WILEY-VCH

Haifei Zhang

Ice Templating and Freeze-Drying for Porous Materials and Their Applications

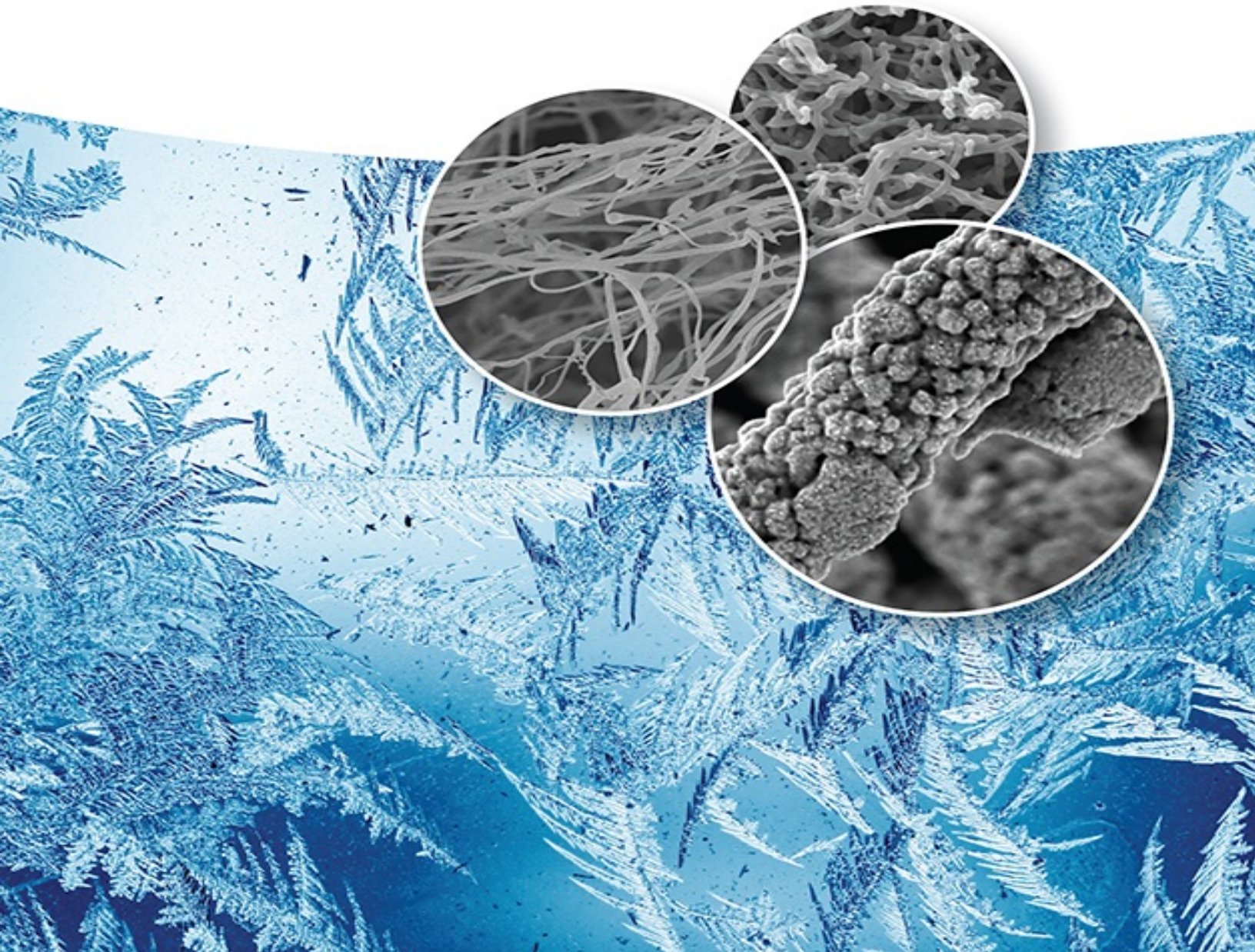

Table of Contents

List of Tables

List of Illustrations

Chapter 3

Chapter 8

Photo of the Pd aerogel. (b) The Pd nanoparticles assemble together (in direct contact) to form the structure. ; (c) The structure of the porous bead prepared by injecting Au nanoparticle suspension into liquid nitrogen and subsequent freezedrying. (d) The aligned structure from the radially aligned part of the bead in (c). (e) The randomly porous structure consisting of nanowires in the outer shell of the beads in (c). (f) The freezeinduced nanowire consisting of aggregated Au nanoparticles.

Figure 9.4 Selfassembly of Au nanoparticles and Au nanorods on Si substrate by ice templating and the encapsulation within polyaniline. (a and b) A typical chain and a nodeshaped structure obtained from 40 nm Au nanoparticles; (c and d) Single chain and multiplelayered chains formed from Au nanorods; (e) A single line chain of Au nanoparticles formed by freezing the nanoparticle suspension in −80 °C ethanol; (f–h) The chain of Au nanoparticles encapsulated by polyaniline.

Figure 9.5 Aligned surface patterns fabricated by directional freezing of liquid suspension thin film on substrates. (a) The spacing between the ridges decrease with the increase of freezing rate, demonstrated with the aqueous suspension containing 5 wt% HS30 silica colloids and 5 wt% poly(vinyl alcohol). (b) The structure prepared from aqueous suspension of 15 wt% HS30 colloids and 1.5 wt% SCMC. (c) The aligned patterns with the selfassembled silica microspheres fabricated from the suspension containing 15 wt% silica microspheres and 5 wt% PVA.

Figure 9.6 1D structures fabricated by directional freezing of polymer nanoparticle/colloid suspensions. (a–c) The structures prepared from polystyrene nanoparticles (80 nm). (d) The nanofibers obtained from polypyrrole nanoparticles (20–50 nm). (e–g) The structures fabricated from polystyrene colloids (450 nm).

Figure 9.7 3D structures fabricated from nanowires via ice templating. (a and b) The porous structures from Ag nanowires. The inset shows the original Ag nanowires. ; (c and d) Aligned nanofibrous networks from phenylalanine nanofibers. ; (e and f) The nanofibrous networks generated from chitin nanofibers.

Figure 9.8 Freezeinduced selfassembly of boron nitride microplates. (a) The structure obtained at the flow rate of 15 μm s^{-1}. (b) The structure from a fast freezing rate of 25 μm s^{-1}. (c) The scheme showing the assembly of the microplates. Scale bar 10 μm.

Figure 9.9 The silica monoliths with microhoneycomb structure and ordered, interconnected macroporous walls fabricated by ice templating with silica nanoparticles and polymer colloids and subsequent removal of polymer colloids by calcination. (a) The crosssectioned area parallel to the freezing direction; (b) the crosssectioned surface perpendicular to the freezing direction; (c) the magnified area parallel to the freezing direction; (d) the polymer colloidtemplated macropores.

Figure 9.10 Nanofibrous structures prepared by ice templating from core–shell particles. (a and b) The structures made from silica nanoparticles (250 nm) with poly(*N*isopropylacrylamide) shell. (c) The scheme showing the selfassembly of

Ice Templating and Freeze-drying for Porous Materials and their Applications

Haifei Zhang

WILEY-VCH

Copyright

Author

Dr. Haifei Zhang

University of Liverpool

Department of Chemistry

Oxford Street

L69 7ZD Liverpool

United Kingdom

Cover Images: Inset cover images
were kindly provided by Haifei Zhang;
(background) © michael1959/iStockphoto

Library of Congress Card No.: applied for

British Library Cataloguing-in-Publication Data

A catalogue record for this book is available from the British Library.

Bibliographic information published by the Deutsche Nationalbibliothek

The Deutsche Nationalbibliothek lists this publication in the Deutsche Nationalbibliografie; detailed bibliographic data are available on the Internet at http://dnb.d-nb.de.

Print ISBN: 978-3-527-34272-3

ePDF ISBN: 978-3-527-80741-3

ePub ISBN: 978-3-527-80742-0

Mobi ISBN: 978-3-527-80740-6

oBook ISBN: 978-3-527-80739-0

Preface

Freezing has long been used as a method for preservation and storage. Freezedrying has been widely used industrially for the production of solid formulations of pharmaceutics, biologics, and foods, aiming for easy transport and longterm storage while maintaining the stability during preparation, storage, and reconstitution. Recently, freezing and freezedrying have been employed to fabricate a wide range of porous materials and nanostructures. The key aspect is the freezing stage, where ice crystals are formed and grow with tuneable size and morphology. During freezing, molecules and/or particles are excluded from the freezing front. The freeze drying process is then utilized to remove ice crystals from the frozen sample and produce *ice templated* structures. This technique, thus known as *ice templating*, has been explored for the fabrication of a wide range of porous materials and nanostructures. In addition to the wide use of water as solvent, some organic solvents and even compressed CO_2 are also used to form solutions or suspensions for the icetemplating process. Although freezedrying is usually used to remove ice crystals, solvent exchange in the frozen state and ambient vacuum drying after polymerizing or crosslinking the frozen samples have also been used, thus avoiding the high cost of freezedrying. Ice templating, also known as freeze casting or simply freeze drying among researchers, can be combined with other approaches in order to produce functional materials with complex porous structures.

There seems to be confusion about freezedrying and icetemplating among researchers from different research fields. However, due to the simplicity and versatility of the icetemplating approach, it can be employed, in principle, by materials scientists from differing backgrounds and expertise for the preparation of desired materials with target applications in mind.

There are several books published on freezedrying or lyophilization, on the topics of food, pharmaceutics, and biological products. This book gives an extensive review of ice templating and freezedrying and the use of ice templating for the fabrication of porous materials and their applications. Chapter 1 introduces the freezedrying process, ice templating for porous structures, and some practical points for ice templating based on our lab experience. Chapter 2 describes the fundamentals of the freezing process and the equations/parameters that are investigated and may be used to guide materials fabrication. Owing to the close relationship between ice templating and freezedrying, the use of freezedrying is discussed extensively for pharmaceutics, biopharmaceutics, and foods in Chapter 3. The stabilization mechanisms and the formulation tips described in Chapter 3 may be also applied for icetemplated materials. Chapters 4-9 focus on the fabrication and applications of different types of ice templated materials, covering porous polymers, porous ceramics and metals, ceramic composites, porous carbon and carbonbased materials, drug nanoparticles, and nanostructured materials from colloids/nanoparticles. Chapter 10 describes the combination of ice templating and other techniques/systems for the fabrication of novel materials. A general summary and perspectives are also given in Chapter 10.

It has been a long but highly exciting journey in compiling this book. I hope this book can

provide useful insights and knowledge for researchers who use freezedrying or ice templating during their investigations. Furthermore, it is expected that this book can also give a general overview and provide expertise and useful tips about ice templating for new researchers coming into this field.

I am grateful to Dr Lifen Yang who has initiated the dialogue of writing a book about ice templating. I thank the project editor Ms Shagun Chaudhary (at the early stage of my writing) and then Mr Lesley Jebaraj for their suggestions, patience, and great support. This book has been mostly written during the evenings and weekends. I am grateful to my family. It would not have been possible to complete this book without their support, patience, and encouragement.

Liverpool, 19 November 2017

Haifei Zhang

University of Liverpool

1
Introduction to Freezedrying and Ice Templating

1.1 Introduction

Freezedrying is a widely used drying technique in pharmaceutics, biologics, and food industries. It is a preferred drying technique when dealing with temperaturesensitive chemicals/substances, as it can produce dry powders or cakes for easy storage and transport. From the perspective of pharmaceutical applications, the freezedried products should also have a reasonable shelf life and be readily reconstituted with the anticipated drug activity [1–4].

A freezedrying process, especially for pharmaceutics and biologics, consists of three steps, i.e. freezing on a cold shelf in a freezedryer chamber, primary drying, and secondary drying [1, 4]. The freezedrying process is usually applied to aqueous solutions or suspensions. When freezing aqueous solutions or suspensions (usually in small vials), the majority of the water in the sample is either free water or gets frozen. However, a small percentage of the water bound to or having strong interaction with pharmaceutics/excipients remains as liquid. The amount of liquid water present in the frozen sample depends on the freezing temperature as well as the components in the solution. The frozen ice crystals are sublimed in the primary drying process, i.e. a change from solid state to vapour state to remove the ice crystals. In the secondary drying step, the bound water needs to diffuse and transport outside of the porous matrix to be removed. Therefore, the rate of primary drying may be controlled or enhanced by careful control of the freezing temperature, the shelf temperature, and the vacuum, whilst the nature and the porosity of the matrix is more important for the secondary drying stage.

In chemistry, biological and materials research, freezedrying is more commonly known as a *drying approach*. The cool samples may be either directly placed on a shelf in a freezedryer or frozen in a freezer or in liquid nitrogen before being placed into a freezedryer. The main purpose is to keep the samples at low temperature (to maintain the component activity) and to prevent dense aggregation or considerable shrinkage during the drying process. This is in contrast to a conventional drying process of aqueous solution or wet samples, e.g. drying in open air, N_2 flow drying or vacuum drying. Because of water's high surface tension, removing liquid water can generate significant surface force that brings small particles together (hence aggregation of particles) or the collapse of porous structure. For this reason, freezedrying has been frequently used in materials science in order to prepare materials with highly interconnected porosity and high surface areas.

During a freezedrying process, either in a pharmaceutical industry environment or in a research lab practice, the process needs to be conducted so that the samples remain frozen, avoiding partial melting and annealing, following which porous cakes or structures without dense skin and shrinkage are prepared. This is, of course, not just intended to produce a

material with an ‘aesthetic look’ [4]. Such materials can have desirable properties for subsequent applications. After the removal of ice crystals, the voids left behind are pores within the materials, hence the porous materials. In the pharmaceutical industry and other relevant research areas, good cakes with homogeneous structures are desirable for their subsequent applications. The porous structures of such cakes are examined with the intention of relating the quality of the freezedried materials with subsequent application performance, rather than as a technique to prepare porous materials with controllable porosity and morphology.

Porous materials are used in a wide range of applications and have been intensively investigated [5, 6]. According to the IUPAC definition, the pores can be categorized as macropores (>50 nm), mesopores (2–50 nm), and micropores (<2 nm) [7]. Templating is probably the most common approach used for the preparation of porous materials. The templates used may be hard templates (e.g. colloids, particles, sacrificial preformed porous structures) or soft templates (e.g. assembly of surfactants, polymers, droplets, emulsions) [5]. In recent years, ice templating has been developed and intensively investigated as an effective approach to the production of a variety of porous materials [8–11]. This templating method exhibits some unique characteristics that the other techniques do not have. For instance, a directional freezing process can be employed to prepare aligned porous materials. By careful control of the freezing conditions, layered porous materials can be formed and can be subsequently utilized to produce tough composite materials mimicking natural structures. Furthermore, the ice templating method is not restricted to waterbased solutions or suspensions. It can be used for organic solutions/suspensions, compressed CO_2 solutions, and emulsions [8].

Sometimes, there is a misconception that freezedrying and ice templating may be the same, as seen in some published articles. However, they are different but are related with each other. In brief, freezedrying is a drying method (in pharmaceutical industry the freezing process is usually completed on the freezedryer shelf). Figure 1.1 shows the schematic representation of a freezedrying process. Ice templating is a templating method where ice crystals are used as templates in order to produce the desired templated structures. A controlled freezing process is usually required in order to control the orientation, size, and morphology of the ice crystals. As in any other templating methods for the preparation of porous materials, the ice templates need to be removed. The most common method to remove ice crystals is by freeze drying. However, freezedrying is not the only method that can be used. Solvent exchange may be employed in a cold miscible solvent (and it is an insoluble solvent to the solute in the frozen solvent) where the temperature is below the melting point of the frozen sample. After the frozen solvent is completely removed, the materials may be dried by usual drying methods such as air drying or vacuum drying. There is another option when monomers and crosslinkers or reactive reagents are included in the frozen samples. A frozen polymerization/crosslinking process can be applied, which will lock in the frozen structure [12]. After polymerization, the frozen samples may be warmed up to room temperature and then dried in air or by vacuum drying.

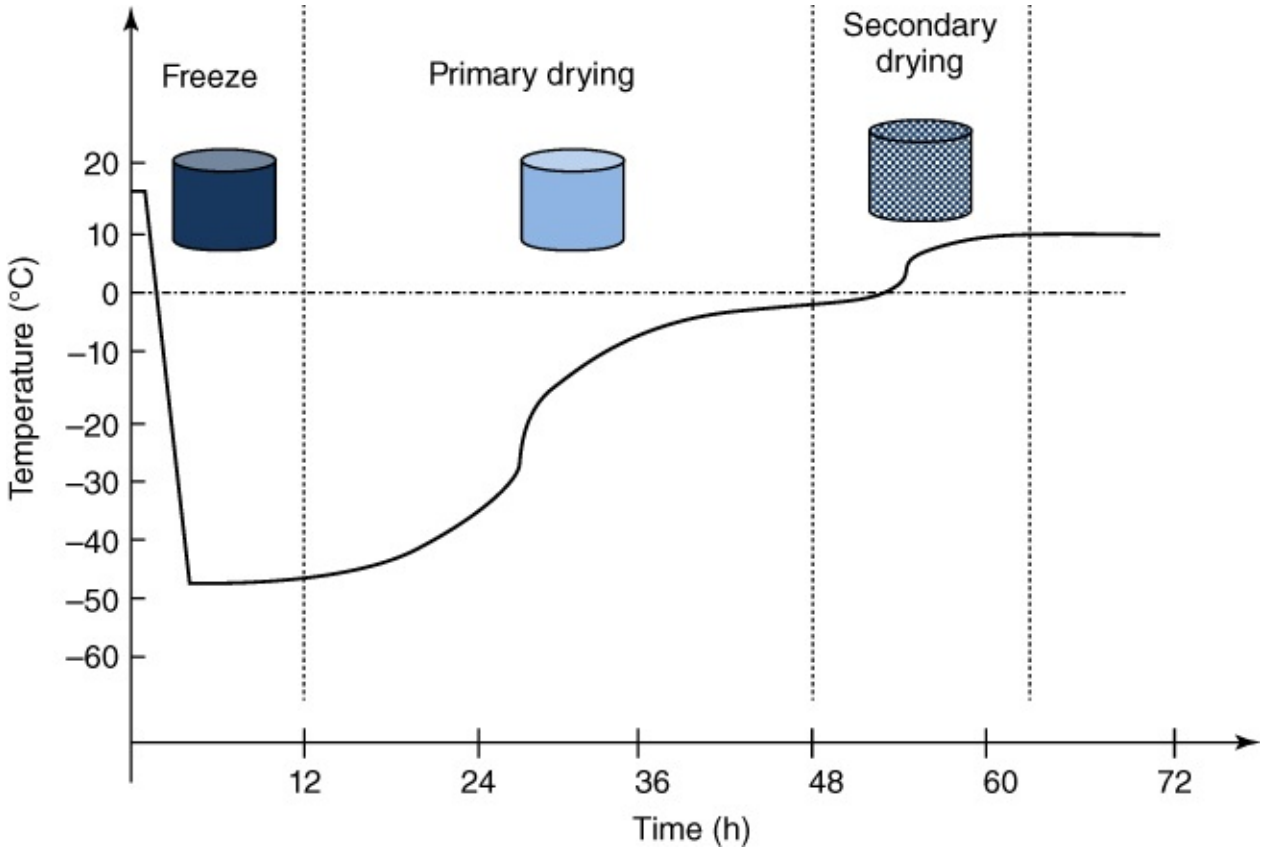

Figure 1.1 Schematic representation of a freezedrying process. The temperature and time scales are approximate and for indication only.

Because of the close link between freezedrying and ice templating, in this chapter, we will first introduce the basics and key aspects/parameters of a freezedrying process. The same controls applied in freezedrying may be applied to the ice templating approach as well when ice crystals are removed by a freezedrying process. However, it must be pointed out that there is very limited research on the effects of the freezedrying process on porous materials or nanostructures. Secondly, the key aspects, important parameters and progress of ice templating method will be covered. The practice and experience of the Zhang group in ice templating and freezedrying for porous materials will be described last, hopefully to provide useful and practical information for researchers who are new to this research area.

1.2 The Freezedrying Process

Water is essential for life. However, the presence of water tends to make materials or products degrade fast. To preserve samples, to make storage longer and transport easier, suitable drying methods are required. This is particularly important for biological and pharmaceutical samples. Indeed, freezing itself is a drying technique. During the freezing process, water turns into ice crystals, which can exclude any impurities, including polymers, particles, and dissolving molecules. The freezing front rejects the solutions from forming ice crystals; this concentrates the solution and makes the dissolved substances ‘dry’. However, the frozen ‘dry’ samples have to be kept at low temperature (below the melting point) and are normally stored in a freezer. This incurs storage costs and difficulty in transporting. Potential freezer break

down or power cut can melt and damage the samples. Thus, a freezedrying process is a preferred drying process.

The use of freezedrying has a long history, tracing back to 1250 BCE for preserving materials by dehydrating, which involves the freezing stage and drying at low temperature under vacuum. Freezedrying is also widely known as ‘ *lyophilization*’, a term mostly attributed to Rey LR's work in 1976. Because the process produces a dry porous structure, its high porosity and exposed surface can rapidly resorb the solvent, e.g. the water, vapour or moisture in the surrounding environment. The freezedried materials exhibit such ‘lyophil’ characteristics towards the solvent (mostly water), hence the term ‘*lyophilization*’ process [4].

But it is not all positive for a freezedrying process. The disadvantages associated with freezedrying processes are low scaleup potential, longer drying time and energyintensive processing. This results in high operational costs. A freezedrying process is therefore only viable for highvalue products, such as pharmaceutics and biologics. There is continuing effort in developing new procedures and/or optimizing the freezing stage and drying stage in order to reduce the operation costs. It is critically important for biological and pharmaceutical samples not to be damaged or deactivated during the freezing stage as the growth of ice crystals can be harmful.

1.2.1 Additives in the Solution

1.2.1.1 Additives to Maintain Integrity/Activity of Biological Samples

Freezedrying can be used for cryopreservation, i.e. longterm storage of biological materials such as in biomedical applications and agriculture. The use of additives can help stabilize biomolecules in the freezedried samples, probably more importantly to reduce the damaging impact of growing ice crystals on biological samples.

During a freezing process, extremely low temperature (e.g. −196 °C of liquid nitrogen) may be applied. The growing ice crystals can pierce (from outside) or tear apart the cells (from inside) by mechanical force. Further, due to the freezing concentration effect, the composition in the liquid phase may change, for example, leading to high ion concentrations or dramatic pH change. This can be detrimental to the cells. Furthermore, because of the freezing dehydrating and concentration effect, this can also cause the change of osmotic pressure across cell membranes and dehydrate the cells [13].

To mitigate these adverse effects, additives acting as cryoprotectants are added to the solution. These additives should be nontoxic or low toxic, can help balance the surrounding environment of the cells, and reduce the size and amount of ice crystals during the freezing stage. Alcohols, glycerols, and polymers (e.g. polyvinyl alcohol (PVA)) have been often used. Antifreeze proteins, as observed in some arctic fish, may be also utilized [14]. It can help lower the ice nucleation temperature and inhibit ice nucleation and crystal growth so to produce small ice crystals without damaging cell activity.

1.2.1.2 Lyoprotectants to Prevent Denaturation of Biopharmaceutics or Enhance Reconstitution of Pharmaceutics

In order to be effective, it is suggested that the lyoprotectants must be retained in the amorphous state. Crystallization of lyoprotectants during the freezedrying process or subsequent storage may potentially damage the stability of proteins. For this purpose, non reducing sugars, especially sucrose and trehalose have been widely used. It should be mentioned that the amorphous state in the freezedried product does not necessarily mean that no crystallization occurs during the freeze stage and drying stage. Indeed, one study found that trehalose could crystallize during annealing and form amorphous materials after freezedrying [15].

As it is widely known, polymer excipients are processed with active pharmaceutical ingredients (API) as tablets or in other formulations. Similar excipients, e.g. hydroxypropyl methyl cellulose (HPMC), may be included in the solution, which can help to stabilize and re constitute the freezedried formulations [16].

1.2.1.3 Stabilizer/Binders for Particulate Suspensions

Suspensions are frequently freezedried to produce porous structures. To ensure a high quality freezedried product, a homogeneous and welldispersed suspension is required [10, 17]. In order to achieve this, polymeric stabilizers such as PVA, polyvinylpyrrolidone, and industrygrade commercial stabilizers may be used. In order to produce samples with good mechanical stability, binders are usually required in the suspensions. It is possible for the same polymer to act as both a stabilizer and a binder. This part is particularly important for the preparation of porous ceramics by freeze casting and more details may be found in Chapter 5.

1.2.2 Optimizing the Freezing Stage

It is recognized that freezedrying is a timeconsuming and energyintensive process. For an industrial freezedrying process, freezing usually takes a few hours whilst the drying process requires days with the primary drying taking much longer than that of the secondary drying. In the primary drying stage, the driving force for the removal of ice crystals is the difference of vapour pressure between the sample chamber and the condenser chamber. It is known that vapour pressure is proportional to temperature. It is more efficient to raise the temperature of the frozen sample rather than to reduce the temperature in the condenser chamber. Therefore, designing a freezing stage that allows nucleation and ice growth at higher temperature can considerably benefit the primary drying process [18, 19].

Freezing is a very complicated process. Water may look like a simple molecule but it has over 10 crystalline phases. The presence of hydrogen bonds between water molecules and the interaction with solutes result in complex phenomena. The nucleation temperature determines the size, number, and morphology of ice crystals. A good process should lead to homogenously dispersed small ice crystals, which can in turn contribute to a faster drying process and a highquality freezedried cake.

Typically, the process of freezing water or water solutions consists of four steps: (i) cooling the solution below the equilibrium freezing temperature; (ii) formation of ice nucleus that acts as primary nucleation; (iii) Secondary nucleation that allows the growth to ice crystals; and (iv) complete freezing to form frozen solids [20]. However, formation of ice nucleus does not occur just below the equilibrium freezing temperature. Pure water can be supercooled to −48 °C to initiate ice nucleation whilst impurities/solutes in a solution may act as nuclei and allow growth of ice crystals under less supercooled conditions (often seen as −15 to −20 °C) [21, 22]. A higher freezing temperature that allows the spontaneous formation of ice crystals would in principle lead to a faster primary drying process. Among different polymorphic forms of ice, cubic shape and more often hexagonal shape crystals are observed under typical freezing conditions. For the hexagonal ice crystals where each oxygen atom is tetrahedrally surrounded by four other oxygen atoms, it can form dense structures with crystal growth thus excluding the solutes from the ice front. Controlling the freezing condition is also important in tuning the size of crystals, where the spontaneous formation of a large number of nuclei and higher temperature gradient may contribute to small ice crystals. There is a link between the drying rate and ice crystal size. Larger ice crystals, usually generated involving an annealing process, increase sublimation rates. This is due to the larger pores left behind by the removal of large ice crystals, which facilitate the transport of water vapours [19]. Controlling the freezing process may also lead to the formation of more homogeneous ice crystals in the frozen samples, which may result in freezedried pharmaceutical cakes of better quality.

In order to maintain and improve freezedried product quality whilst reducing freezedrying time, different freezing methods have been developed. Some of the common ones are described below:

i. *Ice fog technique*. This technique was first reported by Rowe [23]. After the vials are cooled to the desired nucleation temperature, ice nuclei are introduced to facilitate ice crystal growth by a flow of cold N_2. N_2 gas is transported into the chamber through a metal coil immersed in liquid nitrogen. Water vapour already present in the chamber can be cooled by the cold N_2 and forms a vapour suspension of ice crystals (a ‘fog’). The N_2 gas enters the chamber at minimum overpressure and passes the ice nuclei into precooled vials to induce crystallization. Different types of ice fog techniques have been described in the review paper by Geidobler and Winter [19].

ii. *Electrofreezing*. In this method, a high voltage pulse is applied to generate ice nuclei on an electrode, which induces ice crystallization [24]. For this method to be successful, suitable electrodes have to be developed and fixed into a freezedryer. Each vial requires one electrode, which makes this method impractical and difficult to scaleup.

ii. *Ultrasoundinduced freezing* . Applying ultrasonic waves to liquids produces acoustic cavitation, the formation of gasfilled bubbles with shortlived high temperature and pressure [25]. The collapse of the cavitating bubbles results in the increase of equilibrium freezing temperature due to very high pressures. This increases the supercooling level and is the driving force for ice nucleation. The method can be easily realized by attaching an ultrasound generator to an aluminium plate combined with the freezing shelf. Therefore,

there is no direct contact with the freezing solution, thus avoiding a potential contaminating issue. This technique was demonstrated by freezedrying of pharmaceutical proteins. It was found that larger and directional ice crystals were formed at high temperatures whilst smaller and heterogeneous ice crystals were produced at lower temperatures [26].

iv. *Directional freezing*. In this case, ice nucleation is induced at the bottom of the vial by contact with a cold stage. Ice propagation is orientated in the vertical direction and either lamellar or vertical dendrite ice crystals are formed [27]. The directional freezing process may also be realized by applying a gradient freezing stage which may allow the advance of freezing front at a constant velocity, facilitating homogenous cooling of the samples. This technique may be very important for cryopreservation of cells. When ice crystals grow outside the cell, causing water to osmotically move out of the cells, as a result of which the cells shrink and eventually get damaged and die. The directional freezing process contributes to uniform cooling of the samples, producing lamella ice crystals between which the cells are trapped [13]. To achieve uniform cooling, the dissipation of heat of fusions during water freezing is very important, which can be done in two ways: the metal block closely surrounding the sample and from the ice front into the unfrozen part.

Other freezing methods may also be used. For example, shelframped freezing, precooled shelf freezing, and an annealing process (to make ice crystals more uniform) can be readily performed by using different shelf temperature programs on a modern freezedryer. Quench freezing is basically freezing a solution in a cool liquid such as liquid nitrogen or dry ice bath with a chosen organic solvent (e.g. ethanol, acetone). The frozen samples are then placed in a freezedryer. This is the typical method that materials researchers use to produce freeze dried porous materials. By varying the vacuum in the chamber (evaporation of water to reduce local temperature), pressurizing/depressurizing (using the principle of the freezing temperature of water lowered at high pressure and vice versa) the chamber, ice nucleation can be induced. But these methods are not practical or difficult to scale up [18, 19].

1.2.3 Primary Drying in Freezedrying

During the freezing process, the solute is excluded from the freezing front and the solute phase becomes concentrated, which is termed as *freeze concentrate*. By the end of the freezing process, the majority of the water in the solutions turns into ice crystals [28]. The primary drying stage is to remove the ice crystals by sublimation.

During primary drying, the chamber is under vacuum and the pressure is used as the partial pressure of the water vapour. In the chamber, the temperature of the sample is lower than the shelf temperature. The driving force for the primary drying is the difference between the water vapour pressure at the sample temperature and partial pressure in the chamber. Therefore, in order to speed the primary drying process, the sample temperature should be as high as possible without the collapse of the sample structure and a high level of vacuum is maintained in the chamber. It should be mentioned that raising the sample temperature is more efficient for a faster primary drying process. A very high vacuum is not only difficult to maintain but also may hinder the drying process. This is because when ice crystals are sublimed, heat input into

the frozen sample is required (so to maintain the sample temperature). The heat transfer is usually achieved from the shelf (higher temperature) to the sample (lower temperature) and by radiation from the surrounding. At very high vacuum, a Thermos flask effect may be developed in the chamber, which inhibits heat transfer from the shelf. The heat transfer by gas/vapour is reduced as well at high vacuum. This leaves the heat for sublimation provided predominantly by the inefficient radiation. It has been reported that moderate chamber pressure (100–150 mTorr, 100 mTorr is 13.3 Pa) could give optimal heat transfer in a set of vials [29].

Primary drying can take days depending on the freezedryer setup, much longer than the freezing stage and secondary drying (both taking hours). To reduce the freezedrying cycle time without an impact on product quality, the most important thing is to optimize primary drying parameters. The fine tuning of the sample temperature and the shelf temperature is the key to a fast primary drying process. It is known that each 1 °C increase in sample temperature can reduce the primary drying time by about 13% [30]. Therefore, the sample temperature should be as high as possible but below the temperature of sample structure collapse (usually several degrees). The safety margin between the sample temperature and the collapse temperature may be selected by considering the benefit of fast primary drying or higher risk of sample collapse [28]. The shelf temperature is typically 5–40 °C higher than the sample temperature. At constant chamber pressure and shelf temperature, the sample temperature increases 1–3 °C from beginning to the end of primary drying [29]. The bigger the difference between sample temperature and shelf temperature, the faster the primary drying process, but the higher the risk of the sample collapse (Figure 1.2) [28].

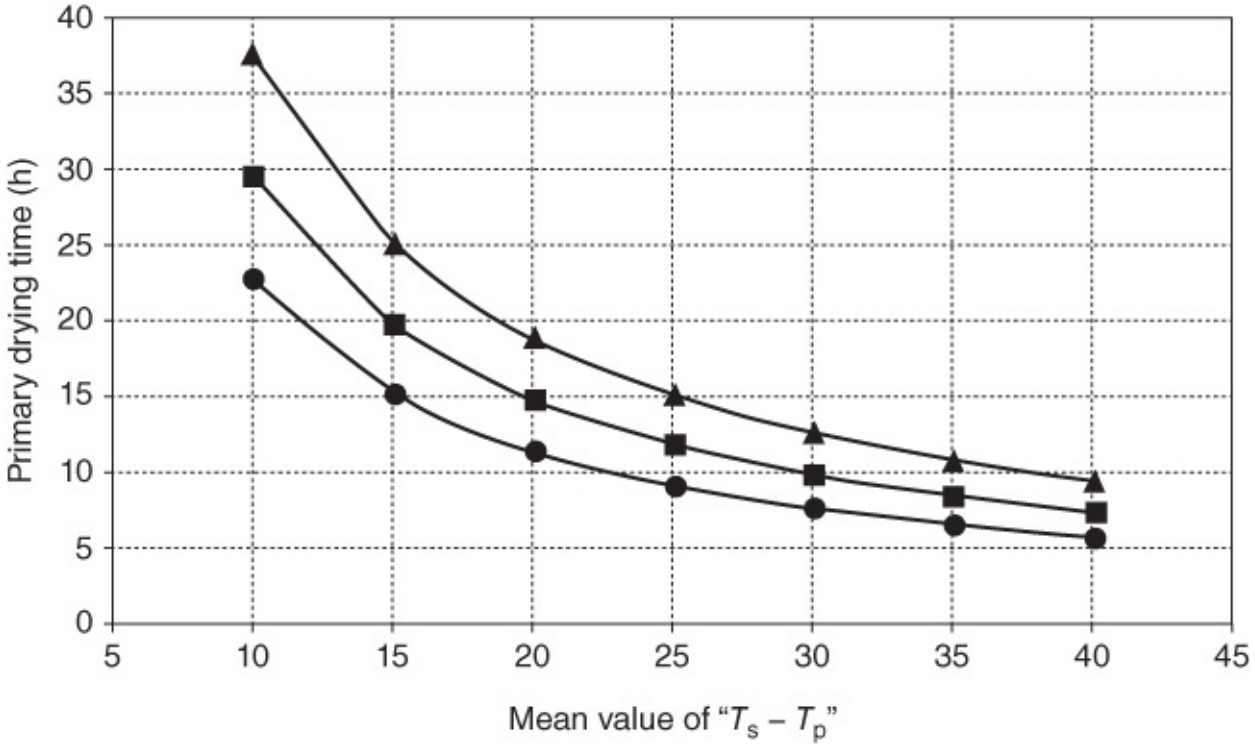

Figure 1.2 The diagram shows the relation of primary drying time with the temperature difference between the shelf temperature (T_s) and the product sample temperature (T_p). Solid circles, low dry layer resistance (solids ≤ 1%); solid square, medium dry layer resistance (10% > solids > 1%); solid triangles, high dry layer resistance (solids ≥ 10%).

Source: Tang and Pikal 2004 [28]. Reprinted with permission from Springer.

By the end of primary drying, all the ice crystals have been removed by sublimation. The sample temperature increases to the shelf temperature because there is no more ice sublimation and there is no heat removal by sublimation. Therefore, it signals the end of the primary drying stage when a steep rise of sample temperature is observed. There are different ways to measure sample temperatures [28], for example, thermocouples or RTD (resistance temperature detector) temperature sensors in the sample vials (invasive, measuring the bottom temperature), and manometric temperature measurement (MMT, measuring the temperature at the sublimation interface, more relevant to the drying process). The temperature discrepancy between the measured sample and the rest of the samples in the chamber should be noticed as a result of the invasive impact of thermocouple and the layout/locations of the samples in the chamber. The sample temperature is usually higher at the front and side but lower in the interior due to additional radiation heat transfer from the door and chamber walls.

1.2.4 Secondary Drying in Freezedrying

The secondary drying is to remove the unfrozen water by desorption from the highly concentrated solute phase. The water transports from the desorption site across the interconnected porosity in the dry matrix and then vaporizes and is removed under vacuum. At the start of secondary drying, there is still a relatively large amount of residual water (5–20% on dry solid) present. With the increase of sample temperature, there is a great risk of sample

collapse. At the end of the secondary drying, the residual moisture content is usually less than 1%, which ensures a good stability and long storage capability.

Although there is an increase of sample temperature, the shelf temperature is still higher because the heat of transfer is required for the vaporization of liquid water phase. Corresponding to the increase of sample temperature, the shelf temperature should increase slowly because the fast increase can cause the collapse of the not completely dry sample. Owing to the high residual moisture content in the amorphous sample early in secondary drying and thereby low glass transition temperature, the possibility of structural collapse is quite high. It is usually regarded as a safe procedure if the shelf temperature increases at a rate of 0.1–0.15 °C min^{-1} for amorphous solids. For crystalline solids, they do not have potential collapse during secondary drying and, therefore, a higher ramp rate (0.3–0.4 °C min^{-1}) is suggested [28].

The shelf temperature is directly related to secondary drying time. It is better to run a high shelf temperature for a short time rather than low temperature for a long period, provided that the sample quality can be maintained. Longer drying period at this region of temperature may be detrimental to the stability of biomolecules such as proteins. The drying time may vary depending on the solution concentration. A higher solute concentration can lead to a solid with smaller surface areas, less porosity, and enhanced barrier for water transport, and thereby a longer drying time. Usually, secondary drying times of 3–6 h is probably best with the terminal temperature varying in the region of 40–50 °C, even for protein formulations [31].

1.3 Ice Templating for Porous Structures

Ice templating has been used widely for the preparation of different types of porous materials. This section describes the key but general parameters that have been investigated. Detailed discussion and specific information are given in the following chapters. Unlike freezedrying for pharmaceutics and foods, the icetemplating method is mainly used in research for the fabrication of novel porous materials and their potential applications. There is either no mass production or rare mass production of materials reported by the icetemplating approach, to the best of the author's knowledge. As such, the preparation time and cost of icetemplated materials have not been evaluated as a priority, as with freezedrying in industries.

1.3.1 Solutes or Particles

i. *Solutions widely used for icetemplating processes* . Small molecules, polymers or biomacromolecules are dissolved in suitable solvents. The solutes are excluded from the freezing ice front during freezing. To form a porous material, it is difficult to work with only small molecules because powders with low porosity are usually formed. It seems like a prerequisite to have polymer or large biomolecules in the solution to form porous structures with tuneable morphology. The larger polymer molecules can entangle or interconnect together to give stability and porosity.

ii. *Particles suspended in liquid medium*. These particles can include nanoparticles,

nanofibres, platelets, and microparticles. To form a homogenous structure, a stable suspension is required before freezing. Therefore, surfactants or stabilizers are always present in the suspensions. For nanoparticles or nanofibres, because of their small sizes, it is generally easy to form stable dispersions. For larger nanoparticles or even microparticles, a higher concentration of stabilizer (usually polymeric, also to increase the viscosity of the suspension) is normally required. This has been observed frequently when using ceramic powders to prepare porous ceramic materials by ice templating.

ii. *Emulsions where liquid droplets dispersed in another liquid phase*. An emulsion can be formed, usually by stirring or homogenization, to disperse liquid droplets in another immiscible continuous liquid phase [32]. A surfactant (either ionic or nonionic polymeric surfactant) is added to stabilize the droplets by preventing them from coalescing. When monomers or polymers are dissolved in the continuous phase, freezing the emulsion followed by freezedrying can produce porous polymers, combining ice templating and emulsion templating. Small molecules or polymers can be also dissolved in the droplet phase, which produces complex materials after freezedrying the emulsion [33, 34].

1.3.2 Solvents

i. *Water*. There is no doubt that water is the mostly used solvent. In the freezedrying formulations for pharmaceuticals and biologics, water is the only solvent used although some polar organic solvents may be added as additives. When employing ice templating for porous materials, as the name ‘ice’ suggests, waterbased solutions or suspensions have been mostly used.

ii. *Organic solvents*. Organic solvents can also be frozen and the resulting frozen solvent or ice crystals (‘ice’ here means the general frozen solvent) are used as templates to generate porous materials. This is particularly important when preparing hydrophobic porous materials or when the precursors are insoluble in water. Despite the potential toxicity, flammability, and environmental concerns, similarly to the use of organic solvents in chemical plants, it is sometimes necessary to utilize these organic solvents. When choosing suitable organic solvents, their melting points and vapour pressures are important parameters to be considered. Owing to the limit in shelf temperature or the temperature of condensing chamber, only organic solvents that have relatively high melting points should be selected, e.g. melting points higher than −60 °C, depending on vapour pressure, type of solutes, freezing volume, and exposed surface area of the frozen sample. Table 1.1 shows the organic solvents that have been used in literature. An important application is the use of organic solvents including dichloroethane, *o*xylene, dioxane as templates for the preparation of hydrophobic biodegradable poly(εcaprolactone) and poly(lactide *co* glycolide) materials. Dimethyl sulfoxide (DMSO) is often used because of its high melting point and the ability to dissolve polar polymers. Tertiarybutanol has been employed quite often for the preparation of silica and porous ceramics. Another unique solvent is camphene, which is solid at room temperature with high vapour pressure. Camphene melts at a moderate temperature of around 60 °C so it is still convenient to form solutions or suspensions. The subsequent freezedrying process can be operated at room temperature

compared to the usual freezedrying process, thus reducing the operation costs.

ii. *Compressed CO_2*. Supercritical CO_2 or compressed CO_2 has been regarded as a green and sustainable solvent. CO_2 is not toxic, inflammable, and cheaper and has low critical points. The solvent properties can be readily tuned by changing temperature and pressure. Below the critical temperature, compressed CO_2 acts like an organic solvent and can be used as a solvent for reactions or separation [35]. The very attractive point is that compressed CO_2 can be easily removed by depressurization. Zhang et al. reported the freezing of compressed CO_2 solution for the preparation of a porous organic material. The process used no organic solvent, and there was no need for freezedrying because the frozen CO_2 could be just sublimed when the reactor valve was open and the frozen sample warmed up gradually [36].

iv. *Mixing solvents*. Two miscible solvents may be mixed together. The point is that each solvent may exhibit different sizes or morphology of ice crystals upon freezing. The mixing solvents may be used accordingly to tune the pore morphology and pore sizes.

v. *Emulsions*. This is an extended use of organic solvents. Oilinwater emulsions have been mostly investigated. In addition to the preparation of porous materials with systematically tuneable porosity, the emulsionfreezedrying method has been explored to form poorly watersoluble drug nanoparticles [33, 37]. Cyclohexane (high melting point, high vapour pressure, low toxic) and chloroform (good solvent for many poorly watersoluble drugs and relatively high melting point) have been mostly used for this purpose [33, 38].

Table 1.1 Properties of common organic solvents used in the icetemplating approach.

Solvent	**Density (ml g^{-1} at 25 °C)**	**Melting point (°C)**	**Vapour pressure (mmHg)**
Dichloroethane	1.256	−35	87 at 25 °C
Chloroform	1.48	−63	160 at 20 °C
*O*xylene	0.879 at 20 °C	−26 to −23	7 at 20 °C
Dimethyl sulfoxide	1.10	16–19	0.42 at 20 °C
1,4Dioxane	1.034	10–12	27 at 20 °C; 40 at 25 °C
Cyclohexane	0.779	4–7	77 at 20 °C
tert Butanol	0.775	23–26	31 at 20 °C
Camphene	0.85	48–52	2.5 at 25 °C

1.3.3 Controlled Freezing

1.3.3.1 Control Orientation of Ice Crystal Growth

i. *Random freezing*. This usually means freezing without control; for example, placing a

solution in a freezer, in a cold bath of dry ice/acetone, or even just immersing in liquid nitrogen. There is no longrange order for the orientation of ice crystals. A schematic diagram is shown in Figure 1.3a. This, however, does not exclude locally ordered arrangement of ice crystals. As long as the temperature gradient exists, the local order of ice crystals will be present. This is also reflected in the pore structure of the freezedried materials.

ii. *Directional freezing*. In contrast to random freezing, directional freezing indicates the orientated growth of ice crystals [22]. It has also been called *unidirectional freezing* by other researchers [9, 10]. This is usually realized by applying a constant temperature gradient to the liquid sample. The greater the temperature gradient, the faster the freezing and the smaller the ice crystals (and hence narrower spacings). A schematic representation of directional freezing process is given in Figure 1.3b. A directional freezing process can be performed by a simple and manual way, for example, by dipping a test tube containing liquid phase into liquid nitrogen slowly. In a more controlled way, one can use a motor to lower the sample vial into liquid nitrogen or keep the sample vial still but use the motor to push the liquid nitrogen dewar up. A dip coater may be used to dip a glass slide with the spread of liquid phase into liquid nitrogen, thus forming a thin film on the glass slide. A computercontrolled freezing stage can be employed to produce 2dimensional surface patterns. A detailed description for this process is given in Section 1.4.

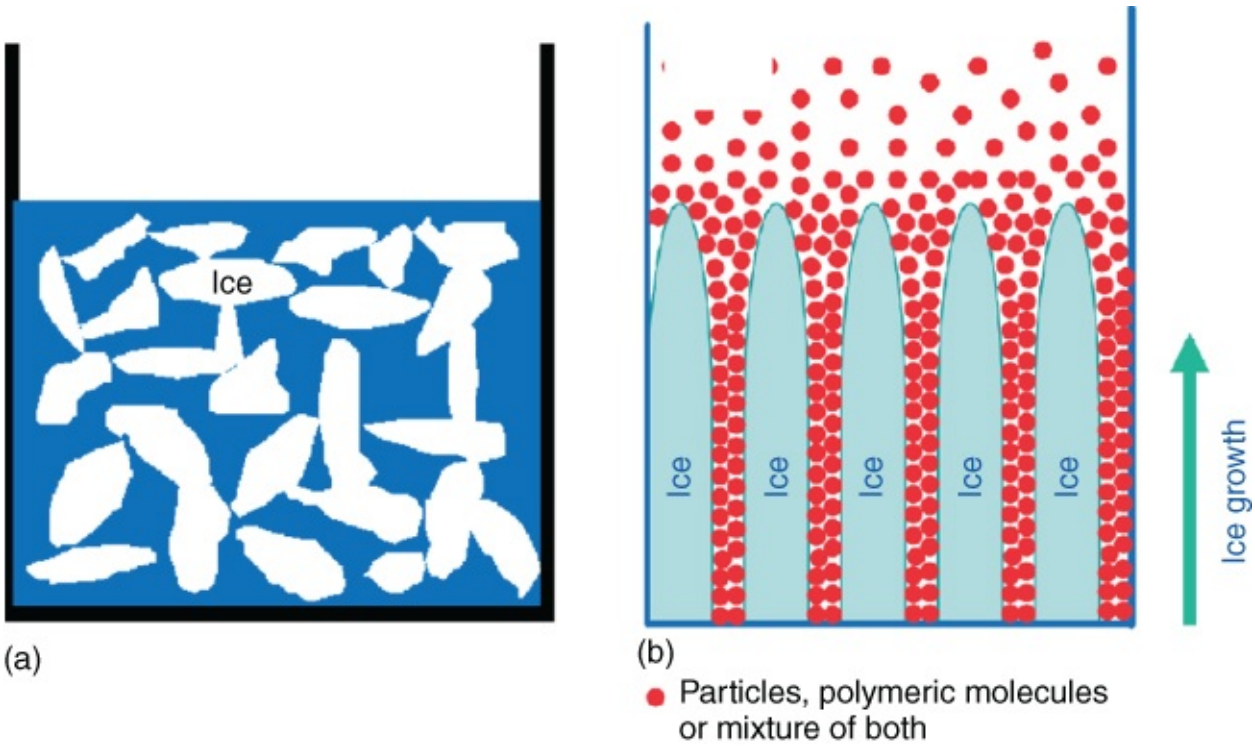

Figure 1.3 Schematic representation of controlled freezing: random freezing (a) versus directional freezing (b).

Source: Qian and Zhang 2011 [8]. Reprinted with permission from John Wiley & Sons.

1.3.3.2 Ways of Freezing Samples

i. *Freezing bulk samples*. The solutions or suspensions contained in a vial, beaker, or mould can be frozen and then freezedried to produce monoliths of different shapes (conforming to the shape of the container). The sample volume may vary from 1 to 100 ml, or even bigger volumes. The key point is that the fill depth or the thickness of the frozen sample should be normally less than 2 cm. Otherwise there is a risk of pore structure collapse or a very long drying time may be required. Indeed, in the freezedrying of pharmaceutics, it is suggested that the fill depth in the vial should be no greater than 2 cm. Otherwise, the quality of the freezedried cakes may be compromised.

ii. *Injection into liquid nitrogen*. Instead of freezing the whole sample, the solution or suspension can be injected using a syringe pump and dropped into liquid nitrogen. The drops allow fast freezing and the resulting frozen beads contribute to fast freezedrying, usually facilitating the formation of nice porous structures. For these freezedried beads, it is very easy to transfer them into different vessels or weigh out the required amount. These beads are usually quite uniform and can pack together nicely, e.g. for better separation. The down side is that it takes longer time to inject the solutions compared to just freezing the whole solution.

ii. *Spray freezing*. This is quite often used for the production of protein or pharmaceutical powders. Basically, a solution is sprayed into liquid nitrogen using a nozzle. The nozzle can be either above the surface of liquid nitrogen [8, 33] or beneath it [39]. In the latter case, the nozzle is usually pressurized to avoid freezeblocking or other measures are taken to prevent nozzle blocking. The sprayed droplets are fast frozen, which may help maintain the amorphous stage of pharmaceutics and avoid/reduce denaturation of proteins. The frozen particles are usually in the micron range. The larger surface area and short transport path allow a fast and uniform drying.

1.3.4 Removal of Ice Crystal Templates

i. *Freezedrying of frozen solutions or suspension* . The common feature for this type of samples is that upon warming up, the frozen samples melt and turn back into the liquid phase. Pharmaceutical formulations, polymer solutions and colloidal suspensions are normally in this category. The freezedrying process is performed to allow the complete sublimation of ice crystals and the subsequent secondary drying to remove the unfrozen bound water (or other solvent). If for any reason the freezedrying process goes wrong, the frozen sample may completely collapse, partially melt or shrink significantly. As a result, the icetemplated porous structure may be lost. Another general characteristic is that these freezedried materials can be readily dissolved into the original solvent (and other soluble solvents) and produce the solutions or suspensions again [1, 4, 8]. This is what is called as *reconstitution* in freezedried pharmaceutics. This feature is also employed to produce aqueous drug nanoparticle dispersions by the emulsionfreeze drying approach [33, 37].

ii. *Freezedrying of gels or crosslinked samples* . For this type of samples, precursors or monomers are dissolved in a suitable solvent. After freezing the solutions, instead of

immediate freezedrying, a gelation process or crosslinked polymerization is allowed to occur while the samples remain frozen to maintain the icetemplated structures. Reported examples include the silica gelation in the frozen state [40], UVinitiated frozen polymerization (a UV initiator and a crosslinker present with the monomers) [12], and the crosslinking polymerization in the freezeconcentrated monomerrich phase in a frozen sample [41]. After the gelation or polymerization, a freezedrying process is applied to remove the ice templates with the main purpose of generating highly interconnected porous structures with minimal shrinkage. Usually, if the materials are highly crosslinked, it is possible to dry them using the traditional vacuum oven instead of freezedrying. To avoid shrinkage or porestructure collapse by drying from water (due to the high surface tension of water), an immiscible organic solvent may be used to replace water and then removed by a common drying method. This can usually reduce the degree of shrinkage considerably. There are instances where freezedrying is used as a technique to produce porous materials with higher porosity and minimal shrinkage. Examples include the freezedrying of metal–organic framework [42], gels [43], resorcinol–formaldehyde resins [44]. Under these circumstances, the materials are chemically crosslinked, physically assembled or stable frameworks containing solvents. The materials are not so flexible and hence a freezing process is not thought to change the original material structures. Freezedrying is only functional as a better drying technique but there is no ice templating involved that leads to icetemplated materials.

ii. *Solvent exchange with frozen samples*. It is possible to prepare icetemplated porous materials without performing a freezedrying process. Apart from the frozen polymerization/reaction and subsequent conventional drying process mentioned in the earlier section, a solvent exchange process may be employed. For this method to work for a frozen sample, a second solvent that is miscible with the frozen solvent but which does not dissolve the solute should be selected. The melting point of this second solvent should be lower than the glass transition temperature (T_g) of the frozen solvent. The frozen sample is soaked in the second solvent at the temperature where the second solvent is still liquid and the frozen sample remains frozen. After replacing with fresh solvent at regular intervals, the frozen solvent is dissolved and completely removed. The materials can then be dried by vacuum drying to produce icetemplated porous materials. This method has been demonstrated by processing frozen DMSOpolymer samples with icy water [45]. It is expected that this approach can be extended to other systems.

1.3.5 Icetemplated Materials

1.3.5.1 Shape and Form

When making bulky or monolithic samples, the shapes of the materials can be controlled by choosing different vessels or moulds. This can be very important for engineering materials where the materials may be too hard, brittle or soft to be cut into the desirable shapes. Powered samples can be fabricated by a spray freezing process or by iceinduced self assembly of colloids. Beads with diameters in millimetres can be prepared by injection into

liquid nitrogen. Figure 1.4 shows examples of the freezedried materials with different forms.

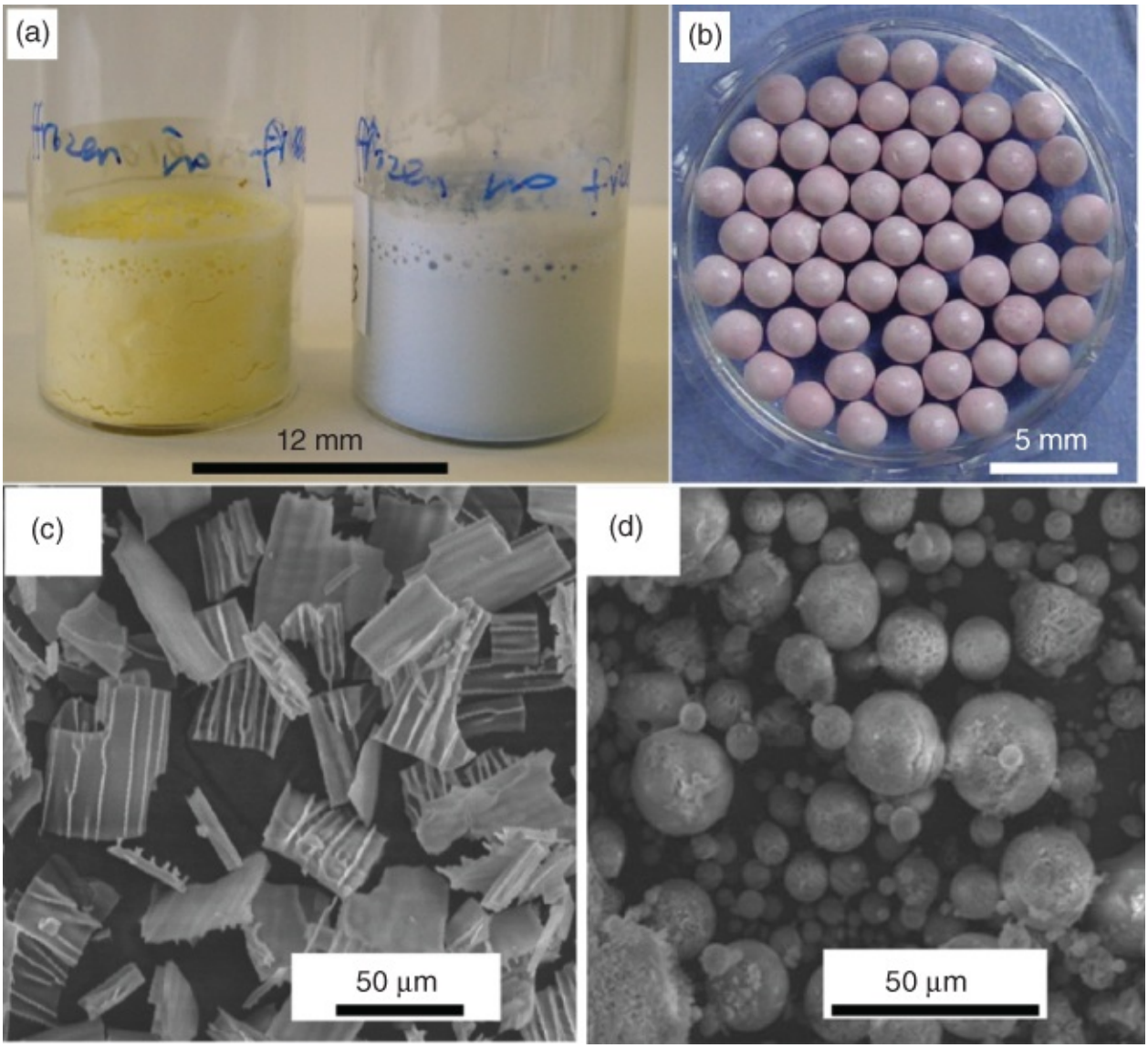

Figure 1.4 Examples showing different shapes and forms of freezedried materials. (a) Monoliths in glass vials; (b) polymer beads containing gold nanoparticles; (c) powders of silica microplates; and (d) powder of porous microspheres.

1.3.5.2 Pore Structure and Morphology

Freezedrying of a solution or suspension produces porous materials. By controlling the freezing process, it is possible to generate porous materials with random pores, aligned microchannels or layered porous structures (Figure 1.5a–c). It has been found that when a very diluted solution or suspension (e.g. 0.1 wt%) is processed, onedimensional nanostructures can be generated. For example, polymer nanofibres can be formed from dilute aqueous polymer solutions (Figure 1.5d) [46]. In the case of nanoparticle suspensions, microwires/nanowires consisting of assembled nanoparticles can be constructed (Figure 1.5e,f) [47]. When combining emulsion templating and ice templating, porous materials with tuneable porosity exhibit both icetemplated and emulsiontemplated pore morphologies (Figure 1.5g). Moreover, when a second polymer is dissolved in the droplet phase, a

composite of aligned porous microspheres embedded in an aligned porous matrix can be formed (Figure 1.5h). Simply dissolving the porous matrix can generate the icetemplated microspheres (Figure 1.5i).

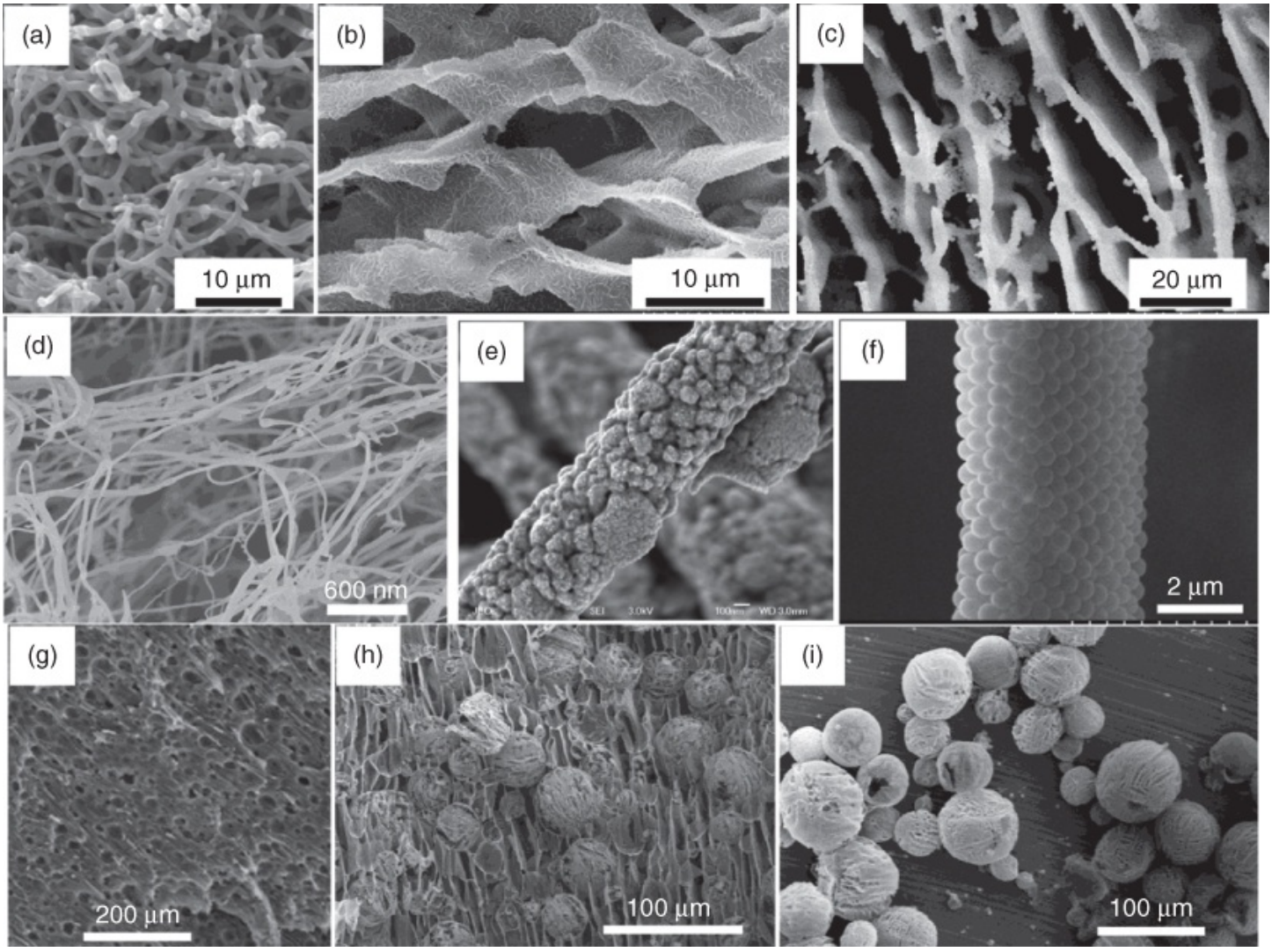

Figure 1.5 Illustration of various morphologies of freezedried materials produced in our laboratory. (a) Porous poly(lactide *co*glycolide); (b) porous poly(vinyl alcohol) with inorganic salt; (c) silica colloids with poly(vinyl alcohol); (d) sodium carboxymethyl cellulose. (e) Nanowires consisting of gold nanoparticles. (f) Microwire consisting of polystyrene colloids; (g) emulsion (with 50% oil phase)templated porous poly(vinyl alcohol) with sodium dodecyl sulfate as surfactant; (h) porous poly(εcaprolactone) microspheres in aligned porous poly(vinyl alcohol); and (i) aligned porous poly(ε caprolactone) microspheres.

Source: Reprinted with permission from Ref. [47].

Source: Reprinted with permission from Ref. [46].

1.3.5.3 Type of Materials

As the icetemplating method can be used for solutions, suspensions or emulsions, and water or organic solvents, a wide range of materials can be prepared. Some of the examples are

illustrated in Figure 1.5. Hydrophilic polymeric materials can be prepared from aqueous polymer solutions whilst hydrophobic organic materials are formed from organic solutions. Porous silica and metal oxides can be constructed either directly from the precursor or by using the preformed polymer structures as templates [48]. For porous metals, usually porous metal oxides can be prepared first and followed by reduction, e.g. in H_2 atmosphere [49]. It is also possible to start with metal nanoparticles and fuse the nanoparticles into metal materials by heating in an inert atmospheres. Porous carbon materials can be generated as well. This may be achieved by freezedrying of carbon nanotubes or graphene suspensions [50]. Or a porous carbonrich polymer may be prepared first followed by carbonization in N_2 or argon [51]. A large number of activities have been carried out on the fabrication of porous ceramics, which normally starts with the suspensions of ceramic particles either in aqueous medium or in a suitable organic medium [10, 17].

1.4 The Practice in Our Laboratory

These are the procedures and setups we have been using in our laboratory. It works well from a research point of view but is not necessarily the optimized procedures or can work on a large scale. The purpose is to give new researchers in this area or relevant research areas basic practices and some ideas to start with.

1.4.1 Controlled Freezing

The controlled freezing process usually refers to directional freezing, in order to allow orientated growth of ice crystals. This is in contrast to random freezing where we usually place the solutions/suspensions in a freezer or a fridge depending on the freezing temperature of the solvent or solution. The directional freezing may be simply carried out by using tweezers or a tong to hold the sample vial and slowly dip into liquid nitrogen. It is still the practice we are using when a new student needs to be familiar with the directional freezing procedure (Figure 1.6a). An alternative approach is to fix the sample vial and to raise the level of liquid nitrogen (Figure 1.6b). It would be best to use a motor to raise the platform that supports the liquid nitrogen dewar. It is also fine to use a jack and raise the level of the jack manually. This works quite well for our experiments.

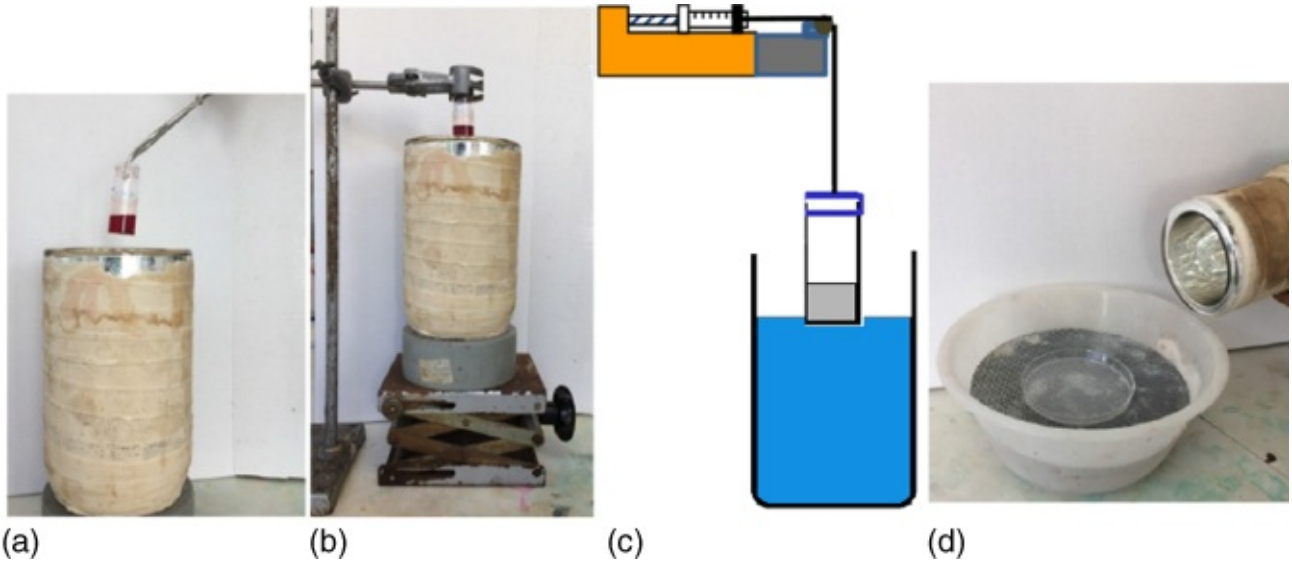

Figure 1.6 Photographs or diagrams show the setups that have been used. (a) Dip the glass vial into liquid nitrogen manually; (b) fix the glass vial into the level of liquid nitrogen dewar on a jack manually; (c) dip the glass vial via a syringe pump; and (d) a petri dish on a metal mesh which is stacked in a bowl. Liquid nitrogen is added from the side. (Note: This photograph is for illustration only with the plastic bowl. For the experiments, an open mouthed dewar is always used.)

To better control the directional freezing process, we have also used a syringe pump to lower a sample vial into liquid nitrogen at a defined rate (Figure 1.6c). Of course, a motor may be also used similarly. More precisely, a computercontrolled dip coater can be used. A sample vial (or glass slide with spreading liquid) can be lowered into liquid nitrogen at the controlled rates. But trial experiments need to be conducted before establishing a suitable procedure. This is because when setting the sample up, the liquid nitrogen vapour may just freeze the sample particularly when the volume is small. A suitable starting point and the lowering rate are key parameters.

Directional freezing has been used to produce aligned porous materials. By contacting the vial bottom with liquid nitrogen and then lowering down into liquid nitrogen gradually, nucleation starts at the bottom and ice crystals grow upwards in a parallel way. To produce a uniformly aligned porous structure, it is important to allow a continuous upward growth of ice crystals and reduce disturbance from sample moving and from the sidewall. It is believed it is better to have a sample vial with a good thermal conductive bottom (e.g. metal) and a poor thermal conductive wall (e.g. plastic, PTFE). Another way is to use a vial with a large diameter to reduce the sidewall effect to the majority of the samples. For example, a large petri dish can be filled with solution or suspension at shallow depth and placed on a metal mesh that is just located at the level of liquid nitrogen. Once nucleation and ice crystal growth starts (that can be observed quite easily), more liquid nitrogen can be poured from the side (Figure 1.6d). The raising level of liquid nitrogen contributes to the continuous freezing and growth of ice crystals until completion.

The above procedures are used to produce relatively bulky or monolithic samples. Similar

procedures may be used to prepare thin films and twodimensional surface patterns, especially with the dip coater approach. In our lab, we have used computeraided two temperaturecontrolled freezing stages to prepare aligned patterns on flat substrates. This instrument is largely used to observe the freezing process (see discussion in section 1.4.2). The difference is that after the slide is completely frozen, it is moved to liquid nitrogen quickly (to keep being frozen) and then transferred into a freezedryer.

In order to produce icetemplated beads, a solution or an emulsion can be simply injected into liquid nitrogen using a syringe pump at a controlled slow rate (Figure 1.7a). It takes some time to fully freeze the drops. Indeed, once the drops move off from the needle and hit the surface of liquid nitrogen, the heat of fusion from freezing water leads to the rapid evaporation of liquid nitrogen, which drives the drops moving around quickly on the surface of liquid nitrogen. The drop will then fully freeze and sink into liquid nitrogen. The time taken to fully freeze the drop varies depending on solvent type (or emulsion), solute, and concentration. In order to prepare discreet beads, the injection rate should be slow enough to allow one drop to be fully frozen and sinking before another drop hits on the surface of liquid nitrogen. When there are two drops rapidly moving around the surface, it is highly likely they will collide and form fused particles. Owing to this slow injection rate, the needle should be well above the surface of liquid nitrogen to prevent the cold liquid nitrogen vapour to freeze the liquid in the needle and block it. Even from a laboratory point of view, the production of beads by injection with one syringe is very slow. To improve the productivity, a peristaltic pump can be used, where a number of silicone tubes may be used to inject a solution (or emulsion) into multiple dewars containing liquid nitrogen. Figure 1.7b shows the setup we have used in our laboratory. Before using this setup, a suitable injection rate must have been established for the liquid system in question.

Figure 1.7 (a) The diagram shows a solution/emulsion/suspension injected into liquid nitrogen. (b) The photograph shows parallel injection into liquid nitrogen using a peristaltic pump. In this case, a milky oilinwater emulsion is injected into liquid nitrogen contained in a few dewars. (c) Illustration of a solution/suspension/emulsion being sprayed into liquid nitrogen using a simple aerosol sprayer. (Note: This photograph is for illustration only with the plastic bowl. For the experiments, an openmouthed dewar is always used.)

To produce icetemplated microspheres, we have used a simple aerosol sprayer (bought from

Fisher Scientific) to spray either aqueous solutions or emulsions into liquid nitrogen. The spraying nozzle is above the surface of liquid nitrogen. Once the fine droplets are sprayed onto the liquid nitrogen, they will rapidly freeze and settle into the liquid nitrogen. The frozen powders can then be collected after decanting the liquid nitrogen and subjecting to normal freezedrying.

1.4.2 Observation of Freezing and Freezedrying

Observation of the freezing process and more specifically the growth of ice crystals have been investigated by various researchers, with the aim to understand the process and provide fundamental evidence for freezing theories. The detailed discussion on this topic can be found in Chapter 2.

We have used an Olympus CX41 microscope equipped with a digital camera and a computer controlled freezing stage (Linkam software, shown in Figure 1.8, borrowed from Dr Michael Butler of Unilever). There are two separately temperaturecontrolled metal plates (a gap of 2 mm between them) achieved by pumping liquid nitrogen at controlled rates. A sample holder connected to a micromotor (which is controlled by the computer) can move a glass slide at different rates (usually 10–200 $\mu m\, s^{-1}$). Thin metal rings (different heights) are placed on a glass cover slide and a defined volume of solution is deposited in the metal ring (to control the thickness of the liquid film) and then covered by another glass cover slide (to prevent solvent evaporation for longer observation). This setup has been used to observe the directional growth of ice crystals for aqueous PVA solution, aqueous PVA/silica colloidal suspension, and aqueous gold nanoparticle suspensions. The study with the controlled freezing stage has provided direct observation for orientated ice crystal growth and demonstrated the viability to control the width of the aligned channels by varying the freezing rate.

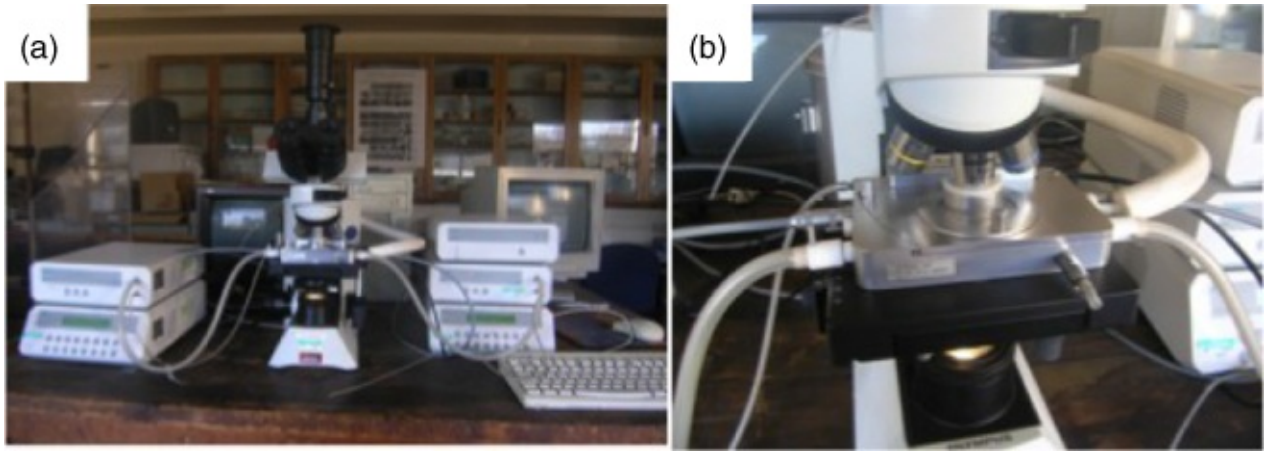

Figure 1.8 Photographs showing the setup used to observe the freezing process – an optical microscope equipped with a computercontrolled freezing stage. (a) The whole setup and (b) close view of freeze stage connections just under the optical lens.

In extended studies, the freezing stage can be tightly sealed and connected to a vacuum pump. After the freezing process is completed (no top cover glass slide is used), the vacuum pump is switched on so that the freezedrying process can be directly observed using the microscope.

We did not observe the gradual sublimation of ice crystals (as we had hoped). It was difficult to get clear optical images during the freezedrying process. After some time, suddenly, it seemed that all the ice crystals have been moved and clear optical images could be obtained (Figure 1.9). For easy observation, an oilinwater emulsion (cyclohexane emulsified into aqueous PVA solution containing sodium dodecyl sulfate as surfactant) is investigated. The emulsion is spread on a glass slide (no cover glass on the top used) and then subjected to freezing and freezedrying. As can be seen from Figure 1.9, there is no visible difference between the emulsion prepared and the emulsion frozen. However, after freezedrying, some cellular pores are really bright because that allows complete light through them while the PVA part looks a bit dark.

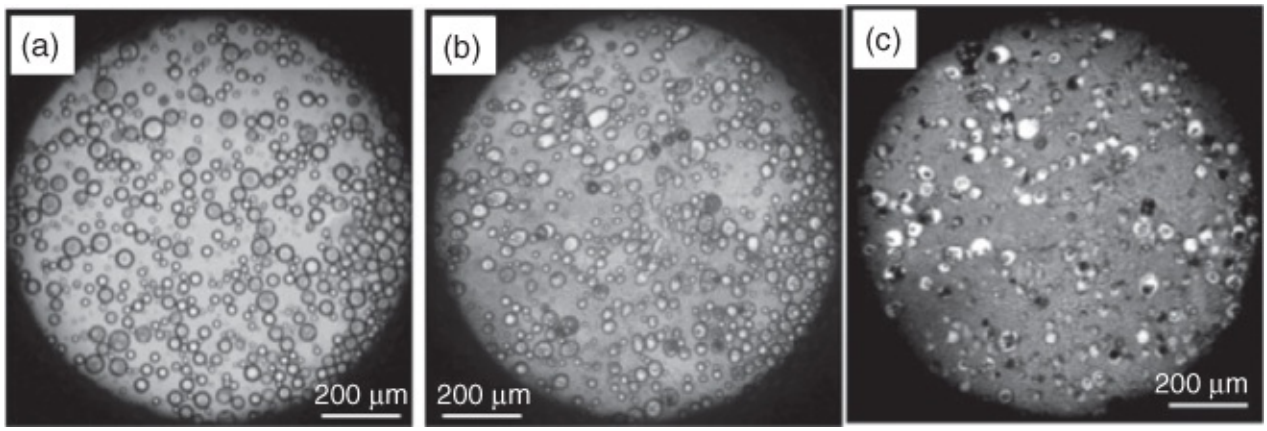

Figure 1.9 Observation of freezedrying an oilinwater emulsion (cyclohexane emulsified into aqueous PVA solution) using an optical microscope. (a) The emulsion as prepared, spread on a glass slide; (b) this emulsion is frozen in the freezing stage; and (c) the same sample after freezedrying by subjecting the freezing stage compartment to a vacuum pump.

Because of the fine control on the freezing process using a computercontrolled freezing stage, this setup has been used to produce aligned polymer (and with silica or metal oxide nanoparticles) patterns and grid structures [52]. These patterned substrates can be used to guide stem cell growth.

1.4.3 Freezedrying Procedure

We have rarely freezedried the samples with a total volume of >200 ml. In principle, provided that the freezedrying capacity is sufficient, the frozen samples with large exposed surface area and a thickness <2 cm (we usually freezedry samples with a fill depth of 1 cm or smaller in the lab) can be freezedried to produce icetemplated porous materials with minimal shrinkage. When the solvents other than water are used, the removal of cyclohexane or DMSO can be equally efficient. For the solvents with lower melting point, a smaller volume and higher exposed surface area should be used to ensure the production of freezedried porous materials.

It is known that small molecules, particularly inorganic solvents, may considerably reduce the freezing point (not the supercooled temperature) when dissolved in water. However, this has not impacted the preparation of polymer materials in our laboratory. Indeed, the use of

polymers either as main solutes or as stabilizers is essential for the preparation of freeze dried porous materials, both in aqueous and organic solutions. For a mixture solution of polymer and inorganic salts, the melting point can be still much lower than frozen water or polymer solution. This should be taken into account and a trial and error process may be required for such types of solutions. The freezedrying process works well with nanoparticle suspensions (usually > 15 nm) although stabilizers are still required.

Once the freezing process is completed, the frozen samples may be stored in liquid nitrogen for a short while before being placed in a freezedryer. One may choose to leave the frozen samples in a freezer overnight (depending on the solvents used) for freezedrying next day. The icetemplated macroporous structures seem stable but we have not investigated the possible annealing or other effects on the pore structures.

Below is the procedure adopted in our laboratory. We have used benchtop freezedryers. The current freezedryer is CoolSafe 90.

1. Before switching on, check that any liquid in the condenser chamber has been completely drained.
2. Switch on the freezedryer and keep running at least 15 min. Ensure that the vacuum level and the required condenser temperature are reached.
    - Close the draining valve.
    - Ensure that the acrylic chamber is properly positioned
    - Switch on the freezedryer.
    - Switch on the pump, ensure that the valve between the pump and freezedryer is open.
    - Ensure that the freezedryer is running stably when the yellow light (on the panel) is not flashing and the condenser temperature is down to about −100 °C.
3. Place the frozen samples into the freezedryer.
    - Ensure you have all the frozen samples ready (not one by one) beside the freezedryer. The frozen samples should be stored in liquid nitrogen (it may be alright for water samples to be stored in a freezer, but liquid nitrogen is recommended to avoid partial melting during transferring because of the small volumes involved).
    - Close the valve between the pump and the freezedryer.
    - Open the draining valve to release the vacuum.
    - Open the acrylic chamber, immediately place the frozen samples (it helps to have some liquid nitrogen with the frozen samples) on the stack. Do not place the frozen samples directly on the acrylic base because the low temperature may stiffen the plastics.
    - Once the samples are placed, immediately reposition the acrylic chamber.
    - Close the draining valve and open the valve to the pump.
4. Leave the samples to be freezedried normally for 48 h. Check the status of the frozen

samples in the first 30 min. If for any reason the freezedrying is not running properly, for example, the acrylic chamber is misplaced, or is leaking somewhere, one will notice the partial melting of the frozen samples. If this happens, stop the freezedrying process and sort out the problems.

5. When the freezedrying is finished, it is alright to repeat procedure 3 and freezedrying another batch of frozen samples. Because we only freezedry small volumes of frozen samples, this should not exceed the cold chamber capacity or impact the freezedrying process obviously. But this should be examined carefully if large volumes of frozen samples are freezedried.
6. Switch off the freezedryer when no further samples are to be freezedried
    - Switch off the freezedryer.
    - Open the draining valve to release the vacuum.
    - Take out the freezedried samples and store in a desiccator.
    - Switch off the pump.
    - Allow the condenser to warm up, melted solvent is drained, and flush the condenser chamber using water (only do this at room temperature) if it does not look clean.

Other types of freezedryers can also be used. For example, we have also used a VirTis AdVantage freezedryer where the shelf temperature can be programmed to facilitate the freezedrying process. The important thing is to know the melting points of the frozen sample, vapour pressure of the frozen solvent (or approximately judge based on the volatility), the sample depth, and the volume. Different labs may have different freezedrying practices but the overall target is the same–to produce icetemplated materials with desirable pore structures and pore volumes.

References

1 Franks, F. and Auffret, T. ed. (2007). FreezeDrying of Pharmaceuticals and Biopharmaceuticals: Principles and Practice. RSC Publishing.

2 Rey, L. and May, J.C. ed. (2010). FreezeDrying/Lyophilization of Pharmaceutical and Biological Products. CRC Press.

3 Hua, T.C., Liu, B.L., and Zhang, H. ed. (2010). FreezeDrying of Pharmaceutical and Food Products, Food Science, Technology and Nutrition. Woodhead Publishing Limited.

4 Varshney, D. and Singh, M. ed. (2015). Lyophilized Biologics and Vaccines: Modality Based Approaches. Springer.

5 Roberts, A.D., Li, X., and Zhang, H. (2014). Porous carbon spheres and monoliths: morphology control, pore size tuning and their applications as Liion battery anode materials. *Chem. Soc. Rev.* 43: 4341–4356.

6 Silverstein, M.S., Cameron, N.R., and Hillmyer, M.A. ed. (2011). Porous Polymers. Hoboken: Wiley.

7 Sing, K.S.W., Everett, D.H., Haul, R.A.W. et al. (1985). Reporting physisorption data for gas/solid systems with special reference to the determination of surface area and porosity. *Pure Appl. Chem.* 57: 603–619.

8 Qian, L. and Zhang, H. (2011). Controlled freezing and freeze drying: a versatile route for porous and micro/nanostructured materials. *J. Chem. Technol. Biotechnol.* 86: 172–184.

9 Gutierrez, M.C., Ferrer, M.L., and del Monte, F. (2008). Icetemplated materials: sophisticated structures exhibiting enhanced functionalities obtained after unidirectional freezing and icesegregationinduced selfassembly. *Chem. Mater.* 20: 634–648.

10 Deville, S. (2010). Freezecasting of porous biomaterials: structure, properties and opportunities. *Materials* 3: 1913–1927.

11 Pawelec, K.M., Husmann, A., Best, S.M., and Cameron, R.E. (2014). Icetemplated structures for biomedical tissue repair: from physics to final scaffolds. *Appl. Phys. Rev.* 1: 021301.

12 Barrow, M., Eltmimi, A., Ahmed, A. et al. (2012). Frozen polymerization for aligned porous structures with enhanced mechanical stability, conductivity, and as stationary phase for HPLC. *J. Mater. Chem.* 22: 11615–11620.

13 Wolkers, W.F. and Oldenhof, H. ed. (2015). Cryopreservation and FreezeDrying Protocols. New York: Human Press, Springer.

14 Deville, S. (2013). Icetemplating, freeze casting: beyond materials processing. *J. Mater. Res.* 28: 2202–2219.

15 Sundaramurthi, P. and Suryanarayanan, R. (2010). Trehalose crystallization during freeze drying: implications on lyoprotection. *J. Phys. Chem. Lett.* 1: 510–514.

16 Levina, M. and RajabiSiahboomi, A.R. (2004). The influence of excipients on drug release from hydroxypropyl methylcellulose matrices. *J. Pharm. Sci.* 93: 2746–2754.

17 Li, W.L., Lu, K., and Walz, J.Y. (2012). Freeze casting of porous materials: review of critical factors in microstructure evolution. *Int. Mater. Rev.* 57: 37–60.

18 Kasper, J.C. and Friess, W. (2011). The freezing step in lyophilisation: physiochemical fundamentals, freezing methods and consequences on process performance and quality attributes of biopharmaceuticals. *Eur. J. Pharm. Biopharm.* 78: 248–263.

19 Geidobler, R. and Winter, G. (2013). Controlled ice nucleation in the field of freeze drying: fundamentals and technology review. *Eur. J. Pharm. Biopharm.* 85: 214–222.

20 Searles, J.A., Carpenter, J.F., and Randolph, T.W. (2001). The ice nucleation temperature

determines the primary drying rate of lyophilization for samples frozen on a temperature controlled shelf. *J. Pharm. Sci.* 90: 860–871.

21 Moore, E.B. and Molinero, V. (2011). Structural transformation in supercooled water controls the crystallization rate of ice. *Nature* 479: 506–508.

22 Zhang, H., Hussain, I., Brust, M. et al. (2005). Aligned two and threedimensional structures by directional freezing of polymers and nanoparticles. *Nat. Mater.* 4: 787–793.

23 Rowe, T.D. (1990). A technique for the nucleation of ice. *Proceedings of International Symposium on Biological ProductFreezeDrying and Formulation* , Basel, New York: Karger, c1992. ISBN 3805554664.

24 Petersen, A., Rau, G., and Glasmacher, B. (2006). Reduction of primary freezedrying time by electric field induced ice nucleus formation. *Heat Mass Transfer* 42: 929–938.

25 Bang, J.H. and Suslick, K.S. (2010). Applications of ultrasound to the synthesis of nanostructured materials. *Adv. Mater.* 22: 1039–1059.

26 Nakagawa, K., Hottot, A., Vessot, S., and Andrieu, J. (2006). Influence of controlled nucleation by ultrasounds on ice morphology of frozen formulations for pharmaceutical proteins freezedrying. *Chem. Eng. Process.* 45: 783–791.

27 Patapoff, T.W. and Overcashier, D.E. (2002). The importance of freezing on lyophilisation cycle development. *BioPharm* 15: 16–21.

28 Tang, X. and Pikal, M.J. (2004). Design of freezedrying processes for pharmaceuticals: practical advice. *Pharm. Res.* 21: 191–200.

29 Pikal, M.J., Roy, M.L., and Shah, S. (1984). Mass and heat transfer in vial freezedrying of pharmaceuticals: role of the vial. *J. Pharm. Sci.* 73: 1224–1237.

30 Pikal, M.J. (1990). Freezedrying of proteins. Part I: Process design. *BioPharm* 3: 18–28.

31 Pikal, M.J., Shah, S., Roy, M.L., and Putman, R. (1990). The secondary drying stage of freeze drying: drying kinetics as a function of temperature and chamber pressure. *Int. J. Pharm.* 60: 203–217.

32 Zhang, H. and Cooper, A.I. (2005). Synthesis and applications of emulsiontemplated porous materials. *Soft Matter* 1: 107–113.

33 Zhang, H., Wang, D., Butler, R. et al. (2008). Formation and enhanced biocidal activity of waterdispersible organic nanoparticles. *Nat. Nanotechnol.* 3: 506–511.

34 Zhang, H., Edgar, D., Murray, P. et al. (2008). Synthesis of porous microparticles with aligned porosity. *Adv. Funct. Mater.* 18: 222–228.

35 Cooper, A.I. (2000). Polymer synthesis and processing using supercritical carbon dioxide.

J. Mater. Chem. 10: 207–234.

36 Zhang, H., Long, J., and Cooper, A.I. (2005). Aligned porous materials by directional freezing of solution in liquid CO_2. *J. Am. Chem. Soc.* 127: 13482–13483.

37 Grant, N. and Zhang, H. (2011). Poorly watersoluble drug nanoparticles via an emulsionfreezedrying approach. *J. Colloid Interface Sci.* 356: 573–578.

38 McDonald, T.O., Martin, P., Patterson, J.P. et al. (2012). Multicomponent organic nanoparticles for fluorescence studies in biological systems. *Adv. Funct. Mater.* 22: 2469–2478.

39 Yu, Z., Garcia, A.S., Johnston, K.P., and Williams, R.O. (2004). Spray freezing into liquid nitrogen for highly stable protein nanostructured microparticles. *Eur. J. Pharm. Biopharm.* 58: 529–537.

40 Mukai, S.R., Nishihara, H., and Tamon, H. (2004). Formation of monolithic silica gel microhoneycombs (SMHs) using pseudosteady state growth of microstructural ice crystals. *Chem. Commun.* 874–875.

41 Gun'ko, V.M., Savina, I.N., and Mikhalovsky, S.V. (2013). Cryogels: morphological, structural and adsorption characterisation. *Adv. Colloid Interface Sci.* 187–188: 1–46.

42 Ma, L., Jin, A., Xi, Z., and Lin, W. (2009). Freeze drying significantly increases permanent porosity and hydrogen uptake in 4,4connected metal–organic frameworks. *Angew. Chem. Int. Ed.* 48: 9905–9908.

43 Sai, H., Xing, L., Xiang, J. et al. (2013). Flexible aerogels based on an interpenetrating network of bacterial cellulose and silica by a nonsupercritical drying process. *J. Mater. Chem. A* 1: 7963–7970.

44 Tamon, H., Ishizaka, H., Yamamoto, T., and Suzuki, T. (2000). Influence of freezedrying conditions on the mesoporosity of organic gels as carbon precursors. *Carbon* 38: 1099–1105.

45 Roberts, A.D., Lee, J.S.M., Wong, S.Y. et al. (2017). Nitrogenrich activated carbon monoliths via ice templating with high CO_2 and H_2 adsorption capacities. *J. Mater. Chem. A* 5: 2811–2820.

46 Qian, L., Willneff, E., and Zhang, H. (2009). A novel route to polymeric submicron fibers and their use as templates for inorganic structures. *Chem. Commun.* 3946–3948.

47 Zhang, H., Lee, J.Y., Ahmed, A. et al. (2008). Freezealign and heatfuse: microwires and networks from nanoparticle suspensions. *Angew. Chem. Int. Ed.* 47: 4573–4576.

48 Qian, L., Ahmed, A., Foster, A. et al. (2009). Systematic tuning of pore morphologies and pore volumes in macroporous materials by freezing. *J. Mater. Chem.* 19: 5212–5219.

49 Ran, H., Feng, P., Liu, Z. et al. (2015). Complexshaped porous Cu bodies fabricated by

freezecasting and vacuum sintering. *Metal* 5: 1821–1828.

50 Nardecchia, S., Carriazo, D., Ferrer, M.L. et al. (2013). Three dimensional macroporous architectures and aerogels built of carbon nanotubes and/or graphene: synthesis and applications. *Chem. Soc. Rev.* 42: 794–830.

51 Roberts, A.D., Li, X., and Zhang, H. (2015). Hierarchically porous sulfurcontaining activated carbon monoliths via icetemplating and onestep pyrolysis. *Carbon* 95: 268–278.

52 Qian, L., Ahmed, A., GlennonAlty, L. et al. (2015). Patterned substrates fabricated by a controlled freezing approach and biocompatibility evaluation by stem cells. *Mater. Sci. Eng. C* 49: 390–399.

2
Fundamentals of Controlled Freezing for Icetemplated Porous Materials

2.1 Introduction

Freezing has been known to be an effective way for food storage and cell cryopreservation [1, 2]. Because molecules, particles, or impurities can be rejected and condensed between ice crystals during freezing, it has also been used as a drying technique or a method for cleaning water [3]. Owing to the phase separation that results from freezing, the removal of ice crystals by sublimation or washing after gelation of a concentrated solute phase can produce ice templated porous materials or fibrous structures. This was probably first demonstrated by the formation of silica fibres after Mahler et al. froze a silica sol [4]. More examples have been reported on the preparation of porous ceramics, biomaterials, and polymers [5–7]. Some early examples include the initial description of freeze casting by Maxwell et al. in 1954 for fabricating dense ceramics [8], porous polymers from agar gels in 1984 [9], porous ceramics in 2001 [10], and biomaterials from collagen [11].

The term ‘ice templating’ is referred to the process where ice crystals are used as template and a porous material can be generated after removing such a template. This process is also widely termed as *freeze casting* (particularly for preparation of porous ceramics) or *simply freeze drying* (although this name does not accurately describe the process) [5–7, 12]. The ice templating method has been widely used to produce a wide range of porous materials with a variety of morphologies. Because ice crystals are used as template, the icetemplated structure and/or pore morphology can be controlled by the various ice morphologies that are formed during the freezing process. Therefore, the fundamental study on the formation and behaviour of ice crystals under controlled freezing conditions is critical for the production of advanced porous materials with desirable properties. Indeed, the investigation on freezing aqueous polymer and particulate systems is of wider scientific interests such as in frozen soils, freezing sea water/glaciers, and cryopreservation [12].

Although some organic solvents other than water have been used for icetemplated porous materials, the fundamental study in controlled freezing in literature has been nearly exclusively focused on the systems using water. In this chapter, the basics of ice crystals is first described. In the freezing or solidification of aqueous systems, the majority of the articles in literature are based on aqueous particulate systems, either experimentally or theoretically. Different mathematic models describing the freezing phenomena have been developed, which are evidenced by experimental observation. We will then introduce the instruments or techniques used for observation or investigation of freezing phenomena and follow this by description/discussions of models/equations and observations in the freezing of aqueous particulate systems.

2.2 The Basics of Ice Crystals

Ice crystals may be formed when the temperature of the water is lowered below the equilibrium freezing point (i.e. 0 °C) and nucleation can be started. In practice, ice crystals do not form just below the equilibrium freezing point because a large energy barrier must be overcome so that water molecules may move closer and become ordered [1]. Supercooled water (e.g. as low as −40 °C) is usually required to initiate the nucleation and crystallization [13]. Very often, foreign particles (or impurities) and even the wall of the container act as nuclei to promote the growth of ice crystals.

There are about 10 crystalline phases available for ice crystals, as shown in Figure 2.1 [14]. Most of these phases are stable in a certain range of temperature and pressure. The structures of these crystalline phases, mostly investigated by the neutrondiffraction crystallographic method, can be rationalized in terms of fully connected tetrahedral networks of water molecules, with each molecule donating hydrogen bonds to two neighbours and accepting two hydrogen bonds from two others. Although the oxygen atoms are related to an underlying lattice, the hydrogen atoms are in disorder [14]. The crystalline phases that are encountered daily, which are formed from atmospheric pressure and a temperature not lower than −200 °C, is the hexagonal ice (Ih). In the Ih, the O–O–O angles are close to the ideal tetrahedral angle of 109.47° [14]. The density of Ih is lower than that of water, which is essential for the lift on Earth. However, with the increase of pressure, other forms of ice crystals can be formed, with a higher density than water [15]. As the pressure is increased, water molecules have to rearrange themselves to occupy less volume. This can change the network structure (which can still remain tetrahedral) and increase the distortion of the O–O–O angles, e.g. the angles varying between 80° and 129° [14].

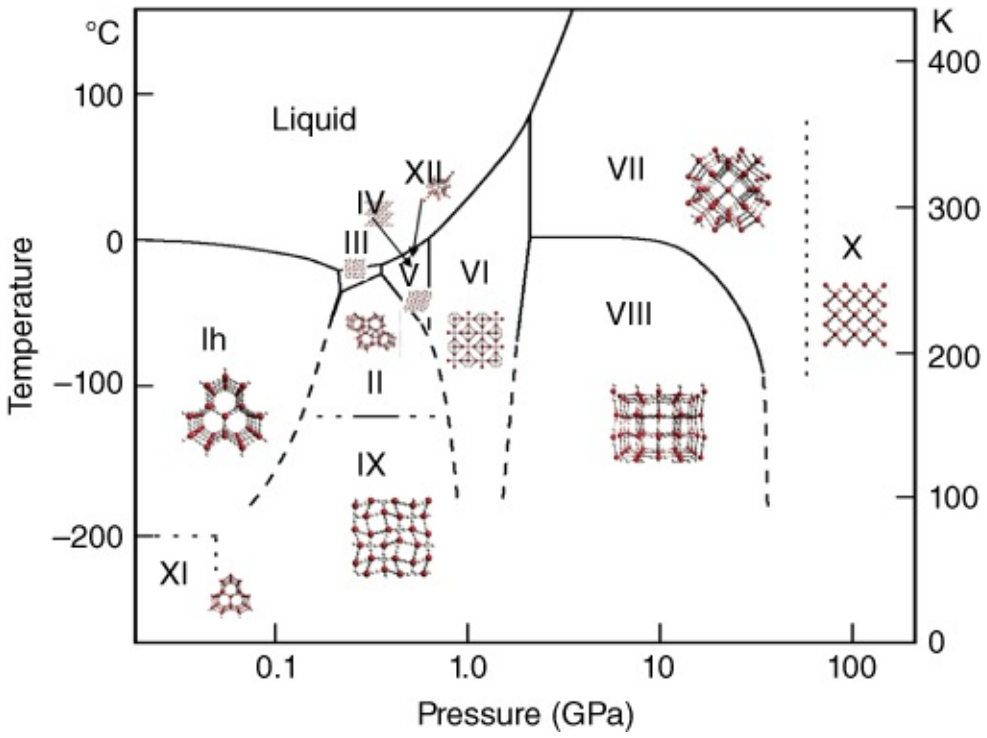

Figure 2.1 The solid–liquid phase diagram of ice (1 GPa = 10 000 bars).

Source: BartelsRausch et al. 2012 [14]. Reprinted with permission from APS.

Ih shows a lattice of 'puckered' hexagonal crystal structure, with the basic ice crystal growth form being the hexagonal prism [16]. The overall morphology of natural ice crystals (e.g. snowflakes) or ice crystals formed under relatively ambient conditions can take different forms, e.g. they can be platelike, columnar, or dendritic, depending on the relative growth rate of ice crystals on the basal facet and prism facet. At ambient conditions, there exists another crystalline form, the cubic ice (Ic). Ic is metastable and is thought to exist in the coldest regions of the Earth. Ic is believed to be a benign form of ice crystals for cryopreservation. However, the observation of Ic is difficult because it can rapidly transform to the stable hexagonal phase Ih. The structures of both Ih and Ic consist of sixmembered puckered rings. However, the difference between them lies in the stacking of these layers [13]. It is also thought that Ic may be a poorly crystallized phase and may be placed between the crystalline and amorphous phases [14]. From Xray diffraction data and Monte Carlo simulations, Malkin et al. showed that ice crystals formed homogeneously from supercooled water (231.7 ± 1.0 K) were neither of Ih and Ic phases, but were composed of randomly stacked layers of cubic and hexagonal sequences [13]. Based on this study, they argued that almost all ice that had been identified as Ic was most likely stackingdisordered ice with varying degrees of stacking disorder.

The morphologies of ice crystals have been mostly observed and investigated for snowflakes or snow crystals. Snow crystals grow from water vapour and they have been known for their beautiful and symmetrical patterns. When snow crystals are formed in air at atmospheric pressure near 1 bar, the morphologies vary, depending on the change of temperature and water vapour supersaturation [16]. Although the ice crystals are formed from a liquid phase in the icetemplating technique, the morphologies of snow crystals grown from water vapour may be

controlled by careful selection of freezing conditions when freezing aqueous solutions or suspensions. Indeed, most of the snow crystal morphologies have been observed in ice templated materials, as discussed by Deville in the review article [12].

In a study related to the ice templating or freezecasting technique, Shibkov et al. established the morphology diagram of ice crystal patterns growing freely in supercooled water [17]. The study classified eight nonequilibrium macroscopic structures from heterogeneous nucleation of ice in pure water at atmospheric pressure and the temperature range of −0.1 to −30 °C. The morphology spectrum of nonequilibrium crystal of ice crystals includes fragment of dense branching structure, dendrite, needlelike crystals, fractal needled branch, compact needled branch, and the platelet, depending on the range of supercooling temperatures. Some of the structures coexist. Three different scenarios, tipsplitting, dynamical tip oscillation, and selective application of noise, were thought to induce the initial perturbations and the formation of sidebranches. Based on the results of the realtime tipvelocity measurements, the morphology diagram of ice crystals (average tip velocity υ_t vs supercooling temperature ΔT) was constructed (Figure 2.2) [17]. It is clear that the ice crystal morphology could be tuned by varying the supercooling temperature/tip velocity. The morphology transition between different phases is achievable and can be investigated. For example, the transition between stable needle and platelet was found to be a firstorder kinetic transition because there was a υ_t (ΔT) jump by a factor of about 2 at about 7.5 °C.

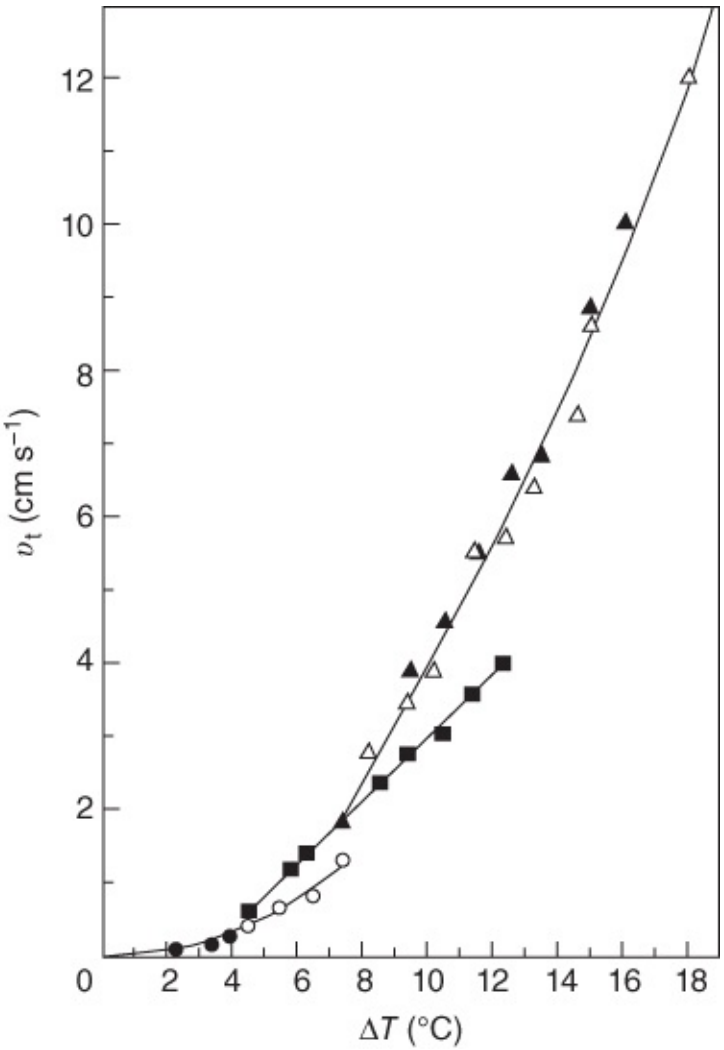

Figure 2.2 Morphology diagram of nonequilibrium growth patterns in υ_t–ΔT phase space: •, dendrite; ○, stable needlelike crystal; solid square, fractal needled branch; solid triangle, compact needled branch; hollow triangle, platelet.

Source: Shibkov et al. 2003 [17]. Reprinted with permission from Elsevier.

2.3 Instruments and Techniques for Investigation of Freezing Aqueous Particulate Systems

When the icetemplating technique or freeze casting is used to produce porous materials, the dissolution of polymers/small molecules and the suspended particles can considerably impact the growth of ice crystals. The morphologies of ice crystals and hence the icetemplated pore structures can be directly related to the freezing system and the freezing condition. In order to investigate how the ice crystals grow, the impact of particles (the studies on impact of polymers are highly limited), and the interaction of particles and freezing front, a variety of instruments and techniques have been employed and are described further.

2.3.1 Optical Microscope Equipped with a Freezing Stage

The sizes of ice crystals or ice lenses during freezing of aqueous suspensions are normally in the micron range, which can be observed by a standard optical microscope. Of course, the macroscopic ice lenses rather than single ice crystals are observed. A CCD camera can be attached to the optical microscope to record the images or videos. The key element in the set up is the freezing stage that should allow directional solidification or freezing of aqueous suspensions. This is probably the most used technique discussed in literature to observe the initiation and growth of ice lenses [18–21].

An example of such a freezing stage setup is illustrated in Figure 2.3 [18]. A similar system was used by our group [19] and a photo of such a setup is given in Figure 1.8. In order to investigate the directional freezing of aqueous colloidal silica suspensions (average diameter of ~1.5 μm), a Linkam GS350 stage was employed with a homebuilt Köhler lens microscope [18]. The temperature of the two metal plates, with a gap of 2 mm between them, is controlled by electrical resistance heaters and a pumpcontrolled flow of liquid nitrogen. The temperature gradient is created by the difference in the temperatures of the two plates. Usually, the temperature of a cold plate (T_c) is lower than the freezing temperature T_f while the temperature of a warm plate (T_w) is higher than T_f. A computercontrolled stepper motor holds the sample cell in contact with the plates and pulls along the temperature gradient (from the warm plate to the cold plate) at a defined moving velocity. The sample depth is small so that the ice lens can be clearly observed from the gap between the two plates. The sample cell is usually contained within a sealed box to prevent the condensation of water vapour, which could make the clear observation very difficult.

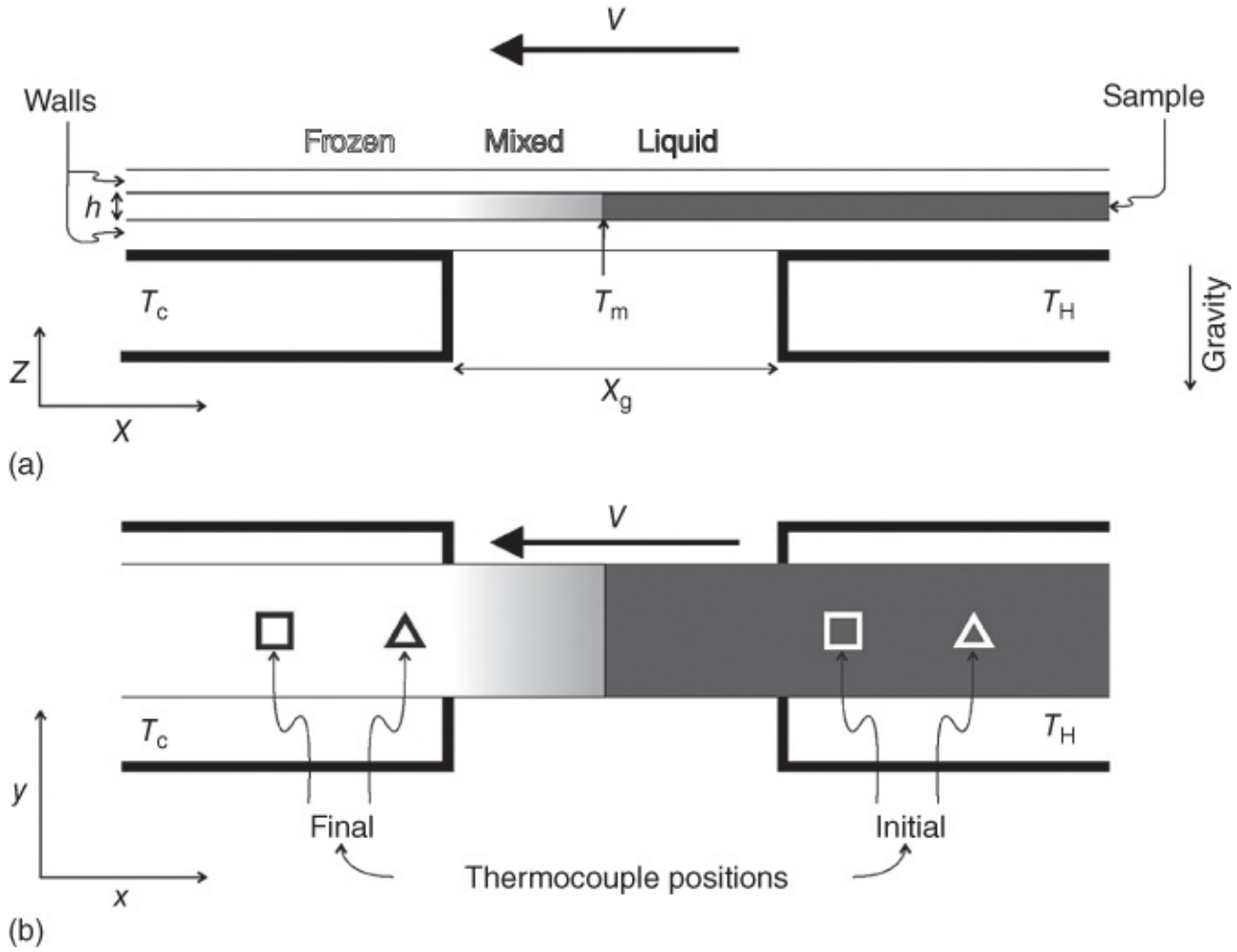

Figure 2.3 Schematics of a freezing stage setup used to directionally freeze the aqueous silica colloidal suspension. (a) The sample is contained within two glass walls and has depth *h*. (b) Initial and final positions of two thermocouples, represented by square and triangle symbols, placed inside the sample.

Source: Schollick et al. 2016 [18]. Reprinted with permission from American Chemical Society.

Different freezing stages may be used [19–21]. To allow the observation of directional solidification of ice lens, they should always have two independently temperaturecontrolled plates and a facility to allow the accurate moving velocity of samples across the plates.

2.3.2 Optical Interferometry

Optical interferometry is a good technique to study interfacial instability and dendritic ice growth because of its ability to measure small relative changes in refractive index in two dimensions. This method has been applied in the form of Michelson, Mach–Zehnder, wedge, and holographic interferometry. For example, Mach–Zehnder optical interferometry (a schematic diagram is shown in Figure 2.4) has been used to measure the concentration gradient at the ice–solution interface and the ice–solution interface morphology [21]. Like the optical microscope, a temperature gradient microscope stage (TGMS) is required to directly freeze the sucrose and pullulan solutions. Similarly, the TGMS consists of two plates kept at different temperatures with a gap of 5 mm. A drop of the solution is placed on a glass slide surrounded

by a 75 μm spacer on the top of which a standard cover slip is placed. The slide is placed across the two plates and held by a movable sprung plate connected to a motor capable of moving the sample across the gag at speeds between 0.5 and 80 μm s^{-1}. A constant stream of dry nitrogen gas is passed over the sample to prevent condensation from forming on the top of the coverslip.

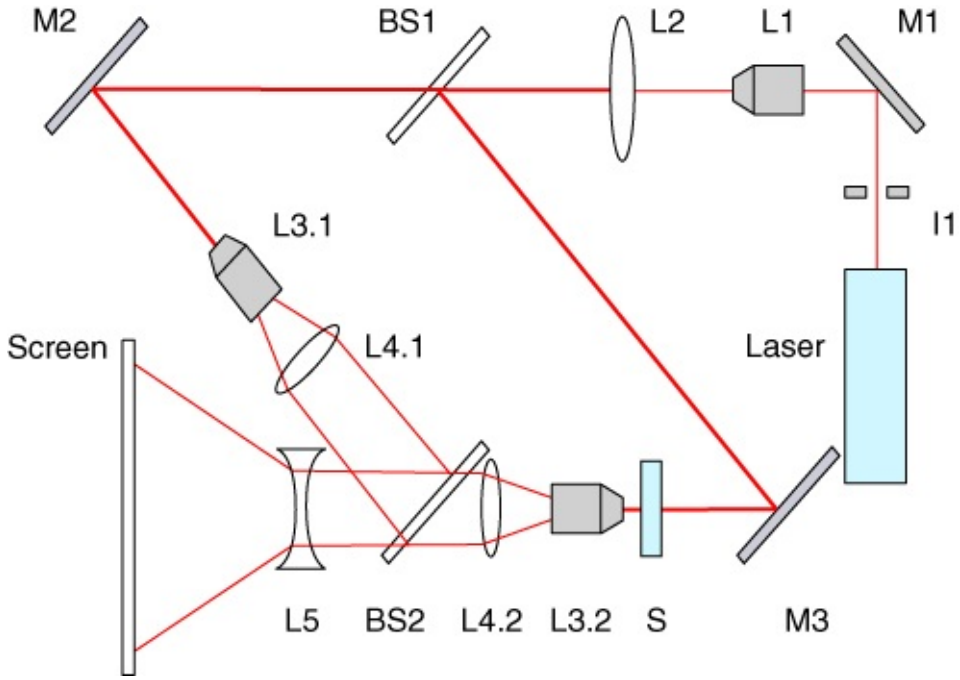

Figure 2.4 Schematic diagram of the Mach–Zehnder optical interferometer.

Source: Butler 2000 [21]. Reprinted with permission from American Chemical Society.

In the Mach–Zehnder setup, an interference pattern, consisting of dark and light areas, is produced when the two beams are recombined, which can be analysed to obtain information on the refractive index. Usually, reference fringes are set up prior to introducing the samples into the sample path. The solution concentrations may be derived by analysing the optical difference from fringe positions, using the following equation [21]:

$$\frac{C - C_0}{C} = \frac{\lambda \, \Delta\chi}{(n(C) - n_0)hw}, \tag{2.1}$$

where C is the local solution concentration, C_0 is the bulk concentration, λ is the wavelength, $\Delta\chi$ is the deviation of fringe position from that of the reference fringe, $n(C)$ is the refractive index of the solution with concentration C, n_0 is the refractive index of pure water (1.333), h is the sample thickness, and w is the separation of the reference fringes.

The ice–solution interface morphology can be observed directly from the interference images using the interferometer. The change of position of the interface as the planar interface develops instability is used to calculate the growth velocity at the point of instability.

2.3.3 Cryogenic Transmission Electron Microscopy (CryoTEM)

Optical microscopy cannot be used to investigate the nanoscale structure or the crystalline polymorphs of ice crystals due to its limited magnification power. Cryogenic transmission electron microscopy (CryoTEM) is ideal for direct experimental observation of hexagonal or cubic ice polymorphs. First of all, the aqueous solution or suspension must be frozen for the observation. To allow the electron beam to go through the sample, the thickness of the sample must be carefully controlled. However, because of the high vacuum in the CryoTEM system and also because the high current density of the electron beam irradiation can generate heat at the sample, the ice sample may be easily sublimed, thus causing great difficulty in observing the ice sample.

Dillon and coworkers developed an in situ CryoTEM sample stage by joining an environmental cell with a copper cold finger stage [22]. This platform could access nanoscale information about ice crystallization. A gold nanoparticle (~30 nm) suspension was pipetted (about 100 nl) onto a cleaned 50 nm thick SiNx window. A second SiNx window sealed the liquid within the cell. An average thickness of ~300–500 nm was detected. A low beam current density (~0.5–1.5 mA cm^{-2}) was used to minimize the heating and charging effects. Both images and videos were recorded on the observation. The microstructures of ice crystallized at 220–260 K were imaged using this technique. It was found that the growth of nanotwinned cubic ice aligned along the $[21\bar{1}]$ plane with dendritelike morphology occurred between 220 and 245 K. Hexagonal ice was formed at 260 K growing along the $\langle\bar{1}100\rangle$ plane with a planar ice/water interface [22].

A highresolution TEM was used by Kobayashi et al. to investigate the morphology and crystal structure of ice nanoparticles [23]. Both Ih and Ic crystals were found and assigned. The dynamic transition between Ih and Ic phases of individual ice nanoparticles was monitored by in situ transmission electron diffractometry. The preparation of ice nanoparticles was quite delicate. A TEM microgrid, wetted with distilled methanol, was held in a cryo holder. The grid was quenched by dipping the tip of the holder into liquid nitrogen, and subsequently cooled by supplying liquid nitrogen. The grid was then exposed to a moist atmosphere with a specific water vapour pressure of 1.2 kPa and a temperature of 298.9 K for 20 s. The specimen was then directly induced into a TEM column (vacuum of ~10^{-5} Pa, keeping the low temperature). The TEM was operated at 120 kV with the point resolution better than 0.106 nm. The average size of the ice nanoparticles was around 390 nm and the larger ice nanocrystals tended to be faceted. To avoid instant evaporation of ice nanoparticles under the incident beam, the exposure time was minimized to 0.5 s, from a very thin region with a rapidly moving and evaporating frontier.

2.3.4 Xray Radiography and Tomography

Compared to the techniques mentioned earlier (and also the scanning electron microscopy (SEM) that can usually only image the surface of a freezedried and/or sintered sample), X ray radiography and tomography provide obvious advantages: transparent materials are no longer required because opaque materials can be imaged by Xray absorption contrast; a high spatial resolution (μm) can be obtained on synchrotron instrument; and a threedimensional

(3D) reconstruction of the particle arrangement and the ice crystals after complete freezing is possible [24, 25]. Xrays are at the high energy end of the electromagnetic spectrum, with the energy level in the approximate range of less than 1 to over 100 keV. Although there is no clear classification, Xrays with energy levels higher than 10 keV are termed as hard Xrays while Xrays with energy levels lower than 10 keV are termed as soft Xrays. The wavelengths of soft Xrays are in the order of 1 nm while the wavelengths are in the fraction of nanometres for hard Xrays. Because of such short wavelengths (in the similar length region as atoms), the reflection is minimal when the Xray hits a material surface. The Xray can penetrate between the atoms and then interact with atoms and absorbed by the material. Different materials exhibit different attenuation coefficients, which are determined by the electron density of the material and the atomic weight of its chemical elements.

There are different modes of Xray imaging [26]. For Xray absorption imaging, as traditionally used in medical applications, there is almost no distance between the sample and the detector. However, for a homogeneous material with low attenuation coefficient or a heterogeneous material with a range of small attenuation coefficients, it is insufficient to produce absorption image with satisfactory contrast. Thus, Xray phase contrast imaging has been developed where there is a fixed distance between the sample and the detector. Phase contrast is possible because the beam is not only absorbed by the material but that the phase of the wave is also affected, depending on the material's refractive index. This technique requires a homogeneous and spatially coherent beam. Based on this, holotomography is introduced, which uses a combination of several distances as well as combines the phase shift information to produce phase maps that are subsequently used for the tomographic reconstruction. This technique can be employed for the materials that have very small variations in attenuation coefficients, which lead to insufficient imaging results even with phase contrast techniques. Holotomography is defined as quantitative phase tomography with micrometre resolution using coherent hard synchrotron radiation Xrays [27]. The approach is based on the Fresnel diffraction approximation and is efficiently implemented using fast Fourier transform (FT) functions. The use of different distances reduces the challenge of finding a local optimum or a nonunique solution. It should be mentioned that only two dimensional (2D) images (radiographs) can be produced by Xray imaging. However, once the phase maps are obtained via holographic reconstruction (disengaging the phase map from the image), it is then rather straightforward to bring many maps corresponding to different orientations of the sample together and produce the 3D tomographic reconstruction with quantitative information. For example, the quantitative phase maps of polystyrene foam from 700 angular positions were used to produce a 3D tomographic reconstruction, giving the 3D distribution of the refractive index decrement, or of the electron density [27].

The nucleation and growth of ice crystals during solidification of aqueous alumina slurries were investigated by direct in situ highresolution Xray radiography and tomography on the beamline ID19 of European Synchrotron Radiation Facility (ESRF) [25]. The energy was set to 20.5 keV. The distance between the sample and the detector was 20 mm. A set of 1200 projections were taken within 180°. Radiographs taken with different viewing angles of the sample provided a dynamic visualization of the solidification process. Using the HST program

at the ESRF, the computing reconstruction provided a 3D map of the local absorption coefficients in each elementary volume of the sample from the set of absorption radiographs. An example of the radiographs showing global instabilities and the 3D local observation by Xray tomography of ice crystals are given in Figure 2.5. With this study, it was possible to establish global instabilities and the structure diagrams for the solidification of colloidal suspensions [25]. The dynamics of the freezing front during the solidification of aqueous alumina slurry was investigated by in situ Xray radiography, tomography, and modelling [28]. Freezing of alumina slurry was carried out by pouring it into a polypropylene cylindrical mould, invisible to Xrays, placed at the tip of a copper cold finger inside a cryogenic cell. A set of 900 projections were taken within 180°. This work showed that the control of the morphology of packed alumina structures in the freezing direction could be achieved by choosing the suitable temperature profile at the base of the suspension. The effects of additives during directional freezing of aqueous titania suspensions were investigated by synchrotron Xray radiography on beamline 8.3.2 at the Advanced Light Source (Berkeley, CA) [29]. The freezing stage consisted of a cylindrical Teflon mould placed on a copper cold finger with the temperature controlled using liquid nitrogen via a thermocouple linked to a power unit and ring heater. The cooling rate was 2.5 °C min^{-1} starting from the ambient temperature. Samples were scanned with a 24 keV monochromatic beam. A field view of 3 mm was obtained using 5 × lens and a voxel size of 1.7 μm. It was concluded that adding binder could induce a transition from a disorientated structure to a lamellar structure. A depletion mechanism could be used to explain the particle redistribution at the ice/water interface.

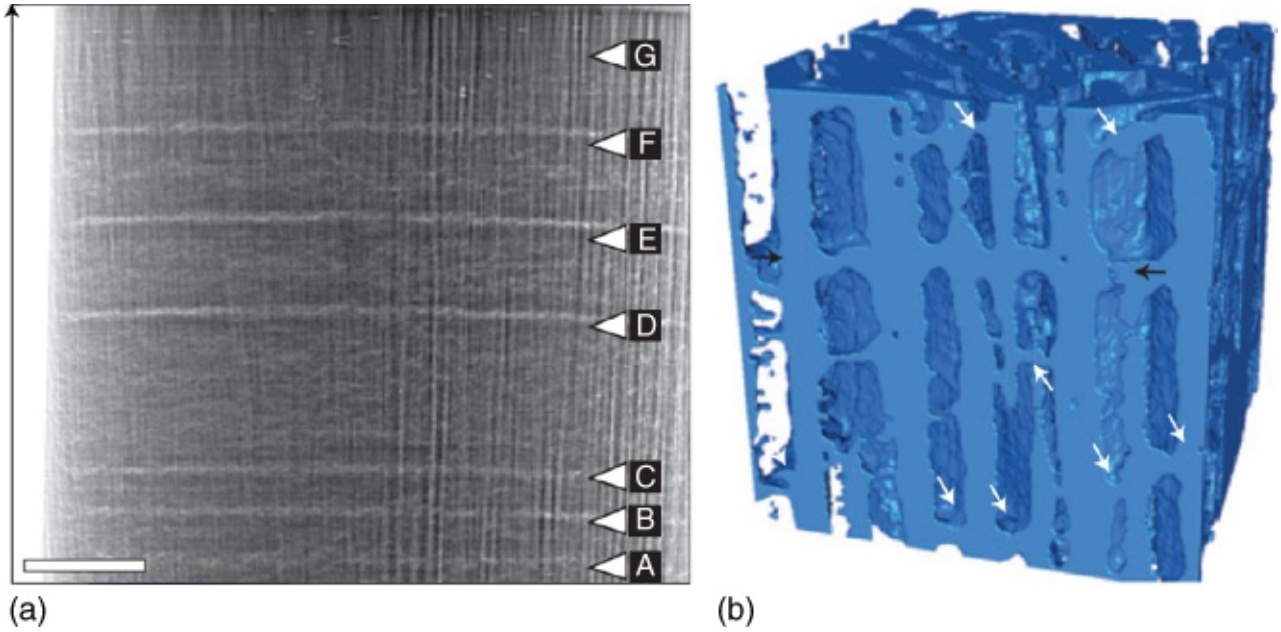

Figure 2.5 Experimental observations of the development of global interface instabilities and their impact on the ice structure when directionally freezing aqueous alumina (0.2 µm particles) suspension. (a) The radiograph showing bright bands (less absorption of the beam, particlespoor region) and interface displacement direction. (b) 3D local observation by X ray tomography of ice crystals, revealing lateral growth of ice crystals from localized (white arrows) and global (black arrows) instabilities.

Source: Deville et al. 2009 [25]. Reprinted with permission from Nature Publishing Group.

2.3.5 Small Angle Xray Scattering

In general, the Xray scattering techniques collect the information on variation of a sample's electron density to generate contrast. A spatial variation of electron density at the nanometre scale scatters an Xray beam to low angles while the high angle scattering results from the atomic scale [30]. Small angle Xray scattering (SAXS) is a technique used to characterize the samples based on a spatially averaged intensity distribution between the scattering angles of 0° and 5°. SAXS can provide detailed structural analysis and physical information for a variety of 1–100 nm and beyond particles or polymers, in various states (e.g. gaseous, liquid, solid) [30, 31]. SAXS uses small beams (submillimetre down to a micrometre). Thin samples with low to intermediate atomic number density for low absorption or intermediate to high atomic number density for scattering contrast can usually generate good quality data. This technique can benefit from the extreme brightness of Xray synchrotron source that provides excellent photon counting statistics [32]. The theoretical foundation for SAXS can be correlated with both the form factor and structure factor. The SAXS profile has three distinct regions [33, 34] that can be used to extract for information on the radius of gyration (the Guinier region), crosssection structures (the Fourier region), and surface per volume (the Porod region) (Figure 2.6). In the Guinier region, the radius of gyration R_g may be obtained by fitting a line to the natural log of the intensity as a function of the square of the scattering vector q^2. In the Fourier region, the pair distribution function may be determined by an indirect

Fourier transformation of the experimental form factor, providing significant information regarding the particle shape $P(q)$. In the Porod region, by determining the Porod invariant Q, it can provide surface information such as the surface to volume ratio and specific surface estimation for compact particles [33].

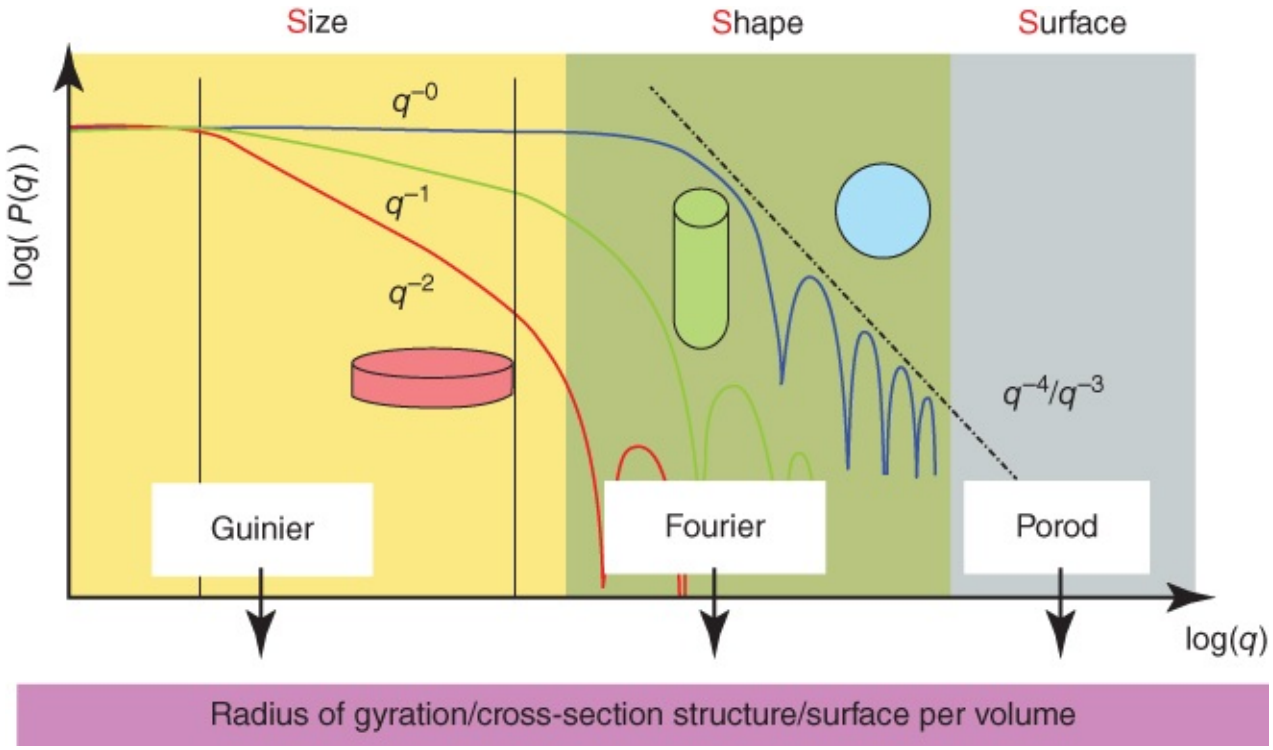

Figure 2.6 Diagram showing the regions of SAXS profile and the type of data that can be extracted from each region.

Source: Boldon et al. 2015 [33]. Reprinted with permission from Taylor & Francis.

During the process of freezing aqueous particulate suspension, the particles can be rejected from the freezing front and pack densely between the ice crystals. Understanding the packing at the particle scale is important both for the theoretical description and the potential for production of advanced icetemplated materials. However, none of the above techniques described can provide information about the particlescale structure during freezing or for a completely frozen sample. CryoTEM would have the high resolution required to observe the particles. However, the densely packed particles region will have very low transparence and make it really difficult if not impossible to be observed by CryoTEM.

However, this structural information on the packing particles during freezing may be obtained by SAXS, via a Fourierspace representation of the mass distribution within the samples on the scale of one to several times the particle radius. The directional solidification of aqueous silica colloidal suspensions (radii of silica colloids about 32 nm) was investigated by Spannuth et al. using SAXS [35]. The sample chamber within the cell was formed by sandwiching an approximately 400 μm thick aluminium washer between two copper blocks. The actual thickness of the chamber could be varied between 200 and 400 μm due to the flexibility of the windows combined with manual positioning of the cold finger abutting one window. The Xray scattering experiments were carried out at beam line 8ID of the

Advanced Photon Sources at Argonne National Laboratory. It was first verified that the scattering pattern was isotropic and did not change significantly while acquiring a set of images. Thus, the images could be averaged azimuthally and over time to produce the intensity as a function of scattering vector $I(q)$. The normalized intensity curve is given as in the following equation [35]:

$$I(q) = \mathrm{d}T_{\mathrm{r}}\emptyset V_{\mathrm{part}}(\Delta\rho)^2 P(q)S(q) \equiv AP(q)S(q), \tag{2.2}$$

where d is the cell thickness, T_{r} is the transmission coefficient, V_{part} is the average particle volume, and $\Delta\rho$ is the electron density difference between silica and water or ice. The coefficients are grouped to the amplitude A which is $q$independent. $P(q)$ is the particle form factor and $S(q)$ is the structure factor.

One typical example of the SAXS profile (the scattering intensity $I(q)$ vs scattering vector) is shown in Figure 2.7 [35]. The unfrozen data decrease smoothly as q increases, whereas the frozen profile has two features: a peak at high q and an upturn at low q. By fitting the intensities to a theoretical model for the unfrozen data and an empirical function for the frozen data, the structural information about the samples can be obtained. By comparing with the images acquired, the main peak from the SAXS profile from the frozen data can be attributed to the close packing of the particles in the densely packed particle region. The close packing of the silica colloids (so closely packed as to be touching) by freezing allows the shortrange attractive interparticle interaction to dominate, thereby forming longlived particle aggregates.

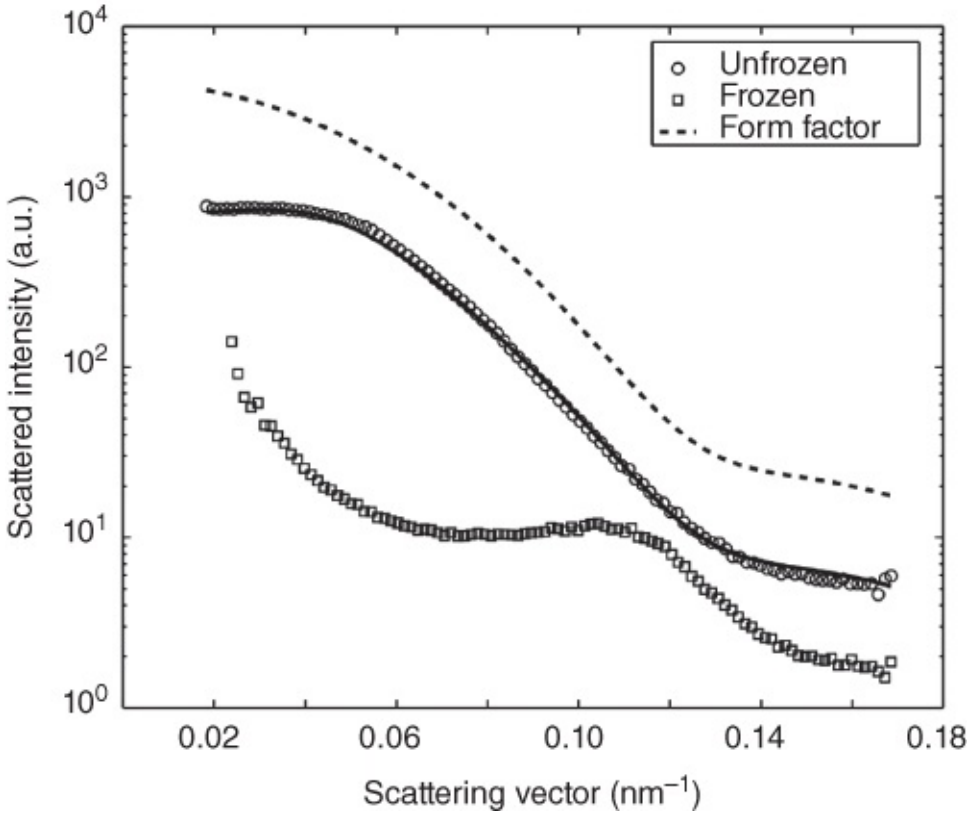

Figure 2.7 The SAXS profiles showing aqueous alumina slurry before freezing (circles) and when frozen (squares). The solid curve represents the fit of the unfrozen data to a polydisperse sphere form factor and monodisperse hardsphere structure factor. For comparison, the dotted line shows only the form factor with the same parameters but an arbitrary amplitude. For clarity, the unfrozen data have been offset from the frozen data.

Source: Spannuth et al. 2011 [35]. Reprinted with permission from APS.

2.4 The Interactions Between a Particle and the Freezing Front

2.4.1 Basic Models and Equations for the Critical Freezing Velocity

To obtain experimental evidence for theoretical studies, diluted particle suspensions are usually being directionally solidified. In order to develop theoretical models to describe the interactions between particles and the ice/water interface, the particles may be treated simply as hard spheres and the models may be described based on the interactions of a particle and the freezing front. This is, of course, not the real situation when ice templating is used to make porous materials. But it can help to develop the basic theoretical models and work towards the more complicated system.

During the freezing step, the advancing ice/water front pushes a particle ahead at a low freezing velocity. Figure 2.8 schematically depicts a spherical particle being pushed away by the freezing front [19]. The particle is not directly in contact with the freezing front. Instead, there is a flowing liquid film around the particle that is present in order to maintain the

transport of molecules and growth of ice crystals around the particle. The particle experiences two counteracting forces: an attractive force resulting from viscous drag due to fluid flow that tends to trap the particle, and a repulsive force originating from van der Waals forces between the particle and freezing front. Theoretical models have been developed based on, to be more specific, nonretarded van der Waals forces where the separation between the particle and the freezing front is small, compared to the particle radius.

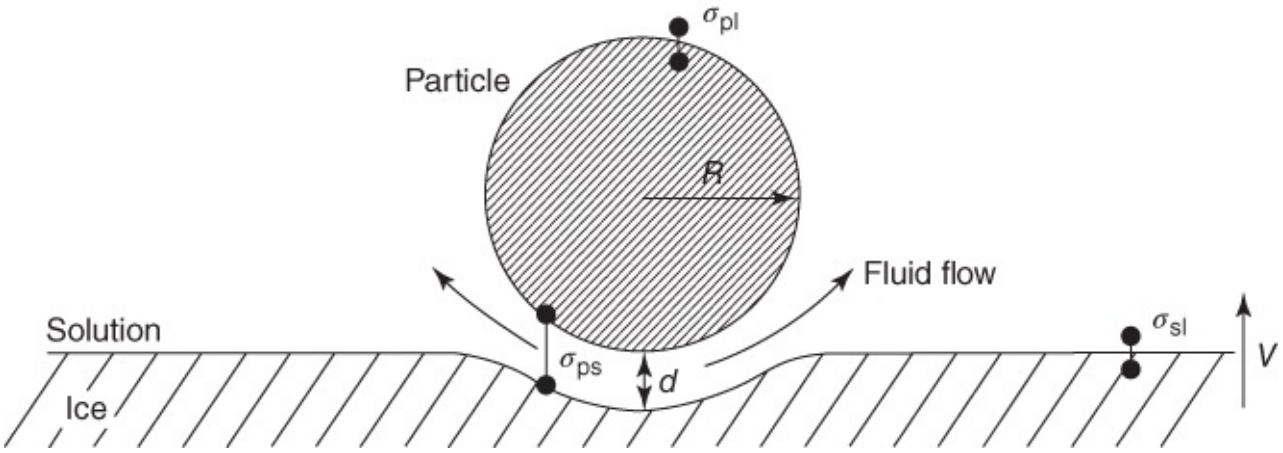

Figure 2.8 Schematic representation for the movement of a particle in front of the freezing front.

Source: Zhang et al. 2005 [19]. Reprinted with permission from Nature Publishing Group.

The attractive drag force can be expressed as in the following equation, derived for the case of a flat interface [36, 37]:

$$F_\eta = 6\pi\eta v r^2/d, \tag{2.3}$$

where η means the viscosity of the liquid suspension medium, v is the velocity, r is the particle radius, and d is the vertical distance of the particle ahead of the freezing front.

By thermodynamics, a particle can be rejected from the freezing front if the interfacial free energy between the particle and the solid phase, σ_{sp}, is greater than the sum of surface free energies of solid–liquid, σ_{sl}, and liquidparticle, σ_{lp}. That is:

$$\Delta\sigma_0 = \sigma_{sp} - (\sigma_{sl} + \sigma_{lp}) > 0. \tag{2.4}$$

If the above equation is not satisfied, the particle will be entrapped by the ice crystals to achieve the state of lowest energy.

For a spherical particle of radius r, with a thin film of liquid between the particle and the freezing point, the repulsive (disjoining) force can be expressed as:

$$F_\sigma = 2\pi r\Delta\sigma_0\left(\frac{a_0}{d}\right)^n, \tag{2.5}$$

where a_0 is the average intermolecular distance in the liquid film, d is the vertical distance

from the particle to the freezing front, and the exponent n ranges from 4 to 5 [36, 37]. However, there are also reports on $n = 2$ for small d, $n = 3$ for larger d, or $n = 1–4$ sometimes used [[37], and references therein].

The critical velocity, indicating the transition from particle rejection to encapsulation by increasing freezing velocity, can be derived by balancing the attractive force and the disjoining force ($F_\eta = F_\sigma$) [37]:

$$v_c = \frac{\Delta\sigma_0 d}{3\eta r}\left(\frac{a_0}{d}\right)^n. \tag{2.6}$$

This equation is based on a flat freezing front. The critical velocity is inversely proportional to the particle radius. It is important to determine the values for d, n, and $\Delta\sigma_0$.

Another equation can be used to calculate the critical velocity. Based on the numerical variation of some parameters affecting the shape of the solid/liquid interface, the critical velocity can be determined from the critical distance, the ratio of thermal conductivities, and a dimensionless parameter (X) including the solute concentration. It is assumed that the crystal and the melt have the same thermal conductivity and no gravitational action, and that the viscosity is independent of concentration and the surface free energies are independent of concentration and temperature. In the case of a pure melt, the critical velocity can be expressed as [38]:

$$v_c = \frac{\Delta\sigma_0 a_0}{12\eta}\frac{1}{r}, \tag{2.7}$$

where the critical distance is kept constant for all particle radii: $d_c = 2a_0$. When the thermal conductivities of the particles and the liquid are different, a parameter μ (the ratio of the thermal conductivities of the particles and the liquid) can be introduced into Equation (2.7) in the denominators.

2.4.2 Effects of Thermal Gradient, Particle Radius, and Viscosity on Critical Velocity

For large particles, both the gravitational force and buoyance force cannot be ignored. During a freezing process, the forces experienced by the particle include the attractive forces (gravity and viscous drag forces), which favour settling and entrapment, and the repulsive forces (buoyance and van der Waals forces), which facilitate the floating of the particles in the liquid and hence more likely the particles being pushed along. By balancing these forces and assuming that the velocities of the particles and the freezing front are the same, an equation to calculate the critical velocity is given as [5, 39, 40]:

$$v_c = \frac{\rho_l}{9\eta\rho_s}\left[\frac{-A^*}{2\pi D d_0} - gDd_0(\rho_p - \rho_l)\right], \tag{2.8}$$

where D is the particle diameter, η is the viscosity of the liquid phase, A^* is the Hamaker constant (= -7.0×10^{-20} J for the ice–water–particle system) [41], d_0 is the minimal distance between the particle and the freezing front, g is the gravitational constant, and ρ_s, ρ_l, and ρ_p are the densities of the solid frozen phase, the liquid phase, and the particle, respectively.

There are other forms of equations that take into account these factors. For a temperature gradient G applied across the sample system, the critical velocity can be expressed as [37]:

$$v_c = k'' \frac{d}{\eta} \frac{1}{r} G. \tag{2.9}$$

When the influence of surface curvature phenomena (Gibbs–Thomson effect) can be ignored and for a 'large' particle, the equation can be given in Equation (2.10), where B_3 is an interaction constant [42]:

$$v_c \propto \frac{1}{\eta r} B_3^{3/4} G^{1/4}. \tag{2.10}$$

Equation (2.7) is based on a pure melt. When a solute is dissolved in the liquid phase, the critical velocity is influenced by the temperature gradient as:

$$v_c \propto \frac{\sqrt{G}}{r}. \tag{2.11}$$

The velocity can be independent from the particle radius if the solute concentration is very high:

$$v_c \propto \frac{G}{C_0}. \tag{2.12}$$

When calculating the interaction energy between macroscopic bodies (the van der Waals force for two polarizable atoms can be expressed as $W = -C/r^6$, where C is the coefficient in the atom–atom pair potential and r is the distance between the two atoms) it can be separated into two independent parts, the Hamaker constant (generally, $A^* = \pi^2 C \rho_1 \rho_2$, where ρ_1 and ρ_2 are the number of atoms per unit volume in the two bodies; A is approximately 10^{-19} J), containing information about the materials involved, and a force equation taking into account the geometric parameters of the interactions. Equations (2.7) and (2.10) can be compared or linked by the interaction constant B_3 and the Hamaker constant A^* as given in the equation below [42]:

$$B_3 = -6\pi A^* = 72\pi^2 d_c^2 \Delta\sigma_0. \tag{2.13}$$

In a study on engulfment of latex particles (negatively charged polystyrene microspheres with the radii in the range of 1–10 μm), Lipp and Körber proposed an empirical function of particle radius r, temperature gradient G, and the viscosity η to fit the obtained data [42]:

$$v_c = P\left(\frac{G^x}{r^y \eta^z}\right). \tag{2.14}$$

The best fit of the data produced different values of x, y, z. When the value of $x = 0.25$, $y = 1.0$, and $z = 1.0$, Equation (2.14) corresponds to Equation (2.10).

The deformation of the ice–liquid interface and the presence of the liquid film (Figure 2.10) may be attributed to interfacial premelting. When the particle is large enough, the effects of interface curvature may be minimal. However, the thermal conductivity and density of the particles can influence the freezing phenomena. It has been found that the critical velocity is less sensitive to the temperature gradient and the precise dependence changes with different interaction types. Particle buoyancy can enhance or reduce the tendency for the particle to be captured [43].

2.4.3 Geometry and Interfacialcurvature Effects

When the particle is small, the effect of interfacial curvature is eminent. For a smooth spherical particle and freezing fronts of different geometry, the critical velocity equation can be generalized as [36, 37]:

$$v_c = k' \frac{1}{\eta} \frac{1}{r^m}, \tag{2.15}$$

where the exponent m varies between 1 and $^3/_2$ and k' is a proportionality factor depending on the geometry and $\Delta\sigma_0$.

The interface curvature can be considered specifically when developing theoretical models. When deviated from a planar freezing interface, the melting temperature of a pure substance is reduced by an amount proportional to the interface curvature $\mathcal{K}$ and the surface energy σ_{sl} (Equation (2.16)). This phenomenon is often called as the Gibbs–Thomson effect. Intermolecular interactions can cause the formation of melted fluid between the particle and the freezing interface, even when the interface is planar. The interface temperature T_i can be expressed as [44]:

$$T_i = T_m - \frac{T_m \sigma_{sl}}{\rho_s q_m} \mathcal{K} - T_m \left(\frac{\lambda}{d}\right)^v, \tag{2.16}$$

where T_m is the equilibrium melting temperature, ρ_s and q_m are the solid density and the latent heat, respectively, and λ is a length scale characterizing the strength of the intermolecular interactions. The exponent v depends on the type of intermolecular forces that dominate; $v = 2$ for longrange electrical interactions; $v = 3$ for nonretarded van der Waals forces; and $v = 4$ for retarded van der Waals interactions [44, 45].

By comparing the relative importance of intermolecular interactions and interface curvature in controlling the interface temperature, the characteristic radius of the particle r_c can be given as

[44]:

$$r_c = \frac{\sigma_{sl}}{\rho_s q_m}\left(\frac{T_m}{\lambda G}\right)^{\nu/(\nu+1)}. \tag{2.17}$$

Typically, r_c is of order 10^{-4} m. When the particle radius r r_c, the curvature effects may be neglected.

The calculated interface profile is used to evaluate the force balance and the particle behaviour. Both the nonretarded van der Waals forces (controlling the thickness of the pre melted film) and the longrange electrical interactions are considered. A generalized velocity scale *ú*, by balancing the counteracting forces, is expressed as [44]:

$$\acute{u} \equiv \frac{\sigma_{sl}\lambda^2}{6\eta r^2}\left(\frac{\rho q_m r}{\sigma_{sl}}\right)^{\frac{2}{\nu}}. \tag{2.18}$$

When longrange electrical interactions dominate ($\nu = 2$), this indicates that $v_c \propto r^{-1}$. When retarded van der Waals interactions dominate ($\nu = 4$), $v_c \propto r^{-3/2}$. When nonretarded van der Waals interactions dominate ($\nu = 3$, r r_c), this will give $v_c \propto r^{-4/3}$. It is noted that the velocity scale is independent of the temperature gradient G. The film thickness in the inner region is determined mainly by the balance between interfacialcurvature effects and nonretarded van der Waals interactions. Because the lubrication force (attractive force) and the thermomolecular force (disjoining force) are strongest here, the particle velocity is insensitive to G [44].

2.5 Morphology Instability at the Freezing Front

During the freezing of particle suspension, the freezing front rejects and pushes the particles at low freezing rate. With the increase of freezing rates (usually by applying a higher temperature gradient across the liquid sample), the planar interface is disturbed and broken into dendritic or cellular ice crystals while the particles are closely packed between the ice dendrites. This is the key point that indicates that the icetemplating technique via directional freezing can be used to produce porous materials with different pore morphologies [7, 12, 19, 46, 47].

The interface instability is a result of constitutional supercooling in the liquid phase just in front of the freezing front. This indicates a lower freezing temperature in the local zone than the equilibrium temperature. The reason for supercooling in a colloidal system is the higher concentration of the particles close to the freezing front. In the constitutionally supercooled region, a small protrusion of ice crystals experience a greater driving force than the planar front and hence grow faster. With the protrusions becoming larger, a cellular or dendritic morphology is formed [21].

2.5.1 Mullins–Sekerka Equation

A theoretical equation was developed by Mullins and Sekerka by calculating the time dependence of the amplitude of a sinusoidal perturbation of infinitesimal initial amplitude introduced into the planar shape. The critical mathematical simplification was the use of steadystate values for the thermal and diffusion fields [48]. The equation was developed to investigate the stability of a planar interface during solidification of a dilute binary alloy. But it has also been applied to the freezing of aqueous colloidal suspensions. The equation is given below [19, 21, 48, 49]:

$$\frac{\dot{\delta}}{\delta} = \frac{\left\{V\omega\left\{-2T_M\Gamma\omega^2\left[\omega^* - \frac{V}{D}(1-k)\right] - 2G\left[\omega^* - \frac{V}{D}(1-k)\right] + 2mG_c\left[\omega^* - \frac{V}{D}\right]\right\}\right\}}{\left\{2G\left(\frac{k_s - k_l}{k_s + k_l}\right)\left[\omega^* - \frac{V}{D}(1-k)\right] + 2\omega mG_c\right\}}, \tag{2.19}$$

$$\omega^* = \frac{V}{2D} + \left[\left(\frac{V}{2D}\right)^2 + \omega^2\right]^{1/2}, \tag{2.20}$$

where δ is the size of the perturbation,V is the growth velocity, ω is the frequency, T_M is the equilibrium melting point, Γ is the ratio of the surface energy and the latent heat of fusion, D is the diffusion coefficient, k is the partition coefficient, G is the temperature gradient, G_c is the solute concentration gradient at the interface, m is the slope of the liquidus line on the phase diagram, and k_s and k_l are the thermal conductivities of the ice and solution, respectively.

When using this equation to predict instability, there is always a sinusoidal perturbation of certain wavelength λ_0, above which waves grow, below which waves decay, and at which the wave must have constant amplitude.

Usually, the actual primary spacing of the formed ice dendrites is greater than the instability wavelength, which is likely the result from some degree of coarsening of the structure during growth. Different models have been developed to predict the primary spacing, based on different assumptions. However, the expression for the primary spacing (λ_d) can be generally given as [21]:

$$\lambda_d = AG^{-1/2}V^{-1/4}, \tag{2.21}$$

where A is dependent on variables such as the diffusion coefficient, partition coefficient, and liquidus slope; G is the temperature gradient and V is the ice crystal growth velocity.

In a directional solidification study of ice crystallization in sucrose and pullulan solutions, it was found that the Mullins–Sekerka equation could provide a reasonable prediction of the instability wavelength over a range of velocities. The primary spacing found is in agreement with Equation (2.21). However, it was not good for the pullulan solution. The discrepancy was attributed to the long polymer chains and hence the hindered diffusion mechanism [21].

From the investigation of freezing colloidal suspensions or polymer/colloidal suspensions [19,

46], the primary spacing or the lamellae thickness is inversely proportional to the freezing velocity. That is, the faster the freezing velocity, the narrower the primary spacing. An empirical dependence can be correlated between the primary spacing λ (or wavelength) and the freezing velocity v in parallel to the temperature gradient:

$$\lambda = Av^{-n}, \tag{2.22}$$

where n may be in the range of 1–4 [6, 50].

2.5.2 Linear Stability Analysis

It is well known that dissolution of ionic compounds can significantly reduce the freezing temperature. The degree of freezing temperature depression is directly related to the concentration of the particles. It has been noticed that a colloidal suspension can become constitutionally supercooled as well. Peppin et al. developed a mathematical model for the solidification of a suspension of hardsphere colloids [51]. It showed that the highly non linear functional dependence of the diffusion coefficient on the volume fraction gave rise to a range of behaviours. For small particles where Brownian diffusion dominates, constitutional supercooling occurs at the interface. For larger particles where Brownian diffusion is weak, the particles form a porous layer above the interface.

In a further study, following the hardsphere equation of state, a linear stability analysis of a planar freezing interface has been described [52]. After solving steadystate configuration, the steady profile is perturbed via normal modes. The governing equation in the perturbed quantities is linearized and the resulting ordinary differential equation is solved to determine conditions under which the interface is stable (perturbations decay in time) or unstable (perturbations grow in time). Considering the dilute limit (the concentration $C \to 0$ so that the diffusion coefficient $D \to 0$), the characteristic equation can be obtained as [51]:

$$\sqrt{1 + 4(\sigma + \alpha^2)} = 1 - 2k_s - 2(\sigma + k_s)(M^{-1} - 1 + \alpha^2\Gamma)^{-1}, \tag{2.23}$$

where σ is the growth rate of the disturbance and α is the wavenumber of the normal modes along the interface. The growth rate σ determines whether or not a particular perturbation will grow in time. k_s is the segregation coefficient that depends on the interfacial concentration and the solidification velocity. M is the morphological number while Γ is a surface energy parameter (detailed definition can be found in Ref. [52]). This equation is similar to the Mullins–Sekerka equation developed from dilute alloys, with an important distinction that here the coefficients depend on the particle radius. It is found that the interfacial stability depends strongly on the size and concentration of the particles. A stabilizing effect is observed when increasing the particle sizes whilst increasing the concentration can destabilize the interface.

Experimental evidence has been obtained to verify the morphological instability [20]. The compressibility (osmotic pressure) is measured to predict the freezing point depression as a function of particle volume fraction (bentonite particles). The freezing point may decrease to −8 °C at a volume fraction of about 0.5. Measurement of permeability is used to predict the

concentrationdependent diffusivity. By considering these parameters, for a given temperature gradient, the critical conditions for the onset of constitutional supercooling can be obtained from the following equation [20]:

$$\hat{G}_T \leq \frac{d\hat{T}_f}{d\hat{z}}|_{\hat{z}=0} = -P_e \hat{T}_{f\emptyset} \frac{\emptyset_i}{\hat{D}}, \tag{2.24}$$

where dimensionless temperature gradient and diffusivity are used. P_e is the Peclet number and ∅ is the particle volume fraction. This theoretical threshold can be determined experimentally, demonstrating that the colloidal suspensions can be treated analogously to atomic or molecular alloys [20].

2.5.3 Morphology Zones and Stability Diagram

From the initial freezing of a colloidal suspension to the steadystate freezing, the morphologies in different zones can vary significantly. This may be shown by imaging the freezedried and sintered samples (Figure 2.9) [47]. When freezing aqueous alumina slurry by contacting cold finger on two sides, the initial freezing rate is fast and the freezing fronts encapsulate all the particles. This results into a dense layer of the materials. With the increasing distance from the cold finger, the freezing velocity decreases gradually and the microstructures of the resulting material change from columnar, lamellar, lamellar/dendritic, to a more steadystate of lamellar/dendritic ice front with homogeneous lamellar thickness (Figure 2.9). Two possibilities can be considered for the ice morphology transition from planar to columnar [47]. The first possibility is the constitutional supercooling as described in the Mullins–Sekerka theory. The second possibility for the breakdown of the planar interface may be triggered by the presence of particles in the liquid. The breakdown may occur when the velocity is below the threshold for the onset of constitutional supercooling [20].

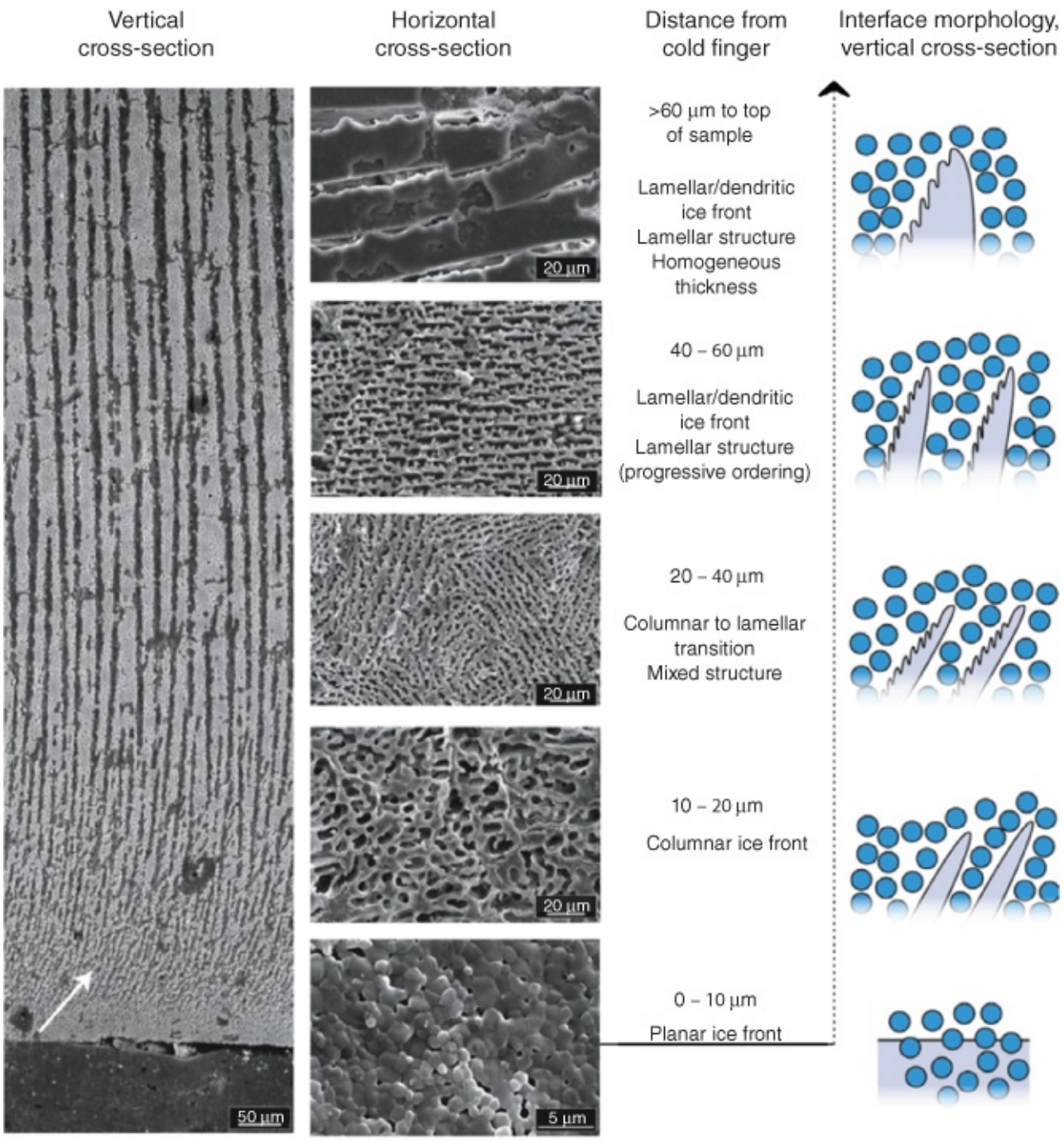

Figure 2.9 Scanning electron microscopic (SEM) images of a sintered freezecast alumina sample, showing the change of ice front morphology with varying distance from the cold finger. The schematic on the right represents how the particles are encapsulated in or rejected from the ice front.

Source: Deville et al. 2007 [47]. Reprinted with permission from Elsevier.

The morphological change of ice front during the freezing of aqueous alumina slurry has also been directly observed by in situ Xray radiography and tomography [53, 54]. The morphology and evolution of the ice crystals are classified based on the presence and percentage of crystal orientations. Two types of ice crystals are described: zcrystals where the crystals are orientated to the freezing direction (zaxis) and are growing faster in this direction, and *r*crystals (*r* means random) where the crystals are more or less in the *xy* plane (radial

direction). In the zone very close to the cold surface, because nucleation is spatially homogeneous, the populations of *z*crystals and *r*crystals are spatially homogenously distributed. In the next zone, the crystals grow larger and the packing of the particles become more efficient, the percentage of *z*crystals slowly increase. In the zones further away from the cold surface, the *r*crystals stop growing and then only *z*crystals grow from the suspension [53]. This leads to a steadystate freezing stage where the particles are rejected from *z*crystals and particle redistribution occurs in the *xy*plane. Particle redistribution depends on the interface velocity. From moderate to slow velocities (1 μm s^{-1}), the particles migrate by Brownian diffusion, leading to a builtup layer of concentrated particles ahead of the interface. However, for the conditions normally used in the freezing of colloidal suspensions for freeze cast materials, the Brownian diffusion may be neglected, as observed in this study [54]. The concentrated particle layers observed in the radiographs may be due to the larger particles approaching the crystal separation distance that cannot be accommodated between the primary dendrites.

Theoretical models are often developed based on single particle in dilute colloidal suspensions [36–52]. For real situations where freezing of colloidal suspensions is used for the preparation of porous materials, those models cannot predict the complex behaviour. Direct observation of such a freezing system and the corresponding explanation by multiparticle models, where the possible interactions between the particles are considered, are required in this research field. Global and localized interface instabilities have been observed by in situ Xray radiographs (Figure 2.5) [25]. The instability can be regarded as inducing growth of ice crystals in the plane perpendicular to the freezing direction. The localized instabilities are transverse crystals between the ice crystals. A stability diagram can be built based on this study (Figure 2.10), including unstable domains and metastable domains. The metastable domains are defined as those where no instabilities are observed and homogeneous crystals are obtained at high interface velocity and/or large particles. The instability is attributed to partial diffusion of the particles ahead of the freezing interface. Thus, the resulting higher concentration of the suspension in front of the freezing front leads to the depressing of the freezing point [20], hence a constitutional supercooling situation. For high freezing velocity, the diffusion is very limited and the freezing zone (in a constitutional supercooling state) is within the growing crystal tips. The zone ahead of the crystal tips is in a stable state, which does not incur instability and yields homogenous materials. This situation is referred to be in the metastable domains. At lower freezing velocities, the diffusion is enhanced. The particle redistribution leads to the formation of a diffusion layer (still in a constitutional supercooling state) appearing beyond the growing crystal tips. The nucleation of the crystals occurs in the supercooled zone and hence the instability [25].

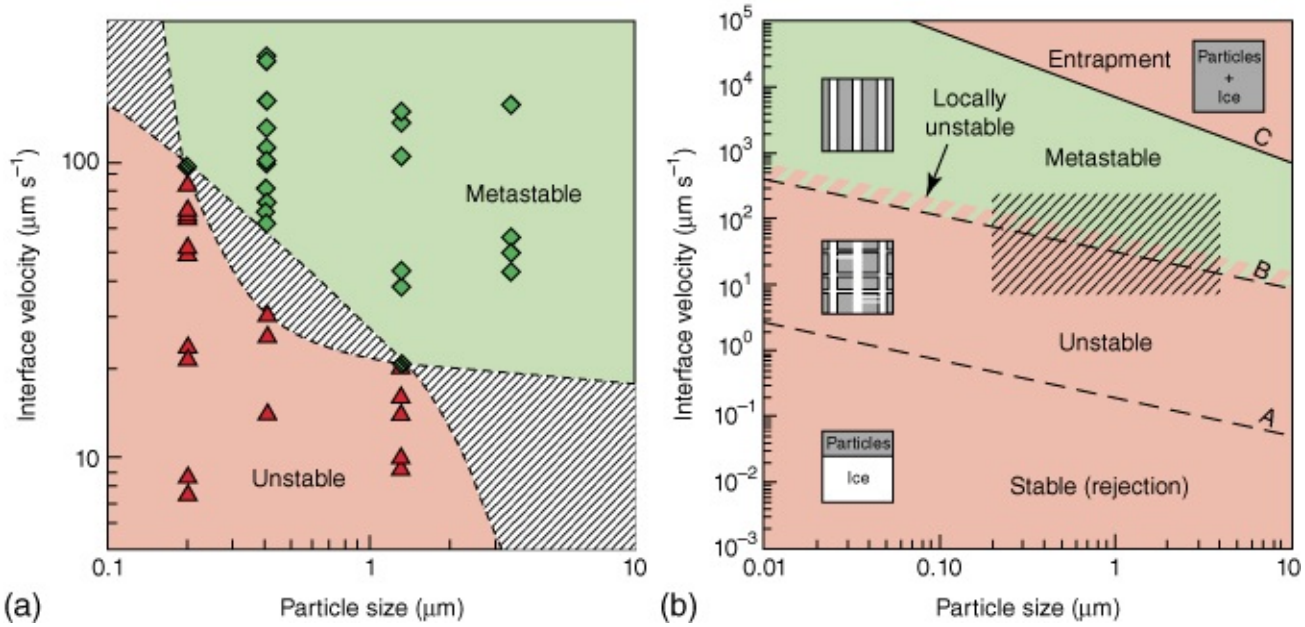

Figure 2.10 The stability diagrams constructed from freezing aqueous alumina slurry as observed by in situ Xray radiography. (a) The ice stability diagram. The hatched area is an estimated domain where the metastable to unstable regime transition can occur. (b) General stability and the structural diagram. The hatched area indicates the conditions investigated. The diamond and triangle symbols indicate the data points that are measured.

Source: Deville et al. 2009 [25]. Reprinted with permission from Nature Publishing Group.

The traverse ice crystals caused by the localized instability can lead to porosities in the wall of the freezecasting material. This may explain why many of the materials are prepared under similar freezing conditions although the compression stabilities can vary considerably among different reports [55]. The traverse growth of ice crystals can be regarded as ice lenses, which is often observed in geophysics. Ice lenses are the ice crystals growing in the supercooled zone in the direction perpendicular to the freezing direction or the temperature gradient. The formation of the supercooled zone has been attributed to the partial diffusion of the particles. During the freezing of alumina dispersions with varying concentrations of ionic additives, different zones ahead of the crystals tips are observed [55]. At a low concentration of the ionic additive (but in the optical range to obtain the strongest repulsion), accumulated particle layer (APS), particledepleted region (PDR), and then the liquid suspension are in front of the crystals tips in turn. With the increasing concentration of the ionic additive, the PDR becomes thinner and then disappears. The formation of the PDR is quite unusual. This is explained by the concentration of free ions rejected from the freezing front, increased ionic strength compressing the repulsion charged layer of the alumina particles, and the flocculation and aggregation of the particles. The settlement of large aggregates leads to the formation of a PDR [55]. As such, the supercooled zone should originate from the particle flocculation rather than the partial particle diffusion. The PDR is initially formed between the ice crystals but can move above the crystals tips when the suspension contains low concentration of ionic dispersants, favoured by low viscosity and high zeta potential. The ice lenses formed in the PDR can explain the defects formed in the freezecasting materials. The growth of ice lenses in the high velocity region, sometimes termed as ‘banding’, may question the credibility of the

assumption of local equilibrium at the freezing interface. In order to model this non equilibrium segregation of ice crystals, the Boltzmann velocity distribution of a particle has been used to derive an expression for the segregation coefficient at the interface as a functional of the freezing velocity and particle radius [56]. A phase diagram can be constructed and used to explain the formation of bandlike defects.

Timelapse, 3D in situ imaging shows that the thickness of the ice crystals and the horizontal growth of ice crystals (ice lenses) increase with freezing time [57]. The thickness of the horizontal crystals reaches a plateau of about 25 μm after about 60 s. A closeup view of the 3D reconstruction of the ice crystals shows the tilted growth of ice crystals from the imposed freezing direction and also the dendrites on one side of the ice crystals. This is also observed by SEM imaging of the sintered freezecasting alumina [47]. As schematically shown in Figure 2.11, tilting of the ice crystals is the result of the direction imposed by the temperature gradient and the favoured direction of anisotropic crystal growth [57]. Tilting of the ice crystals becomes greater when the freezing rate (usually corresponding to the temperature gradient) decreases. A threshold below which ice crystals tilt exists in the 3–3.5 $\mu m\, s^{-1}$ range [57]. The dendrites grow on one side with respect to the temperature gradient direction. Dendrite growing on the other side is energetically unfavourable [47, 57].

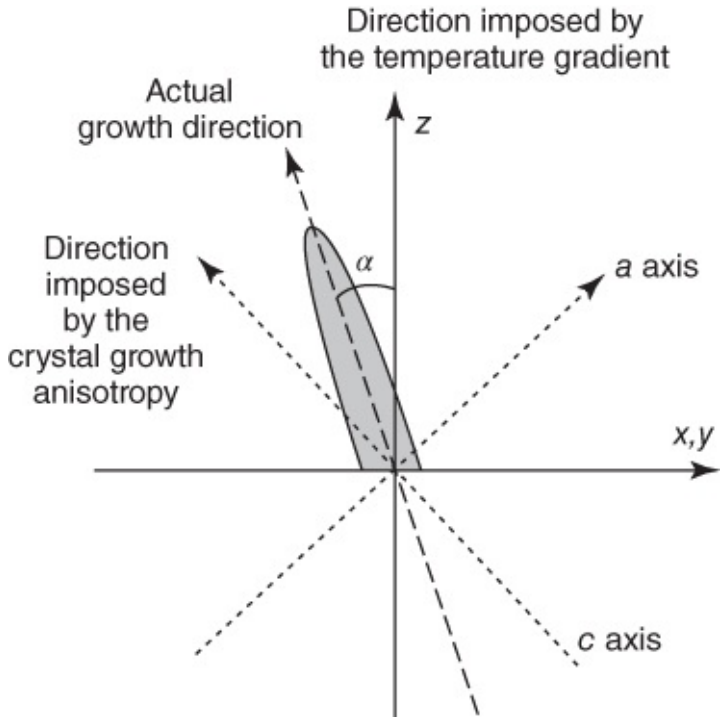

Figure 2.11 The schematic representation shows the tilted growth of ice crystals, resulting from the relationship between the imposed temperature gradient and the preferred growth direction.

Source: Deville et al. 2013 [57]. Reprinted with permission from Elsevier.

Ice banding is a pattern of ice segregation that results from freezing concentrated colloidal suspensions, which is a familiar phenomenon seen in geophysics such as frost heave. Directional solidification of the concentrated alumina slurry (mean particle diameter ~0.32 μm, 60 wt% or 27 vol%) was performed to investigate the ice segregation patterns [58]. As

shown in Figure 2.12, at the low freezing rate (0.5–2 μm s^{-1}), the segregated ice lenses are formed in the frozen solid with a partially frozen layer and a compacted layer above the freezing interface [58]. When the freezing velocity is increased (3–4 μm s^{-1}), like the breakdown of planar interface in the dilute system, the ice lenses become disordered with the compact layer diminishing. In the high velocity region (5–10 μm s^{-1}), with no ice lenses or compacted layer, the ice banding is highly modulated, giving a wavy and jagged appearance. The compacted layer is randomly closely packed, with particle fraction $\Phi_p \approx 0.64$. The compaction of the particles occurs as a sol–gel transition because they cannot be redispersed in the solvent. It indicates an irreversible aggregation, overcoming the maximal repulsion between the particles. According to the Derjaguin–Landau–Verwey–Overbeek (DLVO) theory, there is a peak of repulsion force at a critical distance between the particles. Passing that critical distance, the cohesive force is dominating and the particles are aggregated. The cryostatic suction during ice segregation can easily produce compressive stresses that are much larger than the typical repulsive force value (≤10 kPa), ensuring the particles bond together [59]. This is also evidenced by a SAXS study demonstrating the particles in touching distance [35].

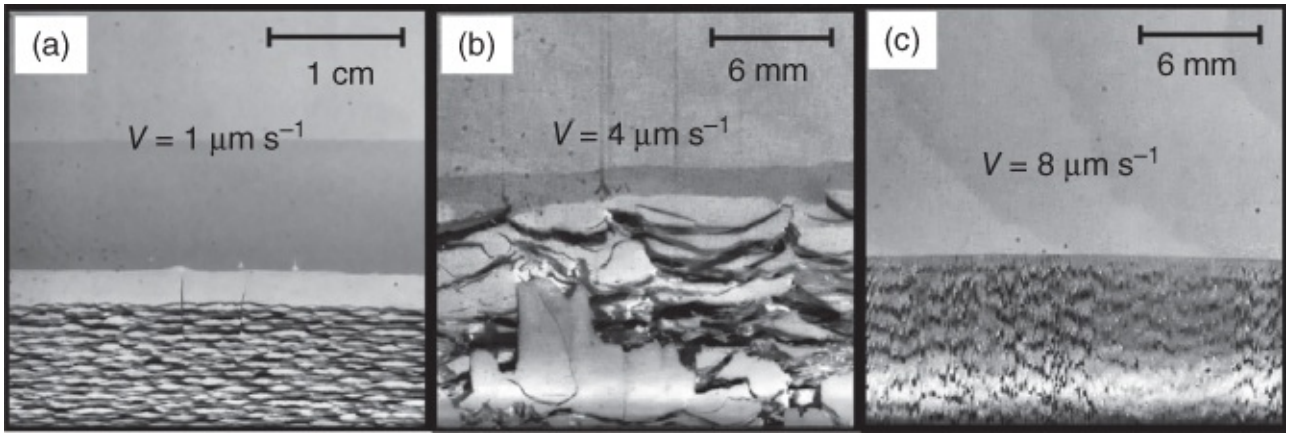

Figure 2.12 Images show the quasisteady ice segregation patterns from directional solidification of concentrated alumina slurries at different pulling speed. The segregated ice appears black while the colloid appears grey. (a) At low velocity, the ice bands are crack like in the frozen region, illustrating the formation of ice lenses, with compacted layers (dark grey) and partially frozen layer (light grey). (b) At medium velocity, ice lenses become disordered, with diminishing compaction layer. (c) At high velocity, periodic ice banding with a wavy appearance forms. Vertical icefilled cracks can also be observed.

Source: Anderson and Worster 2012 [58]. Reprinted with permission from American Chemical Society.

Quite importantly, the partial frozen layer can be regarded as a frozen fringe, which is an interconnected liquid network maintained in the frozen fringe due to the existence of unfrozen water near the particle surface and in the pendular region near the pore throat. This supercooled water is the result of curvature near the throat of the pore and interfacial pre melting. The thermomolecularly generated pressure gradient pushes the particles towards the warmer region and drives the liquid moving towards the colder region to sustain ice lens growth. When a new ice lens is nucleated within the frozen fringe, it can intercept the water

supply of its predecessor that will stop growing. The repeating of this process can eventually produce a regular pattern of ice lenses and compaction layer [59].

Rigidice models have been developed for this ice segregation phenomenon (ice lenses and compaction). It assumes that the pore ice and ice lens form a rigid interconnected body of ice and the forces generated do not deform the poreice network [60]. A related theoretical framework in the context of frost heave is developed, where the forces are derived directly from the thermophysical interactions between the constituents of partially frozen suspension [61]. This model is extended to allow for an evolving compaction front, where particles aggregate and form a cohesive matrix. The developed model is able to elucidate the role of compaction layer in ice segregation [59].

2.6 Effect of Parameters on the Structure and Morphology of Icetemplated Materials

There are not many studies on how the freezedrying process impacts the structure of ice templated materials, except the evaluation of freezedried cakes in the pharmaceutical and food industries. The parameters that have been investigated extensively can be classified into two categories: formulation of solution/suspensions and control of the freezing conditions.

2.6.1 Formulation of Solution/Suspensions

2.6.1.1 Solutes or Particles

A solute can be dissolved in a solvent (usually water) to form a solution, which is then frozen and freezedried to produce an icetemplated material. Because small molecular compounds would normally form powders after freezedrying, polymers are usually added to the solution. The entanglement of long polymer chains can lead to the formation of stable porous structures. The main parameters for polymers include molecular weight, hydrophobicity, and charges. Stronger interaction between the polymer chains, e.g. H bonding, π–π interaction, and electrostatic interaction, can have big impacts on the stability and pore morphology of the resulting structures. Small molecules may be included in polymer solutions as additives to introduce additional functions or properties into the icetemplated materials.

Both microparticles and nanoparticles have been extensively used for freezecasting materials. Different solvents have been used but water is always the most preferred one because of its low cost and green credentials. The main parameters for particles include: particle size, nature of particle material (e.g. organic, metal, or metal oxide), and particle shape. As particulate suspensions are the most commonly investigated systems both for materials preparation and fundamental studies, the following discussion of parameters is mostly relevant to particles.

2.6.1.2 Particle Size and Shape

For large particles, depending on their density (particularly the density difference compared to

the density of the solvent), the gravitational force/buoyance force can play an important role on rejection/encapsulation of the particles by the freezing front, resulting in a significant impact on the morphology and stability of the resulting materials. Although most models are based on spheres, the shapes of microparticles (which are usually prepared by grinding or precipitation) used in freeze casting may not be spherical. The irregular shape and larger size of the particles can result in low packing efficiency and slow moving during freezing, which may have significant effects on porosity, morphology, and stability of the prepared materials [5, 6, 62]. Nanoparticle suspensions are usually quite stable. They may be readily selfassembled into microwire or nanowire structures by the icetemplating process [7, 12].

The size of the polymers can be varied by molecular weight. But the difference in the structures can be quite subtle, providing that icetemplated materials can be formed.

2.6.1.3 Concentration of Polymers or Particles

The concentration of a polymer solution can have a distinct effect on the structure of the ice templated polymeric materials. At medium or high concentrations (e.g. 5 wt% or higher), aligned porous or randomly porous polymers can be produced [7, 19]. However, at very low concentrations (e.g. 0.5 wt% or lower), polymeric nanofibres may be formed [63, 64]. This effect of polymer concentration depends on the type and molecular weight of the polymers, and also the type of the solvent used.

Similarly, the concentration of particulate suspensions may result in wire structures or porous materials [7, 65]. Most of the reports have employed suitable concentrations in a view to produce porous ceramics with controlled morphology and mechanical stability [5, 6, 12]. However, the concentrated particulate suspensions may generate porous ceramics with periodic ice lenstemplated structures rather than the usual layered or unidirectional microchannel structure [55, 58].

2.6.1.4 Additive or Binder

Additives and/or binders are required when processing particulate suspensions [5, 6]. First, it helps to stabilize a homogeneous suspension which is crucial for the freezecasting process. Common surfactants (e.g. ionic surfactants) or polymers with stabilizing effects, including commercial polymers with trade names, poly(vinyl alcohol) and poly(vinyl pyrrolidone), can be added for this purpose. The binder is to hold the particles together and maintain a stable structure after freezedrying. A polymer additive may act both as a stabilizer for the suspension and as a binder for the freezedried material. If the target is to produce porous ceramics, the amount of additives used is usually kept to optimum and minimum. This is to reduce the processing costs and also to reduce the potential shrinkage or defects after sintering the freezedried bodies.

This approach can be further utilized to produce porous composite materials. Depending on what is required, the main component can be polymer or particles. The distribution of particles in the polymer and the interaction between polymer and particles are two important parameters. Usually, it is required to have a homogenous distribution of particles and strong

interaction between the polymer and particles to generate porous composites with desired pore structure and mechanical stability.

2.6.1.5 Solvent

In addition to the cost and environmental consideration, the selection of solvents mainly depends on their suitability for freezedrying. In this regard, high melting point and high vapour pressure are the criteria to be considered. There is no doubt that water is the most used solvent. But other solvents have been used as well. For example, camphene, *tert*butylalcohol, naphthalenecamphor have been used as solvents for particle suspensions to produce freeze casting materials [5, 6, 12]. Dichloroethane, *o*xylene, dimethyl sulfoxide (DMSO), cyclohexane, and compressed CO_2 have been used for solutions or emulsions [7, 19, 66–69].

2.6.1.6 Emulsion

In addition to solution and suspensions, freezing and freezedrying of emulsions have also been used to prepare porous polymers and composite materials. Emulsion is a mixture of two immiscible liquids (usually water and an immiscible organic solvent), with one liquid as droplet phase dispersed in the other continuous liquid phase. Surfactants are usually required to stabilize the droplets in the emulsion. The volume percentage of an emulsion can be varied in a wide range. This can be very powerful when emulsion templating is used to prepare porous materials [70]. The emulsion structure is usually locked in by polymerization. Freezing has provided an effective and alternative way of locking in the emulsion structure. Usually, a polymer can be dissolved in the continuous phase with the droplets only consisting of solvent. After the removal of the solvents from both the continuous phase and the droplet phase by freezingdrying, porous materials can be produced. For an oilinwater emulsion (where oil phase is the droplet phase), hydrophobic compounds may be dissolved in the droplet phase. After freezedrying, hydrophobic nanoparticles in hydrophilic porous polymer matrix can be formed [68, 69]. This nanocomposite can be readily redissolved in water, producing stable aqueous nanoparticle dispersions, which have important applications for nanomedicine [71]. While particles can be suspended in the continuous phase for preparation of composite materials, colloids or nanoparticles can also be used as surfactants to form Pickering emulsions to make either inorganic or composite materials. By varying the percentage of the oil droplet phase in an emulsion, combining emulsion templating and ice templating, a highly efficient route can be established for producing porous materials with systematically tuned pore morphology and porosity. This approach can also be extended to double emulsions [72].

2.6.2 Control of the Freezing Conditions

In order to produce the icetemplated materials with the desired pore structure and formats, the freezing process may be carried out in different ways, as detailed in Chapter 1. The key point in controlled freezing is the control of freezing velocity. Indeed, the theoretical models described above are always related to the freezing velocity. Qualitatively, the freezing velocity can be varied to tune the pore sizes [6, 19, 50]. In general, fast freezing leads to small ice crystals and hence small pores in the resulting freezedried materials while the freezing rate

should be reduced if a material with larger pore sizes is required.

However, it is very difficult to accurately control the freezing velocity when preparing porous materials via the icetemplating approach. It is generally accepted that the freezing velocity may be determined by the temperature between the freezing front and the cooling plate and the thermal conductivities of solid phases involved. For the fundamental studies in freezing, quite often, a sample cell is placed across two separately temperaturecontrolled metal plates and is pulled at certain speeds towards the cold plate. A temperature gradient is created between the two plates (the temperature difference divided by the gap between them), which is the driving force for the directional solidification of solutions or colloidal suspensions. However, the same temperature gradient can be obtained from different temperatures of the plates, as long as the temperature difference is the same. This may have a significant impact on the removal of the heat generated by the freezing (solidification) of the solvent.

When a layer of liquid freezes at its thermal transition temperature T_E, the solidification enthalpy h_E is given out as heat and has to be conducted away through the frozen solid to the cooling plate. The velocity at a given time t where the solidification front progresses can be described as [6]:

$$v(s) = \frac{ds}{dt} = \frac{\lambda_S(T_E - T_0)}{\rho_L h_E}\left(s + \frac{\lambda_S}{k}\right)^{-1}, \tag{2.25}$$

where s is the thickness of the liquid layer, λ_S is the thermal conductivity of the frozen solid, k is the heat–transfer resistance, ρ_L is the liquid density, and T_0 is the temperature of the cold plate (or the temperature of the cold liquid that cools the plate). It is clear that to maintain a constant velocity, T_0 should vary according to Equation (2.25).

When freezing a slurry, in order to calculate the thermal conductivity of the solidified particles, the packed particles between the ice lamellae crystals can be treated as a bed of closed particles. The thermal conductivity of such a packed bed can be predicted using the Krischer–Kröll model, from the amount of the serial component, the volume fraction of the continuous ice phase, and the thermal conductivities of the particles and ice. Assuming that the frozen slurry has alternate ice lamellae and packed particle layers and the lamellae to be parallel to the heat flow direction, the total thermal conductivity of the frozen slurry can be calculated by the following equation [6]:

$$\lambda_S = \Psi\lambda_I + (1 - \Psi)\lambda_B, \tag{2.26}$$

where Ψ is the volume fraction of the ice phase and λ_I is the thermal conductivity of pure ice, while λ_B is the predicted thermal conductivity of the packed particles between ice lamellae. Once λ_S is obtained, one can use Equation (2.25) to calculate the freeze velocity.

2.7 Summary

In this chapter, the fundamental aspects of controlled freezing for icetemplated materials have been described. The basics of ice crystals, the instruments used for the fundamental study, and the different theoretical models to predict particle fate and ice morphology and dimensions when freezing aqueous colloidal suspensions are covered. The important processing parameters, with the aim to fabricate the icetemplated materials of desired structures and properties, are outlined.

References

1 Petzold, G. and Aguilera, J.M. (2009). Ice morphology: fundamentals and technological applications in foods. *Food Biophys.* 4: 378–396.

2 Hubel, A., Darr, T.B., Chang, A., and Dantzig, J. (2007). Cell partitioning during the directional solidification of trehalose solutions. *Cryobiology* 55: 182–188.

3 Halde, R. (1980). Concentration of impurities by progressive freezing. *Water Res.* 14: 575–580.

4 Mahler, W. and Bechtold, M.F. (1980). Freezeformed silica fibers. *Nature* 285: 27–28.

5 Li, W.L., Lu, K., and Walz, J.Y. (2012). Freeze casting of porous materials: review of critical factors in microstructure evolution. *Int. Mater. Rev.* 57: 37–60.

6 Wegst, U.G.K., Schecter, M., Donius, A.E., and Hunger, P.M. (2010). Biomaterials by freeze casting. *Phil. Trans. R. Soc. A* 368: 2099–2121.

7 Qian, L. and Zhang, H. (2011). Controlled freezing and freeze drying: a versatile route for porous and micro/nanostructured materials. *J. Chem. Technol. Biotechnol.* 86: 172–184.

8 Maxwell, W., Gurnick, A.R., and Francisco, A.C. (1954). Preliminary Investigation of the FreezeCasting Method for Forming Refractory Powders. *NACA Research Memorandum, Lewis Flight Propulsion Laboratory*.

9 Tong, H.M., Noda, I., and Gryte, C.C. (1984). Formation of anisotropic ice–agar composites by directional freezing. *Colloid Polym. Sci.* 262: 589–595.

10 Fukasawa, T., Deng, Z.Y., Ando, M. et al. (2001). Pore structure of porous ceramics synthesized from waterbased slurry by freezedrying process. *J. Mater. Sci.* 36: 2523–2527.

11 Schoof, H., Apel, J., Heschel, I., and Rau, G. (2001). Control of pore structure and size in freezedried collagen sponges. *J. Biomed. Mater. Res.* 58: 352–357.

12 Deville, S. (2013). Icetemplating, freeze casting: beyond materials processing. *J. Mater. Res.* 28: 2202–2219.

13 Malkin, T.L., Murray, B.J., Brukhno, A.V. et al. (2012). Structure of ice crystallized from

supercooled water. *PNAS* 109: 1041–1045.

14 BartelsRausch, T., Bergeron, V., Cartwright, J.H.E. et al. (2012). Ice structures, patterns, and processes: a view across the icefields. *Rev. Mod. Phys.* 84: 885–944.

15 Akyurt, A., Zaki, G., and Habeebullah, B. (2002). Freezing phenomena in ice–water systems. *Energy Convers. Manage.* 43: 1773–1789.

16 Libbrecht, K.G. (2005). The physics of snow crystals. *Rep. Prog. Phys.* 68: 855–895.

17 Shibkov, A.A., Golovin, Y.I., Zheltov, M.A. et al. (2003). Morphology diagram of nonequilibrium patterns of ice crystals growing in supercooled water. *Physica A* 319: 65–79.

18 Schollick, J.M.H., Style, R.W., Curran, A. et al. (2016). Segregated ice growth in a suspension of colloidal particles. *J. Phys. Chem. B* 120: 3941–3949.

19 Zhang, H., Hussain, I., Brust, M. et al. (2005). Aligned two and threedimensional structures by directional freezing of polymers and nanoparticles. *Nat. Mater.* 4: 787–793.

20 Peppin, S.S.L., Wettlaufer, J.S., and Worster, M.G. (2008). Experimental verification of morphological instability in freezing aqueous colloidal suspensions. *Phys. Rev. Lett.* 100: 238301.

21 Butler, M.F. (2000). Instability formation and directional dendritic growth of ice studied by optical interferometry. *Cryst. Growth Des.* 1: 213–223.

22 Tai, K., Liu, Y., and Dillon, S.J. (2014). In situ cryogenic transmission electron microscopy for characterizing the evolution of solidifying water ice in colloidal systems. *Microsc. Microanal.* 20: 330–337.

23 Kobayashi, K., Koshino, M., and Suenaga, K. (2011). Atomically resolved images of Ih ice single crystals in the solid phase. *Phys. Rev. Lett.* 106 (206101).

24 Maire, E., Buffière, J., Salvo, L. et al. (2001). On the application of Xray microtomography in the field of materials science. *Adv. Eng. Mater.* 3: 539–546.

25 Deville, S., Maire, E., BernardGranger, G. et al. (2009). Metastable and unstable cellular solidification of colloidal suspensions. *Nat. Mater.* 8: 966–972.

26 Heethoff, M. and Cloetens, P. (2008). A comparison of synchrotron Xray phase contrast tomography and holotomography for noninvasive investigation of the internal anatomy of mites. *Soil Org.* 80: 205–215.

27 Cloetens, P., Ludwig, W., Baruchel, J. et al. (1999). Holotomography: quantitative phase tomography with micrometer resolution using hard synchrotron radiation X rays. *Appl. Phys. Lett.* 75: 2912–2914.

28 Bareggi, A., Maire, E., Lasalle, A., and Deville, S. (2011). Dynamics of the freezing front

during the solidification of a colloidal alumina aqueous suspension: in situ Xray radiography, tomography, and modelling. *J. Am. Ceram. Soc*. 94: 3570–3578.

29 Delattre, B., Bai, H., Ritchie, R.O. et al. (2014). Unidirectional freezing of ceramic suspensions: in situ Xray investigation of the effects of additives. *ACS Appl. Mater. Interfaces* 6: 159–166.

30 Li, T., Senesi, A.J., and Lee, B. (2016). Small angle Xray scattering for nanoparticle research. *Chem. Rev.* 116: 11128–11180.

31 Ingham, B. (2015). Xray scattering characterization of nanoparticles. *Crystallogr. Rev.* 21: 229–303.

32 Allen, A.J. (2005). Characterization of ceramics by Xray and neutron smallangle scattering. *J. Am. Ceram. Soc*. 88: 1367–1381.

33 Boldon, L., Laliberte, F., and Liu, L. (2015). Review of the fundamental theories behind small angle Xray scattering, molecular dynamics simulations, and relevant integrated application. *Nanotechnol. Rev.* 6: 25661.

34 Schnablegger, H. and Singh, Y. (2013). The SAXS Guide: Getting Acquainted with the Principles, 3ee. Austria: Anton Paar GmbH.

35 Spannuth, M., Mochrie, S.G., Peppin, S.S.L., and Wettlaufer, J.S. (2011). Particlescale structure in frozen colloidal suspensions from smallangle Xray scattering. *Phys. Rev. E* 83: 021402.

36 Uhlmann, D.R., Chalmers, B., and Jackson, K.A. (1964). Interaction between particles and a solid–liquid interface. *J. Appl. Phys*. 35: 2986–2993.

37 Körber, C., Rau, G., Cosman, M.D., and Gravalho, E.G. (1985). Interaction of particles and a moving ice–liquid interface. *J. Cryst. Growth* 72: 649–662.

38 Pötschke, J. and Rogge, V. (1989). On the behaviour of foreign particles at an advancing solid–liquid interface. *J. Cryst. Growth* 94: 726–738.

39 Casses, P. and Azouniaidi, M.A. (1994). A general theoretical approach to the behaviour of foreign particles at advancing solid–liquid interfaces. *Adv. Collolid Interface Sci* 50: 103–120.

40 Chino, Y. and Dunand, D.C. (2008). Directionally freezecast titanium foam with aligned, elongated pores. *Acta Mater.* 56: 105–113.

41 Larson, I., Drummond, C.J., Chan, D.Y.C., and Grieser, F. (1993). Direct force measurements between TiO_2 surfaces. *J. Am. Chem. Soc*. 115: 11885–11890.

42 Lipp, G. and Körber, C. (1993). On the engulfment of spherical particles by a moving ice–liquid interface. *J. Cryst. Growth* 130: 475–489.

43 Rempel, A.W. and Worster, M.G. (1999). The interaction between a particle and an advancing solidification front. *J. Cryst. Growth* 205: 427–440.

44 Rempel, A.W. and Worster, M.G. (2001). Particle trapping at an advancing solidification front with interfacialcurvature effects. *J. Cryst. Growth* 223: 420–432.

45 Wettlaufer, J.S., Worster, M.G., Wilen, L.A., and Dash, J.G. (1996). A theory of premelting dynamics for all power law forces. *Phys. Rev. Lett.* 76: 3602–3605.

46 Deville, S., Saiz, E., Nalla, R.K., and Tomsia, A.P. (2006). Freezing as a path to build complex composites. *Science* 311: 515–518.

47 Deville, S., Saiz, E., and Tomsia, A.P. (2007). Icetemplated porous alumina structures. *Acta Mater.* 55: 1965–1974.

48 Mullins, W.W. and Sekerka, R.F. (1964). Stability of a planar interface during solidification of a dilute binary alloy. *J. Appl. Phys.* 35: 444–451.

49 Sekerka, R.F. (1965). A stability function for explicit evaluation of the Mullins–Sekerka interface stability criterion. *J. Appl. Phys.* 36: 264–267.

50 Deville, S. (2008). Freezingcasting of porous ceramics: a review of current achievements and issues. *Adv. Eng. Mater.* 10: 155–169.

51 Peppin, S.S.L., Elliott, J.A.W., and Worster, M.G. (2006). Solidification of colloidal suspensions. *J. Fluid Mech.* 554: 147–166.

52 Peppin, S.S.L., Worster, M.G., and Wettlaufer, J.S. (2007). Morphological instability in freezing colloidal suspensions. *Proc. R. Soc. A.* 463: 723–733.

53 Deville, S., Maire, E., Lasalle, A. et al. (2009). In situ Xray radiography and tomography observations of the solidification of aqueous alumina particle suspensions – part I: initial instants. *J. Am. Ceram. Soc.* 92: 2489–2496.

54 Deville, S., Maire, E., Lasalle, A. et al. (2009). In situ Xray radiography and tomography observations of the solidification of aqueous alumina particle suspensions – part II: steady state. *J. Am. Ceram. Soc.* 92: 2497–2503.

55 Lasalle, A., Guizard, C., Maire, E. et al. (2012). Particle redistribution and structural defect development during ice templating. *Acta Mater.* 60: 4594–4603.

56 Elliott, J.A.W. and Peppin, S.S.L. (2011). Particle trapping and banding in rapid colloidal solidification. *Phys. Rev. Lett.* 107 (168301).

57 Deville, S., Adrien, J., Maire, E. et al. (2013). Timelapse, threedimensional in situ imaging of ice crystal growth in a colloidal silica suspension. *Acta Mater.* 61: 2077–2086.

58 Anderson, A.W. and Worster, M.G. (2012). Periodic ice banding in freezing colloidal

dispersions. *Langmuir* 28: 16512–16523.

59 Anderson, A.W. and Worster, M.G. (2014). Freezing colloidal suspensions: periodic ice lenses and compaction. *J. Fluid Mech.* 758: 786–808.

60 O'Neil, K. and Miller, R.D. (1985). Exploration of a rigid ice model of frost heave. *Water Resour. Res.* 21: 281–296.

61 Rempel, A.W., Wettlaufer, J.S., and Worster, M.G. (2004). Premelting dynamics in a continuum model of frost heave. *J. Fluid Mech.* 498: 227–244.

62 Bouville, F., Maire, E., and Deville, S. (2014). Selfassembly of faceted particles triggered by a moving ice front. *Langmuir* 30: 8656–8663.

63 Qian, L., Willneff, E., and Zhang, H. (2009). A novel route to polymeric submicron fibers and their use for inorganic structures. *Chem. Commun.* 3946–3948.

64 Qian, L. and Zhang, H. (2010). Green synthesis of chitosanbased nanofibers and their applications. *Green Chem.* 12: 1207–1214.

65 Zhang, H., Lee, J.Y., Ahmed, A. et al. (2008). Freezealign and heatfuse: microwires and networks from nanoparticle suspensions. *Angew. Chem. Int. Ed.* 47: 4573–4576.

66 Roberts, A.D., Wang, S., Li, X., and Zhang, H. (2014). Hierarchical porous nitrogenrich carbon monoliths via icetemplating: high capacity and highrate performance as lithium ion battery anode materials. *J. Mater. Chem. A* 2: 17787–17796.

67 Zhang, H., Long, J., and Cooper, A.I. (2005). Aligned porous materials by directional freezing of solution in liquid CO_2. *J. Am. Chem. Soc.* 127: 13482–13483.

68 Zhang, H., Wang, D., Butler, R. et al. (2008). Formation and enhanced biocidal activity of waterdispersible organic nanoparticles. *Nat. Nanotechnol.* 3: 506–511.

69 Grant, N. and Zhang, H. (2011). Poorly watersoluble drug nanoparticles via an emulsionfreezedrying approach. *J. Colloid Interface Sci.* 356: 573–578.

70 Zhang, H. and Cooper, A.I. (2005). Synthesis and applications of emulsiontemplated porous materials. *Soft Matter* 1: 107–113.

71 Qian, L., Ahmed, A., Foster, A. et al. (2009). Systematic tuning of pore morphologies and pore volumes in macroporous materials by freezing. *J. Mater. Chem.* 19: 5212–5219.

72 Qian, L. and Zhang, H. (2013). Onestep synthesis of proteinencapsulated microspheres in a porous scaffold by freezedrying double emulsions and tuneable protein release. *Chem. Commun.* 49: 8833–8835.

3
Applications of Freezedrying in Pharmaceuticals, Biopharmaceuticals, and Foods

3.1 Introduction

Freezedrying is usually an essential procedure when the icetemplating technique is used for the preparation of porous and nanostructured materials. However, this technique has so far rarely been used to produce materials in industrial sectors. However, as a drying technique, the freezedrying method has been widely used in pharmaceutical, biopharmaceutical, and food industries. The objectives are usually to prepare welldefined cakes with interconnected macroporous structures (to ensure easy and highstandard reconstitution) and improved stability for storage and transport. Different types of excipients and/or control of pH have been investigated to maintain the activity or native state of the active ingredients in these materials whilst still producing the fine macroporous structures [1, 2]. Although the focuses are not on the porosity and properties of these materials, the freezedried products in these industrial applications can be linked with or can provide insights into the preparation of porous materials by ice templating. Indeed, many of the icetemplated materials, particularly polymeric materials, show similar pore structures or characteristics as the freezedried pharmaceutical cakes [3, 4]. In this chapter, the purposes are twofold: (i) to give readers a general idea on how freezedrying processes have been employed in relevant industries, focusing on excipients, stability, and processing parameters and design and (ii) to provide thoughts/ideas for the preparation of icetemplating materials, particularly polymeric materials and nanomedicine.

3.2 Excipients in Pharmaceutical Formulations

In brief, pharmaceutical excipients are components in a pharmaceutical dosage formulation other than the active pharmaceutical ingredients (APIs). The role of the pharmaceutical excipients is to guarantee the dosage, stability and bioavailability of the APIs [5, 6]. The excipients can be any component added intentionally to the medicinal formulations and the impurities in the formulations. More specifically, the excipients can act as fillers, binders, diluents, bulking agents, lubricants, wetting agents, solvents, preservatives, flavours, colouring agents, antiadherents, sorbents, coating agents, surfactants, etc. [5]. Excipients can be obtained from different sources, including animals (e.g. gelatin, stearic acid, lactose, natural polymers), plants (e.g. starches, sugars, flavours, cellulose, polymers), minerals (e.g. silica, buffer solutions, inorganic salts, oxides) as well as synthesized polymers and stabilizers [5, 6].

In a pharmaceutical formulation, the percentage of excipients is usually very high. These excipients have their own properties and, similarly to APIs, may participate in adsorption and

biodistribution. Therefore, the safety of the excipients is equally important. The excipients should be subjected to the same toxicity studies as demanded by APIs. When choosing certain compounds as excipients, it is always suggested to choose from those being used previously in pharmaceutical products or those originating from food industry and generally recognized as safe (GRAS). The second choice may be compounds chemically modified from those being approved and utilized in the pharmaceutical or food industry. The use of new compounds as excipients will need to be assessed to meet the requirements of the regulation bodies. The safety assessments comprise: (i) toxicity of the excipients; (ii) interactions of APIs–excipients at different stages; and (iii) impacts from production, distribution, and use.

Polymers have been widely used as pharmaceutical excipients for various roles including as diluents, bulking agents, stabilizers, in protective coating, osmotic pumps, and contribute to controlled drug release [5]. These polymers may be either natural or synthesized. Some frequently used polymers include hydroxypropyl methylcellulose (HPMC), hydroxypropyl cellulose (HPC), poly(vinyl alcohol) (PVA), polyvinylpyrrolidone (PVP), alginate, dextran, poly(ethylene glycol) (PEG), starch, and so on. PVA, a synthetic polymer, is not only widely used as an excipient in food and pharmaceutical applications but also as a stabilizer for emulsion formulations and drug nanoparticles [3, 7, 8]. This may be attributed to its excellent safety properties. Based on a comprehensive evaluation of the scientific literature, it is inferred that PVA is not mutagenic or clastogenic, does not accumulate in the body when administered orally, poorly absorbed from the gastrointestinal tract (GI), and has very low acute oral toxicity (LD_{50} in the range of 15–20 g kg^{-1}) [9].

Sugars are a type of excipients that have been employed for a variety of solid dosage formulation, either via freezedrying or other techniques [10–12]. As a filler/binder, mannitol has been widely used, and has even been compared to the conventionally lowpriced excipients such as lactose, microcrystalline cellulose, and calcium hydrogen phosphate. This is because of its very unique properties: low hygroscopicity, inertness towards the APIs and patient body, good taste, good compactibility, and the ability to produce stable tablets [13]. Mannitol can exist in four polymorphic forms (α, β, γ, δ), of which the β form is the stable polymorph and dominantly available in the market.

The abovementioned polymers and sugars are mainly used as hydrophilic matrix to stabilize hydrophilic pharmaceuticals or biopharmaceuticals. There are also excipients that are more effective in stabilizing and delivering lipophilic drugs. Two excellent examples are cyclodextrin and lipids. Cyclodextrins are a family of cyclic oligosaccharides composed of α(1,4) linked glucopyranose subunits. There are three types of cyclodextrins: α, β and γcyclodextrins, composed of 6, 7, 8glucopyranose units, respectively. The unique properties of the cyclodextrins are their hydrophobic internal cavity and hydrophilic external surface. As molecular carriers or chelating agents, via molecular complexation or encapsulation of hydrophobic compounds, cyclodextrins have been extensively investigated and utilized in a wide range of applications such as pharmaceutical excipients, drug delivery, separation, food, and catalysis [14]. Lipidbased pharmaceutical formulations have drawn considerable interest from the pharmaceutical industry and from researchers. Most of the

lipidbased formulations use lipid vesicles, emulsions or excipients to solubilize lipophilic drugs that are poorly water soluble, and thereby improve drug absorption in the body. An important question is whether the drug remains in solubilized form inside the GI after being administered [15].

A recent development is on excipient foods, i.e. designing food matrices to improve oral bioavailability of pharmaceuticals and nutraceuticals [16]. This is different from medical food, which contains one or more APIs. By analogy to a pharmaceutical excipient, excipient food does not exhibit any therapeutic properties or bioactivity itself. But when consuming with pharmaceuticals, it can help increase the efficacy of any pharmaceuticals codigested with it. This may be achieved through bioactive liberation, increase in membrane permeability, and inhibition of efflux mechanism. Excipient food ingredients may include lipids, carbohydrates, proteins, minerals, surfactants, chelating agents, and phytochemicals [16].

There are additional requirements when excipients are used in freezedried formulations. Because the freezedrying process has been mostly used in proteinbased solid formulations, the excipients must play the role of maintaining the integrity and stability of the proteins at different stages of the freezedrying process and during storage and reconstitution. Specifically, excipients that act as a cryoprotectant, lyoprotectant, or stabilizer in solid form should be added into the formulations. Fortunately, some excipients, e.g. sugars, can have all the protecting properties during freezedrying and act as a stabilizer in solid protein formulations. As it has been well documented, nonreducing disaccharides trehalose and sucrose have been mostly used as stabilizers [1, 10]. Mannitol and glycine are good choices as tonicity modifiers [17]. Bulking agents in freezedried formulations usually include mannitol, glycine, lactose, dextran, povidone, and disaccharides [1, 18]. It is possible that one single sugar excipient can act in differing capacities such as a freezedrying protectant, stabilizer, bulking agent, and disintegrating agent.

When the excipients are present in or added to parenteral formulations, they can enhance or maintain API solubility and/or stability. The excipients also play important roles in assuring safety, minimizing pain and irritation, and controlling drug delivery [18]. However, these excipients can have significant effects on the distribution and elimination of the co administered APIs. In a review focusing on the effects of pharmaceutical excipients on drug disposition, Buggins et al. summarized the effects of cosolvents (e.g. DMSO, ethanol, propylene glycol, PEGs, cyclodextrins, and surfactants (e.g. Cremophor, Tween, Solutol) on distribution, metabolism, renal elimination, oral adsorption, hepatic elimination, etc. [19].

Physicochemical properties of excipients, such as solubility, ionization, hydrogen bonding tendency, molecular size and shape, have significant impact on their fate in the body. When assessing safety and therapeutic efficacy of pharmaceutical formulations, it is thus very important to obtain the data about the excipient pharmacokinetics and profiling [20]. Pharmacokinetics is the kinetics of drug absorption, distribution, metabolism, and excretion (ADME). The parameters used to characterize ADME usually include volume of distribution (V_D), elimination halflife ($t_{1/2}$), clearance (Cl), and bioavailability (F). The pharmacokinetic processes usually follow firstorder kinetics. V_D describes how the compound is distributed

within the body. A larger V_D indicates that the API is in the blood plasma and is also highly tissue bound. Elimination $t_{1/2}$ of the API is the time it takes to reduce its blood plasma concentration by 50%. Cl indicates how rapidly the API is eliminated from the body. It can be divided into hepatic clearance (Cl_H) and renal clearance (Cl_R). Bioavailability is the fraction (hence the symbol *F*) of an API absorbed from the GI into the general blood circulation [21]. Whilst the excipient pharmacokinetics data should be reliably measured, some simple methods may be used to predict the ADME properties. The ruleoffive approach developed by Lipinski et al. is widely used to predict absorption from the GI and overall druglike properties of biologically active compounds [22]. The Biopharmaceutics Classification System (BCS) [23] and The Biopharmaceutics Drug Disposition Classification System (BDDCS) [24] are also used to provide useful information on solubility, permeability and the extent of API metabolism. The physicochemical properties (M_w, solubility, Log *P*, Hbond donors, and Hbond acceptors) of 26 common pharmaceutical excipients and their pharmacokinetic parameters ($t_{1/2}$, V_D, *F*) have been summarized by Loftsson [20]. The size/hydration diameter and the surface properties of the excipients are very important for clearance from the body. For example, PVP with $M_w < 10$ kDa is readily excreted via kidney by glomerular filtration, PVP of M_w up to 25 kDa is completely excreted within one day, while it can take 8 days to excrete PVP with $M_w = 37$ kDa [25]. Polymer nanoparticles less than 8 nm are mainly excreted by renal clearance while the larger particles must disassemble into smaller particles before being excreted from the body [26]. Although the safety and the pharmacokinetic parameters of pharmaceutical excipients have to be rigorously examined for pharmaceutical products, some insights may be gained from the pharmacokinetic data of the known excipients. For example, the sizerelated effects are less likely to have an impact when the excipients can be readily excreted from the body. Hydrophilic low M_w polymers with small V_D fall into this category, with $t_{1/2}$ of about 2 h [20].

3.3 Improving the Freezedrying Process

Freezedrying processes are only industrially viable for pharmaceutical solid formulations or other high valueadded products. This is due to the long, energyintensive and complex freezedrying process. A freezedrying process may take 2–4 days, with the majority time used in the primary drying process. There are other important factors to consider – the activity and stability of the active ingredients in the formulations, e.g. proteins, vaccines, and food bacteria. Therefore, the efforts for improving freezedrying processes usually focus on reducing the freezedrying time and producing welldefined cakes with high stability of APIs.

3.3.1 The Types of Freezedrying Processes

3.3.1.1 Spray Freezedrying Process

In a conventional freezedrying process, the vials containing solutions or suspensions are

frozen on the shelf in a freezedryer and then subjected to vacuum to allow the sublimation of the frozen solvent (usually water). The exposed surface area of the frozen body is directly proportional to the rate of sublimation. In other words, in order to increase the sublimation rate and reduce the freezedrying time, the size of the frozen sample should be reduced. This can be achieved by a spray freezedrying process, where a solution or suspension is either atomized into cold vapour over a cold liquid (usually liquid nitrogen) (Figure 3.1) or directly atomized into liquid nitrogen. The frozen powders (with the sizes of the particles in the micron range) can be subjected to a conventional freezedrying process [27]. By analogy, in a spray drying process, the liquid or suspension is atomized into a chamber. Hot air or nitrogen flows inside the chamber in a cocurrent or countercurrent direction, evaporating water from the sprayed droplets and producing a dry powder product [27, 28]. The spray drying process is not suitable for temperaturesensitive compounds while there will be no such limit for a spray freezedrying process. The spray freezedrying processes are mainly used in drying of pharmaceutical products and high value foods, and in the encapsulation of active but sensitive compounds [27]. Avoiding the blocking of the atomizing nozzles and preventing aggregation of sprayed droplets before they are fully frozen are the main operational difficulties [29–31].

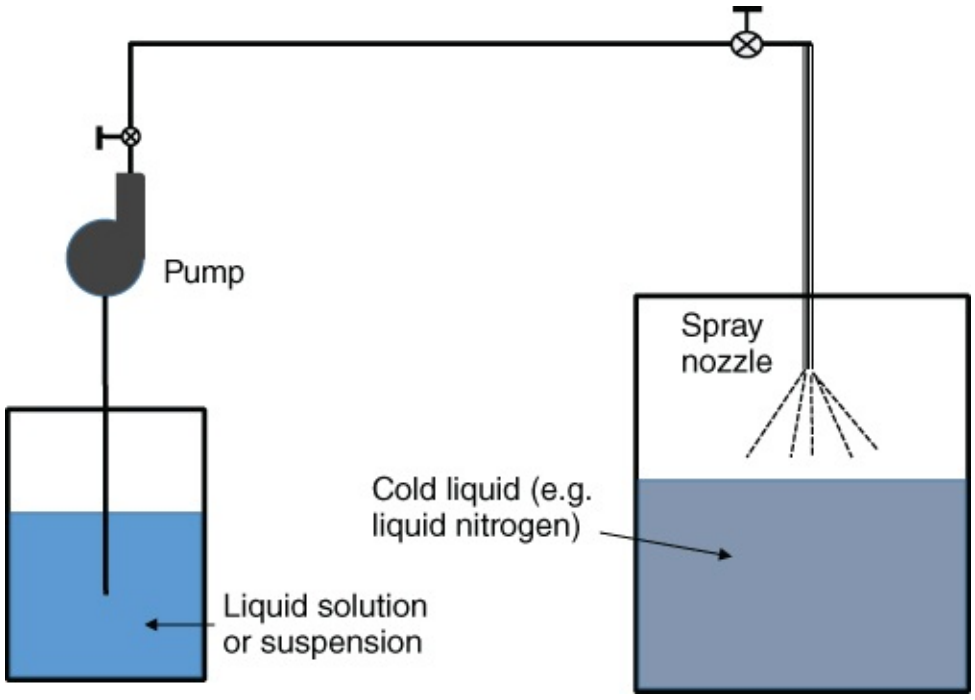

Figure 3.1 The schematic representation shows the spray into vapour over a cold liquid. The nozzle may be immersed into the cold liquid for the process of spray into liquid.

3.3.1.2 Spin Freezing

Another way to reduce the size of the frozen body is by spin freezing. This is achieved by rotating the vials filled with liquid solution or suspension along their longitudinal axis. The liquid phase forms a thin layer coating the inner wall of the vial, which is cooled and frozen by using a flow of sterile gas with a controllable low temperature around the rotating vial (Figure 3.2) [32]. The frozen sample is thin and spread over a larger surface. This can lead to faster freezedrying. It also has the great potential to realize a continuous freezedrying process. In

a study to evaluate spin freezing versus conventional freezing as part of a continuous freeze drying concept (Figure 3.2), De Meyer et al. estimated that the total process time could be reduced by a factor of 10–40, depending on the specific formulation properties and vial dimensions [32].

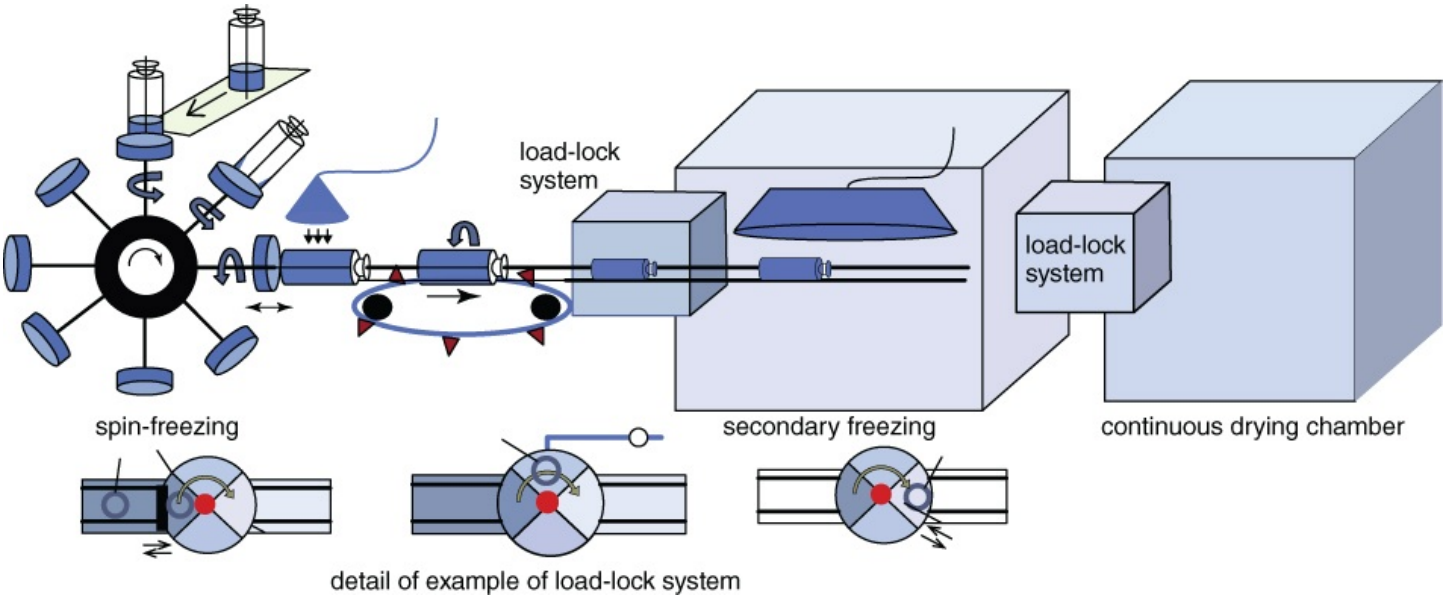

Figure 3.2 The use of spin freezing in a continuous freezing and drying system.

Source: De Meyer et al. 2015 [32]. Reprinted with permission from Elsevier.

3.3.1.3 Atmospheric Freezedrying

In a conventional freezedrying process, the frozen samples are subjected to high vacuum to allow the sublimation of the frozen solvent. This can significantly add costs to energy usage and limit the scaleup of the freezedrying process. However, high vacuum is not necessary for a freezedrying process. It has been observed for long that a frozen sample can be dried naturally in dry and cold winter. As such, atmospheric freezedrying has been introduced [33, 34]. This process is viable provided the partial pressure of water vapour in the drying chamber is lower than the water vapour pressure of the frozen sample. This is usually achieved by circulating a cold and dry gas through the frozen sample [27]. As expected, this method is very slow for bulky frozen samples. It is thus reasonable to combine a spray freezedrying process with atmospheric freezedrying to produce poorly watersoluble drug formulations [29]. Contacting the frozen microparticles with cold dry gas in a fluidized bed is proposed for a faster atmospheric freezedrying process [35]. This allows better mixing between the frozen particles and the cold gas, enhancing mass transfer between the two phases and thereby a faster drying process. A problem with atmospheric freezedrying is the use of huge quantity of cold gas (albeit recirculation). The temperature of the cold gas should be lower than the collapse temperature of the frozen samples. The need for such a large quantity of cold gas supply is highly demanding [27]. This problem has been partially addressed by subatmospheric pressure freezedrying as it allows for shorter drying time and reduced use of cold gas [35, 36]. Owing to these issues with atmospheric freezedrying, conventional freezedrying process is still mostly used in research and industrial applications.

3.3.2 Process Development and Design

There are several stability issues during the freezedrying process for solid protein formulations. These issues include denaturation stresses from cold temperature, pH change, solute concentration as well as phase separation during freezing and critical temperatures during freezedrying [37]. Various formulations have been investigated in order to achieve specific optimal conditions [11]. In an effort to facilitate the adoption of modern techniques and move the investigations of freezedrying processes from the empirical and datadriven approach to a more knowledgebased route, the Food and Drug Administration (FDA) introduced 'Pharmaceutical cGMP for the 21st Century: A Riskbased Approach' and 'Guidance for Industry: Process Analytical Technology – A framework for Innovative Pharmaceutical Development, Manufacturing and Quality Assurance', in 2004 [38]. For a freezedrying process, this includes implementing quality by design (QbD) for proposing experiments, identifying quality target product profile and critical quality attributes, performing risk assessments, and defining the design space and process control strategy [39].

Based on the QbD approach, a fractional factorial design has been applied to investigate the effects of buffer type, pH, and excipients on glass transition temperature; monoclonal antibody concentration; unfolding transition temperature and particle size of the reconstitute solutions [40]. The Pareto ranking analyses showed that pH, NaCl, and polysorbate 20 were the most important factors [40].

The design space can be regarded as the combination and interaction of input variables and process parameters that can generate the products with the desirable quality. For a freeze drying process, the product temperature at the sublimation interface is crucial in determining cake structure and residual moisture content. The other important parameters include shelf temperature, chamber pressure, collapse temperature, glass transition temperature (for amorphous products) or eutectic temperature (for crystalline products) [39]. Mathematical modelling can be used to build the design space for a pharmaceutical freezedrying process. One such study was carried out on the primary drying stage to investigate the effect of shelf temperature and chamber pressure on product temperature and sublimation flux [41]. In addition to shelf temperature and chamber pressure, the dried layer thickness was used as the third coordinate to construct the diagram.

The process control is then required to ensure that the freezedrying process can be performed within the variation of process parameters as defined in the design space. Usually, non invasive and realtime monitoring and control of the process are preferred. This relies on the use of the stateoftheart process analytical technologies (PAT). PAT is used to design, analyse, and control manufacture via timely measurement of critical objectives of the final products [39, 42]. For the lyophilization of biopharmaceutics, the PAT tools can be used in the freezing step to monitor the degree of supercooling, in the primary drying step to probe product temperature and end point of primary drying, and in the secondary drying to monitor and control the residual moisture content [39]. Table 3.1 summarizes the main analytic methods used as PAT during freezedrying processes [39, 42]. Various techniques that can be used to characterize the freezedried products, include scanning electron microscopy (SEM),

transmission electron microscopy (TEM), Fourier transform infrared spectroscopy (FTIR), powder Xray diffraction (PXRD), differential scanning calorimetry (DSC), solid nuclear magnetic resonance (solid NMR), and circular dichroism (CD) spectroscopy. These characterization data can provide the feedback on experimental design and process control. The application of PAT is expected to facilitate process transfer from laboratory to production or between manufacturers because the process is less equipment dependent but relies more on sound scientific and engineering knowledge.

Table 3.1 Summary of PAT tools used in pharmaceutical freezedrying.

Source: Zhang et al. 2008 [31]. Adapted from Nature Publishing Group. Read et al. 2010 [42]. Adapted from John Wiley & Sons.

Analytic technique	**Measuring attributes**	**Probe position**
Resistance temperature detectors (RTD)	Product temperature	Inside sample vials, primary drying
Manometric temperature measurements (MTM)	Product temperature	Noninvasively at the sublimation interface
Nearinfra red (NIR) spectroscopy	Moisture content, sublimation rate	Bottom of the vials
Raman spectroscopy	Water to ice conversion, purity and polymorphs of the drug	Top surface of the frozen body
Tuneable diode laser absorption spectroscopy (TDLAS)	Water vapour concentration, sublimation rate, predict the end of primary drying	Laser beam attached to the freezedryer spool

3.4 Applications of Freezedrying in Pharmaceutics

Pharmaceutics can be classified into three categories based on their molecular weights [43]. As schematically shown in Figure 3.3, small molecule drugs with molecular weights of <500 Da are conventionally termed as pharmaceutics. Proteins, or biologics/biopharmaceutics, usually have molecular weights of >5000 Da. Between them, researches are emerging on peptidebased drugs. Peptidebased drugs, proteins, and vaccines are often classified together as biopharmaceutics, which are the focus of Section 3.5. In this section, the discussion is mainly on pharmaceutics or small molecular drug.

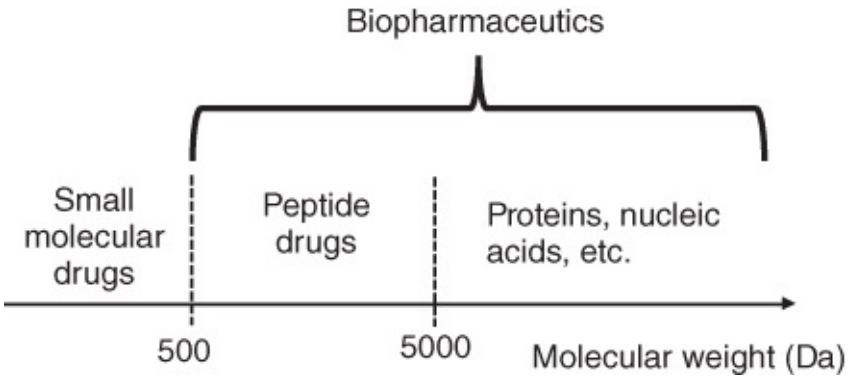

Figure 3.3 A schematic representation of drug classification based on their molecular weights.

With the use of modern highthroughput synthesis and screening techniques, a large number of potentially active compounds have been identified. However, a high percentage of them are poorly soluble in water, leading to poor bioavailability and therapeutic efficacy [44]. These drug compounds may be classified into different categories, based on certain criteria: e.g. BCS classification based on solubility and permeability [23] and BDDCS classification based on solubility and metabolism [24]. These classifications offer clarity and benefits for pharmaceutical research and regulatory bodies [45]. Corrections and additional drugs may be continuously added to the list of the classifications [46]. A simple and effective 'ruleof five' was developed by Lipinski et al. to predict the likely poor absorption or permeation if the drug compounds have more than five Hbond donors, molecular weights over 500 Da, Log P over 5, and more than 10 Hbond acceptors. The rule is not applicable for compounds that can be used as substrates for biological transporters and biopharmaceutics [22].

Solid pharmaceutical formulation aims to improve apparent solubility and thereby permeability and bioavailability for poorly watersoluble drugs [47]. This usually involves the reduction in size of drug particles and the use of excipients, particularly polymers, as amorphous matrices to stabilize the drug particles [5, 44]. The dissolution rate of a compound is proportional to the exposed surface area. Therefore, smaller drug particles can increase the dissolution rate, supersaturation, or apparent solubility in the GI. This, however, does not necessarily transfer to equally higher permeability. The selection of excipients in drug formulations is very important because it can influence the solubility–permeability interplay [48]. The lipophilic drugs in amorphous solid formulations can enhance both apparent solubility and flux across the intestinal membrane [49]. However, as the amorphous glass state is not thermodynamically stable, crystallization can occur with time. This may bring out the stability and toxicity issues of the pharmaceutical products, which will have to be carefully examined [50].

Different solid formulation methods have been reported [47]. The use of freezedrying in pharmaceutical formulations can usually offer fast dissolution of the solid formulation or provide high porosity for light and/or floating drug delivery system (FDDS). Of course, it is a necessary option for processing temperaturesensitive drug compounds. Because the processed drugs are generally poorly soluble in water, nonaqueous cosolvents can be added to facilitate initial liquid formulation [51]. This may also help to increase sublimation rate, due to the usually high vapour pressure of the nonaqueous solvent. However, with the

use of the cosolvents, additional storage and processing safety need to be considered. The contents of residual solvent in the solid formulations should be assessed and, within the required limits, enforced by the regulatory bodies.

3.4.1 Spray Freezedrying

As described in Section 3.3.1, the spray freezedrying process can be used to produce pharmaceutical powder formulations. The produced formulations can enhance dissolution rate and apparent solubility of poorly watersoluble drugs [29, 30]. When comparing spray freezedrying and spray drying, the powders produced by spray freezedrying may exhibit superior aerosolization efficiency and hence finer particles [52]. Sugars and/or polymers are usually added as protectants or stabilizers to produce stable powder formulations. As a result of the spray freezedrying process, spherical, light, and porous micronsized powders are produced. This offers fast dissolution and good aerodynamics. In addition to spray freeze drying in vapour over liquid and spray freezedrying in liquid, it is possible to directly spray into a cold atmosphere in a chamber, which is like a direct opposite version of spray drying (cold atmospheres versus hot atmosphere). Another option is to spray onto a solid surface, where the liquid droplets form a thin film which is frozen ultrarapidly. Therefore, this process is sometimes called thin film freezing [53]. To realize the thin film freezing process, the droplets of a liquid formulation can simply fall on a cold surface or spray onto a rotating steel drum containing a cryogen such as dry ice or liquid nitrogen [53–55]. To minimize water vapour condensation on the cold surface, the whole apparatus can be placed in a dry box with controlled humidity. The spray freezedrying process has been widely used for both poorly watersoluble drugs and a variety of proteins and vaccines [52–56]. The powder formulations have been used for pulmonary, nasal, and needlefree ballistic intradermal applications [56].

3.4.2 Orally Disintegrating Tablets (ODTs)

The orally disintegrating tablets (ODTs) are also known as orally dispersible drug delivery systems. The feature of the ODTs is that they can release drugs immediately when coming into contact with saliva [57]. This type of drug formulations can be highly beneficial for patients who have difficulty in administering drugs via the oral route. Paediatrics, geriatrics, psychiatrics, nauseated or unconscious patients fall into this category of patients. Upon administration into mouth, the saliva penetrates into the highly porous ODTs that rapidly disintegrate to form a suspension of fine particles. The ODTs usually contain flavours and sweeteners (for taste marking) to enhance patient compliance. Hydrophilic polymers are usually used as porous matrices to stabilize drug particles, and with good wettability for fast disintegration [5]. Unit size and disintegration time are the two main parameters to consider when assessing ODTs. The disintegration time is usually expected to be less than 1 min [58]. ODTs can be categorized into three delivery groups: sublingual route, buccal route, and localized drug delivery [57].

Various methods have been used to fabricate the ODTs, e.g. spray drying, moulding, compression, and the cotton candy process, to name a few [57]. The hotmelt extrusion method may be of more industrial importance because the process can be operated

continuously and is easy to scale up. The use of freezedrying is unique because highly interconnected porous and soluble polymeric structures can always be produced [3]. This can lead to fast dissolution of the freezedried products and instant formation of stable aqueous nanoparticle dispersions [8, 31, 59]. By using the freezedrying method, ODTs with ibuprofen have been produced [60]. A factorial design approach was further used to optimize the conditions for the performance of the ODTs [61]. Tastemarking ingredients could be added into the freezedrying formulations and evaluated [62]. Some examples of commercial ODTs available in the market include Zydis® tablets, Lyoc®, and Quicksolv® [57]. The disadvantage for the ODTs produced by freezedrying is the weak mechanical stability and the potential to adsorb moisture. Thus, suitable seals and packaging are required for these ODTs.

3.4.3 Floating Drug Delivery System

The FDDS is one type of gastroretentive drug delivery system for improving gastric retention time [63, 64]. The prolonged presence or release of drugs can improve bioavailability and stable plasma concentration of the drugs, thereby reducing potential side effects and the amount of dosage. For orally administered drugs, their release and adsorption are directly related to gastrointestinal transit time. The stomach can be anatomically divided into three regions: fundus, body, and antrum pylorus. The fundus and body act as a reservoir for nondigested mixtures while the antrum is the main site for mixing motion and pumping actions [64]. The particle size of disintegrated drug dosages should be in the range of 1–2 mm to be pumped into the small intestine via the pyloric valve. The pH of the stomach in fasting state is 1.5–2.0, and 2.0–6.0 in fed state. A large volume of water or other liquids may raise the pH to 6.0–9.0 in the stomach. The resting volume of the stomach is approximately 25–50 ml [63].

There are different mechanisms for gastroretentive drug delivery, including mucoadhesion, sedimentation, and expansion [63]. For the FDDS, once administered into the stomach, the density of the wetted dosage is lower than that of the gastric liquid, thereby floating and preventing it from pumping into the small intestine rapidly. This can be achieved by effervescent dosages and noneffervescent dosages. In an effervescent dosage, swellable polymer and effervescent compounds (e.g. sodium bicarbonate) are included. When in contact with the acidic gastric fluid, CO_2 is formed and released, which provides the buoyancy for the dosage to float. For the noneffervescent dosage, a highly porous structure with good wetting and/or swellable property is required. When absorbing liquid in the stomach, the swollen gel like material with the trapped air can float and provide sustained release of the drug [63]. The freezedrying is well placed to produce highly porous materials with tuneable pore structures [8] and hence is an effective technique to prepare the FDDS. For example, highly porous HPMCbased tablets were prepared by freezedrying for the gastroretentive delivery of ecabet sodium (a locally acting antigastric ulcer drug). The porous structure lowered the tablet density and kept the tablets floating without any lag time, until the tablets were disintegrated and released [65]. As expected, the FDDS is not suitable for drugs that may cause gastric lesions or are unstable under acid conditions.

3.4.4 Emulsion Freezedrying

Owing to the hydrophobic nature of many drug compounds, oilinwater (O/W) emulsions have been employed for delivery and enhanced bioadsorption. Emulsion is a mixture of two immiscible liquid phases with one phase in the form of droplets dispersed in the other continuous liquid phase, usually stabilized by amphiphilic polymers or surfactants [66, 67]. Colloids or nanoparticles may be also used as stabilizers, producing Pickering emulsions. As per the requirement of immiscible liquid phases, emulsions are always composed of water and one immiscible organic solvent. Depending on which phase is the continuous phase, the emulsions can be classified as O/W emulsion (where water is the continuous phase) or water inoil (W/O) emulsion (where oil is the continuous phase) or double emulsions O/W/O and W/O/W (basically the preformed emulsion disperses into another phase). Based on the size of the droplets, emulsions can be categorized into emulsions (droplet sizes from submicron to 100 microns, thermodynamically unstable), miniemulsions or nanoemulsions (droplet sizes approximately 50–500 nm, better kinetic stability), and microemulsions (clear and thermodynamically stable, droplets <100 nm in diameter) [67].

O/W emulsions are usually used for lipophilic drug formulations, where the lipophilic drugs are dissolved in the oil droplet phase. The oils usually used include lecithin, soyabean oil, lipid, triglycerides, etc. Freezedrying is employed to improve the formulation stability and reconstitution properties. Because the oils may be liquidlike but exhibit very low vapour pressure, they remain in the formulation after freezedrying. Cryoprotectants and bulking agents are added to generate stable lyophilized formulations. A submicron emulsion of antitumour drug Cheliensisin A with soyabean lecithin and medium chain triglycerides as the oil phase and sucrose (10 w/v%) added as cryoprotectant was freezedried. The lyophilized formulation showed improved stability, lower IC_{50} values, and enhanced antitumour activity [68]. Dry emulsion tablets produced by the emulsionfreezedrying technique were studied for the delivery of a poorly watersoluble drug hydrochlorothiazide [69]. Medium chain triglyceride was the oil phase while the aqueous phase contained the bulking agent maltodextrin. The tablet strength increased significantly with the concentration of maltodextrin and decreasing pore sizes. Methylcellulose as an emulsifier–tablet binder also showed significant influence on tablet strength and disintegration time [69]. Bufadienolidescontaining submicroemulsions and nanoemulsions were formed and freezedried. The optimum cryoprotectants were found to be 20% maltose for nanoemulsions and 20% trehalose for sub micron emulsions. The freezedried powders showed stability up to 3 months with no change in visual appearance, reconstitution stability, and particle aggregation [70]. O/W microemulsions containing Amphotericin B were freezedried, resulting in oily cakes, which could be easily reconstituted and stablized under the conditions studied. The microemulsion was prepared by adding polysorbate 80water solution to a lecithin/isopropyl myristate mixture under stirring. Amphotericin B solution in sodium hydroxide solution (1 M) was then added to the formed microemulsion at a temperature of 80 °C [71].

The emulsionfreezedrying approach has been further developed by Zhang et al. to produce aqueous poorly watersoluble drug nanoparticle suspensions [8, 31]. Unlike the use of non

volatile oil phase in the emulsions and producing oily cakes [68–71], volatile organic solvents such as cyclohexane or *o*xylene are used to dissolve hydrophobic drugs. The formed organic solutions are then emulsified into aqueous phase containing polymer and surfactant to form O/W emulsions. Upon freezedrying, both water and the organic solvent are removed to generate dry porous nanocomposites. The highly interconnected porous structure allows the dry materials to dissolve in water in seconds to form stable aqueous drug nanoparticle suspensions. This will be the focus of Chapter 8 on freezedrying for nanomedicine.

3.5 Applications of Freezedrying in Biopharmaceutics

Based on World Preview 2016 Outlook to 2022 by EvaluatePharma, biologics will contribute 50% of the Top 100 product sales by 2022. Among the top 20 most valuable R&D projects, the majority of them deal with biologics, with monoclonal antibodies leading the way. Currently, in clinical applications or industrial research, the majority of the biologics/biopharmaceutics are proteins. Proteins function when they remain in the native secondary and/or tertiary structures. Many factors can lead to protein denaturation and aggregation. Indeed, this is one important reason that protein pharmaceuticals are traditionally administered by injection. This is the main barrier for biopharmaceutics during bioprocessing [72].

Because protein pharmaceutics are usually administered in parenteral formulations, liquid formulations would be preferred. However, due to relatively fast molecule motion and water facilitated reactions, the stability of proteins is a major issue during transport and longterm storage. The stability issues may be addressed by suitable solid formulations, mostly prepared by freezedrying [10]. This is because the degradation reactions can be avoided or slowed down sufficiently in the dry solid state. However, during a freezedrying process, the proteins experience freezing (cold) stress and dehydration stress, followed by the stability issue during solidstate storage. When designing a freezedrying formulation and processing, protein stability is the ultimate target [1, 17]. All the formulation parameters (e.g. protein concentration and type and amount of excipients) and processing conditions should be optimized based on protein stability.

In this section, we describe first the different types of protein degradation mechanisms and procedures that can be taken to avoid or minimize such degradation routes. Then we will discuss the freezedrying of different biopharmaceutics and the important parameters investigated.

3.5.1 The Freezedrying Process for Biopharmaceutics

3.5.1.1 During Freezing

The dominant protein conformational motions are controlled by the hydration shell and the bulk solvent [73]. The degree of hydration h can be defined as the weight ratio of water to protein. Dehydrated proteins do not function (some proteins begin to function at $h \geq 0.2$) while full functions may require $h > 1$. Largescale motions are significantly affected by variation in the bulk solvent and controlled by solvent viscosity [73]. When freezing a liquid protein

formulation, solute concentration, increasing viscosity, and formation of ice crystals can all contribute to protein denaturation.

Cold denaturation. The majority of proteins show cold denaturation well below the freezing point of water. This suggests that it may not have a significant impact on protein denaturation. However, with ice formation and protein concentration, the influence can be huge.

Protein concentration. At a high concentration (whether because of initial preparation or freezing induced), the number of proteins in a certain volume is high. This can lead to stronger interaction between proteins and greater potential for aggregation and precipitation [10]. Also, the surrounding bulky solvent may have higher viscosity, exerting impact on protein dynamics [73]. However, there is potential advantage with higher concentrations: the percentage of proteins exposed to freezing stress may be lower [1]. Since the percentage degradation during protein formulation is a critical parameter, suitable protein concentrations should be selected.

pH change. Proteins are usually stable in a narrow pH range and many of them are only stable at physiological pH. During freezing, because of the solute or ion concentration effect and possible crystallization of certain salts, the pH can vary considerably and cause protein denaturation. Buffering species are usually added to stabilize the pH change but some buffering salts should be avoided due to the crystallization during freezing. Na_2HPO_4 crystallizes more easily than NaH_2PO_4, which can result in a significant pH drop [10]. With potassium phosphate, the crystallization of dihydrogen salt may give a final pH near 9 [17]. Therefore, the sodium phosphate and potassium phosphate buffers should be avoided. Buffers with minimal pH change upon freezing may be selected from citrate, histidine, and Tris [17].

Ice–water interface. Adsorption of proteins at the interface can lead to protein instability. This is because the interaction with interface is favoured when a protein is partially unfolded to give greater exposure of hydrophobic amino acid side chains (usually in the core of protein) to the interface [11]. Air–water interface exists in the liquid formulation whilst the ice–water interface develops during freezing. To minimize the interface damage, surfactants can be added to the formulations. Owing to their amphiphilic nature, surfactants tend to adsorb at the interface thereby preventing or reducing the adsorption of proteins at the interfaces.

To start with a stable formulation, buffers, ions, nonaqueous organic solvents, and surfactants may be included [1, 11, 17]. In order to protect the freezing stresses as outlined earlier, excipients such as sugars, polymers, surfactants, and amino acids may be added depending on the specific proteins. The protection of proteins by sugars (used very often) during freezing (and also freezedrying) may be attributed to the universal thermodynamic mechanism developed by Timasheff for control of protein stability and reactions with weakly interacting cosolvents [74]. It has been established that, nearly any sugar or polyol, acting as excluded salts, can provide increased conformational stability of proteins. Furthermore, addition of

amino acids, salts, and many polymers may also fall into this category [11].

3.5.1.2 During Freezedrying

Dehydration stresses are experienced by proteins through the partial removal of water molecules from the hydration shell. Generally, the water content in freezedried solids is less than 10%. This can denature proteins and prevent their functioning [73]. During a dehydrating process, the proteins may transfer protons to ionized carboxy groups and reduce the charges in the structural proteins. The resulting low charge density can lead to stronger protein–protein hydrophobic interaction and cause protein aggregation [10]. Another stress is the increased surface (interface of solid/air) generated by sublimation of ice. In addition to the instability related with surface adsorption, this may have a pronounced effect during storage of the solid formulations.

FTIR has been mostly used to monitor protein denaturation during freezedrying, with the focus in the amide I, II or III region [10]. Moreover, hydrogen bonds are disrupted during freezedrying, leading to an increase in frequency and a decrease in the intensity of hydroxyl bond stretching. As observed in protein solid formulations, βsheet contents are increased while the contents of αhelix are decreased. An increase in βsheet content usually indicates protein aggregation and/or intermolecular interaction. This can be monitored by two major IR bands at about 1617 and 1697 cm^{-1} [75].

Because freezing and freezedrying are two separate processes with different stresses induced, both cryoprotectants and lyoprotectants are required for solid protein formulations generated by freezedrying. Fortunately, the widely used excipients such as sugars or disaccharides function in both processes to stabilize the proteins. Sugars such as trehalose and sucrose are the mostly used excipients. A ‘water replacement’ mechanism is generally utilized to emphasize how sugars can stabilize proteins during freezedrying. That is, sugar replaces water molecules from the hydration shell and then interacts/stabilizes the proteins through hydrogen bonding [11, 76].

3.5.1.3 During Solid State Storage

The instability of solid protein formulations during storage has been reviewed from the perspective of chemical and physical factors and also from the angle of thermodynamic and kinetic influences [10, 11, 77, 78]. In this section, we describe how chemical reactions and physical interactions contribute to protein denaturation/aggregation, what excipients may be added to stabilize the proteins, and then explain stabilizing mechanisms proposed in literature.

Chemical Reactions

There are several typical reactions involved in the instability of solid protein formulations.

1. *Deamidation*. This is a common degradation route for peptides and proteins containing Asn and Gln [10, 11]. For the Asn deamidation, it generates two degradation products (Asp and isoAsp) at the site of the original Asn residual. The mechanism and more detailed information may be found in the reviews [[10, 11], and references therein] and the website

on this topic (www.deamidation.org).

2. *Hydrolysis*. The degradation by hydrolysis at As/Asp residues and Aspassociated hydrolysis of the peptide backbone. This type of reaction shows the sensitivity to pH and buffer species [11]. The hydrolysis of peptide backbone is also observed in antibodies containing no Asp.
3. *Protein glycation(Maillard reaction)*. This type of reaction occurs between the carbonyl groups of reducing sugars and the lysine and arginine residues (the base) in proteins. A reducing sugar exhibits a free aldehyde group or ketone group and can act as a reducing agent. All monosaccharides (e.g. galactose, glucose, and fructose) are reducing sugars. Disaccharides can be either reducing or nonreducing. Nonreducing disaccharides include sucrose and trehalose. Their glycosidic bonds between anomeric carbons cannot convert to the openchain form with aldehyde group at the end. The examples of reducing disaccharides include lactose and maltose. The Maillard reaction is named after French chemist Louis Maillard and has been widely investigated in food industry. It is related to aroma, taste, and colour and is involved in cooking processes such as roasting, baking, and grilling. It is also known as nonenzymatic browning reactions because of the colour developed during the reaction. The Maillard reaction is very complicated but the initial basic reaction is the condensation of a reducing sugar with a compound containing an amino group (e.g. lysine or lysine residuals in peptides and proteins). The condensation product is Nsubstituted glycosilamine, which rearranges via Amadori rearrangement and then follows different mechanisms under different pHs to finally form Melanoidins (brown nitrogenous polymers) [79].

Oxidation. Proteins containing His, Met, Cys, Tyr, and Trp amino acids can be denatured by potential oxidation reactions on these side chains. The reactions may be easily initiated by atmospheric oxygen or the presence of other oxidation agents. The reactions may be photocatalysed or metalcatalysed. Apart from the intrinsic nature of the amino acids, surface area, moisture content, pH, and the presence of metal ions or other impurities in the solid protein formulations can have significant impact on the rate of oxidation. To avoid or limit the oxidation reactions, the solid formulations should be sealed properly (to reduce moisture or other solvent adsorption), exposure to oxygen (air) and potential UV irradiation should be minimized, and excipients should be added to reduce oxidation rate (e.g. mannitol as free radical scavengers, ethylenediaminetetraacetic acid (EDTA) to chelate metal ions) [11].

1. *Disulfide formation*. The Cys residues can form disulfide bonds, which may cause aggregation and affect the overall protein conformation. This process may be retarded by the removal of free Cys residues [11].

Physical Instability

Physical instability mainly involves thermal denaturation (particularly at high storage temperature) and denaturation from surface adsorption. Freezedrying usually leads to a highly porous structure with high surface areas, which may contribute significantly to surface adsorption. Thermally induced denaturation, characterized by DSC, is usually irreversible

because the unfolded protein molecules form aggregation. There are different mechanisms of protein aggregation induced by various factors [11, 80]. For a freezedrying process, protein aggregation can occur from freezing and lyophilization stresses. During storage of the solid formulations, the aggregation is likely to result mainly from chemical modifications, motion through the amorphous matrix, and surfaceinduced aggregation. Moisture content, pH, and other impurities can considerably influence the protein stability. The interaction of excipients with proteins and glass transition temperature (T_g) of the amorphous matrix are two important factors for storage of protein formulations. Generally, amorphous matrices with higher T_g reduce protein motion ability and contribute to higher stability. The presence of moisture can considerably reduce the overall T_g of the matrix and thereby the stability of the protein. In addition to the common stabilizing excipients such as sugars and surfactants, bulking agents (e.g. mannitol) can help produce an elegant cake structure and stabilize the proteins. However, the crystallization of the excipients or bulking agents can have detrimental effects on protein stability.

Upon reconstitution, small aggregates may be soluble (reversible aggregates) or well dispersible (for sizes 1–100 nm). The larger particles may be suspended or precipitated from the liquid formulations. Protein aggregates may show significant cytotoxic effects and immune response. The relationship between protein aggregates and immunogenicity has been examined and a mixed picture has been shown [81]. This may depend on the specific formulations and specific proteins. The important thing is that the protein aggregates in the formulations should be properly characterized and provided as a pharmaceutical product.

Improving Protein Stability

Depending on the proteins involved, suitable excipients should be selected for the formulations. Some aspects of choosing excipients have already been discussed earlier, for example, the use of nonreducing sugars, surfactants, suitable buffers, etc. The pH of the formulations should be considered both in the freezedrying process and in the reconstitution stage. The solution pH of the liquid solution after reconstitution can be regarded as a measure of the solid state microenvironment pH. This can help monitor the possible ‘pH’ of the solid formulation and its effect on protein stability and improve on the general protein formulation.

As mentioned earlier, the moisture content plays an important role. Maintaining a low moisture content is favourable for protein stability. Moisture transfer from the stopper to the solid formulation should be avoided. The proper seal on the vials should be kept all the time. The vials containing solid protein formulations may be stored in a dry and inert atmosphere. This will also decrease the chance of oxygen exposure.

Storage temperature is another important parameter. The degradation kinetics is faster at higher temperature. A low storage temperature is always preferred although this is not always possible particularly during shipping. Another potential problem is the crystallization of amorphous matrix. The rate of crystallization generally increases with increasing temperature and moisture content. Crystallization of the matrix can denature a protein because of the loss of closer excipient interaction with proteins and the possible decrease in T_g of the amorphous

matrix. With the crystallization, water molecules can be excluded from the crystalline phase and thereby increase the moisture content of the amorphous phase. The increasing moisture can result in the decrease of T_g. For example, with the widely used excipient/bulking agent mannitol [13], a metastable phase of mannitol can crystallize when storage/shipping temperature is higher than 45 °C, leading to disastrous destabilization of proteins [17]. For mannitol, there are three anhydrous crystalline forms (α, β, δ forms) and two metastable phases (hemihydrate and amorphous). Mannitol tends to form crystalline forms during freezedrying but the addition of an excipient such as sucrose can facilitate the formation and stabilize the metastable forms [82].

Stabilization Mechanisms in Solid Protein Formulations

'Water replacement' mechanism. This falls into the category of thermodynamic consideration. As mentioned in the stabilization measures during freezedrying, excipients such as sugars or polyols replace water in the hydration shell. This involves the interaction (mostly hydrogen bond formation) between the excipients and the proteins to maintain the native conformations of the proteins. Amorphous states of proteins and excipients allow closer contact between them and greater Hbonding opportunities. The crystallization of excipients (e.g. mannitol) during storage can cause increasing instability due to less hydrogen bonding [10]. The residual water in the matrix residing at the protein–sugar interface (socalled 'water entrapment') is also able to provide thermodynamic stabilization of the proteins via hydrogen bonding [78].

Matrix vitrification. This is dynamic (kinetic) control of protein degradation in amorphous matrix. The very high viscosity in the glass state can significantly slow down the motion, conformation relaxation, and chemical denaturation of the protein. As the storage temperature may vary, amorphous matrix with higher T_g is usually thought to offer higher stabilization, although this may not always be the case. The vitrification mechanism is related to the slow α relaxation of the sugar matrix. A longer α relaxation time τ_α may indicate slower degradation [78]. In the pharmaceutical field, it is common to assume that log (τ_α) scales approximately with ($T_g - T$) [83]. τ_α may be also determined by positron annihilation spectroscopy or by enthalpy relaxation techniques [77].

βRelaxation of the matrix . Although there are plenty of experimental observations that can be explained by the above two mechanisms, they cannot adequately account for the observation of protein stability in amorphous sugar matrix with antiplasticizing additives. Instead, the observed protein stability is directly linked to highfrequency β relaxation processes [78]. Amorphous solids exhibit three characteristic dynamic processes over a wide range of timescales: β_{fast} relaxation (picoseconds, temperature independent), Johari–Goldstein β (β_{JG}) relaxation (microsecond to millisecond), and the slow α relaxation (seconds to months) [77]. In the study of protein in sugar matrix with antiplasticizing additives, a linear relationship between degradation rates and β relaxation was observed. It was proposed that the high frequency β relaxation process impacts protein degradation through coupling of the β relaxation to local protein motions and diffusion of small

molecular reactive species in the amorphous matrix [77].

3.5.2 Biopharmaceutical Formulations

In Section 3.5.1, the routes to protein degradation and the ways of improving protein stability have been described. Selection and addition of suitable excipients are key to stable protein formulations. Figure 3.4 shows the molecular structures of the common excipients employed in protein solid formulations. In this section, we discuss, through some examples (without attempting to cover the literature comprehensively), how freezedrying processes have been applied in biopharmaceutical solid formulations and how the processing conditions and the selected use of excipients improve the stability of the biopharmaceutics.

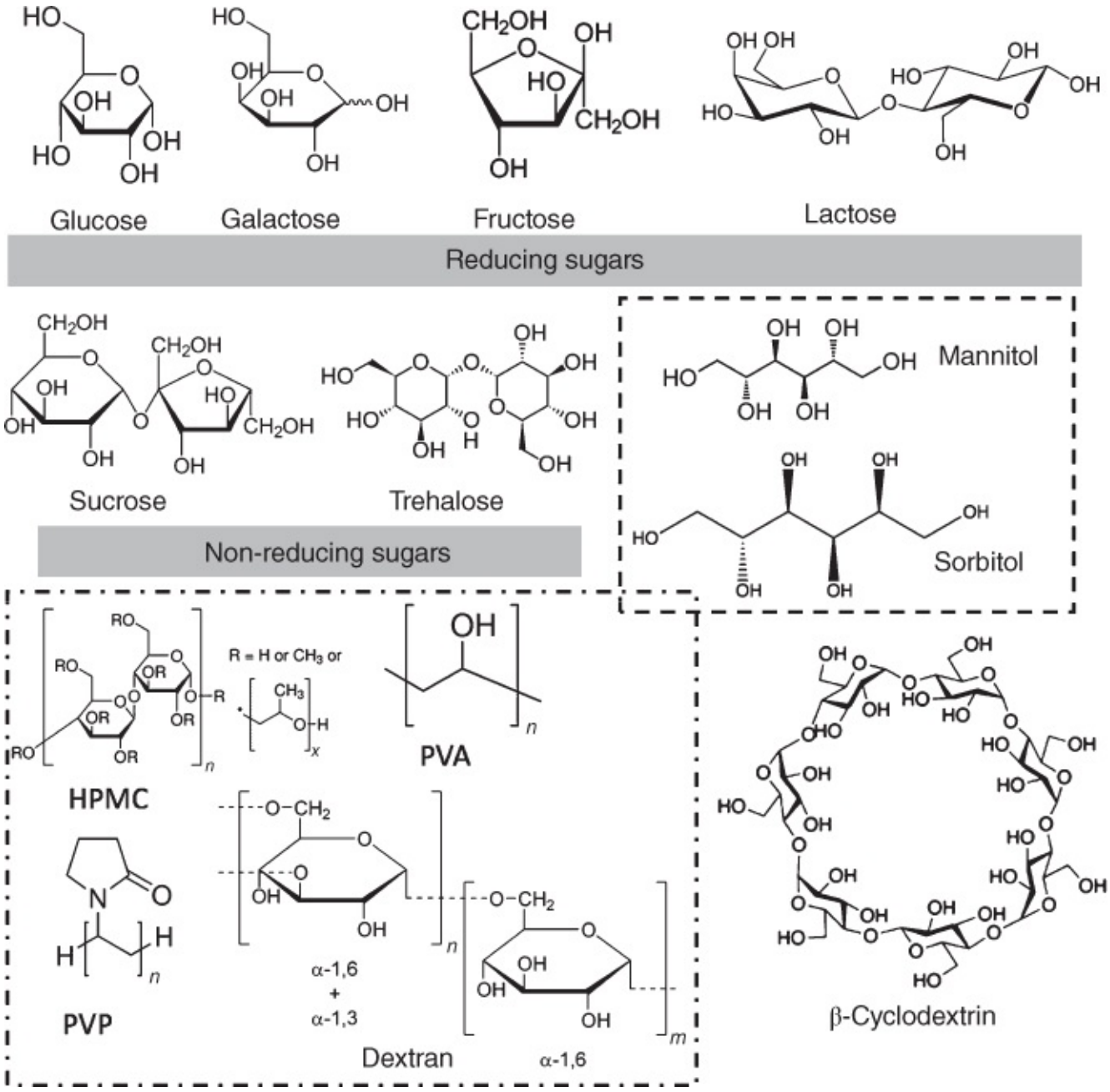

Figure 3.4 Molecular structures of commonly used excipients. Many of them also serve as cryoprotectants and/or lyoprotectants.

3.5.2.1 Peptide Formulations

In the classification spectrum of drugs based on molecular weight (M_w) (Figure 3.3), peptides can be positioned in the M_w region of 500–5000. Compared to small molecular drugs and proteins, pharmaceutical peptides are underinvestigated, although certainly emerging. There are more than 60 US FDAapproved peptide medicines and around 140 peptide drugs are in clinical trials [84]. But there are only approximately 20 new chemical entities (NCEs) for peptides and this number has not changed too much over the years [43]. Generally, small molecule drugs exhibit good solubility, membrane permeability, oral bioavailability, and metabolic stability, but poor target selectivity. Biopharmaceuticals such as proteins show target specificity and high potency but low stability and permeability. It is thought that the peptide drugs may combine the advantages of small drugs and proteins [43]. It should be pointed out that the classification based on M_w of 500–5000 is quite arbitrary. There are no distinctly different properties or scientific meaning for peptides and proteins around M_w 5000. For example, some researchers put insulin in the category of peptides and some others have reported it as a protein. Peptides may be defined as molecules containing fewer than 50 amino acids [43].

Native peptides in general do not cross cell membranes. Therefore, membrane permeability elements are inserted into the peptide molecules to form ‘cell penetrating peptides’ [84]. Via rational design and chemical modifications, e.g. introducing αhelixes, forming salt bridge, lactam bridge, the peptides can show better pharmaceutical properties [84]. Peptides with cyclic backbone are better resistant to proteolytic degradation [43]. Currently, most of the peptide drugs have less than 20 amino acids, representing 75% of existing marketed peptides [43]. Greater effort may be made to discover peptide drugs with the size up to 50 amino acids.

To improve the stability of peptide drugs, suitable excipients may be added into the formulations. Micro and nanoencapsulations are also effective and have been investigated [85]. Freezedrying is an effective method to prepare stable dry peptide formulations. For example, glucagon was dissolved in three different buffer solutions and then mixed with the excipient solutions. Polysorbate 20 was added as a polymeric surfactant. Three carbohydrate excipients, trehalose, hydroxyethyl starch, and βcyclodextrin, were investigated. The freezedried formulations were characterized by MS, HPLC, FTIR, DSC, and turbidity [86]. Contrary to proteins, it was thought that stabilizing the secondary structure of glucagon was not a prerequisite for its stability. The study showed that stable freezedried glucagon formulations could be produced. The presence of polysorbate 20 facilitated the decrease of glucagon aggregation and chemical degradation [86].

In a freezedrying study with a model peptide hormonehuman secretin (0.002 w/v%), excipients of NaCl (0.9 w/v%), cysteineHCl (0.15 w/v%), and mannitol (2 wt%) were investigated [87]. After reconstitution, the amount of secretin was measured by HPLC while the aggregated particles were examined by dynamic laser scattering (DLS). The storage of the solid formulations was studied at different temperatures (−20, 4, 25 and 25 °C/60% RH) and different periods (0, 1, 4, and 8 weeks). The study demonstrated that the increased crystallinity of mannitol occurred with time. The aggregated particles and increased reconstitution time

were observed with longer storage period and higher temperature/humidity [87].

3.5.2.2 Protein Formulations

Freezedrying has been mostly employed in solid protein formulations [1, 10, 11, 17, 56]. Some of the examples include monoclonal antibody (e.g. IgG) [88, 89], insulin [90, 91], cytokine [92], and enzymes [76, 90, 93]. Ó'Fágáin and Collition described the practical procedures of freezedrying protein formulations, aiming to achieve protein stability during freezedrying and storage [94]. Prevention of bacterial contamination, selection of suitable excipients, low temperature storage, and the operational procedures of the freezedrying were all covered, with useful notes on best practice and common pitfalls [94]. The research and development on solid protein formulations have focused on optimizing the excipients, formulations, and freezedrying process controls.

For example, alkaline phosphatase (a protein enzyme) was stabilized with inulin or trehalose and also ammediol as a plasticizer. The enzymatic activity of the protein remained stable when the T_g was well above the storage temperature [76]. It was concluded that the vitrification mechanism played a dominant role in stabilization when the storage temperature was up to 10–20 °C higher than T_g whilst the water replacement mechanism was the main factor for stabilization at higher T_g [76]. For the same protein, the freezedrying process was also performed with waterbinding substrates (sucrose, lactose) or nonwaterbinding substrates (mannitol, PVP). Not all the waterbinding substrates (the reducing sugar, lactose) could help to maintain the protein activity [93]. In the freezedried insulin formulation with trehalose or dextran, the two types of formulations showed different stability behaviours during storage with regard to storage temperature and relative humidity. βRelaxation mechanism seemed to be responsible for the degradation of insulin in the matrix of trehalose and dextran [95].

There are many studies focusing on the use of different excipients and newly designed excipients. It is important to find out what exactly affects the stability of the target proteins and what alternative methods may be taken to improve the stability. Oligosaccharides dextran and inulin of approximately the same M_w was combined with four proteins of different M_ws (6–540 kDa). It showed that molecular flexibility played a significant role in stabilizing the proteins. As long as the matrices are amorphous, smaller and more flexible sugar molecules can provide better stabilization due to less steric hindrance [90]. New excipients may be designed and synthesized to give better stabilization of protein pharmaceutics. For example, a series of polyethermodified *N*acy amino acids were synthesized and they were used as non ionic surfactants in protein formulations. The surfactant containing a phenylalanine moiety has shown slow thermal degradation and aggregation of IgG and IgGderived pharmaceutics, compared to the commonly used polysorbate surfactants [89].

Different freezing techniques, including freezedrier shelf [96], spray freezedrying [56], and thin film freezing [53], have been used for the preparation of solid protein formulations. An inhibition of mannitol crystallization was observed by addition of sucrose and NaCl during freezing. However, the annealing step promoted the formation of mannitol hydrate, which is known to undergo conversion into the anhydrous polymorph upon storage [97]. It was found

that the drying step was necessary to cause aggregation of the recombinant human interferonγ in a freezedried sucrose formulation, not the adsorption to the ice/liquid interface. However, an additional annealing step resulted in more nativelike protein structures and suppressing the aggregation upon reconstitution [98].

It is favourable to perform the freezedrying step at a higher temperature as this will considerably shorten the freezedrying cycle and it is economically beneficial. It is widely accepted that the product temperature during freezedrying should be below the T_g in order to get an elegant cake structure. Higher temperature freezedrying may be achieved by selecting suitable excipients that have high T_g. Recently, it was shown that it was possible to freezedry above the T_g in amorphous IgG formulations while maintaining the product quality. This was achieved by using highconcentration protein formulations [88]. However, this should be carefully examined, depending on specific protein formulations. This is because high protein concentration and the drying procedure could promote the transformation of excipient polymorphs [99].

Proteins have been encapsulated to protect their stability (either in the storage or in the GI) and enhance the chance of oral administration with better patient compliance [85]. Spray drying and spray freezedrying are some of the widely used methods [56, 100]. Dry micronsized particle powders are usually produced. Precipitation and emulsion evaporation are the mostly used methods to produce proteinencapsulated nanospheres [85, 100]. As these nanospheres are prepared as aqueous suspension, freezedrying of the nanoparticle suspensions is usually required to produce dry formulations with improved stability for shipping and storage [101]. Similarly to freezedrying of liquid protein formulation, the proteins in nanoparticle suspensions during freezedrying are highly likely to experience the same freezing stress, freezedrying stress, and the stability issues during solid storage. This indicates that suitable excipients should be also included in the proteinencapsulated nanoparticle suspensions.

Insulinloaded poly(lactic *co*glycolic acid) (PLGA) nanoparticles were prepared by an emulsion evaporation method based on W/O/W double emulsions and were freezedried with different cryoprotectants (trehalose, glucose, sucrose, fructose, and sorbitol) at a concentration of 10 w/v% [102]. In general, the addition of cryoprotectants improved the protein stability. Compared to the formulations without cryoprotectants, the content of insulin native structure in the freezedried formulations was enhanced from 71% to 79% on average. Among these formulations, the sorbitolbased formulation showed better stabilization capability [102]. Effects of different carbohydrates and polymeric cryoprotectants (Microcelax®mixture of lactose and Avicel, AvicelPH102microcrystalline cellulose, mannitol, sucrose, Avicel RC591, maltodextrin, Aerosil, and PEG4000) on freezedrying of nanostructured lipid carriers were investigated. Among the tested excipients, Avicel RC591 was found to be most effective in maintaining the particle sizes [103]. Different sugar excipients at the concentrations of 1–3 w/v% were applied to the freezedrying of nonloaded and doxorubicinloaded PEGylated human serum albumin (HSA) nanoparticle suspensions. It was found that 3 w/v% concentration generated the best stabilization result and sucrose and trehalose displayed better longterm storage stability than mannitol [104]. Later, a similar

finding for freezedrying of HI6loaded recombinant HSA nanoparticles was reported [105]. Instead of adding sugar excipients into the nanoparticle suspensions, the co encapsulation of cryoprotectants (trehalose, sucrose or sorbitol) into insulinloaded PLGA nanoparticles could also mitigate the freezing stresses to maintain protein activity [85]. Similar to freezedrying protein formulations, annealing of frozen nanoparticle samples could affect the drying process. This was shown by the accelerated sublimation rate but without affecting the nanostructure when annealing a nanocapsule sample [106].

3.5.2.3 Vaccine Formulations

Vaccines save millions of people over the years by immunization against tuberculosis, polio, diphtheria, tetanus, measles, hepatitis B, and pertussis. It is estimated that these vaccines can save about 2.5 million lives each year. However, the significant issue of vaccine shortage remains and vaccines are not accessible to every person in developing countries. It is the goal of the Global Vaccine Action Plan (GVAP), to deliver full access to immunization by 2020. Vaccine shortage has been enhanced by stability problems during storage and shipping as well as by the lack of medical workers (because vaccines are usually available as injection formulations). Vaccines can be classified into different types: live attenuated vaccines, inactivated vaccines, subunit vaccines, toxoid vaccines, conjugate vaccines, DNA vaccines, and recombinant vector vaccines [107]. Live attenuated vaccines consist of viruses that have lost their virulence but are still able to provide a protective immunity against a virulent virus. These types of vaccines are easier to produce (than inactivated vaccines) and are the most successful of the human vaccines because they can offer longterm immunity [108].

Adjuvants are materials added to vaccine formulations in order to improve immunological response. The criteria for an adjuvant are safety, stability, and the cost. Adjuvants are usually introduced to subunit and recombinant protein vaccines [109]. These vaccines are highly purified antigens, contain only a part of the pathogen to generate immune response, and are safer because they have no ability to revert to a virulent form. The often used adjuvants include aluminium salts, emulsions, and liposomes, which have been proven to be safe and cheaper [109, 110]. There are newly developed adjuvants that combine the usual adjuvants and immune potentiators, e.g. AS04 [109, 110]. For vaccine formulations, the interaction of vaccine and adjuvant and the stability of both vaccine and adjuvant should be considered [110].

Vaccines are conventionally produced in liquid forms. The stability of vaccines may be maintained in a cold medium with suitable cryoprotectants such as nonreducing sugars, polymer surfactants, and buffers. The storage temperatures may go down to −20 °C or even −60 °C. A storage temperature above 8 °C is always harmful for vaccines [109]. Whenever the cold temperature cannot be maintained during storage, shipping, or delivering, the outcome of the accelerated degradation in aqueous medium can be disastrous.

Like solid protein formulations, the freezedrying of vaccine can also provide higher stability and the potential for oral administration [108, 111]. The latter development can be highly beneficial because a trained medical worker may not be required to deliver the vaccine to patients. Similar stabilizing mechanisms and approaches from solid protein formulations may

be applied to vaccine freezedrying [110, 112]. However, for live attenuated vaccines, additional freezing stabilization may be required, like what has been required in cell cryopreservation [108, 113]. The control of ice nucleation and crystal growth is critical in cryopreservation where the dehydration stress during freezing and mechanical damage of ice crystal growth should be minimized. The effects of change in pH, osmolarity, and solute concentration can be more significant. In the vaccine freezedrying applications, similar excipients as those used in solid protein formulations have also been employed, e.g. potassium phosphate (pH 6–8, in the range of virus activity, despite small pH change during freezing), sucrose/trehalose/sorbitol [108]. Usually, the vaccine and adjuvant are mixed together before using. This can generate financial and technological barriers. By freezedrying a nanoemulsion containing both tuberculosis antigen and adjuvant, one single vial containing the dry formulation of both components can be produced, reducing the coldchain dependence of the vaccine product [114]. Although freezedrying is very promising, other drying methods such as foam drying should still be considered, depending on the type of vaccines. In a recent study, it was found that the dry formulation of live attenuated influenza vaccines prepared by foam drying was an order of magnitude more stable than those prepared by freezedrying and spray drying [115].

3.5.2.4 Nucleic Acidbased Formulations

Nucleic acids are biopolymers composed of monomers called nucleotides. A nucleotide is formed from the condensation reaction of phosphoric acid, 2deoxyribose (or ribose), and Ncontaining organic bases. The polynucleotides formed from 2deoxyribose are called deoxyribonucleic acids, abbreviated as DNA, while the ones from ribose are called ribonucleic acids, abbreviated as RNA. DNA are double strands formed from pairing bases. Three kinds of RNAs are identified: ribosomal RNA (rRNA, the majority), messenger RNA (mRNA), and transfer RNA (tRNA). In both RNA and DNA, the acidity and negative charges result from the phosphoric acid in the polymer chains.

Nucleic acids are used as biopharmaceutics to treat infectious diseases and incurable diseases such as cancer and genetic disorders. The therapeutic treatments depend on either replacing a modified gene with the healthy one or completing a missing one to express the required proteins [116]. This means that the nucleic acid pharmaceutics need to transport through cell membrane (for RNAs) and further move into the nucleus (for DNAs). It is very difficult for the naked RNAs or DNAs to survive the transporting process. Viruses are initially used as carriers to transport RNA/DNA into the cell or cell nucleus. However, the risk of triggering immune response by using viruses as delivering vectors can be disastrous. Furthermore, the costs of preparation and storage of virus formulations are very high. Nonvirus gene carriers have thus been widely investigated and used [116].

The nucleic acidbased therapeutics include plasmid DNAs (pDNAs, introduce transgenes into cells), oligonucleotides (short singlestranded segments of DNA, duplex with mRNA for antisense applications, triplex with DNA for antigene applications), ribozymes (RNA molecules able to sequencespecifically cleave mRNA), DNAzymes (analogues of ribozymes with greater stability), aptamers (small singlestranded or doublestranded segments,

directly interact with proteins), and small interfering RNAs (siRNAs, short doublestranded RNA segments, downregulate diseasecausing genes via RNA interference) [117]. pDNAs typically contain 5000 base pairs or more while siRNAs usually have only 20–25 base pairs [118]. In order to deliver DNAs/RNAs, the commonly used nonvirus carriers are cationic, forming complex with DNAs/RNAs via electrostatic interactions. These carriers include lipids (forming lipoplex), polymers (forming polyplex), and nanoparticles with positive surface charges [116]. Different lipids and polymers such as polyethyleneimine (PEI), poly(lysine), chitosan, and dendrimer polyamidoamine have been widely used. The complexation of polycations and pDNAs can condense the large pDNA molecules into very small structures that can enhance its transport across cellular barriers. But this condensation effect may be limited to polynucleotides greater than 400 bases [118].

Liquid formulations can be readily prepared and are convenient to use particularly in parenteral administration. However, polyplexes and lipoplexes in aqueous media are not favoured for shipping and longterm storage [119]. Freezedrying the liquid formulations is an effective route to enhancing storage stability. Linear PEI (M_w 800 Da–800 kDa) was complexed with oligodeoxynucleotide (ODN) and ribozyme. The freezedried products showed no loss of activity for ODN–PEI and ribozyme–PEI but a decrease of the transfection efficiency was observed for plasmid–PEI. However, this could be addressed by adding trehalose, mannitol or sucrose as lyoprotectants [120]. In another study, the freezedried plasmid/PEI (M_w 22 kDa) polyplex showed longterm stability. The products from isotonic formulations with 14% lactosucrose, 10% hydroxypropylbetadex/6.5% sucrose or 10% povidone/6.3% sucrose showed no particle size change after storage for 6 weeks at 40 °C. Polyplexes with lactosucrose or hydroxyproplybetadex/sucrose showed high transfection efficiencies and cellular metabolic activities [121]. Mesoporous silica nanoparticles were coated with PEI and then complexed with DNA. The freezedried formulations showed enhanced gene expression and higher efficiency. The use of trehalose as lyoprotectant facilitated the formulation stability – maintaining the activity for at least 4 months storage at room temperature [122]. Freezedried lipid/DNA complexes with glucose, sucrose, or trehalose as lyoprotectants were investigated for longer term storage (up to 2 years) at temperatures of −20 to −60 °C. Degradations were observed in terms of transfection rates, particle size, dye accessibility and supercoil content in all the temperatures. It was found that preventing the formation of reactive oxygen species in the dry state storage was very important to maintain the stability [123].

It was observed that freezedrying siRNA–liposome in ionic solutions led to the functionality loss of 65–75% while the addition of sugars (trehalose, sucrose, lactose, glucose) could maintain transfection efficiency with no loss [124]. The freezedried siRNA with PEGylated lipids showed the mucoadhesive property and could be rehydrated by body fluid to form a hydrogel and achieve the sustained release of siRNA [125]. Trehalosebased block copolycations were synthesized and could form stable complex with pDNA. These polymers could act both as stabilizer and lyoprotectant. Without adding sugar as lyoprotectant, the freezedried formulation showed good stability and high gene expression after reconstitution. From the study of the in vivo pDNA delivery, these polymers exhibited favourable properties

in cytotoxicity, cellular uptake, and transfection ability [126].

Spray freezedrying is an alternative technique for lyophilization of nucleic acidbased formulations, particularly for lipid nanoparticle [127, 128]. In addition to the enhanced stability, spray freezedrying is highly effective in producing porous powders for pulmonary delivery via inhalation devices [119]. Particularly, due to its poor pharmacokinetics, it is preferred to deliver siRNA for local administration, e.g. inhalation for respiratory diseases [129]. Sugars are usually added as lyoprotectants to enhance the formulation stability. This has been demonstrated by lipid/pDNA [130] and PEI/DNA with sugar additives (sucrose, trehalose, mannitol) [131]. Biodegradable polycations were synthesized and formed complex with pDNA. Porous particle powders (5–10 μm in diameter) were produced by the spray freezedrying process, with the integrity of pDNA maintained [132]. It was also noted that the addition of LLeucine in the formulation could improve the inhalation performance [132]. pH responsive peptides were complexed with DNA. Mannitol was added as lyoprotectant for the preparation of inhalable dry powders [133]. This study also compared the performance of the formulations produced both by spray freezedrying and spray drying. The spray drying powders showed some advantages [133]. pH responsive peptides were also used in the inhalable siRNA formulations, which showed antiviral activity against H1N1 influenza virus, although prepared by a spray drying method [134].

3.6 Freezedrying in Food Applications

3.6.1 Simple Freezedrying

Drying is a process used to preserve food. Industrial production of foods is generally achieved by convective drying or hot air drying. However, these drying methods often lead to significant shrinkage and quality loss of the foods. Freezedrying has been widely used for food preservation to improve the longterm storage, but mainly for highvalue foods. The high value foods may include but are not limited to: (i) seasonal and perishable commodities; (ii) baby foods with maximum quality and nutrition; (iii) nutraceutical foods; (iv) organoleptic foods (e.g. flavours, aromatic herbs, coffee); and (v) specially designed foods for outdoor activities such as military foods, space foods, etc. [135]. The drying process may cause changes in the physical aspects including colour (although this may be a result of chemical degradation/reaction), structure (e.g. hard casing, shrinkage), and chemical deterioration of aroma compounds and degradation of nutritional components. Generally, freezedrying can lead to minimal shrinkage, maintain the porous structure and texture, and offer the best potential for rehydration. For example, when drying berries, the volume shrinkage during freezedrying is around 5–15% while it is approximately 80% for air drying [136]. Owing to the greater costs than air drying, freezedrying can only be economical for the production of highvalue foods. But it has been widely used in the production of dry meat, fruits, vegetables, and functional foods [135–138].

Although freezedrying is a better drying technique in preserving food quality, the freeze dried food may be not as nutritious or delicious as fresh food. For example, the content of

phenolics is lower in the freezedried extract [139]. After freezedrying fruit pulps, the activity, texture, and browning index should be evaluated against the fresh ones [140]. Other techniques may be combined with freezedrying to reduce the drying time and/or improve shelf time. For example, during atmospheric freezedrying of shrimps, pretreatment by vacuum thermal drying and osmotic dehydration were used to reduce the drying time and the effects were investigated [141]. Broiler chicken meat was treated by a flow of ozone before freezedrying. This process could extend the shelflife up to 8 months [142].

3.6.2 Encapsulation

For sensitive and/or volatile food additives, simple freezedrying would not be able to preserve these additives. Encapsulation of these additives into matrix or nanospheres/microspheres has been an effective approach to addressing this problem. The encapsulation can protect the active/volatile ingredients from the surrounding environment, prevent or reduce the loss, and control the release of these ingredients in a timely manner at the right place. This method can transfer the liquid form to an easily handled solid form, also offering longerterm storage [28, 143]. The encapsulation procedure involves the core materials that are incorporated into particles or matrix and the wall materials that encapsulate or surround the active core materials. A variety of food components, protein powders, oils, flavours, cells, and enzymes have been used as core materials. The common wall materials include maltodextrin, chitosan, modified starch, gums, whey protein, skimmed milk powder, soya protein isolate, gelatin, cyclodextrin, lecithin, and modified cellulose [28, 143–145].

Different methods have been used for the encapsulation, including spray drying, extrusion, coacervation, emulsification, molecular inclusion, and fluidizedbed coating [28, 143–145]. Freezedrying is unique in that it can result in minimal shrinkage, has a good structure and is suitable for heatsensitive actives. The encapsulation can be carried by directly freeze drying aqueous solutions containing the wall material and food ingredients (e.g. fruit extract) [146]. The prerequisite is that these food actives should be soluble in water although it is possible to suspend powders in the aqueous medium. For the hydrophobic compounds or oils, an emulsion may be formed first and then subjected to freezedrying [147, 148]. However, the mostly used method is spray freezedrying. Different liquid formulations, including aqueous solutions, suspensions, and emulsions, can be spray freezedried to produce dry encapsulated powders [28, 36, 143–145, 149]. These powders can be easily handled for packaging or mixing with other food ingredients. The type of the wall materials and the porosity and the size of the microparticles may be tuned for controlled release or fast rehydration.

3.6.3 Probiotic Foods

Probiotics can be defined as live microorganisms that benefit the host when administered. Probiotic foods can benefit the immune system, strengthen the mucosal barrier and suppress intestinal infection. High levels of viable microorganisms (in excess of 10^9 cfu day^{-1}) may be required in probiotic foods for efficacy [150]. For probiotics to be used in foods successfully, several criteria must be met: good viability and activity, stability during processing and

storage, being alive during passage in the upper GI tract and arriving at the action site, and functioning in the gut environment [151]. The dairy fermentation industries, including production of cheese, yoghurt, and sour cream, are ranked second only to the production of alcoholic beverages. It has been well established that some lactic acid bacteria play a very important role in the fermentation processes [152]. In fermented probiotic processes, it is common to culture probiotic bacteria with other types of bacteria (starters) in order to generate good sensory properties.

Freezedrying is a preferred method to make dry formulations of microorganisms, which offer the benefit of easy handling, transport, and longterm storage [153]. Again, the low shrinkage and porosity associated with freezedrying contribute to fast rehydration with the maximal activity of microorganisms. Like cell cryopreservation [113] or freezedrying of live vaccines, the control of the freezing process is very important for maintaining the probiotic bacteria activity. Cryoprotectants should be added. Fast freezing with small ice crystals may be beneficial for the bacteria [150].

Similar to what has been described for freezedrying of biopharmaceutics, a variety of sugars and polymers can act as cryoprotectants and lyoprotectants for the freezedrying process as well as stabilizers for storage. The protectants that are usually used include trehalose, sorbital sucrose, glucose, lactose, maltodextrin, skim milk powder, whey protein, betaine, dextran, and PEG [150, 152]. The protecting compounds may be added to the probiotic bacteria suspensions before freezedrying. For example, glucose, lactose, trehalose, and skim milk were added either alone or combined before freezedrying *Lactobacillus rhamnosus* and *Lactobacillus casei/paracasei*. Survival rates greater than 94% were observed immediately after freezedrying. When stored under refrigeration, the freezedried formula with skim milk alone or supplemented with trehalose or lactose showed the best performance after 39 weeks of storage. The lowest survival was found with glucose and glucose plus milk for non refrigerated storage; no viable cells were left at the end [154]. Conventional freezedrying and spray freezedrying were compared for the microencapsulation of *L. paracasei*. The spray freezedrying method was found to be better, with >60% of probiotic cell viability. In the freezing stage, high concentrations of trehalose helped preserve the cell viability. Overall, higher concentrations of protectants (maltodextrin, trehalose) contributed to high probiotic viability during freezedrying and storage [155]. In addition to sugars and disaccharides, polymerbased formulations could also support the viability of probiotic cells effectively [156].

Sugar protectants may be also added to the culture media prior to fermentation to facilitate the adaptation of probiotic cells to the environment. When grown in batch culture, the growth of bacterial culture may be divided into four stages: log, lag, stationary, and death phases. At the stationary phase, the cells develop a general stress resistance and are thus more resistant to the surrounding stresses. Therefore, freezedrying the probiotic cells at the stationary phase is the optimal stage to maintain cell viability [150]. When adding sugar protectants in the culture media, they can accumulate within the cells. The osmotic difference between the internal and external environment is reduced. This can help mitigate the stresses induced by freezing. For example, the presence of sugars such as lactose, sucrose, and trehalose during the growth of

probiotic cells was found to help adapt to freezing and thawing stresses [157]. The lower decrease in viability after freezedrying was observed when *Lactobacillus bulgaricus* was grown with mannose (the best), fructose, and sorbital [158]. Metabolites such as mannitol, sorbitol, and glutamate, which in most cases remain inside the cells, may contribute to the improved survival rate during freezedrying [159].

The selection of protectants for the freezedrying process can have significant impact on the storage. Nonreducing sugars may be a better choice due to the potential Maillard reactions of reducing sugars with cell proteins [79]. Storage temperature, relative humidity, powder composition, and exposure to oxygen and light are the important factors on the viability of probiotic cells in the dry powders during storage. Rehydration is the final critical step for the revival of probiotic cells after storage. It has been suggested that freezedrying the cells at the stationary phase and employing a slow rehydrating procedure may produce the best results [150].

3.7 Summary

Freezedrying has been widely used in solid pharmaceutical and biopharmaceutical formulations, with the main objective being high stability during longterm storage and reconstitution. Excipients have been added to the formulations to maintain the functions of APIs, reduce the stresses during freezing and freezedrying, and enhance the stability during storage. Different types of excipients are described and some of the common excipients are given as examples. From the industrial point of view, reducing the freezedrying costs, by reducing freezedrying time or raising the freezedrying temperatures is essential; this has been addressed in this chapter. This may be achieved by the use of different freezing techniques (e.g. spray freezedrying, spin freezing) and various freezedrying options.

This chapter has also focused on the applications of freezedrying in pharmaceutics, biopharmaceutics, and foods (especially probiotic foods). Special attention is paid to solid protein formulations, with stabilizing mechanisms, degradation routes, and stabilizing options being discussed extensively. A variety of solid formulations in each category are described in detail, emphasizing the advantages resulting from freezedrying, providing examples for freezedried formulations, and comparing with other formulation approaches. This demonstrates the importance and uniqueness of the freezedrying technique in industrial applications. The principles and formulations that are used to produce highquality products may be adopted to fabricate icetemplated materials as will be discussed in the following chapters.

References

1 Carpenter, J.F., Chang, B.S., GarzonRodriguez, W., and Randolph, T.W. (2002). Rational design of stable lyophilized protein formulations: theory and practice. In: Rationale Design of Stable Protein Formulations – Theory and Practice (ed. J.F. Carpenter and M.C. Manning), 109–133. New York: Kluwer Academic/Plenum Publishers.

2 Ógáin, O.N., Li, J., Tajber, L. et al. (2011). Particle engineering of materials for oral inhalation by dry powder inhalers. I – Particles of sugar excipients (trehalose and raffinose) for protein delivery. *Int. J. Pharm.* 405: 23–35.

3 Qian, L. and Zhang, H. (2011). Controlled freezing and freeze drying: a versatile route for porous and micro/nanostructured materials. *J. Chem. Technol. Biotechnol*. 86: 172–184.

4 Deville, S. (2013). Icetemplating, freeze casting: beyond materials processing. *J. Mater. Res*. 28: 2202–2219.

5 Debotton, N. and Dahan, A. (2017). Applications of polymers as pharmaceutical excipients in solid oral dosage forms. *Med. Res. Rev.* 37: 52–97.

6 Pifferi, G. and Restani, P. (2003). The safety of pharmaceutical excipients. *Il Farmaco* 58: 541–550.

7 Qian, L. and Zhang, H. (2013). Onestep synthesis of proteinencapsulated microspheres in a porous scaffold by freezedrying double emulsions and tuneable protein release. *Chem. Commun.* 49: 8833–8835.

8 Grant, N. and Zhang, H. (2011). Poorly watersoluble drug nanoparticles via an emulsion freezedrying approach. *J. Colloid Interface Sci*. 356: 573–578.

9 DeMerlis, C.C. and Schoneker, D.R. (2003). Review of the oral toxicity of polyvinyl alcohol (PVA). *Food Chem. Toxicol*. 41: 319–326.

10 Wang, W. (2000). Lyophilization and development of solid protein pharmaceuticals. *Int. J. Pharm.* 203: 1–60.

11 Manning, M.C., Chou, D.K., Murphy, B.M. et al. (2010). Stability of protein pharmaceuticals: an update. *Pharm. Res.* 27: 544–575.

12 Walters, R.H., Bhatnagar, B., Tchessalow, S. et al. (2014). Next generation drying technologies for pharmaceutical applications. *J. Pharm. Sci*. 103: 2673–2695.

13 Ohrem, H.L., Schornick, E., Kalivoda, A., and Ognibene, R. (2014). Why is mannitol becoming more and more popular as a pharmaceutical excipient in solid dosage forms? *Pharm. Dev. Technol*. 19: 257–262.

14 Del Valle, E.M.M. (2004). Cyclodextrin and their uses: a review. *Process Biochem.* 39: 1033–1046.

15 Chen, M.L. (2008). Lipid excipients and delivery systems for pharmaceutical development: a regulatory perspective. *Adv. Drug Delivery Rev.* 60: 768–777.

16 McClements, D.J. and Xiao, H. (2014). Excipient foods: designing food matrices that improve the oral bioavailability of pharmaceuticals and nutraceuticals. *Food Funct*. 5: 1320–1333.

17 Carpenter, J.F., Pikal, M.J., Chang, B.S., and Randolph, T.W. (1997). Rational design of stable lyophilized protein formulations: some practical advice. *Pharm. Res.* 14: 969–975.

18 Akers, M.J. (2002). Excipient–drug interactions in parenteral formulations. *J. Pharm. Sci.* 91: 2283–2300.

19 Buggins, T.R., Dickinson, P.A., and Taylor, G. (2007). The effects of pharmaceutical excipients on drug disposition. *Adv. Drug Delivery Rev.* 59: 1482–1503.

20 Loftsson, T. (2015). Excipient pharmacokinetics and profiling. *Int. J. Pharm.* 480: 48–54.

21 Loftsson, T. (2015). Essential Pharmacokinetics: A Primer for Pharmaceutical Scientists. Elsevier Science.

22 Lipinski, C.A., Lombardo, F., Dominy, B.W., and Feeney, P.J. (2001). Experimental and computational approaches to estimate solubility and permeability in drug discovery and development settings. *Adv. Drug Delivery Rev.* 46: 3–26.

23 Amidon, G.L., Lennernas, H., Shah, V.P., and Crison, J.R. (1995). A theoretical basis for a biopharmaceutic drug classification: the correlation of in vitro drug product dissolution and in vivo bioavailability. *Pharm. Res.* 12: 413–420.

24 Wu, C.Y. and Benet, L.Z. (2005). Predicting drug disposition via applications of BCS: transport/absorption/elimination interplay and development of a biopharmaceutics drug disposition classification system. *Pharm. Res.* 22: 11–23.

25 Wessel, W., Schoog, M., and Winkler, E. (1971). Polyvinylpyrrolidone (PVP), its diagnostic, therapeutic and technical application and consequence thereof. *Arzneim.Forsch.* 21: 1468–1482.

26 Longmire, M., Choyke, P.L., and Kobayashi, H. (2008). Clearance properties of nano sized particles and molecules as imaging agents: considerations and caveats. *Nanomedicine* 3: 703–717.

27 Ishwarya, S.P., Anandharamakrishnan, C., and Stapley, A.G.F. (2015). Spray–freeze drying: a novel process for the drying of foods and bioproducts. *Trends Food Sci. Technol.* 41: 161–181.

28 Ray, S., Raychaudhuri, U., and Chakraborty, R. (2016). An overview of encapsulation of active compounds used in food products by drying technology. *Food Biosci.* 13: 76–83.

29 Rogers, T.L., Nelsen, A.C., Sarkari, M. et al. (2003). Enhanced aqueous dissolution of a poorly water soluble drug by novel particle engineering technology: sprayfreezing into liquid with atmospheric freezedrying. *Pharm. Res.* 20: 485–493.

30 Hu, J., Rogers, T.L., Brown, J. et al. (2002). Improvement of dissolution rates of poorly water soluble APIs using novel spray freezing into liquid technology. *Pharm. Res.* 19: 1278–1284.

31 Zhang, H., Wang, D., Butler, R. et al. (2008). Formation and enhanced biocidal activity of waterdispersible organic nanoparticles. *Nat. Nanotechnol.* 3: 506–511.

32 De Meyer, L., Van Bockstal, P.J., Corver, J. et al. (2015). Evaluation of spin freezing versus conventional freezing as part of a continuous pharmaceutical freezedrying concept for unit doses. *Int. J. Pharm.* 496: 75–85.

33 Merymann, H.T. (1959). Sublimation freezedrying without vacuum. *Science* 130: 628–629.

34 Lewin, L.M. and Mateles, R.I. (1962). Freeze drying without vacuum: a preliminary investigation. *Food Technol.* 16: 94–96.

35 Leuenberger, H., Plitzko, M., and Puchkov, M. (2006). Spray freeze drying in a fluidized bed at normal and low pressure. *Drying Technol.* 24: 711–719.

36 Anandharamakrishnan, C., Rielly, C.D., and Stapley, A.G.F. (2010). Sprayfreezedrying of whey proteins at subatmospheric pressures. *Dairy Sci. Technol.* 90: 321–334.

37 Lim, J.Y., Kim, N.A., Lim, D.G. et al. (2016). Process cycle development of freeze drying for therapeutic proteins with stability evaluation. *J. Pharm. Invest.* 46: 519–536.

38 US Food and Drug Administration (2004). *Guidance for Industry PAT – A Framework for Innovative Pharmaceutical Development, Manufacturing, and Quality Assurance*, (accessed September 2014). http://www.fda.gov/downloads/drugs/guidances/ucm070305.pdf.

39 AwotweOtoo, D. and Khan, M.A. (2015). Lyophilization of biologics: an FDA perspective. In: Lyophilized Biologics and Vaccines (ed. D. Varshney and M. Singh). New York: Springer Science + Business Media.

40 AwotweOtoo, D., Agarbi, C., Wu, G.K. et al. (2012). Quality by design: impact of formulation variables and their interactions on quality attributes of a lyophilized monoclonal antibody. *Int. J. Pharm.* 438: 167–185.

41 Fissore, D., Pisano, R., and Barresi, A.A. (2011). Advanced approach to build the design space for the primary drying of a pharmaceutical freezedrying process. *J. Pharm. Sci.* 100: 4922–4933.

42 Read, E.K., Shah, R.B., Riley, B.S. et al. (2010). Process analytical technology (PAT) for biopharmaceutical products: part II. Concepts and applications. *Biotechnol. Bioeng.* 105: 285–295.

43 Craik, D.J., Fairlie, D.P., Liras, S., and Price, D. (2013). The future of peptidebased drugs. *Chem. Biol. Drug Res.* 81: 136–147.

44 Wais, U., Jackson, A.W., He, T., and Zhang, H. (2016). Nanoformulation and encapsulation approaches for poorly watersoluble drug nanoparticles. *Nanoscale* 8: 1746–1769.

45 Chen, M.L., Amidon, G.L., Benet, L.Z. et al. (2011). The BCS, BDDCS, and regulatory guidances. *Pharm. Res.* 28: 1774–1778.

46 Hosey, C.M., Chan, R., and Benet, L.Z. (2016). BDDCS predictions, selfcorrecting aspects of BDDCS assignments, BDDCS assignment corrections, and classification for more than 175 additional drugs. *AAPS J.* 18: 251–260.

47 Janssens, S. and Van den Mooter, G. (2009). Review: Physical chemistry of solid dispersions. *J. Pharm. Pharmacol*. 61: 1571–1586.

48 Dahan, A., Beig, A., Lindley, D., and Miller, J.M. (2016). The solubility–permeability interplay and oral drug formulation design: two heads are better than one. *Adv. Drug Delivery Rev.* 101: 99–107.

49 Dahan, A., Beig, A., IoffeDahan, V. et al. (2013). The twofold advantage of the amorphous form as an oral drug delivery practice for lipophilic compounds: increased apparent solubility and drug flux through the intestinal membrane. *AAPS J.* 15: 347–353.

50 Roberts, C.J. and Debenedetti, P.G. (2002). Engineering pharmaceutical stability with amorphous solids. *AIChE J.* 48: 1140–1144.

51 Teagarden, D.L. and Baker, D.S. (2002). Practical aspects of lyophilisation using non aqueous cosolvent systems. *Eur. J. Pharm. Sci*. 15: 115–133.

52 Yu, H., Teo, J., Chew, J.W., and Hadinoto, K. (2016). Dry powder inhaler formulation of highpayload antibiotic nanoparticle complex intended for bronchiectasis therapy: spray drying versus spray freeze drying preparation. *Int. J. Pharm.* 499: 38–46.

53 Overhoff, K.A., Johnston, K.P., Tam, J. et al. (2009). Use of thin film freezing to enable drug delivery: a review. *J. Drug Delivery Sci. Technol*. 19: 89–98.

54 Engstrom, J.D., Lai, E.S., Ludher, B.S. et al. (2008). Formation of stable submicron protein particles by thin film freezing. *Pharm. Res.* 25: 1334–1346.

55 Overhoff, K.A., Engstrom, J.D., Chen, B. et al. (2007). Novel ultrarapid freezing particle engineering process for enhancement of dissolution rates of poorly watersoluble drugs. *Eur. J. Pharm. Biopharm.* 65: 57–67.

56 Wanning, S., Süverkrüp, R., and Lamprecht, A. (2015). Pharmaceutical spray freeze drying. *Int. J. Pharm.* 488: 136–153.

57 Manyikana, M., Choonara, Y.E., Tomar, L.K. et al. (2016). A review of formulation techniques that impact the disintegration and mechanical properties of oradispersible drug delivery technologies. *Pharm. Dev. Technol*. 21: 354–366.

58 Schiermeier, S. and Schmidt, P.C. (2002). Fast dispersible ibuprofen tablets. *Eur. J. Pharm. Sci*. 15: 295–305.

59 Roberts, A.D. and Zhang, H. (2013). Poorly watersoluble drug nanoparticles via solvent evaporation in watersoluble porous polymers. *Int. J. Pharm.* 447: 241–250.

60 Ahmed, I.S., Nafadi, M.M., and Fatahalla, F.A. (2006). Formulation of fastdissolving ketoprofen tablet using freezedrying in blisters technique. *Drug Dev. Ind. Pharm.* 32: 437–442.

61 Ahmed, I.S., Shamma, R.N., and Shoukri, R.A. (2013). Development and optimization of lyophilized orally disintegrating tablets using factorial design. *Pharm. Dev. Tech.* 18: 935–943.

62 Strange, U., Führling, C., and Gieseler, H. (2014). Formulation, preparation, and evaluation of novel orally disintegrating tablets containing tastemasked naproxen sodium granules and naratriptan hydrochloride. *J. Pharm. Sci.* 103: 1233–1245.

63 Arora, S., Ali, J., Ahuja, A. et al. (2005). Floating drug delivery systems: a review. *AAPS PharmSciTech* 6: E372–E390.

64 Yadav, S., Nyola, N.K., Jeyabalan, G., and Gupta, M. (2016). Gastroretentive drug delivery system: a concise review. *Int. J. Res. Pharm. Sci.* 6: 19–24.

65 Kim, J.Y., Seo, J.W., Rhee, Y.S. et al. (2014). Freezedried highly porous matrix as a new gastroretentive dosage form for ecabet sodium: in vitro and in vivo characterizations. *J. Pharm. Sci.* 103: 262–273.

66 Zhang, H. and Cooper, A.I. (2005). Synthesis and applications of emulsiontemplated porous materials. *Soft Matter* 1: 107–113.

67 Morais, A.R., Alencar, E., Junior, F.H. et al. (2016). Freezedrying of emulsified systems: a review. *Int. J. Pharm.* 503: 102–114.

68 Zhao, D., Gong, T., Fu, Y. et al. (2008). Lyophilized Cheliensisin A submicron emulsion for intravenous injection: characterization, in vitro and in vivo antitumor effect. *Int. J. Pharm.* 357: 139–147.

69 Corveleyn, S. and Remon, J.P. (1998). Formulation of a lyophilized dry emulsion tablet for the delivery of poorly soluble drugs. *Int. J. Pharm.* 166: 65–74.

70 Li, F., Wang, T., He, H.B., and Tang, X. (2008). The properties of bufadienolidesloaded nanoemulsion and submicroemulsion during lyophilisation. *Int. J. Pharm.* 349: 291–299.

71 Moreno, M.A., Frutos, P., and Ballesteros, M.P. (2001). Lyophilized lecithin based oil water microemulsions as a new and low toxic delivery system for Amphotericin B. *Pharm. Res.* 18: 344–351.

72 Cromwell, M.E.M., Hilario, E., and Jacobson, F. (2006). Protein aggregation and bioprocessing. *AAPS J.* 8: E572–E579.

73 Frauenfelder, H., Chen, G., Berendzen, J. et al. (2009). A unified model of protein dynamics. *PNAS* 106: 5129–5134.

74 Timasheff, S.N. (1998). Control of protein stability and reactions by weakly interacting cosolvents: the simplicity of the complicated. *Adv. Protein Chem.* 51: 355–432.

75 Alison, S.D., Dong, A., and Carpenter, J.F. (1996). Counteracting effects of thiocyanate and sucrose on chymotrypsinogen secondary structure and aggregation during freezing, drying and rehydration. *Biophys. J.* 71: 2022–2032.

76 Grasmeijer, N., Stankovic, M., de Waard, H. et al. (2013). Unravelling protein stabilization mechanisms: vitrification and water replacement in a glass transition temperature controlled system. *Biochim. Biophys. Acta* 1834: 763–769.

77 Cicerone, M.T., Pikal, M.J., and Qian, K.K. (2015). Stabilization of proteins in solid form. *Adv. Drug Delivery Rev.* 93: 14–24.

78 Cicerone, M.T. and Douglas, J.F. (2012). βRelaxation governs protein stability in sugar glass matrices. *Soft Matter* 8: 2983–2991.

79 Martins, S.I.F.S., Jongen, W.M.F., and van Boekel, M.A.J.S. (2001). A review of Maillard reaction in food and implications to kinetic modelling. *Trends Food Sci. Technol.* 11: 364–373.

80 Philo, J.S. and Arakawa, T. (2009). Mechanisms of protein aggregation. *Curr. Pharm. Biotechnol.* 10: 348–351.

81 Wang, W., Singh, S.K., Li, N. et al. (2012). Immunogenicity of protein aggregates – concerns and realities. *Int. J. Pharm.* 431: 1–11.

82 Cao, W., Xie, Y., Krishnan, S. et al. (2013). Influence of process conditions on the crystallization and transition of metastable mannitol forms in protein formulation during lyophilisation. *Pharm. Res.* 30: 131–139.

83 Williams, M.L., Landel, R.F., and Ferry, J.D. (1955). The temperature dependence of relaxation mechanisms in amorphous polymers and other glassforming liquids. *J. Am. Chem. Soc.* 77: 3701–3707.

84 Fosgerau, K. and Hoffmann, T. (2015). Peptide therapeutics: current status and future directions. *Drug Discovery Today* 20: 122–128.

85 Antosova, Z., Mackova, M., Kral, V., and Macek, T. (2009). Therapeutic application of peptides and proteins: parenteral forever? *Trends Biotechnol.* 27: 628–635.

86 Fang, W., Qi, W., Kinzell, J. et al. (2012). Effects of excipients on the chemical and physical stability of glucagon during freezedrying and storage in dried formulations. *Pharm. Res.* 29: 3278–3291.

87 Srinivasan, C., Siddiqui, A., KorangYeboah, M., and Khan, M.A. (2015). Stability characterization and appearance of particulates in a lyophilized formulation of a model peptide hormonehuman secretin. *Int. J. Pharm.* 481: 104–113.

88 Depaz, R.A., Pansare, S., and Patel, S.M. (2016). Freezedrying above the glass transition temperature in amorphous protein formulations while maintaining product quality and improving process efficiency. *J. Pharm. Sci.* 105: 40–49.

89 Katz, J.S., Tan, Y., Kuppannan, K. et al. (2016). Aminoacidincorporating nonionic surfactants for stabilization of protein pharmaceutics. *ACS Biomater. Sci. Eng.* 2: 1093–1096.

90 Tonnis, W.F., Mensink, M.A., de Jager, A. et al. (2015). Size and molecular flexibility of sugars determine the storage stability of freezedried proteins. *Mol. Pharm.* 12: 684–694.

91 Fonte, P., Andrade, F., Azevedo, C. et al. (2016). Effect of the freezing step in the stability and bioactivity of proteinloaded PLGA nanoparticles upon lyophilisation. *Pharm. Res.* 33: 2777–2793.

92 Lipiäinen, T., Peltoniemi, M., Sarkhel, S. et al. (2015). Formulation and stability of cytokine therapeutics. *J. Pharm. Sci.* 104: 307–326.

93 Pisano, R., Rasetto, V., Barresi, A.A. et al. (2013). Freezedrying of enzymes in case of waterbinding and nonwaterbinding substrates. *Eur. J. Pharm. Biopharm.* 85: 974–983.

94 Ó'Fágáin, C. and Collition, K. (2017). Storage and lyophilization of pure proteins. In: Protein Chromatography: Methods and Protocols, Methods in Molecular Biology (ed. D. Walls and S.T. Loughran), 159–190. New York: Springer Science + Business Media.

95 Yoshioka, S., Miyazaki, T., and Aso, Y. (2006). βRelaxation of insulin molecule in lyophilized formulations containing trehalose or dextran as a determinant of chemical reactivity. *Pharm. Res.* 23: 961–966.

96 Geidobler, R. and Winter, G. (2013). Controlled ice nucleation in the field of freeze drying: fundamentals and technology review. *Eur. J. Pharm. Biopharm.* 85: 214–222.

97 Hawe, A. and Frieβ, W. (2006). Impact of freezing procedure and annealing on the physicochemical properties and the formation of mannitol hydrate in mannitolsucrose NaCl formulations. *Eur. J. Pharm. Biopharm.* 64: 316–325.

98 Webb, S.D., Cleland, J.L., Carpenter, J.F., and Randolph, T.W. (2003). Effects of annealing lyophilized and spraylyophilized formulations of recombinant human interferonγ. *J. Pharm. Sci.* 92: 715–729.

99 Grohganz, H., Lee, Y., Rantanen, J., and Yang, M. (2013). The influence of lysozyme on mannitol polymorphism in freezedried and spraydried formulations depends on the selection of the drying process. *Int. J. Pharm.* 447: 224–230.

100 TruongLe, V., Lovalenti, P.M., and AbdulFattah, A.M. (2015). Stabilization challenges

and formulation strategies associated with oral biologic drug delivery systems. *Adv. Drug Delivery Rev.* 93: 95–108.

101 Fonte, P., Reis, S., and Sarmento, B. (2016). Facts and evidences on the lyophilisation of polymeric nanoparticles for drug delivery. *J. Controlled Release* 225: 75–86.

102 Fonte, P., Soares, S., Sousa, F. et al. (2014). Stability study perspective of the effect of freezedrying using cryoprotectants on the structure of insulin loaded into PLGA nanoparticles. *Biomacromolecules* 15: 3753–3765.

103 Varshosaz, J., Eskandari, S., and Tabbakhian, M. (2012). Freezedrying of nanostructured lipid carriers by different carbohydrate polymers used as cryoprotectants. *Carbohydr. Polym.* 88: 1157–1163.

104 Anhorn, M., Mahler, H.C., and Langer, K. (2008). Freeze drying of human serum albumin (HSA) nanoparticles with different excipients. *Int. J. Pharm.* 363: 162–169.

105 Dadparvar, M., Wagner, S., Wien, S. et al. (2014). Freezedrying of HIloaded recombinant human serum albumin nanoparticles for improved storage stability. *Eur. J. Pharm. Biopharm.* 88: 510–517.

106 Abdelwahed, W., Degobert, G., and Fessi, H. (2006). Freezedrying of nanocapsules: impact of annealing on the drying process. *Int. J. Pharm.* 324: 74–82.

107 NIAID, 2017, https://www.niaid.nih.gov/research/vaccinetypes (accessed 27 January 2017).

108 Hansen, L.J.J., Daoussi, R., Vervaet, C. et al. (2015). Freezedrying of live virus vaccines: a review. *Vaccine* 33: 5507–5519.

109 Shah, R.R.; Hassett, K.J.; Brito, L.A. (2017) Overview of vaccine adjuvants: introduction, history, and current status, Chapter 1 *Vaccine Adjuvants: Methods and Protocols, Method in Molecular Biology*, Fox, C.B., Springer Science + Business Media New York.

110 Kumru, O.S., Joshi, S.B., Smith, D.E. et al. (2014). Vaccine instability in the cold chain: mechanisms, analysis and formulation strategies. *Biologicals* 42: 237–259.

111 Amorij, J.P., Hickriede, A., Wilschut, J. et al. (2008). Development of stable influenza vaccine powder formulations: challenges and possibilities. *Pharm. Res.* 25: 1256–1273.

112 Brandau, D.T., Jones, L.S., Wiethoff, C.M. et al. (2003). Thermal stability of vaccines. *J. Pharm. Sci.* 92: 218–231.

113 Morris, G.J. and Acton, E. (2013). Controlled ice nucleation in cryopreservation – a review. *Cryobiology* 66: 85–92.

114 Orr, M.T., Kramer, R.M., Barnes, L. V et al. (2014). Elimination of the coldchain dependence of a nanoemulsion adjuvanted vaccine against tuberculosis by lyophilisation. *J.*

Controlled Release 177: 20–26.

115 Lovalenti, P.M., Anderl, J., Yee, L. et al. (2016). Stabilization of live attenuated influenza vaccines by freeze drying, spray drying, and foam drying. *Pharm. Res.* 33: 1144–1160.

116 Ibraheem, D., Elaissari, A., and Fessi, H. (2014). Gene therapy and DNA delivery systems. *Int. J. Pharm.* 459: 70–83.

117 Patil, S.D., Rhodes, D.G., and Burgess, D.J. (2005). DNAbased therapeutics and DNA delivery systems: a comprehensive review. *AAPS J.* 7: E61–E77.

118 Xu, L. and Anchordoquy, T. (2011). Drug delivery trends in clinical trials and translational medicine: challenges and opportunities in the delivery of nucleic acidbased therapeutics. *J. Pharm. Sci.* 100: 38–52.

119 Chow, M.Y.T. and Lam, J.K.W. (2015). Dry powder formulation of plasmid DNA and siRNA for inhalation. *Expert Opin. Drug Delivery* 21: 3854–3866.

120 Brus, C., Kleemann, E., Aigner, A. et al. (2004). Stabilization of oligonucleotide–polyethylenimine complexes by freezedrying: physicochemical and biological characterization. *J. Controlled Release* 95: 119–131.

121 Kasper, J.C., Schaffert, D., Ogris, M. et al. (2011). Development of a lyophilized plasmid/LPEI polyplex formulation with longterm stability – a step closer from promising technology to application. *J. Controlled Release* 151: 246–255.

122 Zhang, X., Zhang, J., Quan, G. et al. (2017). The serumresistant transfection evaluation and longterm stability of gene delivery dry powder based on mesoporous silica nanoparticles and polyethyleneimine by freezingdrying. *AAPS PharmSciTech* 18: 1536–1543.

123 Molina, M.C., Armstrong, T.K., Zhang, Y. et al. (2004). The stability of lyophilized lipid/DNA complexes during prolonged storage. *J. Pharm. Sci.* 93: 2259–2273.

124 Yadava, P., Gibbs, M., Castro, C., and Hugues, J.A. (2008). Effect of lyophilization and freezethawing on the stability of siRNA–liposome complexes. *AAPS PharmSciTech* 9: 335–341.

125 Furst, T., Dakwar, G.R., Zagato, E. et al. (2016). Freezedried mucoadhesive polymeric system containing PEGylated lipoplexes: towards a vaginal sustained released system for siRNA. *J. Controlled Release* 236: 68–78.

126 Tolstyka, Z.P., Philips, H., Cortez, M. et al. (2016). Trehalosebased block copolycations promote polyplex stabilization for lyophilization and in vivo pDNA delivery. *ACS Biomater. Sci. Eng.* 2: 43–55.

127 Ali, M.E. and Lamprecht, A. (2017). Spray freeze drying as an alternative technique for lyophilization of polymeric and lipidbased nanoparticles. *Int. J. Pharm.* 516: 170–177.

128 de Jesus, M.B. and Zuhorn, I.S. (2015). Solid lipid nanoparticles as nucleic acid delivery system: properties and molecular mechanisms. *J. Control. Release* 201: 1–13.

129 Merkel, O.M., Rubinstein, I., and Kissel, T. (2014). siRNA delivery to the lung: what's new? *Adv. Drug Delivery Rev.* 75: 112–128.

130 Seville, P.C., Kellaway, I.W., and Birchall, J.C. (2002). Preparation of dry powder dispersions for nonviral gene delivery by freezedrying and spraydrying. *J. Gene Med.* 4: 428–437.

131 Kuo, J.S. and Hwang, R. (2004). Preparation of DNA dry powder for nonviral gene delivery by sprayfreeze drying: effect of protective agents (polyethyleneimine and sugars) on the stability of DNA. *J. Pharm. Pharmacol.* 56: 27–33.

132 Okuda, T., Suzuki, Y., Kobayashi, Y. et al. (2015). Development of biodegradable polycationbased inhalable dry gene powders by spray freeze drying. *Pharmaceutics* 7: 233–254.

133 Liang, W., Kwok, P.C.L., Chow, M.Y.T. et al. (2014). Formulation of pH responsive peptides as inhalable dry powders for pulmonary delivery of nucleic acids. *Eur. J. Pharm. Biopharm.* 86: 64–73.

134 Liang, W., Chow, M.Y.T., Lau, P.N. et al. (2015). Inhalable dry powder formulations of siRNA and pHresponsive peptides with antiviral activity against H1N1 influenza virus. *Mol. Pharmaceutics* 12: 910–921.

135 Ratti, C. (2001). Hot air and freezedrying of highvalue foods: a review. *J. Food. Eng.* 49: 311–319.

136 Jankovié, M. (1993). Physical properties of convectively dried and freezedried berrylike fruits. *Rev. Res. Work Fac. Agric. Belgr.* 38: 129–135.

137 Nijhuis, H.H., Torringa, H.M., Muresan, S. et al. (1998). Approaches to improving the quality of dried fruit and vegetables. *Trends Food Sci. Technol.* 9: 13–20.

138 Duan, X., Yang, X., Ren, G. et al. (2016). Technical aspects in freezedrying of foods. *Drying Technol.* 34: 1271–1285.

139 Materska, M. (2014). Bioactive phenolics of fresh and freezedried sweet and semi spicy pepper fruits (*Capsicum annuum* L.). *J. Funct. Foods* 7: 269–277.

140 Souza, D.S., Marques, L.G., Gomes, E.B., and Narain, N. (2015). Lyophilization of avocado (persea Americana mill.): effect of freezing and lyophilization pressure on antioxidant activity, texture, and browning of pulp. *Drying Technol.* 33: 194–204.

141 Donsi, G., Ferrari, G., and Di Matteo, P. (2001). Utilization of combined processes in freezedrying of shrimps. *Trans IChemE, Part C* 79: 152–159.

142 Cantalejo, M.J., Zouaghi, F., and PerezArnedo, I. (2016). Combined effects of ozone and freezedrying on the shelflife of Broiler chicken meat. *LWT Food Sci. Technol.* 68: 400–407.

143 Desai, K.G.H. and Park, H.J. (2007). Recent developments in microencapsulation of food ingredients. *Drying Technol.* 23: 1361–1394.

144 Fang, Z. and Bhandari, B. (2010). Encapsulation of polyphenols – a review. *Trends Food Sci. Technol.* 21: 510–523.

145 Madene, A., Jacquot, M., Scher, J., and Desobry, S. (2006). Flavour encapsulation and controlled release – a review. *Int. J. Food Sci. Technol.* 41: 1–21.

146 Ezhilarasi, P.N., Indrani, D., Jena, B.S., and Anandharamakrishnan, C. (2013). Freeze drying technique for microencapsulation of Garcinia fruit extract and its effect on bread quality. *J. Food Eng.* 117: 513–520.

147 Silva, K., Coelho, M.A.Z., Calado, V.M.A., and RochaLeão, M.H.M. (2013). Olive oil and lemon salad dressing microencapsulated by freezedrying. *LWT Food Sci. Technol.* 50: 569–574.

148 Imamura, K., Kimura, Y., Nakayama, S. et al. (2013). Characteristics of amorphous matrices composed of different types of sugars in encapsulating emulsion oil droplets during freezedrying. *Food Res. Int.* 51: 201–207.

149 Karthik, P. and Anandharamakrishnan, C. (2013). Microencapsulation of docosahexaenoic acid by spray–freezedrying method and comparison of its stability with spraydrying and freezedrying methods. *Food BioprocessTechnol.* 6: 2780–2790.

150 Meng, X.C., Stanton, C., Fitzgerald, G.F. et al. (2008). Anhydrobiotics: the challenges of drying probiotic cultures. *Food Chem.* 106: 1406–1416.

151 MattilaSandholm, T., Myllärinen, P., Crittenden, R. et al. (2002). Technological challenges for future probiotic foods. *Int. Dairy J.* 12: 173–182.

152 Carvalho, A.S., Silva, J., Ho, P. et al. (2004). Relevant factors for the preparation of freezedried lactic acid bacteria. *Int. Dairy J.* 14: 835–847.

153 Morgan, C.A., Herman, N., White, P.A., and Vesey, G. (2006). Preservation of micro organisms by drying: a review. *J. Microbiol. Methods* 66: 183–193.

154 Jofré, A., Aymerich, T., and Garriga, M. (2015). Impact of different cryoprotectants on the survival of freezedried *Lactobacillus rhamnosus* and *Lactobacillus casei*/*paracasei* during longterm storage. *Benef. Microbes* 6: 381–386.

155 Semyonov, D., Ramon, O., Kaplun, Z. et al. (2010). Microencapsulation of *Lactobacillus paracasei* by spray freeze drying. *Food. Res. Int.* 43: 193–202.

156 Wessman, P., Mahlin, D., Akhtar, S. et al. (2011). Impact of matrix properties on the survival of freezedried bacteria. *J. Sci. Food Agric.* 91: 2518–2528.

157 Panoff, J.M., Thammavongs, B., and Gueguen, M. (2000). Cryoprotectants lead to phenotypic adaptation to freezethaw stress in *Lactobacillus delbrueckii* ssp. Bulgaricus CIP 101027T. *Cryobiology* 40: 264–269.

158 Carvalho, A.S., Silva, J., Ho, P. et al. (2004). Effects of various sugars added to growth and drying media upon thermotolerance and survival throughout storage of freezedried *Lactobacillus delbrueckii* ssp. Bulgaricus. *Biotechnol. Progress* 20: 248–254.

159 Wisselink, H.W., Weusthuis, R.A., Eggink, G. et al. (2002). Mannitol production by lactic acid bacteria: a review. *Int. Diary J.* 12: 151–161.

4
Porous Polymers by Ice Templating

4.1 Introduction

Porous materials, including polymers, are used in a very wide range of applications, including separation, catalysis, energy storage, tissue scaffolds, to name a few [1–4]. The pore sizes may be categorized as micropores (<2 nm), mesopores (2–50 nm), and macropores (>50 nm) [1]. The pores may be arranged either in order or at random. The pore shapes may be designed and synthesized for shapecontrolled molecular separation or catalysis [5–8]. A porous material containing pores of different sizes (particularly in different categories) is called a hierarchically porous material [1].

Mesoporous polymers and macroporous polymers are usually prepared by templating techniques [9–12]. The templates may be classified as hard (e.g. rigid objects such as colloids, particles, preformed porous solid structures) or soft (usually the selfassembled structures of surfactants/block copolymers or liquid drops) [11, 12]. Emulsion templating, where the liquid droplets are used as templates, has been an effective route to producing macroporous polymers and other materials [13–15]. Gas foaming or supercritical fluid foaming are also efficient in fabricating highly interconnected macroporous polymers [9, 10]. Soft templating (mainly, micelles, microemulsions) [11, 12] and selfassembly of block copolymers and associated processing techniques are widely known to generate mesoporous and/or microporous materials [16].

Microporous polymers, with pore sizes <2 nm, can be directly synthesized, with the potential to control pore shape and pore size. This has been a highly intensive research area, particularly due to the extremely high surface area, pore surface functionality, tailored pore shape for great potential in gas storage, gas separation, catalysis and biomedical applications [2–8]. Wellknown examples of microporous polymers include hypercrosslinked polymers [2, 17], polymers of intrinsic microporosity (PIMs) [3, 4], conjugated microporous polymers [5, 18], covalent organic frameworks (COFs) [5–7], and porous organic cages [6, 8]. Among them, COFs and porous organic cages are crystalline polymers, which is the basis for Xray diffraction and neutron diffraction studies to elucidate the pore structure and pore arrangement. It is also relatively easier to carry out simulation studies on these crystalline polymers [6–8].

A hierarchically porous polymer may be synthesized by employing dual or multiple templates or combining direct synthesis and templating [1, 6, 11]. Different templating techniques may be combined to tune porosity and pore morphologies. In this chapter, we introduce and focus on another templating technique, namely, ice templating and/or freezedrying, for the preparation of porous polymers. For the icetemplating method, water (or other solvents) in a solution, suspension, or emulsion is frozen to form ice crystals. The ice crystals, acting as templates, are then removed (usually by freezedrying) to produce a porous structure (Figure 4.1) [10,

19–21].

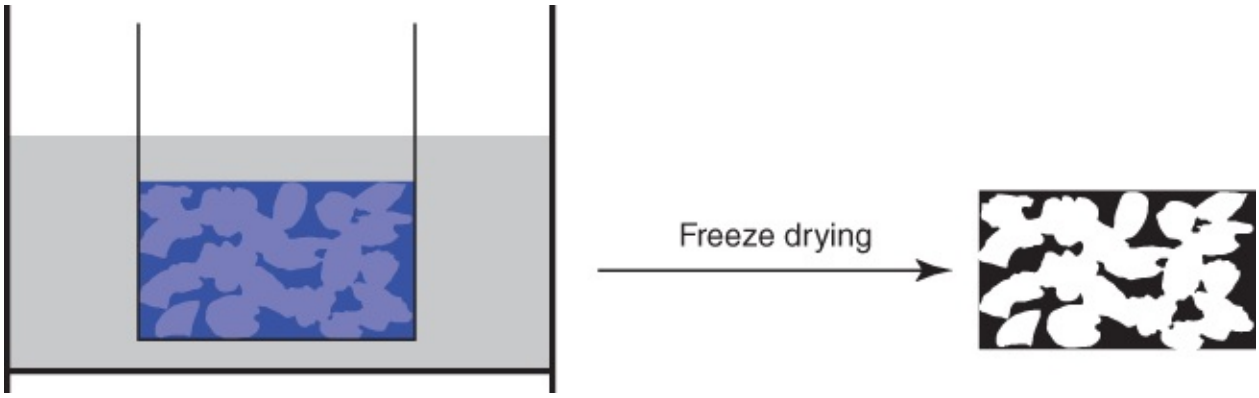

Figure 4.1 Schematic representation of an icetemplating process for the preparation of a porous material.

Source: Qian and Zhang 2011 [10]. Reprinted with permission from John Wiley & Sons.

Porous polymers may be prepared by freezedrying solutions, suspensions, gels, and highly crosslinked polymer. When producing porous structures, ice templating is essential for aqueous solutions and suspensions where the solutes or particles may be excluded from the growing ice crystals and concentrated between ice crystals. For the weakly crosslinked gels, the flexible and loosely linked polymer chains may be partially pushed away by ice crystals, leading to the formation of icetemplated structures. Indeed, the structures of the freezedried gel and hydrated gel are usually different even if the freezedrying process is carefully performed [22]. However, for highly crosslinked polymers or framework materials, the rigid structure may prevent the templating effect caused by ice crystal growth. The freezedrying of such materials is mainly to maintain the highly porous structure (the sublimation of solid ice exerts much lower interface stress than drying by liquid phase evaporation). There are also some new developments in material preparation facilitated by the freezing process. For example, the freezinginduced concentration of solutes can lead to surfactant selfassembly and formation of mesoporous silica [23] or selfassembly of peptides for peptide nanostructures [24]. Because these types of structures do not result from ice templating, they are not included in the discussion below.

4.2 Porous Polymers by Freezedrying of Solutions and Suspensions

4.2.1 Polymer Sponges

The sponge structure usually indicates a highly interconnected 3D macroporous structure. The distribution of pores in a sponge is usually random although local ordering may be present. Aqueous solutions or suspensions are mostly used for the preparation of polymer sponges. In brief, the suspensions/solutions contained in plastic vials (e.g. polystyrene, polypropylene, Teflon) or glass vials are placed in a cold environment such as a freezer or a cold room [25–28], shelf of a freezedryer with varying freezing rates [29, 30], or simply immersing in a

cold liquid (e.g. liquid nitrogen) [28–31]. The growth and orientation of ice crystals are not controlled but the local alignment is usually observed due to the presence of local temperature gradient.

Porous polymers can be readily prepared from aqueous solutions of hydrophilic polymers such as cellulose, chitosan, poly(vinyl alcohol) (PVA), etc [25, 28, 32]. However, these porous polymers are mechanically very week, shrink when exposed to moisture or in air, and rapidly dissolve when in contact with water or aqueous medium. This severely restricts their applications.

Cellulose nanofibers can be prepared by mechanical shearing and disintegrating of cellulose fibers with the widths in the range of 10–100 nm. Alternatively, bacterial cellulose nanofibers may be synthesized by disintegrating cellulose via the use of microorganism. The diameters are in the range of <100 nm but consist of much finer fibrils (2–4 nm). Cellulose nanocrystals are sometimes used as well, exhibiting crystalline defectfree rodlike structures. These nanocelluloses can be chemically modified to offer a variety of surface functionalities [33].

Cellulose nanofibrous foams or aerogel can be readily prepared by the icetemplating technique from their nanosuspensions [34, 35]. The nanocellulose foams can be silyated to enhance surface hydrophobicity and hence the performance in the selective removal of oil from water [36, 37]. They are also widely used to enhance the mechanical stability of other foams by including cellulose nanofibers as additives in the formulations [38].

Great efforts in this area have been made in the preparation of porous scaffolds with useful biological properties. Silk fibroin is a natural fibrous protein with desirable properties such as high strength, elasticity, and haemocompatibility [39]. In addition to the use as a luxurious texture material, it has also been used as surgical suture thread and as scaffold for tissue engineering [26, 39]. Ice templating has been an effective method for the preparation of 3D silk fibroin scaffolds [29] and silk composite foams/gels, for example, poly(*N* isopropylacrylamide)/silk [40] and lactosesilk fibroin conjugate sponge [26].

Biocompatible sponges have been prepared from collagen, collagen biowastes (extracted from animal skin waste) [41], and collagenglycosaminoglycan [29]. Wheat gluten was dispersed in water and then heated to 90 °C. The heated dispersion was homogenized to a 300% foam which was frozen and freezedried. The foam could be chemically crosslinked by glutaraldehyde or thermally polymerized, exhibiting antimicrobial properties [28]. A solution of egg white powders was processed to generate a macroporous sponge that was chemically crosslinked to be used as scaffold for tissue engineering [27]. A 3D macroporous scaffold of poly(3,4ethylenedioxythiophene):poly(styrenesulfonate) (PEDOT:PSS) could be formed by ice templating [30]. Owing to its electrical conducting property and biocompatibility, this scaffold was used for the electrical control of protein conformation and for supporting cell growth [30].

Ice templating has been used to prepare highly interconnected macroporous materials that are advantageous for tissue engineering and liquid phase separation. However, due to the difficulty in forming nanosized ice crystals, the formation of icetemplated materials with nanopores or

mesopores has been highly challenging. Recently, the mixture solvents of tertiarybutanol (TBA) and water was employed to produce porous polysaccharides (pectin, starch, and alginic acid) with both macropores and mesopores [42]. The macropores were formed by ice templates while the mesopores were attributed to the eutectic points of TBA–water. Figure 4.2 shows the phase diagram of the binary TBA–water system, exhibiting two eutectic compositions at ≈23 and 90 wt% TBA. For the porous polysaccharides prepared from the TBA–water mixture solvents (with different TBA compositions), the pore volumes measured by the Barrett–Joyner–Halenda (BJH) method (gas sorption) were the largest around the eutectic points (the maxima of 2.34 and 1.8 $cm^3\ g^{-1}$ for the two eutectic points, respectively) [42].

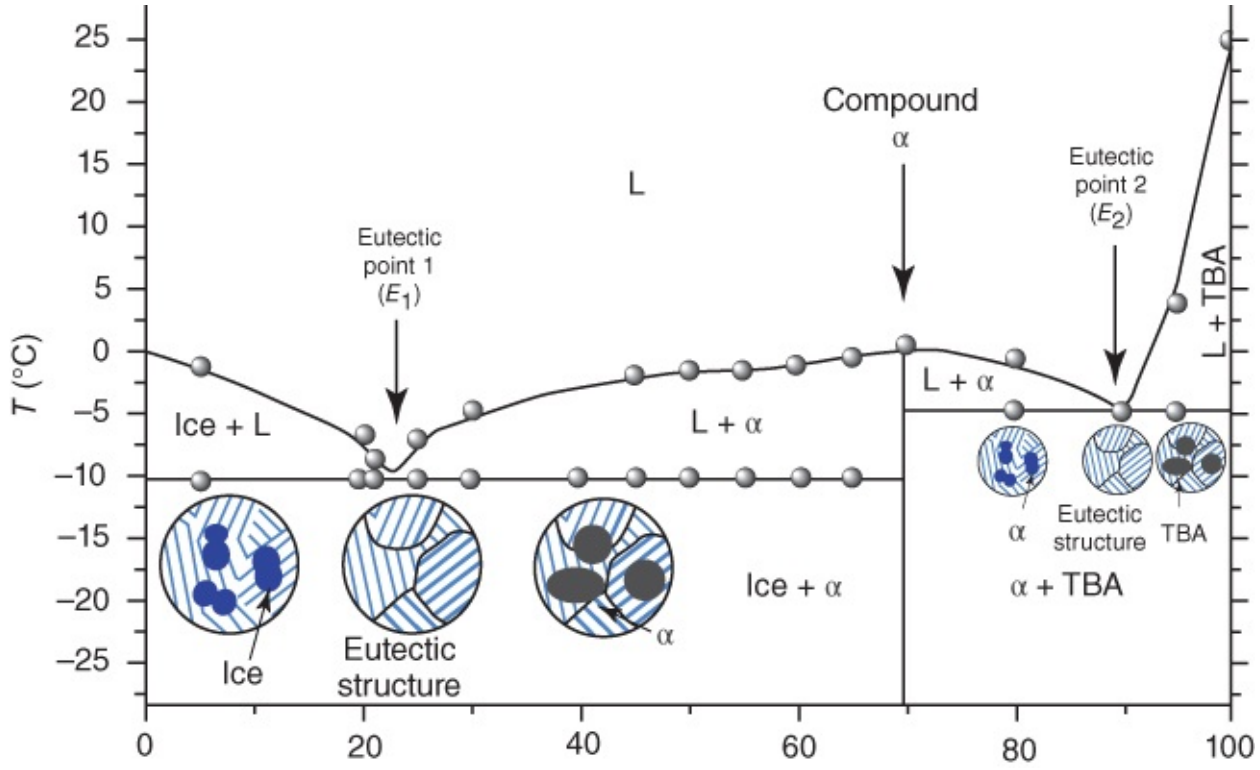

Figure 4.2 The phase diagram of *tert*Butanol (TBA)water (compound α is a TBA hydrate and L = liquid) shows two eutectic points.

Source: Borisova et al. 2015 [42]. Reprinted with permission from John Wiley & Sons.

4.2.2 Aligned Porous Polymers by Directional Freezing

The significant development in icetemplated porous materials in the last decade has been the development of directional freezing process for the preparation of aligned porous or layered materials [43, 44]. This process is also widely known as ‘unidirectional freezing’ or ‘ice segregation induced selfassembly (ISISA)’ [21]. It has been employed to generate a wide range of aligned porous and composite materials with anisotropic properties [19–21]. In principle, the directional freezing process is very simple, where a temperature gradient is applied across a liquid phase sample. The higher the temperature gradient, the faster the freezing rate and the smaller the icetemplated pore sizes. The aligned pore structure is a result of directed growth of the ice crystals along the temperature gradient and the exclusion of

molecules/particles from the ice front and concentration of molecules/particles between the ice crystals. This is demonstrated by the directional freezing of gold nanoparticle suspensions and is schematically represented in Figure 4.3 [45]. In practice, a vial containing solutions or suspensions can be dipped into liquid nitrogen (or another cold liquid) at a controlled rate. Alternatively, a vial or a mould can be placed on a cold finger, a cold plate, or sandwiched between two plates with a set temperature gradient. It is also possible to fabricate the substrates with surface patterns by the dipping method or via a motordriven freezing stage (where a substrate or glass slide with a spread of liquid film can be placed and moved between two temperaturecontrolled metal plates/stages). The directional freezing technique has been applied to solutions or suspensions with water, organic solvents, and even compressed CO_2.

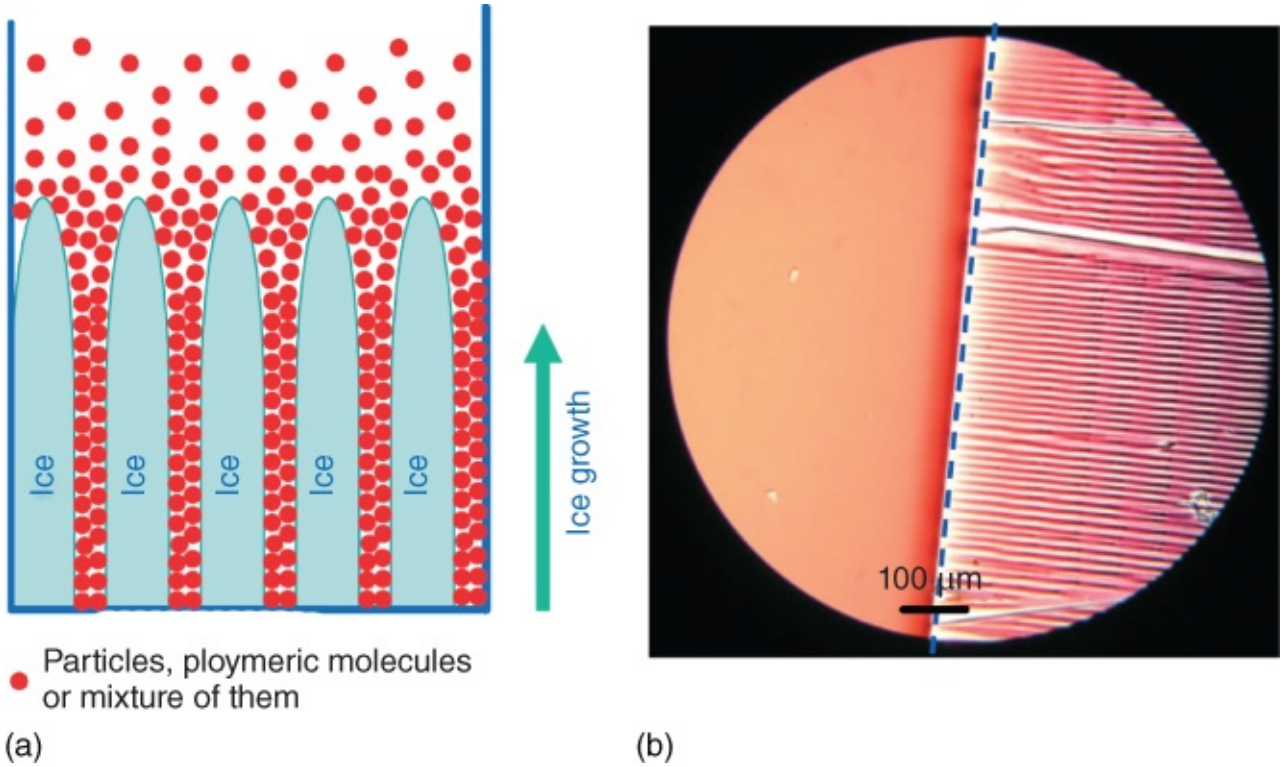

Figure 4.3 (a) The scheme shows the directional freezing process. (b) An optical microscopic image shows the directional freezing of aqueous gold nanoparticle suspension. The white stripes are the orientated ice crystals while the red lines are excluded gold nanoparticles from ice crystals and concentrated between ice crystals. The blue dashed line indicates the interface of the frozen pattern and the liquid suspension.

Source: Zhang and Cooper 2007 [45]. Reprinted with permission from John Wiley & Sons.

4.2.2.1 Waterbased Systems

Aqueous PVA solutions were directionally frozen to fabricate the aligned fishbone like structure. It was demonstrated that the freezing rate could be varied to tune the aligned spacings of the frozen PVA solution with a computercontrolled freezing stage as observed by optical microscopy [43]. By varying the molecular weight and hydrolysis degree of PVA, different freezing rates could be applied to tailor the morphologies of PVA, which could then be used

for the controlled release of ciprofloxacin [46].

Another widely investigated hydrophilic polymer is chitin or chitosan. Chitin nanowhisker suspension was mixed with PVA and then processed to produce the aligned porous structures. The content of PVA could significantly influence the interlamellar spaces (from 180 to 30 μm) from a PVA concentration of 0–2.0 wt% with an initial chitin nanowhisker concentration of 0.8 wt% [47]. 2.4 w/v% chitosan (low molecular weight) in 1 v/v% aqueous glacial acetic acid solution was directly frozen on a copper cold finger and then freezedried. The aligned porous chitosan was used to direct neurite growth [48]. Recently, aligned porous chitosan with shapememory has been generated [49]. The diameters of the aligned channels could be tuned by varying the freezing temperature while the thickness of the channel wall could be controlled by chitosan concentration. When compressed, the channels squeezed the water out; they were deformed but not damaged and the shape could change back when the water was reabsorbed into the channel. A variety of nanostructures including nanoparticles and nanowires could be readily incorporated and absorbed onto the channel wall mostly via electrostatic interaction. These structures could then be used to generate interesting macroscale assemblies [49].

Some other examples include cellulose and collagen [50, 51]. Cellulose was dissolved in aqueous NaOH/urea (5 wt%) and the solution was frozen from the bottom of the mode. Porous cellulose scaffolds with aligned columnar and open porosity were fabricated [50]. A wedge based system was used to produce a range of collagen scaffolds with unidirectional pores. The collagen suspension (0.7 w/v%) was prepared by incubating collagen fibrils overnight at 4 °C in 0.25 M acetic acid (pH 2.7) and homogenized on ice. The wedgebased system consisted of an anodized aluminium wedge and a polyurethane wedge with thermal conductivities of 205 and 0.03 W $(m\,K)^{-1}$, respectively. The freezing medium (liquid nitrogen) was in contact only with the polyurethane wedge. In addition to the large vertical temperature gradient, the wedge shape induced a small horizontal temperature gradient, likely facilitating local nucleation and growth of laterally directed ice crystals. This horizontal temperature gradient could result in small differences in height between adjacent upward growing ice crystals, thus stabilizing the upward growth of ice crystals by blocking inclined ice crystal growth [51].

4.2.2.2 Organic Solventbased Systems

The directional freezing process has also been applied to a range of organic solutions, mainly to prepare porous biodegradable polymers such as poly(εcaprolactone) (PCL) and poly(lactic *co*glycolic acid) (PLGA). For example, aligned porous PCL was prepared by directional freezing of 10 wt% PCL solution in dichloroethane [43]. Aligned porous PCL/zein composites were prepared from chloroformethanol or chloroformacetic acid glacial solution [52]. Zein is a prolaminrich and alcoholsoluble protein, available in corn at 2.5–10% dry basis.

For the preparation of porous PLGA, 1,4dioxane seems to be the most commonly used solvent, probably because of its high melting point (~10 °C) for easy freezedrying. Porous poly(Llactic acid) (PLA) monoliths were prepared from 1,4dioxane solution [53]. The presence of small amounts of water in the solution could lead to the formation of small pits on

the PLA structure. Creating pores in the wall of porous PLA could enhance mass transport for various applications. For this purpose, poly(ethylene glycol) (PEG) of different molecular weights (600, 2000, 4000, 6000 Da) and different ratios to PLA (50/50, 30/70, 10/90) were mixed with PLA. After freezedrying, PEG was leached out using ethanol. This approach allowed the formation of pores in the PLA wall. The pore sizes could be tuned by varying PEG molecular weight and the PEG/PLA ratio [54]. In order to enhance the interconnectivity of the aligned channels in porous PLGA scaffolds, an improved thermalinduced phase separation by adding the second solvent (chloroform, benzene, ethanol or water) into the dioxane solution was employed [55]. The mould containing the solution was first cooled from bottom to top to −20 °C and then further treated in liquid nitrogen. Water is a benign solvent and seemed to be most effective in creating pores in the wall (with water content 3–5 w/w%). This was attributed to the crystallization of the second solvent after the initial crystal growth of dioxane [55].

Blaker et al. combined directional freezing and ice microspheres to prepare highly porous PLA scaffolds with the pore surface lined by bacterial cellulose nanowhiskers (BCNW, to provide hydrophilicity) [56]. The ice microspheres were formed by freezing a water mist generated from an ultrasonic fogger in liquid nitrogen. The frozen spheres were sieved and those in the diameter range of 100–500 μm were used as sacrificial templates. Ice spheres and BCNW were suspended in the PLA–chloroform solution at −25 °C. Owing to the hydrophilic interaction, BCNW migrated from the nonpolar solution to the polar surface of ice microspheres and formed a network coating the spheres. After freezedrying to remove both frozen chloroform and ice microspheres, the porous scaffold with BCNW lining the pore surface could be formed [56].

Polyacrylonitrile (PAN) is a semiconducting polymer and has been widely used to produce fibres and carbon materials. PAN is poorly soluble in water but can be readily dissolved in polar solvents such as dimethyl sulfoxide (DMSO) and dimethylformamide (DMF). Owing to its higher melting point, PAN–DMSO solution was directly frozen and freezedried to produce aligned porous PAN [57]. In an effort to avoid using the freezedrying procedure, it was possible to remove the frozen DMSO by solvent exchange with water. The temperature was maintained at 0 °C using the ice/water mixture. Aligned porous PAN could be successfully formed by this approach [58].

A homemade mould consisting of two plates (one steel plate and one glass plate) was developed to generate 2D temperature gradients for the preparation of aligned porous PLGA and a range of other polymers [59]. A degassed solution (formed with solvents of high melting points) was sealed between the two plates. The mould was then vertically placed into a water reservoir with different temperatures. The vertical temperature gradient was formed due to the relatively low reservoir temperature while the horizontal temperature gradient resulted from the different thermal conductivities of the steel and glass plates. Similarly to the wedgebased system [51], the 2D temperature gradients facilitated the generation of polymer membranes with vertically aligned pores [59].

4.2.2.3 Compressed CO_2 Solution

Supercritical fluids, with the temperature above the critical temperature and the pressure above the critical pressure, exhibit liquidlike density and gaslike diffusivity, and the properties can be tuned readily by varying the pressure and temperature, particularly near the critical region. Owing to its mild critical parameters, nontoxicity, and nonflammability, supercritical CO_2 is the mostly investigated and used supercritical fluid. Supercritical CO_2 foaming is an effective route to preparing highly interconnected porous scaffolds [60]. Compressed CO_2, where the temperature is lower than the critical temperature (~31 °C) but the pressure is higher than the critical pressure (~72 bar), exhibits higher density and strong solvation power. It may be used as a reaction medium or solvating phase such as in the foaming process [60–62]. In the foaming process, the polymers are softened and expanded by high pressure CO_2. Releasing CO_2 by depressurization leaves interconnected but disordered pores behind.

It is possible to freeze a CO_2 solution or suspension and produce an aligned porous material. However, most of the polymers have very low solubility in CO_2. Its low viscosity and low density make it difficult to be used as a medium for suspensions as well. Sugar acetates, including β1,2,3,4,6pentaacetyl Dgalactose (BGAL), α1,2,3,4,6pentaacetyl D glucose (AGLU), and β1,2,3,4,6pentaacetyl Dglucose (BGLU), can be dissolved in compressed CO_2 in sufficient solubility. For example, the BGAL solution in liquid CO_2 (12 wt%) at 72 bar/21 °C in a stainless steel column was directionally frozen in liquid nitrogen [63]. Unlike aqueous or organic solutions, a freezedrying step was not required. Solid CO_2 was readily sublimed when the stainless steel column warmed up at room temperature with the valve open. A dry monolith with aligned porous structure was successfully produced (Figure 4.4). Other CO_2soluble or suspendable additives may be added into the solution to make porous composite materials, as demonstrated by a hydrophobic dye Oil Red O [63].

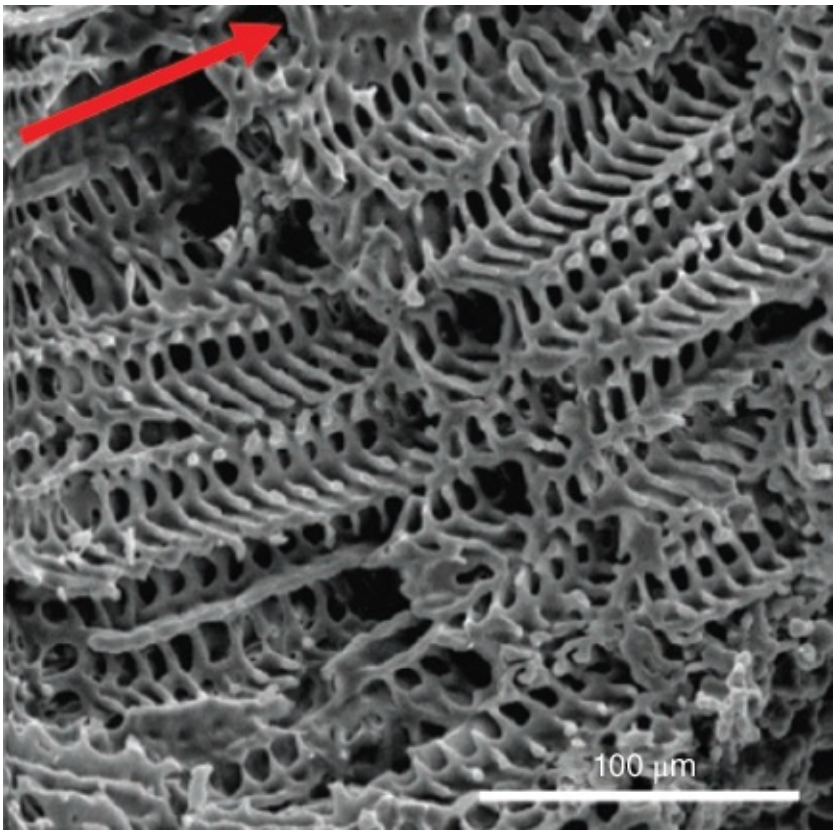

Figure 4.4 Aligned porous BGAL prepared by directional freezing of its solution in compressed CO_2. The red arrow indicates the freezing direction.

Source: Zhang et al. 2005 [63]. Reprinted with permission from American Chemical Society.

Directional freezing of CO_2 solution to fabricate aligned porous materials is a highly attractive method, because no organic solvent is required, there is no issue of solvent residual, and the energyintensive freezedrying step can be avoided. Although it is limited by the low solubility of most polymers in compressed CO_2, with sugar acetate dissolved in CO_2, it may pave the way for directional freezing of a variety of CO_2 suspensions.

4.2.3 Nanofibrous Polymers

Porous polymers are usually formed when using ice templating as the preparation method. It has been noticed that porous polymers with nanofibrous network may be formed when the concentration is reduced [64]. Qian et al. investigated the freezing of highly diluted aqueous polymer solutions, with concentrations in the range of 0.02–0.1 wt% depending on the type and molecular weight of the polymers. Nanofibres can be successfully prepared from PVA, sodium carboxymethyl cellulose (SCMC), dextran, and sodium alginate (Figure 4.5) [65]. The diameters of the nanofibres fall in the range of 100–600 nm. In spite of the diluted solution, it is relatively easy to prepare a large quantity of nanofibres by this approach because the bulky solution can always be frozen in a vessel with a large surface to facilitate freezedrying. This is favourable compared to the electrospinning method that is the common method to prepare polymer nanofibres. The resulting hydrophilic polymer nanofibres may be further used as templates to produce hollow titania microtubes or iron oxide nanofibres [65].

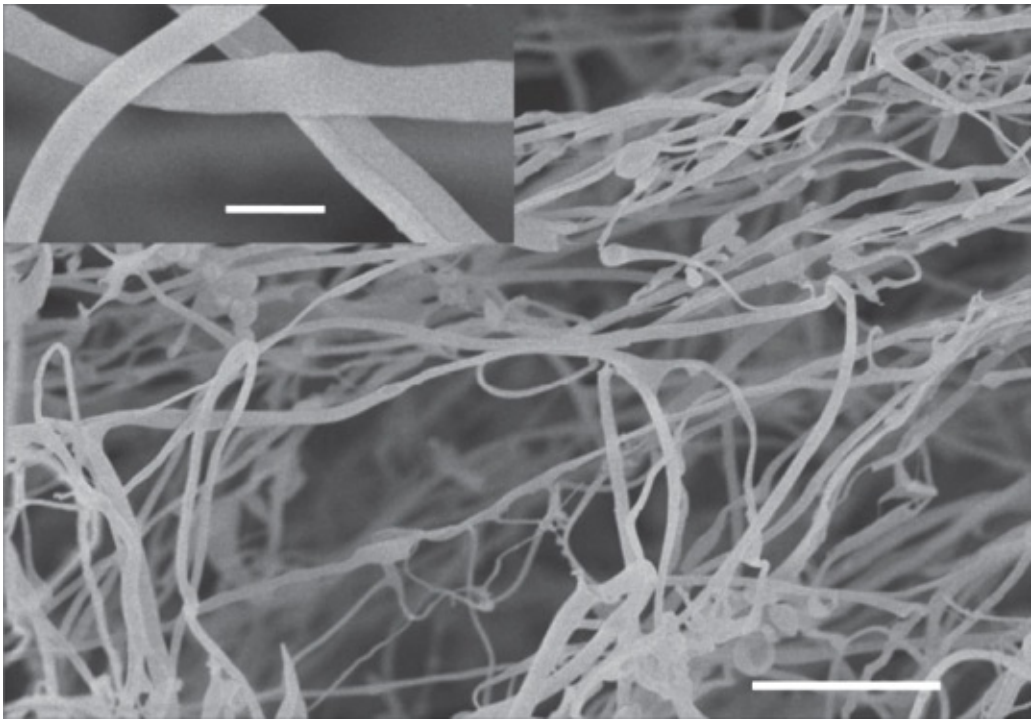

Figure 4.5 An example of polymer nanofibers (SCMC, M_w = 250 K) prepared by freeze drying the dilute aqueous solution (0.02 wt%). Scale bar 5 μm, inset scale bar, 600 nm.

Source: Qian et al. 2009 [65]. Reprinted with permission from Royal Society of Chemistry.

This approach was also used to prepare chitosan nanofibres that were preferred to porous chitosan for the controlled release of proteins (bovine serum albumin (BSA)) and small molecules (Rhodamine B as a model). The release profile could be tuned by varying the morphologies of porous chitosan [32]. In another development, lignin nanofibres were produced continuously by a custombuilt setup (where aqueous solution could spread onto a rotating metal drum whose temperature was controlled by liquid nitrogen; the frozen fibres were removed by a blade and freezedried) and then carbonized to make carbon nanofibres as electrode materials [66]. However, so far, this method has not been found to be very effective in the preparation of hydrophobic nanofibres by directional freezing of organic solutions.

Porous polymers with nanofibre networks may be also formed directly by freezedrying some hydrogels. Hydrogels are highly interconnected 3D porous networks that contain a high percentage of water. Hydrogels with entangled nanofibres may be formed. However, the control on the size of the nanofibres is usually limited. By pHinitiated selfassembly of perylenebased molecules, driven by hydrophobic interaction and π–π stacking, well defined nanofibrous network can be formed, with diameters around 25 nm [67, 68]. After a proper washing procedure with water/acetone/cyclohexane and freezedrying, dry monoliths with nanofibrous networks could be produced [67, 68].

4.2.4 Combining Ice Templating and Other Templating Methods

In addition to its templating impact, freezing is an effective way to lock in the fluid structure. This has been used to combine ice templating and emulsion templating for the preparation of

porous polymers and composite materials. For emulsion templating, the monomers in the continuous phase are polymerized and crosslinked to lock in the emulsion structure and the removal of solvents from the droplet phase and the continuous phase produces emulsion templated structures [14]. By freezing an emulsion (even with limited stability) both phases in the emulsion are frozen to lock in the structure. Similarly, removing the solvents from both internal phase and continuous phase by freezedrying generates a dry and highly porous structure [69]. Because the volume percentage of droplets in an emulsion can be varied in a wide range, this can be translated into systemic control of porosity and pore morphologies in the produced materials [25]. Figure 4.6 shows the evolution of pore structures in ice templated and emulsiontemplated SCMC (M_w = 90 K). Cyclohexane was emulsified into aqueous SCMC solution with sodium dodecyl sulphate (SDS) as the surfactant. The volume ratios of cyclohexane to the total volume of the emulsion were varied at 0, 20, 40, 60, and 75 v/v%. It can be clearly seen from Figure 4.6 that the icetemplated structure is obtained from the emulsion with 0% cyclohexane (basically aqueous solution). Then, the number of cellular emulsiontemplated pores increases with the increasing ratio of the internal droplet phase, until a highly interconnected porous structure is formed with the 75 v/v% emulsion. Accordingly, the bulk densities of the SCMC materials decrease from 0.11 to 0.031 g cm^{-3} and the pore volumes (as measured by Hg intrusion porosimetry) increases from 7.75 to 29.67 cm^3 g^{-1} [25].

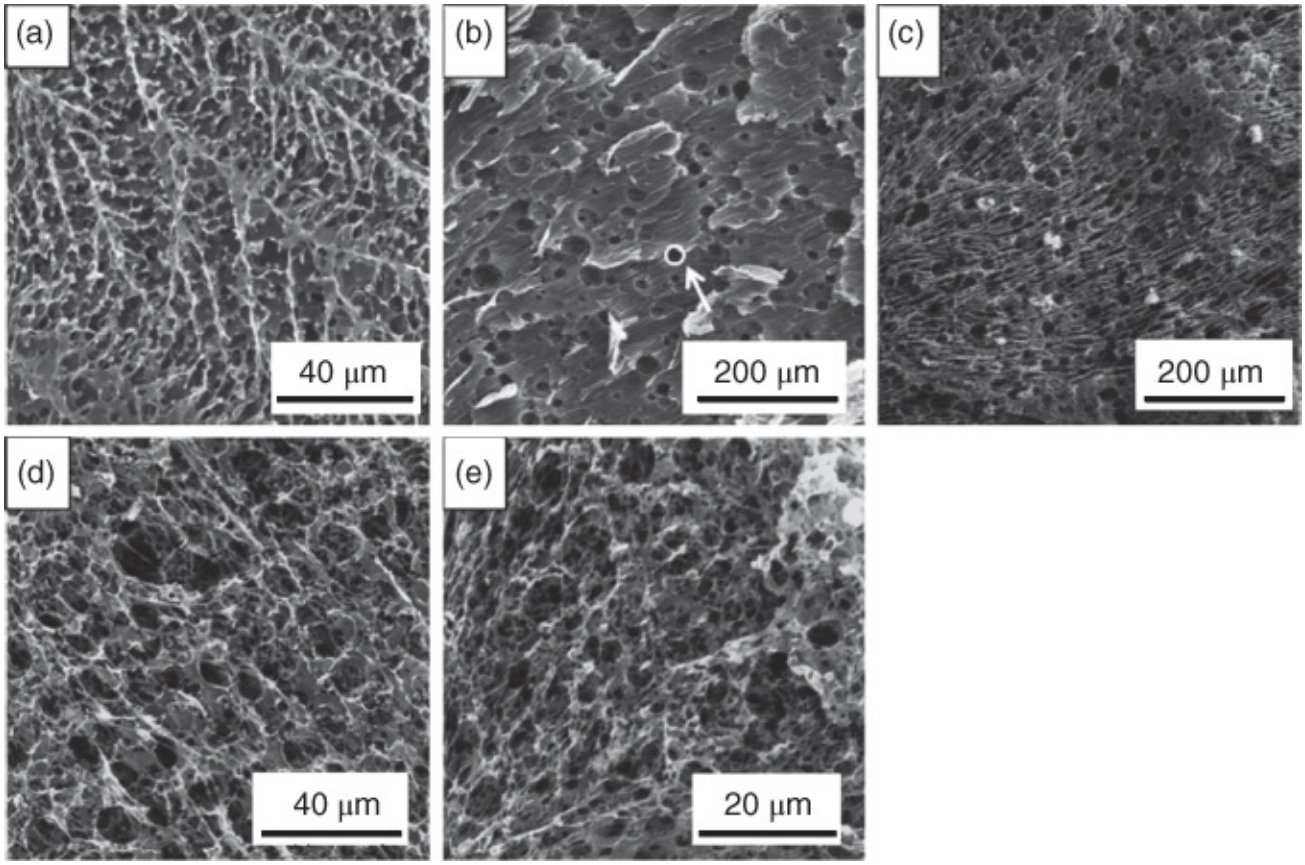

Figure 4.6 The evolution of pore structures by emulsion templating and ice templating based on porous sodium carboxymethyl cellulose. The emulsions are prepared with different volume percentages of internal phase. (a) 0%, (b) 20% v/v. The white circle indicates one of the emulsiontemplated pores. (c) 40%, (d) 60%, (e) 75% v/v.

Source: Qian et al. 2009 [25]. Reprinted with permission from Royal Society of Chemistry.

An emulsion is usually formed from an organic phase and an aqueous phase, e.g. the oilin water (O/W) emulsion. The difference in the densities of organic solvent and aqueous phase can be explored by centrifugation. For example, when an O/W emulsion is formed with cyclohexane, the lighter oil droplets can move upward while those in the heavier aqueous phase mainly remain at the lower part when the emulsion is centrifuged. Thus, a distribution of oil droplets is formed with more droplets at the top and few droplets at the bottom. This emulsion can then be rapidly frozen and freezedried to produce an emulsiontemplated gradient porous material [70]. This was demonstrated with the polymer (PVA and polyacrylamide) and polymer/silica composites [70]. For the O/W emulsion, hydrophobic compounds may be dissolved in the organic droplet phase. Freezedrying of such emulsions can produce porous polymers with the *in situ* formation of organic nanoparticles [69]. This method has been investigated for the production of aqueous nanodispersion of poorly water soluble drug nanoparticles [71].

In addition to liquid emulsions, a gasinliquid foam may be also freezedried to generate porous scaffolds. This has been demonstrated with polysaccharidebased scaffolds (chitosan, alginate, hyaluronic acid tetrabutylammonium) [72]. The foam was generated inside a glass reactor with the introduction of an inert gas (argon). The foam was frozen immediately in

liquid nitrogen and then freezedried. The diameters of the voids were around 200–300 μm [72]. In another study, ice microspheres were used as additional templates to fabricate highly porous PLA scaffold [56]. Both approaches produced porous materials with large macropores, which can be highly useful for tissue engineering.

4.3 Hydrogels and Crosslinked Porous Polymers

The porous polymers produced by freezedrying solutions, suspensions, and emulsions usually exhibit weak mechanical properties and significant shrinkage or dissolution in the presence of the solvent. This can considerably limit their uses in some applications. This problem may be addressed by crosslinking the polymer before, during or after freezedrying. The crosslinking processes may be performed either physically or chemically. Hydrogels are crosslinked polymers containing a large amount of water, which may be freezedried to produce crosslinked porous polymer. A freezing process is always involved for the hydrogels discussed in this chapter.

4.3.1 Hydrogels By a Freeze–thaw Process

This process is widely known for the preparation of physically crosslinked PVA hydrogels. PVA hydrogels are widely used in pharmaceutical and biomedical applications. Compared to chemical crosslinking, the freeze–thaw process avoids the use of toxic solvents and reagents. During the freeze–thaw process, aqueous PVA solution is frozen for a certain period and then allowed to thaw to form aqueous solution again. Multiple freeze–thaw cycles are usually employed to produce stable PVA hydrogels [73]. The preparation of PVA hydrogels is attributed to the formation of small crystallites, which connect the amorphous PVA chains, as illustrated in Figure 4.7 [74]. The PVA crystallites may be described as a layered structure held together by hydrogen bonding and van der Waals forces. Folded PVA chains can lead to the formation of crystallites (small ordered region) distributed in an amorphous matrix [73–75]. It is believed that the concentration of PVA during freezing facilitates the crystallization while the crystallization may be enhanced or weakened in the thawed state. The increased motion of PVA chains or sections may initially facilitate the crystallization but may subsequently break down the crystallites. It was observed that the size of the crystallites increased first and subsequently decreased [73].

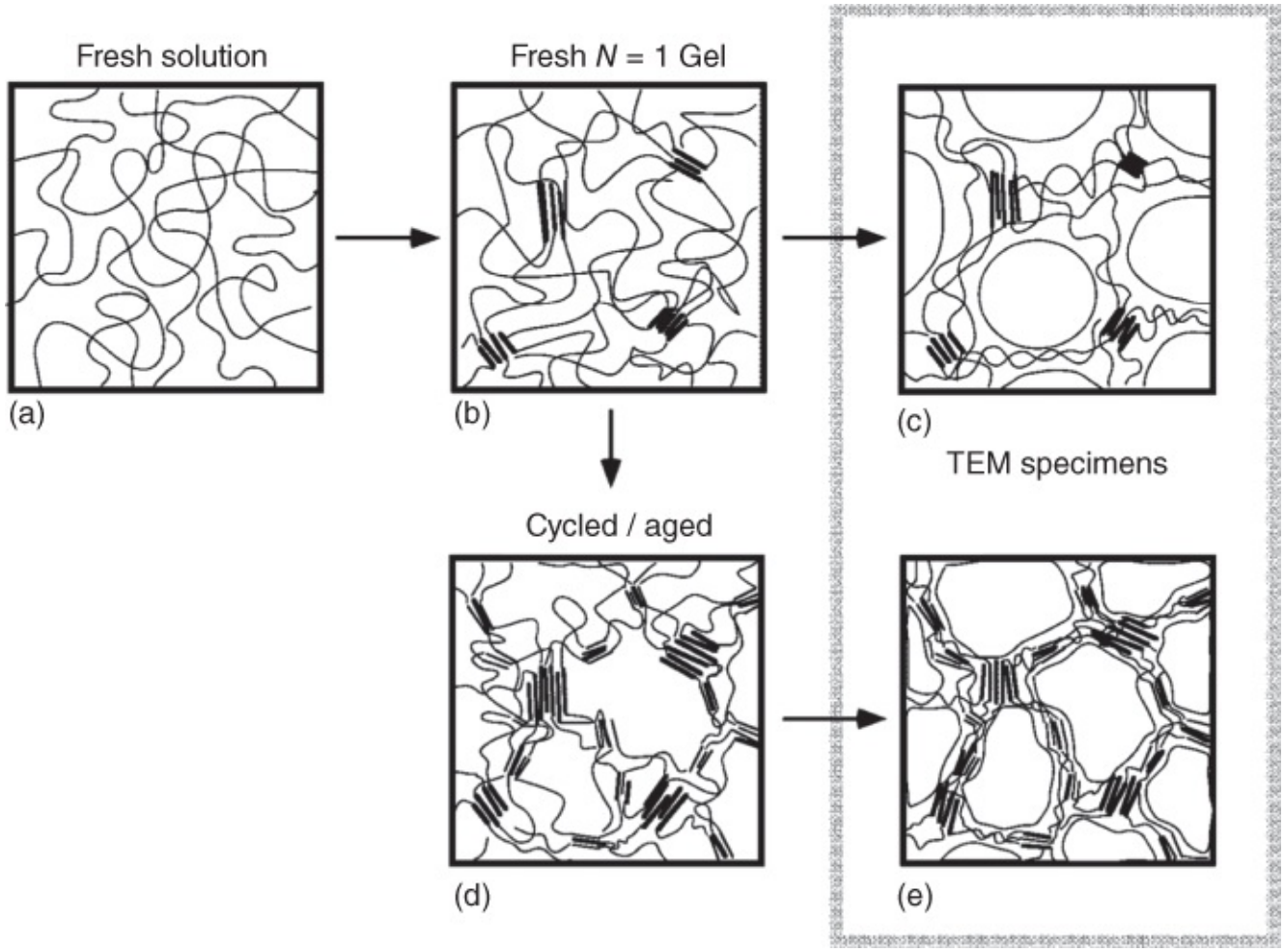

Figure 4.7 Schematic representation of a PVA gel structure during freeze–thaw cycling/aging/imaging. Starting with a fresh solution (a), primary crystallites appear after the first freeze–thaw cycle (b), and these may be enhanced by secondary crystallites after cycling/aging (d). Removal of the frozen water for microscopic imaging collapses the amorphous chains, creating either a network of rounded pores (c), or a network of fibrils (e).

Source: Willcox et al. 1999 [74]. Reprinted with permission from John Wiley & Sons.

The factors that influence the freeze–thaw PVA hydrogels include the properties of PVA (molecular weight, degree of hydrolysis, and concentration) and processing parameters (the number of freeze–thaw cycles, freeze temperature/time, thawing temperature/time). The properties of PVA hydrogels, e.g. mechanical stability, elasticity, and strength under external stresses, are considerably influenced by the size, number, and distribution of PVA crystallites [73, 75]. The degree of crystallinity is in the order of 2–6% for freshly prepared gels [75]. The average size of the crystallites is in the region of 7 nm and the distance between the crystallites is approximately in the range of 15–20 nm [73].

Owing to the importance of the crystallites to PVA hydrogels, the crystallinity of PVA hydrogels has been investigated by various techniques [22, 73–76]. These techniques include density measurement [73], infrared spectroscopy (the intensity of the peak at 1141 cm^{-1} relating to the degree of crystallinity) [73]; cryogenic transmission electronic microscopy (cryoTEM) [74]; differential scanning calorimetry (DSC, the crystallinity degree is expressed as the ratio of the

heat of crystallization of PVA hydrogel and 100% crystalline PVA, $\Delta H/\Delta H_c$, with $\Delta H_c = 150$ J g^{-1}) [73–76]; wide angel Xray diffraction (the crystallinity degree is described as the ratio of the peak area of crystalline aggregates at 18–21° to the sum area of the peaks of crystalline aggregates and amorphous swollen PVA) [22, 75]; and solid state ^{1}H NMR (based on the fraction of rigid protons in PVA hydrogel, measured for the fractions of protons that relax during the first 20 μs) [75]. Based on the comparison study of freeze–thaw gels and aged gels (no freezing involved, gelation at room temperature), even with similar degree of crystallinity, the compressive modulus of the freeze–thaw gel was found to be higher. This led to the suggestion that phase separation during freeze–thaw cycles contributed to the gels with higher modulus [22]. This may be also linked to the effect of PVA concentration during freezing on the formation of crystallites (e.g. size, distribution).

PVA is produced by hydrolysis of poly(vinyl acetate) (PVAc) but 100% hydrolysis is very difficult to achieve. Therefore, the PVA is always a copolymer with PVAc. PVA has a simple linear polymeric chain with pendant hydroxyl groups. This can facilitate the formation of hydrogen bonding between PVA chains, which limits the solubility in water for PVA with high degree of hydrolysis. For PVA with lower degree of hydrolysis, residual hydrophobic groups can weaken or disrupt the interaction between PVA chains. This leads to higher solubility in water for PVA with low degree of hydrolysis [73]. In the studies of freeze–thaw hydrogels, PVAs with the degree of hydrolysis >98% and more often >99% are used. Usually, there is a minimum of PVA molecular weight required for the formation of hydrogels. Different molecular weights have been utilized, including, 115 K, 89–98 K, and 64 K, 36 K [22, 75, 76]. For example, PVA solutions with concentrations of 7, 10, and 15 wt% were frozen at −20 ° for 8 h and thawed at +25 °C for 4 h for different number of cycles [76]. Some general trends were observed. Increasing the number of freeze–thaw cycles can reinforce the PVA hydrogels. The higher PVA concentration leads to initially higher crystallinity and stability upon swelling. An increase in PVA molecular weight results in crystallites of higher lamellar thickness and broader crystallite size distribution [76].

Watermiscible organic solvents have been added to aqueous PVA solution in an effort to generate hydrogels with improved mechanical stability or transparency. Among them, DMSO has been mostly investigated [73]. Preparation of PVA blend/composite hydrogels has also been investigated because they can provide additional useful properties. Some of the examples include pHsensitive PVAPAA (poly(acrylic acid)) hydrogel [77], PEGmodification of PVA hydrogels to reduce protein adsorption [78], PVAchitosan hydrogel [79], PVAalginate hydrogel further crosslinked by Ca^{2+} [80], PVASalecan (a watersoluble extracellular glucan) hydrogel [81], and reinforced PVA hydrogels by cellulose nanocrystals [82]. Recent developments in the freeze–thaw hydrogels include selfhealing PVA hydrogel (attributed to hydrogen bonding between PVA chains at the cutting interface) [83], strong hemicellulose based hydrogel [84], and different types of polysaccharide hydrogels [85].

4.3.2 Macroporous Cryogels

The macroporous cryogels are produced by polymerization or crosslinking reactions at sub

zero temperatures, hence the name ‘cryogels’. The cryogels can be formed from monomers or polymers, in water (the focus of this section) or organic solvent, exhibiting a highly interconnected porous structure [86–88]. For the cryogels to form, the solutions are usually cooled down to between −5 and −20 °C. The frozen (or sometimes called ‘semifrozen’) samples are stored in a cold environment to allow the polymerization to complete, sometimes facilitated by UV irradiation. It is understood that the polymerization can be very slow at low temperatures. However, the freezing process concentrates the monomers and initiators. The resulting higher concentrations can enhance the polymerization, which may balance out the negative effect of low temperature on the reaction rate. The accompanying depression effect on the melting point due to concentration leads to the nonfrozen monomerrich phase segregated within the frozen matrix, which is why such systems may be termed as ‘semi frozen’ and is the basis for the polymerization at subzero temperatures.

The most often used system for cryogels is the redoxinitiated free radical polymerization with potassium persulfate (KPS)/ammonium persulfate (APS) and tetramethyl ethylenediamine (TMEDA). They are usually used for hydrophilic monomers such as acrylamide (AM), *N* isopropylacrylamide (NIPAM) or 2hydroxyethylmethacrylate (HEMA) [89]. For example, PAM cryogel with *N*, *N*′methylenebis(acrylamide) (MBAM) as a crosslinker was formed after freezing the solutions with APS/TMEDA and kept at –12 °C for 16 h [90]. PAM cryogel beads were prepared by emulsifying AM/MBAM/APS/TMEDA into *n*hexane using Span80 as the surfactant at 0–5 °C. The emulsions were then cooled to different temperatures (−12, −15, −18 °C) and kept at the respective low temperatures for 24 h before stopping the reaction and removing *n*hexane and unreacted reagents [91]. Similarly, PNIPAM cryogel was prepared by freezing NIPAM/MBAM/APS/TMEDA and then stored at −12 °C for 12 h [92].

In addition to the concentrations of monomers, the crosslinkers and the reaction temperatures are important parameters that can affect the physical properties of the cryogels. Specific to cryogels, the freezing temperature and probably more importantly the cooling rate can influence the size of ice crystals and hence the pore size of the cryogel. The fast freezing rate leads to a higher number of ice nucleation and smaller size of ice crystals [19–21, 86]. To form a cryogel, the rate of polymerization must be slower than the rate of freezing. Otherwise, the polymer network may be formed before the formation of ice crystals is completed. Owing to the low temperature involved in preparing cryogels, a longer cryopolymerization time is usually required [86, 88]. However, a UV irradiated polymerization may be adopted to facilitate the polymerization. Such a reaction system contains a photoinitiator and the polymerization is initiated under UV irradiation. The UV frozen polymerization is usually applied to acrylate monomers or crosslinkers [86]. For example, PAM, PNIPAM, and polyHEMA cryogels were synthesized using poly(ethylene glycol) diacrylate (PEGDA, M_w ~ 575) and H_2O_2 as the catalyst. The solutions in a mould (4 mm thick) were frozen in a freezer (−20 °C) and then polymerized in a thermostat using a UV curing instrument (power 400 W) for up to 10 min [93]. A similar approach was employed for the *in situ* entrapment of urease in PNIPAM cryogel [94]. However, for acrylate monomers (rather than PEGDA as crosslinker in ref [186), their poor solubility in water signifies that a polar organic solvent is better for the reaction system. 1,4dixoane has been often used to produce polyacrylate cryogels [95–97].

In addition to the use of monomer solutions, cryogels may be also prepared by crosslinking polymer molecules under the freezing conditions. This has been widely known for the preparation of PVA and chitosan cryogels using glutaraldehyde as the crosslinker. However, glutaraldehyde is cytotoxic and it is not easy to completely remove it from the cryogel by washing. Since cryogels have been used widely in biomedical applications and the separation of biomolecules [86, 98], biocompatible crosslinkers such as genipin and oxidized dextran or the crosslinking mechanism via 1ethyl33dimethylaminopropylcarbodiimide hydrochloride (EDC) may be employed [86]. The recently developed cryogels provide biocompatibility and functionality for bioseparation or tissue engineering applications, for example, silk fibroin cryogels (fibroin with TMEDA as catalyst, ethylene glycol diglycidyl ether as crosslinker at −18 °C for one day) [99], transparent hyaluronate cryogel (disaccharides as additives, 2(*N*morpholino)ethanesulfonic acid as crosslinker, storage at −20 °C overnight) [100], and starPEGHeparin cryogels (via the EDC/ *N* hydroxysulfosuccinimid (sulfoNHS) crosslinking chemistry at −20 °C overnight) [101].

Porosity and pore morphology are important properties of porous materials. For hydrogels and particularly supermacroporous cryogels described here, the difference in porosity and pore morphology should be noticed for the hydrogels and their dry structures. It is quite convenient to observe pore morphology by scanning electronic microscopy (SEM) and measure the porosity by Hg intrusion porosimetry. However, both techniques require the use of dry materials. The change in pore structure and porosity is unavoidable when drying the hydrogels, even by freezedrying or the timeconsuming supercritical fluid drying. These changes can be significant. As hydrogels are used in a hydrated state, the characterization of hydrogels is highly important. Cryogels are macroporous materials with pore diameters in the range of 1–300 μm and pore wall thickness of a few micrometers [89]. The pore sizes in this range can be observed by optical microscopy [22]. In order to observe the contrast between polymer network and the contained aqueous medium clearly, confocal laser scanning microscopy (CLSM) is often used. The autoreflection mode may be used to image the hydrogels, based on the difference in reflection from the polymer network and the aqueous medium [102]. Fluorescent dyes may be trapped in the hydrogels, either in the aqueous medium (e.g. Nile Red in water) [102] or by staining the polymer networks with different dyes (e.g. fluorescein isothiocyanate (FITC) or Rhodamine B) [103]. Other techniques include Xray micro computed microscopy (μCT), environmental SEM, and cryoSEM [86]. The porosity may be estimated from the 3D pore structures built from these characterization methods. It may be also determined by squeezing the excess water from a hydrated hydrogel and then calculating the percentage of the squeezed water to the swollen gel [86]. This approach, however, may be only suitable for rather stable hydrogels.

The state of water in a hydrated hydrogel is important because it can affect the water removal during a freezedrying process or the secondary/tertiary structure of adsorbed proteins. Gun'ko et al. have divided the water into five states: free unbound, weakly bound, strongly bound, weakly associated, and strongly associated. The states of water may be distinguished by various techniques such as ^{1}H NMR, DSC and thermogravimetric analysis (TGA) [89].

4.3.3 Aligned Porous Materials By Frozen Polymerization

The chemical process discussed in this section is quite similar as that described in Section 4.3.2, i.e. a crosslinking or polymerization or both occur in the frozen state, providing a crosslinked porous structure. However, the focus is different. In Section 4.3.2, the focus is on the cryogels using water as solvent and the highly interconnected cellular porous structures. This section emphasizes the materials with aligned porous structures, using either water or organic solvents. After the frozen polymerization, the frozen samples are allowed to thaw and dry under vacuum (instead of freezedrying) for their intended applications.

Frozen polymerization has been used to prepare crosslinked aligned porous structures with good mechanical stability from monomer solutions instead of the commonly used polymer solutions [95, 96]. Because the frozen solutions cannot be thermally polymerized and the polymerization rate by free radical polymerization may be too slow, initiation and polymerization by UV irradiation would be a better choice. A photoinitiator and suitable monomers should be used for frozen polymerization. Most of photopolymerizations involve the use of acrylate monomers. For example, tetraethyleneglycol dimetharylate (TEGDMA) was dissolved in 1,4dioxane, cyclohexane, or camphene (by heating to 60 °C) with 1 wt% 2,2 dimethoxy2phenylacetophenone (DMAP) as a UV initiator. After directionally freezing in liquid nitrogen, the frozen samples were placed on ice or dry ice under a UV lamp for 2 h with the samples being turned every 30 min to allow complete polymerization. The warmed samples were then dried in a vacuum oven (no need for freezedrying) overnight at room temperature [95]. Figure 4.8 shows the porous structure of polyTEGDMA from the solutions with 1 : 5 (v/v) TEGDMA to the relative solvent (the same mass ratio for camphene because it is solid at room temperature and it is easier to measure by mass). The Young modulus of these aligned porous materials was up to 9 MPa while the freezedried porous polymers are normally in the range of 0.003–0.0175 MPa [95]. The same methodology has been used to prepare crosslinked polyHEMA, pHsensitive poly[2(dimethylamino) ethyl methacrylate] (PDMAEMA) [96], poly(butyl methacrylate *co*ethylene glycol dimethacrylate) (dioxane as solvent) [97], poly(urethane diacrylate) (dehydrated 1,4dioxane as solvent, diphenyl(2,4,6 methylbenzoyl)phosphine oxide (TPO) as initiator) [104], and polyHEMA (using *t*butyl alcohol as solvent by γ irradiation) [64]. Okaji et al. utilized a binary solvent system (1,4 dioxane and *t*butanol) to prepare a unique multihollowcore honeycomb structure [105]. Diurethane dimethacrylate was the monomer whilst Irgacure 184 was selected as the photoinitiator. For a 1.2 mm thick frozen sample, the UV irradiation was performed for 3 min using a mercury xenon lamp at 365 nm at light intensity of 35 mW cm^{-2}. It was proposed that 1,4dioxane was firstly frozen to form orientated crystals, excluding both the monomer and *t* butanol between them. The crystallization of *t*butanol was initiated within the monomerrich phase to form aligned needle crystals. This resulted in the formation of aligned porous materials with needlelike porosity in the wall [105].

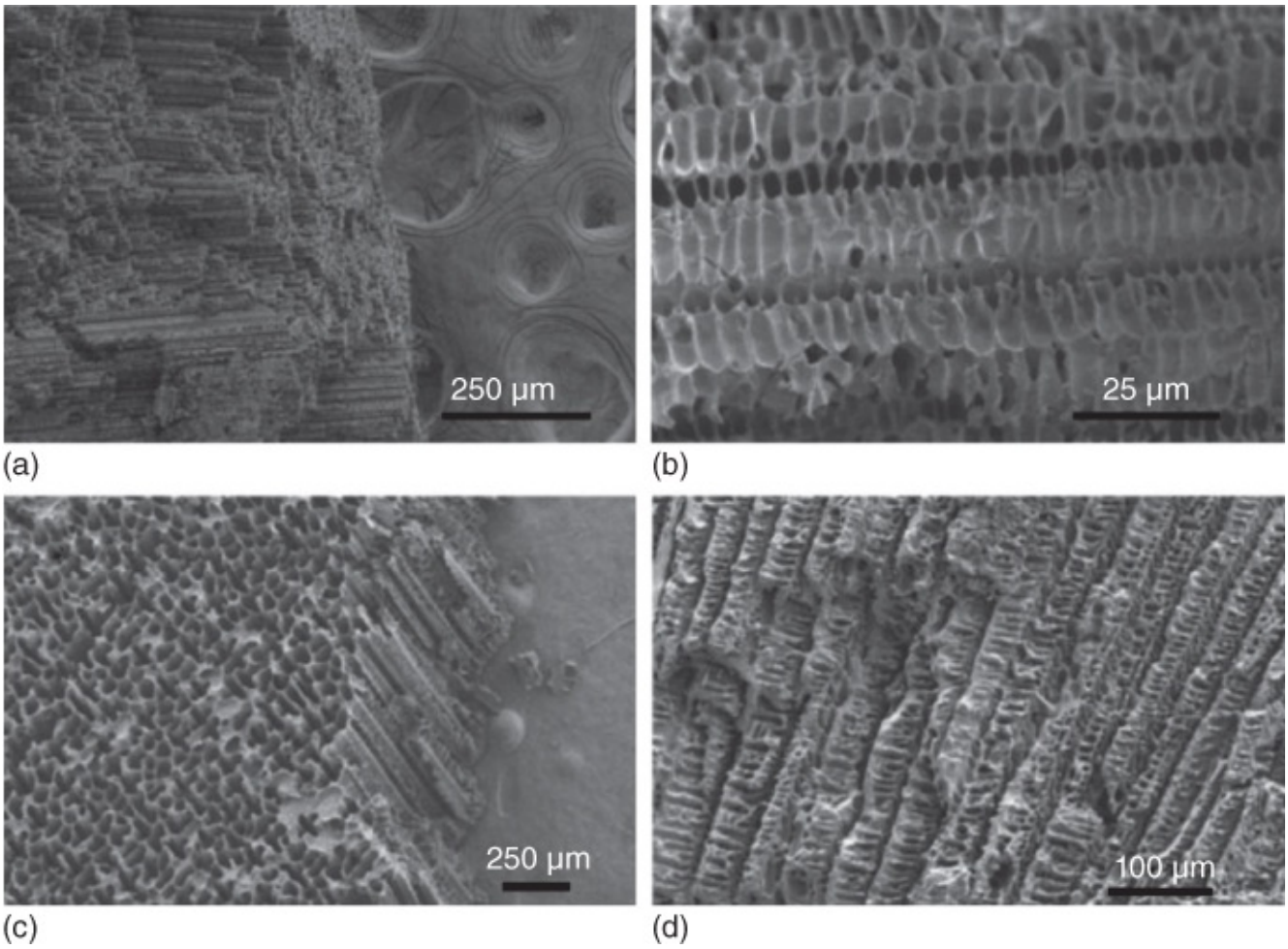

Figure 4.8 Aligned porous polyTEGDMA prepared by UVirradiated frozen polymerization from camphene solution (a,b), cyclohexane solution (c), and dioxane solution (d).

Source: Barrow et al. 2012 [95]. Reprinted with permission from Royal Society of Chemistry.

Similarly to the preparation of cryogels, cryopolymerization to form aligned porous hydrogels can be achieved by employing a directional freezing process instead of freezing in a freezer. For example, aligned porous polyHEMA hydrogels were prepared by directional freezing of aqueous HEMA/KPS/TMEDA solution and then allowed to polymerize at −15 °C for 48 h [106]. PEG hydrogels were generated from aqueous solutions of PEGDA (M_w = 200, 700, 2000) containing APS and TMEDA by cryopolymerization at −15 °C for 12 h [107] and were further used to generate PEG/PNIPAM dualnetwork with temperaturesensitive volume change [103]. A similar procedure was used to prepare aligned porous poly(HEMA *co*AM) hydrogels [108].

Other types of chemical crosslinkers may be also used to prepare cryogels. For example, glutaraldehyde was used to form aligned porous agarosegelatin cryogels. The solutions were contained in 5 ml plastic syringe and placed in a cryostat at −12 °C for 16 h [109]. In another study, dextran was oxidized using sodium periodate (1–2 h at room temperature). The oxidized dextran was then dissolved in water and mixed with chitosan solution (in acetic acid water) at 0 °C. After freezing the mix solution completely at different temperatures (liquid nitrogen −196 °C, freezing ethanol −110 °C, freezing acetic ether −80 °C), the frozen samples were left

in a freezer preset at −8 °C for 3 days to allow the cryopolymerization to complete [110]. A crosslinker, sulfur monochloride (S_2Cl_2), was added to butyl rubbercyclohexane solution. The resulting solutions were frozen in a freezer or cryostat at different temperatures (−2, −7, −10, −18 °C) and maintained at these temperatures for 1–3 days to complete the cryopolymerization. This method produced tough organogels [111].

4.3.4 Postfreezedrying Crosslinking

Instead of frozen polymerization, it is possible to crosslink the freezedried materials to improve their mechanical stability and their stability in liquid medium. Thermal treatment may be employed directly to crosslink the freezedried scaffolds. Biopolymeric scaffolds such as collagenglycosaminoglycan (dehydrothermal crosslinking at 140 °C under vacuum for 24 h) [29] and wheat gluten hybrids (thermal treatment at 130 °C) have been processed in this way. However, it may be necessary to include a crosslinker or prepolymer in the formulation to allow thermal crosslinking. For example, 3glycidoxypropyltrimethoxysilane (GOPS) was added to an aqueous dispersion of PEDOT:PSS. After freezedrying, the scaffolds were heated to 140 °C for 1 h to complete the crosslinking reaction [30]. In another study, poly(glycerol sebacate) (PGS) prepolymer and PLA were dissolved in 1,4dioxane. The freezedried scaffolds were placed in a vacuum oven for 24 h at 150 °C for the curing of PGS prepolymer [112].

Alternatively, the freezedried scaffolds can be crosslinked in a liquid medium. For this approach, the selection of crosslinker, solvent, and concentration is critical for successful crosslinking without damaging the pore structure. A nonsolvent to the scaffold may be used. It is also possible to use a very high concentration of a crosslinker in the solution. The crosslinking reaction can be completed before the dissolution occurs or the damage is done. For example, highly watersoluble porous PVA beads were crosslinked in toluene using toluene 2,4diisocyanate as crosslinker and triethylamine as catalysts. The reaction was refluxed for 3 days. The longer reaction time may be attributed to poor solvation of PVA by toluene [25]. For biocompatible scaffold, the crosslinking via EDC in a polar solvent has been used very often. For example, egg white scaffolds were crosslinked with EDC and NHS in 4 morpholineethanesulfonic acid (MES) buffer in 70% ethanol at 4 °C overnight [27]. Similarly, hyaluronic acid (HA) and alginate scaffold can be crosslinked by EDC chemistry, in a mixing solvent of acetonitrile/ethyl acetate (3 : 2) and acetone/water (9 : 1), respectively. The chitosan scaffold can be crosslinked by genipin (1 w/v%) in ethanol/water (8 : 2) [72].

There are some other options as well. Lactosesilk fibroin sponges were soaked in a series of aqueous methanol solution to induce crystallization and water insolubility. The size of the sponge was very small during this treatment [26]. The SCMC nanofibres prepared by freeze drying were immersed in saturated aqueous $FeCl_3$ solution. The crosslinking of carboxylic acid groups by Fe^{3+} and the low solubility of SCMC in the saturated solution allowed the intact SCMC nanofibres to be crosslinked in aqueous solution. The calcination of Fe^{3+} crosslinked SCMC nanofibres produced Fe_2O_3 nanofibres, confirming that Fe^{3+} crosslinking did happen [65].

4.4 Applications

4.4.1 Biocompatibility and Tissue Engineering

The characteristics of highly interconnected sponges and hydrogels mimic the feature of an extracellular matrix (CEM). It is not surprising that these materials have been widely evaluated and used to support cell growth for tissue engineering. The ability to use different materials, to tune pore morphology and porosity as well as to modify the surface chemistry by different preparation approaches, provides a solid platform to generate suitable scaffolds for different applications.

When a scaffold is in contact with cells and tissues, it is important to make sure there is no unacceptable degree of harm to the body and that the scaffold can perform its intended function [113]. Therefore, it is a rather routine assessment of biocompatibility of porous materials or scaffolds if they are to be used for biomedical applications. Biocompatibility, at its basic level, indicates noncytotoxicity towards the targeted cells or tissues. It is now widely accepted that biocompatibility involves two principle levels [114]. The first one is 'biosafety', covering cytotoxicity and the complex mutagenesis and carcinogenesis. The second level is about 'biofunctionality', where cell adhesion, cell spreading, and cell biosynthetic function are assessed [114]. It should be pointed out that there are different biocompatibility assessment criteria for different parts of the tissues or longterm medical devices [113]. The cytotoxicity assessment is focused on cell damage, cell growth, and cellular metabolism, using methods such as 3(4,5dimethylthiazol2yl)2,5diphenyl tetrazolium bromide (MTT) assay, DNA synthesis, and membrane integrity tests [114].

For a scaffold, in addition to porosity and pore morphology, other properties such as mechanical stability, transparency, and degradability are important parameters [40, 41, 100]. For example, PNIPAM/silk hybrid hydrogels are evaluated by mechanical stability tests and enzymatic degradation by protease XIV [40].

Many studies are carried out to assess the biocompatibility of 3D porous scaffolds or hydrogels. The agarosegelatin cryogels were evaluated by MTT test and by culturing with fibroblast (Cos70). Good cell adhesion and cell proliferation were observed [109]. Human foreskin fibroblast cells were found to easily migrate within silk fibroin scaffolds and reach scaffold periphery within 28 days of culture. Cell attachment and alignment of actin filaments within the scaffold were also confirmed by CLSM [39]. The collagenglycosaminoglycan scaffold was evaluated with human dermal fibroblasts and epidermal keratinocytes. For the potential to be used as engineered skin substitutes, the resulting structures were assessed for surface hydration and mitochondrial metabolism [29].

Laminincontaining gelatin cryogels (glutaraldehyde as crosslinker) and dextran cryogels (with dextran macromer) were generated by cryopolymerization and then assessed for neural tissue regeneration [115]. The optimal pore size range was 80–100 μm. The scaffold seeded with the stem cells from human umbilical cord blood could generate a network of neurons and glia after differentiation. It was possible to transplant the scaffold into the brain tissue as

demonstrated by rat models [115]. The transparent HA cryogels were formed by additives of mono/disaccharides and were still transparent after removing the additives. The transparence facilitates the observation of 3D growth of T47D breast cancer cells with immobilized growth factors by confocal microscopy [100]. Starshaped PEG was crosslinked with heparin via the EDC/sulfoNHS chemistry by cryopolymerization. The gels contained a porosity of up to 93% and interconnected large pores with the size in the range of 30–180 μm. As demonstrated with human umbilical vein endothelial cells, the scaffolds showed cell attachment and even spreading of the cells within the porous scaffold [101].

The scaffolds can also be fabricated from biowastes or easily available biosources. For example, egg white macroporous scaffolds were prepared and found to support active metabolism, proliferation, and migration of human dermal fibroblasts. The *in vivo* evaluation by subcutaneous implantation in mice showed negligible immune reaction and efficient cell and tissue ingrowth [27]. The collagen sponges made from bovine hide trimming pieces were found to be viable towards 293 T cells [41]. For the scaffolds made from semiconducting polymer PEDOT:PSS, in addition to supporting the growth of mouse fibroblasts (3T3L1), protein conformation, cell adhesion, and proangiogenic capability could be tuned electrically by the volt change of +1 to −1 V [30].

Hydrogels with aligned pores can also be used as support for cell growth, just like the sponges or highly interconnected macroporous gels. More importantly, the aligned pores can act as guides to direct cell growth or differentiation. For example, porous PLGA scaffolds with aligned microtubule structures could guide rabbit aortic smooth muscle cells to grow better along the microtubule direction [55]. Porous chitosan was prepared with a highly regular and aligned lamellar architecture, with uniform ridges of controlled height and width on the lamellar surface. The ridges in the 3D aligned porous chitosan could direct DRG neurite growth, as shown in Figure 4.9a [48]. A lamella with the parallel ridges could be isolated from the 3D chitosan, which acted as a 2D substrate to clearly direct the DRG neuron growth (Figure 4.9b) [48].

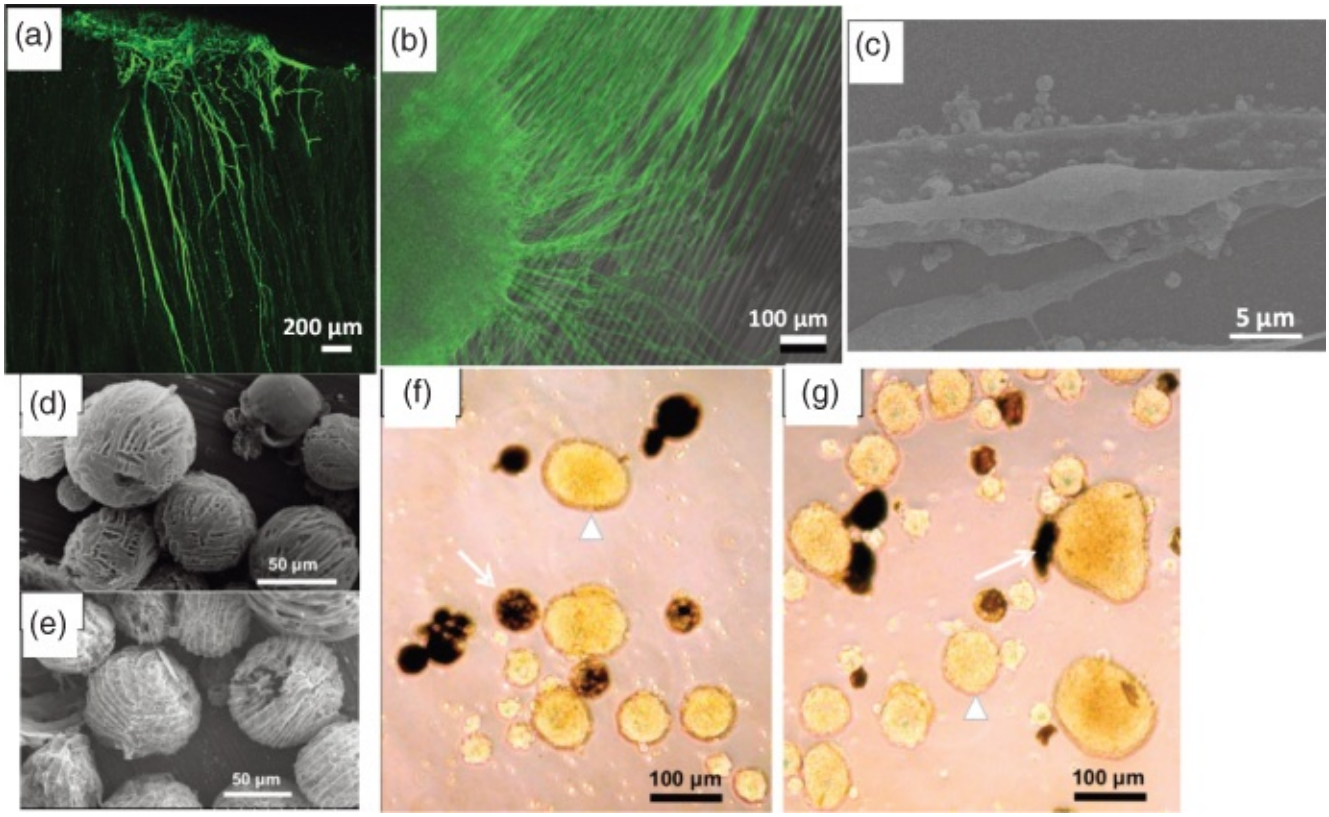

Figure 4.9 Cell growth in the presence of aligned structures. (a) Confocal microscopy image of the aligned growth of DRG neurite in a 3D laminincoated porous chitosan; (b) Fluorescent image of the DRG neurite seeded on an isolated lamella from the 3D chitosan. ; (c) SEM image showing the growth of mMSCs parallel to ridges of the aligned PLGAchitosan substrate. ; (d) SEM image showing aligned porous PCL microspheres; (e) SEM image showing aligned porous PS microspheres; and phase contrast photomicrographs showing the growth of mESCs after 72 h culture in the presence of (f) PS microspheres; and (g) PCL microspheres.

Source: Zhang et al. 2008 [117]. Reprinted from Elsevier.

Source: Reprinted from Ref. [116]

Source: Reprinted from Ref. [48]

It is possible to directly fabricate the 2D aligned patterns by directional freezing of thin liquid phase spreading on a glass slide via a motorcontrolled freezing stage and followed by freezedrying [116]. All the aligned patterns of PLGA (prepared from PLGAdioxane solution), chitosan containing PLGA nanospheres and silica (prepared from silica suspension) could be used to direct the growth of mouse mesenchymal stem cells (mMSCs). The fluorescent microscopic imaging confirmed the cell growth along the aligned ridges. The SEM image in Figure 4.9c shows that the mMSCs are aligned, parallel to the ridges. The spindle shaped cells are seen on the ridges or with the extended filopodia contacting the ridges for the PLGA nanospherecontaining chitosan patterns [116].

Aligned porous PCL microspheres and polystyrene (PS) microspheres can be prepared by directional freezing of O/W emulsions where PCL or PS is dissolved in the oil droplet phase [117]. The freezedried composites can be readily dissolved in water and the aligned porous microspheres are collected by centrifugation, as shown in Figure 4.9d and e. The microsphere

suspension was examined by culturing with mouse embryonic stem cells (mESCs). It was found that the mESCs could grow after 72 h with the microspheres suspended in the culture medium. PS microspheres were not binding to the cell clusters (Figure 4.9f) while PCL microspheres were shown to bind to one or more mESC clusters (Figure 4.9g). There was no cytotoxicity observed for both PS and PCL particles for 7 days of culturing [117].

The freezedrying approach is also effective for encapsulation of enzymes [94], bacteria [118], and cells [119]. The processing is straightforward. The biological entities are suspended in aqueous medium containing monomers or polymers. The resulting suspension can be either cryopolymerized [94] or directly freezedried [119]. In the latter case, cryoprotectants may be added to help maintain the biological activity. The choice of encapsulation materials is highly important. These materials should be biocompatible and the formed matrix surrounding the biological entities should be porous and semipermeable. That allows the diffusion of oxygen, nutrients, and biomolecules, and also for the removal of wastes [120]. Some natural polymers have been widely used as encapsulation materials, including alginate [118, 119], agarose, chitosan, and HA, and proteins including collagen, gelatin, fibrin, and silk fibroin [120]. Other polymers may be also used, e.g. PVA [118] and PNIPAM [94].

4.4.2 Controlled Drug Release

Hydrogels and porous polymers have been widely used for drug delivery. For the ice templated structures, the capability to tune pore morphology by varying freezing conditions and solution compositions may translate to better control in drug delivery. PVA scaffolds have been prepared with tailored porosity and morphology by changing concentration, molecular weight, and freezing rates [46]. The tests on drug release are always performed in aqueous medium such as simulated body fluids (SBF) or phosphate buffer solutions. Apart from instant drug release by dissolving the matrix, water insolubility and stability in water are prerequisites for the icetemplated structures to be used in drug release. Low molecular weight PVAs are readily soluble in water but high molecular weight PVAs with high degree of hydrolysis are dissolved in water only at high temperatures. This is why porous PVA (M_w 72 K, 98% hydrolysis) has been used as scaffold for the diffusional release of ciprofloxacin. The release could be tuned from minutes to days by using PVA scaffolds with different structures and drug loadings [46]. Physically crosslinked PVA hydrogels by the freeze–thaw approach have also been used for drug delivery. For example, the release of flurbiprofen from PVA hydrogels was investigated. The addition of sodium alginate or Pluronic L62 could enhance the gel strength but decrease the drug release [121]. Freeze–thaw PVA hydrogel could be formed onto a PVA/PAA substrate, which could increase the gel strength. Such a system could be used for localized delivery of theophylline [122].

Another widely used polymer is chitosan. Chitosan is soluble in acidic water but not in water with neutral pH. Therefore, porous chitosan can be prepared by freezedrying the acidic solution. Hydrophilic drugs can be easily included in the solution (or similarly suspending fine hydrophobic particles in the solution) and then incorporated in the porous matrix after freeze drying. In a study with chitosan by freezedrying, Rhodamine B and BSA were encapsulated

in porous chitosan. The morphologies of freezedried chitosan changed from interconnected porous structure to nanofibres by varying chitosan concentrations (from 1 to 0.02 wt%). Slow release was observed for porous chitosan while a much faster release was found for nanofibrous chitosan for both Rhodamine B and BSA [33]. However, to encapsulate water soluble proteins in a degradable hydrophobic porous polymer matrix, an emulsion system instead of aqueous solution may be used. Proteinencapsulated microspheres are usually prepared by this method. By freezedrying a waterinoilinwater (W/O/W) double emulsion, proteincontaining PLGA microspheres can be formed in a porous hydrophilic matrix [123]. The release of proteins (e.g. BSA) may be adjusted directly from hydrophobic microspheres with different porosity or entrapping the microspheres within a hydrophilic matrix.

Owing to the nature of the interconnected macropore structures, a burst release and then significantly slowingdown release are the features of release from hydrogels. In terms of therapeutic treatment, it is desirable that the plasma drug concentration should reach the therapeutic concentration region quickly and then maintain in that region. This may be achieved by a fast initial release followed by a near linear release to complement the drugs being metabolized or removed by the body. It is apparent that hydrogels alone are difficult to achieve this target but it may be realized by incorporating a slow release vehicle into the polymer matrix. As such, a model drug, curcumin was loaded into mesoporous silica microspheres that were then suspended in aqueous curcuminchitosan solution. The suspensions were then freezedried to produce curcumincontaining porous composites [124]. Figure 4.10a shows a network of nanofibres containing silica microspheres. The silica microspheres are either attached to the surface or partly embedded into the fibres. When curcumin was loaded into both chitosan and the mesoporous silica microspheres, a twostage release profile can be achieved, a fast initial release followed by near linear release (Figure 4.10b**)**. Clearly, by varying the loading of silica microspheres in the composites, the release profile can be tuned accordingly. The other factors that may be further investigated include porosity of the polymer, drug loading level, and other physically/chemically crosslinked biopolymers.

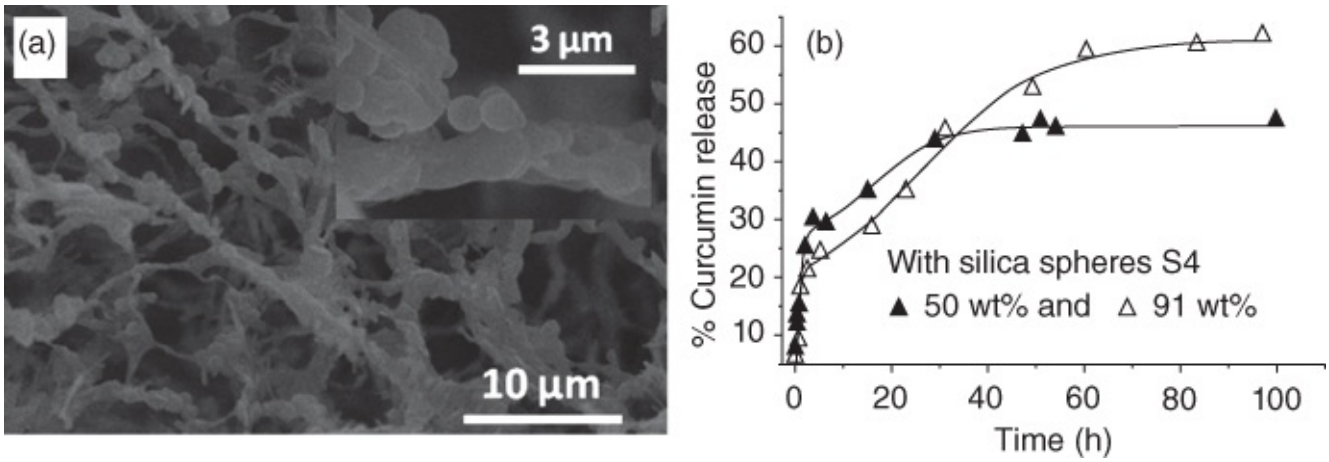

Figure 4.10 Dualcontrolled release of curcumin from porous silica/chitosan composite. (a) SEM image showing the network of chitosan fibers with embedded silica microspheres (with equal mass of silica and chitosan); (b) The release profiles of curcumin from the composites with different loadings of curcuminloaded silica microspheres (50% and 91%, based on chitosan).

Source: Ahmed et al. 2012 [124]. Reprinted with permission from Royal Society of Chemistry.

4.4.3 Encapsulation

Freezedrying and spray freezedrying are effective methods to encapsulate oil, flavours, and proteins in a hydrophilic matrix, towards improving stability and easy transportation. For a detail description on this topic, interesting readers are referred to Chapter 3. The encapsulation efficiency and the stability and activity of the compounds or particles after reconstitution in water are important parameters. For example, chitosan (a polymer with positive charges) was found to improve retention and redispersibility of a flavour oil in a freezedried emulsion containing a negatively charged emulsifier [125]. Maltodextrin was added as a bulk agent. Under optimal conditions, ~95% retention levels were obtained and the redispersed droplets were only slightly bigger than the ones before freezedrying [125].

One interesting development is to prepare hydrophobic organic nanoparticles [69, 71] or microspheres [117] within porous hydrophilic polymers. PVA has been frequently used as the hydrophilic polymer. The freezedried composites can be readily dissolved in water to release the microspheres [117] or produce stable aqueous nanoparticle dispersions [69, 71]. The hydrophobic organic particles can be extended to poorly watersoluble drugs. The emulsionfreezedrying approach has been highly effective to address poor water solubility and prepare sizecontrolled drug nanoparticles [69, 71, 126, 127]. This concept is described in more detail in Chapter 8.

Alternatively, the freezedried scaffolds can be used directly to absorb oil or organic solutions. Once dissolved in water, the oil phase localized in the pores could be released into water, forming an emulsion or dispersion stabilized by the dissolved polymer molecules. An example is the use of porous PVA containing surfactant SDS prepared by freezedrying aqueous solutions or O/W emulsion for the instant formation of emulsions [128]. After soaking porous PVA in cyclohexane for the defined times, the soaked PVA can be directly placed back

into water and an O/W emulsion is formed immediately simply by shaking. By controlling the soaking time of cyclohexane in PVA, O/W emulsions with varying percentages of droplet phase can be formed, with the droplet sizes changing in the range of 8–100 μm (the peak size as measured by MasterSizer). This approach has been demonstrated with a variety of oils including soy oil, mineral oil and perfluorocarbons [128]. When the porous PVA is soaked in organic solutions, by evaporating the solvent afterwards, the hydrophobic solute can form nanoparticles *in situ* within the porous PVA and other polymers. Similarly, dissolution of the polymer in water releases the organic nanoparticles and stable aqueous nanoparticle dispersions are formed [129]. This has proved to be highly effective for the preparation of aqueous poorly watersoluble drug nanoparticle dispersions [129, 130].

4.4.4 Water Treatment

In water treatment, the removal of heavy metal ions, dyes, and oil from aqueous phase is an important research area with significant practical importance. Molecular imprinted polymer (MIP) hydrogels are efficient for the removal of heavy metal ions [87]. Chitosan nanofibres can be used to remove Cu^{2+} from aqueous solution at a capacity of 2.57 mmol g^{-1} [33]. A sponge with a nanofibrous structure prepared by freezedrying of cyanobacterial anionic megamolecules shows selective removal of In^{3+} over Sn^{4+} at concentrations below 50 mM, which may by significant in recycling indium metal [131].

Owing to their highly interconnected macroporosity, icetemplated sponges may be more suitable for high capacity oil absorption. However, a hydrophobic environment or hydrophobic surface functionality is required for effective absorption of oils. For example, due to its internal hydrophobic environment, macroporous cyclodextrin materials prepared by freeze drying aqueous cyclodextrin solutions showed remarkable absorption of organic solvent including 1,4dioxane and ethanol, with the maximum capacities over 20 ml g^{-1} for soybean oil [132]. A polymeric sponge was prepared by cryocrosslinking of polyethyleneimine using 1,4butanediol diglycidyl ether as crosslinker at −15 °C for 24 h. The thawed and washed gel was incubated in tetrahydrofuran (THF) for 24 h and dried in a vacuum oven at 55 °C. The dry gel was modified with different acid chlorides (valeroyl chloride (C4), nonanoyl chloride (C8), and palmitoyl chloride (C17)) in dry chloroform at room temperature under Ar. This produced omniphilic sponges that could effectively absorb hexane under water [133]. The C4modified sponge could absorb 12 times its weight of water or hexane whilst the C17 modified sponge could absorb 15 times its weight of hexane or five times its weight in water [133].

Porous sponges made of cellulose nanofibres have recently drawn much attention in removing oil from water [36, 37]. This may be attributed to their highly accessible surface area, extremely high porosity (or ultralightweight), and the interconnected network structure leading to good flexibility. However, because cellulose nanofibres are hydrophilic, surface modification to enhance hydrophobicity and hence oil absorption is necessary. For example, methyltrimethoxysilane (MTMS) was partially hydrolyzed in water at pH 4 with HCl and mixed with aqueous cellulose nanofibre suspension. Freezedrying then led to the porous

scaffolds with different level of silylation [36]. These sponges proved to be highly efficient in removing dodecane from water with excellent selectivity and recyclability. Depending on the density of the oil liquids, the absorption capacities could be up to 100 times their own weight [36]. In a recent study, bacterial cellulose nanofibres were modified by trimethylsilylation with trimethylchlorosilane and triethylamine in dichloromethane under reflux. The freezedried scaffolds exhibited low density (<6.77 mg cm^{-3}), high surface area (>169 m^2 g^{-1}) and high porosity (~99.6%). As illustrated in Figure 4.11a, the porous scaffold shows high absorption capacity for a range of oils or organic solvents (86–185 g/g, depending on oil density). The equilibrium absorption time varied, depending on the viscosity of the oil phase. It took about 20 s for paraffin oil and plant oil whilst it took only 12 s for an organic solvent to achieve the absorption equilibrium. Owing to the high flexibility, the scaffold showed remarkable reusability (no obvious change in absorption capacity after 10 cycles (Figure 4.11b). This was completed by compressing the absorbed solvent out of the scaffold, rinsing with *t*butanol three times, and freezedried again for the next test [37].

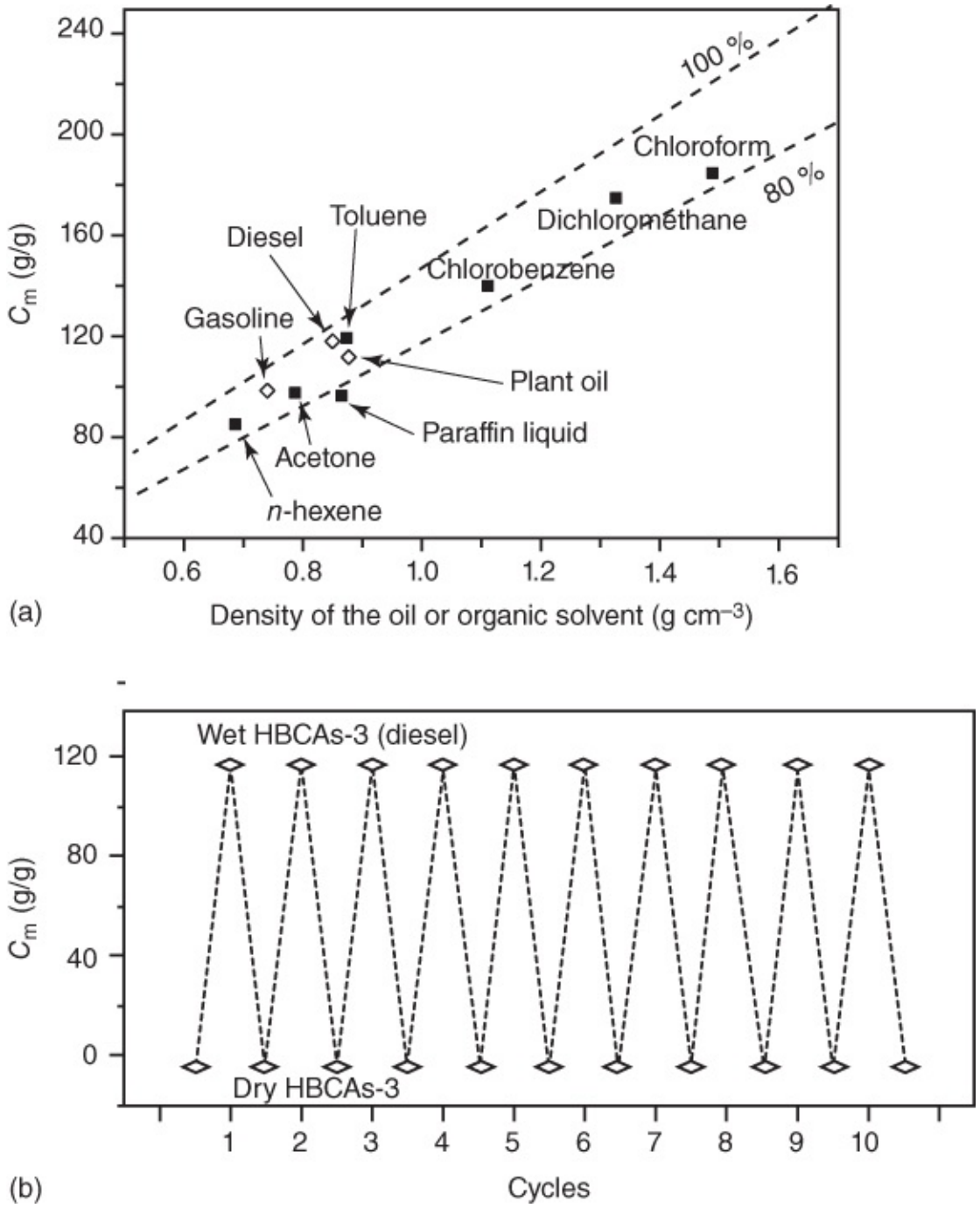

Figure 4.11 Absorption of oils/organic solvents by trimethylsilylated cellulose nanofibrous scaffolds. (a) Graph of the massbased absorption capacity for different solvents with different densities. The upper dashed line represents the theoretical volumebased absorption capacity based on total porosity of the scaffold while the lower dashed line is for 80% of the capacity. It can be seen that most of organic phases can reach ~90% of theoretical volume capacity. (b) The reusability tests for diesel oil over 10 rinsing–absorption cycles.

Source: Sai et al. 2015 [37]. Reprinted with permission from American Chemical Society.

4.4.5 Liquid Chromatography and Separation

The highly interconnected macroporous cryogels are well suited for bioseparation [98]. There are various reports where the cryogels are reported to be immobilized with biomolecules for

cell capture and separation [98]. Vertically orientated porous poly(vinylidene fluoride) (PVDF) membrane was fabricated by ice templating and used for separation of yeasts and lactobacilli based on the sizeexclusion properties. The PVDF membrane prepared from 20 wt% solution (pore sizes ≤ 4.6 μm) could achieve almost 100% separation of yeasts (elliptical cells with diameter 4–6 μm) from lactobacilli (spherical cells with an average diameter of 0.7 μm) [57]. Recently, a solvent crystallization and polymer migration approach was used to construct PVDF membrane with nanopores (much smaller than the usual icetemplated pores). Such porous membranes demonstrated high water permeation flux, stable flux after fouling, superior mechanical properties and better abrasion resistance, compared to the membranes prepared by the conventional phaseseparation process [134].

Cryogels have also been used as monolithic columns for liquid chromatography because they are able to provide high flow rates at low operating pressures and the macropores can be highly beneficial for separation of large biomolecules and cells [98, 135]. Aligned porous materials have been evaluated as monolithic columns for chromatographic separation with a view to offer low back pressure owing to the aligned microchannel structure. For example, aligned porous silica monoliths in fusedsilica capillaries were prepared from TM50 silica colloids and used for normal phase separation (back pressure 9 bar at a flow rate of 0.1 ml min^{-1}) and reversed phase separation (C18modification, back pressure 17 bar at a flow rate of 0.1 ml min^{-1}) [136]. A highly crosslinked polyacrylate column was fabricated by UV frozen polymerization [95]. The column was used for the separation of a mixture containing five compounds (uracil, caffeine, phenol, ethylbenzene, phenylene) using 50/50 v/v acetonitrile water as the mobile phase. Four wellresolved peaks were observed, with phenol and caffeine peak overlapping due to the lack of hydroxyl groups on the monolith. The back pressure was 59 bar at a flow rate of 1 ml min^{-1} [95]. PEG dimethacrylate and poly(butylmethacrylate *co*ethylene dimethacrylate) monoliths were also assessed for the separation of protein mixtures under the reverse phase condition and hydrophilic interaction chromatography (HIC) condition, respectively. The proteins could be separated but the performance was not better than that seen in polymer monoliths prepared by convention approaches [97]. This was attributed to the fact that the polymer monolith was not fully attached to the cycloolefin copolymer (COC) tubing even when the COC was pretreated with a 1 : 1 (wt%) stock solution of methyl methacrylate (MMA) and ethylene glycol diacrylate (EDA) containing benzophenone as photoinitiator [97]. The full attachment of the monolith to the column wall is critical because that will remove voids near the wall. The presence of voids can lead to heterogeneous flow rates and partial mixing. Better attachment of the polymer monolith to the column also provides improved mechanical stability. Indeed, when preparing the silica monolith column, the fusedsilica capillary was pretreated by soaking in 1 M NaOH at 40 °C for 3 h and then flushed with water and acetone. This could increase the density of hydroxyl groups on the wall surface and enhance the interaction with silica colloids [136].

4.4.6 Other Applications

High porosity of icetemplated polymers can be explored for other applications. PolyHEMA hydrogels with nanowire structures were prepared by cryopolymerization. Ag nanoparticles

were then formed on polyHEMA nanowires by simply soaking in $AgNO_3$ solution and subsequent chemical reduction. The aligned nanowire structure provided high surface area and enhanced mass transport to and from the active surface. This was demonstrated by conversion of *o*nitroaniline to 1,2benzenediamine with excellent catalytic activity (apparent rate constant up to 0.165 min^{-1}) and reusability (by washing and immersing in water and then used again for 10 cycles) [64].

The high macroporosity of chitosan was utilized to upload an enzyme (glucose dehydrogenase) towards enzymecatalyzed flowthrough electrodes [31]. Aqueous enzymechitosan solution was simply pipetted onto a prechilled electrode at −20 °C and kept frozen at this temperature for 1 h. The electrode could then be freezedried for evaluation. The chitosan scaffold prepared this way performed 3.25 times better than the airdried chitosan film on electrode, in terms of power density. This could be attributed to greater surface area and enhanced mass transport [31].

The icetemplating technique may be also used to produce closedcell structures that are useful as insulation materials. The solution of wheat gluten in water at a concentration of 14 wt% was processed to produce a homogeneous porous structure with a high content of closed cells [137]. 20 wt% glycerol was added to plasticize the porous material. Owing to the close porosity, the wheat gluten materials were investigated for their thermal conductivity and combustion properties [138]. Both unplasticized and glycerolmodified materials showed a significantly long time to ignition, a lower effective heat of combustion and a higher char content by cone calorimetry measurement. However, the plasticized materials showed better properties overall. The flammability test by the UL 94 method also demonstrated no dripping from the unplasticized structure [138].

4.5 Summary

Ice templating is a highly effective route to fabricating porous polymers and cryogels. This technique may be applied to solutions (including water, organic solvent, and compressed CO_2), suspensions, and emulsions. All the processes involve a freezing step. The frozen samples may be directly freezedried, or cryopolymerized and then freezedried, to produce dry porous polymers. The directly freezedried porous polymers are usually mechanically weak and soluble either in water or the originally used solvent. A postfreezedrying crosslinking step may be performed to enhance the stability of the freezedried materials. Alternatively, the frozen sample may undergo a polymerization or crosslinking reaction in the frozen state. Afterwards, the frozen sample is allowed to thaw to generate cryogels. In addition to chemical crosslinking approaches, a physically crosslinking method, multiple cycles of freeze–thaw, can also be used to produce hydrogels (mainly PVA hydrogel).

The porous scaffolds and cryogels by the icetemplating method have found wide range of applications, particularly as scaffolds for tissue engineering, controlled release, water treatment, separation, and catalysis. For the majority of these applications, crosslinked porous structures or hydrogels are required. For some of the applications, the mechanical stability is

an important parameter. There are other applications that utilize the fast dissolution property of the freezedried polymers in water. These include the applications in the instant formation of emulsions and aqueous organic nanoparticle dispersions. The future development in this area will focus on the fabrication of new scaffolds with superior biocompatibility, green credentials, desirable surface functionalities, and required mechanical stability, and immobilization of biomolecules or nanostructures for biomedical applications and separations.

References

1 Sun, M., Huang, S., Chen, L. et al. (2016). Applications of hierarchically structured porous materials from energy storage and conversion, catalysis, photocatalysis, adsorption, separation, and sensing to biomedicine. *Chem. Soc. Rev.* 45: 3479–3563.

2 Tan, L. and Tan, B. (2017). Hypercrosslinked porous polymer materials: design, synthesis, and applications. *Chem. Soc. Rev.* 46: 3322–3356.

3 McKeown, N.B. and Budd, P.M. (2006). Polymers of intrinsic microporosity (PIMs): organic materials for membrane separations, heterogeneous catalysis and hydrogen storage. *Chem. Soc. Rev.* 35: 675–683.

4 Ramimoghadam, D., Gray, E.M., and Webb, C.J. (2016). Review of polymers of intrinsic microporosity for hydrogen storage applications. *Int. J. Hydrogen Energy* 41: 16944–16965.

5 Díaz, U. and Corma, A. (2016). Ordered covalent organic frameworks, COFs and PAFs. From preparation to application. *Coord. Chem. Rev.* 311: 85–124.

6 Slate, A.G. and Cooper, A.I. (2015). Functionalled design of new porous materials. *Science* 348: 989–999.

7 Diercks, C.S. and Yaghi, O.M. (2017). The atom, the molecule, and the covalent organic framework. *Science* 355: 924–931.

8 Zhang, G. and Mastalerz, M. (2014). Organic cage compounds – from shapepersistency to function. *Chem. Soc. Rev.* 42: 1934–1947.

9 Jaroniec, M. and Schüth, F. (2008). Preface to the special issue: templated materials. *Chem. Mater.* 20: 599–600.

10 Qian, L. and Zhang, H. (2011). Porogen incorporation and phase inversion. In: Porous Polymers (ed. M.S. Silverstein, N.R. Cameron and M.A. Hillmyer), 79–117. Hoboken: John Wiley & Sons, Inc.

11 Petkovich, N.D. and Stein, A. (2013). Controlling macro and mesostructures with hierarchical porosity through combined hard and soft templating. *Chem. Soc. Rev.* 42: 3721–3739.

12 Liu, Y., Goebl, J., and Yin, Y. (2013). Templated synthesis of nanostructured materials.

Chem. Soc. Rev. 42: 2610–2653.

13 Silverstein, M.S. (2014). PolyHIPEs: recent advances in emulsiontemplated porous polymers. *Prog. Polym. Sci* 39: 199–234.

14 Zhang, H. and Cooper, A.I. (2005). Synthesis and applications of emulsiontemplated porous materials. *Soft Matter* 1: 107–113.

15 Zhang, H. and Cooper, A.I. (2005). New approaches to the synthesis of macroporous metals. *J. Mater. Chem.15*: 2157–2159.

16 Wu, D., Xu, F., Sun, B. et al. (2012). Design and preparation of porous polymers. *Chem. Rev.* 112: 3959–4015.

17 Tsyurupa, M.P. and Davankov, V.A. (2006). Porous structure of hypercrosslinked polystyrene: stateoftheart minireview. *React. Funct. Polym.* 66: 768–779.

18 Xu, Y., Jin, S., Xu, H. et al. (2013). Conjugated microporous polymers: design, synthesis and application. *Chem. Soc. Rev.* 42: 8012–8031.

19 Qian, L. and Zhang, H. (2011). Controlled freezing and freeze drying: a versatile route for porous and micro/nanostructured materials. *J. Chem. Technol. Biotechnol.* 86: 172–184.

20 Deville, S. (2013). Icetemplating, freeze casting: beyond materials processing. *J. Mater. Res.* 28: 2202–2219.

21 Gutiérrez, M.C., Ferrer, M.L., and del Monte, F. (2008). Icetemplated materials: sophisticated structures exhibiting enhanced functionalities obtained after unidirectional freezing and icesegregationinduced selfassembly. *Chem. Mater.* 20: 634–648.

22 Hollow, J.L., Lowman, A.M., and Palmese, G.R. (2013). The role of crystallization and phase separation in the formation of physically crosslinked PVA hydrogels. *Soft Matter* 9: 826–833.

23 Dhainaut, J., Piana, G., Deville, S. et al. (2014). Freezinginduced ordering of block copolymer micelles. *Chem. Commun.* 50: 12572–12574.

24 Scanlon, S., Aggeli, A., Boden, N. et al. (2009). Organization of selfassembling peptide nanostructures into macroscopically ordered lamellalike layers by ice crystallization. *Soft Matter* 5: 1237–1246.

25 Qian, L., Ahmed, A., Foster, A. et al. (2009). Systematic tuning of pore morphologies and pore volumes in macroporous materials by freezing. *J. Mater. Chem.* 19: 5212–5219.

26 Gotoh, Y., Ishizuka, Y., Matsuura, T., and Niimi, S. (2011). Spheroid formation and expression of liverspecific functions of human hepatocellular carcinomaderived FLC4 cells cultured in lactosesilk fibroin conjugate sponges. *Biomacromolecules* 12: 1532–1539.

27 JaliliFiroozinezhad, S., RajabiZeleti, S., Mohammadi, P. et al. (2015). Facile fabrication of egg white macroporous sponges for tissue engineering. *Adv. Healthc. Mater.* 4: 2281–2290.

28 Wu, Q., Yu, S., Kollert, M. et al. (2016). Highly absorbing antimicrobial biofoams based on wheat gluten and its biohybrids. *ACS Sustain. Chem. Eng.* 4: 2395–2404.

29 Lloyd, C., Besse, J., and Boyce, S. (2015). Controlledrate freezing to regulate the structure of collagenglycosaminoglycan scaffolds in engineered skin substitute. *J. Biomed. Mater. Res. Part B* 103: 832–840.

30 Wan, A.M., Inal, S., Williams, T. et al. (2015). 3D conducting polymer platforms for electrical control of protein conformation and cellular functions. *J. Mater. Chem. B* 3: 5040–5048.

31 Clooney, M.J., Lau, C., Windmeisser, M. et al. (2008). Design of chitosan gel pore structure: towards enzyme catalysed flowthrough electrodes. *J. Mater. Chem.* 18: 667–674.

32 Qian, L. and Zhang, H. (2010). Green synthesis of chitosanbased nanofibers and their applications. *Green Chem.* 12: 1207–1214.

33 Habibi, Y. (2014). Key advances in the chemical modification of nanocelluloses. *Chem. Soc. Rev.* 43: 1519–1542.

34 Martoia, F., Cochereau, T., Dumont, P.J.J. et al. (2016). Cellulose nanofibril foams: links between icetemplating conditions, microstructures and mechanical properties. *Mater. Design* 104: 376–391.

35 Pääkkö, M., Vapaavuori, J., Silvennoinen, R. et al. (2008). Long and entangled native cellulose I nanofibers allow flexible aerogels and hierarchically porous templates for functionalities. *Soft Matter* 4: 2492–2499.

36 Zhang, Z., Sèbe, G., Rentsch, D. et al. (2014). Ultralightweight and flexible silyated nanocellulose sponges for the selective removal of oil from water. *Chem. Mater.* 26: 2659–2668.

37 Sai, H., Fu, R., Xing, L. et al. (2015). Surface modification of bacterial cellulose aerogels' weblike skeleton for oil/water separation. *ACS Appl. Mater. Interfaces* 7: 7373–7381.

38 Svagan, A.J., Jensen, P., Dvinskikh, S.V. et al. (2010). Towards tailored hierarchical structures in cellulose nanocomposite biofoams prepared by freezing/freezedrying. *J. Mater. Chem.* 20: 6646–6654.

39 Mandal, B.B. and Kundu, S.C. (2009). Cell proliferation and migration in silk fibroin 3D scaffolds. *Biomaterials* 30: 2956–2965.

40 Gil, E.S., Park, S., Tien, L.W. et al. (2010). Mechanically robust, rapidly actuating, and biologically functionalized macroporous poly(*N*isopropylacrylamide)/silk hybrid hydrogels.

Langmuir 26: 15614–15624.

41 Ashokkumar, M., Chipara, A.C., Narayanan, N.T. et al. (2016). Threedimensional porous sponges from collagen biowastes. *ACS Appl. Mater. Interfaces* 8: 14836–14844.

42 Borisova, A., De Bruyn, M., Budarin, V.L. et al. (2015). A sustainable freezedrying route to porous polysaccharides with tailored hierarchical meso and macroporosity. *Macromol. Rapid Commun.* 36: 774–779.

43 Zhang, H., Hussain, I., Brust, M. et al. (2005). Aligned two and threedimensional structures by directional freezing of polymers and nanoparticles. *Nat. Mater.* 4: 787–793.

44 Deville, S., Saiz, E., Nalla, R.K., and Tomsia, A.P. (2006). Freezing as a path to build complex composites. *Science* 311: 515–518.

45 Zhang, H. and Cooper, A.I. (2007). Aligned porous structures by directional freezing. *Adv. Mater.* 19: 1529–1533.

46 Gutiérrez, M.C., GarcíaCarvajal, Z.Y., Jobbágy, M. et al. (2007). Poly(vinyl alcohol) scaffolds with tailored morphologies for drug delivery and controlled release. *Adv. Funct. Mater.* 17: 3505–3513.

47 Zhou, Y., Fu, S., Pu, Y. et al. (2014). Preparation of aligned porous chitin nanowhisker foams by directional freeze–casting technique. *Carbohydr. Polym.* 112: 277–283.

48 Riblett, B.W., Francis, N.L., Wheatley, M.A., and Wegst, U.G.K. (2012). Icetemplated scaffolds with microridged pores direct DRG neurite growth. *Adv. Funct. Mater.* 22: 4920–4923.

49 Gao, H., Lu, Y., Mao, L. et al. (2014). A shapememory scaffold for macroscale assembly of functional nanoscale building blocks. *Mater. Horiz.* 1: 69–73.

50 Flauder, S., Heinze, T., and Muller, F.A. (2014). Cellulose scaffolds with an aligned and open porosity fabricated via icetemplating. *Cellulose* 21: 97–103.

51 Pot, M.W., Faraj, K.A., Adawy, A. et al. (2015). Versatile wedgebased system for the construction of unidirectional collagen scaffolds by directional freezing: practical and theoretical considerations. *ACS Appl. Mater. Interfaces* 7: 8495–8505.

52 Fereshteh, Z., Fathi, M., Bagri, A., and Boccaccini, A.R. (2016). Preparation and characterization of aligned porous PCL/Zein scaffolds as drug delivery systems via improved unidirectional freezedrying method. *Mater. Sci. Eng., C* 68: 613–622.

53 Kim, J., Taki, K., Nagamine, S., and Ohshima, M. (2008). Preparation of poly(llactic acid) honeycomb monolith structure by unidirectional freezing and freezedrying. *Chem. Eng. Sci.* 63: 3858–3863.

54 Kim, J., Taki, K., Nagamine, S., and Ohshima, M. (2009). Preparation of porous poly(l

lactic acid) honeycomb monolith structure by phase separation and unidirectional freezing. *Langmuir* 25: 5304–5312.

55 Shen, H., Niu, Y., Hu, X. et al. (2015). A biomimetic 3D microtubuleorientated poly(lactide *co*glycolide) scaffold with interconnected pores for tissue engineering. *J. Mater. Chem. B* 3: 4417–4425.

56 Blaker, J.J., Lee, K.Y., Mantalaris, A., and Bismarck, A. (2010). Icemicrosphere templating to produce highly porous nanocomposite PLA matrix scaffolds with pore selectively lined by bacterial cellulose nanowhiskers. *Compos. Sci. Technol.* 70: 1879–1888.

57 Roberts, A.D., Wang, S., Li, X., and Zhang, H. (2014). Hierarchical porous nitrogenrich carbon monoliths via icetemplating: high capacity and highrate performance as lithium ion battery anode materials. *J. Mater. Chem. A* 2: 17787–17796.

58 Roberts, A.D., Lee, J.M., Wong, S.Y. et al. (2017). Nitrogenrich activated carbon monoliths via icetemplating with high CO_2 and H_2 adsorption capacities. *J. Mater. Chem. A.* 5: 2811–2820.

59 Liang, H., Ji, K., Zha, L. et al. (2016). Polymer membranes with vertically orientated pores constructed by 2D freezing at ambient temperature. *ACS Appl. Mater. Interfaces* 8: 14174–14181.

60 Bhamidipati, M., Scurto, A.M., and Detamore, M.S. (2013). The future of carbon dioxide for polymer processing in tissue engineering. *Tissue Eng. Part B* 19: 221–232.

61 Zhang, H. and Cooper, A.I. (2003). Compressed fluid sedimentation polymerization. *Macromolecules* 36: 5061–5064.

62 DiazGomez, L., Yang, F., Jansen, J.A. et al. (2016). Low viscosityPLGA scaffolds by compressed CO_2 foaming for growth factor delivery. *RSC Adv.* 6: 70510–70519.

63 Zhang, H., Long, J., and Cooper, A.I. (2005). Aligned porous materials by directional freezing of solution in liquid CO_2. *J. Am. Chem. Soc.* 127: 13482–13483.

64 Mao, Q., Shi, S., and Wang, H. (2015). Biomimetic nanowire structured hydrogels as highly active and recyclable catalyst carriers. *ACS Sustainable Chem. Eng.* 3: 1915–1924.

65 Qian, L., Willneff, E., and Zhang, H. (2009). A novel route to polymeric submicron fibers and their use for inorganic structures. *Chem. Commum.* 3946–3948.

66 Spender, J., Demers, A.L., Xie, X. et al. (2012). Method for production of polymer and carbon nanofibers from watersoluble polymers. *Nano Lett.* 12: 3857–3860.

67 Liu, X., Roberts, A.D., Ahmed, A. et al. (2015). Carbon nanofibers by pyrolysis of self assembled perylene diimide derivative gels as supercapacitor electrode materials. *J. Mater. Chem. A* 3: 15513–15522.

68 Liu, X., Ahmed, A., Wang, Z., and Zhang, H. (2015). Nanofibrous microspheres via emulsion gelation and carbonization. *Chem. Commun.* 51: 16864–16867.

69 Zhang, H., Wang, D., Butler, R. et al. (2008). Formation and enhanced biocidal activity of waterdispersible organic nanoparticles. *Nat. Nanotechnol.* 3: 506–511.

70 Ahmed, A., Smith, J., and Zhang, H. (2011). Gradient porous materials by emulsion centrifugation. *Chem. Commun.* 47: 11754–11756.

71 Wais, U., Jackson, A.W., He, T., and Zhang, H. (2016). Nanoformulation and encapsulation approaches for poorly watersoluble drug nanoparticles. *Nanoscale* 8: 1746–1769.

72 Barbetta, A., Carrino, A., Costantini, M., and Dentini, M. (2010). Polysaccharide based scaffolds obtained by freezing the external phase of gasinliquid foams. *Soft Matter* 6: 5213–5224.

73 Hassan, C.M. and Peppas, N.A. (2000). Structure and applications of poly(vinyl alcohol) hydrogels produced by conventional crosslinking or by freezing/thawing methods. *Adv. Polym. Sci.* 153: 37–65.

74 Willcox, P.J., Howie, D.W., SchmidtRohr, K. et al. (1999). Microstructure of poly(vinyl alcohol) hydrogels produced by freeze/thaw cycling. *J. Polym. Sci., Part B: Polym. Phys.* 37: 3438–3454.

75 Ricciardi, R., Auriemma, F., Gaillet, C. et al. (2004). Investigation of the crystallinity of freeze/thaw poly(vinyl alcohol) hydrogels by different techniques. *Macromolecules* 37: 9510–9516.

76 Hassan, C.M. and Peppas, N.A. (2000). Structure and morphology of freeze/thawed PVA hydrogels. *Macromolecules* 33: 2472–2479.

77 McGann, M.J., Higginbotham, C.L., Geever, L.M., and Nugent, M.J.D. (2009). The synthesis of novel pHsensitive poly(vinyl alcohol) composite hydrogels using a freeze/thaw process for biomedical applications. *Int. J. Pharm.* 372: 154–161.

78 Llanos, G.R. and Sefton, M.V. (1991). Immobilization of poly(ethylene glycol) onto a poly(vinyl alcohol) hydrogel. 1. Synthesis and characterization. *Macromolecules* 24: 6065–6072.

79 Mathews, D.T., Birney, Y.A., Cahill, P.A., and McGuinness, G.B. (2008). Mechanical and morphological characteristics of poly(vinyl alcohol)/chitosan hydrogels. *J. Appl. Polym. Sci.* 109: 1129–1137.

80 Xi, L., Jiang, M., Dong, X. et al. (2012). Controlled mechanical and swelling properties of poly(vinyl alcohol)/sodium alginate blend hydrogels prepared by freeze–thaw followed by Ca^{2+} crosslinking. *J. Appl. Polym. Sci.* 124: 823–831.

81 Qi, X., Hu, X., Wei, W. et al. (2015). Investigation of Salecan/poly(vinyl alcohol) hydrogels prepared by freeze/thaw method. *Carbohydr. Polym.* 118: 60–69.

82 Abitbol, T., Johnstone, T., Quinn, T.M., and Gray, D.G. (2011). Reinforcement with cellulose nanocrystals of poly(vinyl alcohol) hydrogels prepared by cyclic freezing and thawing. *Soft Matter* 7: 2373–2379.

83 Zhang, H., Xia, H., and Zhao, Y. (2012). Poly(vinyl alcohol) hydrogel can autonomously selfheal. *ACS Macro Lett.* 1: 1233–1236.

84 Guan, Y., Bian, J., Peng, F. et al. (2014). High strength of hemicelluloses based hydrogels by freeze/thaw technique. *Carbohydr. Polym.* 101: 272–280.

85 Zhang, H., Zhang, F., and Wu, J. (2013). Physically crosslinked hydrogels from polysaccharides prepared by freeze–thaw technique. *React. Funct. Polym.* 73: 923–928.

86 Henderson, T.M.A., Ladewig, K., Haylock, D.N. et al. (2013). Cryogels for biomedical applications. *J. Mater. Chem. B* 1: 2682–2695.

87 Choudhury, S., Connolly, D., and White, B. (2015). Supermacroporous polyHIPE and cryogel monolithic materials as stationary phases in separation science: a review. *Anal. Methods* 7: 6967–6982.

88 Kirsebom, H. and Mattiasson, B. (2011). Cryostructuration as a tool for preparing highly porous polymer materials. *Polym. Chem.* 2: 1059–1062.

89 Gun'ko, V.M., Savina, I.N., and Mikhalovsky, S.V. (2013). Cryogels: Morphological, structure and adsorption characterization. *Adv. Colloid Interface Sci.* 187188: 1–46.

90 Plieva, F.M., Karlsson, M., Aguilar, M. et al. (2005). Pore structure in supermacroporous polyacrylamide based cryogels. *Soft Matter* 1: 303–309.

91 Zhan, X., Lu, D., Lin, D., and Yao, S. (2013). Preparation and characterization of supermacroporous polyacrylamide cryogel beads for biotechnological application. *J. Appl. Polym. Sci.* 130: 3082–3089.

92 Srivastava, A., Jain, E., and Kumar, A. (2007). The physical characterization of supermacroporous poly(*N*isopropylacrylamide) cryogel: mechanical strength and swelling/deswelling kinetics. *Mater. Sci. Eng., A* 464: 93–100.

93 Petrov, P., Petrova, E., and Tsvetanov, C.B. (2009). UVassisted synthesis of super macroporous polymer hydrogels. *Polymer* 50: 1118–1123.

94 Petrov, P., Pavlova, S., Tsvetanov, C.B. et al. (2011). In situ entrapment of urease in cryogels of poly(*N*isopropylacrylamide): an effective strategy for noncovalent immobilization of enzymes. *J. Appl. Polym. Sci.* 122: 1742–1748.

95 Barrow, M., Eltmimi, A., Ahmed, A. et al. (2012). Frozen polymerization for aligned

porous structures with enhanced mechanical stability, conductivity, and as stationary phase for HPLC. *J. Mater. Chem.* 22: 11615–11620.

96 Barrow, M. and Zhang, H. (2013). Aligned porous stimuliresponsive hydrogels via directional freezing and frozen UV initiated polymerization. *Soft Matter* 9: 2723–2729.

97 Arrua, R.D. and Hilder, E.F. (2015). Highly ordered monolithic structures by directional freezing and UVinitiated cryopolymerisation: evaluation as stationary phases in high performance liquid chromatography. *RSC Adv.* 5: 71131–71138.

98 Ertürk, G. and Mattiasson, B. (2014). Cryogelsversatile tools in bioseparation. *J. Chromatogr. A* 1357: 24–35.

99 Ak, F., Oztoprak, Z., Karakutuk, I., and Okay, O. (2013). Macroporous silk fibroin cryogels. *Biomacromolecules* 14: 719–727.

100 Tam, R.Y., Fisher, S.A., Baker, A.E.G., and Shoichet, M.S. (2016). Transparent porous polysaccharide cryogels provide biochemically defined, biomimetic matrices for tunable 3D cell culture. *Chem. Mater.* 28: 3762–3770.

101 Welzel, P.B., Grimmer, M., Renneberg, C. et al. (2012). Macroporous starPEGheparin cryogels. *Biomacromolecules* 13: 2349–2358.

102 Zhang, H., Hardy, G.C., Khimyak, Y.Z. et al. (2004). Synthesis of hierarchically porous silica and metal oxide beads using emulsiontemplated polymer scaffolds. *Chem. Mater.* 16: 4245–4256.

103 Wu, J., Lin, Y., and Sun, J. (2012). Anisotropic volume change of poly(N isopropylacrylamide)based hydrogels with an aligned dualnetwork microstructure. *J. Mater. Chem.* 22: 17449–17451.

104 Okaji, R., Taki, K., Nagamine, S., and Ohshima, M. (2012). Preparation of porous honeycomb monolith from UVcurable monomer/dioxane solution via unidirectional freezing and UV irradiation. *J. Appl. Polym. Sci.* 125: 2874–2882.

105 Okaji, R., Taki, K., Nagamine, S., and Ohshima, M. (2013). Preparation of a unique, multihollowcore honeycomb structure via the unidirectional freezing of a binary solvent system. *J. App. Polym. Sci.* 130: 526–534.

106 Zhu, J., Wang, J., Lin, Q. et al. (2013). Anisotropic tough poly(2hydroxyethyl methacrylate) hydrogels fabricated by directional freezing redox polymerization. *J. Mater. Chem. B* 1: 978–986.

107 Wu, J., Zhao, Q., Sun, J., and Zhou, Q. (2012). Preparation of poly(ethylene glycol) aligned porous cryogels using a unidirectional freezing technique. *Soft Matter* 8: 3620–3626.

108 Zhao, D., Zhu, J., Zhu, Z. et al. (2014). Anisotropic hierarchical porous hydrogels with unique water loss/absorption and mechanical properties. *RSC Adv.* 4: 30308–30314.

109 Tripathi, A., Kathuria, N., and Kumar, A. (2009). Elastic and macroporous agarose–gelatin cryogels with isotropic and anisotropic porosity for tissue engineering. *J. Biomed. Mater. Res.* 90A: 680–694.

110 Wu, J., Zhao, Q., Liang, C., and Xie, T. (2013). Enzymatically degradable oxidized dextranchitosan hydrogels with an anisotropic aligned porous structure. *Soft Matter* 9: 11136–11142.

111 Dogu, S. and Okay, O. (2008). Tough organogels based on polyisobutylene with aligned porous structures. *Polymer* 49: 4626–4634.

112 Frydrych, M. and Chen, B. (2013). Large threedimensional poly(glycerol sebacate) based scaffolds – a freezedrying preparation approach. *J. Mater. Chem. B* 1: 6650–6661.

113 Williams, D.F. (2008). On the mechanisms of biocompabitility. *Biomaterials* 29: 2941–2953.

114 Kirkpatrick, C.J., Bittinger, F., Wagner, M. et al. (1998). Current trends in biocompatibility testing. *Proc. Inst. Mech. Eng. H* 212: 75–84.

115 Jurga, M., Dainiak, M.B., Sarnowska, A. et al. (2011). The performance of laminin containing cryogel scaffolds in neural tissue regeneration. *Biomaterials* 32: 3423–3434.

116 Qian, L., Ahmed, A., GlennonAlty, L. et al. (2015). Patterned substrates fabricated by a controlled freezing approach and biocompatibility evaluation by stem cells. *Mater. Sci. Eng., C* 49: 390–399.

117 Zhang, H., Edgar, D., Murray, P. et al. (2008). Synthesis of porous microparticles with aligned porosity. *Adv. Funct. Mater.* 18: 222–228.

118 Gutiérrez, M.C., GarcíaCarvajal, Z.Y., Jobbágy, M. et al. (2007). Hydrogel scaffolds with immobilized bacteria for 3D cultures. *Chem. Mater.* 19: 1968–1973.

119 Christoph, S., Kwiatoszynski, J., Coradin, T., and Fernandes, F.M. (2016). Cellularized cellular solids via freezecasting. *Macromol. Biosci.* 16: 182–187.

120 Gasperini, L., Mano, J.F., and Reis, R.L. (2014). Natural polymers for the microencapsulation of cells. *J. R. Soc. Interface* 11, 20140817.

121 Takamura, A., Ishii, F., and Hidaka, H. (1992). Drug release from poly(vinyl alcohol) gel prepared by freezethaw procedure. *J. Controlled Release* 20: 21–28.

122 Nugent, M.J.D. and Higginbotham, C.L. (2007). Preparation of a novel freeze thawed poly(vinyl alcohol) composite hydrogel for drug delivery applications. *Eur. J. Pharm. Biopharm.* 67: 377–386.

123 Qian, L. and Zhang, H. (2013). Onestep synthesis of proteinencapsulated microspheres

in a porous scaffold by freezedrying double emulsions and tuneable protein release. *Chem. Commun.* 49: 8833–8835.

124 Ahmed, A., Hearn, J., Abdelmagid, W., and Zhang, H. (2012). Dualtuned drug release by nanofibrous scaffolds of chitosan and mesoporous silica microspheres. *J. Mater. Chem.* 22: 25027–25035.

125 Kaasgaard, T. and Keller, D. (2010). Chitosan coating improves retention and redispersibility of freezedried flavour oil emulsions. *J. Agric. Food Chem.* 58: 2446–2454.

126 Grant, N. and Zhang, H. (2011). Poorly watersoluble drug nanoparticles via an emulsionfreezedrying approach. *J. Colloid Interface Sci.* 356: 573–578.

127 Wais, U., Jackson, A.W., Zuo, Y. et al. (2016). Drug nanoparticles by emulsionfreeze drying via the employment of branched block copolymer nanoparticles. *J. Controlled Release* 222: 141–150.

128 Qian, L. and Zhang, H. (2010). Direct formation of emulsions using watersoluble porous polymers as sacrificial scaffolds. *J. Chem. Technol. Biotechnol.* 85: 1508–1514.

129 Qian, L., Ahmed, A., and Zhang, H. (2011). Formation of organic nanoparticles by solvent evaporation within porous polymeric materials. *Chem. Commun.* 47: 10001–10003.

130 Roberts, A.D. and Zhang, H. (2013). Poorly watersoluble drug nanoparticles via solvent evaporation in watersoluble porous polymers. *Int. J. Pharm.* 447: 241–250.

131 Okajima, M.K., Nakamura, M., Ogawa, T. et al. (2012). Spongy hydrogels of cyanobacterial polyanions mediate energysaving electrolytic metalrefinement. *Ind. Eng. Chem. Res.* 51: 8704–8707.

132 Marui, Y., Kikuzawa, A., Kida, T., and Akashi, M. (2010). Unique organogel formation with macroporous materials constructed by the freezedrying of aqueous cyclodextrin solutions. *Langmuir* 26: 11441–11445.

133 Chatterjee, S., Gupta, S.S., and Kumaraswamy, G. (2016). Omniphilic polymeric sponges by ice templating. *Chem. Mater.* 28: 1823–1831.

134 Wang, B., Ji, J., and Li, K. (2016). Crystal nuclei templated nanostructured membranes prepared by solvent crystallization and polymer migration. *Nat. Commun.* 7: 12804.

135 Hayes, R., Ahmed, A., Edge, T., and Zhang, H. (2014). Core–shell particles: Preparation, fundamentals and applications in high performance liquid chromatography. *J. Chromatogr. A* 1357: 36–52.

136 Ahmed, A., Myers, P., and Zhang, H. (2012). Preparation of aligned porous silica monolithic capillary columns and their evaluation for HPLC. *Anal. Methods* 4: 3942–3947.

137 Blomfeldt, T.O.J., Kuktaite, R., Johansson, E., and Hedenqvist, M.S. (2011). Mechanical

properties and network structure of wheat gluten foams. *Biomacromolecules* 12: 1707–1715.

138 Blomfeldt, T.O.J., Nilsson, F., Holgate, T. et al. (2012). Thermal conductivity and combustion properties of wheat gluten foams. *ACS Appl. Mater. Interfaces* 4: 1629–1635.

5
Porous Ceramics and Metals by Ice Templating

5.1 Introduction

Porous ceramics have unique applications as filters for water treatment/hot gases/molten metals, hightemperature thermal insulation, catalysts or catalyst support, and bioscaffolds for tissue engineering (particularly bone engineering) [1]. These applications require porous ceramics with specific properties including high temperature stability, mechanical strength, interconnected porosity or closed pores, low density, and low thermal conductivity [2]. A variety of fabrication methods have been developed for the preparation of macroporous ceramics because most of these applications would require the presence of macropores (>50 nm by IUPAC definition, and indeed mostly in the micron range) in order to enhance mass transport or to accommodate cells. These methods usually fall under three categories: (i) the replicating approach by impregnation into a preformed structure; (ii) the sacrificial templating method where the templates are removed by washing, pyrolysis or evaporation; and (iii) the direct foaming method [1, 2].

Recently, ice templating and freezedrying have been used for fabrication of a wide range of porous structures including polymers, composites, ceramics, and nanostructured materials [3–5]. Indeed, the most investigated area is probably the preparation of porous ceramics, as evidenced by the large number of publications and reviews [6–9]. The advantages of ice templating for porous ceramics include: (i) simple processing procedures and hence high versatility; (ii) tuning porosity and pore sizes by the use of various additives and varied freezing conditions; and (iii) different freezing techniques to produce aligned porous structures and monoliths/films. Different terms have been used in literature for this technique, including ice templating, freezedrying, freeze casting, cryoconstruction, and cryosynthesis. Among them, the terms freeze casting (particularly for ceramics) and ice templating are used most often. The techniques used for the preparation of aligned porous materials may be termed as *directional freezing*, *unidirectional freezing*, *orientated freezing*, *directional solidification* or ice segregation induced selfassembly (ISISA). Similarly, the resulting structures may be called *aligned porous*, *parallel microchannels*, *aligned tubular*, *aligned channels* or *honeycomb structures*. These structures may differ in their detail but they are usually produced by similar directional freezing techniques.

In this chapter, the focus is on porous ceramics by ice templating, covering formulations, freezing conditions, and freeze casting combined with gelation, which are prepared from ceramic particle slurries with the help of different solvents and additives. This is followed by the preparation of porous silica and metal oxides from the sols, with or without additives. The preparation of porous metals, either by direct freeze casting of metal particles or more often by reduction of porous metal oxides, is then described. The chapter concludes with the

applications of porous ceramics fabricated by ice templating.

5.2 Porous Ceramics by Ice Templating

Ceramic particles are formulated as slurries, which are then frozen in controlled ways, depending on the targeted pore structure. The frozen samples are then freezedried (or cryo gelled and vacuum dried) to produce green bodies. The green bodies are treated at high temperatures (usually in air) to remove the organic components and to sinter the ceramic particles to generate strong porous ceramics.

The pore structures in icetemplated ceramics may be classified into homogeneous pores or heterogeneous pores [6]. The homogeneous pores are usually created by slow freezing in a cold chamber or by immersing in a cold liquid (such as liquid nitrogen), with a feature of highly interconnected cellular pores. The heterogeneous pores may be divided into aligned pores or graded pores. Applying a temperature gradient across a liquid sample is critical for the production of aligned pores or graded pores, known as *directional freezing*. This is often realized by dipping the liquid sample in a suitable container into liquid nitrogen at controlled rates [10, 11] or by the use of cold finger (as shown in Figure 5.1) [12]. For the dipping method, by using the suitable dipping rate, it is possible to maintain a constant temperature gradient at the freezing front and thereby a more uniform aligned structure. For the cold finger approach, the temperature of the cold finger may be controlled precisely by the temperature controlling unit. However, because the liquid sample is placed on the temperaturecontrolled plate (Figure 5.1), the temperature gradient may change with the progress of the freezing interface, which creates a pore structure of three zones: dense structure, cellular structure, and then transition to lamellar structures [13, 14]. There are other ways of applying directional freezing, some of which are illustrated in Chapter 1. However, the aim is always the same: creating a controlled temperature gradient for the liquid sample.

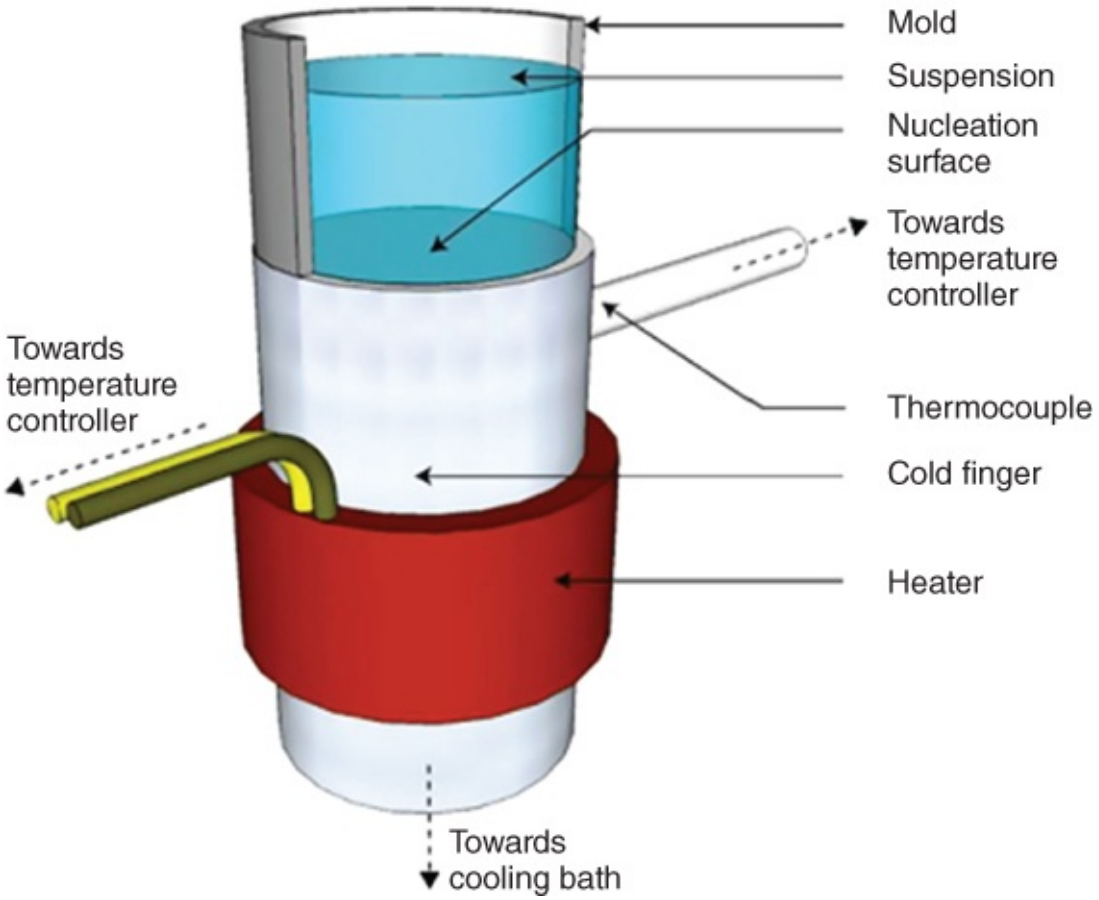

Figure 5.1 The schematic representation of the experimental setup used for directional freezing by cold finger.

Source: Munch et al. 2009 [12]. Reprinted with permission from John Wiley and Sons.

5.2.1 Effect of Formulations

5.2.1.1 Ceramic Particles

A variety of ceramic particles (usually submicron or nanoparticles) have been processed to produce porous ceramics. Among them, alumina particles are the most investigated for the preparation of porous alumina [12, 14–20] or as model particles for theoretical freezing studies [21–25]. Examples of other particles include silica [10, 26–28] or zeolite particles [29], hydroxyapatite [13, 30–33], titania [34–37], calcium phosphate [38, 39], yttria stabilized zirconia (YSZ) and hybrids [40–42], perovskite material LSCF [43, 44], Gddoped ceria (GDC) [45], SiC [46], silicon nitride [47], perovskitetype $LaCoO_3$ [48], barium titanatehydroxyapatite [49], kaolinitesilica [50], mullitezirconia [51], and alumina zirconia [52]. It should be pointed out that this is not an exhaustive list of porous ceramics fabricated by the icetemplating technique. More examples can be found from the reviews on this topic [6–9].

Solid content is primarily related to porosity in porous ceramics. As summarized by Deville from the published data, the porosity is inversely proportional to the solid content in the slurries (Figure 5.2) in the concentration range of 5–60 vol% [8]. In general, the higher the

ceramic particle concentration, the lower the porosity in the fabricated porous ceramics. The pores become less interconnected as well. If the percentage of the binder and stabilizer are similar, the freezedried green bodies are weaker and are difficult to handle at lower ceramic contents. However, when the ceramic content is too high (>80 wt%), the desired pore structure and the pore interconnectivity may be lost [14]. For slurries with high solid contents (>50 vol%), the rejection of particles can be hindered by the larger number of surrounding particles. This can lead to the transition from cellular pores to dendritic patterns [6]. The solid content can also affect pore shapes when sintering at high temperatures. It has been observed that porous kaolinite–silica composites could generate rounded pores at high temperature of sintering and lead to more closed pores at high solid content. In contrast, for the ceramics prepared from low solid content slurries, the pore shrinkage and thickening of pore walls were heterogeneous, leading to elongated pores [50].

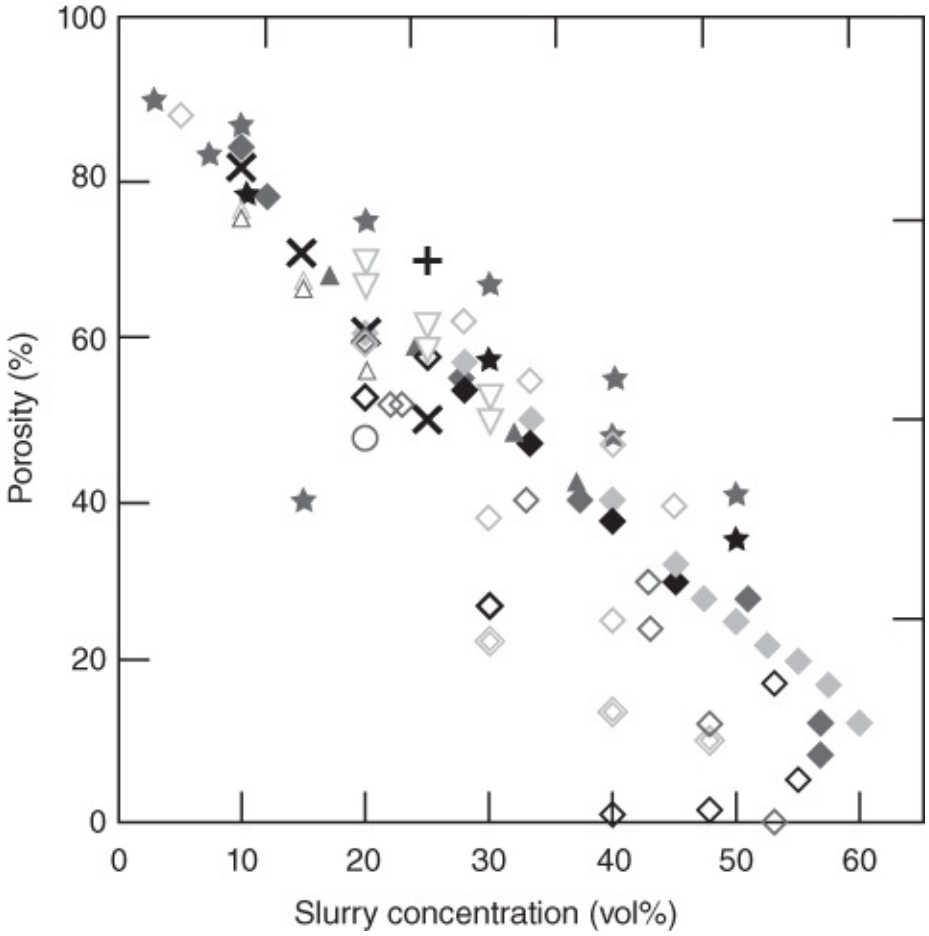

Figure 5.2 The relationship between the porosity in porous ceramics and the concentration in the slurries used to prepare such ceramics by freeze casting.

Source: Deville 2008 [8]. Reprinted with permission from John Wiley and Sons.

Particle size can have significant impacts on pore morphology and porosity and thereby mechanical stability. Deville et al. investigated the influence of alumina particles of different sizes (0.2, 0.4, 1.3 and, 3.4 μm) on nucleation and crystal growth [19]. Large particles provide less nucleation sites, which leads to highly supercooled systems before irreversible nucleation starts. In contrast, small particles have higher surface area and offer more nucleation sites.

This results in a less supercooled state. Thus, by comparing the nucleation between large and small particles, a higher temperature gradient is created for large particles. It should be pointed out that this impact of particle size is mainly related to the initial nucleation and the transition to the stable progress of a freezing interface. A longer transition zone has been observed for larger particles whilst the freezing interface velocity is independent of particle sizes [19]. The size effect (1.69 and 3.9 μm) of hydroxyapatite particles on the formed scaffolds was investigated with regard to sintering, shrinkage, porosity, and compression strength [33]. For the cooling rates investigated, it was observed that higher cooling rates led to stronger scaffolds. Larger shrinkage, lower porosity, and higher compressive strength were found during sintering of the scaffolds made of larger particles [33].

The effects of particle sizes can be multiple, depending on particle density, shape, and slurry composition. The ceramic particles should be relatively small so that a stable particle suspension can be formed for the preparation of homogeneous ceramic materials. Owing to their higher density than those of the solvents, large particles may sediment rapidly in slurry. Even if a suspension is macroscopically stable, the movement of large particles when excluded from the freezing front can be limited. As a result, the targeted pore morphology may be lost. This is more significant when preparing ceramic films and membranes. In general, in relation to freezing velocity, it can be inferred that particle size can influence the entrapment of particles in ice as well as the stability of freezing front, which are the main causes for the formation of different icetemplated morphologies [21].

5.2.1.2 Solvent

Unsurprisingly, water is the most used solvent when preparing porous ceramics by freeze casting. This is because of its low cost and environmentfriendly nature. However, there are some limitations as well: e.g. poor ability to suspend hydrophobic particles, low vapour pressure of ice, and higher freezedrying costs. However, there are also some other solvents that have been frequently used in freeze casting.

*tert*Butyl alcohol (TBA) can freeze below 25 °C and volatilize rapidly above 30 °C. This property is used to prepare porous alumina via freezegel casting. The frozen sample may be thawed, with direct evaporation of TBA [20]. TBA exhibits high melting point (~25 °C), low surface tension, and high saturation vapour pressure, which ensure fast freezedrying at higher drying temperature. TBA also shows low toxicity and has been often used as a cosolvent with water for pharmaceutics [53]. TBA was used as the solvent to prepare porous alumina with long straight pores. The nondendritic morphology was different from the alumina prepared using water and camphene [16]. A sequential slurry casting method was used to prepare three layered aluminazirconia composites from the TBA slurries, with the layers being 95/5 alumina/zirconia, 85/15 alumina/zirconia, and 95/5 alumina/zirconia. Aligned microchannels were formed through the layers, with the bottom layer showing the smallest pores at ~11 μm [54].

Camphene is another commonly used solvent. Camphene is one of three terpenes (the others being menthol and camphor), which can be used as a freezing vehicle for porous ceramics.

They are nontoxic aromatic substances derived from plants [55]. Terpenes are volatile solids that can be readily removed by sublimation at room temperature. Camphene is more widely used than the other two because of its suitable melting point (44–48 °C) and higher vapour pressure in solid state (0.330 kPa at 20 °C) (data from UNEP Publications, http://www.inchem.org). YSZ slurry in camphene was formed by ball milling at 60 °C for 20 h and then frozen in a water bath (15 °C). Conveniently, camphene was removed at room temperature to produce the green body. After sintering at 1450 °C for 3 h, YSZ foam with high compressive strength was produced [56]. A similar procedure was applied to fabricate porous ZrB_2–SiC [57]. βSiAlON particles were suspended in prewarmed camphene at 60 °C to fabricate gradient porous ceramic materials [58].

Mixing solvents are also used to produce porous ceramics with varied morphologies. This is attributed to the changing composition of the solvents and the different crystal morphologies of each solvent. Water with another polar organic solvent (e.g. TBA and dioxane) is often employed. A TBAwater system with varying contents of TBA (0, 10, 20, 30, 40, 50, 60, 70, 80, 90, and 100 wt%) was used to fabricate porous alumina [59]. With the increasing content of TBA, the prepared alumina showed the change of pore morphologies from lamellar, snowflake, and needlelike, to hexagonal. Porous alumina with hexagonal pores made from TBA slurry exhibited the best mechanical strength [59]. The TBAwater system was also employed to produce porous YSZ. In the TBAwater phase diagram, two eutectic compositions (about 16 and 90 wt% of TBA) were identified. When the slurry was formed in the mix solvent with a TBA content of <16 wt% and frozen under suitable conditions, ice crystals formed first, concentrating the TBA content. As a result, a eutectic structure was formed. This resulted in the generation of large main pores and small pores in the large pore wall. In the other end of the phase diagram, when a slurry with 5 wt% water/95 wt% TBA was processed, the freezedried structure exhibited large TBAtemplated faceted pores and smaller pores templated from the eutectic structure with around 90 wt% water [40].

5.2.1.3 Dispersant or Stabilizer

Ammonium polymethacrylate (anionic dispersant) is mostly used for aqueous slurries, usually at the concentration of 1 wt% for alumina powder [12, 14, 17, 21–23], hydroxyapatite particles [13, 31], βtricalcium phosphate particles (βTCP, 1–2 μm) [39], YSZ particles [41, 42], and perovskite LSCF particles [43]. Zeta potential and viscosity of aqueous alumina slurries with different dispersants (ammonium polymethacrylate, sodium polymethacrylate, and ammonium polyacrylate) in the concentration range of 0.2–2 wt% were investigated. It was found that the viscosity was irrespective of the dispersant type, with the lowest viscosity at the concentration of ~0.3 wt%. The concentration range of 0.2–0.4 wt% was found to be optimal for slurries with strong repulsive interactions between the particles. The dispersant concentration could significantly affect the development of a particle depletion zone and formation of ice lenses, which could considerably influence the mechanical strength of the porous ceramics formed [24].

Citric acid was used as a dispersant (1 wt% based on alumina powder) in slurries in TBA [16] or with acrylamide in TBA [20]. Similarly, citric acid was also employed in

alumina/zirconia slurries in TBA [54]. Both citric acid (1 wt%) as dispersant and Dynol 604 (0.25 wt%, ethoxylated acetylenic diol) as surfactant were included in the slurries of biphasic calcium phosphate (BCP) particles (sieved under 75 μm) with acrylamide and methylenebisacrylamide in TBA in order to produce porous bioceramics [38]. For the mixing solvent of TBA and water, citric acid was used as the dispersant with polyvinylpyrrolidone (PVP) as binder (>50 wt% TBA). However, for the mixture solvent with <50 wt% TBA, sodium polyacrylate was the dispersant with carboxymethylcellulose (CMC) as binder [59]. In another study where the TBAwater system was used to prepare porous YSZ, ProxB03 (a polyacrylate ammonium salt) and PEG6M were used as the dispersant and binder for TBA content up to 40 wt%. Only polyvinyl butyral was used as binder without dispersant for TBA content above 70 wt% [40].

Texaphor 963 at a concentration of 5 wt% to the solid powder was added to YSZ–camphene slurry for processing (with no other binder added) [56]. Texaphor 963 was also used for ZrB_2-SiC–camphene slurry at the concentration of 3 wt% [57]. The same dispersant was employed at a concentration of 0.6 wt% for TiO_2–camphene slurries (solid loading 10–20 wt%). These TiO_2 particles were prepared by ethanediamine modification of Degussa P25, which inhibited the anatasetorutile phase transformation of TiO_2 during heat treatment [36].

5.2.1.4 Binder

Poly(vinyl alcohol) (PVA) acts like a ‘glue’ to bind the ceramic particles together and obtain icetemplated monolithic materials that can be easily handled [10, 12, 24]. Quite often, PVA also plays the role of additive with the concentrations of 5–10 wt%, leading to the formation of smaller pores in the resulting porous silica or ceramic materials [10, 12]. When PVA is used as a binder, particularly for slurries with high solid contents (e.g. 20–40 vol% solid particles), a low concentration such as 1 wt% may be sufficient for the production of green bodies, as evidenced in the preparation of porous hydroxyapatite [13, 31]. Both the concentrations of PVA as binder and ammonium polyacrylate as dispersant were varied to change the viscosity of the slurries with a subsequent big impact on porosity and compressive strength of the formed ceramic materials [31]. PVA and PVP were both added to silicon slurry (20 vol%) to act as binder and dispersant, respectively [47]. Bentonite clay as inorganic binder and polyethylene glycol (PEG) as sacrificial organic binder were employed in zeolite 13X slurries (particle size 3–5 μm) for the preparation of hierarchically porous silica [29]. PEG (1000 g mol^{-1}) was added to aqueous βTCP slurry as organic binder [39]. PEG (1–4 wt%) was used as binder in perovskite LSCF slurries with solid loading of 40–50 wt% [43].

Poly(vinyl butyral) was used as binder in the slurry of alumina–citric acid–TBA [16] and also alumina–zirconia–citric acid–TBA slurries [54]. PVP and CMC were binders for the slurries of alumina–TBA–water with the varying contents of TBA in the system [59].

5.2.1.5 Additives

Some additives such as sodium chloride, sucrose, trehalose, glycerol, and ethanol are known to depress the solution freezing point (as antifreezers), most likely via the colligative effects

[12]. The pore structure of porous alumina changes from lamellar (no additive, trehalose, sucrose) to cellular (gelatin, glycerol), or to a lamellar structure with a bimodal pore width distribution (ethanol). These additives can have varying impacts on interfacial tension and interparticle force, leading to varied bridge structures [12]. Glycerol (10 and 20 wt%) was added to 35 vol% alumina slurries, facilitating the formation of more defined porous structures [18]. Ethanol or 1propanol was added to aqueous alumina slurries, resulting in increased viscosity and subsequently decreased porosity and increased compressive strength in the sintered ceramics [60]. Glycerol was used as an antifreezer (1 wt% to solid powder) for the preparation of porous silicon [47].

Some polymers were added to the slurries to tune the pore sizes of the freezedried monoliths. However, this does not exclude the polymers from also acting as binders for the monoliths produced [10, 27]. For example, PEG, γcyclodextrin, and dextran were added to 40 wt% aqueous silica colloid suspensions (O40). The average channel size of the silica monoliths prepared by directional freezing decreased with the increasing concentration of dextran (M_W = 17 500). Remarkably, at the dextran concentration of 10 wt%, the average channel size could be reduced to 180 nm [27]. This is a significant progress because most of the ice templated pores are in the micron range. The effect of PEG with different molecular weights (400, 900, 1350, and 3350 g mol^{-1}) at the concentration of 5 wt% (based on water) was investigated on freezecast alumina [61]. The average pore size changed from 10 to 5.5 μm with the increasing molecular weight of PEG. This could be explained by the diffusivity of PEG and constitutional supercooling [61].

Antifreeze proteins (AFPs) have also been used as additives to depress the freezing point of the slurries in order to form homogeneously distributed ice crystals in the whole frozen body [15]. There are two categories of proteins that are reported to depress the freezing temperature: antifreeze glycoproteins (AFGPs) and AFPs (type I, type II, and type III). The mechanism of reducing freezing temperatures from AFPs is noncolligative because of the presence of thermal hysteresis between freezing temperature and melting temperature. Although the freezing temperature is lowered, the melting temperature has always been very close to 0 °C [62]. Also, the level in depressing the freezing temperature for AFPs at a concentration is considerably higher than those for colligative substances at similar concentrations. It has been postulated that reversible adsorption of AFPs on ice nuclei inhibit ice crystal growth (or allow growth on defined facets), leading to supercooled solutions [62]. Porous alumina was prepared by a gelation freezing method where alumina/gelatin solution was blended at the volume ratio of 10 : 90 with the AFP added into the gelatin solution at weight ratios of 0.25 : 99.75 and 0.50 : 99 : 50 to gelatin. The addition of AFP contributed to the generation of smaller and uniform ice crystals. This was evidenced by the decreasing average pores (from 102.5, 37.8 to 12.8 μm) when the gel was frozen at −20 °C. As shown in Figure 5.3, it is clear that porous alumina prepared with addition of AFP exhibits smaller and uniformly distributed pores, compared to the structure without adding AFP [15]. AFGP was also included in the gelatin system for the preparation of porous mullitezirconia insulators [51]. The obtained uniform pore channels led to a mullite insulator with high compressive strength and low thermal conductivity [51].

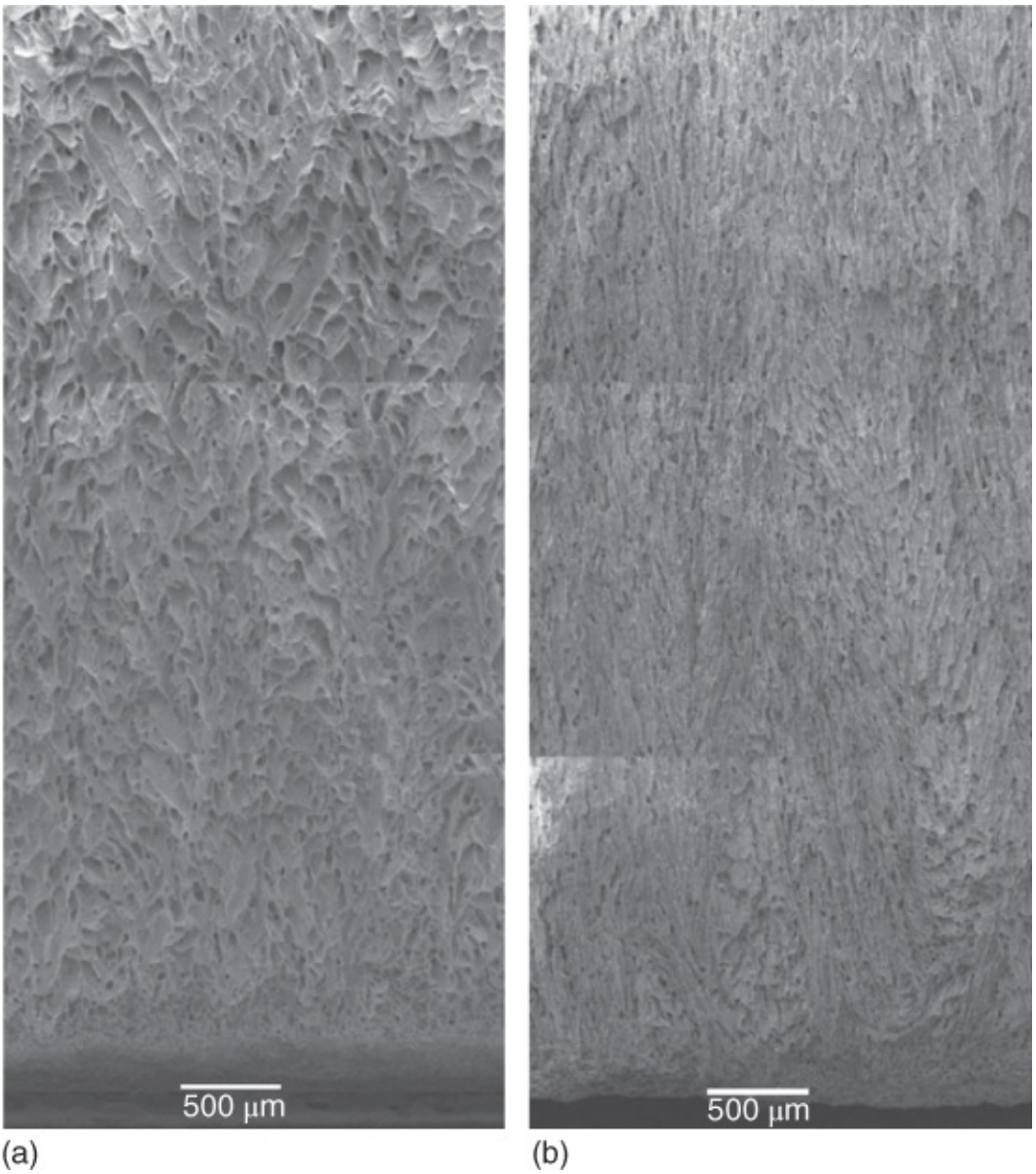

Figure 5.3 Effect of antifreeze protein (AFP) in the slurry on the pore structure of porous alumina prepared by freezing at −40 °C: (a) the pore structure from the slurry containing no AFP and (b) the pore structure prepared from the slurry containing 0.5 wt% AFP relative to gelatin (99.5 wt%).

Source: Fukushima et al. 2013 [15]. Reprinted with permission from John Wiley and Sons.

However, there are no definite differences between dispersant, binder, and additive for some polymers and surfactants included in the slurries. By definition, a dispersant (or stabilizer) is to help disperse the ceramic particles and form a stable dispersion while the binder is to hold the ceramic particles together and generate a monolithic green body after freezedrying. An additive can be anything added into the slurries but usually it is something that can influence pore shape, pore size, and mechanical stability. Some commonly used hydrophilic polymers such as PVA, PVP, CMC, and dextran can play all these roles in aqueous slurries although they are discussed as binders in the earlier sections. The same is true for polymeric surfactants. In general, the amphiphilic property contributes to stabilization whilst molecular weights may have considerable impact as binders and additives. When mixing polymeric and ionic

surfactants, it may be difficult to identify their specific roles. For example, uniform silica microspheres were prepared by a modified Stöber method [63]. These silica microspheres were suspended in water at 30 wt% with 5 wt% PVA. In order to investigate the effect of charges on pore morphology, the cationic surfactant cetyltrimethylammonium bromide (CTAB) and anionic surfactant sodium dodecyl sulfate (SDS) were also included in the slurries. It can be observed from Figure 5.4 that a more cellular pore structure is formed with PVA whilst a much improved aligned structure is obtained with the inclusion of SDS and a layer structure with CTAB [26]. Therefore, although they are wellknown ionic surfactants, the role played by SDS or CTAB may be more like additives. These microspheres are mesoporous. The produced monolith could be coated with silica sol and a hierarchically porous silica monolith with improved mechanical stability could be obtained after calcination [26].

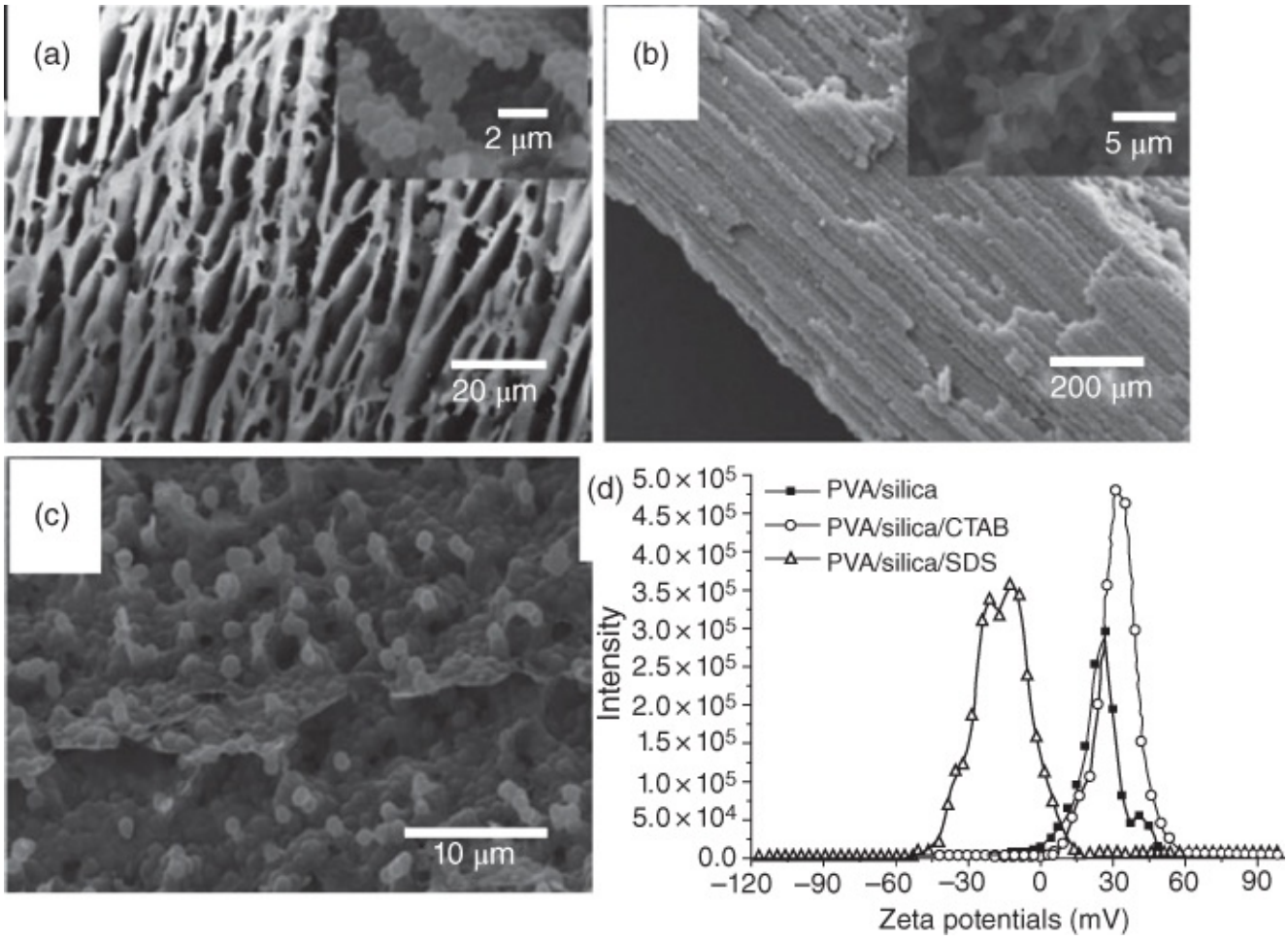

Figure 5.4 Effect of charged additives on the pore structure of porous silica prepared by directional freezing: (a) silica colloids with PVA; (b) silica colloids with PVA + anionic surfactant SDS; (c) silica colloids with PVA + cationic surfactant CTAB; and (d) zeta potentials measured in these three aqueous suspensions.

Source: Ahmed et al. 2011 [26]. Reprinted with permission from Royal Society of Chemistry.

5.2.2 Freezing Conditions

5.2.2.1 Modes of Processing and Freezing

Directional freezing . This is commonly used for the preparation of aligned porous materials, in contrast to the freezing in a cold chamber or freezer (usually slow) for the production of randomly porous (or homogeneous) materials [6]. The key feature of directional freezing is to apply a temperature gradient across the liquid sample or slurry. The solvent nucleation and the crystal growth start at the cold end and move towards the warm end of the sample, as has been described in other literature [64–66]. The directional freezing is usually used for the formation of 3D porous materials [6–10]. Although it has also been used for the preparation of porous films or membranes [34, 37, 43, 58, 67], some specific techniques have been developed to fabricate ceramic films and membranes.

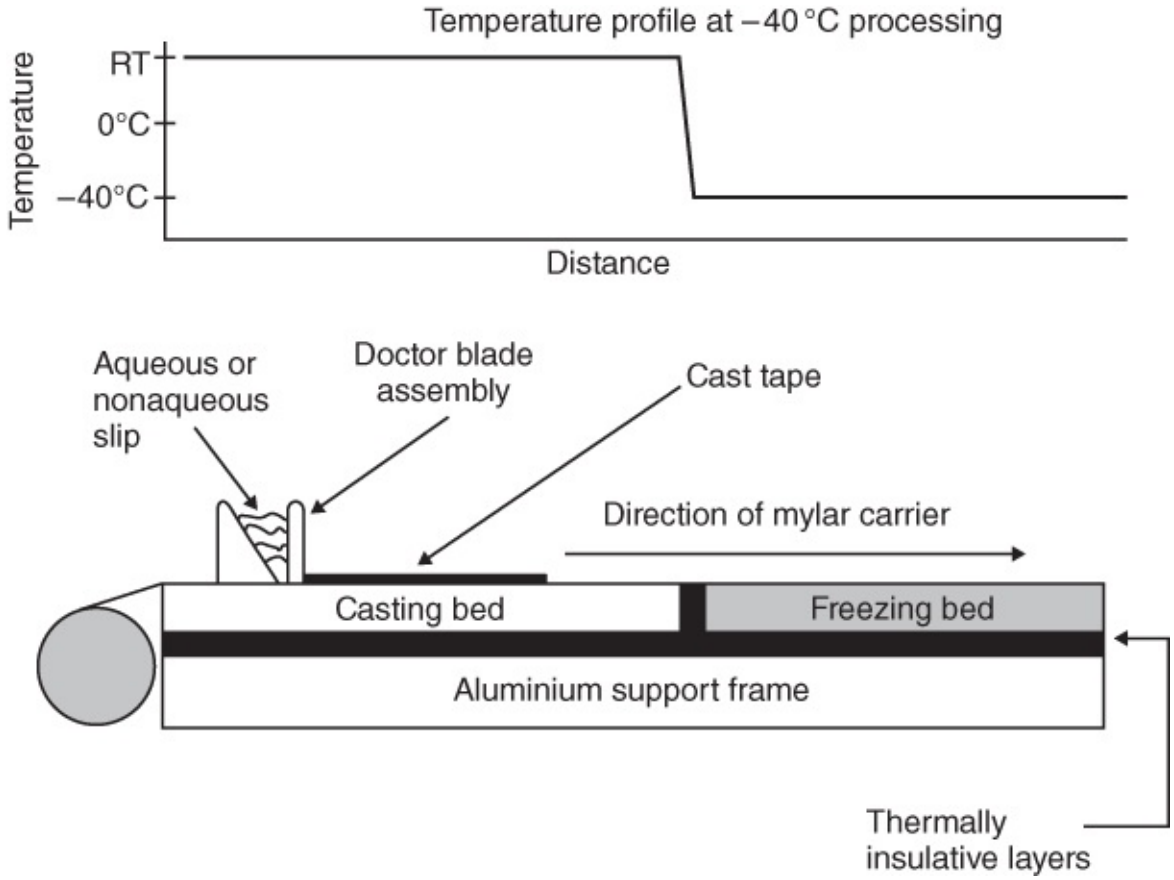

Figure 5.5 The schematic diagram for a freezetapecasting process.

Source: Sofie 2007 [41]. Reprinted with permission from John Wiley and Sons.

Freezetapecasting . Figure 5.5 shows the schematic representation of a freezetape casting process [41]. It is a process to fabricate thin ceramic materials (500–1500 μm in thickness). The process employs a traditional tapecasting process to cast slurry onto a carrier substrate via a doctor blade apparatus. The slurry on the substrate then moves to the next section on a freezing bed to allow for directional freezing of the slurry. This process has been used to form porous YSZ [41] and GDC on NiO substrate [45] for potential energy applications. It should be noted that thin films can also be prepared by directly applying the slurry onto a substrate, which can be dipped into liquid nitrogen at the controlled rate [34] or placed onto a cold finger for directional freezing [37]. Both cases were demonstrated by the formation of ordered porous TiO_2 film but the pore orientation was different; the pores were parallel to the substrate in the dipping approach [34] and

perpendicular to the substrate in the cold finger approach [37].

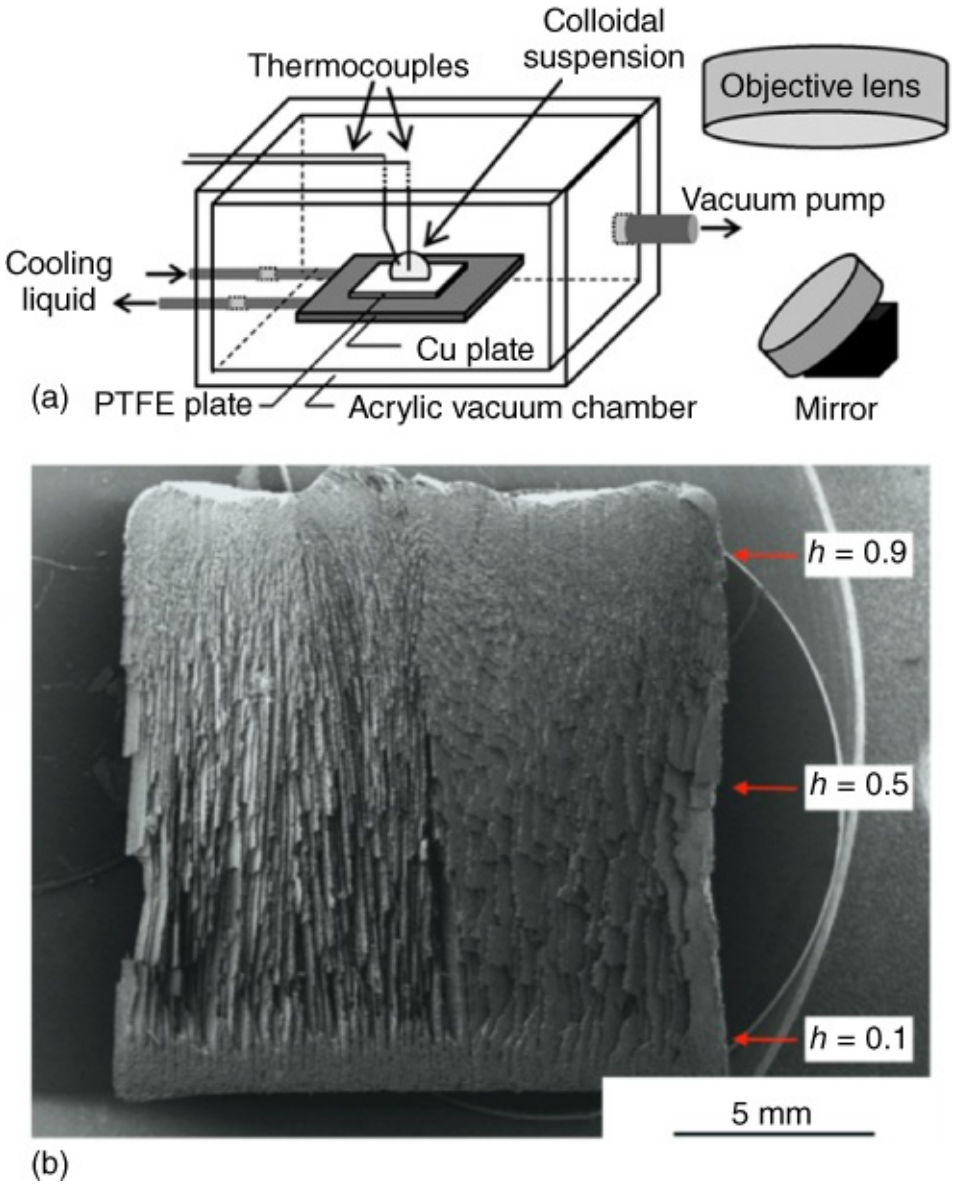

Figure 5.6 (a) The scheme for surface vacuum freezing. (b) Porous alumina prepared by surface vacuum freezing, *h* indicating the relative height of the sample.

Source: Reprinted with permission from Ref. [69].

Source: Reprinted with permission from Ref. [68].

Surface vacuum freezing. In this approach, the freezing process is initiated by introducing a vacuum to the liquid sample, instead of contacting a cold surface below the freezing point. Figure 5.6a shows schematically how the surface freezing by vacuum can be induced [68]. Basically, a drop of liquid on a substrate or a small volume of liquid sample in a vial is placed on a temperaturecontrolled shelf in a chamber. The evaporation of water adsorbs heat, which leads to the surface temperature going down below 0 °C, initiating the freezing process at the surface. The surface freeze prevents further water evaporation but the ice sublimation continuously removes heat from the sample, drives down the temperature and completes the freezing (and freezedrying) process. This was demonstrated with a drop of aqueous silica colloidal suspension (45 nm, solid content

0.01–1 vol%) on a polytetrafluoroethylene (PTFE) plate placed on a shelf (the temperature is set slightly higher than 0 °C). The appearance of the drop did not change after applying the vacuum for 909 s. It was observed that the fibre morphology was formed at a higher rate of pressure decrease whilst a lower rate of pressure decrease led to the formation of porous sponges. It was recorded that the temperature could go down close to −20 °C [68]. Porous alumina can be similarly prepared by this technique. One such example is shown in Figure 5.6b. Three milliliter alumina slurry in a vial was placed on a shelf at 10 °C, with solid contents of 3.2, 6.4, and 12.8 vol%. The vacuum of 150 mTorr (0.2 mbar) was achieved and maintained during the freezedrying process. The alumina monoliths with aligned porous structures could be formed for all these slurries [69]. Similar to the usual directional freezing where the freezing usually starts from the bottom and a dense structure is observed at the bottom, the top surface (where the freezing starts) of the material prepared by surface vacuum freezing exhibits a dense structure followed by welldefined lamellar structure (Figure 5.6b). However, there is also a densestructure layer at the bottom (Figure 5.6b). This may be attributed to the pushingback of freezing fronts due to high shelf temperature (different from the case discussed in Ref. [68]) and accumulation of ceramic particles [69]. The evaporation of water could reduce the surface temperature to below −10 °C and further sublimation could result in a fast declining temperature to below −35 °C. This was the cause for the formation of aligned porous ceramics [70].

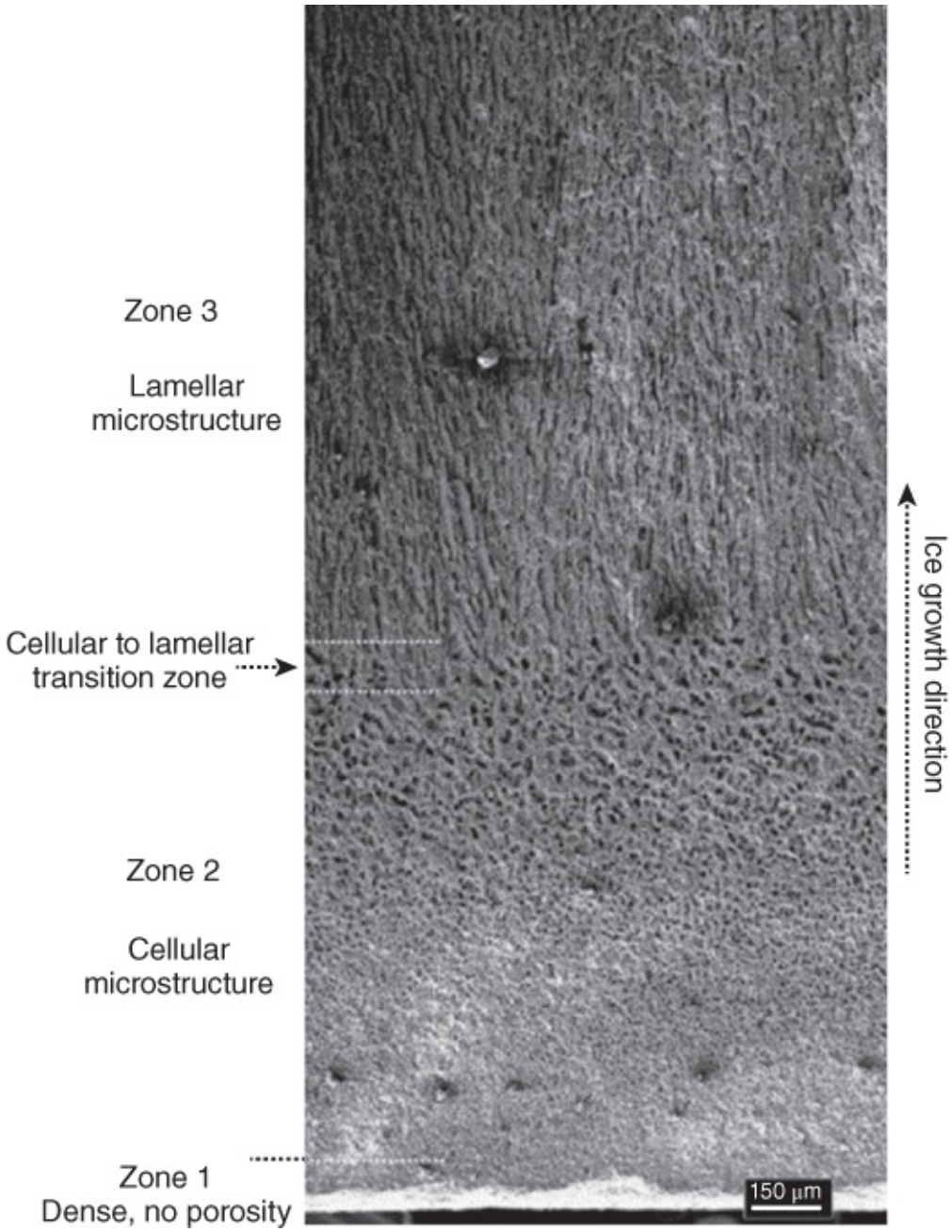

Figure 5.7 The pore structure of porous hydroxyapatite prepared by a directional freezing process using the cold finger setup described in Figure 5.1.

Source: Deville et al. 2006 [13]. Reprinted with permission from Elsevier.

Graded porous ceramics. This type of ceramic material exhibits a gradient change of pore size and/or porosity across the samples. When aligned porous ceramics are prepared by the cold finger approach or the same temperature gradient cannot be maintained, a dense structure is first formed at the cold end (due to the highest temperature gradient and the entrapment of ceramic particles) followed by a transition zone (cellular structure) and subsequently by stable aligned/lamellar structures. One example is shown in Figure 5.7 for porous hydroxyapatite [13]. Similarly, gradient porous βSiAlON could be formed by freeze casting the camphenebased slurry [58]. To better control or improve the graded porous structure, a twosided freezing approach has been employed. The two sides (the top and bottom of the liquid sample) are both cold so that the freezing starts from both

surfaces and moves towards the centre. Alternatively, one side can be set as the cold surface while the other side has a higher temperature (maybe well above the freezing point) [20]. This way, the temperature gradient can be controlled higher or lower, which has a significant impact on the pore structure. In a more controlled way, graded porous ceramics can be fabricated by a serial freezecasting approach. Slurries of different loading or even of different types of solid particles can be placed in order and then frozen [54]. Alternatively, one may add the second layer after the first layer is frozen. Freeze casting may be also combined with screenprinting to produce suitable materials for gas permeation [43, 44]. The freezecast approach produces macroporous ceramics while the dense structure results from screenprinting. The macropores facilitate mass transport but the small pores provide selection/impacts on gas molecules.

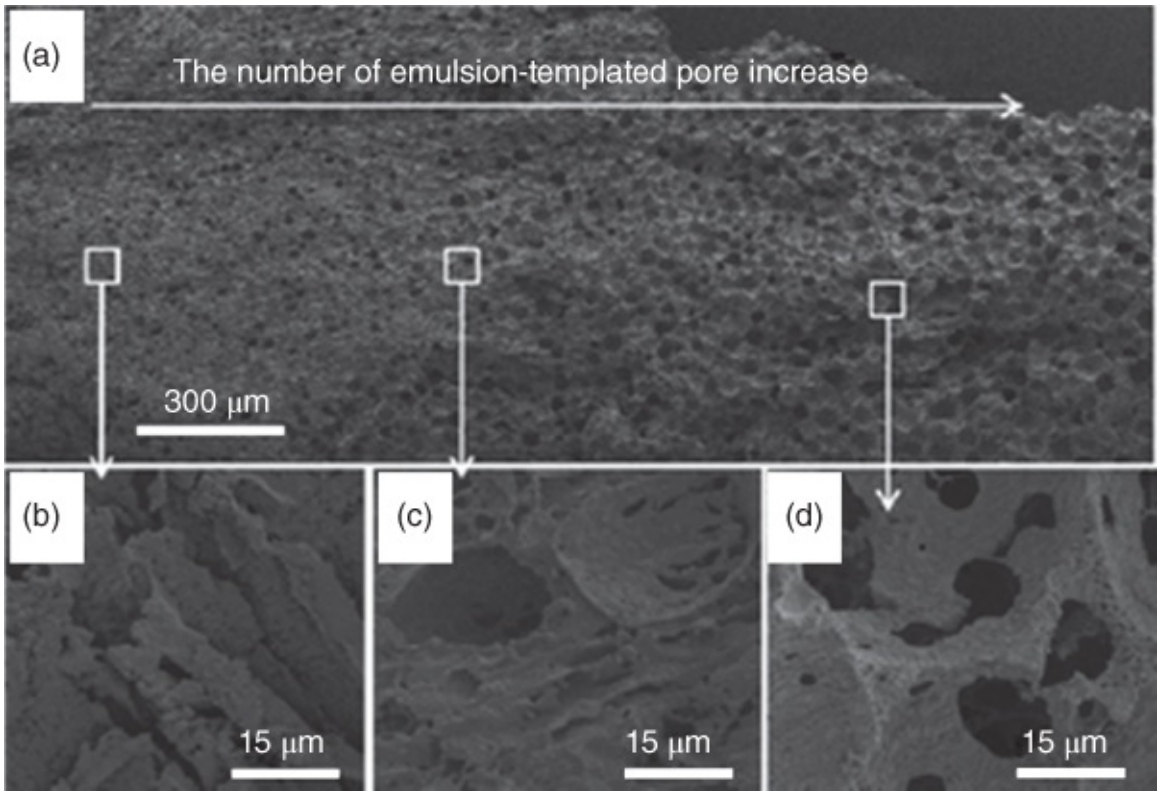

Figure 5.8 Gradient porous PVA–silica composite prepared by freezing the centrifuged emulsion. (a) The evolution of the pore structure in the material, replicated from the centrifugeinduced distribution of oil droplets in the emulsion. (b–d) The expanded views of the pore structures at different parts of the materials. This pore structure remains after calcination to remove PVA.

Source: Ahmed et al. 2011 [71]. Reprinted with permission from Royal Society of Chemistry.

Centrifugation freezing. For a heterogeneous system (e.g. an emulsion, a slurry), the centrifugation force can be explored for the two phases with different densities in order to fabricate gradient porous materials. An oilinwater emulsion, where cyclohexane was the internal oil phase and PVA/SDS/silica colloids were present in the continuous aqueous phase, was centrifuged to create a gradient distribution of oil droplets. This emulsion was then frozen and freezedried to produce a gradient porous material [71]. As shown in

Figure 5.8, from left to right of the image, the number of emulsiontemplated pores increases and the material becomes more porous even with a decreasing degree of ice templated pores. Such composite materials can be easily calcined to produce porous silica with increased porosity (due to the presence of large pores) in one direction and increased surface area (due to the dense silica with larger number of mesopores) in the other direction [71]. Although there seems to be no reports on the use of such technique for slurries (to explore the density difference between ceramic particles and the medium), this method may be readily applied to slurries to fabricate gradient porous ceramics.

Freeze castingwith magnetic field. When magnetic particles are included in the slurry, the magnetic field can exert an impact on the movement of these particles and thus on the final pore structure. High magnetic fields are used for ceramic processing but it requires special equipment and therefore it is inconvenient to be combined with freeze casting. Fe_3O_4 nanoparticles are known to respond to weak magnetic field (<0.18 T). Aqueous slurries of hydroxyapatite particles, ZrO_2, Al_2O_3, and TiO_2 (10 vol%) were mixed with different concentrations (0–8 vol%) of Fe_3O_4 nanoparticles (sizes <50 nm) [72]. Fe_3O_4 nanoparticles moved in the direction of the magnetic field. Particularly, when a rotating magnetic field (0.12 T) was applied around the freezing vial, a spiral dark stripe could be seen for all these freezedried and sintered ceramics except for TiO_2 slurry (Figure 5.9a). The composition of Fe in the Fe_3O_4rich region was 25–80 times higher than those in the Fe_3O_4poor region. For TiO_2 ceramics, Fe_3O_4 were distributed quite homogeneously, with the Fe composition of 1.64 wt% in Fe_3O_4rich region versus the Fe composition of 1.61 wt% in Fe_3O_4poor region. This was attributed to the similar density of Fe_3O_4 and TiO_2 particles. However, the alignment of the pore structure could still be considerably affected by the magnetic field due to the loss of pore alignment in the longitudinal direction [72]. By applying a magnetic field transverse to the freezing direction, movement of Fe_3O_4 nanoparticles could form bridges between the lamellar structures and enhance mechanical stability. This was demonstrated by directional freezing of the slurries containing ZrO_2 (10 vol%) and Fe_3O_4 (0–9 wt%) nanoparticles with a transverse magnetic field (0–0.09 T) [73]. Figure 5.9b shows the bridges formed between the lamellars, with the Fe composition in the bridge about five times higher than that in the lamellars (Figure 5.9c). The compressive strength of the bridged ceramics prepared under the magnetic field of 0.09 T is about five times higher than the ceramics prepared with no magnetic field [73].

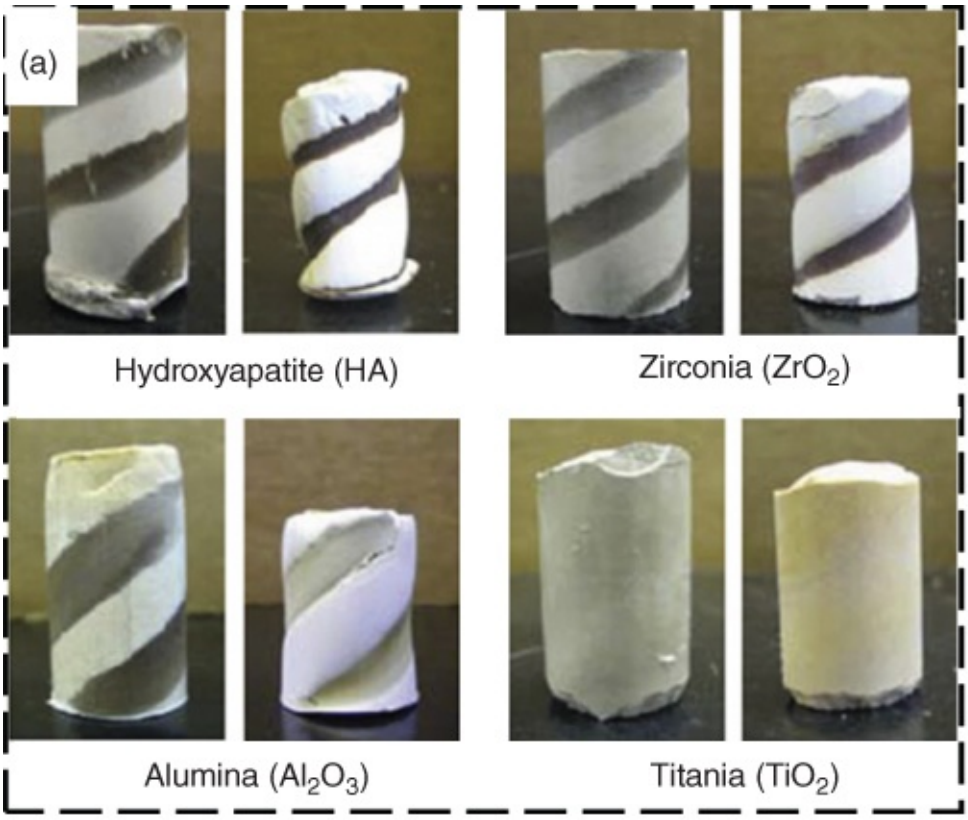
(a)
Hydroxyapatite (HA)
Zirconia (ZrO_2)
Alumina (Al_2O_3)
Titania (TiO_2)

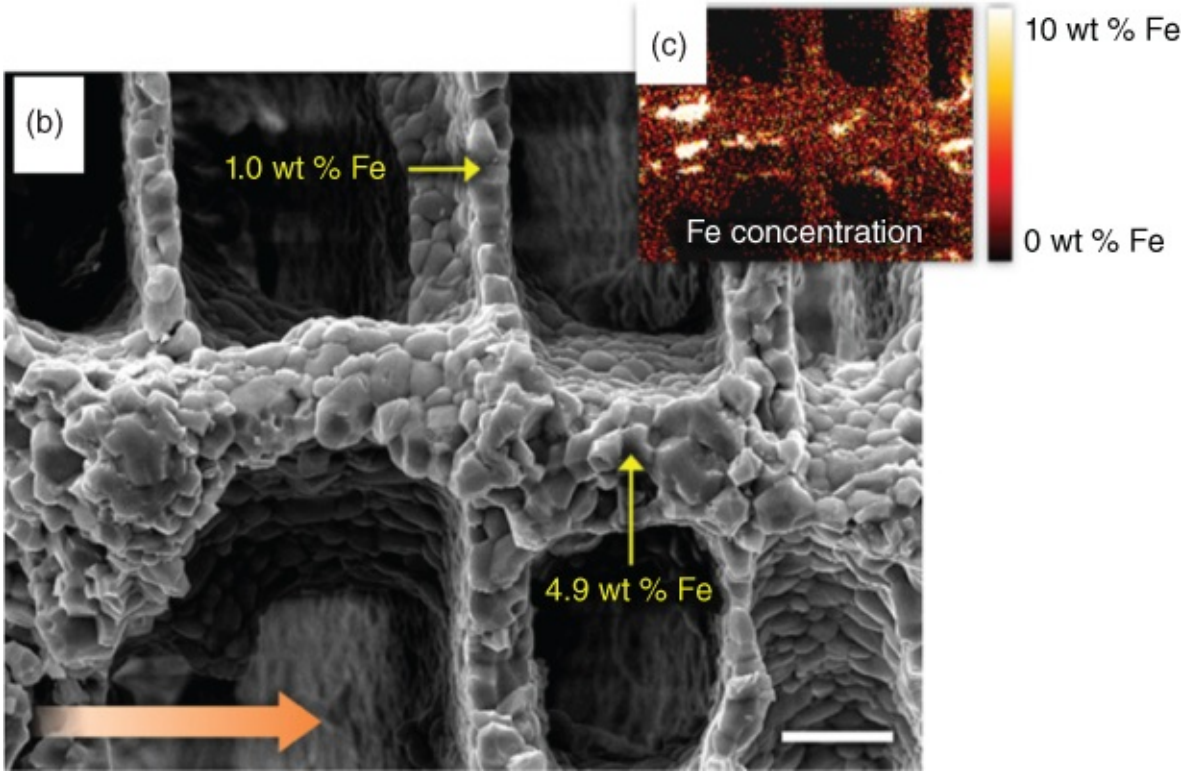
(b)
1.0 wt % Fe
4.9 wt % Fe
(c)
Fe concentration
10 wt % Fe
0 wt % Fe

Figure 5.9 Porous ceramics prepared by freeze casting with magnetic fields. (a) The images of different ceramics containing 3 wt% Fe_3O_4 nanoparticles with a rotating magnetic field of 0.12 T at 0.05 rpm. For each ceramic, the left image is after freeze drying and the right image after sintering. (b) The scanning electron microscopy (SEM) image shows a magnetically aligned porous ZrO_2 with bridges after sintering formed from 10 vol% ZrO_2 + 3 wt% Fe_3O_4 nanoparticles with a transverse magnetic field of 0.09 T (see the direction of the orange arrow); and (c) element map of this structure.

Source: Reprinted with permission from Ref. [73].

Source: Porter et al. 2016 [72]. Reprinted with permission from John Wiley and Sons;

Combining freezing with other templates. Other templates may be employed to generate additional pores in an icetemplated material. Instead of mixing ceramic particles in slurries to make porous hybrid ceramics, sacrificial polymer colloids can be mixed with the ceramic particles. Both types of particles are rejected from the freezing front to form aligned porous materials. Removal of polymer particles by calcination can generate highly interconnected porous ceramic walls. This was demonstrated by a study conducted with silica colloids and poly(styrene *co*methacrylate) particles by directional freezing [74]. Preformed porous structures can be also used as sacrificial templates to make porous ceramics [75, 76]. For example, alumina slurry was impregnated into a porous polyurethane sponge and a directional freezing process was then applied. After the removal of polyurethane by sintering, the resulting ceramics exhibited both icetemplated aligned pores and polymertemplated pores [77]. Emulsion templating and ice templating are combined to produce porous ceramics that contain both emulsiontemplated and ice templated pores [78]. Alternatively, the icetemplated porous polymers can be used as sacrificial templates to fabricate porous silica/metal oxides [78], hollow TiO_2 microtubes and Fe_2O_3 nanofibres [79], and silica spheres on nanofibres [80].

5.2.2.2 Freezing Velocities

It is not surprising that freezing conditions are critical for the preparation of porous ceramics by freeze casting. Freezing setups and freezing temperatures translate to freezing direction and freeze velocity that determine whether porous ceramics can be formed and what the pore morphologies are. Freezing velocity, in combination with particle size and solid loading in slurry, is the most important factor in a freezecasting process. When the freezing velocity is very low, a planar freezing front pushes all the particles along: i.e. particles are concentrated but no icetemplated porous ceramics may be formed. When a critical velocity is reached, the freezing front becomes unstable, leading to cellular, dendrite or lamellar crystal growth. At this stage, the particles are excluded from the freezing front and concentrated between the ice crystals [81]. Further increase of freezing velocity can change the ice crystal patterns and the thickness of ice crystals, which transforms to pore size and pore shape in the freezedried materials [8]. However, very fast freezing leads to immediate entrapment of particles in the freezing front and no icetemplated pores in the ceramics can be obtained after freeze drying. Theoretical studies on predicting and measuring critical velocity and wavelength of

unstable freezing front (i.e. lamellar thickness) have been carried out, mostly using alumina, silica or clay particles as model particles in dilute slurries. This part has been extensively described in Chapter 2.

In a freezecasting process, due to the supercooling requirement for ice nucleation, the initial freezing rate is usually very high and then changes to a steady freezing velocity. This has been well investigated using the cold finger approach by Xray radiography and tomography [22, 23]. Such freezing behaviour is reflected in the structure of freezedried ceramics. As demonstrated by porous hydroxyapatite (Figure 5.7) [13] and alumina [14], a dense structure is formed at the start of the freezing process (the bottom of the sample that contacts the cold finger plate) due to the entrapment of particles in the freezing front, followed by a transition zone and then a stable lamellar structure. It is believed that the discussion of the effects of freezing rates on pore structure/pore size is usually based on the steady freezing stage. In general, the faster the freezing rate, the larger the ice crystals and hence the larger pores. There are theoretical equations developed to predict the pore sizes (see Chapter 2). Empirically, the equation can be given as [8]:

$$\lambda = Av^{-n}, \tag{5.1}$$

where λ is the wavelength of the unstable freezing front (or the lamellae thickness), A is the coefficient related to the slurry system and v is the freezing velocity. For a given system, the data can be fitted into this equation and the values for A and n can be obtained.

Equation (5.1) only describes the simplified effect of freezing velocity on pore sizes. The true effects are complicated and should be considered in the context of particle size, type, and formulation compositions. Under the conditions of differing ionic strength, particle size, concentration, charges, and solvents, ice lenses may be formed transverse to the lamellar structure. After freezedrying and sintering, this defect in structure can considerably weaken the mechanical strength of the porous ceramics [24]. By systematically investigating (and observing) the patterns of ice crystals with those of the ceramic particles under different freezing conditions, diagrams of freezing velocity versus particle size can be constructed based on the stability of the ice freezing front (e.g. particle entrapment, metastable, unstable, stable (particle rejection from planar freezing front) [21]. These diagrams may serve as guides for the fabrication of porous ceramics.

5.3 Porous Ceramics by GelationFreezeCasting

The gelationfreezecasting method allows the gelation of ceramic slurry via thermal gelation or polymerization, followed by controlled freezing of the formed gels. This method has two distinct characteristics: (i) the effect on pore structure, which is different from that of polymer additives and (ii) the crosslinking of the system that holds the ceramic particles together and maintains the icetemplated structure so that the solvent may be removed simply by vacuum or evaporation at room temperature. This means the energyconsuming freeze drying process may not be necessary.

5.3.1 Gelation with Gelatin

This is probably the most used gelationfreezecasting system for the preparation of porous ceramics. Porous ceramics prepared by this method exhibit nearly honeycomblike pore channels, unlike the ellipsoidal, dendritic or lamellar structures formed by conventional freeze casting [82]. Typically, the dry ceramic powder is suspended in warm gelatin solution at around 50 °C. The gelation is initiated when the temperature drops down to room temperature (15–20 °C), with the mixing ratio of powder to gelatin in the range of 1/99–10/90. The slurry gel is then frozen under suitable freezing conditions. In addition to the usual freezedrying, the frozen gel sample may be dried under vacuum at temperatures of 10–35 °C [82]. Unlike aqueous slurries, the movement of water and ceramic particles is limited in the gel state during the freezing process. The confined movement of water molecules in the gel may lead to the segregated ice nucleation and preferential growth of ice crystals as well as inhibit side branch growth from the main ice crystals, helping to eliminate defect formation in the freezing samples [82].

Porous silicon carbide was prepared via gelation with gelatin. The slurries in the moulds were allowed to gel under atmospheric condition and then frozen in cold ethanol bath at various temperatures (−10 to −70 °C). The frozen gels were then dried under vacuum at 10–35 °C for 24 h [83]. Porous alumina was prepared in a similar way but with AFP as additives. The AFP was added to the gelatin solution at the ratio of 0.25 : 99.75 and 0.50 : 99.50 and mixed with the alumina powders. The addition of the AFP led to homogeneously porous alumina with smaller pore sizes [15]. The AFP and gelation were also used to fabricate highly porous mullitezirconia which gave a compressive strength of 11.3 MPa, a porosity of 89.1 vol%, and a thermal conductivity of 0.28 W $(m \cdot K)^{-1}$ [51].

5.3.2 Photopolymerization (or Photocuring) of Frozen Slurry

Frozen polymerization has been used to prepare porous polymers, which removes the need of freezedrying and results in materials with stronger mechanical stability [84–86]. This approach has also been used to fabricate porous ceramics. The UVcurable monomers 4 hydroxybutyl acrylate and PEG 200 diacrylate and the photoinitiator (a liquid blend containing 2,4,6trimethylbenzoylphenylphosphineoxide with a broad absorption peak around 380 nm) were employed to fabricate porous silica and alumina [86]. An emulsion system was also used to form porous alumina microspheres. When $AgNO_3$ was included in the system to prepare TiO_2/polyacrylate composites, the *in situ* reduction of Ag^+ ions on the TiO_2 surface generated Ag nanoparticles, which triggered the photopolymerization without adding a photoinitiator [86]. In another study, PEG (400) diacrylate was dissolved in the terpenes (menthol, camphor, and camphene) above their melting points. Either silica or alumina powders were mixed into the solution with Irgacure 184 added as the photoinitiator. The suspensions in 1 cmhigh dishes were frozen at room temperature and photopolymerized subsequently at room temperature. The terpene solvents could be removed by sublimation or melting away. The usual calcination and sintering procedure was applied to produce porous ceramics [55].

5.3.3 Polymerization (or Gelation) of Slurry

There are other approaches to polymerizing ceramic slurries. One of the frequently used polymerization systems is with acrylamide. The initial polymerization temperature and rate can be finetuned by combining acrylamide (or *N*isopropylacrylamide) and methylene bisacrylamide (the crosslinker) with the initiator ammonium persulfate (APS) and the catalyst tetramethylethylenediamine (TMEDA) with controlled concentrations [87–89]. This polymerization has been used for ceramic slurries. For example, alumina powder was suspended in TBA containing acrylamide to which the initiator APS solution was added just before being frozen. The frozen solid was then heated in an ambient environment at 85 °C. This allowed the melting of TBA, polymerization of acrylamide, and evaporation of TBA in the same process. The polymerization of acrylamide contributed significantly to the strength of the green bodies [20].

In another study, collagenapatite gel was formed by incubating the solution in a sealed vial at 25 °C for 1 h and then increased to 40 °C at 0.5 °C min^{-1} and held at 40 °C for 22.5 h. The formed gel was then left to undergo selfcompression at room temperature for different times before being frozen in a precooled chamber at −25 °C and then freezedried. The increased selfcompression time resulted in higher density of collagen fibres, reduced lamellar spacing, and increased wall thickness in the freezedried scaffold [30]. Chitosan gels were formed by crosslinking with γglycidoxypropyltrimethoxysilane and then mixed with aqueous suspension of TiO_2 particles or TiO_2 sols [90]. The subsequent directional freezing process and lyophilization produced the hybrid TiO_2chitosan scaffolds that were used to degrade methylene blue and orange II dyes [90].

5.4 Porous Ceramics via CryoSolGelation

Porous ceramics, sometimes cited as inorganic gels, can be obtained from a sol–gel process. The process usually starts with the hydrolysis of an inorganic or metalalkoxyl precursor to form a sol. The drying of the gel obtained from the sol is crucial to the porosity and density of the resulting material. The ambient drying process produces a xerogel, which usually exhibits shrinkage, pore structure collapse, and low surface area. To overcome these problems, a supercritical drying process can be applied to produce aerogels or a freezedrying process for cryogels [91].

Porous ceramics (or inorganic cryogels) with high surface area and controlled macropore morphologies can be prepared from the inorganic sols. The investigations were initiated with the directional freezing of silicic acid. After thawing, parallel silica fibres with polygonal crosssections (about 50 μm in diameter and 15 cm long) were formed. The aging time and concentrations were important factors for the formation of silica fibres [92]. This method has been extended to produce porous silica monoliths with aligned pores or microhoneycomb structures by Mukai et al. [11]. Sodium silicate solutions were adjusted using an ionexchange resin (Amberlite IR120B HAG) to give a pH of 3. The pH could also be adjusted by adding a few drops of aqueous ammonium solution while stirring. The obtained clear sol was aged at

303 K and then unidirectionally frozen by dipping a polypropylene tube containing the sol into liquid nitrogen. The frozen sample was then kept in a cold bath at 243 K for 2 h to strengthen the icetemplated structure and then thawed at 323 K. The thawed sample was soaked in TBA for over 1 day to exchange the water in the gel and then freezedried at 263 K to produce dry porous silica monolith with aligned channels of about 11 μm in width and surface areas in the region of 690–780 m^2 g^{-1} [11]. The hydrosols (after adjusting the pH using the ionexchange resin) and the hydrogels (formed after aging the hydrosols with pH < 6) from sodium silicate solutions were further investigated for the preparation of silica gels with a variety of morphologies [93]. The silica gels with aligned channels could be further treated (heated at 800 °C for 2 h, impregnating the structuredirecting agents by soaking and drying at 50 °C, and then crystallized in an autoclave at temperatures of 100–130 °C) to transform into zeolite monoliths [94]. The crystalline zeolite particles (average diameter of 2.5 μm) were clearly seen on the pore surface and on the walls (Figure 5.10). The resulting zeolite monoliths showed type I isotherms of N_2 sorption, which was indicative of the presence of micropores, while the icetemplated macropores were retained [94].

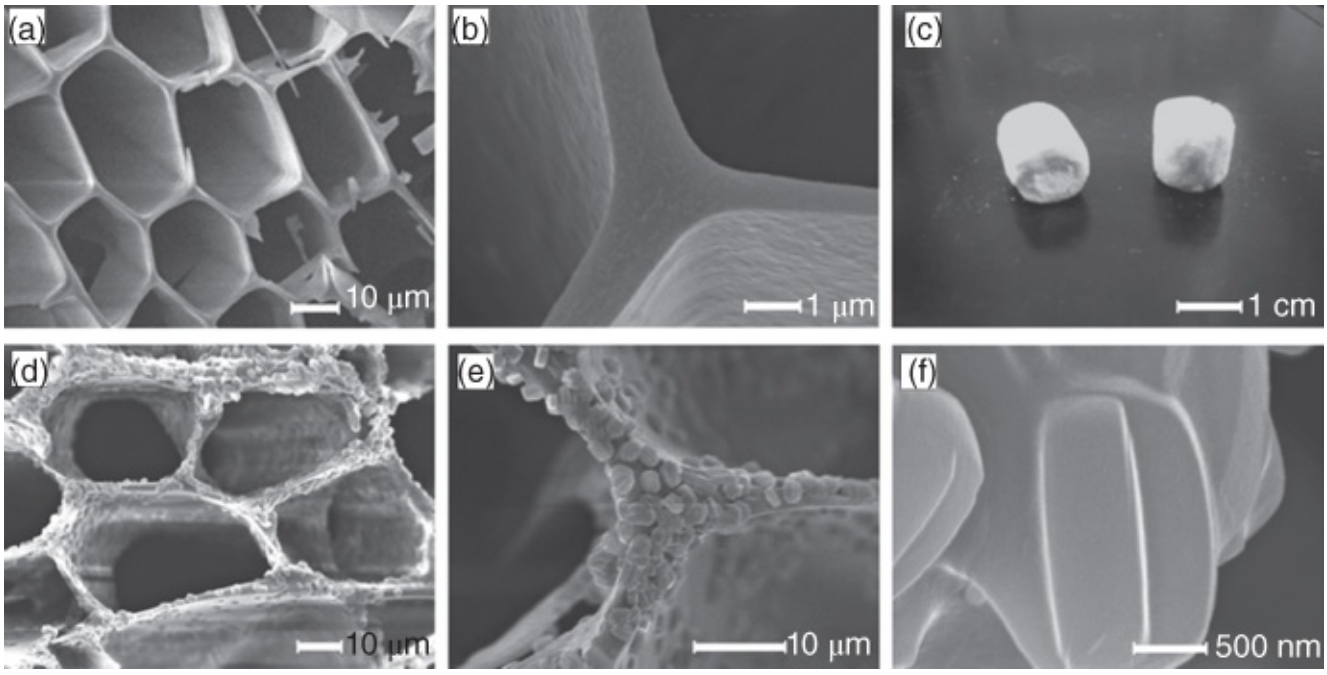

Figure 5.10 Hierarchically porous zeolite monoliths by crystallization treatment of ice templated silica gels. (a–c) The icetemplated silica gel at different magnifications; and (d–f) the macropore structure and the zeolite crystalline particles for the zeolite monoliths.

Source: Mori et al. 2011 [94]. Reprinted with permission from Royal Society of Chemistry.

For the silica sol produced at pH 3, aluminium nitrate was added to achieve the Si/Al ratios of 1.9–9.5. Subsequently, SiO_2–Al_2O_3 monoliths were formed with aligned macropores (10–20 μm and wall thickness 200–500 nm) for the Si/Al ratios of 1.9–3.8 [93]. Al atoms were homogeneously distributed in the monoliths by forming an Al-O-Si polymeric network. Acid sites were confirmed by NH_3TPD (temperatureprogrammed desorption) measurement [95].

Tetraethyl orthosilicate (TEOS) is a common precursor for the preparation of silica via

hydrolysis (usually catalysed by acid or base) and sol–gel processes. This can be used to prepare mesoporous silica via surfactant templating [63] or combined with polymer templates to make macroporous silica [75, 96]. The silica sol obtained by hydrolysis of TEOS is not often directly frozen to produce icetemplated silica. This might be due to the production of ethanol during hydrolysis. Further, the ethanol solutions or gels are not suitable for freeze drying because of the very low melting point. In a study to fabricate bioglass from the TEOS silica sol, TEOS was hydrolysed with triethyl phosphate (TEP) in the presence of HNO_3 (0.06 M) at room temperature with stirring for 1 day. The resulting sol was mixed with an equal volume of water. Ethanol generated during hydrolysis was removed under reduced pressure at 40 °C 30 mbar. The silicaTEP sol was mixed with aqueous $Ca(NO_3)_2$ solution to achieve the desirable concentration and element molar ratio. The obtained sol was aged for 24 h at room temperature and then subjected to a directional freezing process. The green bodies obtained by freezedrying were annealed at 873 K for 5 h [97]. The macroporous bioglass prepared showed good capability for *in vitro* biomineralization [97].

Other types of gels are also freezedried with the main goal being the formation of dry gels with high surface area and high thermal stability. For instance, Co_3O_4 cryogels with interconnected macroporosity and mesoporosity were prepared and tested as an electrode material by a threeelectrode system [98]. $Co(NO_3)_2$ was added to aqueous solution containing citric acid and P123 and the pH was adjusted to 3.33 with ammonia solution. The resulting solution was kept at 70 °C until a dark red gel was formed. The gels were frozen in liquid nitrogen and freezedried, which was further sintered at 300 °C. The icetemplated channels in the dry Co_3O_4 gels facilitated electrolyte diffusion, achieving a specific capacitance of 742.3 F g^{-1} at a potential window of 0.5 V [98]. Manganese oxide cryogels were also synthesized by freezedrying the relevant hydrogels [99]. Two routes were used to prepare the hydrogels. The first was by mixing the solutions of disodium fumarate and sodium permanganate. The second route was by mixing solid fumaric acid with aqueous sodium permanganate solution. The gelation occurred from a few minutes to 1 day depending on the route and the compositions in the solutions [99]. In another study, vanadyl triisopropoxide was mixed with the mixing solvent of water/acetone (each of these precooled in an ice bath for 15 min) and stirred vigorously for 30 s. The gel was formed in about 1 min and aged in a sealed tube for 1–8 days. The aged gel was washed with water, acetone, and solvent exchanged with cyclohexane, followed by freezing in liquid nitrogen and freezedried [100]. The freezedried gels were highly porous with specific surface areas up to 250 $m^2 g^{-1}$ [100]. Instead of porous monoliths, porous TiO_2 fibres were obtained when the hydrogels were unidirectionally frozen and freezedried [101]. The gels were prepared by hydrolysis of titanium tetraisopropoxide via slow addition of HCl at the icecooled temperature and then the dialysis of the obtained solution. The gels were frozen in liquid nitrogen and aged at 243 K for 24 h. TiO_2 fibres were produced after freezedrying and calcination at different temperatures [101].

Alumina cryogels produced via a sol–gel process from aluminium *sec*butoxide (ASB) and subsequent freezedrying showed higher thermal stability particularly at temperatures above

1000 °C [102]. ASB was added to hot water at 86 °C for hydrolysis and refluxed with vigorous stirring. The subsequent addition of nitric acid produced a clear sol. The sol gelation was initiated by adding urea and then allowed to stand for 24 h at 86 °C. The gel was then frozen in liquid nitrogen and freezedried. The higher stability of this alumina cryogel was attributed to the uniform fibres formed in the gel [102]. Aqueous $Pd(NO_3)_2$ solution with ethylenediamine could be added to the sol before adding urea to initiate the gelation. Following the same process, alumina cryogel with uniformly distributed Pd could be produced, which showed high thermal stability and CO oxidation activity [103]. Similarly, cerium nitrate could be added to the sol to prepare CeO_2-Al_2O_3 cryogel [104]. Zirconium dinitrate oxide was dissolved in water before adding ASB and the same procedure was applied to produce tertiary CeO_2-ZrO_2-Al_2O_3 cryogel. The effects caused on the thermal stability, pore structure, and catalytic CO and CH_4 oxidation activities by adding ethylene glycol to the sol were investigated [104].

5.5 Porous Metals via Ice templating

Porous metals can be obtained directly from metal particles via freeze casting. For example, Ti foams were prepared by directional freezing of aqueous Ti slurries, followed by freeze drying and sintering. The sintering was performed under high vacuum at 1150 °C for 8 or 24 h. Longer sintering time was found to reduce the porosity but increase compressive stiffness, strength, and energy absorption [105]. Chemical stability of metal particles at room temperature and moderately elevated temperatures in atmosphere is required for this route. However, the sintering of metal particles at high temperatures is always carried out under inert atmosphere.

More often, porous metals are produced by reducing porous metal oxides that may be fabricated first by the icetemplating approach. For instance, nickel foams were produced after reduction of freezecast NiO scaffolds. NiO powder (<20 μm) slurry with PVA as binder was directionally frozen using a cold finger. The green body obtained by freezedrying was first heated to 300 °C for 2 h to remove PVA and then sintered at 1000 °C under H_2 atmosphere containing 5% Ar. The presence of dispersant Darvan 811 could increase the mean pore size (from 10.9 to 14.2 μm) and total porosity (from 51.2% to 62.1%) [106]. Porous Cu with aligned channels (~100 μm) was fabricated from freezecast camphenebased CuO. The CuO scaffold was reduced at 300 °C for 30 min and then sintered at 700 °C for 1 h under H_2 [107]. CuO powder (~200 mesh) was suspended in water in the presence of PVA as binder. The freezedried sample was heated to 900 °C under vacuum (<0.04 Pa) to decompose CuO to Cu as well as to sinter the Cu particles into porous Cu [108]. In another study, the porous structure prepared by freezedrying of aqueous slurries of $CuSO_4$ with carbon nanotube (CNT) and graphene oxide (GO) were first annealed at 700 °C under N_2 to decompose $CuSO_4$ and reduce GO. Further induction of forming gas (5.5 mol% of H_2 in N_2) could reduce Cu oxides to produce Cu/C composite. The icetemplated macropores were retained [109]. Porous MoO_3 was prepared by the freezecasting approach with camphornaphthalene as

solvent [110]. After freezing in a cold bath at −25 °C, the frozen solvent was removed by sublimation at room temperature with an airflow rate of 0.05 m s^{-1} for 48 h. The reduction to porous Mo was carried out at 750 °C in H_2 atmosphere for 1 h [110].

5.6 Applications of Icetemplated Ceramics

The icetemplating method can be used to fabricate highly interconnected porous ceramics with minimal shrinkage. Furthermore, via the change of slurry formulations and the control of the freezing stage, porous ceramics with desired pore morphology and mechanical stability can be produced. These can be highly advantageous for a number of applications.

5.6.1 Filtration/Gas Permeation

Owing to their chemical stability and mechanical stability, porous ceramics are widely used for filtrations. This is achieved by a sizeexclusion effect, i.e. larger particles are excluded from the ceramic membrane while the solvent or smaller particles can move across the membrane [1]. The control of pore size in icetemplated porous ceramics can be conveniently achieved by changing the solid content in the slurries and the freezing rate. The aligned microchannels created by directional freezing can reduce the operational pressure due to less hindrance to the fluid. More importantly, because of their chemical stability at high temperatures, porous ceramics are widely used for hot gas filtration and molten metal filtrations [1]. The icetemplated macropores in ceramics are usually not suitable for gas separation. However, this feature can be advantageous in enhancing mass transport when porous ceramics are used for other applications. For example, for oxyfuel technology, the porous ceramic membranes fabricated by freezecasting enhanced oxygen permeation [43, 44].

5.6.2 Thermal Insulator

Porous ceramics are extensively used as thermal insulators. The porosity, interconnectivity, and microstructure of the materials can significantly affect thermal conductivity [111]. Closed porosity can prevent convective heat transfer and is usually a good feature for thermal insulation. In general, higher porosity benefits thermal insulation but this should be always considered in conjunction with mechanical stability. This is because higher porosity is usually accompanied by low mechanical strength. For the icetemplated ceramics, the aligned pores or channels may significantly enhance the efficiency of thermal insulation, as demonstrated in Figure 5.11 [1]. This is attributed to the prevention of crossflow convection current due to the aligned pores orthogonal to the heating surface and hence the reduced heat transfer. For example, porous mullitezirconia with aligned pores was prepared by gelation freezing. The materials exhibited low thermal conductivities of 0.23–0.33 W $(m \cdot K)^{-1}$, which were consistent with the values predicted by the Maxwell–Eucken 1 model [51]. The mullite foams were also fabricated using kaolin and Al_2O_3 slurries, using TBA or water as the dispersing medium [112]. Aligned pores were formed in the mullite and their sizes and porosity could be

readily tuned by solid content. At the solid loading of 10 vol%, a porosity of 80% and a compressive strength of 5.6 MPa with TBA as solvent (similarly, 83% porosity and 3.8 MPa strength for the slurry with water) were achieved with a very low thermal conductivity of 0.18 W $(m \cdot K)^{-1}$ (0.17 W $(m \cdot K)^{-1}$ for waterbased slurry). For the TBAbased slurries, when the solid content was increased to 20 vol%, a compressive strength of 49.4 MPa, a porosity of 60.2%, and a thermal conductivity of 0.34 W $(m \cdot K)^{-1}$ were obtained in the resulting mullite [112].

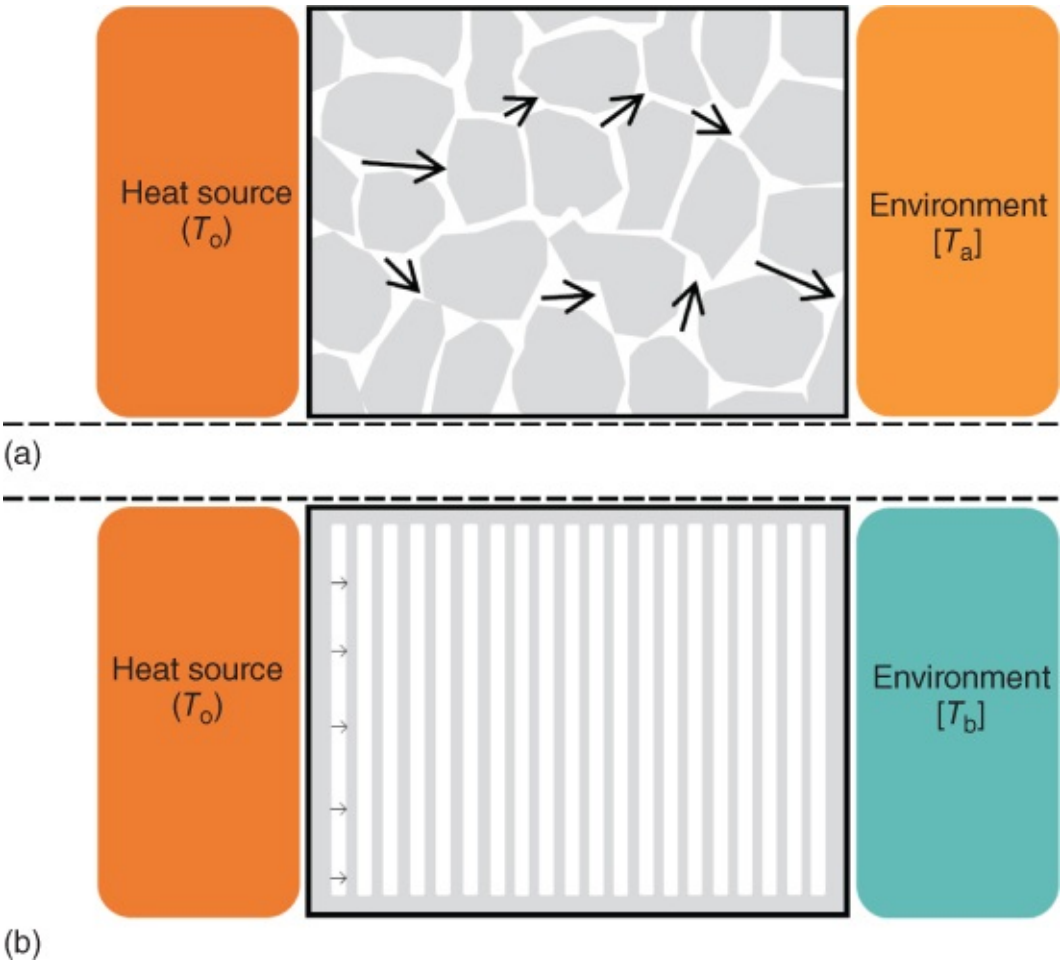

Figure 5.11 Schematic representation of heat transfer in the randomly porous material (a) and the aligned porous material (b). The blue colour in (b) indicates a better thermal insulating efficiency.

Source: Hammel et al. 2014 [1]. Reprinted with permission from Elsevier.

5.6.3 Bioceramics

Icetemplating bioceramics have found wide use as scaffolds for tissue engineering. This is due to the highly interconnected macroporosity and good mechanical stability [7]. In order to be used for bone tissue engineering, the materials should support the growth of bone tissues as well as bond to the living bones. These bioceramics usually contain hydroxyapatite or βTCP [13, 30, 38, 39, 49]. The bonebonding ability can be effectively predicted by mineralization in a simulated body fluid (SBF). Over the years, the recipe of the SBF has evolved to mimic

the ionic concentrations in human blood plasma, which has provided reliable results on bone bioactivity [113]. It has been established that a material able to form apatite on its surface can bond to living bone via the apatite layer, as long as the material does not contain the groups or components that induce toxic or antibody reactions. The short period required for apatite formation usually indicates the short period required to achieve bonding to living bones [113].

Porous hydroxyapatite scaffolds produced by freeze casting showed very high compressive strength, up to 145 MPa for 47% porosity or 65 MPa for 56% porosity [13]. Aligned porous barium titanate/hydroxyapatite composites exhibited high piezoelectric coefficients (d_{33} = 3.1 pC N^{-1}). The 3(4,5dimethylthiazol2yl)2,5diphenyl tetrazolium bromide (MTT) assay with L929 cells confirmed no cytotoxic effects [49]. The collagen–apatite scaffold was fabricated by a gelationfreezedrying approach. This aligned porous scaffold exhibited a 12fold increase in Young's modulus and 2fold increase in the compression modules along the aligned direction, compared to the isotropic porous scaffold [30]. This scaffold's biocompatibility towards bone tissue engineering was demonstrated by the attachment and spreading of MC3T3E1 osteoblasts [30]. BCP scaffolds consisting of hydroxyapatite and βTCP were fabricated by freeze casting using TBA as solvent [38]. The *in vitro* degradation tests were carried out in Hank's balanced salt solution (HBSS), an extracellular solution with an ionic composition similar to human blood plasma. At the start of immersion in HBSS, the precipitation started to form on the scaffold surface. With the increase of soaking time, βTCP was slowly released for the scaffold sintered at 1200 °C whilst α TCP was quickly released for the scaffold sintered at 1300 °C. Further, with the soaking time, the particles gradually grew together and formed a dense layer on the BCP scaffold surface [38]. The icetemplated βTCP scaffolds were subjected to cellular colonization evaluation with MG63 human osteoblastic cells [39]. The tests were carried out with the scaffolds fabricated using the poly(methylmethacrylate) (PMMA) beads (200–800 μm) as templates. It was found that the icetemplated pores >100 μm allowed the cells to grow into the pores and all of the PMMAtemplated pores were colonized by the cells. However, different cell growth behaviours were observed. In the aligned icetemplated tubular structure, the cells penetrated individually into the scaffold. But for the PMMAtemplated porous structure, the cells were grouped and very few isolated cells were observed. Further, the cell penetration depth (250 μm) in the icetemplated scaffold was higher than that in the PMMAtemplated scaffold (150 μm) [39].

Macroporous bioglass scaffolds can also be prepared from the silica precursor with the incorporation of biomineral ions. For example, calcium nitrate was introduced into a TEOS sol. Subsequently, the macroporous bioglass was fabricated by a combination of sol–gel and freezedrying process [97]. The *in vitro* biocompatibility test with the SBF demonstrated the formation of a welldistributed hydroxyapatite nanoparticulate layer [97]. In another interesting approach, silica colloids (HS40) were combined with cow's milk (to provide mineral ions and collagen as additional sacrificial templates) to generate hierarchically porous icetemplated scaffolds [28]. The *in vitro* biomineralization resulted in the formation of a hydroxyapatite nanolayer on the scaffold surface within 24 h exposure time to the SBF [28].

5.6.4 Electric/electrode Materials

Ceramics with photosensitive or electrical properties are used in these types of applications, one example of which is porous titania. Titania films with aligned microgrooves on alumina substrate were fabricated by a directional freezing process. The freezedried films were heat treated at 1000 °C in air for 1.5 h and then at the same temperature for 3 h but under a reducing H_2/Ar (5% H_2) atmosphere [34]. This process generated oxygen vacancies in the rutile TiO_2, resulting in electrically conducting substoichiometric TiO_2 phase (known as *Magnéli phase*). For the TiO_2 film with aligned microgrooves, the electrical resistance was found to be dependent on the orientation of the grooves. This electrical property was explored for electrical simulation. When a simulating electronic circuit was connected to the conducting patterned TiO_2 film, chargebalanced biphasic stimulus pulses with tuneable current amplitude and frequency were delivered [34]. In another study, TiO_2 film with near vertical microchannels on fluorinedoped tin oxide (FTO) glass was prepared by freeze casting and sintered in air at 480 °C for 30 min [37]. This film was then treated by soaking in the N719 (a type of Rubased dye)ethanol solution and sensitized for about 14 h at 60 °C. The sensitized TiO_2 film was used as a photoanode to fabricate a dyesensitized solar cell (DSSC) device. A 13% higher photocurrent density was observed, when compared with the TiO_2 film with randomly porous structure prepared by the conventional doctor blade method. This higher efficiency was attributed to the longer residence time of the light in the pores by reflecting several times from wall to wall and leading to a stronger absorption by the dye molecules [37].

Because of the stability at high temperatures, porous ceramics are used as electrodes for solid oxide fuel cells (SOFCs). Usually, a ceramics paste is applied and sintered to a solid electrolyte via a screening or tapecasting procedure. The isotropic pore structure generated by this procedure exhibits a highly tortuous pathway and a longer transport time, resulting in low efficiencies [42]. This isotropic pore structure is also not ideal for the anisotropic stresses experienced during the cell's lifetime [114]. Porous ceramics with anisotropic porosity, such as NiOYSZ and lanthanum strontium manganite (LSM)YSZ composites, can be readily fabricated by a directional freezecasting process [42, 114].

YSZ electrolyte has been widely used for SOFC due to its superior chemical stability and oxygenionic conductivity over a range of temperatures and oxygen partial pressures. However, the ion conductivity of YSZ decreases when the operation temperature is decreased. There is always a drive to find betterperforming materials at low or intermediate operation temperatures because this can considerably reduce the operation cost and improve the SOFCs stability and safety. GDC has proven to be a good electrolyte suitable for intermediate temperature (500–600 °C) [45]. In a study of the fabrication of hierarchically aligned macroporous anodesupported SOFC, the aligned macroporous NiOGDC anode was first fabricated by a freezedrying tapecasting process. A dropcoating process was then applied to deposit GDC electrolyte slurry on the freezedried NiOGDC. The resulting material was then sintered at 1400–1500 °C for 12 h. An SOFC cell was fabricated with the

NiOGDC as the anode, the dense GDC film as the electrolyte and the LSCFGDC as the cathode. A high cell powder output of 1021 W cm^{-2} at 600 °C was obtained, a value almost two times higher than that achieved with similar cell materials but different NiOGDC pore structure [45].

5.6.5 Catalysis

Porous ceramics can act as a catalyst or as a support for catalyst. The icetemplated interconnected macropores and, particularly, the aligned pores produced by directional freezing can facilitate mass transport or diffusion of reagent molecules to and from the active sites. The thermal stability of the ceramics can make them highly useful for hightemperature catalytic reactions. For example, alumina cryogels with high thermal stability were fabricated from ASB via a sol–gel and subsequent freezedrying process [102]. Pd nanoparticles could be introduced into this alumina cryogel when palladium nitrate was included in the sol during the preparation stage. Compared to other types of dry gels (including xerogel), superior thermal stability of Pd nanoparticles was observed for the alumina cryogel, as demonstrated by the Pd dispersion in alumina (measured by CO chemisorption) when heated in air in the temperature range of 500–900 °C. The dispersion percentage was significantly decreased when the heating temperature was higher than 800 °C. The size of Pd nanoparticles was estimated to be about 2.5 nm after heating at 500 °C and about 3.0 nm after heating at 800 °C. These particle sizes were in good agreement with the slightly larger pore diameters. The uniformly distributed finer Pd nanoparticles in alumina cryogel resulted in high performance for CO oxidation, either after heating at 500 °C or 800 °C [103].

When a catalystactive component is included, the porous ceramics may be directly used as catalysts. Ceria is known to be an effective component to purify exhaust gases or act as promoter for methane reforming. Thus, binary ceramics CeO_2-Al_2O_3 and ternary ceramics CeO_2-ZrO_2-Al_2O_3 were fabricated similarly by the sol–gel and freezedrying process. The addition of ethylene glycol could affect the pore structure and thermal stability of the ceramics. Transmission electron microscopy (TEM) imaging demonstrated the distribution of CeO_2 nanoparticles throughout the cryogel. The cryogels were heated in O_2-N_2 and H_2-N_2 atmospheres separately at 500 °C for 1 h. For the CO oxidation, heating in H_2-N_2 atmosphere and addition of ethylene glycol during preparing gave lower T_{50} (the temperature required to achieve 50% of CO conversion). Similar impacts were observed for CH_4 oxidation but were not as obvious [104]. This was attributed to the high dispersion of smaller CeO_2 nanoparticles in the ceramic matrix under various treatments [104]. Another example was the preparation of $LaCoO_3$ (perovskitetype material) powder prepared by sprayfreezing/freezedrying and its performance for oxidation of methane and CO at low temperatures [48]. The $LaCoO_3$ catalyst showed higher catalytic activity compared to double the amount of Pt/Al_2O_3 (prepared by a conventional impregnation method) under the same conditions (reaction temperatures of 300–440 °C). For CO oxidation, similar catalytic activity of $LaCoO_3$ was observed, compared to five times the amount of Pt/Al_2O_3 catalyst [48].

TiO_2 is well known as a photocatalyst for various catalytic reactions [115]. Porous TiO_2 ceramics were synthesized by the freezecasting method using camphene as solvent [36]. TiO_2 powders (Degussa P25) were treated with ethanediamine before processing. This procedure inhibited the anatasetorutile phase transformation during heat treatment (calcined at 800 °C). The slurry with a solid content of 15 wt% was optimal for the preparation of highly efficient and floating catalyst for photodegradation of atrazine and thiobencarb in water. The total organic carbon (TOC) removal efficiency was 95.7% and 96.7% for atrazine and thiobencarb (5 mg ml^{-1} solution), respectively. The catalyst could be reused at least six times without any obvious impact on its catalytic efficiency. Other pollutants were also tested effectively with this TiO_2 catalyst [36]. The hybrid TiO_2–chitosan scaffolds were fabricated by a gelationfreezecasting method. The photodegradation of methylene blue and Orange II dyes was investigated under irradiation with a UV lamp at $\lambda = 365$ nm. Different TiO_2 nanoparticles were used in this study and their effects on the efficiency of photodegradation were elaborated.

5.7 Summary

Ice templating or freeze casting is a simple and versatile process to produce a wide range of porous ceramics. It can be applied to a variety of particle slurries (either in water or organic solvent or a mixture of solvent) or inorganic sols. The porosity, pore size, and pore interconnectivity, in relation to mechanical strength, can be readily tuned by varying the slurry compositions and the freezing conditions. The most distinct advantage may be the preparation of aligned porous ceramics by the unique directional freezing process. These anisotropic pore structures may facilitate directional transport, guide cell growth, and provide unique properties that are suitable for thermal insulators. The combination of freeze casting with different gelation processes offers additional control on pore morphology and the mechanical strength of the resulting materials.

Icetemplated porous ceramics have been employed for many applications, some of which are described in this chapter. The future development of porous ceramics by this technique may be more applicationorientated. Depending on the requirement of the targeted applications, e.g. large pores with interconnectivity, closed pores, unidirectional microchannels of desirable width, mechanical stability, high temperature stability, and light sensitive property, the ice templating method may be employed to fabricate the porous ceramics that meet these requirements. Additional templating, e.g. nanocasting, colloidal templating or emulsion templating, may be combined with ice templating to produce hierarchical pore structures that mimic biostructured materials including bones and bamboos [116]. Indeed, the layered porous ceramics made by freeze casting can be further processed with organic polymer infiltration, thus generating tough composites, mimicking the structure of nacre. More discussion on this topic is the focus of Chapter 6.

References

1 Hammel, E.C., Ighodaro, O.L.R., and Okoli, O.I. (2014). Processing and properties of advanced porous ceramics: an application based review. *Ceram. Int.* 40: 15351–15370.

2 Studart, A.R., Gonzenbach, U.T., Tervoort, E., and Gauckler, L.J. (2006). Processing routes to macroporous ceramics: a review. *J. Am. Ceram. Soc.* 89: 1771–1789.

3 Qian, L. and Zhang, H. (2011). Controlled freezing and freeze drying: a versatile route for porous and micro−/nanostructured materials. *J. Chem. Technol. Biotechnol.* 86: 172–184.

4 Deville, S. (2013). Icetemplating, freeze casting: beyond materials processing. *J. Mater. Res.* 28: 2202–2219.

5 Gutiérrez, M.C., Ferrer, M.L., and del Monte, F. (2008). Icetemplated materials: sophisticated structures exhibiting enhanced functionalities obtained after unidirectional freezing and icesegregationinduced selfassembly. *Chem. Mater.* 20: 634–648.

6 Li, W.L., Lu, K., and Walz, J.Y. (2012). Freeze casting of porous materials: review of critical factors in microstructure evolution. *Int. Mater. Rev.* 57: 37–60.

7 Wegst, U.G.K., Schecter, M., Donius, A.E., and Hunger, P.M. (2010). Biomaterials by freeze casting. *Phil. Trans. R. Soc. A* 368: 2099–2121.

8 Deville, S. (2008). Freezecasting of porous ceramics: a review of current achievements and issues. *Adv. Eng. Mater.* 10: 155–169.

9 Liu, R., Xu, T., and Wang, C.A. (2016). A review of fabrication strategies and applications of porous ceramics prepared by freezecasting method. *Ceram. Int.* 42: 2907–2925.

10 Zhang, H., Hussain, I., Brust, M. et al. (2005). Aligned two and threedimensional structures by directional freezing of polymers and nanoparticles. *Nat. Mater.* 4: 787–793.

11 Mukai, S.R., Nishihara, H., and Tamon, H. (2004). Formation of monolithic silica gel microhoneycombs (SMHs) using pseudosteady state growth of microstructural ice crystals. *Chem. Commun.* 874–875.

12 Munch, E., Saiz, E., and Tomsia, A.P. (2009). Architectural control of freezecast ceramics through additives and templating. *J. Am. Ceram. Soc.* 92: 1534–1539.

13 Deville, S., Saiz, E., and Tomsia, A.P. (2006). Freeze casting of hydroxyapatite scaffolds for bone tissue engineering. *Biomaterials* 27: 5480–5489.

14 Deville, S., Saiz, E., and Tomsia, A.P. (2007). Icetemplated porous alumina structures. *Acta Mater.* 55: 1965–1974.

15 Fukushima, M., Tsuda, S., and Yoshizawa, Y. (2013). Fabrication of highly porous alumina by gelation freezing route with antifreeze protein. *J. Am. Ceram. Soc.* 96: 1029–1031.

16 Li, D. and Li, M. (2012). Preparation of porous alumina ceramic with ultrahigh porosity

and long straight pores by freeze casting. *J. Porous. Mater.* 19: 345–349.

17 Zheng, J., Salamon, D., Lefferts, L. et al. (2010). Ceramic microfluidic monoliths by ice templating. *Microporous Mesoporous Mater.* 134: 216–219.

18 Tallón, C., Moreno, R., and Nieto, M.I. (2009). Shaping of porous alumina bodies by freeze casting. *Adv. Appl. Ceram.* 108: 307–313.

19 Deville, S., Maire, E., Lasalle, A. et al. (2010). Influence of particle size on ice nucleation and growth during the icetemplating process. *J. Am. Ceram. Soc.* 93: 2507–2510.

20 Chen, R., Wang, C.A., Huang, Y. et al. (2007). Ceramics with special porous structures fabricated by freezegelcasting: using *tert*butyl alcohol as template. *J. Am. Ceram. Soc.* 90: 3478–3484.

21 Deville, S., Maire, E., BernardGranger, G. et al. (2009). Metastable and unstable cellular solidification of colloidal suspensions. *Nat. Mater.* 8: 966–972.

22 Deville, S., Maire, E., Lasalle, A. et al. (2009). In situ Xray radiography and tomography observations of the solidification of aqueous alumina particle suspensions. Part I: initial instants. *J. Am. Ceram. Soc.* 92: 2489–2496.

23 Deville, S., Maire, E., Lasalle, A. et al. (2009). In situ Xray radiography and tomography observations of the solidification of aqueous alumina particle suspensions. Part II: steady state. *J. Am. Ceram. Soc.* 92: 2497–2503.

24 Lasalle, A., Guizard, C., Maire, E. et al. (2012). Particle redistribution and structural defect development during ice templating. *Acta Mater.* 60: 4594–4603.

25 Bareggi, A., Maire, E., Lasalle, A., and Deville, S. (2011). Dynamics of the freezing front during the solidification of a colloidal alumina aqueous suspension: in situ Xray radiography, tomography, and modelling. *J. Am. Ceram. Soc.* 94: 3570–3578.

26 Ahmed, A., Clowes, R., Myers, P., and Zhang, H. (2011). Hierarchically porous silica monoliths with tuneable morphology, porosity, and mechanical stability. *J. Mater. Chem.* 21: 5753–5763.

27 Nishihara, H., Iwamura, S., and Kyotani, T. (2008). Synthesis of silicabased porous monoliths with straight nanochannels using an icerod nanoarray as a template. *J. Mater. Chem.* 18: 3662–3670.

28 Onna, D., Minaberry, Y., and Jobbágy, M. (2015). Hierarchical bioglass scaffolds: introducing the “milky way” for template bioceramics. *J. Mater. Chem. B* 3: 2971–2977.

29 Ojuva, A., Akhtar, F., Tomsia, A.P., and Bergström, L. (2013). Laminated adsorbents with very rapid CO_2 uptake by freezecasting of zeolites. *ACS Appl. Mater. Interfaces* 5: 2669–2676.

30 Xia, Z., Villa, M.M., and Wei, M. (2014). A biomimetic collagen–apatite scaffold with a multilevel lamellar structure for bone tissue engineering. *J. Mater. Chem. B* 2: 1998–2007.

31 Zhang, Y., Zhou, K., Bao, Y., and Zhang, D. (2013). Effects of rheological properties on icetemplated porous hydroxyapatite ceramics. *Mater. Sci. Eng. C* 33: 340–346.

32 Zhou, K., Zhang, Y., Zhang, D. et al. (2011). Porous hydroxyapatite ceramics fabricated by an icetemplating method. *Scr. Mater.* 64: 426–429.

33 Zamanian, A., Farhangdoust, S., Yasaei, M. et al. (2014). The effect of particle size on the mechanical and microstructural properties of freezecasted macroporous hydroxyapatite scaffolds. *Int. J. Appl. Ceram. Technol.* 11: 12–21.

34 Romeo, H.E., Trabadelo, F., Jobbagy, M., and Parra, R. (2014). 2Dice template titanium oxide films as advanced conducting platforms for electrical stimulation. *J. Mater. Chem. C* 2: 2806–2814.

35 Nezafati, N., Hafezi, M., Zamanian, A., and Naserirad, M. (2015). Effect of adding nano titanium dioxide on the microstructure, mechanical properties and in vitro bioactivity of a freeze cast merwinite scaffold. *AIChE* 31: 550–556.

36 Xing, Z., Zhou, W., Du, F. et al. (2014). Facile synthesis of hierarchical porous TiO_2 ceramics with enhanced photocatalytic performance for micropolluted pesticide degradation. *ACS Appl. Mater. Interfaces* 6: 16653–16660.

37 Wang, X., Yang, B., Zhou, K. et al. (2015). Ordered porous TiO_2 films obtained by freezing and the application in dye sensitized solar cells. *Curr. Appl. Phys.* 15: 662–668.

38 Kim, D.H., Kim, K.L., Chun, H.H. et al. (2014). In vitro biodegradable and mechanical performance of biphasic calcium phosphate porous scaffolds with unidirectional macropore structure. *Ceram. Int.* 40: 8293–8300.

39 Meurice, E., Bouchart, F., Hornez, J.C. et al. (2016). Osteoblastic cells colonization inside betaTCP macroporous structures obtained by icetemplating. *J. Eur. Ceram. Soc.* 36: 2895–2901.

40 Guizard, C., Leloup, J., and Deville, S. (2014). Crystal templating with mutually miscible solvents: a simple path to hierarchical porosity. *J. Am. Ceram. Soc.* 97: 2020–2023.

41 Sofie, S.W. (2007). Fabrication of functionally graded and aligned porosity in thin ceramic substrates with the novel freezetapecasting process. *J. Am. Ceram. Soc.* 90: 2024–2031.

42 Lichtner, A.Z., Jauffres, D., Martin, C.L., and Bordia, R.K. (2013). Processing of hierarchical and anisotropic porosity LSMYSZ composites. *J. Am. Ceram. Soc.* 96: 2745–2753.

43 Gaudillere, C., GarciaFayos, J., and Serra, J.M. (2014). Enhancing oxygen permeation

through hierarchicallystructured perovskite membranes elaborated by freezecasting. *J. Mater. Chem. A* 2: 3828–3833.

44 Gaudillere, C., GarciaFayos, J., Balaguer, M., and Serra, J.M. (2014). Enhanced oxygen separation through robust freezecast bilayered dualphase membranes. *ChemSusChem* 7: 2554–2561.

45 Chen, Y., Zhang, Y., Baker, J. et al. (2014). Hierarchically oriented macroporous anode supported solid oxide fuel cell with thin ceria electrolyte film. *ACS Appl. Mater. Interfaces* 6: 5130–5136.

46 Han, D., Mei, H., Xiao, S. et al. (2017). Porous SiC_{nw}/SiC ceramics with unidirectionally aligned channels produced by freezedrying and chemical vapour infiltration. *J. Eur. Ceram. Soc*. 37: 915–921.

47 Kim, D.S. and Kim, D.K. (2015). Hierarchical structure of porous silicon nitride ceramics with aligned pore channels prepared by icetemplating and nitridation of silicon powder. *Int. J. Appl. Ceram. Technol*. 12: 921–931.

48 Lee, S.H., Lee, J.Y., Park, Y.M. et al. (2006). Complete oxidation of methane and CO at low temperature over $LaCoO_3$ prepared by sprayfreezing/freezedrying method. *Catal. Today* 117: 376–381.

49 Zhang, Y., Chen, L., Zeng, J. et al. (2014). Aligned porous barium titanate/hydroxyapatite composites with high piezoelectric coefficients for bone tissue engineering. *Mater. Sci. Eng. C* 39: 143–149.

50 Li, W., Lu, K., and Walz, J.Y. (2013). Effects of solids loading on sintering and properties of freezecast kaolinitesilica porous composites. *J. Am. Ceram. Soc*. 96: 1763–1771.

51 Fukushima, M. and Yoshizawa, Y. (2016). Fabrication of highly porous honeycombshaped mullitezirconia insulators by gelation freezing. *Adv. Powder Technol*. 27: 908–913.

52 Liu, G., Zhang, D., Meggs, C., and Button, T.W. (2010). Porous Al_2O_3–ZrO_2 composites fabricated by an ice template method. *Scr. Mater.* 62: 466–468.

53 Vessot, S. and Andrieu, J. (2012). A review on freeze drying of drugs with *tert*butanol (TBA) + water systems: characteristics, advantages, drawbacks. *Dry. Technol*. 30: 377–385.

54 Choi, H.J., Yang, T.Y., Yoon, S.Y. et al. (2012). Porous alumina/zirconia layered composites with unidirectional pore channels processed using a *tertiary*butyl alcoholbased freeze casting. *Mater. Chem. Phys*. 133: 16–20.

55 Tomeckova, V. and Halloran, J.W. (2012). Porous ceramics by photopolymerization with terpeneacrylate vehicles. *J. Am. Ceram. Soc*. 95: 3763–3768.

56 Hong, C., Zhang, X., Han, J. et al. (2010). Camphenebased freezecast ZrO_2 foam with

high compressive strength. *Mater. Chem. Phys.* 119: 359–362.

57 Du, J., Zhang, X., Hong, C., and Han, W. (2013). Microstructure and mechanical properties of ZrB_2–SiC porous ceramic by camphenebased freeze casting. *Ceram. Int.* 39: 953–957.

58 Hou, Z., Ye, F., Liu, L., and Liu, Q. (2012). Fabrication of gradient porous βSiAlON ceramics via a camphenebased freeze casting process. *Mater. Sci. Eng. A* 558: 742–746.

59 Tang, Y., Qiu, S., Wu, C. et al. (2016). Freeze cast fabrication of porous ceramics using *tert* butyl alcohol–water crystals as template. *J. Eur. Ceram. Soc.* 36: 1513–1518.

60 Zeng, J., Zhang, Y., Zhou, K., and Zhang, D. (2014). Effects of alcohol additives on pore structure and morphology of freezecast ceramics. *Trans. Nonferrous Metals Soc. China* 24: 718–722.

61 Pekor, C. and Nettleship, I. (2014). The effect of the molecular weight of polyethylene glycol on the microstructure of freezecast alumina. *Ceram. Int.* 40: 9171–9177.

62 Yeh, Y. and Feeney, R.E. (1996). Antifreeze proteins: structures and mechanism of function. *Chem. Rev.* 96: 601–617.

63 Ahmed, A., Clowes, R., Willneff, E. et al. (2010). Synthesis of uniform porous silica microspheres with hydrophilic polymer as stabilizing agent. *Ind. Eng. Chem. Res.* 49: 602–608.

64 Yoon, H.J., Kim, U.C., Kim, J.H. et al. (2010). Macroporous alumina ceramics with aligned microporous walls by unidirectionally freezing foamed aqueous ceramic suspensions. *J. Am. Ceram. Soc.* 93: 1580–1582.

65 Zhang, H. and Cooper, A.I. (2007). Aligned porous structures by directional freezing. *Adv. Mater.* 19: 1529–1533.

66 Zhang, H., Long, J., and Cooper, A.I. (2005). Aligned porous materials by directional freezing of solution in liquid CO_2. *J. Am. Chem. Soc.* 127: 13482–13483.

67 Qian, L., Ahmed, A., GlennonAlty, L. et al. (2015). Patterned substrates fabricated by a controlled freezing approach and biocompatibility evaluation by stem cells. *Mater. Sci. Eng. C* 49: 390–399.

68 Inasawa, S., Katayama, T., and Yamaguchi, Y. (2016). Surface freezing and surface coverage as key factors for spontaneous formation of colloidal fibers in vacuum drying of colloidal suspensions. *Soft Matter* 12: 7663–7669.

69 Groβberger, S., Fey, T., and Lee, G. (2016). Vacuuminduced surface freezing to produce monoliths of aligned porous alumina. *Materials* 9: 983.

70 Groβberger, S., Fey, T., and Lee, G. (2017). Freezing kinetics of vacuuminduced surface directional freezing in a glass vial. *Chem. Eng. Sci.* 167: 154–160.

71 Ahmed, A., Smith, J., and Zhang, H. (2011). Gradient porous materials by emulsion centrifugation. *Chem. Commun.* 47: 11754–11756.

72 Porter, M.M., Yeh, M., Strawson, J. et al. (2012). Magnetic freeze casting inspired by nature. *Mater. Sci. Eng. A* 556: 741–750.

73 Porter, M.M., Niksiar, P., and McKittrick, J. (2016). Microstructural control of colloidal based ceramics by directional solidification under weak magnetic fields. *J. Am. Ceram. Soc.* 99: 1917–1926.

74 Kim, J.W., Tazumi, K., Okaji, R., and Ohshima, M. (2009). Honeycomb monolith structured silica with highly ordered, threedimensionally interconnected macroporous walls. *Chem. Mater.* 21: 3476–3478.

75 Zhang, H., Hardy, G.C., Khimyak, Y. et al. (2004). Synthesis of hierarchically porous silica and metal oxide beads using emulsiontemplated scaffolds. *Chem. Mater.* 16: 4245–4256.

76 Zhang, H. and Cooper, A.I. (2005). Emulsiontemplated hierarchically porous silica beads using silica nanoparticles as building blocks. *Ind. Eng. Chem. Res.* 44: 8707–8714.

77 Han, J., Hu, L., Zhang, Y., and Zhou, Y. (2009). Fabrication of ceramics with complex porous structures by the impregnatefreezecasting process. *J. Am. Ceram. Soc.* 92: 2165–2167.

78 Qian, L., Ahmed, A., Foster, A. et al. (2009). Systematic tuning of pore morphologies and pore volumes in macroporous materials by freezing. *J. Mater. Chem.* 19: 5212–5219.

79 Qian, L., Willneff, E., and Zhang, H. (2009). A novel route to polymeric submicron fibers and their use for inorganic structures. *Chem. Commum.* 3946–3948.

80 Ahmed, A., Clowes, R., Willneff, E. et al. (2010). Porous silica spheres in macroporous structures and on nanofibers. *Phil. Trans. R. Soc. A* 368: 4351–4370.

81 Waschkies, T., Oberacker, R., and Hoffmann, M.J. (2011). Investigation of structure formation during freezecasting from very slow to very fast solidification velocities. *Acta Mater.* 59: 5135–5145.

82 Fukushima, M., Yoshizawa, Y., and Ohji, T. (2014). Macroporous ceramics by gelation freezing route using gelatin. *Adv. Eng. Mater.* 16: 607–620.

83 Fukushima, M., Nakata, M., Zhou, Y. et al. (2010). Fabrication and properties of ultra highly porous silicon carbide by the gelationfreezing method. *J. Eur. Ceram. Soc.* 30: 2889–2896.

84 Barrow, M., Eltmimi, A., Ahmed, A. et al. (2012). Frozen polymerization for aligned porous structures with enhanced mechanical stability, conductivity, and as stationary phase for HPLC. *J. Mater. Chem.* 22: 11615–11620.

85 Barrow, M. and Zhang, H. (2013). Aligned porous stimuliresponsive hydrogels via directional freezing and frozen UV initiated polymerization. *Soft Matter* 9: 2723–2729.

86 de Hazan, Y. (2012). Porous ceramics, ceramic/polymer, and metaldoped ceramic/polymer nanocomposites via freeze casting of photocurable colloidal fluids. *J. Am. Ceram. Soc.* 95: 177–187.

87 Zhang, H. and Cooper, A.I. (2002). Synthesis of monodisperse emulsiontemplated polymer beads by oilinwaterinoil (O/W/O) sedimentation polymerization. *Chem. Mater.* 14: 4017–4020.

88 Zhang, H. and Cooper, A.I. (2007). Thermoresponsive "particle pumps": activated release of organic nanoparticles from opencell macroporous polymers. *Adv. Mater.* 19: 2439–2444.

89 Gun'ko, V.M., Savina, I.N., and Mikhalovsky, S.V. (2013). Cryogels: morphological, structure and adsorption characterization. *Adv. Colloid Interf. Sci.* 187–188: 1–46.

90 Suwanchawalit, C., Patil, A.J., Kumar, R.K. et al. (2009). Fabrication of icetemplated macroporous TiO_2chitosan scaffolds for photocatalytic applications. *J. Mater. Chem.* 19: 8478–8483.

91 Eychmüller, A., Ziegler, C., Wolf, A. et al. (2017). Modern inorganic aerogels. *Angew. Chem. Int. Ed.* 56: 13200–13221.

92 Mahler, W. and Bechtold, M.F. (1980). Freezeformed silica fibers. *Nature* 285: 27–28.

93 Mukai, S.R., Nishihara, H., and Tamon, H. (2008). Morphology maps of icetemplated silica gels derived from silica hydrogels and hydrosols. *Microporous Mesoporous Mater.* 116: 166–170.

94 Mori, H., Aotani, K., Sano, N., and Tamon, H. (2011). Synthesis of a hierarchically micro macroporous structured zeolite monolith by icetemplating. *J. Mater. Chem.* 21: 5677–5681.

95 Nishihara, H., Mukai, S.R., Fujii, Y. et al. (2006). Preparation of monolithic SiO_2–Al_2O_3 cryogels with interconnected macropores through ice templating. *J. Mater. Chem.* 16: 3231–3236.

96 Zhang, H., Hardy, G.C., Rosseinsky, M.J., and Cooper, A.I. (2003). Uniform emulsion templated silica beads with high pore volume and hierarchical porosity. *Adv. Mater.* 15: 78–81.

97 Minaberry, Y. and Jobbágy, M. (2011). Macroporous bioglass scaffolds prepared by coupling sol–gel with freeze drying. *Chem. Mater.* 23: 2327–2332.

98 Wang, X., Sumboja, A., Khoo, E. et al. (2012). Cryogel synthesis of hierarchically interconnected macro−/mesoporous Co_3O_4 with superb electrochemical energy storage. *J. Phys. Chem. C* 116: 4930–4935.

99 Yang, J. and Xu, J.J. (2003). Influence of synthesis conditions on the electrochemical properties of nanostructured amorphous manganese oxide cryogels. *J. Power Sources* 122: 181–187.

100 Sudant, G., Baudrin, E., Dunn, B., and Tarascon, J.M. (2004). Synthesis and electrochemical properties of vanadium oxide aerogels prepared by a freezedrying process. *J. Electrochem. Soc.* 151: A666–A671.

101 Mukai, S.R., Nishihara, H., Shichi, S., and Tamon, H. (2004). Preparation of porous TiO_2 cryogel fibers through unidirectional freezing of hydrogel followed by freezedrying. *Chem. Mater.* 16: 4987–4991.

102 Osaki, T., Yamada, K., Watari, K. et al. (2012). Alumina cryogels with superior thermal stability for catalyst supports. *J. SolGel Sci. Technol.* 61: 268–274.

103 Osaki, T., Yamada, K., Watari, K. et al. (2012). Palladiumalumina cryogel with high thermal stability and CO oxidation activity. *Catal. Lett.* 142: 95–99.

104 Osaki, T. Effect of ethylene glycol on structure, thermal stability, oxygen storage capacity, and catalytic CO and CH_4 oxidation activities of binary CeO_2–Al_2O_3 and ternary CeO_2–ZrO_2–Al_2O_3 cryogels. *J. SolGel Sci. Technol.* 82: 133–147.

105 Li, J.C. and Dunand, D.C. (2011). Mechanical properties of directionally freezecast titanium foams. *Acta Mater.* 59: 146–158.

106 Jo, H., Kim, M.J., Choi, H. et al. (2016). Morphological study of directionally freeze cast nickel foams. *Metall. Mater. Trans. E* 3: 46–54.

107 Oh, S., Chang, S., and Suk, M. (2012). Microstructure of porous Cu fabricated by freeze drying process of CuO/camphene slurry. *Trans. Nonferrous Metals Soc. China* 22: s688–s691.

108 Ran, H., Feng, P., Liu, Z. et al. (2015). Complexshaped porous Cu bodies fabricated by freezecasting and vacuum sintering. *Metals* 5: 1821–1828.

109 Charnvanichborikarn, S., Worsley, M.A., BaggeHansen, M. et al. (2014). Ice templating synthesis of lowdensity porous Cu–C nanocomposites. *J. Mater. Chem. A* 2: 18600–18605.

110 Oh, S.T., Kim, Y.D., and Suk, M.J. (2015). Freeze drying for porous Mo with different sublimable vehicle compositions in the camphornaphthalene system. *Mater. Lett.* 139: 268–270.

111 Li, D. and Li, M. (2012). Porous Y_2SiO_5 ceramic with low thermal conductivity. *J. Mater. Sci. Technol.* 28: 799–802.

112 Wang, Z., Feng, P., Wang, X. et al. (2016). Fabrication and properties of freezecast mullite foams derived from coalseries kaolin. *Ceram. Int.* 42: 12414–12421.

113 Kokubo, T. and Takadama, H. (2006). How useful is SBF in predicting in vivo bone bioactivity? *Biomaterials* 27: 2907–2915.

114 Moon, J., Hwang, H., Awano, M., and Maeda, K. (2003). Preparation of NiO–YSZ tubular support with radially aligned pore channels. *Mater. Lett.* 57: 1428–1434.

115 Schneider, J., Matsuoka, M., Takeuchi, M. et al. (2014). Understanding TiO_2 photocatalysis: mechanisms and materials. *Chem. Rev.* 114: 9919–9986.

116 Wegst, U.G.K., Bai, H., Saiz, E. et al. (2015). Bioinspired structural materials. *Nat. Mater.* 14: 23–36.

6
Strong and Tough Ceramic Composites via Ice Templating

6.1 Introduction

6.1.1 Enhanced Applications by Ceramic Composites

The variety of ceramics available offers excellent properties such as mechanical strength, hardness, high temperature stability, optical and electric properties, thermal conductivity, insulation, and biocompatibility [1]. Ceramic composites can be formed between ceramics and metal ceramics and polymer, and between ceramics themselves. These composites provide enhancement in performance by combining the desirable properties of each component and more importantly the possible synergy effect between the components. Ceramics and their composites may be utilized as engineering blocks, in coatings or as porous materials depending on their targeted applications. For example, porous ceramics & composites are used for thermal insulation, filtration, and bioscaffolding [2] while nonporous composites are used in the manufacture of loadbearing objects and abrasionresistant coatings.

Depending on the applications, different types of ceramic materials may be selected. For medical applications including hip replacement, dental implants and restorations, and bone fillers, alumina was initially used and then gradually replaced by zirconia because of its high strength and high fracture toughness. Yttriastabilized zirconia (YSZ) is the standard basic material. However, the presence of water and oxygen can lead to aging problem by penetrating into the gaps due to the trivalent nature of yttria [3]. The development of alumina–zirconia composites and ceria and magnesiadoped zirconia has been improvised to address this aging issue [3]. In the case of scaffolds for bone engineering and biomedical applications, bioglass and calcium phosphate (CaP)based ceramics are mostly used because bioactive hydroxyapatite (HA) can be formed when in contact with the biological fluid [4]. Good mechanical properties are essential for bone tissue engineering. The scaffolds prepared by various approaches are therefore evaluated for their mechanical behaviour in terms of porosity, composition, microstructure, flaws, and reliability [5]. Ultrahigh molecular weight polyethylene (UHMWPE) has been applied as a bearing surface in human joint replacement and artificial bones due to its inert and lowfriction surface and good levels of mechanical properties. Inclusion of HA particles in the UHMWPE matrix leads to improved mechanical & tribological properties and bonding formation between the scaffold and the living bones [6].

Ceramics with high dielectric permittivity (ε_r) are promising candidates for microwave applications. However, the lack of conformity (or bendable property) in ceramic materials hinders their application for small platforms and systemonpackages. Thus, polymer–ceramic composites may be prepared to provide flexible substrates with good permittivity

(ε_r = 20) and low loss, as demonstrated by the composites of barium titanate, MgCaTi, and BiBaNdTitanate with polydimethylsiloxane (PDMS) [7].

For composite materials, the properties may be simply the addition or combination of the properties from each of the components, or more desirably the significantly improved properties made possible by the synergy effect between the components. It is also possible to generate new properties, which the individual components may not exhibit. For example, multiferroic magnetoelectric materials, showing simultaneous ferroelectricity and ferromagnetism, have attracted scientific interest. However, useful natural materials with multiferroic magnetoelectric properties are rare, either due to weak response or because they occur at low temperatures. The composites formed by combining piezoelectric and magnetic compounds can produce a large magnetoelectric response at room temperature. This is the result of the coupling interaction between piezoelectric and magnetic compounds because neither the piezoelectric phase nor the magnetic phase has the magnetoelectric effect [8]. When a magnetic field is applied to this composite, the magnetic phase changes its shape magnetostrictively. The strain generated leads to an electric polarization in the piezoelectric phase [8].

The high temperature stability and corrosion resistance are probably the main reasons for using ceramics in thermal insulation [2], as thermal exchangers [9] and in thermal barrier coatings (TBCs) [10]. For thermal exchangers, silicon carbide (SiC) is probably the most used ceramic due to its high decomposition temperature (~2500 °C), good thermal shock resistance, good flexural strength at high temperature, and high thermal conductivity (about four times higher than that of steel) [9]. Silicon nitride (Si_3N_4, excellent strength and creep resistance but vulnerable to oxidation at high temperatures), alumina (highly resistant under oxidizing and reducing conditions, inexpensive, but comparably low thermal shock resistance), aluminium titanate (low thermal conductivity), and aluminium nitride (good oxidation resistance and thermal stability) have also been used. However, the intrinsic brittleness and lack of reliability limit the applications of these ceramics. Ceramic composites are thus fabricated to address these shortcomings [9]. Lowthermal conductive ceramic coatings are used in the highly demanding hightemperature environment of aircraft and industrial gasturbine engineering. The TBCs provide considerable temperature reduction from the surface temperature to around 100–300 °C. This allows the operation of gasturbine engines at gas temperature well above the melting point of the superalloy (~1300 °C) [10]. The TBCs are formed from four layers: the substrate, the bondcoat, the thermally grown oxide, and the ceramic topcoat. The thermally grown oxide layer is αAl $_2O_3$ with low oxygen ionic diffusivity, limiting the bond coat oxidation. The topcoat ceramic layer is typically made of YSZ by airplasmaspray deposition and electronbeam physicalvapour deposition. YSZ has one of the lowest thermal conductivities at high temperatures (~2.3 W m^{-1} K^{-1} at 1000 °C), a high thermal expansion coefficient (~11 × 10^{-6} $°C^{-1}$) to alleviate the stress between the layers, relatively low density (6.4 Mg m^{-3}), a hardness of ~14 GPa, and a high melting point (~2700 °C) [10].

For the moveable mechanical parts in satellites and spaceborne systems, the reliability of these parts in terms of lubricant degradation and excessive wear is essential because these

systems would remain in space for 10–30 years, exposed to harsh environment and temperature cycling from cryogenic to 400 °C [11]. The tough composite coatings for space tribology may be formed from oxides and dichalcogenides (e.g. PbO/MoS_2, ZnO/MoS_2, ZnO/WS_2), the combination of carbides (TiC, WC)/oxides/dichalcogenides, and also the inclusion of diamondlike carbon particles in the matrix [11]. In responding to the wide range of temperature variation, the coatings can be improved with the encapsulation of YSZ, nanosized MoS_2, and nanodiamonds in a gold matrix [11].

6.1.2 Processing and Mechanical Behaviour of Ceramic Composites

A composite usually consists of a matrix phase and a second/dispersed phase. The second phase can be more than one type of materials. Improving the mechanical properties is essential for nearly all the composites and is paramount for some applications. The matrix can be either polymer or ceramics and the same can be said for the second phase materials as well. The second phase can be a discontinuous phase (e.g. particles) or a continuous phase (e.g. fibres, layered composites). The shape and size of the particles, e.g. spherical particles, irregularly shaped particles, rods, fibres, whiskers, and plates, can have a profound impact on the mechanical behaviour of the resulting composites.

For polymer–ceramics composites where polymer is the matrix, the addition of ceramic particles is often to improve the strength and wear property of the materials [5, 6]. It has been shown that particle loading has a significant impact on Young's modulus while there is little effect from particle/matrix interfacial adhesion [12]. However, for the effect of particle size, there seems to be a critical size (around 30 nm). When the particles are smaller than the critical size, smaller particles in the composites can improve Young's modules more significantly while the effect is not clearly observed when the particles are greater than 30 nm [12].

In this chapter, the focus is on the ceramic composites where the ceramics are the matrix. The second phase can be polymer, metal, or other types of ceramics. Because ceramics usually have high strength but are brittle and the strength or the targeted applications are always compromised by the low toughness, the purpose (or at least one of the main purposes) of making ceramic composites is to improve the fracture toughness. In simple terms, the toughening mechanisms are due to crackbridging, crack deflection, pullout of the dispersed phase, microcracking, and phase transformation toughening [13]. The interface area of the dispersed phase can exert the impactbased pullout friction, debonding, and crack deflection. Therefore, compared to microparticles, the incorporation of nanoparticles in a composite may contribute more significantly to the enhanced mechanical behaviour [14].

The fracture of brittle materials such as ceramics involves little stress dissipation by processes other than crack extension, leading to failure of the materials. In ceramic glasses and single crystalline ceramics, the fracture toughness can be very low (0.5–2 MPa $m^{1/2}$) when compared with metals (15–150 MPa $m^{1/2}$). Despite some improvement, the fracture toughness of polycrystalline ceramics is still very low at ≤5 MPa $m^{1/2}$. In contrast, high flexure strengths can be achieved for most of the ceramics [13]. A substantial fraction of the strength may be lost for

lowtoughness ceramics due to the damage introduced during service. It is therefore highly important to develop toughened ceramics, which is often achieved by fabrication of ceramic composites. Besides the effect of the second phase particles, the shape and size of the matrix ceramic particles can also impact the fracture toughness as it has been shown for elongated alumina particles with SiC whiskers as reinforcement phase [13]. The toughness increases with increasing particle size up to a critical size. In a composite containing tetragonal zirconia, the improved toughness can be attributed to the enhanced matrix toughness and the transformationinduced toughness [13].

Because elastic bridging by ligaments and pullout contribute significantly to the fracture toughness, the dispersed particles with high aspect ratio are usually better for the composite toughness. These include grains, rods, whiskers, platelets, or continuous fibres [13–16]. Particularly for the fibres, a big part of the toughness is attributed to the pullout of the fibres from the matrix, which depends on frictional sliding resistance, the fibre radius, the fibre volume fraction, and the fibre strength statistics [15]. The statistic fibre strength can be taken as the cumulative number of defects, which fails at stress σ and fibre length L by the Weibull expression [15]:

$$\Phi(L,\sigma) = \frac{L}{L_0}(\sigma/\sigma_0)^m, \tag{6.1}$$

where σ_0 is the stress required to cause one failure, on average, in a fibre of length L_0 and m is the variability of measured strengths about the average values.

However, fabrication of long fibrereinforced ceramics is expensive and can be usually realized with limited thickness. Also, the most often used carbon and silicon carbide fibres show limited thermal stability in oxidizing environments. This problem may be addressed by the fabrication of laminar ceramic composites, where alternative layers with thicknesses varying from microns to millimetres, maybe also nanometres although it is highly challenging [16–18]. Various methods are used conventionally for the fabrication of laminar composites. These include: (i) *tape casting:* sequentially depositing a suspension on a support either by spreading under a blade (doctor blade process) or by coating followed by solvent evaporation. The layer thickness is in the range of 50–100 μm [16, 17]; (ii) *centrifugal casting:* achieved by sequential centrifugal casting of slurries with layer thickness down to ~10 μm [17]; (iii) *slip casting:* where a suspension with low viscosity is poured into a porous mould. The extraction of the solvent into the pores via wetting and capillary force leads to the buildup of the solid particle layer. The layer sequence can be achieved by alternating the composition of the suspensions [17]; (iv) *electrophoretic deposition:* this method is driven by the movement of charged ceramic particles under a direct current (DC) electric field [17]; (v) *vapour deposition:* essential for the fabrication of nanoscale layers, by magnetron sputtering [18] or plasma spray [10].

Although great efforts have been made to produce strong materials, strength alone is not enough for many applications. Other mechanical properties such as fracture toughness, creeping behaviour, and fatigue tolerance, are also essential. In addition to intrinsic toughness, fracture

toughness may be highly important. This is because the ceramic materials cannot be prepared perfectly and some flaws or cracks exist during the fabrication process, which can cause catastrophic failure even under relatively low stress. For bone tissue engineering, depending on different parts of the bone system, the scaffolds with different mechanical properties including strength (failure under a single overload), fracture toughness (failure from a modest load with preexisting crack or flaw), and fatigue strength (failure by high number of cycles of small load), should be selected according to the bone types (Figure 6.1) [19].

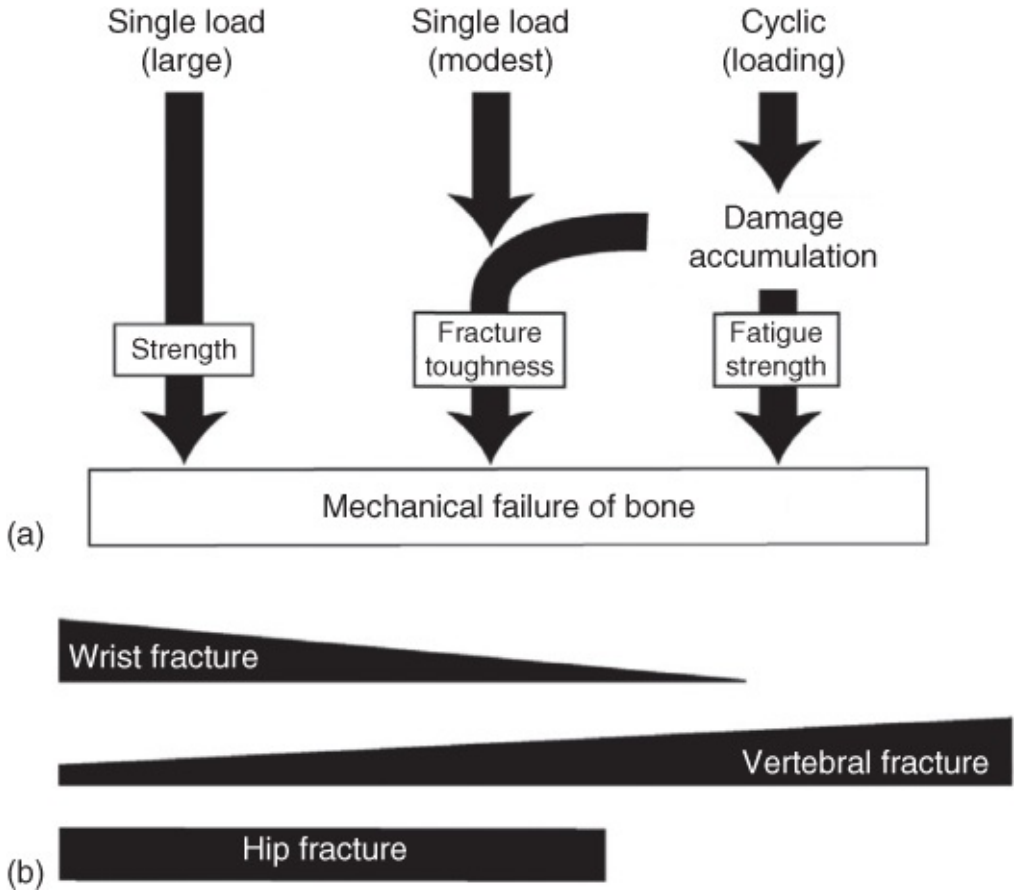

Figure 6.1 Multiple pathways to mechanical failure of different types of bones. (a) Bone fracture may occur by a single large load, a single modest load with preexisting damage in the bone, or accumulated damages by many cycles of loading. (b) Representation showing the likely mode of mechanical failure from different types of bones.

Source: Hernandez and Meulen 2017 [19]. Reprinted with permission from John Wiley and Sons.

However, the strength and toughness in a material are mutually exclusive [20]. When the toughness is increased by fabricating composites, the strength is often decreased. This is because toughness is achieved by adding grains, platelets, or fibres but the resulting interfacial flaws or debonding can reduce the strength [13]. While strength is a stress to resist non recoverable deformation under load, toughening is enhanced by crack deflection/bridging from elastic filament and deformationinduced energy dissipation [20]. It seems there is a trade off between strength and toughness for ceramic composites depending on targeted applications. Some strategies have been developed to make strong and tough composites particularly when learning from natural materials [20].

Nature has produced some extraordinary materials that exhibit exceptionally high strength, toughness, and low density. Some of the wellknown examples include bone, bamboo, teeth, and nacre [21, 22]. The common features of these materials are their hierarchical structures from atomic, nanoscale, to macroscale with relevant interfaces. Some of the materials (e.g. nacre, teeth) consist of a very high inorganic solid content and a low content of organic component (proteins or polymers), with the two phases interfacing at the nanoscale. In an effort to make tough composites, strong research activities have been observed by mimicking the structure of nacre [23]. The fabrication methods include the conventional tape casting, slip casting, layerbylayer (LBL) deposition, electrophoretic deposition, mechanical assembly and freeze casting [23].

In this chapter, the emphasis is on the use of the freezecasting (icetemplating) method to fabricate ceramic composites, particularly biomimetic tough composites [24, 25]. Since mechanical properties are usually the mainstay of fabricating ceramics and ceramic composites, we start with the introduction to the commonly used mechanical parameters when discussing ceramic composites. This is followed by porous ceramic composites, different types of tough composites, and finally the summary.

6.2 Mechanical Characterizations of Ceramic Composites

6.2.1 Strength

Strength is the resistance of the material to the onset of permanent deformation [21]. This can be conveniently measured by uniaxial tension (or compression), the shear force, and the torsion force applied. For a block of material, the tensile stress (σ) is defined as the force (F) divided by the crosssectional area (A):

$$\sigma = \frac{F}{A}. \tag{6.2}$$

Under the tensile stress, the block is deformed or elongated. The deformation can be defined by the strain (ε):

$$\varepsilon = \frac{\delta L}{L}, \tag{6.3}$$

where L is the original length of the block and δL is the extension of the block under the tensile stress [26]. Figure 6.2 shows a representative stress–strain curve.

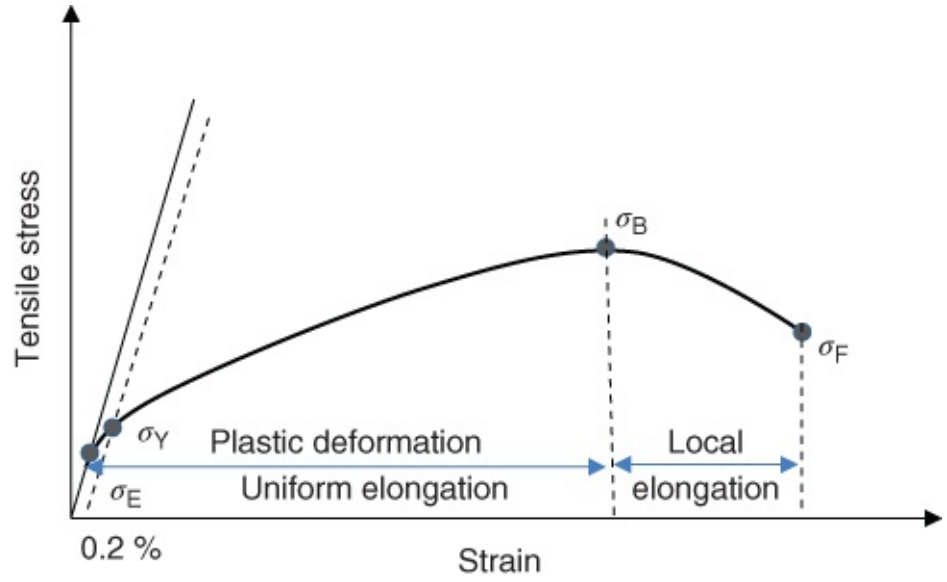

Figure 6.2 The diagram showing a typical tensile stress–strain profile with some important stress parameters indicated. σ_E, the elastic limit stress; σ_Y, the tensile yield stress; σ_B, the ultimate stress; and σ_F, the fracture stress. The solid straight line indicates the linear part of the stress–strain curve that can be used to calculate the Young's modulus (E). The dotted line indicates the deformation at 0.2%.

The definitions mentioned are for engineering stress or engineering strain, where the original area and length are conveniently used. However, under a constant tensile stress, with the elongation of the block, the crosssectional area decreases while the length increases continuously. Therefore, in contrast to engineering strain/engineering stress, true stress and true strain are defined and used where the instantaneous crosssectional area and length are used for the calculation. As shown in Figure 6.3, the true stress–strain curve is always higher than the nominal stress–strain curve.

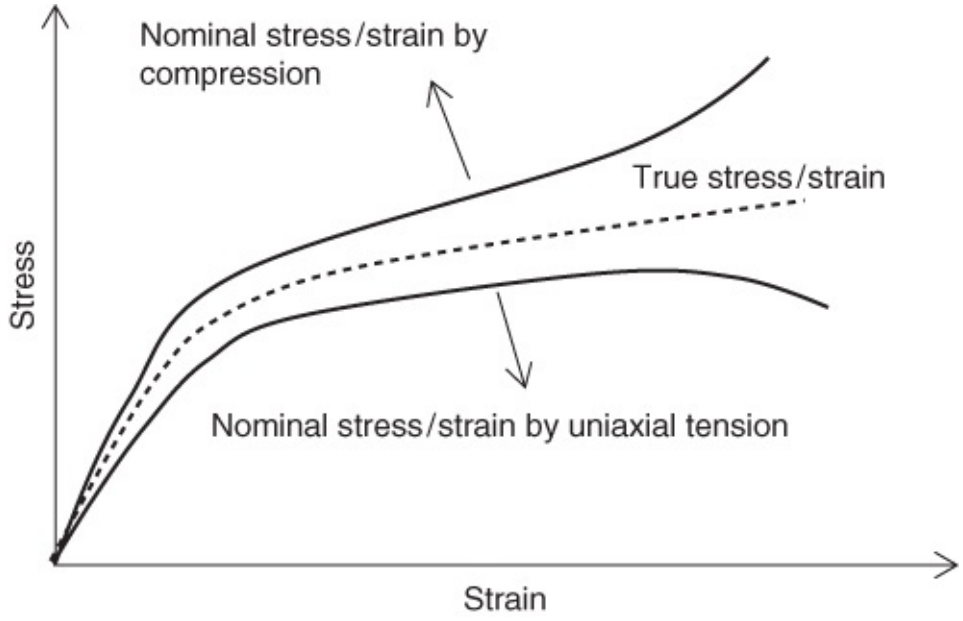

Figure 6.3 The diagram shows the difference between the true stress–strain curve and the nominal stress–strain curves by compression or tension.

As observed from Figure 6.2, the initial part of the stress–strain curve is linear, i.e. the strain is proportional to the stress applied. This normally falls into the elastic deformation region. The elastic deformation means the instantaneous full recovery of the strain when the stress is removed. It is possible that the stress–strain curve may not be linear [26]. *The Young's modulus E* (elastic modulus) is defined as the slope of the initial linear stress–strain curve. The Young's modulus is often used to describe the material's stiffness, meaning the force required to generate elastic deformation [21, 27]. Another parameter under tensile stress is the *Poisson's ratio v*, which is defined as the ratio of the strain parallel to the tensile axis to the strain normal to the tensile axis [27].

The compression stress can be applied like the reverse of the tensile stress. But it is more difficult to obtain reliable stress–strain curves. Under compression, the top and bottom of the specimen should be always parallel and bulging should be avoided. Similar to that for tensile stress, there are also definitions of true compression stress and true strain. The nominal compression can be defined as the compression force divided by the area. Since the area is always increased under compression, the true stress should be lower than the nominal compression stress, as illustrated in Figure 6.3.

When a traction force (T) is applied to the top and bottom surface of a rectangular body specimen, the shear stress τ can be defined as the force (T) divided by the surface area while the strain γ is the ratio of the deformation in the force direction divided by the distance between the top and bottom surface. The *shear modulus* μ can be defined as:

$$\mu = \frac{\tau}{\gamma}. \tag{6.4}$$

Along the stress–strain curve in Figure 6.2, σ_E represents the stress at the elastic limit. Beyond σ_E, the curve moves into a permanent deformation (*plasticity*) region where the strain is not recovered when the stress is removed. The tensile yield stress σ_Y is defined as the stress that generates a permanent strain of 0.2% after the stress is removed. The strain increases continuously with the increasing tensile stress until the maximum stress σ_B (known as ultimate stress). Up to σ_B, the strain or the elongation under tensile stress is uniform. Beyond σ_B, the large local elongation occurs, leading to the decrease of stress. This results in eventually the fracture of the specimen, with the relevant fracture stress σ_F (Figure 6.2). The maximum strain before the fracture, the percentage of elongation or relative change in the crosssectional area, is often described as the *ductility* of the material [21].

Another type of permanent deformation is creep. Figure 6.4 shows the threestage creep profile. The strain (permanent deformation) increases rather rapidly under the applied stress at the start (transient creep or primary creep), then slows down in rate and moves into a steady creep region for a long time. The third stage (also known as tertiary creep) is the accelerated rate of deformation before final failure. Usually the twostage creep profile occurs in polycrystalline ceramics at low stresses and high temperatures while the tertiary stage can be observed for metals [28].

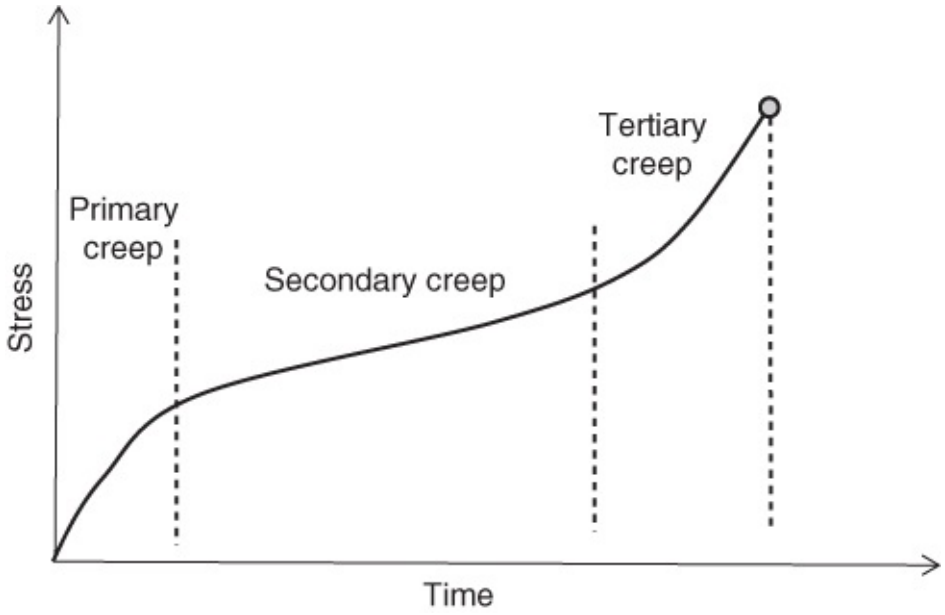

Figure 6.4 The diagram illustrates the creep behaviour under constant load and temperature.

The mechanical tests are usually carried out following the suggested procedures or standards as proposed by the American Society for Testing and Materials (ASTM) or by other internationally tested methods. The recommendations of ASTM E801 are usually used for tension testing of metallic materials. However, due to the nature of brittle fracture, flexure (bending) tests are usually used to evaluate ceramics and ceramic composites. Both three point bending and fourpoint bending tests are frequently employed (Figure 6.5). In the three point bending, the bending stress is highest at the middle and reduces to zero at the support point. Only a very small part of the specimen is exposed to the high stress. For the fourpoint bending test, the central part of the specimen is subjected to uniform bending stress, which is more likely to reflect the real situation. Fourpoint flexure testing is more widely used for strength measurement of ceramics when creep is not significant. Typically, quarterpoint ($D = L/4$) or thirdpoint ($D = L/3$) loading is used. Recommended threepoint and fourpoint flexure tests can be found in ASTM C 116102C [29].

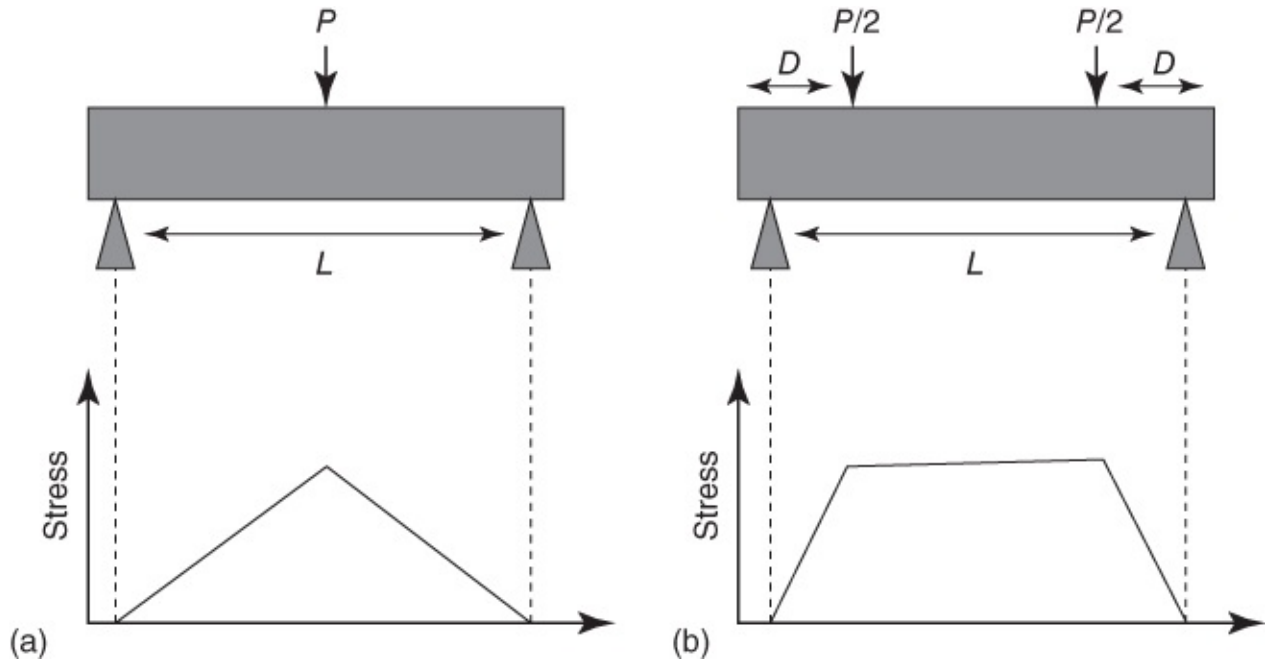

Figure 6.5 The schematic representation of flexural tests. (a) Threepoint bending test. (b) Fourpoint bending test.

6.2.2 Hardness

Hardness is a measure of the material's resistance to permanent deformation when a load is applied on the surface. It can be measured by the extent of penetration by indentation test or indirect methods [29]. The commonly used indentation methods include the Vickers test (the indenter is a squarebased pyramid usually made of diamond), the Krooper test (the indenter with unequal diagonals), and the Brinell test (the spherical indenter) [27, 29].

For the most widely used Vickers test, the hardness (H) can be calculated using the contact area over the four faces of the indenter:

$$H = \frac{1.8544P}{(2a)^2}, \tag{6.5}$$

where P is the applied load and $2a$ is the diagonal length of the indent [29].

In the ceramics industry, the projected area of the indent is often used to calculate the hardness. This gives a small but a significant difference of 7.9%, by comparing the values obtained from Equations (6.5) and (6.6) [29].

$$H = \frac{2P}{(2a)^2}. \tag{6.6}$$

Empirically, the Vickers hardness (H) can be linked with the tensile yield stress (σ_Y) in the following equation:

$$H = c\sigma_Y, \tag{6.7}$$

where the coefficient c is in the range of 2.9–3.0 for metals [27, 30]. The value of the coefficient c varies for different types of materials. Thus, one may use the hardness data to estimate the strength of the materials, or vice versa.

Under mild wear conditions, the hardness is directly related to wear. The relationship can be described as:

$$w_r = k\frac{P}{H}, \tag{6.8}$$

where w_r is the wear rate in volume removed from the surface per unit sliding distance, k is the wear coefficient, P is the force applied against the opposing surface, and H is the hardness. The wear resistance is defined as $1/w_r$ [30].

6.2.3 Fracture Mechanics and Fracture Toughness

In materials, particularly when fabricating engineering materials, the presence of flaws or cracks in these materials is almost unavoidable. The mechanical data obtained from measuring a smooth or 'perfect' specimen cannot be rationally applied for these engineering materials. There is also a huge reliability issue among different batches of the materials. In brief, fracture mechanics investigates how the stress and strain develop around a preexisting crack in a material and how to improve the fracture resistance. It can be classified into two general categories: linear elastic fracture mechanics (LEFM) and elastic–plastic fracture mechanics (EPFM). LEFM is applied to small cracks in the elastic materials with a small plastic zone while the nonlinear EPFM is usually used for largescale conditions within the plastic zone [21, 27].

Fracture mechanics can be characterized by a stress intensity factor K, which is a function of stress, crack size, and boundary conditions. K can be specified based on the modes of crack deformation: K_I for mode I deformation (crack opening), K_{II} for mode II deformation (in place shear of the crack), and K_{III} for mode III deformation (outofplane shear). Because mode I crack deformation is often seen in practical applications, K usually means K_I if not otherwise stated. K is generally expressed as:

$$K = F\sigma\sqrt{\pi a}, \tag{6.9}$$

where F is a dimensionless parameter related to geometry, σ is the applied stress, and a is the crack length. This equation is valid when $a \geq 2.5\left(\frac{K}{\sigma_Y}\right)^2$ for LEFM [27].

There are two parameters used for the EPFM materials: (i) J integral, a pathindependent contour integral for a cracked body, equivalent to the energyrelease rate; (ii) cracktip opening displacement (CTOD), the plastic deformation after blunting an initial sharp crack.

When the intensity factor K reaches a critical value (K_c), the crack becomes unstable and

brittle fracture occurs. K_c is regarded as the fracture toughness for mode I deformation under smallscale yielding and the planestress state. Similarly, for the EPFM materials, J_{IC} or J_c is the toughness for onset of slow crack growth from an initial crack [27].

K_c is usually measured using a singleedge notched (SEM) specimen by flexural tests or a compact test. There are several standards to be followed but ASTM E39990 is widely used. The specimen may contain other types of notch, e.g. a chevron notch.

The procedures and guidelines for the determination of J_{IC} are available in ASTM E1820. The *J–R* (*J* integral – crack Resistance) curve is a plot of *J* integral values versus the corresponding crack extension values, demonstrating the material's resistance to crack extension.

6.2.4 Toughening Mechanism in Ceramics and Ceramic Composites

In ceramics with high toughness, there is usually more than one type of toughening mechanisms. Conventionally, the mechanisms include [31]: (i) *crack deflection* that takes place into the local area (quite often the grain boundaries) with lower resistance to crack propagation. The toughening increases with increasing volume fraction of deflecting particles (until a certain volume fraction, ~20%). Crack deflection may cause partial bridging when a grain/whisker is in the deflection path; (ii) *Crack bowing* that is the development of a nonlinear crack front for a planar crack when a secondphase material is introduced into a brittle material. This is different from crack deflection which occurs as outofplane development of the crack; (iii) *Crack tip shielding* that can be divided into two basic categories: *process zone effects* and *bridging zone effects*. The process zone effects occur around the crack tip. The local compressive or elastic force resulting from the development of crack tip acts to close the crack. The crack bridging is the result of bridging zone effects, occurring at a distance from the crack tip. This effect is usually attributed to the debonding or ligament of the secondphase in the ceramics; (iv) *Contact shielding processes* that includes the resistance to pullout of fibres or grains, sliding interface friction, etc.; (v) *Stressinduced zoneshielding processes* that is found in tetragonal zirconia transformation, microcracking, compressive stress in the outer layer, and residual stress.

As schematically shown in Figure 6.6 [20], toughening mechanisms may be divided into extrinsic toughening and intrinsic toughening. Intrinsic toughening is inherently related to the plasticity zone of the materials ahead of the crack tip and hinders the initiation and propagation of the cracks. The extrinsic toughening is associated with crack tip shielding via crack bridging and wedging behind or at the crack tip. This type of mechanism works via limiting crack growth and usually shows a rising *J–R* curve [20, 21].

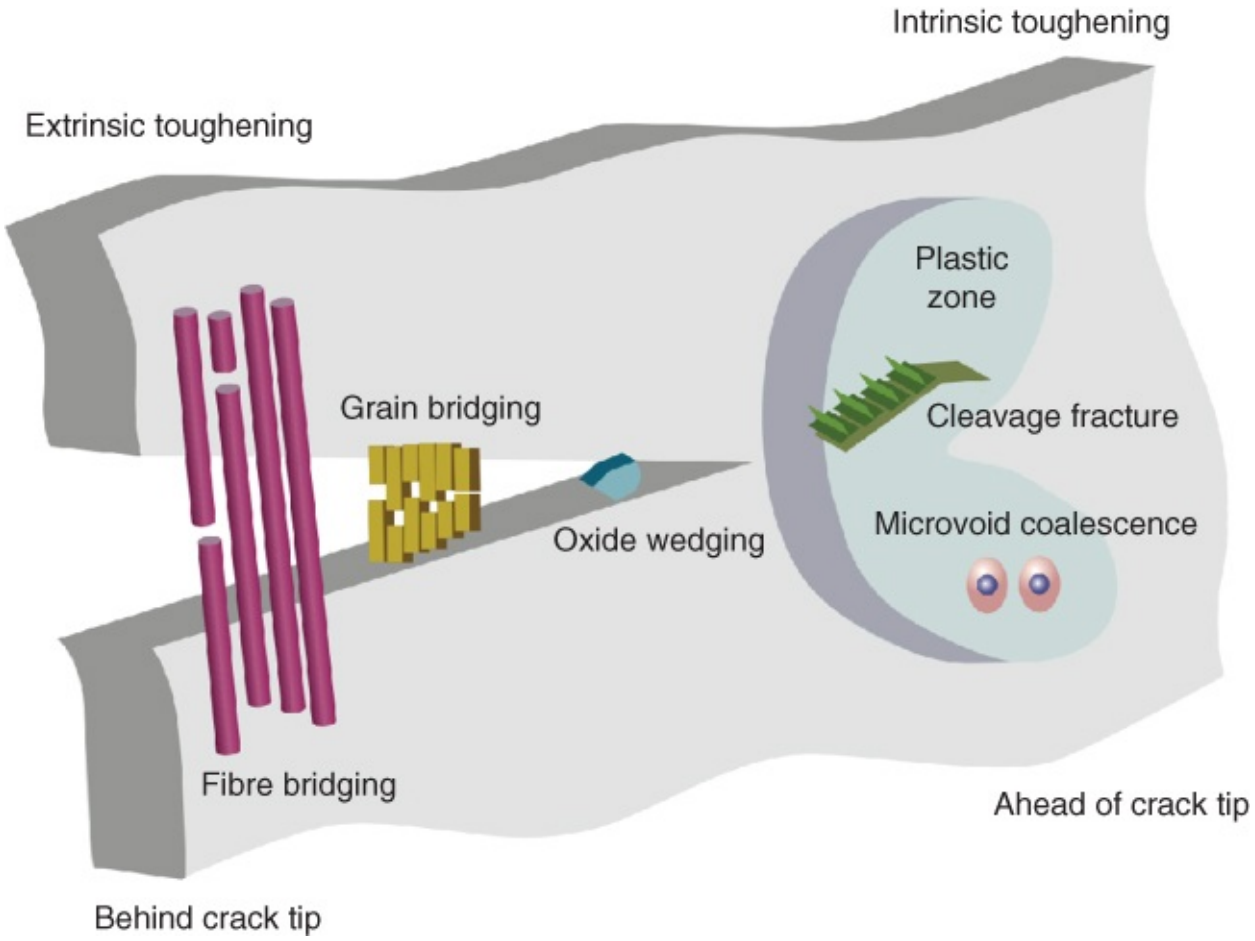

Figure 6.6 The schematic diagram shows the various toughening mechanisms in terms of intrinsic (plasticity) toughening versus extrinsic (shielding) toughening.

Source: Ritchie 2011 [20]. Reprinted with permission from Nature Publishing Group.

Fabrication of ceramic composites by introducing the second phase aims to improve the toughness, mainly via the extrinsic toughening mechanism. As mentioned earlier, discontinuous reinforcing phases including grains, whiskers, and platelets are used to produce toughened ceramics and some equations have been formulated to predict/describe the toughening behaviour [13]. Continuous fibres are found to be more effective in enhancing the toughness of the composites [15, 25]. This has been attributed to crack deflection at the fibre/matrix (preferably weak) interface, better performance in crack bridging by the fibres, and the higher work required for fibre pullout after debonding [32]. Laminar composites have been the focus of recent studies in order to obtain strong and tough composites, stimulated by mimicking the exceptional natural materials such as nacre and teeth [17, 20–23].

6.3 Porous Ceramic/Polymer Composites

The use of freeze casting for the preparation of porous ceramics including the introduction to different freezing techniques and freezecasting parameters is described in Chapter 5. Based on that, it is straightforward to fabricate porous ceramic/polymer composites. This chapter focuses on the composites where the ceramics are the matrix. The composites with dispersed

ceramic particles in a polymer matrix are not covered here.

To make porous ceramic/polymer composites, the ceramic particles can be suspended in a polymer solution (the concentration is usually higher than that of polymer only used as binder or stabilizer) and the resulting suspension is then subjected to a freezing process. The frozen samples are freezedried to form porous ceramic composites. For example, aqueous silica colloidal suspension (Ludox HS30) is mixed with 5 wt% aqueous poly(vinyl alcohol) (PVA). The resulting suspension is unidirectionally frozen and freezedried, producing an aligned porous PVA/silica composite (Figure 6.7a). PVA helps stabilize the silica colloids in the suspension and then acts like a glue to stick the silica colloids together (Figure 6.7b) [33]. When a surfactant such as sodium dodecyl sulfate (SDS) is added into the PVA/silica suspension, an oilinwater emulsion can be formed by emulsifying an organic solvent such as cyclohexane into the aqueous phase. Freezing the emulsion and then freezedrying generates an emulsiontemplated and icetemplated porous composite material. By varying the volume percentages of droplet phase in the emulsion, it is possible to produce porous structures with the systematically tuned pore morphology and porosity [34]. Figure 6.7c shows the porous structure of PVA/silica prepared from the emulsion with a 75 v/v% internal phase. The pore size distribution measured by Hg intrusion porosimetry exhibits the macropores templated from ice and emulsion droplets and mesopores resulted from the assembly of silica colloids (Figure 6.7d). Instead of directional freezing, the emulsion can be sprayed into liquid nitrogen and then freezedried. This produces highly porous silica/polymer microspheres [35] (Figure 6.7e). Other types of ceramic particles can be readily used as well. For example, ceria nanoparticles in PVA suspensions can be processed to generate composite micronsized fibres [33]. Aligned porous columns in capillaries can be prepared by directional freezing of silica colloids (TM50) with PVA or poly(diallyldimethylammonium chloride) (PDDA) and show fast separation with relatively low back pressure by high performance liquid chromatography (HPLC) [37]. Mesoporous silica microspheres (~1 μm in diameter) prepared by a modified Stöber method [38] are employed with PVA to form aligned porous composites [39]. The addition of an anionic surfactant SDS leads to a wellaligned pore structure while the presence of cationic surfactant cetyltrimethylammonium bromide (CTAB) results in a layered porous composite structure [39].

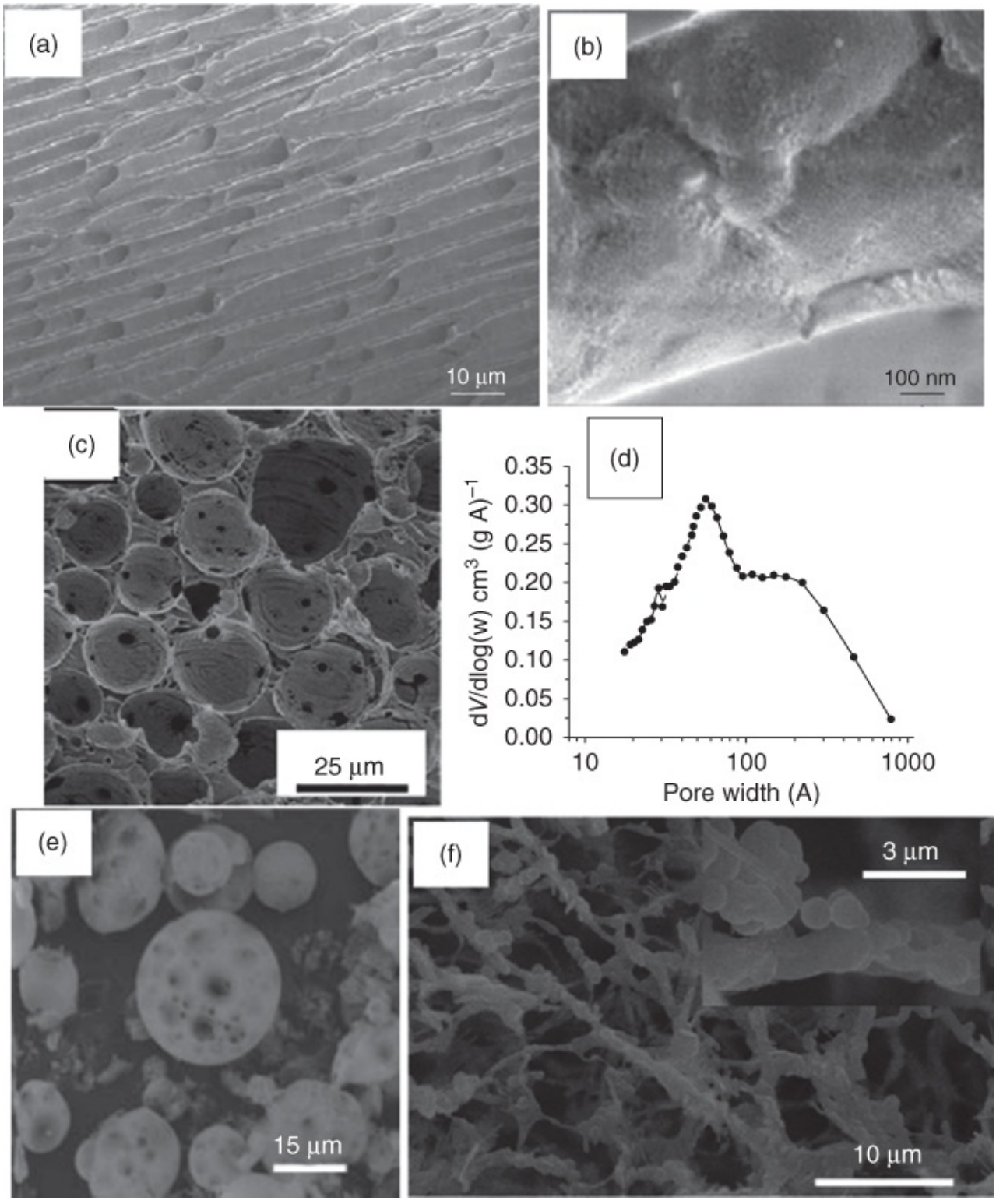
(a)
10 µm
(b)
100 nm
(c)
25 µm
(d)
dV/dlog(w) cm^3 (g A)$^{-1}$
0.35
0.30
0.25
0.20
0.15
0.10
0.05
0.00
10
100
1000
Pore width (A)
(e)
15 µm
(f)
3 µm
10 µm

Figure 6.7 The structures of porous silica–polymer composites. (a) Aligned porous silica (HS30 colloids)PVA and (b) the magnified area shows the packed silica colloids. (c) The emulsiontemplated and icetemplated porous silica (HS30)PVA and (d) the mesopore size distribution measured by N_2 sorption. (e) Porous silicaPVA microspheres prepared emulsionsprayfreezing. (f) Porous chitosansilica.

Source: Ahmed et al. 2012 [36]. Reprinted with permission from Royal Society of Chemistry.

Source: Reprinted with permission from Ref. [35].

Source: Reprinted with permission from Ref. [34].

Source: Reprinted with permission from Ref. [33].

Freezedried porous polymers can be used as scaffolds for drug delivery. However, the highly interconnected macroporous structures by ice templating always contribute to a significant initial burst release [40]. This issue can be addressed by the use of polymer/mesoporous silica composites as the delivery vehicle. For this purpose, a model drug curcumin is uploaded into mesoporous silica spheres that are then suspended in aqueous chitosan solution also containing curcumin. Freezedrying of this suspension generates a porous composite material (Figure 6.7f). A dualcontrolled release profile is achieved with this scaffold – an initial burst release from chitosan (so that a therapeutic drug concentration can be achieved quickly) followed by a steady release from the uploaded mesoporous silica microspheres [36].

Following the same principles as described above, it is possible to produce porous ceramic/polymer composites with different types of ceramic particles. Two type of porous ceramic/polymer composites are described below in detail.

6.3.1 Hydroxyapatite (HA)based Composites

These composites are prepared mainly for bone tissue engineering. The biocompatibility and mechanical strength are the most important parameters for porous HApolymer composites when used as scaffolds. The mechanical properties and the approximate porosity of the human bones are given in Table 6.1 [5, 41]. In natural bone, ~70% of the weight is the mineral content of CaP, in the form of carbonated apatite, with about 22% being organic matrix (90% of which is type I collagen) [42]. There are a range of CaP phases. Among them, hydroxyapatite (HA, $Ca_5(PO_4)_3OH$, Ca:P = 1.67 in mass) and βtricalcium phosphate (βTCP, $Ca_3(PO_4)_2$, Ca:P = 1.5 in mass) are mostly used. This is attributed to their osteogenic property and the ability to form bonds with living bones [5, 42]. In addition, bioglasses are also widely used for bone tissue engineering. However, for both CaP and bioglasses, their mechanical strength and particularly low fracture toughness are serious drawbacks [19]. Fabrication of composite scaffolds provides an effective route to improving the mechanical strength, as illustrated in Figure 6.8**,** based on elastic modulus and compressive strength [41]. By tuning the preparation methods and controlling the compositions of the composite scaffolds, good control of drug delivery from the scaffolds (e.g. proteins, growth factors, antibiotic drugs, etc.) for enhanced bone tissue engineering may be also achieved [41, 42].

Table 6.1 Mechanical properties and porosity of human bone.

Source: Data adapted from Refs [5, 41].

	Compressive strength (MPa)	Tensile strength (MPa)	Elastic modulus (GPa)	Flexural strength (MPa)	Fracture toughness (MPa $m^{1/2}$)	Porosity (%)
Cortical bone	130–180	50–151	12–18	135–193	6–8	5–13
Cancellous bone	4–12	1–5	0.1–0.5	N/A	N/A	30–90

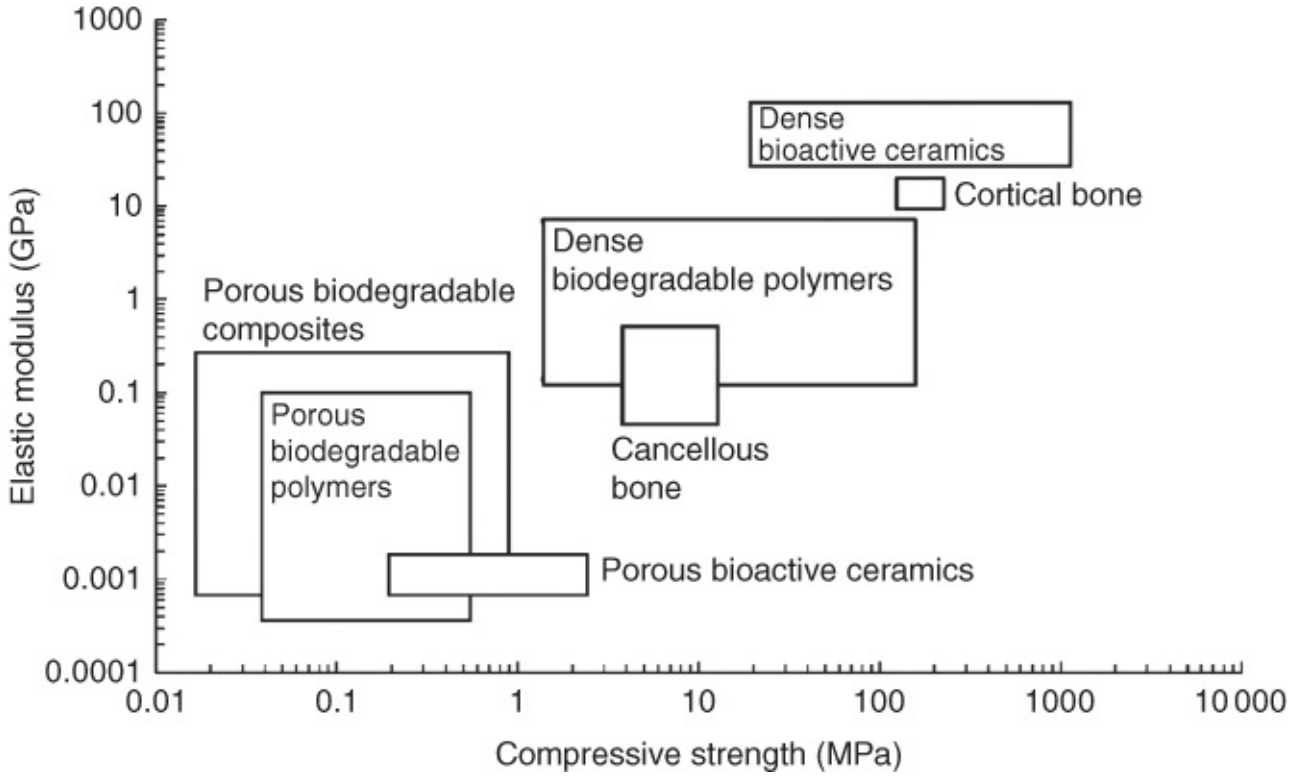

Figure 6.8 Graph of elastic moduluscomposite strength for porous composites in the context of porous polymers, dense polymers, dense ceramics, and bones.

Source: Rezwan et al. 2006 [41]. Reprinted with permission from Elsevier.

When preparing porous HAbased composites, biodegradable aliphatic polyesters are often used. These include poly(lactic acid) (PLA), poly(glycolic acid) (PGA), poly(ε caprolactone) (PCL), and copolymer poly(lacticcoglycolic acid) (PLGA). PLA is available in three forms: LPLA (PLLA), DPLA (PDLA, and racemic mixture of D,LPLA (PDLLA). The degradation occurs via hydrolysis of ester bond, generally following the order of:

PGA > PDLLA > PLLA > PCL.

The factors that affect the degradation rates include molecular weight, chemical composition, polydispersity, porosity, crystallinity, and device configuration [41].

For example, nanocrystalline carbonated apatites were prepared by a deposition method. The PLGA–apatite composites were fabricated by freeze casting using dimethyl carbonate as solvent [43]. The weight percentage of apatites in the PLGA/apatite composites varied from 0% to 60%. With the increasing percentage of PLGA, the porosity decreased from 72.1% to 63.9% whilst the Young's modulus increased from 0.16 to 0.34 MPa and then slightly decreased. This was attributed to the aggregation of apatite particles at higher concentration in the original slurries. A higher percentage of apatite in the composites was also found to reduce the *in vitro* degradation of PLGA [43].

In another study, aqueous CaP slurries with sodium carboxymethyl cellulose (SCMC) as stabilizer were processed by directional freezing and freezedrying to produce porous CaP scaffolds. The PLGA–CaP scaffolds were obtained by soaking the CaP scaffolds in PLGA CH_2Cl_2 solution followed by vacuum drying [44]. In order to improve cell attachment and proliferation, the PLGA–CaP scaffolds were treated by NH_3 plasma and then exposed to collagen solution and subsequent crosslinking with glutaraldehyde. The collagenPLGA–CaP scaffolds showed improved water uptake, porosity, and markedly enhanced cell seeding and growth, while the compressive strength remained unchanged [44].

Other biocompatible natural polymers such as chitosan can also be used to produce porous scaffolds by ice templating [40]. As compared with polyesters such as PLGA, aqueous slurries can be processed via the freezecasting approach, avoiding the use of an organic solvent. For example, aligned porous chitosan/HA scaffolds with high porosity (~85%), large pore sizes (200–500 μm), and interconnected porosity were prepared [45]. MG63 osteoblastlike cells were found to spread and cluster along the walls and grow well into the tubular pores [45].

Most of the ceramic particles used are either irregularly shaped or spherical. Nacre has high strength and toughness and consists of mainly aragonite platelets and a small fraction of polymer (proteins) [21–23]. It is thus impossible to produce strong porous composites with ceramic platelets. For example (although not HA platelets), alumina platelets (diameter 5–10 μm and thickness 300–500 nm) and chitosan and gelatin were used to produce porous scaffolds with nacrelike walls [46]. This has been compared with large and small spheres with diameters similar to the platelet dimensions, as shown in Figure 6.9**.** The alumina platelets were assembled into nacrelike structures by the freezing process, with the polymers holding the platelets together. This nacrelike porous scaffold showed higher stiffness, strength and toughness by a factor of 1.5–4 than the scaffolds with the same porosity but no nacrelike structure [46].

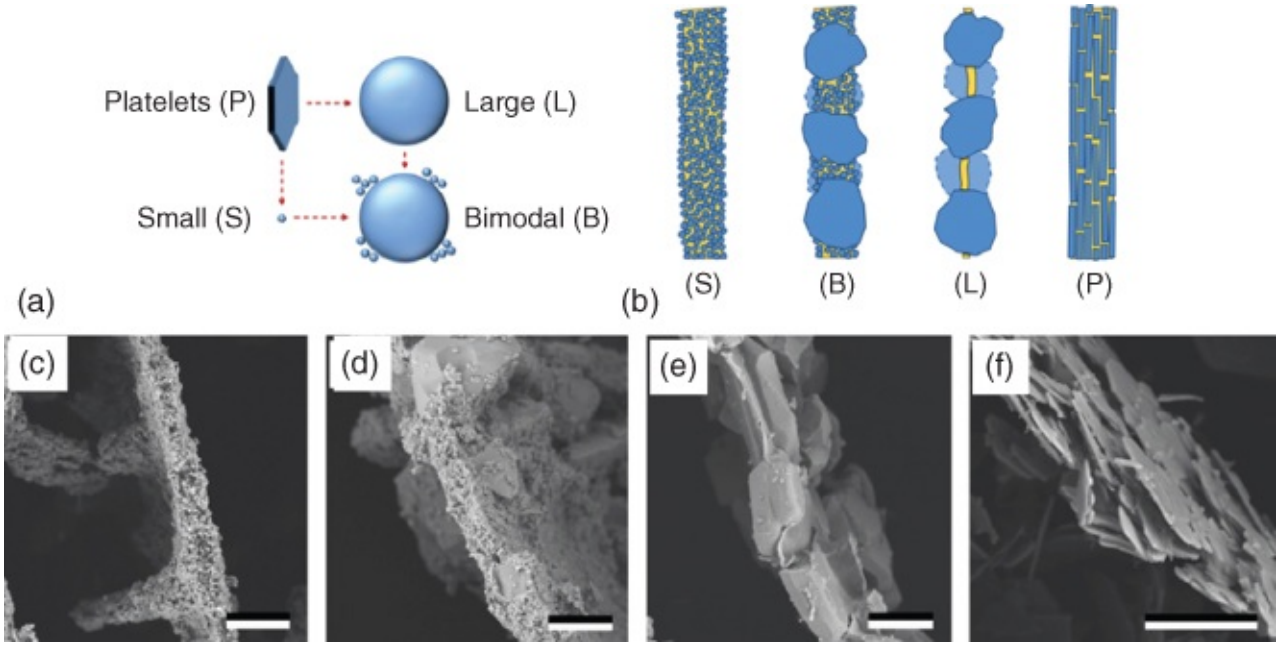

Figure 6.9 Porous alumina–polymer composites prepared by freeze casting of alumina platelets and alumina particles. (a) Diagram showing the platelets, the size of alumina particles, and the bimodal particles. (b) Diagram showing how the particles and platelets assemble during the freezing process. (c–f) Show the structures of the composites formed, comparable to the diagram in (b).

Source: Hunger et al. 2013 [46]. Reprinted with permission from Elsevier.

6.3.2 Claybased Composites

Clays are usually referred to as natural aluminosilicate colloids, which may also include other minerals and metal oxides [47]. There are two terms usually used: ‘clay’ and ‘clay mineral’. Clays are regarded as natural, with grain sizes smaller than 2 or 4 μm, containing phyllosilicates as their main constituents. Clay minerals can be natural or synthetic, not size limiting and can include both phyllosilicates and nonphyllosilicates [48]. However, clay minerals are often referred to as clays in literature [48]. Crystalline clays consist of layers of silica tetrahedrons and alumina octahedrons. Accordingly, they can be classified into 1 : 1 layer (one silica layer and one alumina layer), 2 : 1 layer (one alumina layer between 2 silica layers or trioctahedrons), regular mixed layers, and chainstructure types [47]. There are many types of clay particles. The commonly used clays are given in Table 6.2**.** The surface chemistry (e.g. charges, polarity, edge surface, and planar surface) of the clay particles when suspended in water or incorporated into a matrix can have significant impact on their applications [49]. Clays have been used for adsorption of dyes [50], heavy metal ions [47], proteins and nucleic acids [51], and drug release [52]. Their potential toxicological impacts have been evaluated [53].

Table 6.2 Properties of commonly used clay particles.

Source: Data adapted from Refs [47, 49].

	Crystalline type	Thickness of layers unit	Electronic charge[a]	Comments
Montmorillonite (Smectite)	2 : 1 layer	1–2 nm	−0.522 to −0.741 (O with no cation) −0.800 t0 −0.867 (O with K^+)	Different cation counterions, weak force between two silica layers permitting water and exchange ions (Na^+, NH_4^+)
Kaolinite	1 : 1 layer	0.72 nm	0.152 (inner H) 0.219 (surface H)	Strong bonding, no layer swelling
Bentonite	Consisting of montmorillonite and other crystalline structures			
Perlite				
Illite	2 : 1 type	1.0 nm		Bonded by K^+ ions
Vermiculites	2 : 1 type			Bonded by Mg^{2+}
Chlorites	2 : 1 layer, trioctahedrons	1.4 nm		Mg^{2+}, Al^{3+}, Fe^{3+}, Fe^{2+} on octahedron sites

[a]Charges on surface atoms are obtained by the semiempirical electronegativity equalisation method (EEM).

Polymer–clay composites are extensively investigated with a view to enhance or facilitate the abovementioned applications [50]. In addition to offering new functionalities, the main outcomes of fabricating polymer–clay composites are to enhance their mechanical strength and viscoelastic property and adjust porosity and density [54, 55]. There are various methods that can be used to prepare polymer–clay composites but the icetemplating method offers a simple and versatile route, particularly with the advantage of producing anisotropic porous structures [24, 55, 56].

Various polymers and clays have been used to fabricate porous composites via the ice templating approach. Pectins are complex carbohydrates that can be obtained from plants and fruits. They have been used as coating or packaging for food and pharmaceuticals. Pectins can easily form gels and can be crosslinked by divalent metal ions. To prepare porous pectin–clay composites, pectin and sodium montmorillonite (NaMMT) were dissolved/suspended in water and the resulting suspension was then frozen and freezedried. Alternatively, $CaCl_2$ solution could be added to form a pectin/clay gel before freezing [57]. The solid content of NaMMT could be adjusted to produce the composites with the moduli in the range of 0.04–

114 MPa and the densities of 0.03–0.19 g cm^{-3} [57]. Casein is a naturally available protein, constituting ~80% of cow's milk protein. A similar procedure was used to prepare casein NaMMT composites. The caseinMMT suspension could be crosslinked using glyceraldehyde before the freezecasting procedure. The crosslinking procedure improved the aerogel structure remarkably but with minimal impact on the density [58]. Natural rubber (NR)–MMT composites were prepared by freezing and freezedrying of aqueous NR/Na MMT suspensions. To prepare the crosslinked aerogel, the freezedried samples were immersed in S_2Cl_2benzene solution and crosslinking by S_2Cl_2 at −18 or 18 °C for 24 h. The crosslinking procedure resulted in a 26fold increase of the compressive modulus to 1.8 MPa [59].

In addition to enhanced mechanical strength, the polymer–clay composites have also exhibited lower thermal conductivity and improved performance in flame retardation. Poly(vinyl alcohol) (PVA, Mn = 31–50 K) composites were prepared with different types of inorganic fillers including silica (12 nm), NaMMT, laponite, and halloysite with aqueous suspensions containing 5 wt% PVA and 5 wt% inorganic nanofiller [60]. The suspensions in polystyrene vials were frozen in a solid CO_2/ethanol bath (−80 °C) and freezedried with an initial shelf temperature of 25 °C and a condenser temperature of −80 °C. Compared to the PVA aerogel, the addition of laponite resulted in ~20% decrease in density and an increase of 10% in modulus but this trend was not obvious for other fillers particularly halloysite and silica. The addition of inorganic fillers did not increase the limiting oxygen index values (~24–25) significantly but resulted in significant decrease in heat release (measured by cone calorimetry), smoke release, and CO production. Figure 6.10 illustrates the heat release rates (HRRs) of the composites with time. It can be seen that the heat release occurs in a very short period for the expanded polystyrene (EPS) packing foam and also significant heat release from PVA only. All four composites exhibited considerably reduced heat release, with the PVA/laponite performing the best [60]. In another effort, the PVA/NaMMT suspensions were crosslinked by irradiation using a ^{60}Co source with different absorbed doses before freezing in liquid nitrogen [61]. Higher dosage of irradiation led to higher crosslinking and higher modulus and then the impact became slightly negative. The content of MMT in the composites affected the modulus and density but these were also affected by the absorbed irradiation dosage. However, the higher percentage of MMT in the composites (e.g. 1% PVA–9% MMT) certainly contributed significantly to reduced heat releasing rates [61].

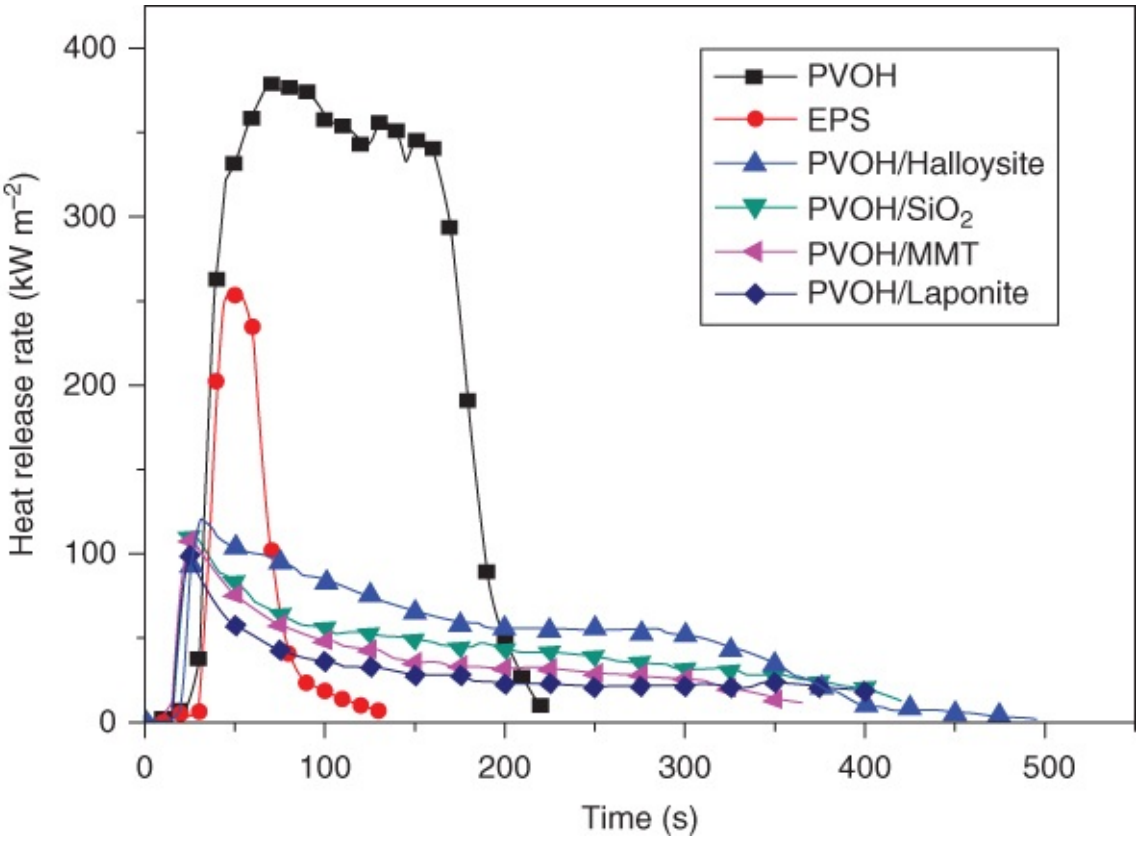

Figure 6.10 The effects of PVOH (polyvinyl alcohol)/clay and PVOH/SiO_2 on heat release rates, compared to PVOH only and the commercial expanded polystyrene (EPS).

Source: Chen et al. 2014 [60]. Reprinted with permission from American Chemical Society.

Furfuryl alcohol (FA) may be produced or converted from biomass. It is soluble in water and compatible with the clays with hydroxylated surfaces such as MMT. FA can be readily polymerized in water or in pure monomer form in the manner of head to head or head to tail, catalysed by acid. Homogeneous aqueous suspension of FA and NaMMT were polymerized by adding a small amount of sulfuric acid while stirring and at a temperature of 100 °C. The contents were poured into polystyrene vials for freezing in dry iceethanol bath and then freezedried [62]. The crosslinked composite aerogels showed low flammability, withstanding a gas flame for over 20 s without noticeable combustions [62].

Nanofibrillated cellulose (NFC)–MMT composites were prepared by both directional freezing (in PTFE mould with copper bottom, on copper cold finger, precooled to 4 °C, a freeze rate of 10 °C min^{-1} then applied until reaching −150 °C) and nondirectional freezing (in aluminium cups, precooled at 4 °C overnight and then freezed in liquid nitrogen) [63]. The freeze dried samples were tested by compression. The anisotropic samples were compressed both parallel and perpendicular to the freezing direction. Young's modulus was observed to increase from isotropic composites, to anisotropic testing by perpendicular direction (~2.5–6 times), then to anisotropic testing by parallel direction (~10–85 times), depending on the content of NFC. For the yield strength, the order of anisotropic (parallel) > isotropic > anisotropic (perpendicular) was observed for all the samples. For the work to failure, the values for isotropic and anisotropic perpendicular tests were close while it was much higher for

anisotropic parallel testing. For each type of material, the increasing content of NFC led to increase of Young's modulus, compressive strength, and toughness. Although NFC is flammable, the addition of MMT improved the heat endurance and shape retention up to 800 °C while the mechanical properties were maintained up to 300 °C [63].

6.4 Porous Ceramic–Ceramic Composites

The objectives of preparing ceramic–ceramic composites usually include obtaining enhanced mechanical properties, combining the useful properties of the ceramic components, and offering a synergy effect between components or new properties [1–10]. When preparing porous ceramic–ceramic composites by the freezecasting method, the ceramic particles can be simply blended and suspended in a suitable solvent. The slurries are then frozen and freezedried. Alternatively, the freezecasting method can be used to fabricate porous ceramics. The second ceramic component is then incorporated into the first icetemplated ceramics by methods such as impregnation or chemical vapour deposition (CVD).

Most of the porous ceramic composites are prepared directly by freezecasting of the blended ceramic slurries, e.g. lanthanum strontium manganite (LSM)–YSZ [64, 65], kaolinite–silica [66], Al_2O_3–ZrO_2 [67–69], mullite–alumina [70], HfB_2–$MoSi_2$ [71], and HAbased composites [72–74]. For the twostage method, porous Si_3N_4 was first formed by freeze casting. A silica sol was impregnated into the pores and the subsequent gelation and solvent replacement and evaporation led to the formation of silica aerogel within the porous Si_3N_4 [75]. In another example, carbon nanotubes (CNTs) aerogel was first prepared by freeze casting and then exposed to methyltrichloromethane in a CVD furnace. The vapour could readily infiltrate into the porous CNT. After the CVD process, porous CNT/SiC composites were generated [76].

For the Al_2O_3–ZrO_2 composites, when the solid content was increased from 40% to 70%, an increase of compressive strength from 15 to 81 MPa was observed, while the porosity decreased from 74% to 35% [67]. The size of the ceramic particles (associated with their densities) could affect the strength of the ceramics and their relative concentration in the ceramic composites [68]. For the threelayer Al_2O_3–ZrO_2 composites, a graded porous structure was observed, with the compressive strength in the range of 63–376 MPa for the sintered ceramics [69]. The mullite–alumina with a gradelayered pore structure also exhibited improved compressive strength [70]. For the kaolinite–silica composites, the improved strength was related to the solid loading and the packing and interfacial contact of silica and kaolinite particles [66]. The aligned porous LSM–YSZ composites combined electronic conduction from LSM and ionic conduction from YSZ while the aligned porous structure could provide a direct percolation pathway for ionic and electronic species [64, 65]. This can be highly beneficial as electrode materials for solid oxide fuel cells. The ultrahigh temperature ceramics were demonstrated by the preparation of HfB_2–$MoSi_2$ composites via a gelcasting route. The solid loading could be used to tune the mechanical properties including flexural strength and fracture toughness. The values of the fracture toughness for the sintered

ceramics were in the range of 2.18–4.24 MPa [71].

For HAbased ceramic composites, HA provides the required biocompatibility for bone tissue engineering while the addition of other ceramics can enhance the mechanical stability of the porous scaffolds. In the HA–SiO_2 composites, the addition of silica nanoparticles introduced the partial phase transformation of HA to βTCP, which improved the thermal stability with less shrinkage after sintering and the attachment and proliferation of human osteoblastlike cells [72]. With the addition of alumina nanoparticles, both the pore size and compressive strength were increased. This could be attributed to the formation of calcium aluminate phases, increased wall density and thickness, and reduced porosity [73]. With the inclusion of barium titanate in the HA ceramic composites, the piezoelectric effect was introduced to the scaffold, which played an important physiological role in bone growth and fracture healing. For the composites containing 70% and 90% barium titanate, the piezoelectric coefficient d_{33} was found to be 1.2 and 2.8 pC/N, respectively [74].

In the composites of Si_3N_4–silica aerogel, Si_3N_4 is a wavetransparent material while the mesoporous silica aerogel provides very good thermal insulation. The icetemplated pores are too large compared to the mean free path of air molecules (~69 nm) and thus cannot provide efficient thermal insulation. Indeed, the prepared composite with silica aerogel showed low thermal conductivity (0.043 W $(m\,K)^{-1}$), low dielectric constant (~1.6) and loss tangent (~0.0018) [75].

6.5 Nacrelike Layered Ceramic–Polymer Composites

6.5.1 Nacre and Nacremimic Composites

It has been long recognized that it is a huge challenge to produce materials with high strength and high toughness because these two properties are usually mutually exclusive [20]. Learning from Nature where extraordinarily strong and tough materials exist [21, 22, 77], it is possible to fabricate such materials by combining minerals/ceramic particles and organic layers such as polymer and proteins. The nanoscale and weak interfaces between minerals and organic layers seem to be the main cause for the toughening effects. The toughening mechanisms include the alleviation of locally high stresses and different extrinsic mechanisms such as crack deflection, bridging, and friction [20, 77].

Among various tough composite materials, nacre and nacremimic layered materials are widely investigated [21–23, 78]. Nacre adopts a unique brickandmortar structure. Nacre consists of 95% volume fraction of inorganic component (aragonite calcium carbonate platelets) and about 5% of organic polymer (chitin and protein) [22, 78]. The inorganic platelets are 8–10 μm wide and 0.4–0.5 μm thick. They are largely stacked/assembled into inorganic layers, with a distance of 20 and 50 nm between them, which is filled with the organic component. There are nanoasperities of 10–30 nm in width (with a distance of 100–200 nm between them) on the surface of the microplatelets. The microplatelets are also connected by mineral bridges [77, 78]. Nacre exhibits exceptional mechanical properties. Its

tensile strength and Young's modulus are in the range of 80–135 MPa and 60–70 GPa [23, 78]. A typical tensile stress–strain curve is shown in Figure 6.11 [79]. The hydrated nacre can give a much higher tensile toughness compared to that of the dry nacre. The elongation of the fibril organic polymer/protein is about 100 nm before stiffening. This corresponds well with the inelastic deformation of nacre (~1%) [23]. The fracture toughness can be as high as 1.5 kJ m^{-2} [78]. It is obvious that the inclusion of a small percentage of organic layer in nacre improves the strength and toughness of 20–30 times compared to the pure monolithic aragonite [22]. This is attributed to multiple energy dissipation mechanisms, as proposed by Mayer [80] and is summarized below:

- Crack deflection, delamination, microcracking due to weak interfaces
- Anchoring, crosslink breaking, polymer chain deformation and unfolding, ligament formation of the organic phase, and crack bridging by organic ligaments
- Pullout of the ceramic phase, friction resistance due to surface toughness/mineral bridges of the platelets, and hole formation at the ends of displaced ceramic phase
- Plasticizing effects on the polymer layer by moisture
- Residual stresses to energy absorption.

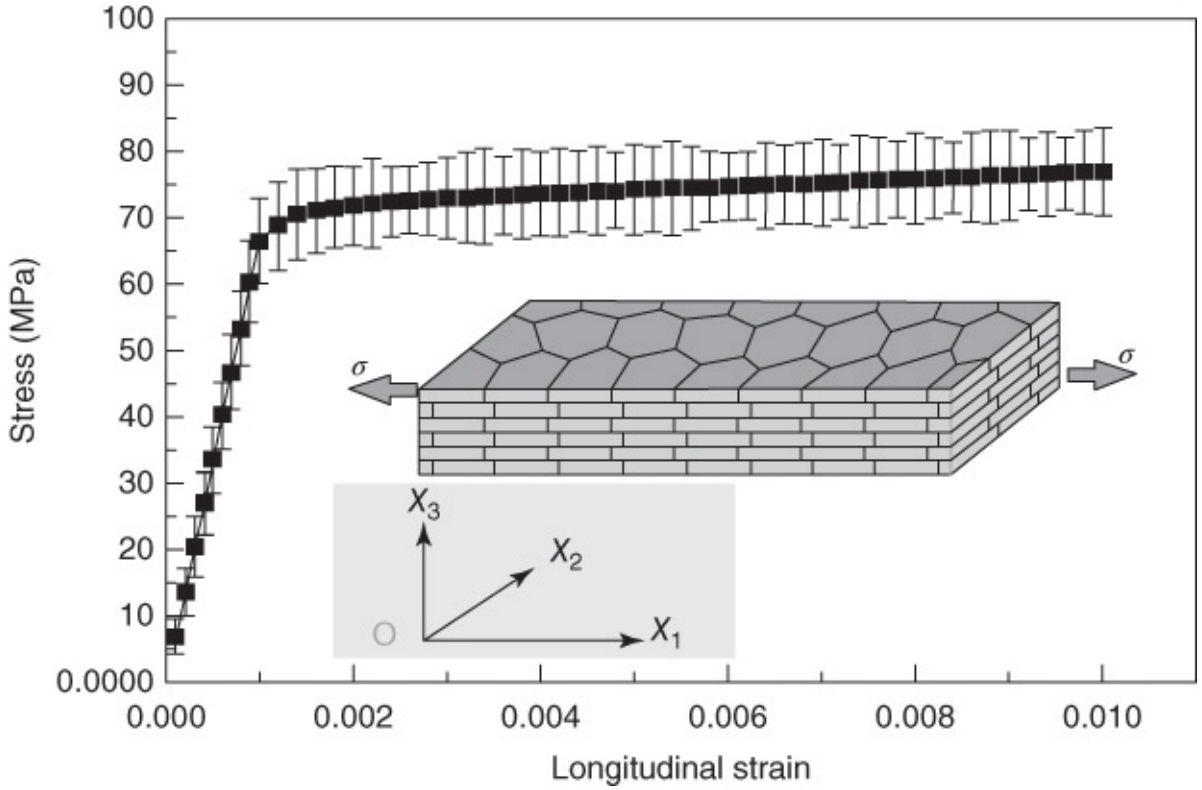

Figure 6.11 A representative stress–strain curve for nacre.

Source: Song et al. 2008 [79]. Reprinted with permission from American Physical Society.

Different methods have been utilized to prepare layered materials. The traditional methods such as tape casting and slip casting may be difficult to produce the layer thickness into the small micron or nanoscale region [17]. The electrophoretic deposition is slow and is difficult

for the preparation of largesized materials [23]. The LBL deposition is a versatile method to prepare layered materials with controllable thickness. The method mainly depends on the electrostatic interaction between the two components. For example, the polymer with positive charges, chitosan, and negatively charged clay particles (e.g. MMT) and alumina particles have been used to prepare composite materials [23]. However, the LBL approach is time consuming and it is very difficult to generate layered composites with high percentage of inorganic components. Recently, the freezecasting approach has been intensively used to fabricate tough nacre–mimic composite materials [21–24, 56]. By controlling the slurry compositions and freezing parameters, ceramic particles can be excluded from the freezing front, forming dense ceramic layers between ice crystals [81]. The layer thickness and the spaces between layers can be adjusted by controlling the freezing conditions (and other post treatments for the dry porous scaffold, see following discussion). This freezing step is also highly effective in assembling ceramic platelets [46, 82]. The layered porous ceramics can be produced after freezedrying and sintering. Subsequently, organic polymers may be incorporated into the pores, resulting in layered composites.

6.5.2 Layered Polymer–Ceramic Composites by Infiltrating Ice templated Porous Ceramics

Porous alumina with layered structures can be fabricated via directional freezing. The thickness of the alumina walls and lamellar spacing can be effectively tuned by changing the velocity of the freezing front [81]. This approach is highly versatile. For example, a layered porous HA scaffold was fabricated by freezecasting and then filled with an organic phase epoxy resin to create a nacrelike composite [81]. The HA–epoxy composite has a much higher loaddisplacement profile. Indeed, the HAbased composite exhibited exceptional stiffness (10 GPa), strength (150 MPa), and work of fracture (220 J m^{-2}) [81]. Porous alumina with lamella length up to 70 mm was fabricated from aqueous slurries with solid alumina (particle size D_{50} = 390 nm) contents of 25–45 vol%. The freezedried green body was sintered at 1550 °C. An epoxy resin was infiltrated into the porous alumina under vacuum and then left for 24 h for the resin to harden [83]. The composite exhibited fracture toughness of 2.92 MPa $m^{½}$, and Weibull strength of up to 117 MPa [83].

Nacre exhibits a very high inorganic component (~95%) and a mortarandbrick structure. It is obvious that simply infiltrating a polymer phase into a layered porous ceramic does not meet this requirement. The issues are as follows: (i) the ceramic layer does not allow sufficient infiltration into itself (i.e. a layered composite but not a mortarandbrick structure); (ii) the content of the inorganic component in the composite is too low; (iii) there appears to be only a limited interaction or no interaction at all between the polymer phase and the ceramic phase. To address these issues, Ritchie and coauthors developed a method to fabricate highly toughened alumina–polymer composites with high yield strength (~210 MPa) and fracture toughness (~30 MPa $m^{½}$) [84, 85]. A procedure was developed to hot press the porous alumina scaffold and condense and break the layered structure. Sucrose was used as an additive in the slurry during the freezing process, which helped to produce a layered porous structure with

rough spiked surface. In order to reduce the porosity (and thereby increase the content of the inorganic component in the composite) and create a brickandmortar structure, the scaffold was firstly infiltrated with paraffin wax and then uniaxially pressed at 80 °C (just melting paraffin wax) at ~50–100 MPa. The wax phase facilitated the densification of the porous structure at 80 °C and then held the bricks (broken lamellar structure) together. A further thermal treatment at 400 °C (2 h) and 1500 °C (2 h) in air removed the organic phase and promoted further densification. In the final step, the scaffold was pressed isostatically at 1.4 GPa followed by another step of heating treatment (1500 °C, 2 h) to facilitate the formation of inorganic bridges between the bricks [84, 85]. The interaction between the polymer phase and alumina phase was addressed by grafting the polymer to the ceramic bricks. This was achieved by first grafting 3(trimethoxysilyl)propyl methacrylate (γMPS) to the alumina washed by a Piranha solution, via the reaction between -OH and SiOMe (methoxysilyl group). A partially polymerized methyl methacrylate (MMA) with high content of initiator was then impregnated into the γMPSgrafted alumina. The impregnated scaffold was annealed at 150 °C under nitrogen for 2 h to complete the polymerization and the grafting. Using this method, PMMA–grafted alumina composite with a brickandmortar structure and an alumina content of ~80% has been produced [84, 85].

For comparison, the brickandmortar composites with nongrafted PMMA and the lamellar composites with both types of PMMA (grafted and nongrafted) were also prepared [84, 85]. High yield strengths (120 and 210 MPa) were obtained for nongrafted and grafted brick andmortar composites, respectively. Remarkably, these composites showed >1% inelastic deformation before failure. *J–R* curves were used to characterize the toughness behaviour of nonLEFM observed in these composites. A rising *R*curve demonstrated the extensive extrinsic toughening. The lamellar and brickandmortar composites could reach fracture toughness of 15 MPa $m^{½}$ (J_c ~ 5000 J m^{-2}) and 30 MPa $m^{½}$ (J_c ~ 8000 J m^{-2}), respectively, much higher than that by nacre and the homogeneously compressed alumina particles). The effects of strong interface (PMMA–grafted alumina) and weak interface (nongrafted PMMA–alumina) on fracture toughness (K_J) were investigated. In general, the strong interface in the composites enhanced the fracture toughness (Figure 6.12). The fracture toughness only slightly increased (e.g. 12–16 MPa $m^{½}$, Table 6.3) for lamellar structures while the values were doubled for the brickandmortar composites [85]. Multiple toughening mechanisms were observed, including ligament bridging, crack deflection/delamination, void growth, microcracking, and inelastic deformation. Particularly, the cracking and the extent of damage were not localized. In the lamellar composites, the relatively thick PMMA layer still played a structural and loadbearing role. However, for the brickandmortar composites, the pull out toughening of the bricks was significant, quite like most of the engineering structural ceramics. The unique toughening mechanism was from the sliding between the alumina blocks facilitated by the submicro PMMA film. This also explained the stronger effect of grafting polymer phase on the fracture toughness of the brickandmortar composites. The grafting could provide a more effective viscoelastic phase that permits but limits the extensive interface sliding [85].

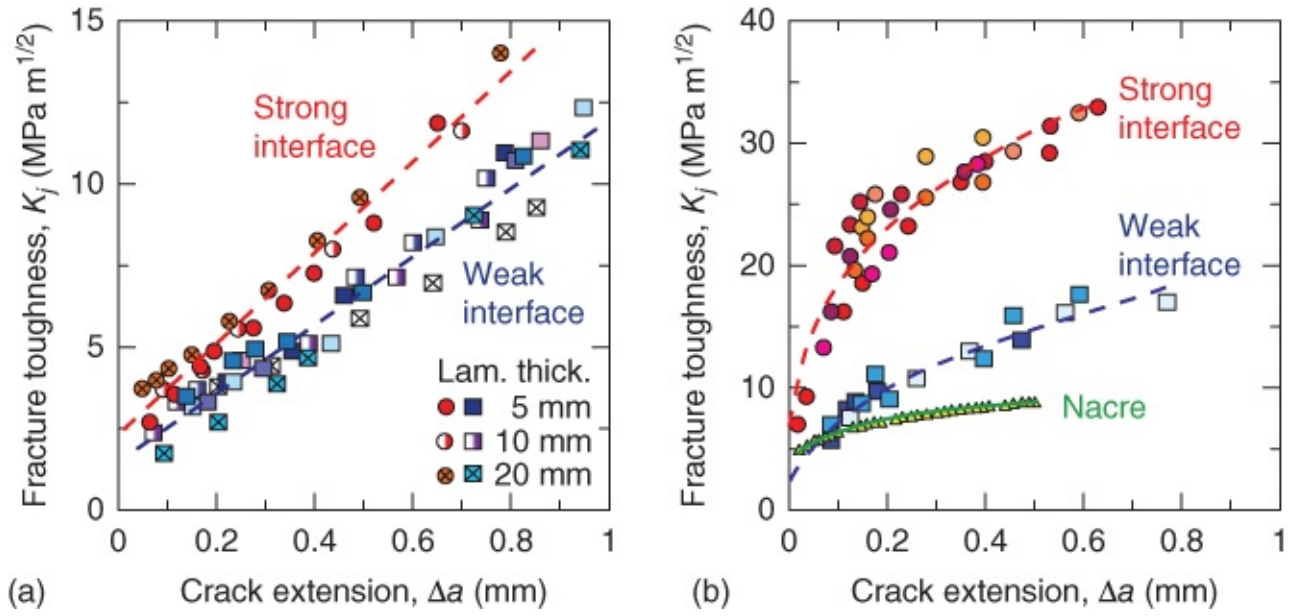

Figure 6.12 The plots of the stress intensity, K_J, as a function of crack extension, show the crackresistance behaviour of (a) lamellar alumina–PMMA composites and (b) brickand mortar alumina–PMMA composites.

Source: Launey et al. 2009 [85]. Reprinted with permission from Elsevier.

Table 6.3 Mechanical properties of layered ceramic composite materials.

Sample	Flexural strength	Hardness	Fracture toughness[a]	Fabrication method	References
HA/epoxy	150 MPa	10 GPa	220 J m^{-2}	Freeze casting	[81]
Alumina/epoxy	117	140 GPa	2.8 MPa m^{½}	Freeze casting	[83]
Alumina–PMMA (nongrafted)	90 MPa		12 MPa m$^{1/2}$ (K_{JC})	Freeze casting	[85]
Alumina–PMMA (grafted)	112 MPa		12 MPa m$^{1/2}$ (K_{JC})	Freeze casting	[85]
Alumina–PMMA (hot pressed, non grafted)	115 MPa		15 MPa m$^{1/2}$ (K_{JC})	Freeze casting, mortar and brick	[84, 85]
Alumina–PMMA (hotpressed, grafted)	210 MPa		32 MPa m$^{1/2}$ (K_{JC})	Freeze casting, mortar and brick	[84, 85]
Alumina–cyanate ester	300 MPa	11 GPa		Freeze casting, interlocked structure	[86]
HA/PMMA	100 MPa	20 GPa	2075 J m^{-2}	Bidirectional freezing, grafting	[87]

Aragonite/silk fibroin			3 MPa $m^{1/2}$ (K_{JC})	Mineralization in icetemplated chitin	[88]
Zirconia/epoxy	160 MPa	4.0 GPa		Freeze casting with *n* butanol clathrate hydrate effect	[89]
Graphene/SiOC	63 MPa		3–3.5 MPa $m^{1/2}$	Graphene network by freeze casting	[90]
CNTs/epoxy	150 MPa	24 GPa	4.26 KJ m^{-2}	CVD for CNT forest	[91]
Alumina/PMMA	220 MPa		8.5 MPa $m^{½}$	Magnetically assisted slip casting	[92]
Zirconia/epoxy	Shear strength 51 MPa	Shear modulus 5.5 GPa		Helixreinforced, magnetic freeze casting	[93]
Alumina/AlSi	300 MPa		40 MPa $m^{½}$	Freeze casting	[94]
SiC/2024Al	931.3 MPa		18 MPa $m^{½}$	Freeze casting	[95]
SiC/AlSiMg	722 MPa	140 GPa		Freeze casting	[96]
Alumina/silica calcia	470 MPa	290 GPa	22 MPa $m^{½}$	Freezing and hot pressing	[97]
Alumina/silica alumina	650 MPa	190 GPa	14 MPa $m^{½}$	MASC	[92]
Alumina/titania	370 MPa	150 GPa	6.5 MPa $m^{½}$ (K_{IC})	MASC	[98]
Alumina/graphene	523 MPa	17.66 GPa	4.49 MPa $m^{½}$	Solvent evaporation and hot pressing	[99]
Si_3N_4/graphene			6.6 MPa $m^{½}$	Solvent evaporation and hot pressing	[100]
ZrB_2SiC/graphene	522 MPa	12.5 GPa	9.45 MPa $m^{½}$	Selfassembled and hot pressing	[101]

[a]These values are quoted from relevant references. The data may not clearly indicate whether they are fracture toughness at initial cracking or the maximum fracture toughness. Readers are suggested to read the original references carefully.

Zhao et al. added SCMC (4–9%) to alumina slurries, which facilitated the formation of highly ordered ceramic bridges between alumina layers (9 wt% SCMC in the slurries) (Figure 6.13) [86]. The freezedried scaffolds were sintered at 1600 °C for 4 h before cyanate ester was infiltrated under vacuum and cured at 220 °C in an aircirculated oven. This method did not

employ the hot pressing procedure but produced a nacre–mimic interlocking composite structure. The composite exhibited a flexural strength of up to 300 MPa, a specific strength of 162 MPa $(g\,cm^{-3})^{-1}$ (i.e. the strength divided by the density), and a failure strain of 5% [86]. Since it has been very difficult to produce ceramics with large domains of lamellar structure (mm) by the conventional freezecasting approach, Bai et al. employed a bidirectional freezing method to fabricate nacrelike composites as large as 4 × 8 x 25 mm [87]. A PDMS wedge was introduced between the cold finger and the slurry, promoting the formation of longrange lamellar structure. This was demonstrated by the fabrication of HA/PMMA composites (grafted mortarandbrick structure). The longrange lamellar structure was pressed uniaxially to give densified scaffolds with porosity of 15–25%. Similarly to that reported previously [84, 85], monomer MMA and initiator 2,2azobisisobutyronitrile (AIBN) were infiltrated into the γMPSgrafted scaffold. The in situ polymerization at 40 °C and aging at 90 °C for another 2 h produced the HA–PMMA composites with high ceramic content (75–85%) and excellent mechanical properties (flexural strength 100 MPa, Young's modulus 20 GPa, and work of fracture up to 2075 J m^{-2}) [87]. In addition to in situ polymerization of the monomers, PMMA may be incorporated into the ceramic scaffolds by emulsion polymerization [102].

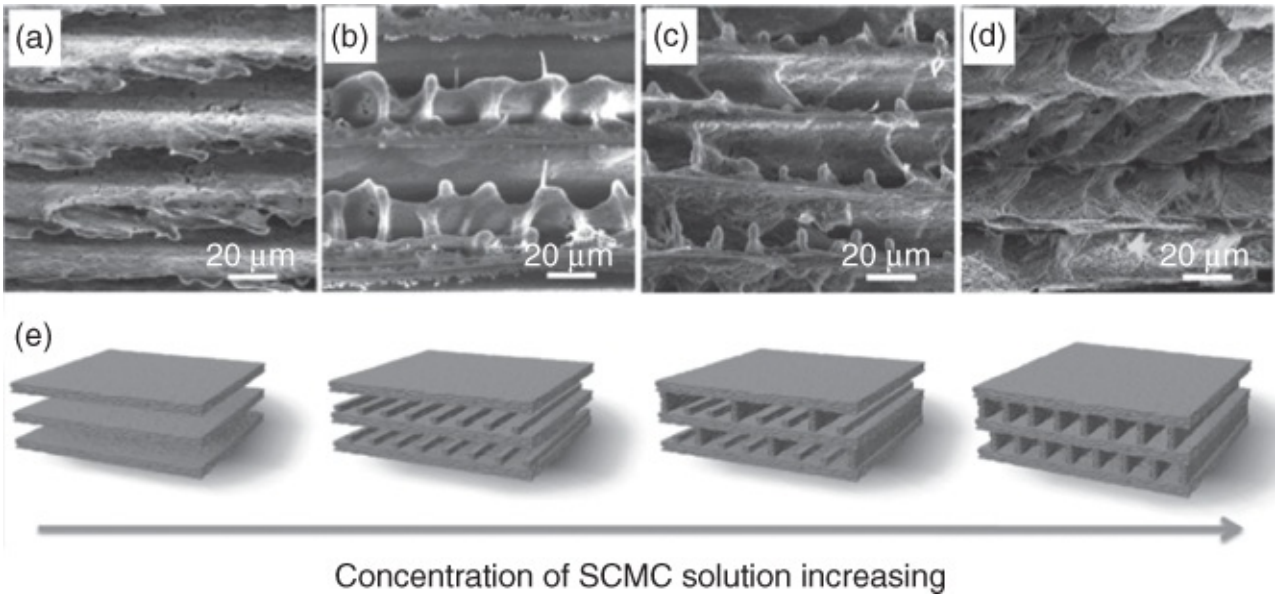

Figure 6.13 Addition of SCMC promotes the formation of bridges between alumina layers as shown by SEM images (a–d) with the SCMC concentrations of 4, 5, 7, 9 wt%, respectively, and the schematic description (e).

Source: Zhao et al. 2016 [86]. Reprinted with permission from John Wiley and Sons.

The incorporation of a second organic phase into layered porous ceramics is also effective in the fabrication of composite scaffolds with stronger mechanical properties. For example, PCLacetone (1.5 and 5.0 wt%) solution was impregnated into an icetemplated porous β TCP. Because the amount of PCL was small, PCL was only infiltrated into the small pores within the lamellar layers and coated the layer surface as thin film while the macroporosity was retained [103]. Compared to the just freezedried βTCP porous scaffold, the porous composites exhibited considerably improved mechanical properties: e.g. flexural strength

increased from 3.4 to 5.3 MPa (4.2 vol% PCL) and 5.6 MPa (5.6 vol% PCL) and compressive strength increased from 4.4 to 6.0 MPa (0.7 vol% PCL), 9.5 MPa (4.4 vol% PCL) and 10.3 MPa (7.6 vol% PCL) for the samples prepared from the slurries with a solid content of 20 vol% and onset freezing velocity 20 μm s^{-1} [103].

Furthermore, the concept of harnessing hydrophobic hydration and clathrate hydrate has been explored for the fabrication of stronger composites [89]. This approach is based on the addition of alcohols into aqueous slurries. In dilute aqueous solution, a hydrophobic molecule (such as alcohol with C-H chain) can bond to water molecules and pattern them around itself, a phenomenon called 'hydrophobic hydration', as illustrated in Figure 6.14. This phenomenon occurs in the liquid state at or around room temperature with an important parameter being the number of molecules being patterned (n_h). The freezing process can transform such structure into a clathrate hydrate (Figure 6.14) [89]. Alcohols, amines, amides, and some polymers such as PVA are potential additives to form clathrates. For example, ethanol, *n*propanol, and *n* butanol were added to aqueous ZrO_2 slurries for the freezecasting process. The green bodies were sintered at 1350 °C for 3 h in air. The important findings were that the pore area reached a maximum point at a suitable concentration. But the concentrations for maximum pore areas were different for different alcohols, 10 vol% for ethanol, 5 vol% for *n*propanol, 3 vol% for *n* butanol [89]. This suggested that the concentration decreased with the increasing chain length of alcohol molecules. Interestingly, after impregnating the porous ceramics with epoxy to produce the composite materials, higher ultimate compression strength (UCS) and Young's modulus were always observed for ceramics made at such additive concentrations, usually higher than >50%. This is different from the eutectic crystallisation formed from the additive alcohol and water under suitable conditions [104]. While studying the eutectic effect, it was observed that, in addition to the usual icetemplated macropores, mesopores were generated in the freezedried material and the porosity was characterized by gas sorption study [104]. However, in the case of clathrate hydrate effects, the pore size and area were calculated from SEM images using ImageJ software, assuming ellipse pores with major axis *a* and minor axis *b*. The enlarged hydrate structures resulted in enlarged ice crystals and hence larger pores, as evidenced by ImageJ calculation. This also led to larger pore area, contributed positively to the strength of the composites [89].

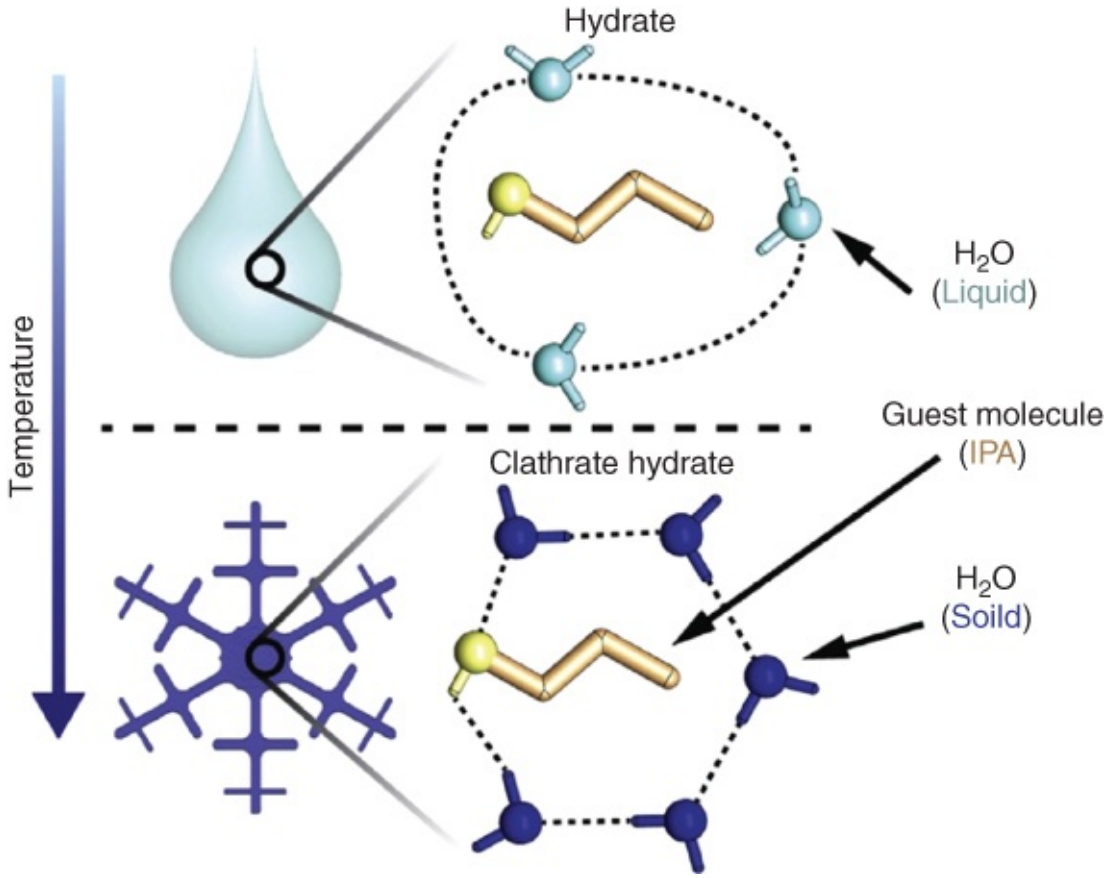

Figure 6.14 The diagram illustrates hydrophobic hydration and transformation into clathrate hydrates via a freezing path, based on the example of npropanol molecule.

Source: Naleway et al. 2016 [89]. Reprinted with permission from Elsevier.

Instead of incorporating an organic phase into a ceramic scaffold to fabricate nacrelike composites, mineralization in preformed matrix has been reported recently to generate synthetic nacre [88]. In this method, porous chitosan was first prepared by the icetemplating approach and then transformed into waterinsoluble chitin by acetylation. The fine dispersion of $Ca(HCO_3)_2$ (in the presence of polyacrylic acid and Mg^{2+}) was pumped into porous chitin. The chitin layers were assimilated with the gradual mineralization of the matrix. The aragonite phase was obtained by decomposition of $Ca(HCO_3)_2$. The nacrelike composite was formed by silk fibroin infiltration and hot pressing at 80 °C. This synthetic nacre exhibited a structure similar to that of natural nacre, with 91 wt% of aragonite phase, 2–4 μm thick aragonite layers, and 100–150 nm silk fibroin layers [88]. Like natural nacre, a rising crackextension profile was observed. This synthetic nacre showed a fracture toughness of ~3 MPa $m^{½}$, a specific strength of ~30 MPa $(g\,cm^{-3})^{-1}$, and a specific toughness of ~1 MPa $m^{½}$ $(g\,cm^{-3})^{-}$ (i.e. toughness divided by the density) [88].

Porous graphene networks were formed by freeze casting aqueous grapheme oxide suspension and subsequently reduced to graphene at 900 °C. A 20% volume shrinkage was observed after this treatment. A preceramic polymer, polymethyl siloxane, was then infiltrated into the graphene network. The graphene/SiOC composites were produced by pyrolysis under N and heat treatment at 1000 °C and densified using spark plasma sintering (SPS) [90]. The

composite contained a network of very thin (20–30 nm) carbon phase and thus was electrically conductive. This could be used to sense the damaging effect in the composite because a rise in voltage could result from microcracking before fracture and the voltage could be recovered if the network connectivity was recovered. The composite showed an initiation toughness of 1.7 MPa $m^{½}$ and a maximum toughness of 3–3.5 MPa $m^{½}$ when the rising *R*curve reached the steady state, a calculated work of fracture around 46 J m^{-2} [90]. Carbon networks could also be formed by other methods and utilized to form strong composites. For example, the CVD technique was used to grow CNT forest perpendicular to woven SiC fabrics [91]. The nanotubegrown fabrics were infiltrated with epoxy and stacked together to produce layered composites. These composites gave rise to excellent mechanical properties such as flexural strength 150 MPa, flexural modulus 24.3 GPa, and work of fracture 4.26 KJ m^{-2} for G_{IC} and 140 J m^{-2} for G_{IIC} [91].

6.5.3 Magnetic Fieldassisted Freezecasting for Strong Composites

The application of magnetic fields is convenient to align particles and control their distribution in composites. The only problem is that most ceramic particles are either paramagnetic or only exhibit very weak magnetic properties. Very strong magnetic fields (>1 or even >10 T) are required to control the distribution of feeble magnetic ceramic particles [105, 106]. This problem can be addressed by coating the ceramic particles with superparamagnetic nanoparticles such as iron oxide. Particularly, by using the correct geometry of coated ceramic particles, an ultrahigh magnetic response can be achieved and hence only a weak magnetic field is required to align the particles. For example, alumina platelets (7.5 μm long and 200 nm thick) and calcium sulphate hemihydrate rods (10 μm long, 1 μm thick) were coated with 12 nm iron oxide nanoparticles. A weak magnetic field of 0.8 mT was required to tune the 3D orientation and distribution in a suspension containing polymers or monomers. The composites could be subsequently produced by evaporating the solvent or polymerizing the monomers [105]. The alumina platelets coated with iron oxide nanoparticles were then used in a magnetically assisted slip casting (MASC) process [92]. The rotating magnetic field could be programmed and applied to control the alignment/angle of the assembled platelets. After heating at 500 °C for 3 h to remove the organic binder, the MASC ceramic was uniaxially hot pressed (up to 100 MPa), which increased the volume fractions of the platelets from 35 to 60 vol%. At this stage, the monomer MMA could be infiltrated and the subsequent polymerization led to the production of alumina–PMMA composite. This composite showed a fracture toughness of 8.5 MPa $m^{½}$, fracture strength of 220 MPa, and specific strength of 76 MPa (g cm^{-3})$^{-1}$ [92].

The magnetic field can be combined with a freezing process [106]. When the orientation of the magnetic field is perpendicular to the freezing direction, the magnetic force could facilitate the formation of bridges between the ceramic layers in slurries containing ceramics such as alumina and a small percentage of iron oxide nanoparticles (e.g. 3 or 9 wt%). When a rotating field is applied, ceramic scaffolds with a spiral pattern of iron oxide can be produced [106].

This method was applied to fabricate helixreinforced composites with enhanced torsional properties [92]. Aqueous ZrO_2 (diameter 0.2–0.5 μm) slurries with solid content of 10 or 20 vol% and 3 wt% (of the solid content) 50 nm Fe_3O_4 nanoparticles were directionally frozen with a rotating magnetic field of 0.12 T. The green bodies were sintered in air at 1300 °C for 3 h, followed by the infiltration with epoxy [93]. Figure 6.15 shows the ZrO_2–epoxy composite containing 40% or 60% zirconia. The spiral patterns can be clearly seen and are affected by the rotating speed of the magnetic field 0.12 T. The dark stripes are concentrated Fe_3O_4 particles and the distance between the stripes becomes smaller with the increasing rotating speed. The helix angle changes with the variation of rotating speed as well. Inorganic bridges can be clearly seen between the ceramic layers (Figure 6.18d and e). Shear strength up to 54 MPa and shear modulus up to 5.5 GPa were recorded for these helixreinforced ZrO_2–epoxy composites [93].

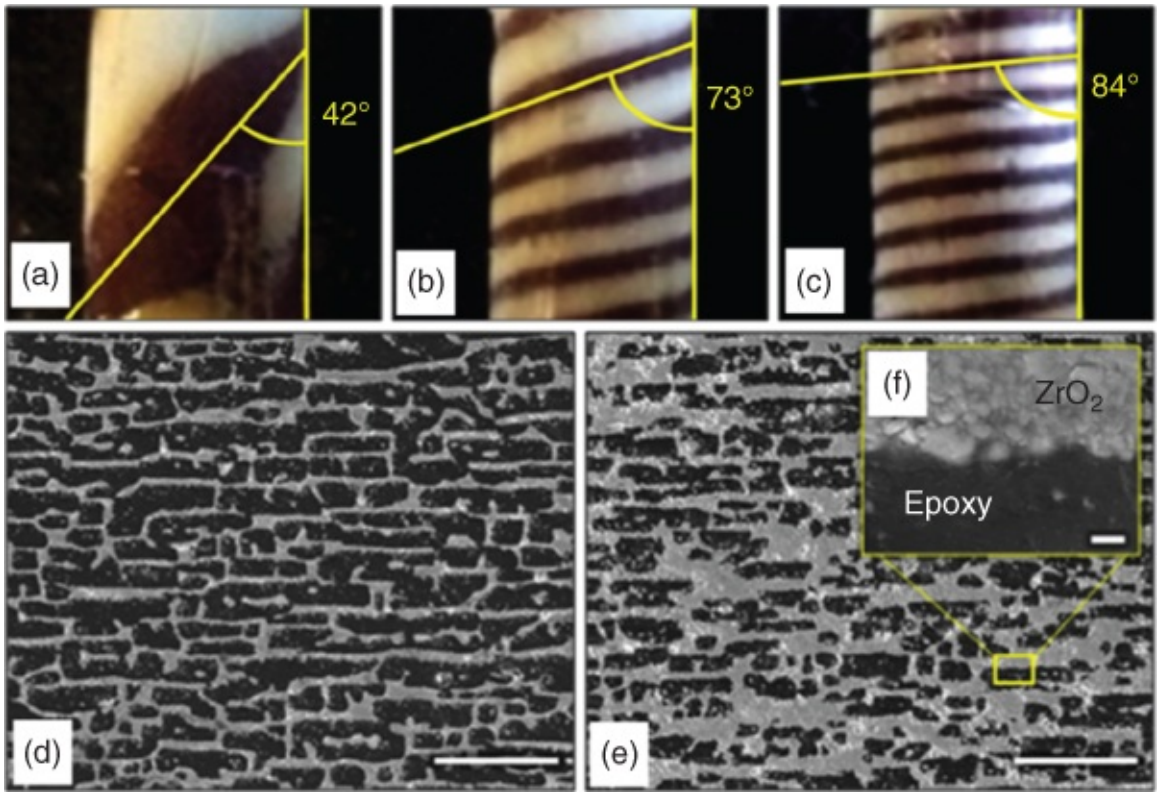

Figure 6.15 Helixreinforced zirconia–epoxy composites via a magnetically assisted freeze casting process. (a–c) Show the images of 40 : 60 composites under a rotating magnetic field of 0.12 T at the speed of (a) 0.05 rpm, (b) 0.20 rpm, and (c) 0.40 rpm. The helix angles are also illustrated in the images. (d–f) Show the structure by SEM imaging of (d) 40 : 60 composite, (e) 60 : 40 composite, and (f) the magnified structure of the 60 : 40 composites.

Source: Porter et al. 2015 [93]. Reprinted with permission from Elsevier.

It is clear that the polymer phase plays a significant role in enhancing fracture toughness in nacrelike composites. While the organic phase in natural nacre consists of chitin and protein, the synthetic nacres investigated so far mostly contain PMMA and epoxy resin as the organic phase (Table 6.3). The use of different polymers and the role of polymer phase in the energy

dissipating toughening mechanisms are essential to fabricate toughened composites. Different polymers were thus infiltrated into the porous alumina produced by the MASC approach (silica nanoparticles included to introduce mineral bridges and nanoasperities) [107]. These polymers were carefully selected with different properties: (i) poly(lauryl methacrylate) (PLMA), a soft and weak elastomer; (ii) PMMA, a strong, stiff and brittle thermoplastic; (iii) polyether urethane diacrylatecopoly(2hydroxyethyl methacrylate) (PUAPHEMA), a polymer of immediate strength and stiffness. The monomers were infiltrated into the hot pressed ceramics and polymerized in situ. The flexural strength and fracture behaviour were assessed by threepoint bending. As shown in Table 6.4, compared to the scaffold without polymer, the effects of the polymer phase on the composites are clearly different, depending on the types of the polymers. With the soft polymer PLMA, the mechanical properties are very similar to the scaffold and the fracture toughness even decreases. For the stiff and brittle PMMA, the fracture strength is the highest while fracture toughness is lower than the composite containing PUAPHEMA. The tougher polymers also contribute to increased strains at failure while flexural modulus does not change much over the four materials. Based on the K_{JC}crack extension graph, the rising *J–R* curves were observed to the crack extension of 0.8 mm and were still not steady for both PMMA and PUAPHEMA composites [107].

Table 6.4 Mechanical data of nacrelike composites of alumina with different polymers.

Source: Niebel et al. 2016 [107]. Adapted with permission from Elsevier.

Materials	**Flexural modulus (GPa)**	**Fracture strength (MPa)**	**Strain at failure (%)**	**Fracture toughness[a] (MPa $m^{½}$)**	**Work of fracture (J m^{-2})**
Alumina scaffold	35.0 ± 8.1	99.7 ± 9.9	0.27 ± 0.06	1.88 ± 0.21	42.6 ± 8.7
Alumina–PLMA	35.3 ± 5.4	99.9 ± 10.3	0.25 ± 0.02	1.43 ± 0.30	42.4 ± 7.8
Alumina–PMMA	36.6 ± 6.7	182.3 ± 13.8	0.43 ± 0.06	2.40 ± 0.35	110.0 ± 4.2
Alumina–PUA PHEMA	36.8 ± 3.8	168.1 ± 17.5	0.44 ± 0.03	3.39 ± 0.28	156.2 ± 1.7

[a]The values are for fracture toughness at crack initiation.

6.6 Nacrelike Ceramic/Metal Composites

In order to enhance fracture toughness, composites are usually fabricated from a brittle material scaffold and a second ductilephase material. Lamellar composites have shown to be mostly effective in increasing toughness, compared to particles and fibres, for the same volume fraction of ductile reinforce phase [94]. Metals have been widely used as ductile phase to

prepare ceramic–metal composites (CMCs). It is thus quite straightforward to fabricate nacrelike CMCs by replacing polymer with metal. Unlike the use of polymer solution or liquid phase monomers, metal melt will have to be infiltrated into a porous icetemplated ceramic scaffold.

Layered porous alumina was fabricated by freeze casting and then sintered at 1550 °C for 1 h. A eutectic aluminium–silicon alloy (Al–12Si) was infiltrated into the porous alumina [108]. The elastic constants of the composites were obtained by a wave velocity approach. The composite fabricated from the scaffold with the finer structure exhibited a density of 3.18 ± 0.04 Mg m^{-3} and an elastic constant (C_{11}) of 240 ± 10 GPa [108]. In another study, the alumina scaffold was heated to 900 °C under a 10^{-4} Pa vacuum. An argon gas pressure of 70 kPa was introduced to facilitate the infiltration of the molten Al–Si eutectic alloy [94]. The composites contained ~40% ceramic phase with Al–Si layer thickness of 10 μm and showed an excellent tensile strength of ~300 MPa and a fracture toughness of 40 MPa m^{½} [94]. Because metals are usually good thermal conductors, anisotropic thermal conductivity can be achieved for the ceramic–metal composites. In this regard, aligned porous alumina and zirconia scaffolds were fabricated by directional freezing [109]. An aluminium alloy ($AlSi_{10}Mg$) was infiltrated into the scaffolds at 740 °C using a vacuum pressure metal casting device. Thermal conductivities of 80 W m^{-1} K^{-1} (parallel to the freezing direction) and 13 W m^{-1} K^{-1} (perpendicular to the freezing direction) were achieved for the zirconia/metal composites [109].

Other CMCs are also prepared by this approach. Lamellar SiC/2024Al composites were fabricated by infiltrating the molten Al alloy into the SiC scaffold at 800 °C. A ram was activated by a 40 ton hydraulic press to force the melt into the scaffold. The highest strength and toughness achieved for the composites were 931.3 MPa and 18.8 MPa m^{½} (measured by threepoint bending test), respectively [95]. For another SiC composite, after sintering the lamellar porous SiC scaffold at 1200 °C for 2 h in air, the Al–Si–Mg alloy melt was infiltrated into the scaffold at 950 °C under the flowing N_2 atmosphere [96]. A new phase of $MgAl_2O_4$ was formed to strengthen the interfacial bonding between the alloy phase and the SiC particles. An ultrasonic pulse echo technique was used to measure the elastic strength and modulus. The elastic modulus was found to increase with the volume percentage of SiC (up to 40 vol%), to a value of 163 GPa. The values were nearly the same between the longitudinal direction and the transverse direction. For the composite with 30 vol% SiC, the compressive strength was the highest, 722 ± 35 MPa for longitudinal direction and 555 ± 27 MPa for transverse direction [96].

The aim for the nacre–mimetic composites with polymer phase, has always been to increase the content of inorganic (ceramic) component and achieve nanoscale thickness of the polymer layers. However, for the nacrelike ceramic–metal composites, the content of metal phase is always very high and often higher than the ceramic phase. The mechanical properties are more like a combination of two components and a balance (or compromise) between toughness (elasticity) and strength. In the Al/TiC composite with 15 vol% TiC, the bending strength was

355 MPa, the elastic modulus was 100 GPa, and the toughness was high at K_{JC} 81.0 MPa $m^{½}$ (measured by threepoint bending test without prefabricated notch). However, for the composite containing 35 vol% TiC, the bending strength increased to 500 MPa while the toughness decreased to 32.9 MPa $m^{½}$ [110]. This could be explained by nonlocalized multiplecrack propagation in the 15 vol% TiC composites (Figure 6.16a and b). The thick metal layer could effectively dissipate the stress at the crack tip. Further, due to the loose ceramic layers, the metal phase was able to infiltrate between the ceramic particles. This could promote the occurrence of nonlocalized cracks. In the case of Al/25 vol% TiC and Al/35 vol% TiC, the thin metal layers were unable to disperse the stress at the crack tip, leading to propagation of cracks and failure (Figure 6.16c and d) [110].

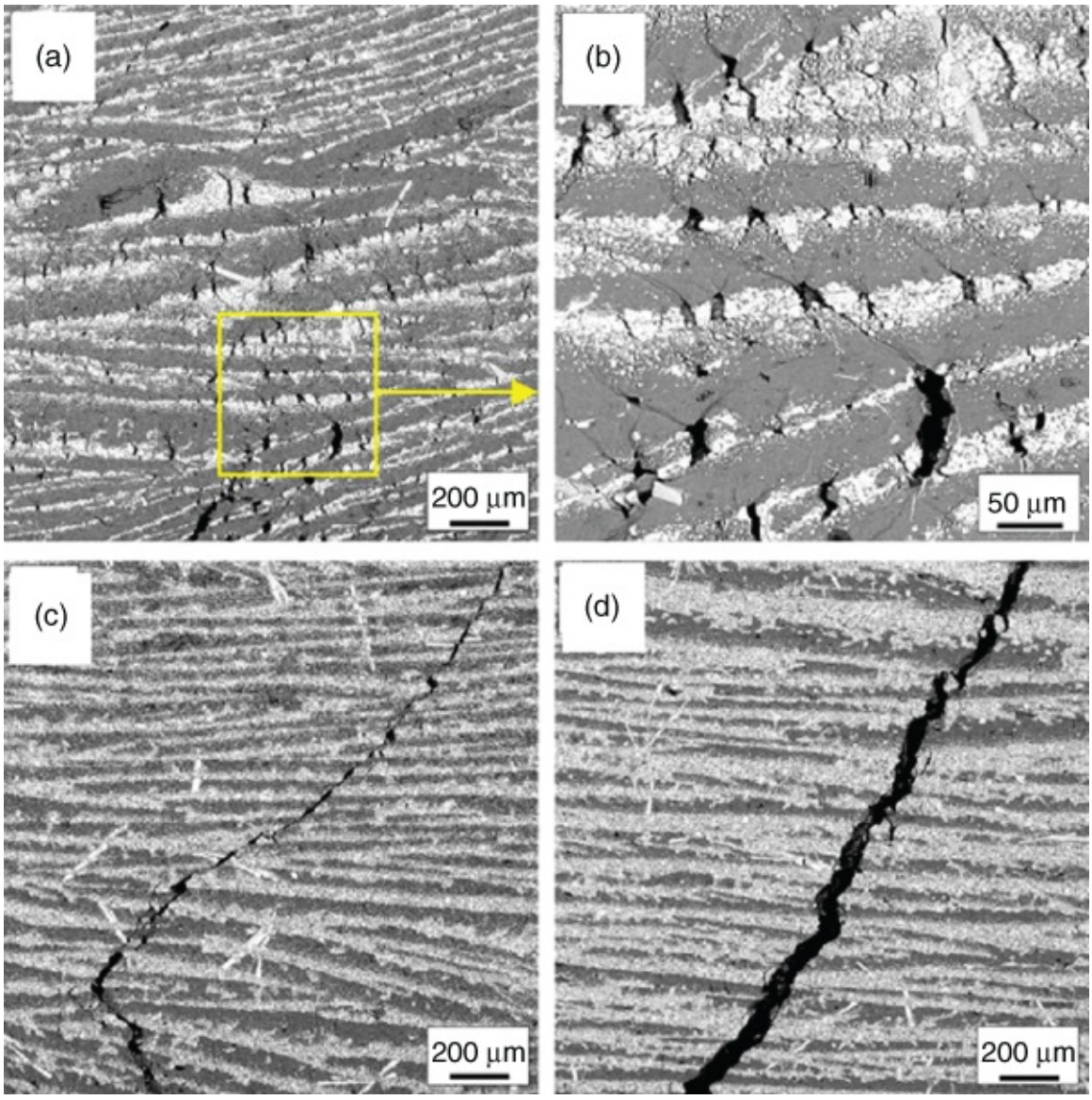

Figure 6.16 The SEM images show the initial cracks of the composite (a and b) Al/15 vol% TiC, (c) Al/25 vol% TiC, and (d) Al/35 vol% TiC after the threepoint bending test.

Source: Wang et al. 2017 [110]. Reprinted with permission from Elsevier.

The mechanical properties of ceramic–metal composites may be enhanced via interfacial reactions [96]. For example, commercial alloy AZ91 (Mg9Al1Zn) was infiltrated into

porous SiC at 650 °C [111]. The SiC scaffold was preoxidized at 1100 °C for 2 h, forming a SiO_2 layer. Mg vapour was generated during infiltration and reacted with the oxidized surface, generating a Mg_2Si phase. This could enhance the mechanical property of the composite. The flexural and compressive strengths of the composite with 30 vol% ceramics were measured to be 599 ± 44 and 743 ± 20 MPa, respectively [111]. ZL107 alloy (Al7Si5Cu) was infiltrated into the freezecast lamellar Al $_2O_3$–ZrO_2 scaffold at 850 °C under a 2 MPa Ar gas. The composite was further heated at 850 °C for a period of 0–120 min. The heating facilitated the reaction between Al and ZrO_2 [112]. After heating for about 60 min, the primary products of the reaction, $(Al_{1-m,}\ Si_m)_3Zr$ and ZiS_2, could develop into bridges between the ceramic layers, thus enhancing the strength and toughness of the composites [112].

6.7 Enamelmimic Ceramic–Polymer Composites

The mammalian tooth can be divided into four parts [113]: enamel, dentin, pulp, and cementum. Enamel is the hardest mineralized tissue in the body and consists of 95–97 wt% carbonated HA and <1 wt% of organic materials. Enamel is the uppermost 1–2 mm part of the tooth crown [114]. It is highly strong but may be brittle. The dentin layer has similar composition and mechanical properties as bones. The dentin layer can dissipate the stress from the enamel and prevent it from cracking. The geological or chemical HA has a formula of $Ca_5(PO_4)_3(OH)$ [42]. However, it is carbonated HA, $Ca_{10}(PO_4,\ CO_3)_6(OH)_2$, that is present in bone and enamel. Carbonated HAs can be classified as type A (carbonate replacing hydroxide) and type B (carbonate replacing phosphate). They can be distinguished by infrared spectroscopy [114]. The compositions of carbonated HA in bones vary because bones serve as a reservoir to maintain homeostasis balance with ions such as Ca^{2+}, Mg^{2+}, and PO_4^{3-}. It is much less the case for enamel because enamel does not resorb and remodel once matured [114].

Enamel is formed in two stages: secretion and maturation. While ameloblast functions in the secretion stage, amelogenin is the dominant organic component in the mature enamel [115]. Amelogenin is hydrophobic and contains C terminus, and can selfassemble into nanospheres (and then maybe chains and ribbons), which promote the orientated growth of HA crystallites along the *c*axis [114, 115]. Therefore, in the enamel, bundles of HA rods are sandwiched (and maybe with an interweaving structure depending on tooth type [116]) by very small amounts of organic components. The structures of some teeth, with aligned and/or bundled columnar features, are illustrated in Figure 6.17 [117]. In addition to the main component amelogenin, the other organic components in enamel are enamelin (a glycoprotein, strongly adsorbed to enamel crystals) and ameloblastin (also known as amelin or sheathlin) [114]. The strength (elastic modulus) of enamels has been measured by various methods and researchers [115]. The obtained values vary. In general, the elastic modulus is in the region of 30 GPa for a cross sectional surface and 10 GPa for an occlusal surface by macroscale tests. For the tests by nanoindentation, the values are in the region of 80–100 GPa [115].

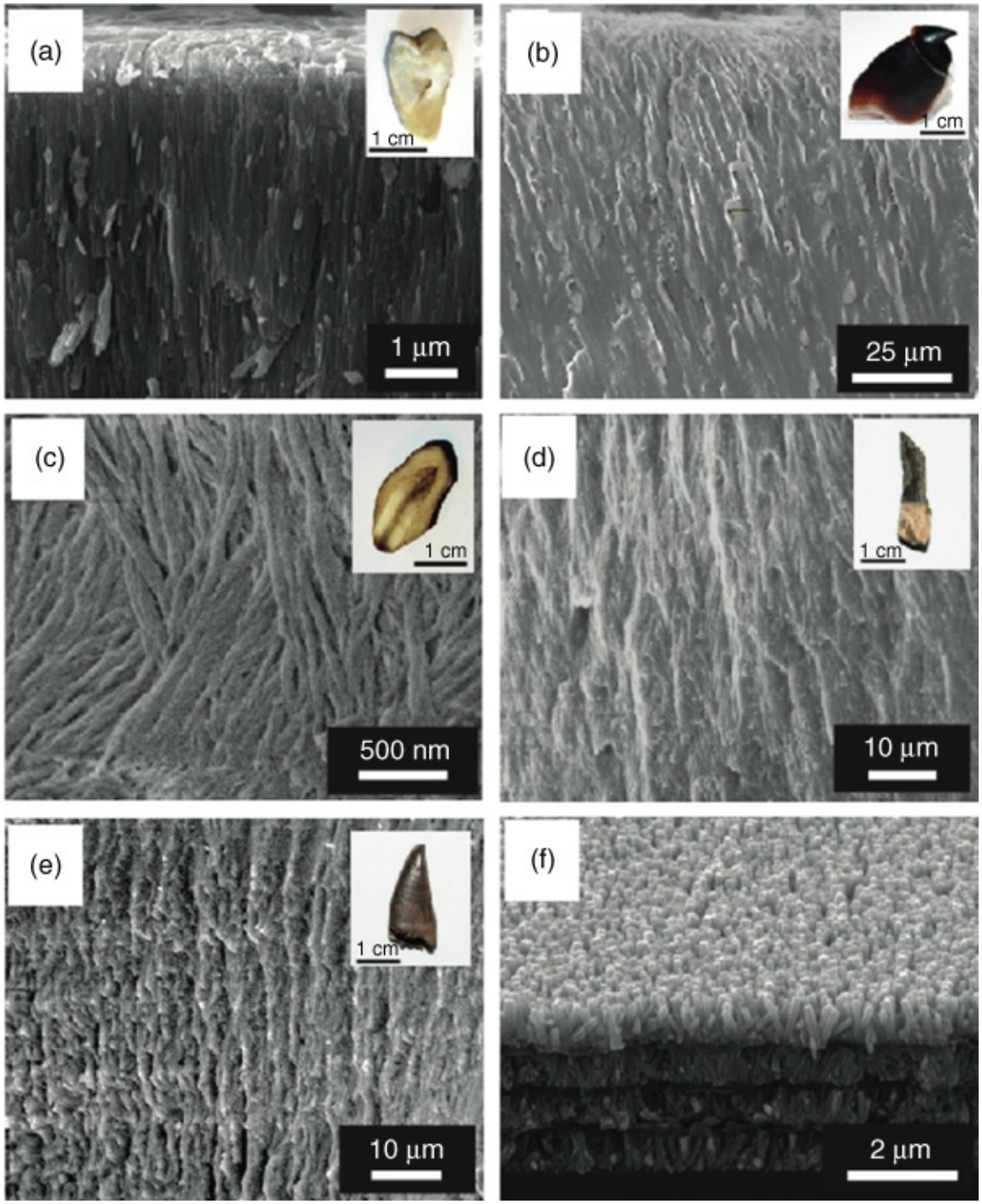

Figure 6.17 The columnar motifs in the teeth of (a) human tooth enamel, (b) beak of *Octopus vulgaris*; (c–e) tooth enamel from the *Odobenidae* family (c), from *Tyrannosaurus rex* (d), and from *Albertosaurus spp* (e). (f) The structure of the composites fabricated by layerbylayer (LBL) coating of vertical ZnO nanowires.

Source: Yeom et al. 2017 [117]. Reprinted with permission from Nature Publishing Group.

Because enamel cannot resorb and regenerate, tooth implant and tooth restoration are clearly required. It is no surprise that dental materials must have high strength and, ideally, high fracture toughness. Ceramic–ceramic and ceramic–metal composites are conventionally used for dental applications [118]. Alumina and silicabased ceramics have been traditionally used. In recent years, zirconia has appeared to be an alternative ceramic. Zirconia exists in

three crystalline forms: monoclinic (low temperature), tetragonal (>1170 °C), and cubic (>2370 °C). Zirconia exhibits superior mechanical properties than alumina, i.e. excellent flexural strength, fracture toughness, and corrosion resistance, particularly for partially stabilized zirconia [119]. Zirconia is chemically inert. It is very difficult to modify a zirconia surface, which hinders the preparation of strong zirconia composites via polymer grafting. This, however, may be addressed by coating zirconia with silica. A variety of silanol chemistry can then be employed to achieve a better adhesive bonding [119]. Zirconia implants have been examined systemically from clinical data. The shortterm cumulative survival rates and marginal bone loss are promising while more data are required for longterm predictability [120].

Traditional dental materials are usually composites with ceramic particles randomly distributed in a polymer matrix. To mimic the structure of enamel or dentin, aligned porous ceramics fabricated by directional freezing can be used to produce such composites. Petrini et al. prepared aligned porous alumina with graded porosity which was then infiltrated with epoxy resin [121]. The composite structure was more like that of dentin (composed of 70 wt% HA, 20 wt% of organic materials, and 10 wt% water, with packed tubule structure). Owing to the graded porosity of the alumina scaffold (dense structure at the bottom and wellaligned porous structure in the upper part), different mechanical properties were obtained for the top and bottom of the composite. For the top part of the composite, the elastic modulus was 9.1 ± 0.3 GPa, flexural strength 213.1 ± 59.9 MPa, and compressive strength 222.4 ± 44.9 MPa. For the bottom part, the elastic modulus was 6.5 ± 2.3 GPa, flexural strength 183.1 ± 49.4 MPa, and compressive strength 140.6 ± 66.6 MPa. Based on these data, it can be inferred that the flexural strength is similar to that of dentin. The mechanical property of the top part of the composite is better than that of the bottom part, despite the high porosity and low ceramic content of the top part. This was attributed to the presence of closed pores in the bottom ceramic [121].

As has been mentioned in Section 6.5, the strategy adopted in the freezecasting approach in the preparation of nacre–mimic composites has been to increase the content of the inorganic component and reduce the thickness of the organic layer. Because of the very high percentage of the inorganic component in enamel (up to ~97 wt%), it is highly challenging to produce such composites via a freezecasting approach. In addition to combining hot pressing with freeze casting, other approaches may be employed to fabricate enamellike composites. Very recently, inspired by the columnar structure of various types of teeth, vertically arranged ZnO nanowires were fabricated via a hydrothermal approach, followed by LBL deposition of polyelectrolytes between the ZnO nanowires (Figure 6.17f) [117]. The polyelectrolytes used were polyallylamine and polyacrylic acid. This produced a composite with a 67 vol% inorganic component. The procedure was repeated and the composites could be stacked to produce strong composites with the Young's modulus at 39.8 ± 0.9 GPa (by the Berkovich probe) or 1.65 ± 0.06 GPa (by the conical probe). These data are comparable with those of tooth enamel with 85 vol% inorganic component (modulus of 62–108 GPa and hardness of 1.1–4.9 GPa) [117].

6.8 Ceramic–Ceramic Composites with the Second Nanoscale Ceramic Phase

Tough ceramic composites have been fabricated via the introduction of a ductile phase such as polymer and metal into a brittle porous ceramic scaffold. This may reduce the strength of the resulting materials (compared to the ceramics) although there are examples of both strength and toughness being improved for the composites. There is, however, another problem with the use of polymer and metal in the composites. The thermal stability of these composites is limited by the presence of polymer or metal. This could be a serious drawback for hightemperature applications. Therefore, there is a need to fabricate ceramic–ceramic composites that also demonstrate high strength and high toughness.

Learning from nacre and nacrelike materials, it has been found that increasing the local density at the interfaces can lead to enhanced toughening, primarily via crack deflection. The increase of local density can be achieved by the use of small nanoscale constituents at the interface. This concept has been demonstrated by Deville and coauthors [97]. The freezing procedure was used to assemble the anisotropic platelets between the ice crystals. The initial slurry contained alumina platelets (7 μm in diameter and 500 nm in thickness), alumina nanoparticles (100 nm, serving as inorganic bridges and nanoasperities at the platelet surface), and smaller nanoparticles of silica–calcia phase (20 nm, filling the remaining gaps during the sintering stage). The fabrication procedure is illustrated in Figure 6.18. After the pressing step, the material was sintered by fieldassisted sintering at 1500 °C [97]. The resulting composite exhibited the combination of high strength (470 MPa), high toughness (22 MPa $m^{½}$), and high stiffness (290 GPa). Because the composite only consisted of ceramics, the mechanical properties were retained at a relatively high temperature of 600 °C. The rising K_{JC}crack extension was still observed, with the initial toughness (K_{IC}) of 4.7 MPa $m^{½}$ and maximum toughness (K_{JC}) of 21 MPa $m^{½}$ [97].

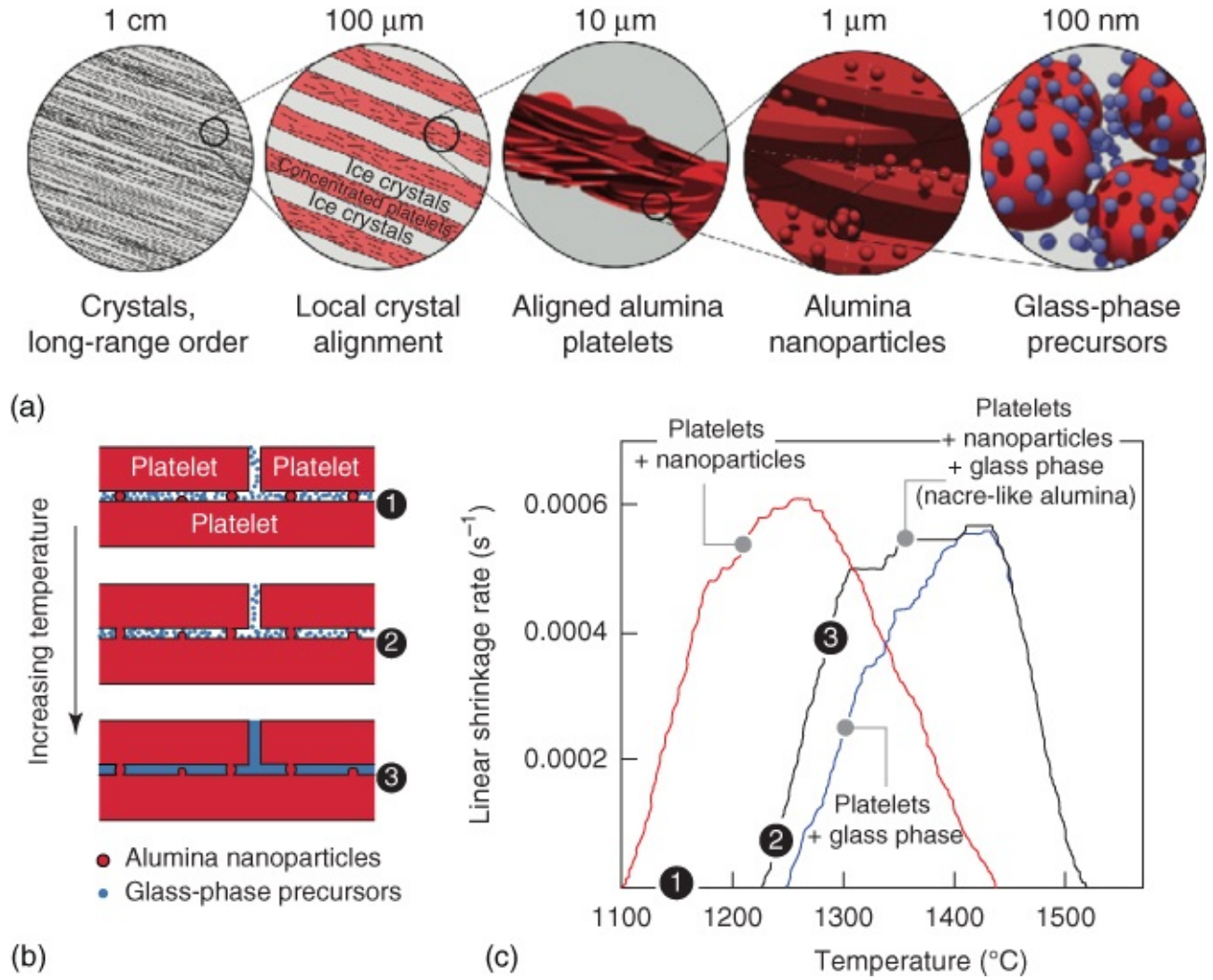

Figure 6.18 Fabrication of all ceramic composites via a freezing path. (a) Selforganization of particles of different shapes and sizes during the freezing procedure. (b) Schematic representation of the densification of the composites by sintering with pressing. (c) Linear shrinkage of the composites with different components during the densification process.

Source: Bouville et al. 2014 [97]. Reprinted with permission from Nature Publishing Group.

In the MASC process for the preparation of composites, inorganic silica and alumina nanoparticles could be added into the initial slurry to fabricate all ceramic composites. The ceramic–ceramic composite exhibited excellent properties, i.e. flexural modulus of ~190 GPa, flexural strength of 650 MPa, initial toughness (K_{IC}) of ~5 MPa $m^{½}$ and maximum toughness (K_{JC}) of 14 MPa $m^{½}$ [92]. In a further study, the alumina platelets were coated with titania and then rendered magnetically responsive by adsorption of iron oxide nanoparticles [98]. Titania could be sintered at lower temperatures (e.g. a temperature higher than 1100 °C is necessary to sinter alumina), which could significantly minimize the processing time and material heterogeneity. During the sintering with pressing, titania particles could form in situ mineral bridges between alumina platelets in the temperature window of 900–1100 °C to form strong composites. Indeed, the composite fabricated around 900 °C exhibited the highest toughness (K_{IC}) of ~6.5 MPa $m^{½}$ and flexural strength of ~370 MPa (flexural modulus ~150 GPa) while

the flexural modulus was highest at ~190 GPa for the composite processed at 1100 °C [98].

Similar methodologies (although the freezing procedure not used) are employed to prepare other types of ceramic composites, mainly graphene–ceramic composites [99–101]. Graphene nanoplatelets were suspended with alumina in dimethyl formamide (DMF) by sonication and ball milling. The solvent DMF was removed in an oven at 90 °C for 3 days. The composite was then sintered with a uniaxial pressure of 50 MPa at 1500–1550 °C by the SPS. Graphene platelets overlapping and uniform distribution in alumina matrix were observed. The incorporation of graphene platelets at 0.38 vol% achieved the best improvement in flexural strength (from 400 to 523 MPa) and fracture toughness (3.53 to 4.49 MPa $m^{½}$) but the hardness was slightly decreased from 18.06 to 17.66 GPa, compared to pure alumina [99]. For the graphene–Si_3N_4 composite, graphene and Si_3N_4 were separately suspended in water, stabilized by CTAB and then combined together and sonicated. The water was removed at ~100 °C and the dry composite was heated in argon at ~500 °C for 1 h to remove CTAB before being densified by the SPS process at 1650 °C with an applied load of 35 MPa. The presence of the graphene platelets was confirmed by Raman spectroscopy in the composite after the harsh treatment. When graphene platelets were included at 1.5 vol%, the fracture toughness was increased more than twofold (from 2.8 to 6.6 MPa $m^{½}$) while the hardness was slightly decreased [100]. In another study, graphene oxide and ZrB_2 (2 μm) were selfassembled in water containing PVA to form layered structures. SiC was also added in order to enhance the mechanical property. The layered composite was collected by filtering the solution and then treated by the SPS at 1950 °C for 15 min with a uniaxial load of 30 MPa under high vacuum. The bioinspired graphene/ZrB_2–SiC composite exhibited a flexural strength of 522 MPa, fracture toughness of 9.45 MPa $m^{½}$, tensile strength of 72.1 MPa, and modulus of 12.5 GPa [101].

6.9 Tough and Functional Composites

Functional ceramics are required to fabricate materials for targeted applications. The incorporation of polymer into the ceramic scaffolds usually aims to improve pliability and mechanical properties. The composites may be readily fabricated by mixing ceramic particles and polymer in suspensions or in melts and then processed by solvent evaporation or hot molding techniques [122, 123]. However, most of the functional properties rely on the good contact between the ceramic particles. In a ceramic–polymer composite where the particles are randomly distributed in the polymer matrix, the desired property may be weakened as a result. The aligned porous or layered porous ceramic structures fabricated by ice templating can be highly effective to address this issue while improving the mechanical stability at the same time.

Aligned porous leadzirconatetitanate (PZT) scaffolds were prepared by the freezecasting process. Epoxy was then filled into the aligned pores of the PZA scaffold and allowed to cure to generate PZT–epoxy composites [124]. The volume fraction of PZT in the composites varied from 36% to 69%. As shown in Figure 6.19, the longitudinal piezoelectric strain

coefficient (d_{33}) is about three times higher than the transverse piezoelectric strain coefficient ($-d_{31}$) for different PZT fractions. This suggests good contact between PZT particles along the longitudinal (freezing) direction and hence a higher d_{33}. Figure 6.19 also shows that d_{33} is the highest (~450 pC/N) at a PZT fraction of 57%. This can be attributed to the dense and well defined aligned structure at this composition. Accordingly, the hydrostatic strain coefficient ($d_h = d_{33} + 2d_{31}$) can be calculated and shows the highest value of 184 pC/N at the PZT fraction of 57%. The mechanical property was evaluated by compression test. The PZT/epoxy composite exhibited an increase of twofold in compressive strength compared to the porous PZT scaffold [124].

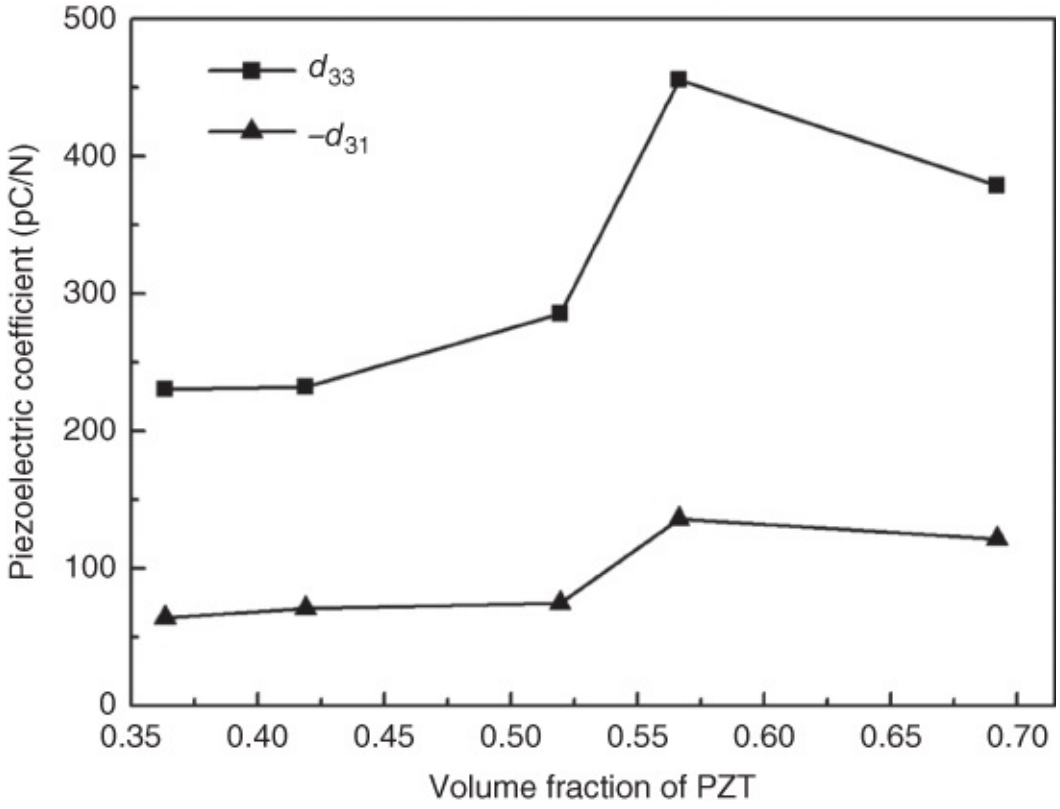

Figure 6.19 PZT/epoxy composites show anisotropic piezoelectric strain coefficient along the longitudinal (freezing) direction (d_{33}) and the transverse direction (d_{31}).

Source: Xu and Wang 2014 [124]. Reprinted with permission from John Wiley and Sons.

The same idea can be used to generate excellent ion conductivity and thermal conductivity in the mechanically enhanced composites. Aqueous $Li_{1+x}Al_xTi_{2-x}(PO_4)_3$ (LATP) nanoparticle (200–500 nm) slurry was frozen unidirectionally and freezedried to form vertically aligned porous scaffolds [125]. After densification by sintering, solid electrolyte PEO(polyethylene oxide)/PEG(polyethylene glycol) was filled into the porous scaffold. An ion conductivity of 0.52×10^{-4} S cm^{-1} was achieved, 3.6 times that of the composite with randomly distributed LATP nanoparticles. The tension and compression moduli for the composites were 6.6 and 3.6 MPa, respectively, whilst they were 1.9 and 1.4 MPa for the PEO/PEG sample [125].

Aligned porous BN was prepared via directional freezing of aqueous BN (10 μm

microplatelets) slurry with SCMC as stabilizer. In comparison, randomly porous BN was also fabricated by freezing slowly in a freezer. Epoxy/3DBN composites were subsequently produced by infiltrating epoxy resin with curing agent and catalyst into the porous scaffolds [126]. Epoxy/BN composites were also prepared by simply mixing BN with epoxy resin and curing. From Figure 6.20a, it can be seen that the thermal conductivity increases with the increase of BN loading in the composites. The epoxy/oriented 3DBN composite shows much higher thermal conductivity than the other two composites. The enhancement in thermal conductivity (measured along the freezing direction) compared to epoxy resin is given in Figure 6.20b. At a BN loading of 35 vol%, an enhancement of 2226 for the epoxy/oriented 3DBN conductivity (conductivity 4.42 W m $^{-1}$ K^{-1}) is obtained, nearly three times higher than that of the epoxy/random3DBN composite and four times higher than that of the epoxy/BN composite made by simple mixing [126]. This can be attributed to the alignment and self assembly of BN platelets during directional freezing, similar to that previously reported [97].

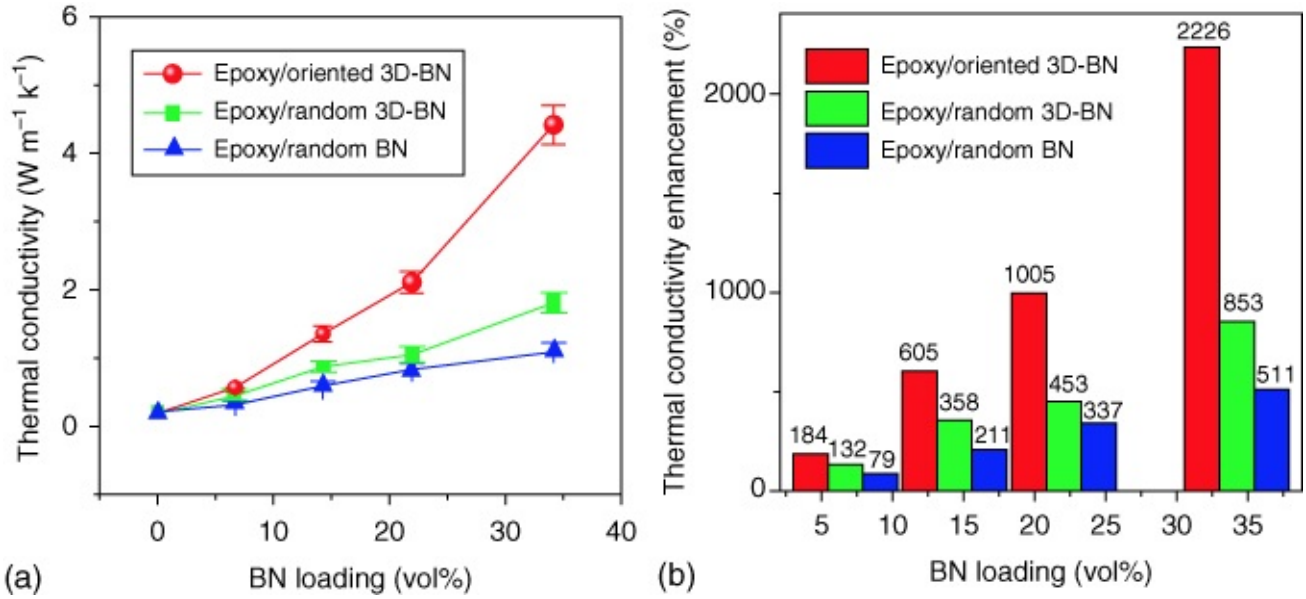

Figure 6.20 (a) The plot shows the relationship of thermal conductivity of the epoxy/BN composites with different BN loadings. (b) The thermal conductivity enhancement of different types of epoxy/BN composites based on the thermal conductivity of pure epoxy matrix.

Source: Hu et al. 2017 [126]. Reprinted with permission from American Chemical Society.

6.10 Summary

Ceramics usually have high strength, high thermal stability, and corrosionresistant property, and different functional properties depending on the type of ceramic. However, ceramics are usually brittle and this can be catastrophic for some applications and thus must be addressed. One of the main goals in the fabrication of ceramics composites is to improve fracture toughness without negatively impacting their strength significantly. There are other advantages in composites such as combined useful properties, newly generated properties, elasticity, etc.

Ceramic composites can be formed by combining ceramics with ductile phases such as polymer or metal and other ceramic particles (parameters including size, shape and aspect

ratio). While the toughness can be enhanced by fabricating such composites, the strength is usually reduced. This is because strength and toughness are mutually exclusive and there is usually a tradeoff between strength and toughness when fabricating ceramic composites. Significant progress has been made recently in preparing strong and tough composites by learning from the wonderful natural materials, such as nacre, bone, and enamel where the hierarchical structure, assembly of inorganic platelets or columnar structure, and most importantly the interfacing between the inorganic phase and the organic phase are the main contributing factors. Different toughening mechanisms have been identified and used in designing and fabricating composite materials.

Nacrelike composites, with high percentage of assembled inorganic platelets (~95 vol%) and the nanoscale layer of organic component, have been mostly prepared and investigated. These usually involve the use of alumina platelets to form layered porous scaffolds by directional freezing (freeze casting). The second phase such as polymer or metal is infiltrated into the porous scaffolds. In order to increase the content of solid inorganic phase in the composites, the freezedried scaffolds are often sintered and pressed uniaxially with loads of 30–50 MPa or even higher. When preparing ceramic–ceramic composites (so that they can be used for hightemperature applications), smaller ceramic nanoparticles (such as silica, titania) can be added into the initial slurries. After a freezecasting process or other processes to assemble the platelets and remove the solvent, the resulting composites are usually treated by SPS at temperatures from 900 up to 1950 °C (depending on the type of ceramic) with applied load on the samples.

By learning from Nature, it has been possible to fabricate tough and strong composites. But there is still a long way to go because our fabrication methods employ very harsh conditions and the composites are still inferior if we use the same components from nature. It is thus still very important to understand the detailed structural arrangement and the toughening mechanism in natural materials. From the engineering and manufacturing point of view, one way to go forward is to increase further the percentage of inorganic components in the composites and decrease the thickness of organic component. For example, as the hardest part in the body, enamel contains 97 wt% of inorganic component. It is hugely challenging to fabricate composites with such a high inorganic content while maintaining the hierarchical and delicate organic/inorganic structure.

So far, the commonly used ceramics, such as alumina, HA, SiC, and BN, have been used to fabricate tough composites. The ductile phases have been polymer (PMMA, epoxy) and metal alloys. It is highly desirable to select suitable ceramic particles and polymers to produce functional and tough ceramic composites. Furthermore, the composites may be subjected to etching/micromolding/3D laser lithography to create structural composites with high strength, high toughness, but low density [127].

References

1 Rosso, M. (2006). Ceramic and metal matrix composites: routes and properties. *J. Mater.*

Proc. Technol. 175: 364–375.

2 Hammel, E.C., Ighodaro, O.L.R., and Okoli, O.I. (2014). Processing and properties of advanced porous ceramics: an application based review. *Ceram. Int.* 40: 15351–15370.

3 Chevalier, J. and Gremillard, L. (2009). Ceramics for medical applications: a picture for the next 20 years. *J. Eur. Ceram. Soc.* 29: 1245–1255.

4 Boccardi, E., Ciraldo, F.E., and Boccassini, A.R. (2017). Bioactive glassceramic scaffolds: processing and properties. *MRS Bull.* 42: 226–232.

5 Johnson, A.J.W. and Herschler, B.A. (2011). A review of the mechanical behaviour of CaP and CaP/polymer composites for applications in bone replacement and repair. *Acta Biomater.* 7: 16–30.

6 Macuvele, D.L.P., Nones, J., Matsinhe, J.V. et al. (2017). Advances in ultra high molecular weight polyethylene/hydroxyapatite composites for biomedical applications: a brief review. *Mater. Sci. Eng. C* 76: 1248–1262.

7 Koulouridis, S., Kiziltas, G., Zhou, Y. et al. (2006). Polymer–ceramic composites for microwave applications: fabrication and performance assessment. *IEEE Trans. Microw. Theory Tech.* 54: 4202–4208.

8 Nan, C., Bichurin, M.I., Dong, S. et al. (2008). Multiferroic magnetoelectric composites: historical perspective, status, and future directions. *J. Appl. Phys.* 103: 031101.

9 Sommers, A., Wang, Q., Han, X. et al. (2010). Ceramics and ceramic matrix composites for heat exchangers in advanced thermal systems – a review. *Appl. Therm. Eng.* 30: 1277–1291.

10 Padture, N.P., Gell, M., and Jordan, E.H. (2002). Thermal barrier coatings for gasturbine engine applications. *Science* 296: 280–284.

11 Voevodin, A.A. and Zabinski, J.S. (2005). Nanocomposites and nanostructured tribological materials for space applications. *Compos. Sci. Technol.* 65: 741–748.

12 Fu, S., Feng, X., Lauke, B., and Mai, Y. (2008). Effects of particle size, particle/matrix interface adhesion and particle loading on mechanical properties of particulate–polymer composites. *Composites B* 39: 933–961.

13 Becher, P.F. (1991). Microstructural design of toughened ceramics. *J. Am. Ceram. Soc.* 74: 255–269.

14 Palmero, P. (2015). Structural ceramic nanocomposites: a review of properties and powders' synthesis methods. *Nanomaterials* 5: 656–696.

15 Curtin, W.A. (1991). Theory of mechanical properties of ceramic–matrix composites. *J. Am. Ceram. Soc.* 74: 2837–2845.

16 Chartier, T., Merle, D., and Besson, J.L. (1995). Laminar ceramic composites. *J. Eur. Ceram. Soc.* 15: 101–107.

17 Chan, H.M. (1997). Layered ceramics: processing and mechanical behaviour. *Annu. Rev. Mater. Sci.* 27: 249–282.

18 Deng, X., Chawla, N., Chawla, K.K. et al. (2005). Mechanical behaviour of multilayered nanoscale metal–ceramic composites. *Adv. Eng. Mater.* 7: 1099–11108.

19 Hernandez, C.J. and van der Meulen, M.C.H. (2017). Understanding bone strength is not enough. *J. Bone Miner. Res.* 32: 1157–1162.

20 Ritchie, R.O. (2011). The conflicts between strength and toughness. *Nat. Mater.* 10: 817–822.

21 Wegst, U.G.K., Bai, H., Saiz, E. et al. (2015). Bioinspired structural materials. *Nat. Mater.* 14: 23–36.

22 Libonati, F. and Buehler, M.J. (2017). Advanced structural materials by bioinspiration. *Adv. Eng. Mater.* 19: 1600787.

23 Wang, J., Cheng, Q., and Tang, Z. (2012). Layered nanocomposites inspired by the structure and mechanical properties of nacre. *Chem. Soc. Rev.* 41: 1111–1129.

24 Porter, M.M., Mckittrick, J., and Meyers, M.A. (2013). Biomimetic materials by freeze casting. *JOM* 65: 720–727.

25 Zok, F.W. and Levi, C.G. (2001). Mechanical properties of porous matrix ceramic composites. *Adv. Eng. Mater.* 3: 15–23.

26 Wachtman, J.B., Cannon, W.R., and Matthewson, M.J. (2009). Stress and strain (Chapter 1). In: Mechanical Properties of Ceramics, 2nd ed, 1–26. John Wiley & Sons, Inc.

27 Czichos, H., Saito, T., and Smith, L. (2006). Mechanical properties (Chapter 7). In: Springer Handbook of Materials Measurement Methods, 283–298. Springer Science + Business Media, Inc.

28 Wachtman, J.B., Cannon, W.R., and Matthewson, M.J. (2009). Types of mechanical behaviour (Chapter 2). In: Mechanical Properties of Ceramics, 2nd ed, 27–34. John Wiley & Sons, Inc.

29 Wachtman, J.B., Cannon, W.R., and Matthewson, M.J. (2009). Measurements of elasticity, strength, and fracture toughness (Chapter 6). In: Mechanical Properties of Ceramics, 2nd ed, 89–118. John Wiley & Sons, Inc.

30 Wachtman, J.B., Cannon, W.R., and Matthewson, M.J. (2009). Hardness and wear (Chapter 22). In: Mechanical Properties of Ceramics, 2nd ed, 405–422. John Wiley & Sons, Inc.

31 Wachtman, J.B., Cannon, W.R., and Matthewson, M.J. (2009). Overview of toughening mechanisms in ceramics (Chapter 10). In: Mechanical Properties of Ceramics, 2nd ed, 189–198. John Wiley & Sons, Inc.

32 Xia, Z. and Li, L. (2014). Understanding interfaces and mechanical properties of ceramic matrix composites (Chapter 12). In: Advances in Ceramic Matrix Composites (ed. I.M. Low), 267–285. Woodhead Publishing Limited.

33 Zhang, H., Hussain, I., Brust, M. et al. (2005). Aligned two and threedimensional structures by directional freezing of polymers and nanoparticles. *Nat. Mater.* 4: 787–793.

34 Qian, L., Ahmed, A., Foster, A. et al. (2009). Systematic tuning of pore morphologies and pore volumes in macroporous materials by freezing. *J. Mater. Chem.* 19: 5212–5219.

35 Zhang, H., Wang, D., Butler, R. et al. (2008). Formation and enhanced biocidal activity of waterdispersable organic nanoparticles. *Nat. Nanotechnol.* 3: 506–511.

36 Ahmed, A., Hearn, J., Abdelmagid, W., and Zhang, H. (2012). Dualtuned drug release by nanofibrous scaffolds of chitosan and mesoporous silica microspheres. *J. Mater. Chem.* 22: 25027–25035.

37 Ahmed, A., Myers, P., and Zhang, H. (2012). Preparation of aligned porous silica monolithic capillary columns and their evaluation for HPLC. *Anal. Methods* 4: 3942–3947.

38 Ahmed, A., Clowes, R., Willneff, E. et al. (2010). Synthesis of uniform porous silica microspheres with hydrophilic polymer as stabilizing agent. *Ind. Eng. Chem. Res.* 49: 602–608.

39 Ahmed, A., Clowes, R., Myers, P., and Zhang, H. (2011). Hierarchically porous silica monoliths with tuneable morphology, porosity, and mechanical stability. *J. Mater. Chem.* 21: 5753–5763.

40 Qian, L. and Zhang, H. (2010). Green synthesis of chitosanbased nanofibers and their applications. *Green Chem.* 12: 1207–1214.

41 Rezwan, K., Chen, Q.Z., Blaker, J.J., and Boccassini, A.R. (2006). Biodegradable and bioactive porous polymer/inorganic composite scaffolds for bone tissue engineering. *Biomaterials* 27: 3413–3431.

42 Bose, S. and Tarafder, S. (2012). Calcium phosphate ceramic systems in growth factor and drug delivery for bone tissue engineering: a review. *Acta Biomater.* 8: 1401–1421.

43 Schardosim, M., Soulié, J., Poquillon, D. et al. (2017). Freezecasting for PLGA/carbonated apatite composite scaffolds: structure and properties. *Mater. Sci. Eng. C* 77: 731–738.

44 He, F., Li, J., and Ye, J. (2013). Improvement of cell response of the poly(lacticco glycolic acid)/calcium phosphate cement composite scaffold with unidirectional pore structure

by the surface immobilization of collagen via plasma treatment. *Colloids Surf. B* 103: 209–216.

45 Cai, X., Chen, L., Jiang, T. et al. (2011). Facile synthesis of anisotropic porous chitosan/hydroxyapatite scaffolds for bone tissue engineering. *J. Mater. Chem.* 21: 12015–12025.

46 Hunger, P.M., Donius, A.E., and Wegst, U.G.K. (2013). Platelets selfassembly into porous nacre during freeze casting. *J. Mech. Behav. Biomed. Mater.* 19: 87–93.

47 Uddin, M.K. (2017). A review on the adsorption of heavy metals by clay minerals, with special focus on the past decade. *Chem. Eng. J.* 308: 438–462.

48 Bergaya, F. and Lagaly, G. (2006). General introductions: clays, clay minerals, and clay science (Chapter 1). In: Handbook of Clay Science, Development in Clay Science, vol. 1 (ed. F. Bergaya, B.K.G. Theng and G. Lagaly), 1–18. Elsevier Ltd.

49 Schoonheydt, R.A. and Johnston, C.T. (2006). Surface and interface chemistry of clay minerals (Chapter 3). In: Handbook of Clay Science, Development in Clay Science (ed. F. Bergaya, B.K.G. Theng and G. Lagaly), 87–113. Elsevier Ltd.

50 Ngah, W.S.W., Teong, L.C., and Hanafiah, M.A.K.M. (2011). Adsorption of dyes and heavy metal ions by chitosan composites: a review. *Carbohydr. Polym.* 83: 1446–1456.

51 Yu, W.H., Li, N., Tong, D.S. et al. (2013). Adsorption of proteins and nucleic acids on clay minerals and their interactions: a review. *Appl. Clay Sci.* 8081: 443–452.

52 de Sousa Rodrigues, L.A., Figueiras, A., Veiga, F. et al. (2013). The systems containing clays and clay minerals from modified drug release: a review. *Colloids Surf. B* 103: 642–651.

53 Maisanaba, S., Pichardo, S., Puerto, M. et al. (2015). Toxicological evaluation of clay minerals and derived nanocomposites: a review. *Environ. Res.* 138: 233–254.

54 Jordan, J., Jacob, K.I., Tannenbaum, R. et al. (2005). Experimental trends in polymer nanocomposites: a review. *Mater. Sci. Eng. A* 393: 1–11.

55 Madyan, O.A., Fan, M., Feo, L., and Hui, D. (2016). Enhancing mechanical properties of clay aerogel composites: an overview. *Composites B* 98: 314–329.

56 Qian, L. and Zhang, H. (2011). Controlled freezing and freeze drying: a versatile route for porous and micro/nanostructured materials. *J. Chem. Technol. Biotechnol.* 86: 172–184.

57 Chen, H., Chiou, B., Wang, Y., and Schiraldi, D.A. (2013). Biodegradable pectin/clay aerogels. *ACS Appl. Mater. Interfaces* 5: 1715–1721.

58 Pojanavaraphan, T., Magaraphan, R., Chiou, B., and Schiraldi, D.A. (2010). Development of biodegradable foamlike materials based on casein and sodium montmorillonite clay. *Biomacromolecules* 11: 2640–2646.

59 Pojanavaraphan, T., Liu, L., Ceylan, D. et al. (2011). Solution crosslinked natural rubber (NR)/clay aerogel composites. *Macromolecules* 44: 923–931.

60 Chen, H., Wang, Y., and Shiraldi, D.A. (2014). Preparation and flammability of poly(vinyl alcohol) composite aerogels. *ACS Appl. Mater. Interfaces* 6: 6790–6796.

61 Chen, H., Liu, B., Huang, W. et al. (2014). Fabrication and properties of irradiation crosslinked poly(vinyl alcohol)/clay aerogel composites. *ACS Appl. Mater. Interfaces* 6: 16227–16236.

62 Wang, T., Sun, H., Long, J. et al. (2016). Biobased poly(furfuryl alcohol)/clay aerogel composite prepared by a freezedrying process. *ACS Sustainable Chem. Eng.* 4: 2601–2605.

63 Donius, A.E., Liu, A., Berglund, L.A., and Wegst, U.G.K. (2014). Superior mechanical performance of highly porous, anisotropic nanocellulose–montmorillonite aerogels prepared by freeze casting. *J. Mech. Behav. Biomed. Mater.* 37: 88–99.

64 Lichtner, A.Z., Jauffrès, D., Martin, C.L., and Bordia, R.K. (2013). Processing of hierarchical and anisotropic porosity LSM–YSZ composites. *J. Am. Ceram. Soc.* 96: 2745–2753.

65 Lichtner, A.Z., Jauffrès, D., Roussel, D. et al. (2015). Dispersion, connectivity and tortuosity of hierarchical porosity composite SOFC cathodes prepared by freezecasting. *J. Eur. Ceram. Soc.* 35: 585–595.

66 Li, W., Lu, K., and Walz, J.Y. (2013). Effects of solids loading on sintering and properties of freezecast kaolinite–silica porous composites. *J. Am. Ceram. Soc.* 96: 1763–1771.

67 Liu, G., Zhang, D., Meggs, C., and Button, T.W. (2010). Porous Al_2O_3–ZrO_2 composites fabricated by an ice template method. *Scr. Mater.* 62: 466–468.

68 Liu, G. and Button, T.W. (2013). The effect of particle size in freeze casting of porous alumina–zirconia composite. *Ceram. Int.* 39: 8507–8512.

69 Choi, H.J., Yang, T.Y., Yoon, S.Y. et al. (2012). Porous alumina/zirconia layered composites with unidirectional pore channels processed using a tertiarybutyl alcoholbased freeze casting. *Mater. Chem. Phys.* 133: 16–20.

70 Kim, K.H., Kim, D.H., Ryu, S.C. et al. (2016). Porous mullite/aluminalayered composites with a graded porosity fabricated by camphenebased freeze casting. *J. Compos. Mater.* . doi: 10.1177/0021998316636460.

71 He, R., Zhang, X., Han, W. et al. (2013). Effects of solids loading on microstructure and mechanical properties of HfB_2–20 vol.% $MoSi_2$ ultra high temperature ceramic composites through aqueous gelcasting route. *Mater. Des.* 47: 35–40.

72 Blindow, S., Pulkin, M., Koch, D. et al. (2009). Hydroxyapatite/SiO_2 composites via freeze

casting for bone tissue engineering. *Adv. Eng. Mater.* 11: 875–884.

73 Ghazanfari, S.M.H. and Zamanian, A. (2013). Phase transformation, microstructural and mechanical properties of hydroxyapatite/alumina nanocomposite scaffolds produced by freeze casting. *Ceram. Int.* 39: 9835–9844.

74 Zhang, Y., Chen, L., Zeng, J. et al. (2014). Aligned porous barium titanate/hydroxyapatite composites with high piezoelectric coefficients for bone tissue engineering. *Mater. Sci. Eng. C* 39: 143–149.

75 Yang, H., Ye, F., Liu, Q. et al. (2015). A novel silica aerogel/porous Si_3N_4 composite prepared by freeze casting and sol–gel impregnation with highperformance thermal insulation and wavetransparent. *Mater. Lett.* 138: 135–138.

76 Han, D., Mei, H., Farhan, S. et al. (2017). Anisotropic compressive properties of porous CNT/SiC composites produced by direct matrix infiltration of CNT aerogel. *J. Am. Ceram. Soc.* 100: 2243–2252.

77 Meyers, M.A., McKittrick, J., and Chen, P. (2013). Structural biological materials: critical mechanicsmaterials connections. *Science* 339: 773–779.

78 Cheng, Q., Jiang, L., and Tang, Z. (2014). Bioinspired layered materials with superior mechanical performance. *Acc. Chem. Res.* 47: 1256–1266.

79 Song, F., Zhou, J., Xu, X. et al. (2008). Effect of a negative Poisson ratio in the tension of ceramics. *Phys. Rev. Lett.* 100: 245502.

80 Mayer, G. (2005). Rigid biological systems as models for synthetic composites. *Science* 310: 1144–1147.

81 Deville, S., Saiz, E., Nalla, R.K., and Tomsia, A.P. (2006). Freezing as a path to build complex composites. *Science* 311: 515–518.

82 Bouville, F., Maire, E., and Deville, S. (2014). Selfassembly of faceted particles triggered by a moving ice front. *Langmuir* 30: 8656–8663.

83 Roleček, J., Salamon, D., and Chlup, Z. (2017). Mechanical properties of hybrid composites prepared by icetemplating of alumina. *J. Eur. Ceram. Soc.* 37: 4279–4286.

84 Munch, E., Launey, M.E., Alsem, D.H. et al. (2008). Tough, bioinspired hybrid materials. *Science* 322: 1516–1520.

85 Launey, M.E., Munch, E., Alsem, D.H. et al. (2009). Designing highly toughened hybrid composites through natureinspired hierarchical complexity. *Acta Mater.* 57: 2929–2932.

86 Zhao, H., Yue, Y., Guo, L. et al. (2016). Cloning Nacre's 3D interlocking skeleton in engineering composites to achieve exceptional mechanical properties. *Adv. Mater.* 28: 5099–5105.

87 Bai, H., Walsh, F., Gludovatz, B. et al. (2016). Bioinspired hydroxyapatite/poly(methyl methacrylate) composite with a nacremimetic architecture by a bidirectional freezing method. *Adv. Mater.* 28: 50–56.

88 Mao, L., Gao, H., Yao, H. et al. (2016). Synthetic nacre by predesigned matrixdirected mineralization. *Science* 354: 107–110.

89 Naleway, S.E., Yu, C.F., Hsiong, R.L. et al. (2016). Bioinspired intrinsic control of freeze cast composites: harnessing hydrophobic hydration and clathrate hydrates. *Acta Mater.* 114: 67–79.

90 Picot, O.T., Rocha, V.G., Ferraro, C. et al. (2016). Using grapheme networks to build bioinspired selfmonitoring ceramics. *Nat. Commun.* 8: 14425.

91 Veedu, V.O., Cao, A., Li, X. et al. (2006). Multifunctional composites using reinforced laminae with carbonnanotube forests. *Nat. Mater.* 5: 457–462.

92 Ferrand, H.L., Bouville, F., Niebel, T.P., and Studart, A.P. (2015). Magnetically assisted slip casting of bioinspired heterogeneous composites. *Nat. Mater.* 14: 1172–1181.

93 Porter, M.M., Meraz, L., Calderon, A. et al. (2015). Torsional properties of helix reinforced composites fabricated by magnetic freeze casting. *Compos. Struct.* 119: 174–184.

94 Launey, M.E., Munch, E., Alsem, D.H. et al. (2010). A novel biomimetic approach to the design of highperformance ceramicmetal composites. *J. R. Soc. Interface* 7: 741–753.

95 Liu, Q., Ye, F., Gao, Y. et al. (2014). Fabrication of a new SiC/2024Al cocontinuous composite with lamellar microstructure and high mechanical properties. *J. Alloys Compd.* 585: 146–153.

96 Shaga, A., Shen, P., Sun, C., and Jiang, Q. (2015). Lamellarinterpenetrated AlSi Ag/SiC composites fabricated by freeze casting and pressureless infiltration. *Mater. Sci. Eng. A* 630: 78–84.

97 Bouville, F., Maire, E., Meille, S. et al. (2014). Strong, tough and stiff bioinspired ceramics from brittle constitutes. *Nat. Mater.* 13: 508–514.

98 Grossman, M., Bouville, F., Erni, F. et al. (2017). Mineral nanointerconnectivity stiffens and toughens nacrelike composite materials. *Adv. Mater.* 29: 1605039.

99 Liu, J., Yan, H., and Jiang, K. (2013). Mechanical properties of graphene platelet reinforced alumina ceramic composites. *Ceram. Int.* 39: 6215–6221.

100 Walker, L.S., Marotto, V.R., Rafiee, M.A. et al. (2011). Toughening in graphene ceramic composites. *ACS Nano* 5: 3182–3190.

101 An, Y., Han, J., Zhang, X. et al. (2016). Bioinspired high toughness graphene/ZrB_2 hybrid composites with hierarchical architectures spanning several length scales. *Carbon* 107: 209–

216.

102 Chen, R., Johnson, M.B., Plucknett, K.P., and White, M.A. (2012). Thermal conductivity of tunable lamellar aluminum oxide/polymethyl methacrylate hybrid composites. *J. Mater. Res.* 27: 1869–1876.

103 Flauder, S., Sajzew, R., and Müller, F.A. (2015). Mechanical properties of porous β tricalcium phosphate composites prepared by icetemplating and poly(εcaprolactone) impregnation. *ACS Appl. Mater. Interfaces* 7: 845–851.

104 Borisova, A., De Bruyn, M., Budarin, V.L. et al. (2015). A sustainable freezedrying route to porous polysaccharides with tailored hierarchical meso and macroporosity. *Macromol. Rapid Commun.* 36: 774–779.

105 Erb, R.M., Libanori, R., Rothfuchs, N., and Studart, A.R. (2012). Composites reinforced in three dimensions by using low magnetic fields. *Science* 335: 199–204.

106 Porter, M.M., Yeh, M., Strawson, J. et al. (2012). Magnetic freeze casting inspired by nature. *Mater. Sci. Eng. A* 556: 741–750.

107 Niebel, T.P., Bouville, F., Kokkinis, D., and Studart, A.R. (2016). Role of the polymer phase in the mechanics of nacrelike composites. *J. Mech. Phys. Solids* 96: 133–146.

108 Roy, S. and Wanner, A. (2008). Metal/ceramic composites from freezecasting ceramic performs: domain structure and elastic properties. *Compos. Sci. Technol.* 68: 1136–1143.

109 Hautcoeur, D., Lorgouilloux, Y., Leriche, A. et al. (2016). Thermal conductivity of ceramic/metal composites from preforms produced by freeze casting. *Ceram. Int.* 42: 14077–14085.

110 Wang, Y., Shen, P., Guo, R. et al. (2017). Developing high toughness and strength Al/TiC composite using icetemplating and pressure infiltration. *Ceram. Int.* 43: 3831–3838.

111 Zhang, H., Shen, P., Shaga, A. et al. (2016). Preparation of nacrelike composites by reactive infiltration of a magnesium alloy into porous silicon carbide derived from ice template. *Mater. Lett.* 183: 299–302.

112 Guo, R., Shen, P., Lin, S. et al. (2017). High compressive strength in nacreinspired Al −7Si−5Cu/Al_2O_3–ZrO_2 composites at room and elevated temperatures by regulating interfacial reaction. *Ceram. Int.* 43: 7369–7373.

113 Tamerler, C. and Sarikaya, M. (2008). Molecular biomimetics: genetic synthesis, assembly, and formation of materials using peptides. *MRS Bull.* 33: 505–512.

114 Palmer, L.C., Newcomb, C.J., Kaltz, S.R. et al. (2008). Biomimetic systems for hydroxyapatite mineralization inspired by bone and enamel. *Chem. Rev.* 108: 4754–4783.

115 He, L.H. and Swain, M.V. (2008). Understanding the mechanical behavior of human

enamel from its structural and compositional characteristics. *J. Mech. Behav. Biomed. Mater.* 1: 18–29.

116 Fincham, A.G., MoradianOldak, J., and Simmer, J.P. (1999). The structural biology of the developing dental enamel matrix. *J. Struct. Biol.* 126: 270–299.

117 Yeom, B., Sain, T., Lacevic, N. et al. (2017). Abiotic tooth enamel. *Nature* 543: 95–99.

118 Denry, I. and Holloways, J.A. (2010). Ceramics for dental applications: a review. *Materials* 3: 351–368.

119 Thompson, J.Y., Stoner, B.R., Piascik, J.R., and Smith, R. (2011). Adhesion/cementation to zirconia and other nonsilicate ceramics: where are we now? *Dent. Mater.* 27: 71–82.

120 Pieralli, S., Kohal, R.J., Jung, R.E. et al. (2017). Clinical outcomes of zirconia dental implants: a systematic review. *J. Dent. Res.* 96: 38–46.

121 Petrini, M., Ferrante, M., and Su, B. (2013). Fabrication and characterization of biomimetic ceramic/polymer composite materials for dental restoration. *Dent. Mater.* 29: 375–381.

122 Dietze, M., Krause, J., Solterbeck, C.H., and EsSouni, M. (2007). Thick film polymer–ceramic composites for pyroelectric applications. *J. Appl. Phys.* 101: 054113.

123 George, S., Anjana, P.S., Sebastian, M.T. et al. (2010). Dielectric, mechanical, and thermal properties of lowpermittivity polymer–ceramic composites for microelectronic applications. *Int. J. Appl. Ceram. Technol.* 7: 461–474.

124 Xu, T. and Wang, C.A. (2014). Piezoelectric properties of a pioneering 31 type PZT/epoxy composites based on freezecasting processing. *J. Am. Ceram. Soc.* 97: 1511–1516.

125 Zhai, H., Xu, P., Ning, M. et al. (2017). A flexible solid composite electrolyte with vertically aligned and connected ionconductivity nanoparticles for lithium batteries. *Nano Lett.* 17: 3182–3187.

126 Hu, J., Huang, Y., Yao, Y. et al. (2017). Polymer composite with improved thermal conductivity by constructing a hierarchically ordered threedimensional interconnected network of BN. *ACS Appl. Mater. Interfaces* 9: 13544–13553.

127 Bauer, J., Hengsbach, S., Tesari, I. et al. (2014). Highstrength cellular ceramic composites with 3D microarchitecture. *Proc. Natl. Acad. Sci.* 111: 2453–2458.

7
Porous Carbon and Carbonbased Materials via Ice Templating and Freezedrying

7.1 Introduction

Porous carbon materials exhibit high chemical stability and high surface area and are used in a wide range of applications. A wellknown example of carbon materials are activated carbons that are usually fabricated by carbonization of polymers or biomass, followed by activation. Activated carbons are microporous materials (pore size <2 nm) and have been extensively used as adsorbents, as catalyst supports, in gas storage, etc. Like for other types of porous materials, the tuning of pore size, porosity, and surface functionality is crucial to optimize the potential of porous carbons for use in various applications. For example, while the micropores provide high surface area and large number of active sites, mesopores (2–50 nm) are important for mass transport of molecules, and macropores (>50 nm) may be essential for viscous systems, large molecules or tissue engineering.

Porous carbons may be fabricated by hard templates (e.g. porous silica, alumina, silica spheres), soft templates (e.g. surfactant assemblies, ionic liquids, liquid droplets, polymeric structures), or nontemplating methods (e.g. sol–gel process, hydrothermal process, self assembly) [1–7]. The pore surface of carbon materials can be specifically functionalized by incorporating heteroatoms in the synthesis, subsequent surface oxidation and activation, halogenation, and sulfonation, or via the coating of polymers and deposition of nanoparticles [8]. These carbon materials may be readily prepared as powders, monoliths, spheres [9], membranes [10] or fibres/nanofibres [11, 12]. Porous carbons can be produced from high carboncontent synthetic polymers [10, 11], sustainable natural polymers/biomass [1, 6], polymeric gels [7], or metal organic frameworks [13]. Carbon nanotubes (CNTs) and graphene (and graphene oxides) have been intensively investigated since their discovery not long ago. This is attributed to their excellent individual properties and great potential in various applications [14–16]. Importantly, they have also been used as building blocks to fabricate films, fibres, spheres, and three dimensional (3D) porous scaffolds [17–20]. Composites and hybrid materials containing CNTs and/or graphene have also been produced in order to improve mechanical properties and induce synergy effects, and also to enhance their properties such as thermal or electrical conductivity [21–25]. These carbon structures have found exciting applications in energy storage (e.g. rechargeable batteries, supercapacitors) [12, 19, 26–28], sensing [29], fuel cells and solar cells [26, 28, 30], pollution management [18, 31, 32], catalysis [22, 33], and biomedical applications [20, 24, 34, 35].

Ice templating has been used as a simple but effective route to preparing a wide range of porous materials and nanostructures [36, 37]. As the name ‘ice templating’ suggests, the ice crystals formed during the freezing stage are used as templates, which are usually removed by

a freezedrying process. Ice templating is highly effective for solutions, suspensions, and lightly crosslinked gels where molecules/particles/gel structures are excluded from the growing ice crystals. However, for strong gels or highly crosslinked wet polymeric or inorganic structures, it is very difficult for the growing ice crystals to change the original pore structure to a noticeable degree and hence the effect of ice templating is minimal (although this does not exclude the potential templating effect from the solvated solvent). For these types of gels or structures, the freezedrying process is employed to minimize the surface tension that is exerted on the pore structures during sublimation of the frozen solvent, prevent or significantly reduce pore structure collapse, and produce highly porous materials. For example, the freezedrying of resorcinol–formaldehydes is performed to produce highly porous cryogels, with porosity on a similar level as supercritical fluid drying but usually much better than airdried xerogels, unless a dense porous structure is required [38]. The organic cryogels can then be carbonized to produce carbon cryogels [39].

In this chapter, for each category of porous carbon materials described, both the freeze dryinginduced cryostructures and the icetemplated structures are covered. The relevant applications and particularly the advantages arising from the freezedrying or icetemplating procedures are discussed. Because of the intensive investigations of porous carbon materials for supercapacitors and rechargeable batteries, key properties and performance data are summarized in Tables 7.1 and 7.2 respectively.

Table 7.1 Supercapacitor performance of porous carbon and hybrids by ice templating/freeze drying.

Materials	**Fabrication method**	**Capacity**	**Surface areas/pore sizes/pore volume**	**References**
TanninF gel	Carbon cryogel	100 F g^{-1} in 4 M H_2SO_4 at scan rate of 2 mV s^{-1} by CV	1420 m^2 g^{-1}, micropore volume 0.28 cm^3 g^{-1}	[40]
Sdoped carbon	Cryogel from 2 thiophene carboxaldehyde and resorcinol	94.4 F g^{-1} in organic electrolyte, by charge/discharge	1105 m^2 g^{-1} Pore size 4.2 nm Mesopore volume 0.46 cm^3 g^{-1} Total pore volume 0.86 cm^3 g^{-1}	[41]
Ndoped carbon	Cryogel from melamine–formaldehyde	59.23 F g^{-1} in 5 M KOH by CV at scan rate of 10 mV s^{-1} 62.13 F g^{-1} in 30% KOH by charge/discharge at the rate of	88.44 m^2 g^{-1} mesopore volume 0.18 cm^3 g^{-1} 10.23% N	[42]

		20 mA		
Ndoped graphene carbon	For the above, 5% graphene oxide incorporated and thermally reduced	297 F g^{-1} by CV 313 F g^{-1} by charge/discharge	261 m^2 g^{-1} mesopore volume 0.36 cm^3 g^{-1} 14.29% N	[42]
Porous carbon	Icetemplated polyamic acid	248 F g^{-1} at 0.5 A g^{-1} in 6 M KOH	2038 m^2 g^{-1} 0.9% N, Mesopore volume 0.26 cm^3 g^{-1}, total pore volume 0.86 cm^3 g^{-1}, pore size 0.7 nm	[43]
Porous carbon	Icetemplating, SiO_2 colloid templating and CO_2 activation	221 F g^{-1} at 2 mV s^{-1} in 1 M H_2SO_4	2096 m^2 g^{-1} pore volume 3.0 cm^3 g^{-1}	[44]
CNF microspheres	Carbonized PDI gel	284 F g^{-1} at 1A g^{-1} in 6 M KOH, 67 retaining after 1000 cycles at 4 A g^{-1}	427 m^2 g^{-1} 3.61% N Hg intrusion volume 10.43 cm^3 g^{-1}	[45]
CNF networks	Carbonized PDI gel	192 F g^{-1} at 1 A g^{-1} 346 F g^{-1} at 1 mV s^{-1} in 2 M H_2SO_4	520 m^2 g^{-1}	[46]
Graphene aerogel	GO reduced to form gel by Lascorbic acid and freeze dried	128 F g^{-1} at 50 mA g^{-1} in 6 M KOH	512 m^2 g^{-1}, 2.48 cm^3 g^{-1}	[47]
Graphene aerogel	GO reduced and functionalized by hydroquinone to form a gel and then freezedried	441 F g^{-1} at 1 A g^{-1} in 1 M H_2SO_4	297 m^2 g^{-1}, Pore volume 0.95 cm^3 g^{-1}, Pore sizes 2–70 nm	[48]
Graphene aerogel on Ni foam	Freezedrying from soaked Ni foam	366 F g^{-1} at 2 A g^{-1} in 6 M KOH		[49]

Graphene paper	Infiltration assembly and freezedrying	137 F g^{-1} at 1 A g^{-1} in PVA/H_2SO_4 solid electrolyte	148 m^2 g^{-1}	[50]
$VOPO_4$–graphene	Ice templating, then reduced by hydrazine vapour	528 F g^{-1} at 0.5 A g^{-1} in 6 M KOH	—	[51]
$NiCo_2S_4$ nanotube@Ni–Mn LDH@graphene	In situ growth in porous graphene	1740 mF cm^{-2} at 1 mA cm^{-2}	—	[52]
Pristine graphene/MWCNT	Room temperature gelation and drying	100 F g^{-1} at 100 A g^{-1} or 167 F g^{-1} at 1 A g^{-1}, organic electrolyte	700 m^2 g^{-1}, 10–200 nm, peaked at 83 nm	[53]

Table 7.2 Porous carbon and hybrids as electrodes for rechargeable batteries (the batteries are LIBs, unless stated otherwise, SIBs for sodiumion batteries).

Materials	Fabrication method	Capacity	Surface areas/pore volume/pore sizes	References
V_2O_5–carbon cryogel	Electrodeposition in cryogel	280 mAh g^{-1} at 100 mA g^{-1}, based on V_2O_5, >250 mAh g^{-1} after 20 cycles	402 m^2 g^{-1} Mesopore volume 0.42 cm^3 g^{-1} Pore size 6 nm	[54]
SnO_2–carbon cryogel	Impregnation and thermal decomposition in cryogels	590 mAh g^{-1} at 100 mA g^{-1} after 50 cycles	153 m^2 g^{-1} Pore volume 0.514 cm^3 g^{-1} Pore size 3.19 nm	[55]
Scarbon composites	S infiltration into porous carbon prepared by ice templating, SiO_2 colloidal templating and CO_2 activation	747 mAh g^{-1} at the Crate of 1C with organic electrolyte, for Li-S battery	2339 m^2 g^{-1} Pore volume 3.8 cm^3 g^{-1}, initial 1 : 1 C:S in mass	[56]
CNF web	Pyrolysed and activated cellulose fibres	858 mAh g^{-1} at 100 mA g^{-1} after 100 cycles	1236 m^2 g^{-1} Total pore volume 1.03 cm^3 g^{-1}	[57]
Graphene paper	Infiltration assembly and freezedrying	420 mAh g^{-1} at 2 A g^{-1}	148 m^2 g^{-1}	[50]
Graphene/CNT sponge	Freezedrying and thermal annealing	436 mAh g^{-1} at 50 mA g^{-1} after 100 cycles for SIBs	498 m^2 g^{-1} Pore volume 1.51 cm^3 g^{-1}	[58]
WS_2/CNT–rGO aerogel	Freezedrying the gel and thermal annealing	749 mAh g^{-1} at 100 mA g^{-1} for LIBs 311.4 mAh g^{-1} at 100 mA g^{-1} and 253 mAh g^{-1} at 200 mA g^{-1} after 100 cycles for SIBs	—	[59]

7.2 Carbon Cryogels and Icetemplated Carbons

7.2.1 Carbon Cryogels

In order to produce carbon cryogels, polymeric (organic) gels are first formed, followed by a freezedrying process and a pyrolysis procedure. The polymeric gels are usually prepared via controlled hydrolysis and polycondensation reactions using different precursors. Figure 7.1 illustrates the molecular structures of some commonly used precursors. Resorcinol and formaldehyde are the mostly used system [7, 39]. Some other systems are also investigated, either to tune pore structures, to induce doping elements, or to improve sustainability by using sustainable precursors. These include phenol–formaldehyde [60], melamine–formaldehyde [42], resorcinol–2thiophenecarboxaldehyde [41], and tannin–formaldehyde [40].

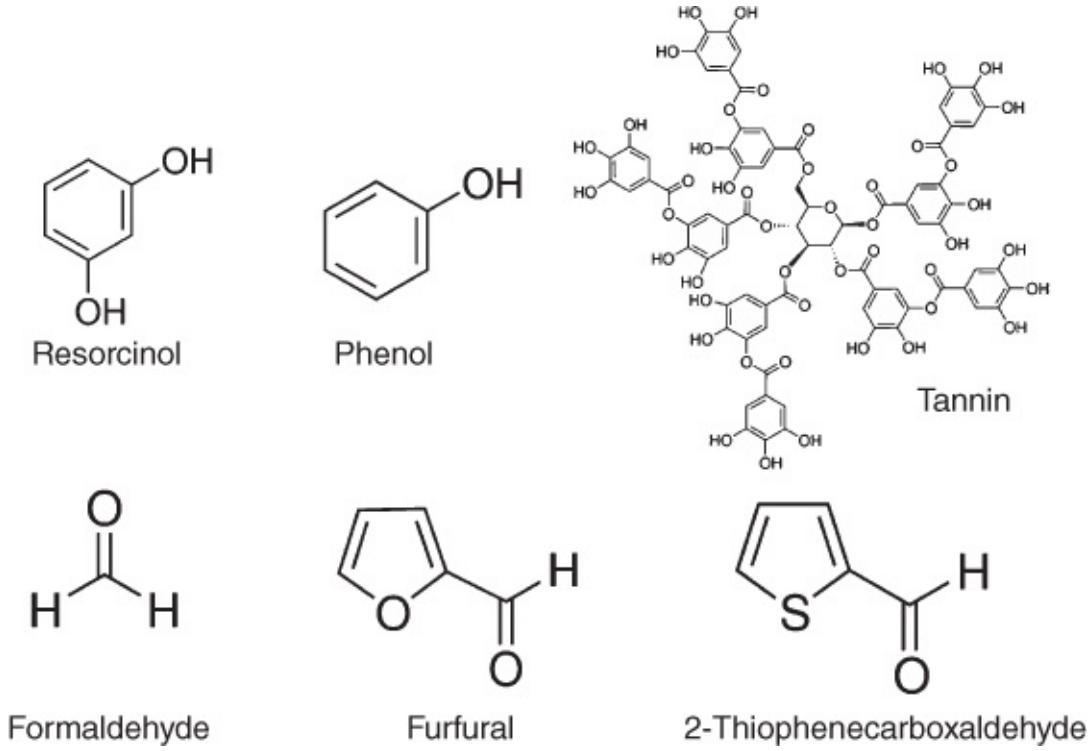

Figure 7.1 Molecular structures of the common organic precursors used for the preparation of carbon cryogels.

For the resorcinol (R)–formaldehyde (F) system, the solvent can be water (W) or organic solvents such as acetone or alcohols of different chain lengths (e.g. methanol, ethanol, propanol, butanol). The catalyst (C) can be a base or an acid. Sodium carbonate (Na_2CO_3) seems to be the most commonly used base catalyst [7]. Sodium hydroxide (NaOH) is also frequently used. Hexamine can be used to introduce N into the carbon cryogel [39]. The R/F molar ratio of 1 : 2 is the widely used condition. The R/C ratios are usually in the range of 50–300. In general, lower R/C ratios lead to the formation of smaller polymer nanoparticles that are connected to form a porous structure with large necks, giving the fibrous gel. For higher R/C ratios, large polymer particles (~15–200 nm) may be formed, resulting in a ‘stringof pearls’ gel structure [7]. The C/W or R/W ratios can have a substantial effect on the pore size and porosity of carbon cryogels [7]. Particularly with hexamine as catalyst in an alcoholic

solvent, the addition of water can decompose hexamine into formaldehyde and ammonia, resulting in a decrease of about 20% in porosity [39]. The type of solvents in RF gels can have a big impact on the pore structure of the resulting dry gels. If water is used as the solvent, it is usually replaced with a polar organic by solvent exchange, for reducing the damages on the pore structure during the drying procedure. When the freezedrying procedure is intended, tertiarybutanol (*t*butanol) is usually used to replace other solvents before freezedrying. This is due to its high melting point and relatively high vapour pressure.

Tamon and coworkers have extensively investigated the fabrication of carbon cryogels from RF gels [61–64]. The reactant solutions (R/C = 25 or 200, R/W (g cm^{-3}) = 0.125 or 0.250, R/F = 0.5) with sodium carbonate as catalyst were gelled at 25 °C for 1 day, 50 °C for 1 day, and then 90 °C for 3 days [61]. The RF gels were washed with water or *t*butanol and then freezedried. The pyrolysis procedure was performed after aging the RF gels at 250 °C for 8 h, following a procedure of heating to 250 °C at 4.2 °C min^{-1}, dwelling for 2 h, heating to 1000 °C at 4.2 °C min^{-1}, dwelling for 4 h and then cooling down to room temperature, under a N_2 flow of 80 cm^3 min^{-1}. Carbon cryogels with surface areas >800 m^2 g^{-1} and mesopore volumes >0.55 cm^3 g^{-1} were formed [61]. It was further found that freezedrying of the RF gels with *t*butanol could generate more mesopores, compared to freezedrying the RF gels with water [62]. The mesoporosity could also be controlled by changing the polycondensation conditions. The C/W ratio was found to be related to the mesoporosity. The mesopore volume, mesopore size, and surface area decreased with the increase of C/W when C/W was in the region of ≤70 mol m^{-3}. It was hard to generate mesopores in the carbon cryogels when C/W was >70 mol m^{-3} [63]. In addition to cryogel monoliths, carbon cryogel microspheres were prepared via an inverse emulsion polymerization approach [64]. Aqueous reaction mixtures (R/C = 400 or 100, R/W = 0.25 or 0.50) were emulsified in cyclohexane with Span 80 as the surfactant. The resulting emulsions were stirred at 25 or 60 °C for 5–10 h in order to allow the gelation in the aqueous droplets [64].

Traditionally, it has been very difficult to prepare carbon cryogels with mesopores >40 nm. This is attributed to the low pH required for the synthesis and the difficulty in reproducing carbon cryogels when a small amount of Na_2CO_3 is used. This problem was addressed by the use of buffer solutions with pHs in the range of 10.0–12.0 (by adding 0.1 M HCl or 0.1 M NaOH into Na_2CO_3 solution). Carbon cryogels with large mesopores (14–108 nm) were successfully produced [65]. HCl aging of frozen RF gels could markedly increase the hydrophobicity of carbon cryogels [66]. This was achieved by immersing the frozen RF gels in 1 N aqueous HCl solution for 1–20 days at room temperature before washing with *t*butanol. The resulting carbon exhibited similar hydrophobicity as the coalderived activated carbon and pure βzeolite [66]. Effect of pyrolysis temperature and partial oxidation by oxygen were also investigated, which had an obvious impact on the adsorption of Pb^{2+} but minimal impact on the adsorption of methylene blue [67].

Modification or doping of carbon cryogels can be achieved by direct incorporation of chemical precursors in the synthesis mixture, impregnation of target entities into the porous

carbon cryogels or chemical modification of carbon surface [7, 8, 39]. For example, Ndoped carbon cryogels were prepared by the reaction between melamine and formaldehyde [42] or with hexamine as catalyst [39]. The organic gels from resorcinol and 2 thiophenecarboxaldehyde could be used to fabricate Srich carbon cryogels [41]. When ammonia borane was added to the RF gel during the solvent exchange stage, the prepared B,Ndoped carbon cryogel showed increased surface area and larger mesopore volume [68]. SnO_2incorporated carbon cryogels were fabricated by impregnating the cyrogel with $SnSO_4$ ethnaol solution, followed by freezedrying and pyrolysis in N_2 at 500 °C for 1 h. The diameters of the SnO_2 particles were approximately 15 nm [55]. $VOSO_4$ solution (pH 1.8) was infused into porous carbon cryogel films. The films were dried under vacuum at 80 °C and then subjected to potentiodynamic electrodeposition to produce V_2O_5incorporated composites [54]. Sulfonated carbon cryogels as acid catalysts were generated by treating the pyrolysed carbon with concentrated sulfuric acid at 80 °C for 10 h and subsequently 150 °C for 5 h under a dry N_2 atmosphere [69].

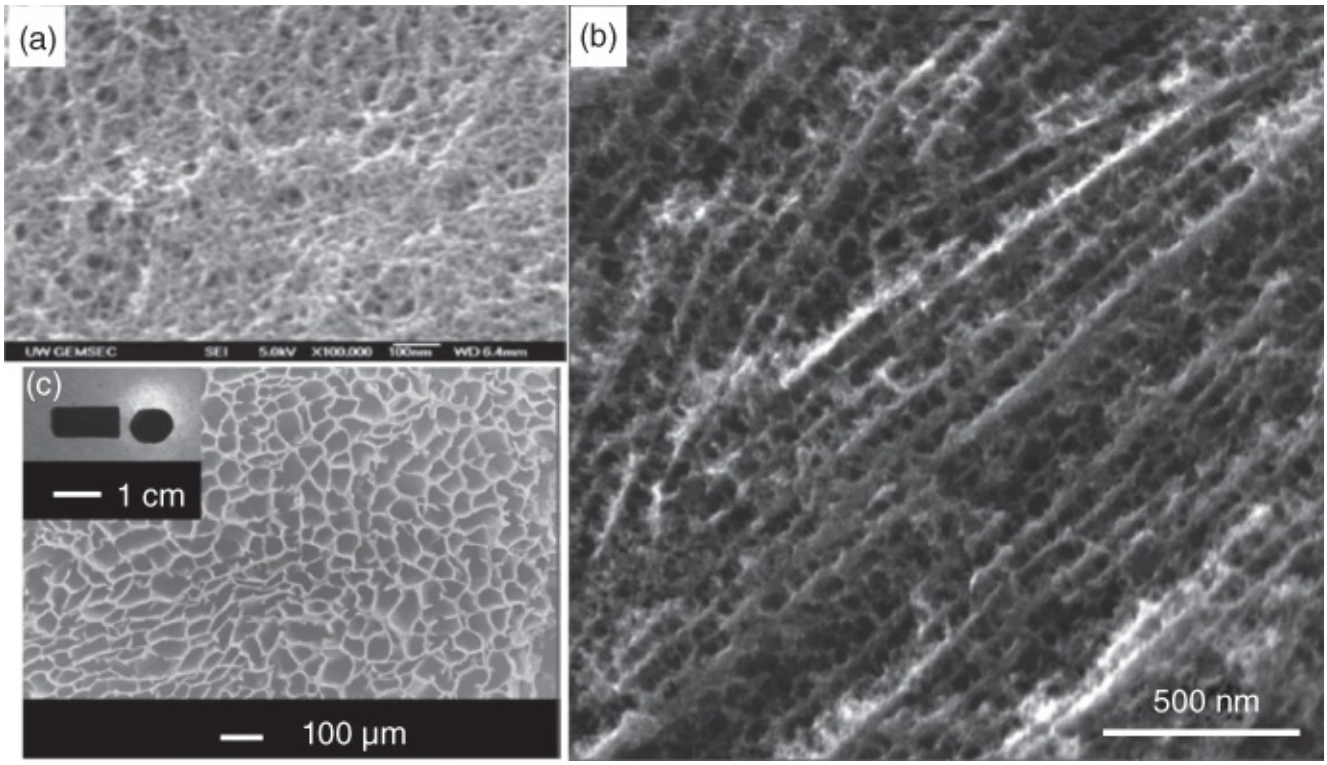

Figure 7.2 Examples of carbon cryogels with different pore structures. (a) Randomly fibre like pore structure. (b) Aligned porous carbon structure. (c) The carbon cryogel with microhoneycomb structure.

Source: Yoshida et al. 2016 [142. Reprinted with permission from Springer Nature.

Source: Minović et al. 2015 [140. Reprinted with permission from Elsevier.

Source: Sepehri et al. 2009 [136. Reprinted with permission from Elsevier.

Carbon cryogels have been used for adsorption (water treatment), electrochemical energy storage, and catalyst support. These applications are enhanced by high surface area, large number of mesopores, and icetemplated macropores in the carbon cryogels. Figure 7.2

shows the pore structures of some carbon cryogels. The icetemplated aligned structure (Figure 7.2b) and the honeycomb structure (Figure 7.2c) in the gels are the results of directional freezing of relatively lightly crosslinked RF gels.

Carbon cryogel microspheres were prepared via inverse emulsion polymerization with surface areas up to 752 $m^2 g^{-1}$, mesopore volume 0.97 $cm^3 g^{-1}$, and micropore volume 0.23 $cm^3 g^{-1}$. These microspheres were packed into a column for high performance liquid chromatography (HPLC) [64]. A similar approach was also employed to prepare carbon microspheres for adsorption of phenol and reactive dyes. The size of the mesopores in the microspheres did not impact the adsorption of phenol. This was likely due to the small size of phenol molecules. For a similar reason, the adsorption of Black 5 and Red E (larger size of molecules) was higher than activated carbon and increased with the size and the volume of mesopores [72]. However, the use of monolithic adsorbents may be easier for the adsorption of pollutants because the monoliths can be easily collected from the solution. Mesoporous carbon cryogels prepared from RF gels was used for the adsorption of As^{3+} (aqueous sodium arsenite solution). The adsorption capacity (~2.1 mg g^{-1} carbon) was similar in the pH range of 2–11 [70]. The carbon cryogels with large mesopores 14–108 nm, prepared by controlling the pH via the use of buffer solution, could be used to distinguish proteins of different sizes. This was achieved by protein adsorption of different molecular weights into the mesopores of different sizes [65]. The hydrophobic carbon cryogels prepared via HCl aging was used to recover 1butanol from dilute aqueous solution (135 mM) at 37 °C. A high adsorption capacity of 3.13 mol kg^{-1} was achieved [66]. In general, the adsorption capacity increased with 1butanol concentration but changed slightly when the concentration was >200 mM [66]. The carbon monolith with a microhoneycomb structure (with straight channels of 25–25 μm in diameter) (Figure 7.2c) was fixed into a heat shrinkable tube. The tube was connected to a setup containing an HPLC pump and a UV–vis detector for the flow adsorption of phenol [71]. The highest adsorption capacity achieved was around 160 mg g^{-1} from aqueous phenol solution of 100 ppm [71]. The carbon microspheres obtained from phenolic resin were embedded in a poly(vinyl alcohol) cryogel and evaluated for the removal of pesticides atrazine (32 mg l^{-1}) and malathion (16 mg l^{-1}) in aqueous solutions. The flow through tests showed that the maximum adsorption capacities were 641 mg (atrazine) and 591 mg (malathion) g^{-1} carbon [73].

Carbon and dopedcarbon cryogels obtained from organic resins are widely used as porous electrodes for supercapacitors. Carbon cryogels obtained from phenol–formaldehyde (PF) resin were tested in 4 M H_2SO_4 aqueous electrolyte and specific capacitances of around 100 F g^{-1} were achieved. There was no direct link between the capacitance and the surface area/micropore volume. The highest capacitance obtained was related to mesopores and not too narrow micropores [60]. For the carbon cryogels prepared from tannin–formaldehyde resin, similar specific capacitance of about 100 F g^{-1} was achieved. However, this study found that the capacitance could be correlated to the micropore volume [40]. Srich carbon obtained from 2thiophenecarboxaldehyde–resorcinol resin could improve the wetting property of the electrode in organic electrolyte (1 M tetraethylammonium tetrafluoroborate in 50–50 propylene carbonate–dimethyl carbonate). Complete wetness could be achieved for the

carbons with 2.5 at.% S. The best capacitance achieved was 94.4 F g^{-1} when the freezedried resin was pyrolysed at 1000 °C [41]. Ndoped carbon from melamine–formaldehyde showed a specific capacitance of 59 F g^{-1} at scan rate of 10 mV s^{-1} in 5 M KOH aqueous electrolyte by cyclic voltammetry or 62 F g^{-1} at the current rate of 20 mA in 30% KOH solution by the charge/discharge approach. However, with the incorporation of 5% graphene oxide (then reduced to graphene by a thermal treatment), the specific capacitance could be increased to 279 F g^{-1} and 313 F g^{-1}, respectively [42]. For the N,Bdoped carbon cryogels with higher mesoporosity, higher surface area, and more uniform mesopore size distribution, the specific capacitance (tested in the organic electrolyte as used in Ref. [41], up to ~120 F g^{-1}) could be correlated with the surface area [68].

Incorporation of metal oxide nanoparticles into carbon cryogels has been used to enhance the performance of lithium ion batteries (LIBs). For example, hydrous vanadium pentoxide ($V_2O_5 \cdot nH_2O$) was formed in porous carbon cryogel by electrodeposition. Owing to the highly interconnected 3D porous structure, the composite electrode reached a discharge capacity of 280 mAh g^{-1} (based on the mass of V_2O_5) at a current density of 100 mA g^{-1}. These values were about twice that of $V_2O_5 \cdot nH_2O$ on Pt foil. The capacity was still higher than 250 mAh g^{-1} after 20 cycles [54]. SnO_2 nanoparticles (~15 nm) were incorporated into carbon cryogel via impregnation and thermal decomposition of stannous sulfate. When used as an electrode for LIBs, a discharge capacity of 590 mAh g^{-1} after 50 cycles at a current density of 100 mA g^{-1} was recorded. This value was much higher than pure SnO_2 nanoparticles, carbon cyrogel and their physical mixture. Again, this performance was attributed to the 3D porous structure and the stabilization of SnO_2 particles in the mesopores [55].

Sulfonated carbon cryogels with icetemplated microhoneycomb structure were used as solid acid catalysts for liquid phase reactions [69]. These catalysts exhibited surface areas of 570–670 m^2 g^{-1}, mesopore volumes of 0.2–1.5 cm^3 g^{-1}, concentrations of sulfuric acid group in the rage of 0.62–0.97 mmol g^{-1}, depending on R/C (50, 200) and pyrolysis temperature (673 K, 1273 K). The catalyst prepared from R/C = 200 and pyrolysis temperature of 1273 K exhibited the best properties in the combination of 570 m^2 g^{-1}, 1.5 cm^3 g^{-1}, and 0.62 mmol g^{-1}. By using these catalysts, higher reaction rate and higher selectivity (>90%) than Amberlyst15 were observed for esterification of acetic acid with ethanol and oleic acid with methanol, and particularly for the condensation reaction of furfural and 2methylfuran [69]. It was believed that the highly interconnected mesopores, larger mesopore volume, and the surface hydrophobicity contributed to the superior catalytic activities.

7.2.2 Icetemplated Carbons

This section covers polymer solutions (instead of gels) that can be processed to produce porous carbons. Both aqueous solutions and organic solutions may be utilized. However, the selection of polymer is very important. The polymers should have high carbon contents and are not sublimed or melting during the pyrolysis process. Polymers that have been used to fabricate porous carbon or carbon membranes may be used in an icetemplating process [10, 74]. Some

of the commonly used polymers are given in Figure 7.3. Polyimides are formed by condensation reactions of dianhydrides and diamines. There are a range of polyimides. They usually show highmelting point and high thermal stability. Because of aromatic rings in the polyimide molecules, these polymers are rigid and can be good precursors for production of carbon materials. Polyetherimide is illustrated in Figure 7.3. Another commonly used commercial polyimide is Kapton produced by DuPont [10]. Biomass is also widely used as a source of carbon materials. However, they are not covered in this section because they are insoluble in most of the solvents although alkaline lignin can be readily dissolved in water.

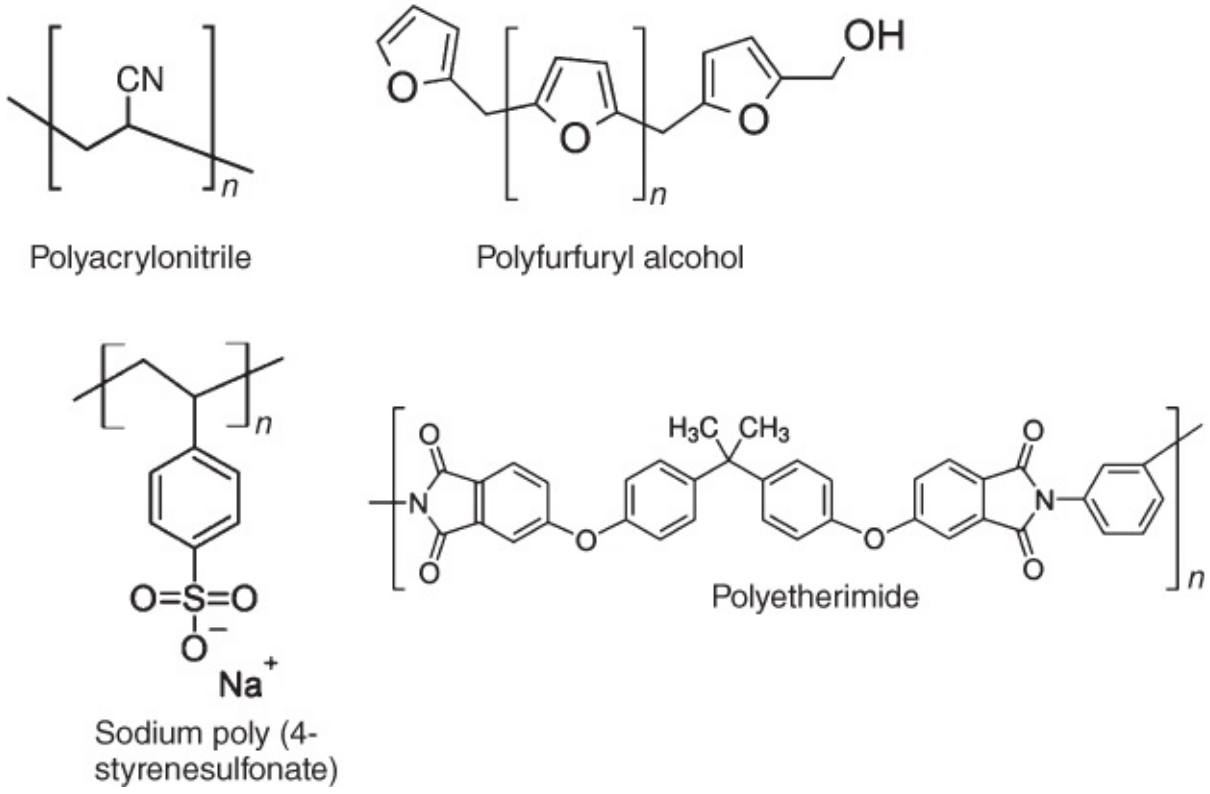

Figure 7.3 Molecular structures of commonly used polymers for icetemplated carbons.

Polyacrylonitrile (PAN) is the mostly used polymer in the preparation of porous carbon or carbon nanofibres (CNFs). PAN was dissolved in dimethyl sulfoxide (DMSO) and the resulting solutions were frozen and freezedried to produce aligned porous polymer. It was found that stable aligned porous monoliths could be formed when the concentrations were not less than 100 mg ml^{-1}. It was essential to anneal the freezedried PAN in air at 280 °C for 1 h before the pyrolysis process at 800 °C [75]. The aligned macroporous structure was retained in the carbon materials. N_2 sorption study showed the surface areas to be below 200 m^2 g^{-1} and lack of mesopores in the resulting carbon materials. The advantage of this method is that doping elements can be easily added in the initial PAN solution. This was demonstrated by incorporation of melamine and graphene oxides to produce Ndoped graphene–carbon composites, which resulted in a substantial increase of reversible capacity for LIBs (300 mAh g^{-1} at a high current density of 10 A g^{-1}) [75]. After freezing the PAN–DMSO solution, the usual freezedrying step could be replaced with a solvent exchange process [76]. The icetemplated structures were retained (Figure 7.4). Owing to relatively low surface

areas after carbonization, varying amounts of KOH were incorporated into the porous PAN, followed by the same annealing and pyrolysing procedure. The incorporation of KOH was simply achieved by soaking porous PAN in aqueous KOH solutions. The highly interconnected macroporosity in PAN facilitated the impregnation of KOH. The activated icetemplated carbons showed hierarchical porosity (Figure 7.4) with a surface area up to 2206 $m^2 g^{-1}$ and varying percentage of N content. Great potential was demonstrated for the uptake of CO_2 and H_2 by these Ndoped icetemplated carbon materials. The carbon material with a surface area of 1049 $m^2 g^{-1}$ and 14.9% N gave a CO_2 uptake of 16.12 mmol g^{-1} at 298 K and 10 bar while the carbon with the surface area of 2206 $m^2 g^{-1}$ and 1.29% N showed the adsorption of H_2 (2.66 wt%) at 77 K and 1.2 bar [76].

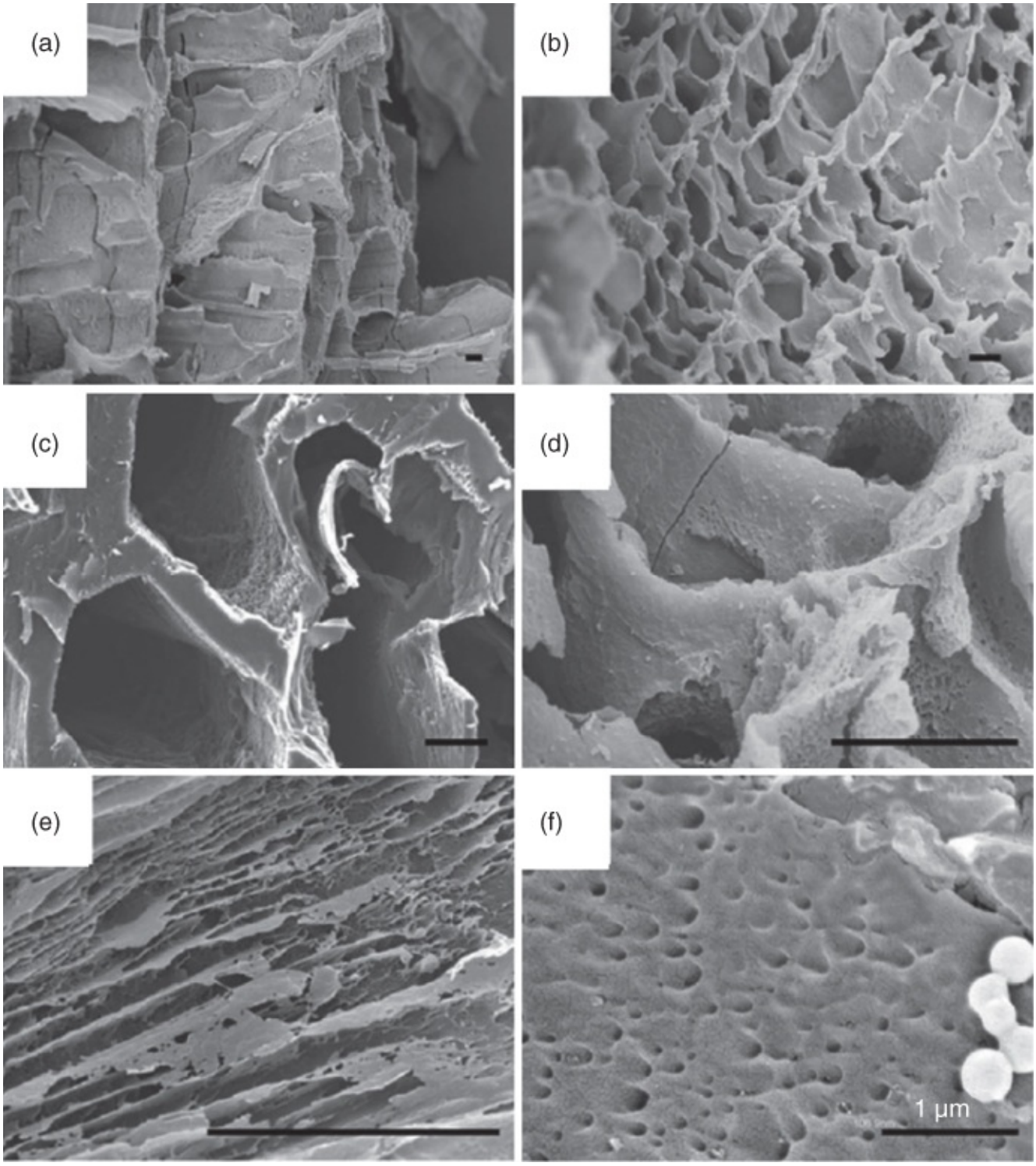

Figure 7.4 Pore structure of the icetemplated carbon prepared from polyacrylonitrile at various magnifications. (a) ×300. (b) ×700. (c) ×1400. (d) ×3700. (e) ×6500. (f) ×30k. Scale bar = 10 μm unless otherwise stated.

Source: Roberts et al. 2017 [152. Reprinted with permission from Royal Society of Chemistry.

Other polymers have also been used. One example is sodium poly(4styrenesulfonate) (PSS). PSS can be dissolved in water and the resulting aqueous solution can be conveniently freeze dried. In the study by Roberts et al. [77], it was found that a single step of thermal treatment at 800 °C under Ar was sufficient to produce icetemplated porous carbon monoliths.

Remarkably, the in situ generated Na_2SO_4 could act as an activating agent during pyrolysis which was further transformed to $Na_2S{\cdot}9H_2O$. Following washing with acidic solution, sulfur was formed in situ within the porous carbon. By varying degassing temperature, the amount of sulfur removed from the carbon materials could be adjusted. Accordingly, the pore volume and the surface area of the carbon materials could be changed. A high specific surface area of 1051 $m^2\ g^{-1}$ was achieved. The S content could be increased from 17.07 wt% to 39.74 wt% by incorporating additional Na_2SO_4 into porous PSS prior to pyrolysis [77]. Polyamic acid (PAA) is an intermediate polymer to produce polyimide. By carbonization of freezedried PAA from its solution in 1,4dioxane, hierarchically porous carbon with icetemplated macropores was produced [43]. The N content decreased with the increase of carbonization temperature. The carbon obtained by carbonization at 1000 °C exhibited a porosity of 90.8%, a surface area of 2038 $m^2\ g^{-1}$ and a N content of 0.9% (by elemental analysis). When used as an electrode, a specific capacitance of 248 F g^{-1} was reached at 0.5 A g^{-1} in 6 M KOH solution [43]. Chitosan and benzoxamine (and montmorillonite also added to reinforce the aerogel) were freezedried and then allowed for thermal crosslinking by stepwise treatment from 100 to 175 °C. The carbonized materials (at 800 °C under N_2) showed excellent CO_2 adsorption (up to 6.25 mmol g^{-1} at 298 K and 2 bar) [78].

Hard colloidal templating and ice templating have been combined to fabricate hierarchically porous carbon monoliths containing micropores, welldefined mesopores and macropores. This was demonstrated by directional freezing and freezingdrying of silica colloids–glucose suspension, followed with carbonization and HF etching to remove silica colloids. Different sizes of silica colloids, e.g. 4, 8, 12 nm, were used. This resulted in the welldefined mesopores templated by silica colloids [44]. The specific surface area and the extent of micropores could be further increased by CO_2 activation. The porous carbon, prepared from 4 nm silica colloids, 1 : 1 ratio of silica to glucose and 4 h of CO_2 activation, showed a BET surface area of 2096 $m^2\ g^{-1}$ and pore volume of 3.0 $cm^3\ g^{-1}$ [44]. The large pores and high pore volumes of such carbon materials facilitated the impregnation of polyethyleneimine, which was then used for CO_2 capture. A capacity of 4.2 mmol g^{-1} could be achieved for CO_2 capture after 45 min. When evaluated for their use in supercapacitors, a specific capacitance of 221 F g^{-1} was recorded at a scan rate of 2 mV s^{-1} in a threeelectrode setup with 1 M H_2SO_4 as the electrolyte [44]. This method was also applied to the suspension of silica colloids (4 nm) and sucrose. The highest surface area of 2339 $m^2\ g^{-1}$ and total pore volume of 3.8 $cm^3\ g^{-1}$ were obtained for the porous carbon with 1 : 1 ratio of silica to sucrose and 2 h CO_2 activation [56]. Sulfur was infiltrated into the porous carbon via melt infusion. The carbonS composite was tested for Li-S battery with 1 M LiTFSi and 1 wt% $LiNO_3$ dissolved in a mixture of 1,3dioxlane and dimethoxyethane (1 : 1 v/v) as the electrolyte. A high specific capacitance of 747 mAh g^{-1} was obtained at the rate of 1C. This electrode was highly stable. High capacitances of 647 mAh g^{-1} and 503 mAh g^{-1} were still recorded after 200 cycles at high Crates of 2C and 5C [56].

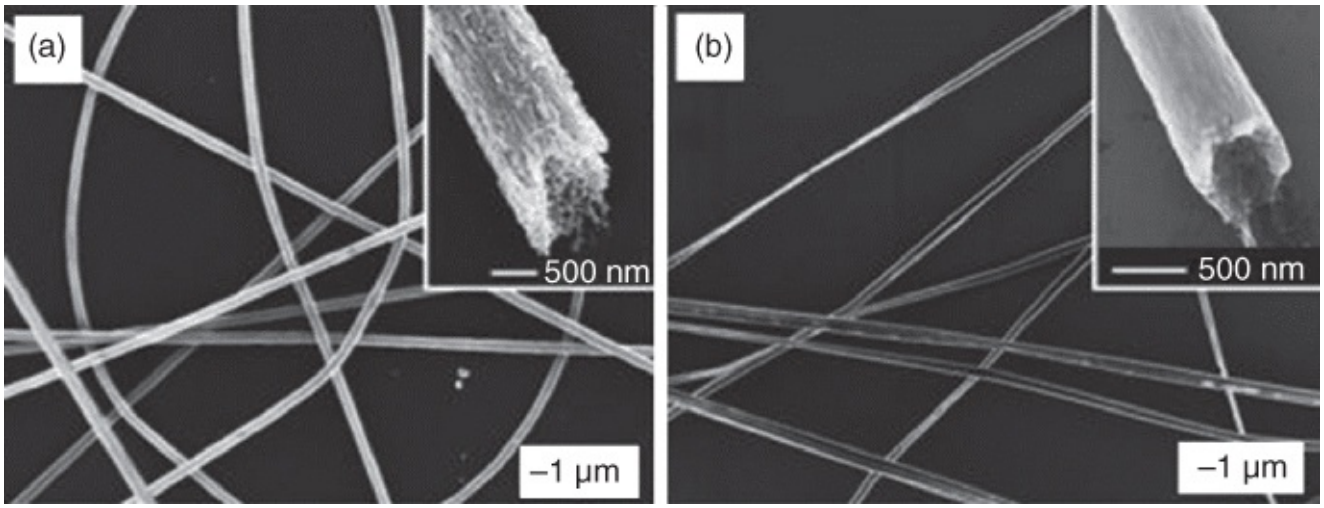

Figure 7.5 (a) Poly(acrylonitrile) fibres prepared by electrospinning into liquid nitrogen. The inset shows the end of a broken fibre, clearly indicating a highly porous structure. (b) Porous carbon fibres obtained by carbonization of the poly(acrylonitrile) fibres.

Source: McCann et al. 2006 [158. Reprinted with permission from American Chemical Society.

7.3 Carbon Nanofibres

CNFs may be directly prepared by chemical vapour deposition (CVD) [12]. But the CVD approach requires hightemperature and highvacuum equipment and it is extremely difficult to produce a large amount of CNFs. Carbonization of polymer fibres has been an effective approach to prepare CNFs. The polymer fibres may be fabricated by traditional spinning (e.g. melt spinning) but this method can only form fibres of larger diameters (>5 μm) [12]. Electrospinning has been extensively used to fabricate polymer fibres and CNFs [11, 12]. Control of fibre morphology and fibre diameter is highly important for the electrospinning method. This may be achieved by adjusting solution viscosity, surface tension, flow rate, electric conductivity and voltage [12]. The commonly used polymers for electrospun CNFs include PAN, pitch, lignin, PI and PVDF. Because of their low carbon yields (<15%), polyvinylpyrrolidone (PVP) and PVA are used mainly for metal oxide/CNF composites [12]. The electrospinning process does not usually involve a freezing step. However, instead of a conductive collection plate, highly porous fibres can be fabricated by electrospinning into a cryogenic liquid (e.g. a liquid nitrogen bath) [79]. As shown in Figure 7.5, the icetemplated porous structure can be observed in the fibres and the highly porous CNFs are generated after thermal annealing and carbonization [79]. Aqueous PVA solution containing $SnCl_2$ was electrospun. The asprepared sample was frozen in an icebox at −12 °C for 2 days. Subsequently, the frozen fibres were heated at 110 °C for 2 h and then 550 °C for 3 h in Ar/H_2 atmosphere. This led to the formation of Sn/SnO_x nanoparticles in the larger icetemplated pores within the CNFs [80]. The volume of the particles was found to be less than half of the pore volume, which provided space to accommodate the volumetric change of Sn/SnO_x nanoparticles during the LIB test. This contributed to the high capacitance of 735 mAh g^{-1} in the 1st cycle and 510 mAh g^{-1} after 40 cycles at the current density of 30 mA g^{-1} [80].

CNFs may be produced by hydrothermal and solvothermal reactions but quite often the products are powders or microspheres [6]. Using nanowires as template can facilitate the formation of CNFs in the form of monoliths. This was demonstrated by the use of Te nanowires in the hydrothermal carbonization of glucose with the production of largescale CNF cryogels [81]. Because this nanowiretemplating approach includes a step of removing the template, it may be more convenient to process polymer nanofibres directly and followed by carbonization. For example, aqueous chitin or wood cellulose nanofibre (~10 nm) suspensions in *t*butanol at a concentration of 0.05 wt% were freezedried and subsequently carbonized to produce CNFs with surface areas of 279 $m^2 g^{-1}$ [82]. Aqueous cellulose nanofibres suspension could be directly freezedried. After pyrolysis at 600 °C, CNFs with diameters of ~20 nm were formed [57]. CNF webs were prepared from freezedrying and pyrolysis of bacterial cellulose and were activated by KOH (700 °C under N_2 1 h) to improve the surface area and induce mesopores to the CNFs [83]. The highest surface area achieved was 1236 $m^2 g^{-1}$ and pore volume 1.029 $cm^2 g^{-1}$ for the activated CNFs was obtained by KOH:cellulose = 6 (by mass). When evaluated as an anode for LIBs, a specific capacity of 857.6 mAh g^{-1} was recorded at a current density of 100 mA g^{-1} after 100 cycles [83].

It is possible to generate polymeric nanofibres by direct freezedrying of aqueous polymer solution [84, 85]. The key to the success of this approach is the use of diluted polymer solutions, e.g. in the range of 0.05–1 wt%, depending on the type and molecular weight of the polymers used. The diameters of the fibres are usually in the range of 100–800 nm. A directional freezing procedure can be applied to fabricate aligned polymer nanofibres. When a watersoluble polymer of high carbon content, such as lignin, is used, CNFs can be readily formed by carbonization of the polymer fibres [86]. This was convincingly demonstrated by a study from Spender et al. [45]. More importantly, by injecting the lignin solution (0.2 wt%) onto a rotating drum cooled by a pressurized liquid nitrogen tank, they showed it was possible to prepare lignin nanofibres continuously and hence the synthesis of large amount of CNFs [45].

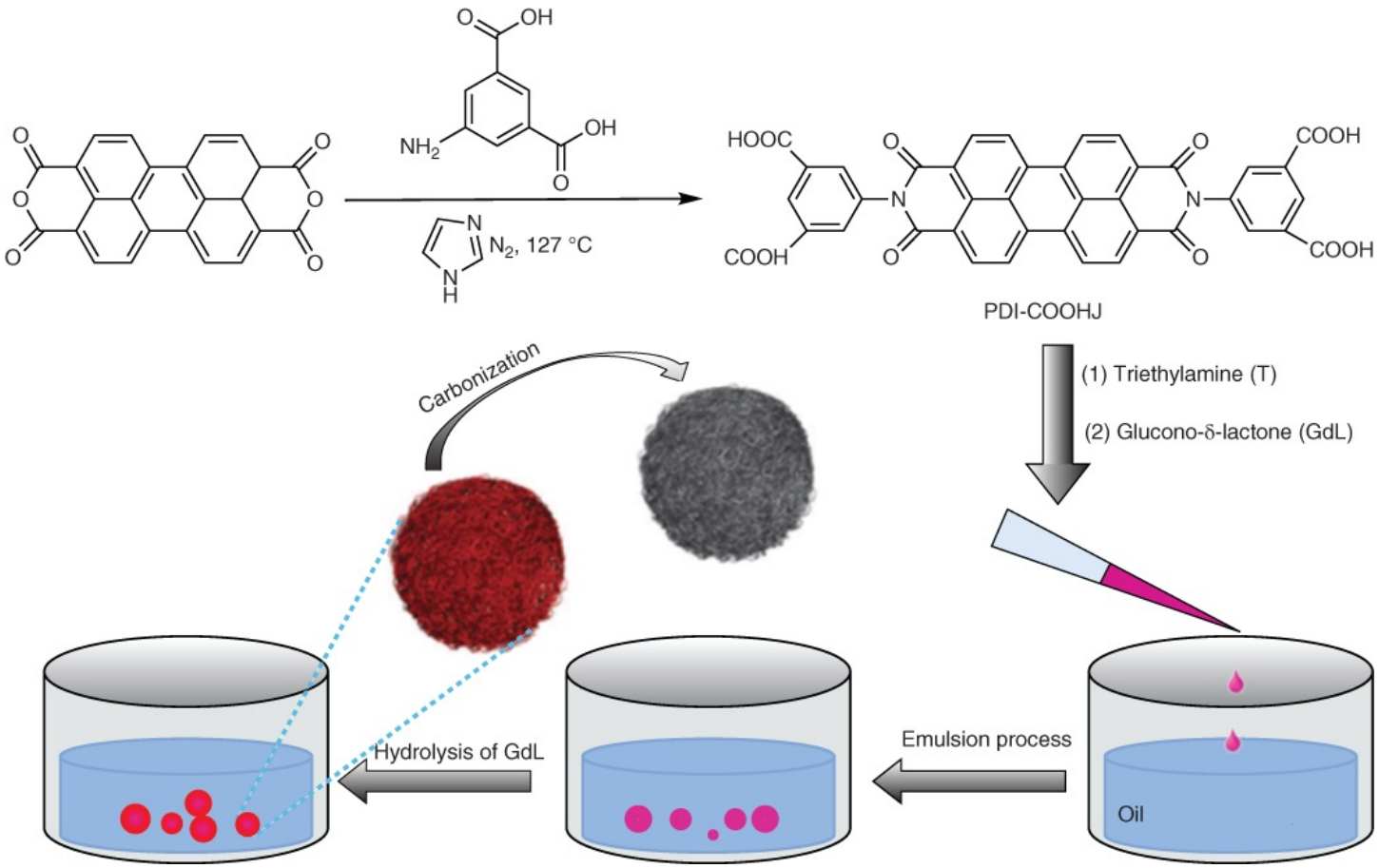

Figure 7.6 The scheme shows the synthesis of perylene diimide derivatives (PDICOOH) and the preparation steps for nanofibrous microspheres. The fibrous monoliths can be readily formed via the gelation of a bulk solution (see Figure 7.7).

Source: Liu et al. 2015 [92. Reprinted with permission from Royal Society of Chemistry.

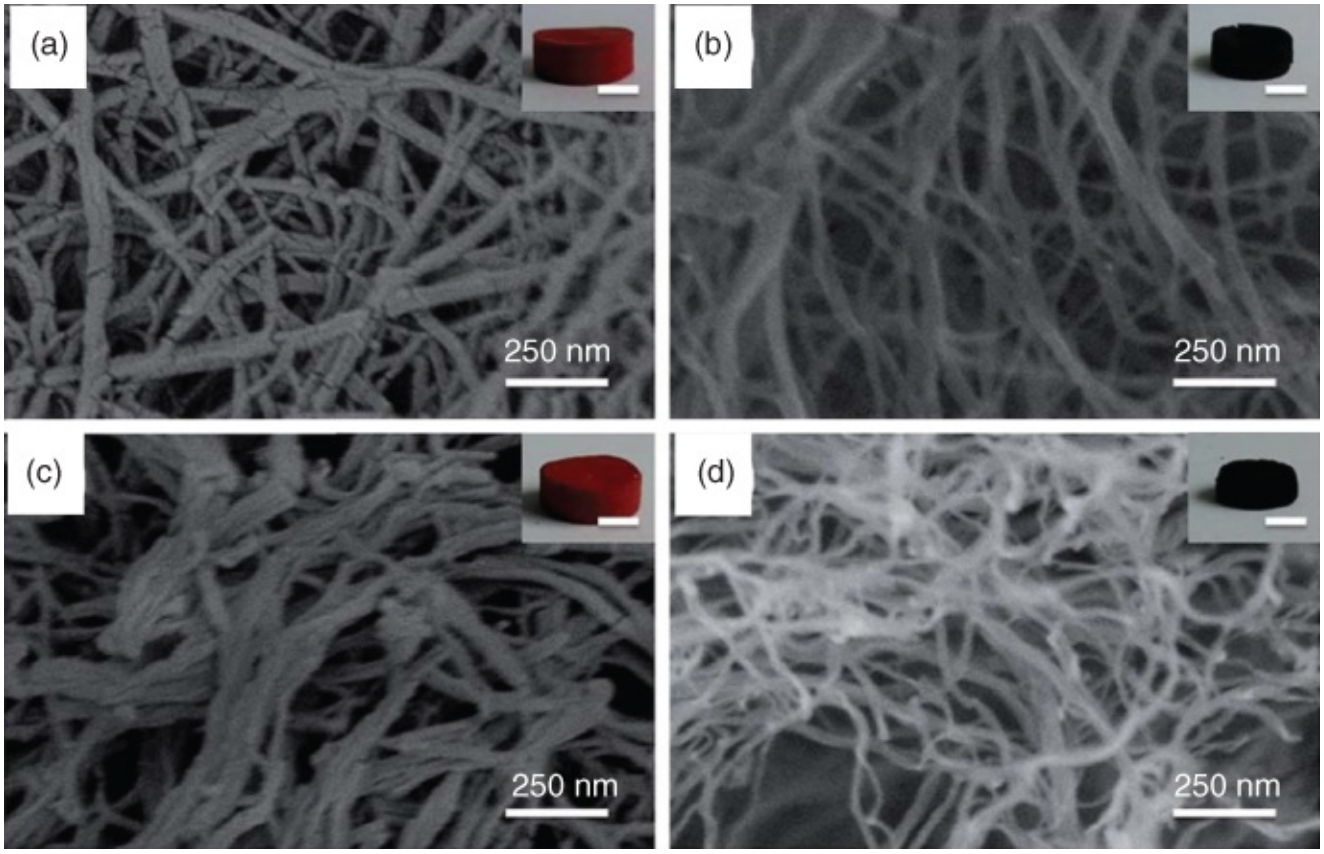

Figure 7.7 The morphologies of nanofibrous gel and carbon monoliths prepared from dissolving the PDICOOH in water with triethyl amine. (a) and (b) The gel monolith and the carbon monolith. (c) and (d) Ndoped gel and carbon monoliths by adding melamine in the PDICOOH solution. Insets show the photos of the relevant monoliths, scale bars = 5 mm.

Source: Liu et al. 2015 [174. Reprinted with permission from Royal Society of Chemistry.

Lowdensity polymeric gels may exhibit nanofibrous networks, which can serve as templates for CNFs. However, there are two limiting issues: (i) quite often these polymers have low carbon content and are thus unsuitable for carbonization; (ii) the diameters of the fibres are not uniform, particularly at the fibre junctions. Zhang and coworkers proposed to form organic nanofibres via pHtriggered selfassembly of perylene diimide derivatives (PDIs) and then carry out carbonization to produce CNF networks [46, 87]. PDIs are multiaromatic molecules with an extended quadrupolar π system and strong hydrophobicity. The pH triggered selfassembly is driven by hydrophobic interaction, π–π stacking and interaction of side chains. Figure 7.6 illustrates the synthesis of PDICOOH that is used as a precursor to form nanofibrous gels. The PDICOOH was dissolved in basic water, assisted by the addition of triethylamine. Gluconoδlactone (GdL) or freshly prepared aqueous GdL solution was added to the PDI solution. The slow hydrolysis of GdL reduced the solution pH and initiated the gelation. This helped to form a uniform hydrogel, compared to the direct addition of acid solution. A monolithic gel could be readily formed, showing a dark red colour, with the uniform fibre diameters around 25 nm. A washing procedure in the order of water, acetone and cyclohexane and the subsequent freezedrying resulted in red nanofibrous monoliths (Figure 7.7). This treatment also facilitated the preparation of CNF monoliths (Figure 7.7). An advantage of this method is that different precursors may be included in the gelation procedure

to prepare modified CNFs. For example, melamine was added to make Ndoped CNFs (Figure 7.7c and d). K_2SnO_3 was used to replace triethylamine to make the solution basic and also introduce SnO_x into the CNF monoliths. Nonionic surfactant F127 was added to improve the surface area of the CNFs (up to 520 $m^2\ g^{-1}$). When tested as the electrode material for a supercapacitor, a specific capacitance of 346 F g^{-1} at the scan rate of 1 mV s^{-1} or 192 F g^{-1} at the current density of 1 A g^{-1} in 2 M H_2SO_4 was achieved. Remarkably, the specific capacitance was increasing with the test cycles, achieving a capacitance of 226 F g^{-1} at 4 A g^{-1} after 1000 charge/discharge cycles [87]. Unlike the electrospinning method, this gelation approach can be combined with emulsification to fabricate nanofibrous microspheres (Figure 7.6). Aqueous PDI solution containing GdL was emulsified into *o*xylene with Span 80 as the surfactant and polystyrene was included as stabilizer. The gelation was initiated in the aqueous droplets to form gel microspheres. The gel microspheres were then collected by centrifuging/filtering and were washed, dried and carbonized to produce nanofibrous carbon microspheres [46]. These microspheres were also evaluated as the electrode for supercapacitors. A highspecific capacitance of 284 F g^{-1} at 1A g^{-1} and good rate capability (retaining 57% after 1000 cycles at 4 A g^{-1}) were recorded [46].

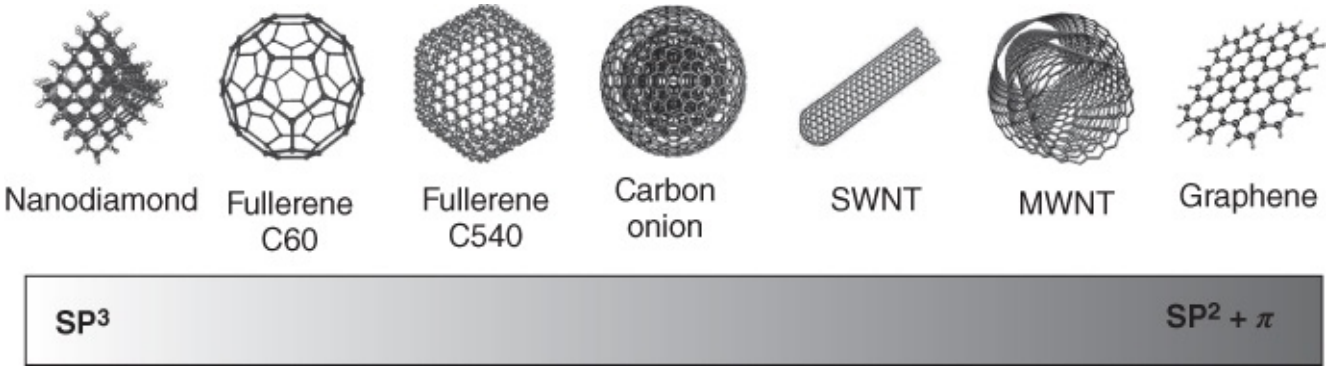

Figure 7.8 Different forms of carbon nanomaterials.

Source: Mauter and Elimelech 2008 [62. Reprinted with permission from American Chemical Society.

7.4 Carbon Nanotubes (CNTs) and CNTbased Materials

7.4.1 Introduction to CNTs

There are different forms of carbon nanomaterials, from nanodiamonds with tetrahedron sp^3 configuration to graphene with the planar sp^2 conformation (Figure 7.8) [31]. Theoretically, an sp^2hybridized CNT can be constructed by rolling up a hexagonal graphene sheet. This can lead to chiral and nonchiral arrangement of carbon atoms [88]. The nonchiral CNT can take the armchair or zigzag configuration, as illustrated in Figure 7.9 [21]. The transformation induced by the stress along the axial direction of the armchair tube, resulting in the structure with two pentagons and two heptagons in pair, is called the Stone–Wales transformation. This transformation contributes to ductile fracture in armchair CNTs.

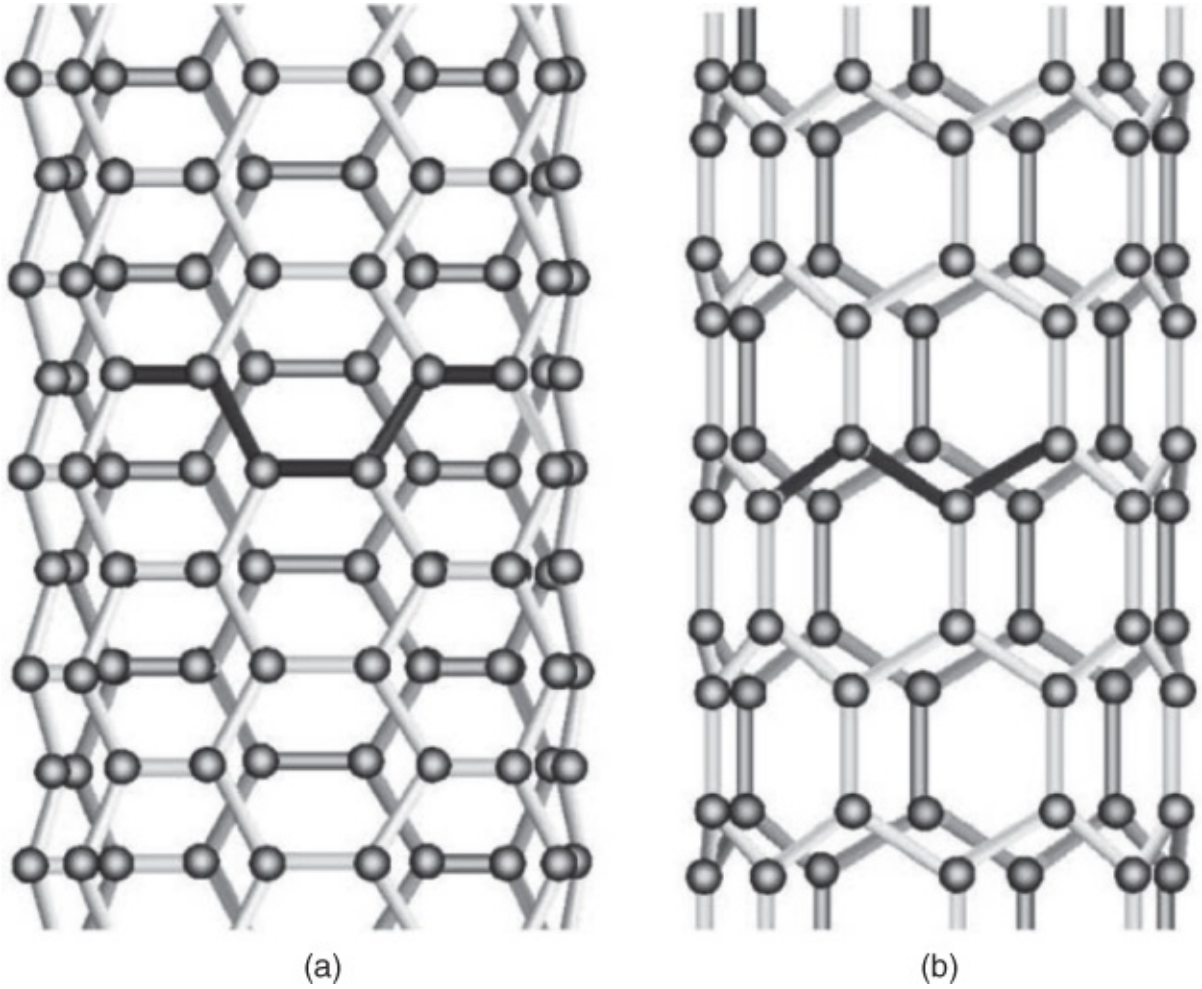

Figure 7.9 Schematic representation of the C arrangement in a carbon nanotube. (a) The armchair structure. (b) The zigzag structure.

Source: Thostenson et al. 2001 [42. Reprinted with permission from Elsevier.

There are singlewalled, doublewalled, and multiwalled CNTs. CNTs may be produced by arc discharge and laser ablation and the widely used CVD [89]. CVD is the main approach used to manufacture CNTs, by cracking gaseous hydrocarbon over transition metal catalysts. The carbon is dissolved in the metal and then grows from the metal to form CNTs and also CNFs. The commonly used hydrocarbons are methane, ethylene, acetylene, benzene and xylene while the catalysts are mostly Fe, Co and Ni due to their high solubility and high diffusion rate to carbon atoms [89]. CNTs have excellent mechanical, electronic and thermal properties. For example, a Young's modulus of 0.9 TPa and tensile strength of 150 GPa, electrical conductivity of 10^7 S m^{-1} and thermal conductivity of 3500 W $(m\ K)^{-1}$ at room temperature, have been reported [26]. Therefore, due to the nanoscale feature and excellent properties, CNTs have been used and have great potential in a wide range of applications such as adsorption of metal ions and environmental applications [18, 90], energy conversion and energy storage [26, 91], catalysis [89] and biomedical applications [24, 91]. Some of the applications are highly promising and, therefore, may be exploited for commercial applications, e.g. CNT yarns and sheets for supercapacitors, sensing and actuators [92, 93].

7.4.2 CNT Aerogels/Cryogels

CNTs and CNT films may be directly produced by the CVD approach. However, solution based CNT processing approaches are much more widely used in the preparation of CNT films, yarns and 3D structures [28]. However, surfactant and/or polymer stabilizer are usually required to form stable CNT dispersion, which is critical to produce uniformly distributed CNT structures. Therefore, the direct processing of CNTonly dispersion is rare. Usually, after the CNT structures are formed, the polymer or surfactant may be removed by washing or thermal treatment. For the term 'aerogels', they usually indicate ultralight and highly porous materials fabricated by either supercritical fluid drying or freezedrying [94].

The icetemplating approach has been used to fabricate CNT aerogels or foams. For example, CNT aerogels were prepared with sodium dodecylbenzene sulfonate [94]. Macroporous CNT foams with a porosity of 97% were produced by freezedrying. Sodium carboxymethylcellulose (SCMC) was used to stabilize the CNTs in the aqueous dispersion [95]. However, these freezedried CNT structures are mechanically very weak. Chemically crosslinking the CNTs in the 3D structures is an effective route to improving mechanical stability. Ajayan and coworkers used the Suzuki crosscoupling reaction between aryl halide and boronic acid derivatives to crosslink the CNTs [96]. Before the reaction, the CNTs were washed with concentrated HNO_3 under reflux to remove impurities and introduce the -COOH groups. The CNTCOOH was then converted to CNTCOCl by reacting with $SOCl_2$, which could then be crosslinked by 1,4phenyldiboronic acid. The crosslinked CNT gels were then freezedried to produce the covalently connected CNT networks [96]. The CNT COCl could also be functionalized by allylamine monomers and then crosslinked by a free radical polymerization initiated by azobisisobutyronitrile (AIBN). A freezedrying process was then employed to fabricate the chemically crosslinked CNT networks [97]. Mechanically stable porous CNT beads were produced by dropping aqueous CNT dispersions (containing CNTCOOH, glutaraldehyde, resorcinol, borax) into liquid nitrogen and subsequently freezedrying [98].

7.4.3 CNTbased Porous Materials

CNT–polymer materials are mainly fabricated by the icetemplating approach. One of the main advantages is to enhance mechanical stability. For example, the freezedried CNT aerogels were fragile, just enough for careful handling while the PVAenhanced CNT aerogel could support 8000 times of its own weight [94].

The introduction of polymer may also offer some properties that promote the applications of CNTbased materials, as has been demonstrated by the CNT–chitosan structures. Chitosan is probably the most widely used polymer in making porous CNT–polymer structures. CNT may be directly dispersed in aqueous chitosan solution. Alternatively, CNTs may be first purified and functionalized by HNO_3 washing. In the latter case, the -COOH groups or other oxygen containing groups can have stronger interaction with the positive amine groups on chitosan. This facilitates the formation of stable porous CNT–chitosan structures. CNT–chitosan

materials have been investigated as scaffolds for cell culturing and tissue engineering. CNT toxicity, e.g. asbestoslike behaviour, has been a big challenge for biomedical applications. The incorporation of biocompatible chitosan into CNT structures has certainly benefited their biomedical applications [24]. Multiwall carbon nanotubes (MWCNTs)–chitosan scaffolds showed good cell adhesion, viability and proliferation when evaluated with C2Cl2 cell line (myoblastic mouse cell). From the *in vivo* tests, the adsorption potential of MWCNTs was exploited to incorporate rhBMP2 into the scaffold, which promoted cell colonization and tissue growth [99]. This scaffold was also compared with chondroitin sulfate–MWCNTs and gelatin–MWCNTs, based on the evaluations using three types of mammalian cells (L929 fibroblasts, Saos2 osteoblasts, EC_{PC} cells). It was concluded that the preparation parameters and scaffold properties could be optimized to serve better for the target cells [100]. Chondroitin sulfate is a major regulatory component of nerve tissue and has been used to fabricate icetemplated scaffolds with MWCNTs [101, 102]. Viable cultures enriched in neuron cells for up to 20 days could be formed, displaying calcium transients and active mitochondria [101]. It was found that the biocompatible MWCNT–chitosan scaffolds could promote the immobilization and proliferation of bacteria such as *Escherichia coli* within the icetemplated pores [103]. This kind of materials may be used as electrodes in microbial fuel cells (MFCs). This was demonstrated by the colonization of electroactive bacteria *Geobacter sulfurreducens* within the 3D microchannelled MWCNT–chitosan scaffold; the pore structure of the scaffold shown in Figure 7.10. The resulting materials were used as a flow through bioanode for the MFC and produced acetate oxidation current densities of up to 24.5 A m^{-2} and a maximum powder density of 2.87 W m^{-2} [104].

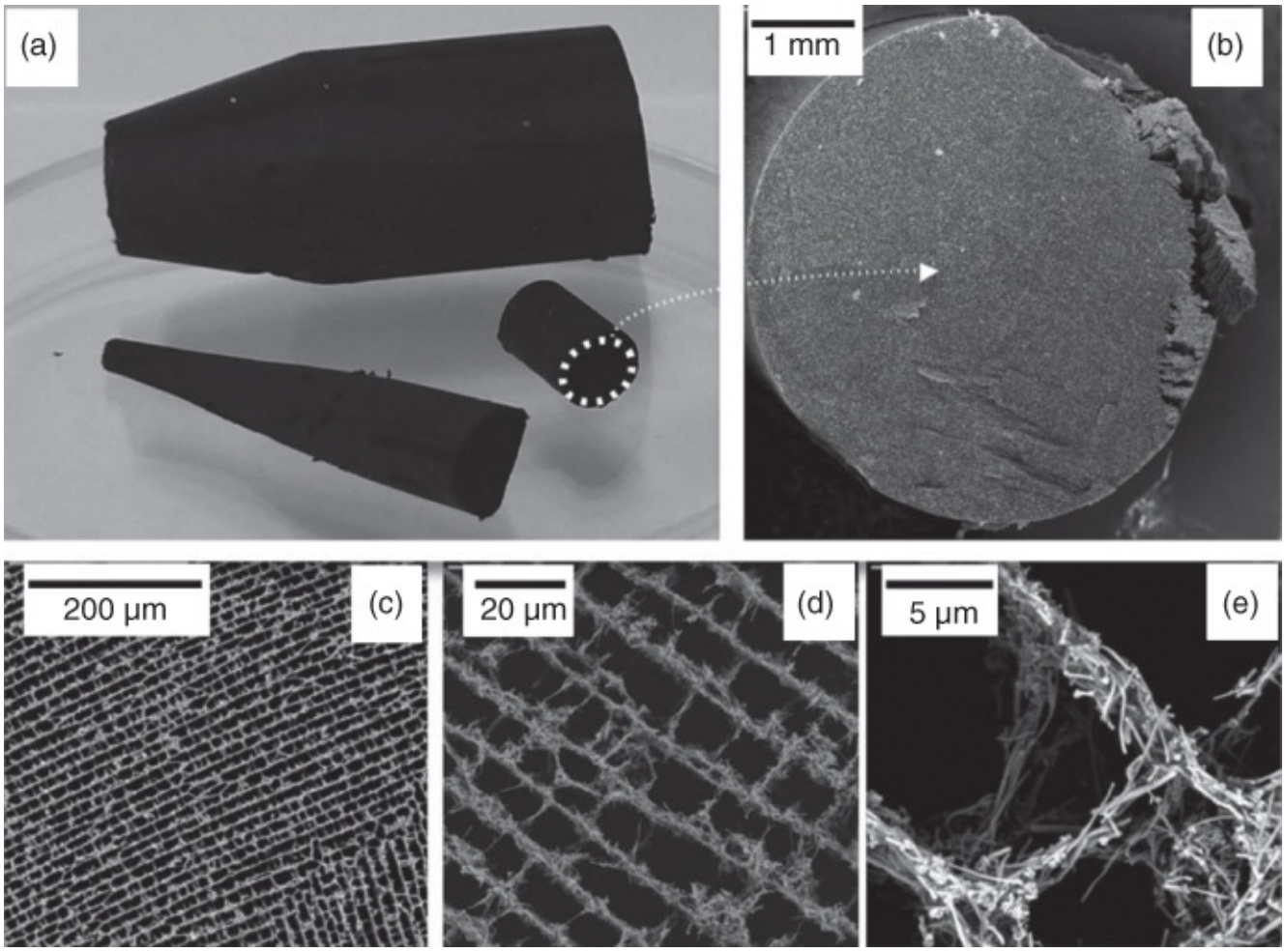

Figure 7.10 (a) Macroscopic monoliths of different shapes composed of MWCNT/chitosan fabricated by the icetemplating process. And the pore structures at different magnifications; scales are 1 mm (b), 200 µm (c), 20 µm, (d) and 5 µm (e).

Source: Katuri et al. 2011 [208. Reprinted with permission from Royal Society of Chemistry.

The hierarchical porosity and highly exposed surface of CNTs in CNT–chitosan scaffolds facilitate adsorption of pollutants or other target components [105]. Despite the high porosity, CNT–chitosan scaffolds or compressed powders can be highly conductive due to the presence of CNTs. A percolation threshold was found to be ~2.5 wt% MWCNTs [106]. The conductivity of such scaffolds facilitates their use as electrodes. For example, a macroporous MWCNT–chitosan scaffold prepared by the icetemplating process, with surfacedecorated Pt nanoparticles, was used as the anode for methanol fuel cell. The electric conductivity was recorded as 2.5 S cm^{-1}, resulting from a high content of MWCNTs. Current densities of up to 242 mA cm^{-2} were obtained [107]. As expected, CNT–chitosan composite foams showed enhanced elastic property. The recovery ability of the composite foams increased with the increasing CNT content until a critical point. After this point, the recovering ability after cyclic compression tests was decreased dramatically. This was attributed to the inadequate chitosan presence and the aggregation of CNTs [108].

Other polymers and additives have also been employed to produce CNTbased materials, achieving improved mechanical stability while still maintaining the electrical and thermal

properties. Cotton cellulose was dissolved in aqueous basic CNT suspension with Brij 76 used as a stabilizer. The Young's modulus of the freezedried composites was measured to be up to 90 MPa. The electrical conductivity was in the range of 2.3×10^{-4}–2.2×10^{-2} S cm^{-1} for the composites containing 3–10 wt% CNTs [109]. MWCNT–silk fibroin scaffolds with randomly porous and aligned porous structures were produced by gelation and flash freezing and directional freezing of the suspensions, respectively [110]. The aligned MWCNT–silk fibroin scaffolds showed superior thermal stability and electrical conductivity [110]. Aqueous suspensions containing MWCNT and polyurethane were processed via the directional freezing approach to fabricate light and aligned porous composites [111]. In addition to the enhanced mechanical properties (compared to porous CNT and polyurethane), the composites showed high electromagnetic interference (EMI) shielding effectiveness, exceeding 50 or 20 dB in the Xband with the density only being 126 or 20 mg cm^{-3}, respectively [111]. V_2O_5 powders were suspended in aqueous H_2O_2 solution, which formed a gel upon continuously stirring. Aqueous CNT dispersion was then added to the gel with vigorous stirring. The sheetlike V_2O_5–CNT composite formed after freezedrying was treated at 300 °C for 1 h and then evaluated as a cathode for LIBs. A discharge capacity of 240 mAh g^{-1} was obtained at the rate of 5C, and 71% of the capacity was retained after 300 cycles [112]. $NiFe_2O_4$ nanoparticles (20 nm in diameter) were dispersed in aqueous chitosan and CNT dispersion. The freeze drying process was then employed to prepare the composite sponges. After dropping glucose oxidase solution onto the sponge to prepare a glucose biosensor, two large linear ranges (0–3.0 and 3.2–12.4 mM) with sensitivities of 84.1 and 24.6 μA $(mM\ cm^2)^{-1}$ were obtained [113].

The polymer phase may be infiltrated into a freezedried porous CNT scaffold to make a composite. For example, liquid epoxy resin was infiltrated into aligned porous CNT scaffold. The curing of epoxy resin was completed at 140 °C for 12 h. The lamellar structure of the original CNTs rendered the composites highly conductive. An electrical conductivity of 0.158 S cm^{-1} at a CNT loading of 1.31 wt% was observed while the Young's modulus and yield strength were improved at 25.5% and 12.2%, respectively, compared to pure epoxy resin [114]. PANbased carbon fibre cloth was soaked with CNT suspension and then freeze dried. The freezedried cloth was thermally treated at 400–650 °C under Ar. Subsequently, epoxy resin was impregnated into the CNF/CNT structure to produce the composite with good electrical conductivity and mechanical strength [115]. Liquid polydimethylsiloxane (PDMS) precursor was infiltrated into an MWCNT foam at room temperature under vacuum. The curing of the liquid precursor was completed to produce the CNT–PDMS composite. The composite showed a high thermal conductivity of 0.82 W $(m\ K)^{-1}$, about 455% that of pure PDMS and 300% higher than that of the physically blended composites. Both the tensile strength and elongation at break were superior to those of the blended composite as well. This property made it a good candidate for thermal management of electronic devices [116].

7.5 Porous Graphene Networks and Graphenebased Materials

7.5.1 Graphene and 3D Graphene Networks

Graphene exhibits excellent properties such as very high Young's modulus (~1100 GPa), fracture strength (125 GPa), thermal conductivity (~5000 W $(m\ K)^{-1}$), mobility of charge carriers (200 000 $cm^2\ (V\ s)^{-1}$), specific surface area (calculated value of 2630 $m^2\ g^{-1}$) and the quantum Hall effect [15, 16]. Graphene may be produced by four different methods: (i) CVD and epitaxial growth; (ii) mechanical exfoliation of graphite or the wellknown 'Scotch tape' method; (iii) epitaxial growth substrates and (iv) preparation of graphene suspensions [16]. Among the four methods mentioned, the first three methods can produce highquality graphene but the quantity is very small. Preparation of graphene suspension is an effective route to addressing this issue with regard to largescale synthesis and application. Graphene is the atomthick sheet of hexagonal sp^2bonded carbon network (Figure 7.8). Owing to the high surface area, hydrophobic interaction and π–π stacking potential, graphene tends to aggregate. So it is impractical to prepare graphene suspension directly. Usually, graphite is oxidized by strong oxidants to produce aqueous graphene oxide dispersion. Graphene oxide is basically a graphene sheet with Ocontaining groups bonded to the carbon atoms, including hydroxyl, epoxide, carboxylic and carbonyl groups, as illustrated in Figure 7.11 [117]. Graphene oxide (GO) sheets are hydrophilic and negatively charged, which promotes their stable dispersion in water. Polymers or surfactants are usually required to stabilize GO in water. GO can be chemically or thermally reduced to produce graphene (or called *chemically converted graphene*) under the stabilization of polymer/surfactant usually in a gel or solid state [17, 19, 29]. However, aqueous graphene dispersion can be produced as demonstrated by hydrazine reduction in the presence of ammonia [118].

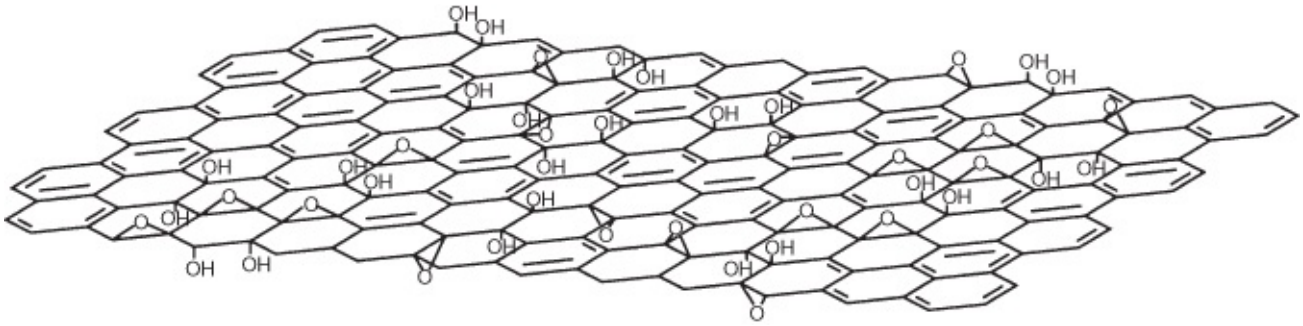

Figure 7.11 The chemical structure of graphene oxide.

Source: He et al. 1998 [234. Reprinted with permission from Elsevier.

Porous graphene or 3D graphene networks combine the excellent properties of graphene, highly interconnected porosity, and the easy manipulation or manufacturing for a wide range of applications [17, 19, 29, 119, 120]. Various approaches have been developed to fabricate 3D graphene materials including hydrothermal gelation [17], selfassembly under chemical reduction [17], modified GO and subsequent crosslinking/polymerization [17, 18], template

directed assembly [19, 29] and 3D printing [121]. Graphene fibres can be fabricated by wet spinning. The anodized aluminium oxide (AAO) may be used as a template to prepare graphene tubes while polymer colloidal particles are used as templates to prepare graphene spheres [19]. In addition, the icetemplating or freezecasting approach has been used to fabricate porous graphene with some unique properties [17–19, 119, 120]. This is the focus in the following sections.

7.5.2 Porous Graphene by Ice Templating/Freezedrying

Pristine graphene may be used directly to prepare graphene aerogels. For example, some solvents that are solid at room temperature but have relatively high vapour pressure were used to disperse graphene flakes at elevated temperatures. When cooling down to room temperature, the dispersions turned into solids. The solvents were conveniently removed by sublimation at room temperature [53]. Phenol (melting point 40.5 °C, vapour pressure 47 Pa at room temperature) and camphene (melting point 51.5 °C, vapour pressure 400 Pa) can be used as such solvents. The produced graphene aerogels showed good elasticity and electrochemical properties [53].

However, the preparation of most porous graphene structures starts with aqueous GO suspensions that are usually prepared by a modified Hummers method [16]. The control of freezing processes and preparation parameters that have been employed for other ice templated materials can be similarly applied for the preparation of porous graphene materials [36, 37]. Based on the methods reported in literature, the use of ice templating or freeze drying for graphene materials can be classified into five categories as described below.

The first approach is by directly freezing the GO suspensions and subsequent freezedrying [122–126]. Directional freezing, flash freezing, or slow freezing may be employed to produce graphene materials with either aligned porous structures or randomly porous structures. The GO may be partially reduced in the suspension before freezing, which leads to partial self assembly of GO sheets in the suspension and better elasticity and stability of the freezedried graphene structures [119, 120]. Figure 7.12 shows the scheme and the typical pore structures of cellular graphene monolith prepared by freezing a partially reduced GO suspension. It was found that the amount of oxygencontaining groups on GO could significantly influence the interactions between GO sheets. The superelastic porous graphene monolith could be produced with the C/O atomic ratio of around 1.93 in the partially reduced GOs [127]. Note that in Figure 7.12 there is a thawing procedure that facilitates the annealing and assembly of GO sheets. Indeed, multiple freezedrying procedures may be utilized to improve the properties of graphene materials. For example, the thermally reduced GO cryogel was soaked in KOH solution, freezedried, activated at 973 K under Ar, washed with dilute HCl and freezedried again. This produced an aligned porous graphene aerogel with additional mesopores and micropores [128]. The freezedried graphene structure may be directly formed in a porous scaffold or on a porous grid. This can be simply achieved by dipping the template in a GO suspension and subsequently freezedrying the GOsoaked scaffold. An example is the formation of graphene aerogel in nickel foam [49].

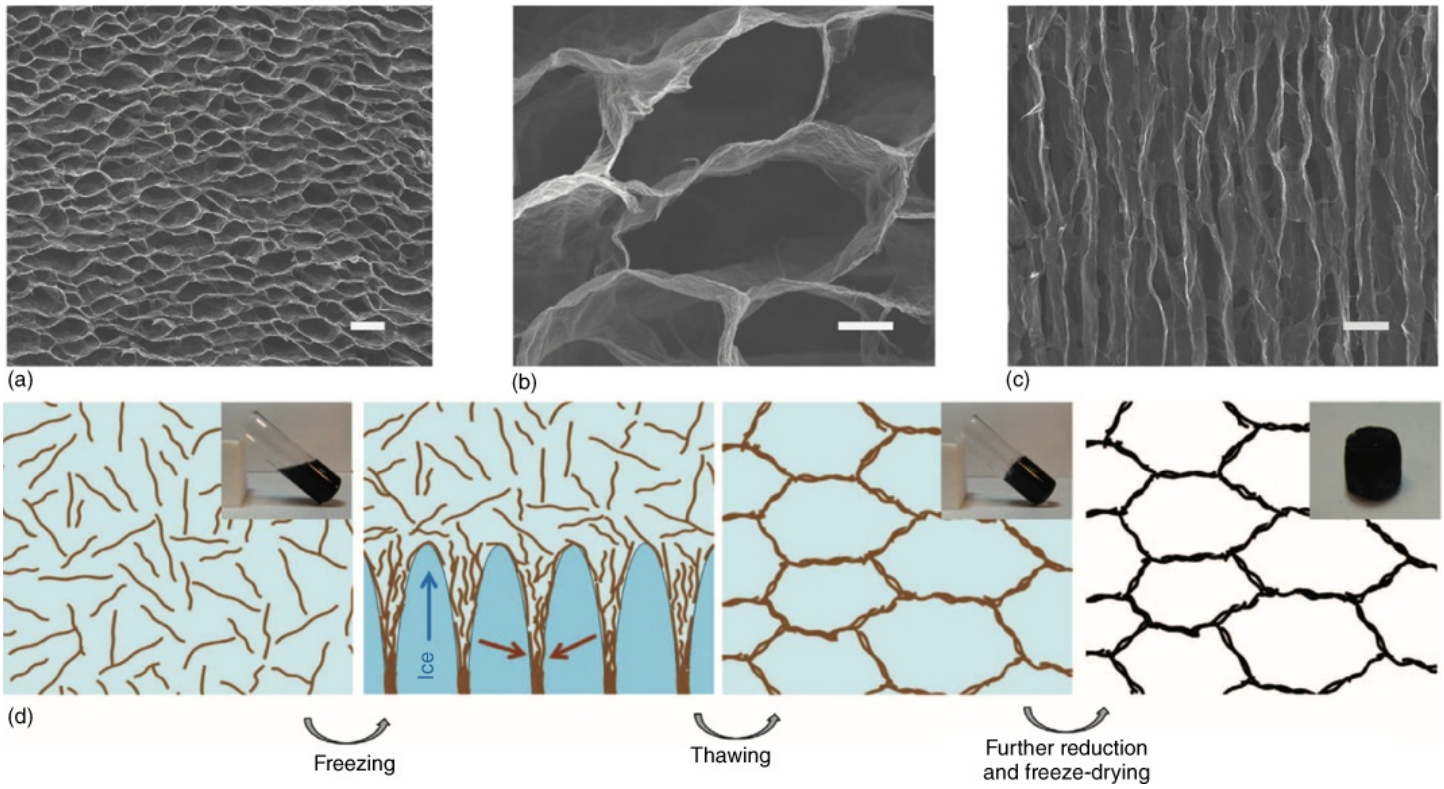

Figure 7.12 Porous graphene materials fabricated by directional freezing of GO suspension and subsequent freezedrying. (a)–(c) Representative pore structures. (d) The preparation scheme.

Source: Qiu et al. 2012 [254. Reprinted with permission from Nature Publishing Group.

The second method is the freezedrying of GO hydrogels. Such an example is given in Figure 7.13. The GO hydrogel was formed by heating aqueous dispersion of GO with hydroquinone at 100 °C for 12 h. The hydrogel was then freezedried to generate a highly porous graphene aerogel [48]. Similarly, a GO gel was formed by heating its aqueous dispersion containing ascorbic acid (1 : 1, w/w) at 70 °C for 4 h and then freezedried [129]. Indeed, all kinds of GO hydrogels formed by hydrothermal treatment or chemical reductions [17–19] may fall into this category.

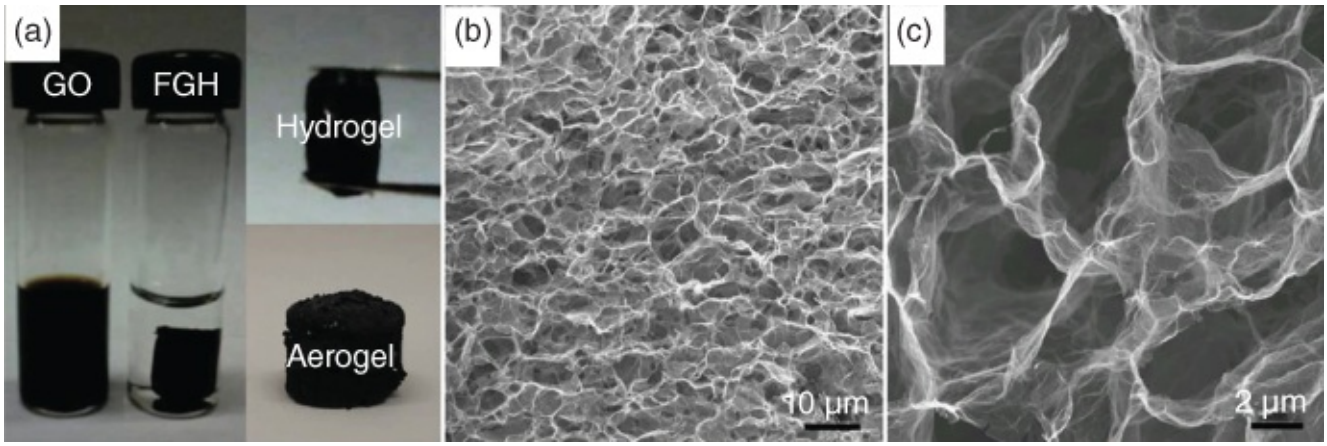

Figure 7.13 Porous graphene monolith fabricated by freezedrying of a graphene (GO) gel. (a) Photos of GO dispersion, functionalized GO hydrogel (FGH) in water and picked up using a tweezer, and the freezedried aerogel. (b) and (c) The pore structure of the aerogel.

Source: Xu et al. 2013 [48]. Reprinted with permission from John Wiley and Sons.

The third method is to combine ice templating and emulsion templating to fabricate porous graphene. This approach has the potential to generate porous materials with very high pore volume and systematically tuned porosity [130, 131]. Figure 7.14 illustrates how this approach is employed to prepare porous graphene materials. An oil phase (e.g. toluene) is emulsified into aqueous chemicallymodified graphene (CMG, or GO) dispersion containing PVA and sucrose (stabilizer and facilitating the freezing process) to form an oilinwater emulsion. This emulsion can be directly frozen and freezedried to produce dry porous graphene (Figure 7.14a). The emulsiontemplated cellular pores can be clearly observed in Figure 7.14b. Highly porous fibres may be formed by injecting the emulsion and then freezedried (Figure 7.14c) [132]. Air bubbles or airinwater emulsion may be formed with surfactants (e.g. sodium dodecyl sulfate, or nonionic polymeric surfactant) [133] or a conventional detergent [134] and then utilized as templates to fabricate porous graphene. After freezedrying, a thermal annealing procedure as well as the removal of surfactant may be necessary to retain the graphene's excellent properties [133].

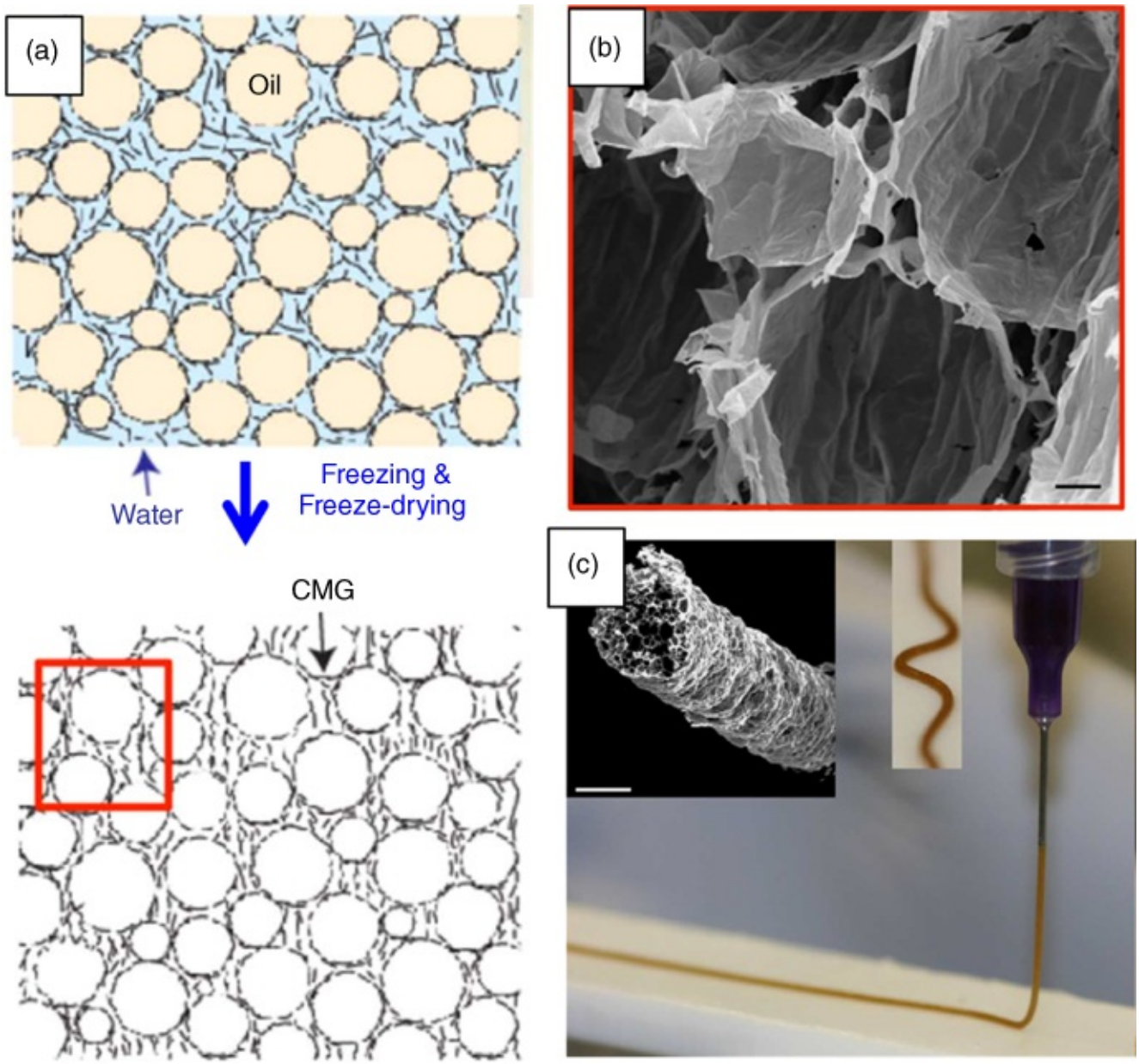

Figure 7.14 (a) Porous graphene scaffolds by freezedrying of oilinwater emulsions with aqueous GO (or chemically modified graphene, CMG) dispersion as the continuous phase. (b) The overview of the pore structure. (c) Porous wires by injecting the emulsion.

Source: Barg et al. 2014. Reprinted with permission from Ref. [264.

The fourth method is the preparation of porous graphene paper via filtration assembly of GO sheets and freezedrying (Figure 7.15). GOs may be partially reduced before filtration (Figure 7.15) [135] or directly infiltrated with a membrane under vacuum [50]. The freezedried GO paper can be thermally reduced and further reduced with ascorbic acid solution to generate graphene paper.

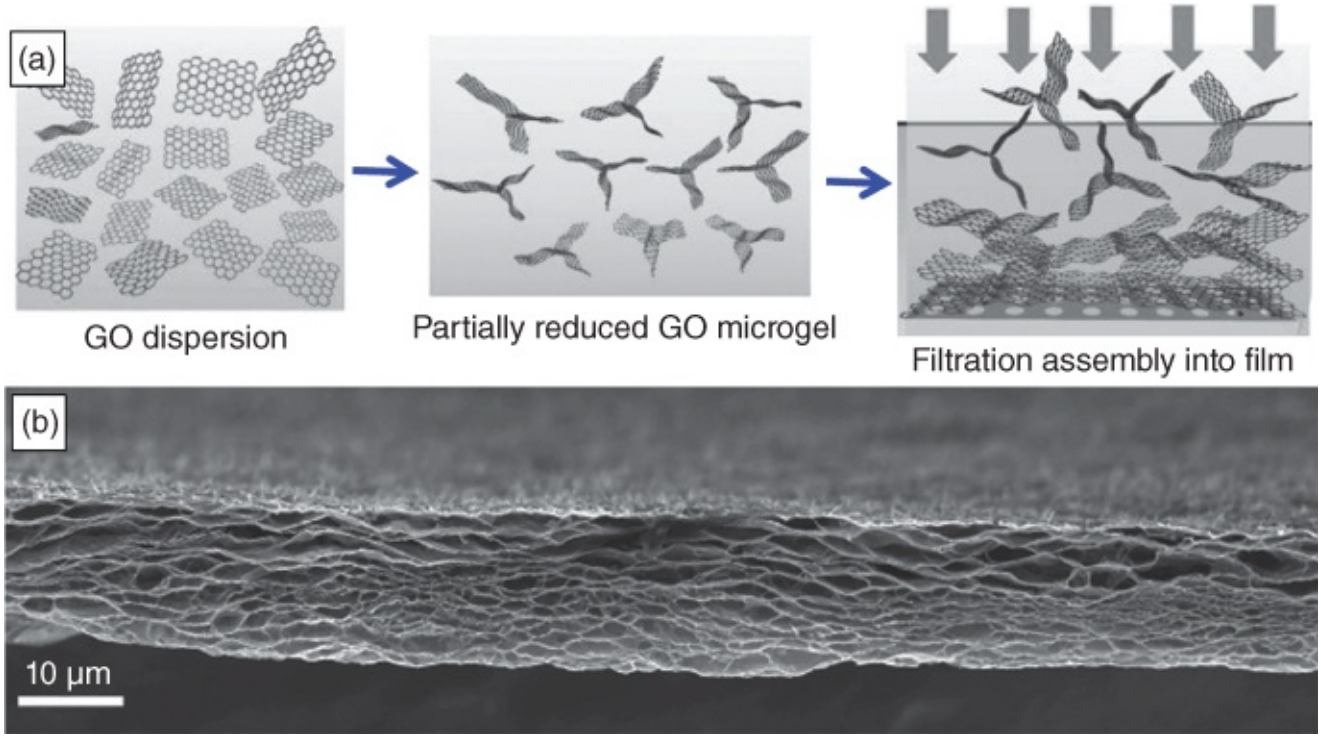

Figure 7.15 Porous graphene papers by freezedrying the wet film formed by filtration assembly of GO suspensions. (a) The schematic representation of the filtration assembly process. (b) The pore structure of the graphene paper.

Source: Shao et al. 2016 [270. Reprinted with permission from John Wiley and Sons.

The final approach is to fabricate porous graphene microspheres by electrospraying aqueous GO suspension into a cryogenic liquid bath (e.g. liquid nitrogen, cooled *n*hexane), as schematically described in Figure 7.16 [136]. The pore structure may be tuned by the concentration and reduced state of GOs while the diameters of the microspheres can be adjusted by the flow rate of electrospraying. It was observed that higher flowing rate resulted in larger microspheres [136]. Similarly to spraying suspensions or emulsions into liquid nitrogen to make porous microspheres [130], aqueous GO suspensions or emulsions may be directly sprayed or atomized into liquid nitrogen (or other cryogenic liquids). The frozen droplets can then be collected and freezedried to generate GO microspheres that may be further thermally annealed and reduced to form porous graphene microspheres. The size of the nozzles and the atomizing pressure can be varied to change the size of the microspheres. Higher atomizing pressure usually leads to the formation of smaller spheres.

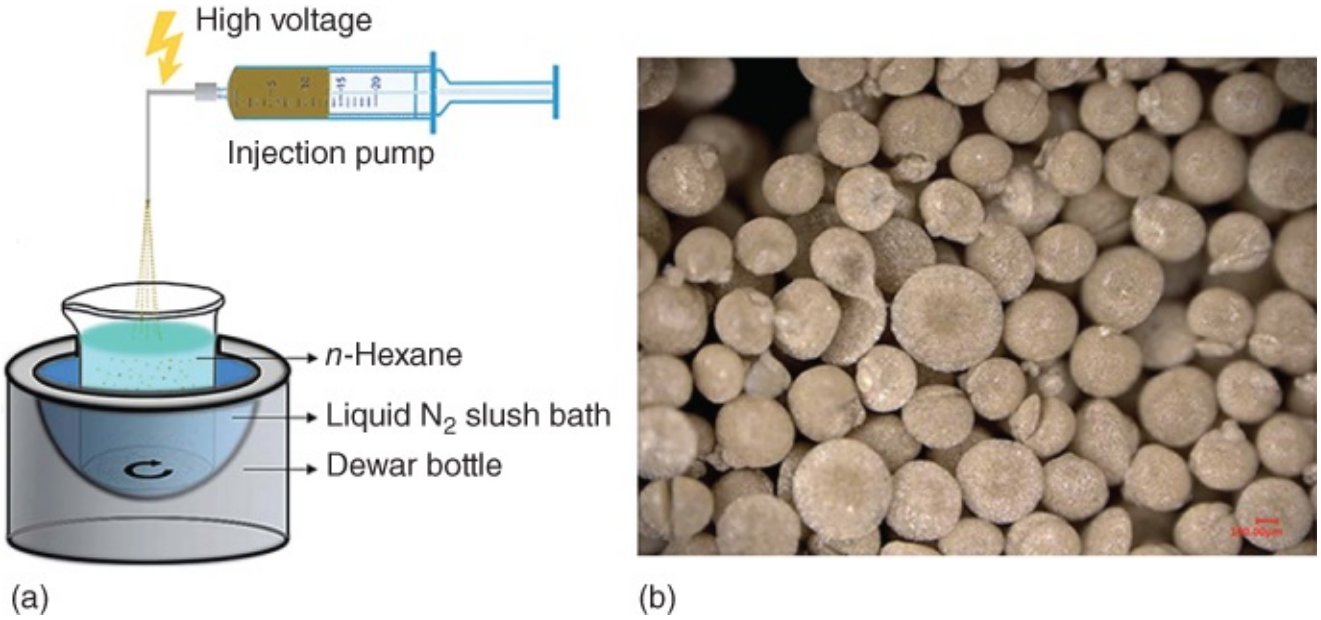

Figure 7.16 Porous graphene spheres by electrospraying into a cryogenic liquid. (a) The schematic preparation process. (b) The optical microscopic image of graphene spheres.

Source: Liao et al. 2016 [272. Reprinted with permission from Royal Society of Chemistry.

Porous graphene monoliths show superelastic behaviour. The cellular monoliths prepared from partially reduced GOs could maintain the structural integrity under loads that were >50 000 times their own weight and rapidly recover from >80% compression [127]. The graphene networks fabricated from both icetemplating and emulsiontemplating showed 98% and 95% recoverable deformation after 1 cycle and 10 cycles of compression, depending on the density of the materials. The Young's modulus increased with the increasing density, reaching a few megapascals [132]. The airbubbled graphene foams exhibited reliably compressive stress of 5.4 MPa and strain as high as 99% at least for 1000 cycles during the compress/release test [133]. Unlike conventional rigid materials and CNTbased polymeric materials, the electrical resistance of the superelastic graphene networks decreases with the compressive strain increments of up to 60%, in a linear fashion. This property makes graphene foam an excellent candidate for strain sensing, for example, in human health monitoring [124]. This piezoresistive response can be ultrafast and provides instantaneous and high fidelity electrical response to dynamic pressures from quasistatic to 2000 Hz or ultralow pressure of 0.082 Pa [137]. This is illustrated in Figure 7.17. It can be seen that the voltage response is spontaneous to the change of stress at frequencies of 20 and 1000 Hz (Figure 7.17a and b). The response sensitivity is generally inversely proportional to the density. The high response sensitivity is achieved from the cellular graphene with a density of 0.54 mg cm^{-3} (Figure 7.17c). This material can detect a very low pressure applied (Figure 7.17d).

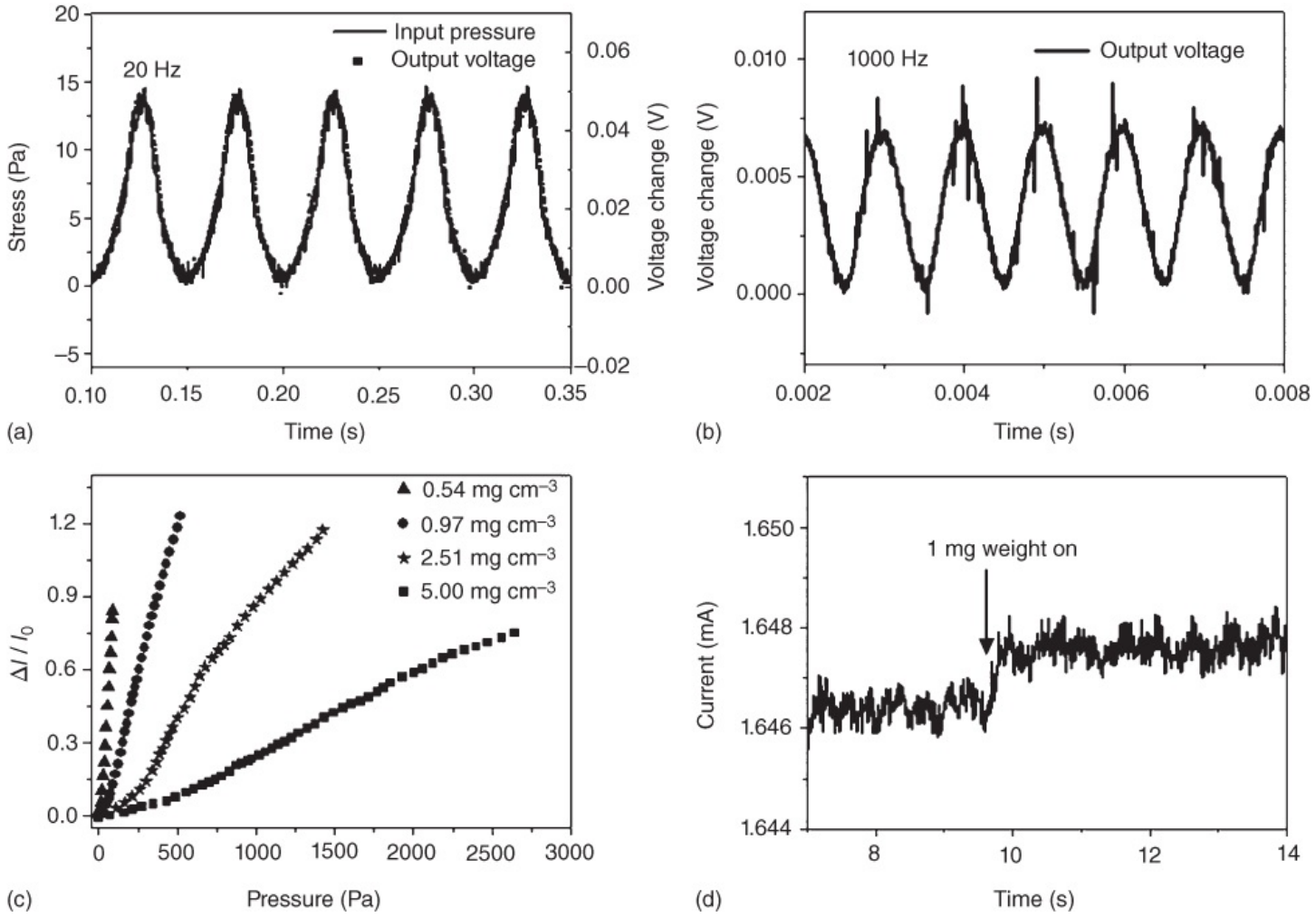

Figure 7.17 Dynamic piezoresistive behaviour of the superelastic cellular graphene material and the relation of sensitivity versus density. (a) and (b) Highfrequency response of the graphene material with a density of 0.54 mg cm^{-3}. (c) Electrical response of the graphene materials with different densities. (d) An example of the graphene material with a density of 0.54 mg cm^{-3} detecting ultralow pressure (1 mg weight on an area of 113 mm^2 is equivalent to 0.082 Pa).

Source: Qiu et al. 2016 [274. Reprinted with permission from John Wiley and Sons.

The high electrical conductivity and the interconnected porosity of porous graphene materials have made them excellent electrodes for supercapacitor. A GO suspension was reduced with L ascorbic acid to form a hydrogel, which was freezedried (or supercritical CO_2 dried) to produce a graphene aerogel. This aerogel exhibited a BET surface area of 512 $m^2\ g^{-1}$, pore volume of 2.48 $cm^3\ g^{-1}$ and electrical conductivity of ~100 S m^{-1} and could support 14 000 times more than its own weight. When evaluated as electrode for supercapacitor, it gave a specific capacity of 128 F g^{-1} at the rate density of 50 mA g^{-1} [47]. Hydroquinone functionalized graphene aerogel showed a specific capacitance of 441 F g^{-1} at 1 A g^{-1} in 1 M H_2SO_4 aqueous electrolyte. When using this material to build a flexible solidstate supercapacitor with H_2SO_4–PVA gel as the electrolyte, a similar performance was obtained, i.e. 412 F g^{-1} at 1 A g^{-1}, 74% capacitance retention at 20 A g^{-1} and 87% capacitance retention

over 10 000 cycles [48]. Flexible freestanding graphene paper showed a specific capacitance of 137 F g^{-1} at 1 A g^{-1} in a solidstate supercapacitor with H_2SO_4–PVA as gel electrolyte [50]. The cellular graphene paper was found to be highly effective for ultrahighpower density supercapacitors, generating power densities in the range of 7.8–14.3 kW kg^{-1}. When increasing the loading of the active materials, the supercapacitor could produce energy density up to 1.11 W h l^{-1} [135]. The pristine graphene aerogels fabricated by freeze gelation at ambient temperature showed better performance as electrode for supercapacitors under high current density [53]. The aerogels made from glucoseassisted reduced GO could produce a capacitance of 157 F g^{-1} at the optimized glucose content of 1 wt% [138]. GO and melamine were mixed to fabricate Ndoped graphene, which showed an improved capacitance of 217 F g^{-1} at a scan rate of 5 mV s^{-1}, three times higher than that of the nondoped graphene gel [126]. The 3D graphene aerogel on nickel foam was evaluated as a binderfree supercapacitor electrode. The tests produced a specific capacitance of 366 F g^{-1} at a current density of 2 A g^{-1} in 6 M KOH. The retained capacitance was 60% after 2000 cycles of tests [49]. The graphene aerogels have also been used as electrodes for recharged batteries or fuel cells. For example, when the graphene paper was used as anode for LIBs, a discharge capacity of 420 mAh g^{-1} was obtained at a current density of 2 A g^{-1} [50]. Graphene sponge was examined as the anode for MFCs. The setup could generate a maximum power density of 427 W m^{-3}, higher than the value of carbon felt at 395 W m^{-3} [139].

Porous graphene materials exhibit high pore volume, highly interconnected porosity, superelasticity and hydrophobicity. These properties make them excellent candidates for oil/water separation or absorption of organic liquids. Anisotropic porous graphene aerogels could absorb organic solvents (such as hexane, heptane to a mass increase of ~140 times, acetone and ethanol to a mass increase of ~160 times) and vegetable oil/pump oil to a mass increase of around 190 times. As tested with the absorption of hexane, the absorbed hexane could be removed by burning, distillation, or more conveniently by squeezing (due to superelasticity) to recycle the graphene aerogels [129]. The hierarchically porous graphene prepared by ice templating and emulsion templating could take up organic liquids 113–276 times their own weight. For a lighter graphene cellular network with a density of 1.5 mg cm^{-3}, the absorption of motor oil could be as high as 605 g/g [131]. The porous graphene spheres showed impressive absorption of organic solvents (60–210 g/g depending on type and density) and oils (~65–105 g/g from gasoline to lubricating oil) [136]. By placing a porous graphene aerogel on the flame of a wax candle and rotating for 3 s, soot was formed on the outer surface of the aerogel. This procedure increased the surface hydrophobicity and enhanced the absorption of organic liquid by 8–10 times. The weight gains were in the range of 140 g/g for soybean oil to 620 g/g for chloroform [140]. When used for absorption of pollutants from wastewater directly, GO scaffolds may perform better. The hydrophilic nature of the GO scaffold may facilitate wetting by water and enhance the interaction with polar pollutants and ions. One study showed the absorption of trichlorophenol in the concentration range of 1–20 mg l^{-1}, achieving an absorption capacity of 21.08 mg g^{-1} [141].

Porous graphene or GO scaffolds have been used for other applications as well. One of them is

for catalysis. Graphene nanoscroll networks [142], N/Sdoped [143] and Ndoped graphene porous structures [144] have been used as efficient electrocatalysts for oxygen reduction reactions. Porous GO scaffolds can be used to catalyse the oxidation of SO_2 to SO_3 [123] and as substrates for neural cell growth [125]. The high thermal conductivity of vertically aligned graphene membranes has been employed for the generation of clean water from seawater via the use of solar energy. The average water evaporation rates could reach 1.62 and 6.25 kg $(m^2\ h)^{-1}$ under 1 and 4 sun illumination [122].

7.5.3 Graphenebased or Graphenecontaining Materials by Ice Templating

This section is divided into two categories: graphene (or GO)–polymer composites and graphene–inorganic nanostructured hybrids.

The graphene (or GO)–polymer composites may be further classified into two types. The first type is the composites with polymer as the matrix or the major component. The main purpose of incorporating graphene is to reinforce the mechanical stability of the freezedried porous polymers. GO, due to its surface functionality and good dispersibility in water, has been usually used as the additive. For example, GO was dispersed with epoxy precursor. After freezedrying and a conventional curing process, the porous GO–epoxy composites (with GO content 3–9 wt%) exhibited very low density (0.09 g cm^{-3}), good mechanical strength (0.231 MPa) and high elasticity [145]. GO was added to the cellulose solution to induce gelation. The composite aerogel was obtained after freezedrying. With the addition of 0.1 wt% GO, the compressive strength and Young's modulus were increased by about 30% and 90%, respectively, compared to that of cellulose aerogel [146]. By combining cellulose nanofibres, GO, and sepiolite nanorod, the anisotropic porous composite (10% GO) showed excellent combustion resistance and a thermal conductivity (15 mW $(m\ K)^{-1}$) only half that of expanded polystyrene. The composite showed high strength in the axial direction and low thermal conductivity in the radial direction, making it an excellent candidate for thermal insulation and as a fireretardant material [147]. With the incorporation of GO at 0.5–3 wt%, the Young's modulus of the gelatin–PVA–GO composite was improved by 67–133%. The porous composite was biocompatible as investigated with MC3T3E1 preosteoblast murine cell line [148]. GO may be reduced and then processed to make reinforced graphene–polymer composites. For example, GO in aqueous suspension was chemically reduced in the presence of poly(sodium 4styrenesulfonate) (PSS). A freezedrying process was employed to fabricate PSSgraphene/PVA composites (1 : 50, w/w). The compressional modulus was nearly an order of magnitude higher than the PVAonly sample [149]. In another study, GO was reduced by hydrazine and then used to prepare the GO–chitosan composite, which was used to detect glucose by electrocatalysis [150].

The second type is the composites where graphene (or GO) is the matrix or has the continuous or skeletal structure. Like the inorganic platelets in nacre (see Chapter 6), the graphene sheets can be used as building blocks, in combination with polymer, to fabricate nacrelike strong and tough composite materials. Porous silk fibroin (15 wt%)–GO composites could be

prepared by freezedrying. When the mixing suspension gel was cast as film and airdried, the resulting film exhibited a tensile strength of 221 ± 16 MPa, a failure strain of 1.8 ± 0.4%, and a modulus of 17.2 ± 1.9 GPa [151]. Aqueous GO and PVA suspensions were processed by a bidirectional freezing approach, followed by reduction with hydroiodic acid and hot pressing at 95 °C. The electrical conductivities were in the range of 16.5–249 S m^{-1}, corresponding to the GO content of about 44–71 wt%. Remarkably, the composite film with 58 wt% GO showed a tensile strength of 150.9 MPa, a fracture strain of 8.84%, toughness of 7.15 MJ m^{-3} and Young's modulus of 2.84 GPa [152].

Quite often, 3D porous graphene networks are fabricated first and the polymer phase is incorporated in the second stage. The resulting composites usually show good mechanical stability and superelasticity while the excellent electrical conductivity and thermal conductivity from graphene networks are retained. A robust, conductive, temperature responsive binary hydrogel was formed by soaking graphene cellular networks in *N* isopropylacrylamide solution containing a crosslinker and initiator and followed by polymerization [153]. Polyborosiloxane (PBS) exhibits an intrinsic selfhealing behaviour due to its dynamic dative triple and quadruple bonds formed between boron and oxygen in the Si-O groups. PBS is a highly viscous liquid at low strain rates but behaves like a solid at high strain rates. A selfhealing composite may be fabricated by incorporating PBS into porous graphene networks. This was demonstrated by Saiz and coauthors, by infiltrating liquid PDMS and boron oxide (which react to form the PBS polymer in situ) into icetemplated graphene networks. 6–8 healing cycles were demonstrated with no structural loss. This composite was used to sensor pressure change based on the piezoresistive response [154]. When epoxy resin was incorporated into vertically aligned porous graphene networks with a low loading of 0.92 vol%, the obtained composite showed a high thermal conductivity (2.13 W $(m\,K)^{-1}$), a reduced coefficient of thermal expansion (~37.4 ppm K^{-1}) and an increased glass transition temperature (135.4 °C) [155].

For the graphene–inorganic hybrid structure, noble metal nanoparticles are usually formed within porous graphene (or GO) networks while inorganic nanostructures may be blended with graphene or grow from the graphene surface. Metal salts can be mixed with aqueous GO suspension and the resulting suspension is freezedried. Metal nanoparticles are formed in situ when the GO scaffold is reduced to graphene. This has been demonstrated by preparation of Pt and Ag nanoparticles within 3D porous graphene. These materials gave ultralow density, good electrical conductivity and excellent EMI shielding effectiveness, and also enhanced electrocatalytic performance [156]. Aqueous suspension containing Nafion, GO and chloroplatinic acid was freezedried to produce a highly porous structure. This structure could be reduced by hydrazine or monosodium citrate to form graphenesupported Pt nanoparticles on a Nafion scaffold, which combined ionic conductivity (from Nafion), electronic conductivity (from graphene) and catalytic activity (from Pt nanoparticles) [157]. In another study, $HAuCl_4$ was added to aqueous GO suspension. After further addition of ascorbic acid and a heating–freezing–heating process, gold nanoparticle/graphene gel was formed. After washing and freezedrying, dry porous graphene structures with Au nanoparticles were produced. Pt and Pd nanoparticles were also produced using a similar

procedure. The composites showed excellent catalytic performance in the reduction of 4 nitrophenol and methylene blue by $NaBH_4$ [158].

Vertically porous composites of layered $VOPO_4$ and graphene were constructed by the directional freezing process [51]. When tested as electrodes for supercapacitors, a high capacitance of 528 F g^{-1} at 0.5 A g^{-1} was obtained with 6 M KOH as electrolyte. For the asymmetric supercapacitor built from this composite as the cathode and vertically porous graphene as the anode, a high cell voltage of 1.6 V and energy density of 108 W h kg^{-1} were achieved [51]. $NiCo_2S_4$ nanotube@Ni–Mn layered double hydroxides were formed on graphene sponge by in situ growth via a multistep hydrothermal synthesis. When evaluated for supercapacitors, the composite electrode exhibited a specific capacitance of 1740 mF cm^{-2} at 1 mA cm^{-2} and 1268 mF cm^{-2} at 10 mA cm^{-2} [52]. C_3N_4–GO aerogel was fabricated directly by freezedrying the mixing suspension. Excellent visiblelight photocatalytic activity was demonstrated by the degradation of dyes (Rhodamine B, methyl orange, methylene blue) and the oxidation of NO at a ppb level [159]. The absorption wavelength of the composite could be extended to about 481 nm from the wavelength of about 453 nm from C_3N_4 powder [159]. Polyethylene glycol was incorporated into an icetemplated boron nitride (BN)/GO scaffold. With a BN content of 19.2 wt%, the composite exhibited a high thermal conductivity of 1.84 W $(m\ K)^{-1}$. It was further demonstrated to possess great potential as phase change materials to realize efficient lighttothermal and lighttoelectric energy conversion and storage [160].

7.6 Porous Graphene/CNT Hybrid Structures

Graphene (or GO) and CNTs can be used as building blocks together to fabricate porous carbon materials. This may avoid or reduce the dilution effect in CNT or graphene composite materials on thermal and electrical conductivity, where additives such as polymers are included to improve mechanical properties. Porous graphene/CNT hybrid structures prepared by the icetemplating approach have shown enhanced properties such as surface area, elasticity, and compressive strength, compared to the individual components. The CNTs can act as structural support and as a separator to prevent graphene (GO) nanosheets from stacking or aggregating. This can result in a higher surface area in the resulting hybrid porous structure [53]. The strong interaction between the CNTs and graphene (via π–π stacking and hydrophobic interaction, or the interaction between the remaining functional groups on the surface of CNT and graphene) may bond the graphene nanosheets together and reduce the sliding under compression and thereby enhance the elasticity and compression strength [161, 162]. The long and flexible CNTs may also serve as threads to ‘bundle’ the nanosheets together [58].

Pristine graphene (PG)–MWCNT and reduced graphene oxide (rGO)–MWCNT aerogels were fabricated via a roomtemperature approach [53]. Higher specific capacitances were achieved for the hybrid aerogels. Between PG–MWCNT and rGO–MWCNT, the specific

capacitance (305 F g^{-1}) was higher for rGO–MWCNT than for PG/MWCNT (167 F g^{-1}) at a current density of 1 A g^{-1} with nonaqueous 1.0 M tetraethyl ammonium tetrafluoroborate/propylene carbonate. This was attributed to the higher surface area in the rGO–MWCNT aerogel. However, PG–MWCNT showed a higher specific capacitance (100 F g^{-1}) at a fast scan rate of 100 A g^{-1} than those of rGO–MWCNT (72 F g^{-1}) and rGO aerogel (0.9 F g^{-1}). This was attributed to the lower internal resistance of PG than that of rGO [53]. Aqueous GO/CNT dispersion was freezedried and then thermally annealed at 800 °C under N_2 for 3 h. The porous hybrid sponge with 20 wt% CNTs showed the highest surface area (498 m^2 g^{-1}) and pore volume (1.51 cm^3 g^{-1}). When tested by cyclic voltammetry (CV) at 10 mV s^{-1} in 1 M NaCl solution, a specific capacitance of 203 F g^{-1} was obtained. When evaluated as the capacitive deionization electrode, a high electrosorption capacity of 18.7 mg g^{-1} was achieved [163]. This composite material was also used as anode for sodium ion batteries, the highest charge capacity was achieved at 436 mAh g^{-1} after 100 cycles with a current density of 50 mA g^{-1}. A capacity of 195 mAh g^{-1} was maintained at 10 A g^{-1} after 7440 cycles [58]. However, not all the graphene–CNT structures produce better performance for supercapacitors. For example, both graphene aerogel and graphene–CNT aerogel were formed on nickel foams. The hybrid material as electrode showed a lower capacitance (207 F g^{-1} at 2 A g^{-1}) than that of graphene aerogel on nickel foam (366 F g^{-1} at 2 A g^{-1}) [49]. The freezedried GO–SWCNT scaffold was annealed at 800 °C under Ar for 2 h and evaluated as a counter electrode for dyesensitized solar cells. A photovoltaic conversion efficiency of 8.70% was achieved [164].

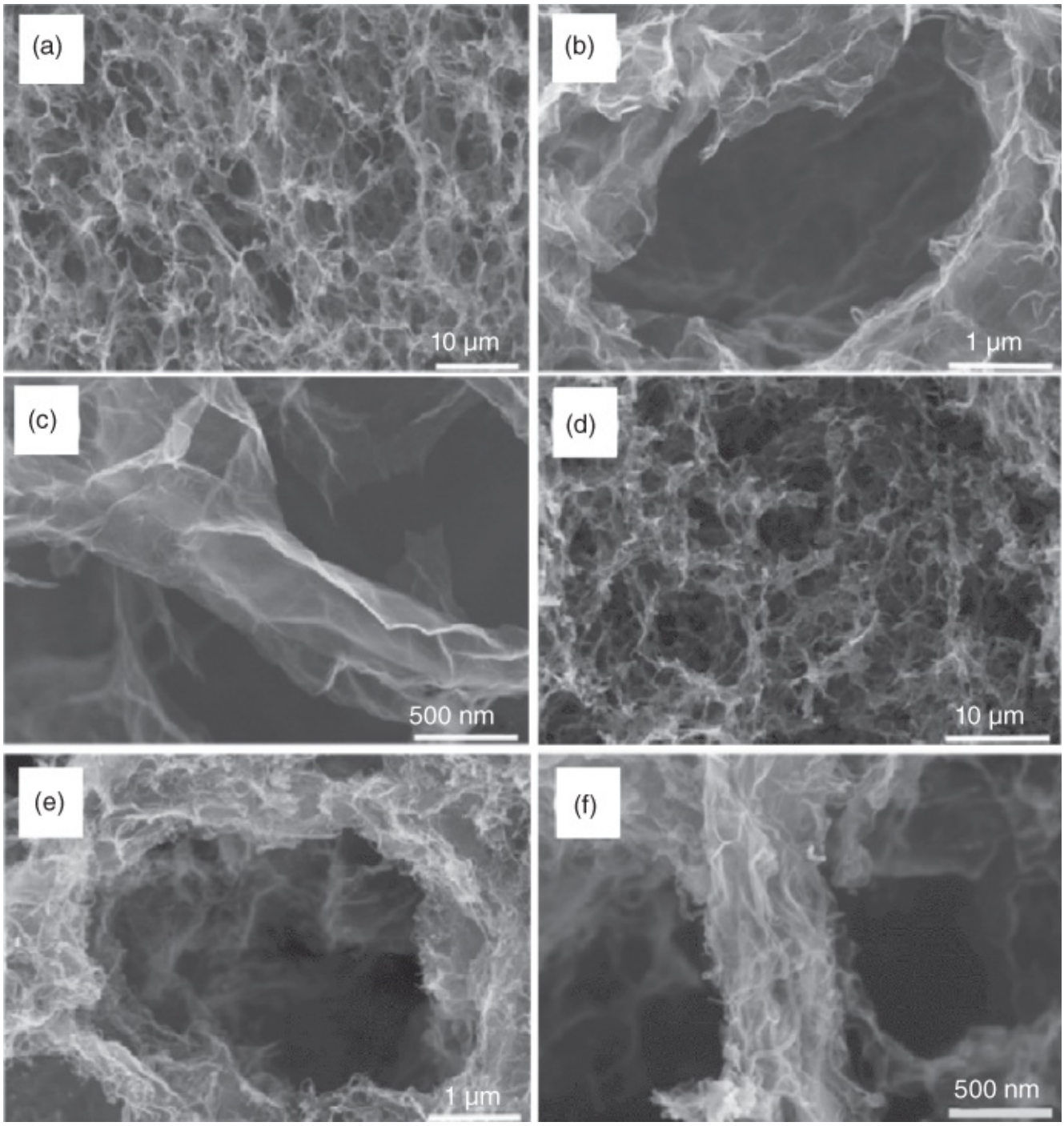

Figure 7.18 The pore morphologies and structures of (a)–(c) 3D porous graphene aerogel and (d)–(f) the graphene/CNT aerogel with similar initial density.

Source: Lv et al. 2016 [324. Reprinted with permission from Elsevier.

Oxidized CNTs (by refluxing in the mixture of concentrated H_2SO_4 and HNO_3 (3 : 1, v/v)) were dispersed in water with GO. The gel was formed after a hydrothermal treatment (180 °C for 12 h) and then freezedried to form the aerogel. Figure 7.18 shows the porous structures of graphene and graphene–CNT aerogels. Both of them are highly porous. At higher magnifications, the entangled CNTs can be seen to cover the ligaments and the cellular walls. The hybrid aerogel showed a high compressibility with the compression strain as high as 80%. The thermal conductivity increased with the density, achieving the highest at 88.5 W $(m\,K)^{-1}$

with a density of 85 mg cm^{-3} (GO:CNT ratio at always 3 : 1). For the thermal interface testing, by locating the aerogels between two Cu blocks with high temperature and low temperature, a low thermal interface resistance of 13.6 mm^2 KW^{-1} was obtained [162]. The oilinwater emulsion with hexane as oil droplets and GO/oxidized CNTs in the continuous aqueous phase was hydrothermally treated at 180 °C for 10 h to form a gel. The hybrid porous scaffold was produced after freezedrying of the gel and then infiltrated with epoxy resin. The resulting composite with a thickness of 9 mm could absorb up to 80% of the incident radiation when evaluated as a microwave absorbing material [165].

The rGO/SWCNT aerogels prepared from a freezing–thawing–freeze drying process were assessed for their thermoelectric (TE) properties [166]. The TE performance is usually evaluated by a dimensionless figure of merit, $ZT = S^2 T/k$, where S is the Seebeck coefficient, T is the temperature and k is the thermal conductivity. The composite aerogel with 37.5 wt% of SWCNT showed an enhanced TE performance with $ZT = 8.03 \times 10^{-3}$ [166]. This was attributed to the interconnected porosity, the energyfiltering effect, and the phonon scattering at interfaces/joints. The same material, also due to its hydrophobicity, exhibited the high capacity to absorb organic liquids. The absorption capacities varied depending on the solvent, dichloromethane 139 g/g, *N*methyl2pyrrolidone 98 g/g, and *n*hexane 130 g/g. For *n*hexane, after 5 cycles, about 92% of the absorption capacity was retained [166]. The graphene–CNT aerogels have also been used for the removal of oil or pollutant by other researchers [159, 166]. The hybrid aerogel obtained by freezedrying the gel formed by hydrothermal treatment in the presence of ethylenediamine (120 °C, 12 h) could absorb organic liquids in the range of 100–270 times their own weight (100 g/g for *n*hexane). The recycling tests by combustion or squeezing to remove *n*hexane showed nearly no decrease in absorption for 10 cycles [167]. In another study, the hybrid aerogels were demonstrated as superior absorbents to remove pollutants, oxytetracycline 1729 mg g^{-1}, diethyl phthalate 680 mg g^{-1}, methylene blue 685 mg g^{-1}, Cd^{2+} 235 mg g^{-1} and diesel 421 g/g [161]. The graphene–CNT aerogels usually have a good combination of compressibility and superelasticity, as shown by squeezing the solvent absorbed aerogel for the recycling purpose. Also, due to the piezoresistive behaviour, the graphene–CNT aerogel could be used as pressure sensors, e.g. in fields related to artificial skin [168].

A third component may be introduced into the graphene–CNT aerogels to improve their applications. For example, transition metal dichalcogenide nanosheets are known as active materials for LIBs and SIBs. Although MoS_2 has been extensively used as the anode for LIBs and SIBs, WS_2 may have greater potential because its intrinsic electronic conductivity is higher than that of MoS_2 [59]. $(NH_4)_2WS_4$ powders were dissolved in the GO and CNT dispersion in DMF. The obtained suspension was solvothermally treated at 200 °C for 10 h to produce a gel. The gel was washed, freezedried, and thermally annealed at 500 °C for 2 h in H_2/N_2 to generate the hierarchically porous WS_2/CNT–rGO aerogel. As the anode, this hybrid material delivered a specific capacitance of 749 mAh g^{-1} at 100 mA g^{-1} for LIBs and 311.4 mAh g^{-1} at 100 mA g^{-1} and 252.9 mAh g^{-1} at 200 mA g^{-1} after 100 cycles for SIBs [59]. Hexagonal nanorods of hydroxyapatite were formed on flexible porous graphene/SWCNT

membrane [169]. This hybrid membrane was found to promote the attachment and proliferation of human foetal osteoblast osteoprogenitor cells and enhance *in vitro* biomineralization in simulated body fluid [169].

7.7 Summary

Porous carbon materials can be prepared by carbonization of porous polymers/polymeric gels or by fabrication directly from carbon building blocks, namely CNTs and graphenes (or graphene oxides). Conventionally, carbon aerogels are produced by carbonization of freeze dried highly crosslinked polymeric gels, with the typical example being resorcinol formaldehyde gel. The freezedrying process ensures the formation of highly porous dry polymeric gels. When the crosslinking density is low, the icetemplated pore structure may be generated in carbon aerogels as well. However, in order to fully realize the icetemplating potential, polymer solutions (where the polymers have high carbon content to facilitate the production of carbon materials by carbonization) are processed by controlled freezing and freezedrying to generate porous polymers, which can be subsequently pyrolysed under inert atmosphere to generate porous carbon materials. Additional colloidal templating may be included to induce high porosity and mesopores in the carbon materials. CNFs can be produced by carbonization of polymer nanofibres produced by freezedrying of dilute polymer solution or nanofibrous organic gels generated by pHtriggered gelation.

More excitingly, CNTs and graphene/graphene oxide nanosheets are used as carbon building blocks, via the icetemplating approach, to produce porous carbon structures, composite structures and CNTs/graphene hybrid structures. Most of these materials show good electrical conductivity, mechanical stability and high surface area. Remarkably, graphene and graphene oxide nanosheets can be used to fabricate porous networks with superelasticity and piezoresistivity.

Owing to the inert chemical stability, electrical conductivity, high surface area and surface hydrophobicity, porous carbon materials have been widely used as absorbents for water treatment, adsorbents for gas uptake, oil/water separation, electrode materials and catalyst supports. Applications for each category of the carbon materials are described in this chapter. The icetemplated anisotropic pore structures can bring additional advantages for certain applications, e.g. anisotropic conductivity and enhanced mass transport in aligned channels. Particularly, the carbon materials made from CNTs and graphenes have been extensively used as electrodes for rechargeable batteries and supercapacitors. Owing to its unique nanosheet structure, graphenes and graphene oxides can be used to fabricate superelastic networks and conductive strong composites, which have been uniquely used for sensing pressure and detecting structure integrity. It is envisaged that the icetemplating and freezedrying approach can be used widely to fabricate various functional carbon materials for advanced applications.

References

1 Dutta, S., Bhaumik, A., and Wu, K.C. (2014). Hierarchically porous carbon derived from polymers and biomass: effect of interconnected pores on energy applications. Energy Environ. Sci. 7: 3574–3592.

2 Liang, C., Li, Z., and Dai, S. (2008). Mesoporous carbon materials: synthesis and modification. Angew. Chem. Int. Ed. 47: 3696–3717.

3 Lee, J., Kim, J., and Hyeon, T. (2006). Recent progress in the synthesis of porous carbon materials. Adv. Mater. 18: 2073–2094.

4 Zhang, H. and Cooper, A.I. (2005). Synthesis and applications of emulsiontemplated porous materials. Soft Matter 1: 107–113.

5 Fechler, N., Fellinger, T.P., and Antonietti, M. (2013). “Salt templating”: a simple and sustainable pathway toward highly porous functional carbons from ionic liquids. Adv. Mater. 25: 75–79.

6 Titirici, M.M., White, R.J., Brun, N. et al. (2015). Sustainable carbon materials. Chem. Soc. Rev. 44: 250–290.

7 AlMuhtaseb, S.A. and Ritter, J.A. (2003). Preparation and properties of resorcinol formaldehyde organic and carbon gels. Adv. Mater. 115: 101–114.

8 Stein, A., Wang, Z., and Fierke, M.A. (2009). Functionalization of porous carbon materials with designed pore architecture. Adv. Mater. 21: 265–293.

9 Liu, J., Wickramaratne, N.P., Qiao, S.Z., and Jaroniec, M. (2015). Molecularbased design and emerging applications of nanoporous carbon spheres. Nat. Mater. 14: 763–774.

10 Saufi, S.M. and Ismail, A.F. (2004). Fabrication of carbon membranes for gas separation – a review. Carbon 42: 241–259.

11 Huang, Z.M., Zhang, Y.Z., Kotaki, M., and Ramakrishna, S. (2003). A review on polymer nanofibers by electrospinning and their applications in nanocomposites. Compos. Sci. Technol. 63: 2223–2253.

12 Zhang, B., Kang, F., Tarascon, J.M., and Kim, J.K. (2016). Recent advances in electrospun carbon nanofibers and their application in electrochemical energy storage. Prog. Mater. Sci. 76: 319–380.

13 Chaikittisilp, W., Ariga, K., and Yamauchi, Y. (2013). A new family of carbon materials: synthesis of MOFderived nanoporous carbons and their promising applications. J. Mater. Chem. A 1: 14–19.

14 Tasis, D., Tagmatarchis, N., Bianco, A., and Prato, M. (2006). Chemistry of carbon nanotubes. Chem. Rev. 106: 1105–1136.

15 Geim, A.K. and Novoselov, K.S. (2007). The rise of graphene. Nat. Mater. 6: 183–191.

16 Park, S. and Ruoff, R.S. (2010). Chemical methods for the production of graphenes. Nat. Nanotechnol. 4: 217–224.

17 Lv, W., Zhang, C., Li, Z., and Yang, Q. (2015). Selfassembled 3D graphene monolith from solution. J. Phys. Chem. Lett. 6: 658–668.

18 Dasgupta, A., Rajukumar, L.P., Rotella, C. et al. (2017). Covalent threedimensional networks of graphene and carbon nanotubes: synthesis and environmental applications. Nano Today 12: 116–135.

19 Cao, X., Yin, Z., and Zhang, H. (2014). Threedimensional graphene materials: preparation, structures and application in supercapacitors. Energy Environ. Sci. 7: 1850–1865.

20 Nardecchia, S., Carriazo, D., Ferrer, M.L. et al. (2013). Three dimensional macroporous architectures and aerogels built of carbon nanotubes and/or graphene: synthesis and applications. Chem. Soc. Rev. 42: 794–830.

21 Thostenson, E.T., Ren, Z., and Chou, T.W. (2001). Advances in the science and technology of carbon nanotubes and their composites: a review. Compos. Sci. Technol. 61: 1899–1912.

22 An, X. and Yu, J.C. (2011). Graphenebased photocatalytic composites. RSC Adv. 1: 1426–1434.

23 Hu, K., Kulkarni, D.D., Choi, I., and Tsukruk, V.V. (2014). Graphenepolymer nanocomposites for structural and functional applications. Prog. Polym. Sci. 39: 1934–1972.

24 Serrano, M.C., Gutiérrez, M.C., and del Monte, F. (2014). Role of polymers in the design of 3D carbon nanotubebased scaffolds for biomedical applications. Prog. Polym. Sci. 39: 1448–1471.

25 Nieto, A., Bisht, A., Lahiri, D. et al. (2017). Graphene reinforced metal and ceramic matrix composites: a review. Int. Mater. Rev. 62: 241–302.

26 Yang, Z., Ren, J., Zhang, Z. et al. (2015). Recent advancement of nanostructured carbon for energy applications. Chem. Rev. 115: 5159–5223.

27 Wood, K.N., O'Hayre, R., and Pylypenko, S. (2014). Recent progress on nitrogen/carbon structures designed for use in energy and sustainability applications. Energy Environ. Sci. 7: 1212–1249.

28 Hu, L., Hecht, D.S., and Grüner, G. (2010). Carbon nanotube thin films: fabrication, properties, and applications. Chem. Rev. 110: 5790–5844.

29 Qiu, H., Guan, Y., Luo, P., and Wang, Y. (2017). Recent advances in fabricating monolithic 3D porous graphene and their applications in biosensing and biofuel cells. Biosens. Bioelectron. 89: 85–95.

30 Chang, H., Joo, S.H., and Pak, C. (2007). Synthesis and characterization of mesoporous carbon for fuel cell applications. J. Mater. Chem. 17: 3078–3088.

31 Mauter, M.S. and Elimelech, M. (2008). Environmental applications of carbonbased nanomaterials. Environ. Sci. Technol. 42: 5843–5859.

32 Ren, X., Chen, C., Nagatsu, M., and Wang, X. (2011). Carbon nanotubes as adsorbents in environmental pollution management: a review. Chem. Eng. J. 170: 395–410.

33 Yu, J.S., Kang, S., Yoon, S.B., and Chai, G. (2002). Fabrication of ordered uniform porous carbon networks and their application to a catalyst supporter. J. Am. Chem. Soc. 124: 9382–9383.

34 Kumar, S., Rani, R., Dilbaghi, N. et al. (2017). Carbon nanotubes: a novel material for multifaceted applications in human healthcare. Chem. Soc. Rev. 46: 158–196.

35 Chung, C., Kim, Y.K., Shin, D. et al. (2012). Biomedical applications of graphene and graphene oxide. Acc. Chem. Res. 46: 2211–2224.

36 Qian, L. and Zhang, H. (2011). Controlled freezing and freeze drying: a versatile route for porous and micro/nanostructured materials. J. Chem. Technol. Biotechnol. 86: 172–184.

37 Deville, S. (2013). Icetemplating, freeze casting: beyond materials processing. J. Mater. Res. 28: 2202–2219.

38 Job, N., Théry, A., Pirard, R. et al. (2005). Carbon aerogels, cryogels and xerogels: influence of the drying method on the textural properties of porous carbon materials. Carbon 43: 2481–2494.

39 Candelaria, S.L., Chen, R., Jeong, Y.H., and Cao, G. (2012). Highly porous chemically modified carbon cryogels and their coherent nanocomposites for energy applications. Energy Environ. Sci. 5: 5619–5637.

40 AmaralLabat, G., Szczurek, A., Fierro, V. et al. (2012). Pore structure and electrochemical performances of tanninbased carbon cryogels. Biomass Bioenergy 39: 274–282.

41 Zhou, Y., Candelaria, S.L., Liu, Q. et al. (2014). Sulfurrich carbon cryogels for supercapacitors with improved conductivity and wettability. J. Mater. Chem. A 2: 8472–8482.

42 Khalid, B., Meng, Q., Li, J., and Cao, B. (2014). Nitrogen rich graphenecrosslinked melamine formaldehyde carbon cryogels for supercapacitors. Electrochim. Acta 142: 101–107.

43 Choi, Y.M., Singh, K.P., Park, J.D. et al. (2016). Hierarchically microcellular microporous carbon from polyamic acid cryogel and its electrochemical capacitance. Energy Technol. 4: 278–287.

44 Estevez, L., Dua, R., Bhandari, N. et al. (2013). A facile approach for the synthesis of monolithic hierarchical porous carbonshigh performance materials for amine based CO_2 capture and supercapacitor electrode. Energy Environ. Sci. 6: 1785–1790.

45 Spender, J., Demers, A.L., Xie, X. et al. (2012). Method for production of polymer and carbon nanofibers from watersoluble polymers. Nano Lett. 12: 3857–3860.

46 Liu, X., Ahmed, A., Wang, Z., and Zhang, H. (2015). Nanofibrous microspheres via emulsion gelation and carbonization. Chem. Commun. 51: 16864–16867.

47 Zhang, X., Sui, Z., Xu, B. et al. (2011). Mechanically strong and highly conductive graphene aerogel and its use as electrodes for electrochemical power sources. J. Mater. Chem. 21: 6494–6497.

48 Xu, Y., Lin, Z., Huang, X. et al. (2013). Functionalized graphene hydrogelbased high performance supercapacitors. Adv. Mater. 25: 5779–5784.

49 Ye, S., Feng, J., and Wu, P. (2013). Deposition of threedimensional graphene aerogel on nickel foam as a binderfree supercapacitor electrode. ACS Appl. Mater. Interfaces 5: 7122–7129.

50 Shu, K., Wang, C., Li, S. et al. (2015). Flexible freestanding graphene paper with interconnected porous structure for energy storage. J. Mater. Chem. A 3: 4428–4434.

51 Lee, K.H., Lee, Y.W., Lee, S.W. et al. (2015). Icetemplated selfassembly of $VOPO_4^-$ graphene nanocomposites for vertically porous 3D supercapacitor electrodes. Sci. Rep. 5: 13696.

52 Wan, H., Liu, J., Ruan, Y. et al. (2015). Hierarchical configuration of $NiCo_2S_4$ nanotube@NiMn layered double hydroxide arrays/threedimensional graphene sponge as electrode materials for highcapacitance supercapacitors. ACS Appl. Mater. Interfaces 7: 15840–15847.

53 Lin, Y., Liu, F., Casano, G. et al. (2016). Pristine graphene aerogels by roomtemperature freeze gelation. Adv. Mater. 28: 7993–8000.

54 Pan, A., Liu, D., Zhou, X. et al. (2010). Enhanced lithiumion intercalation properties of coherent hydrous vanadium pentoxide–carbon cryogel nanocomposites. J. Power Sources 195: 3893–3899.

55 Zhang, M., Li, Y., Uchaker, E. et al. (2013). Homogenous incorporation of SnO_2 nanoparticles in carbon cryogels via the thermal decomposition of stannous sulfate and their enhanced lithiumion intercalation properties. Nano Energy 2: 769–778.

56 Sahore, R., Estevez, L.P., Ramanujapuram, A. et al. (2015). Highrate lithiumsulfur batteries enabled by hierarchical porous carbons synthesized via ice templation. J. Power

Sources 297: 188–194.

57 Jazaeri, E., Zhang, L., Wang, X., and Tsuzuki, T. (2011). Fabrication of carbon nanofiber by pyrolysis of freezedried cellulose nanofiber. Cellulose 18: 1481–1485.

58 Yan, D., Xu, X., Lu, T. et al. (2016). Reduced graphene oxide/carbon nanotubes sponge: a new high capacity and long life anode material for sodiumionbatteries. J. Power Sources 316: 132–138.

59 Wang, Y., Kong, D., Shi, W. et al. (2016). Ice templated freestanding hierarchically WS_2/CNTrGO aerogel for highperformance rechargeable lithium and sodium ion batteries. Adv. Energy Mater. 6. doi: 10.1002/aenm.201601057.

60 Szczurek, A., Jurewicz, K., AmaralLabat, G. et al. (2010). Structure and electrochemical capacitance of carbon cryogels derived from phenolformaldehyde resins. Carbon 48: 3874–3883.

61 Tamon, H., Ishizaka, H., Yamamoto, T., and Suzuki, T. (1999). Preparation of mesoporous carbon by freeze drying. Carbon 37: 2049–2055.

62 Tamon, H., Ishizaka, H., Yamamoto, T., and Suzuki, T. (2000). Influence of freezedrying conditions on the mesoporosity of organic gels as carbon precursors. Carbon 38: 1099–1105.

63 Yamamoto, T., Nishimura, T., Suzuki, T., and Tamon, H. (2001). Control of mesoporosity of carbon gels prepared by sol–gel polycondensation and freeze drying. J. NonCryst. Solids 288: 46–55.

64 Yamamoto, T., Sugimoto, T., Suzuki, T. et al. (2002). Preparation and characterization of carbon cryogel microspheres. Carbon 40: 1345–1351.

65 Hamano, Y., Tsujimura, S., Shirai, O., and Kano, K. (2014). Control of the pore size distribution of carbon cryogels by pH adjustment of catalyst solutions. Mater. Lett. 128: 191–194.

66 Ogino, I., Kazuki, S., and Mukai, S.R. (2014). Marked increase in hydrophobicity of monolithic carbon cryogels via HCl aging of precursor resorcinolformaldehyde hydrogels: application to 1butanol recovery from dilute aqueous solutions. J. Phys. Chem. C 118: 6866–6872.

67 Hotová, G. and Slovák, V. (2015). Effect of pyrolysis temperature and thermal oxidation on the adsorption properties of carbon cryogels. Thermochim. Acta 614: 45–51.

68 Sepehri, S., García, B.B., Zhang, Q., and Cao, G. (2009). Enhanced electrochemical and structural properties of carbon cryogels by surface chemistry alteration with boron and nitrogen. Carbon 47: 1436–1443.

69 Ogino, I., Suzuki, Y., and Mukai, S.R. (2015). Tubing the pore structure and surface

properties of carbonbased acid catalysts for liquidphase reactions. ACS Catal. 5: 4951–4958.

70 Minović, T., Gulicovski, J.J., Stoiljković, M.M. et al. (2015). Surface characterization of mesoporous carbon cryogel and its application in arsenic (III) adsorption from aqueous solutions. Microporous Mesoporous Mater. 201: 271–276.

71 Yoshida, S., Iwamura, S., Ogino, I., and Mukai, S.R. (2016). Adsorption of phenol in flow systems by a monolithic carbon cryogel with a microhoneycomb structure. Adsorption 22: 1051–1058.

72 Kim, S.I., Yamamoto, T., Endo, A. et al. (2006). Adsorption of phenol and reactive dyes from aqueous solution on carbon cryogel microspheres with controlled porous structure. Microporous Mesoporous Mater. 96: 191–196.

73 Busquets, R., Ivanov, A.E., Mbundi, L. et al. (2016). Carboncryogel hierarchical composites as effective and scalable filters for removal of trace organic pollutants from water. J. Environ. Manag. 182: 141–148.

74 Roberts, A.D., Li, X., and Zhang, H. (2014). Porous carbon spheres and monoliths: morphology control, pore size tuning and their applications as Liion battery anode materials. Chem. Soc. Rev. 43: 4341–4356.

75 Roberts, A.D., Wang, S., Li, X., and Zhang, H. (2014). Hierarchical porous nitrogenrich carbon monoliths via icetemplating: high capacity and highrate performance as lithium ion battery anode materials. J. Mater. Chem. A 2: 17787–17796.

76 Roberts, A.D., Lee, J.S.M., Wong, S.Y. et al. (2017). Nitrogenrich activated carbon monoliths via icetemplating with high CO_2 and H_2 adsorption capacities. J. Mater. Chem. A 5: 2811–2820.

77 Roberts, A.D., Li, X., and Zhang, H. (2015). Hierarchically porous sulfurcontaining activated carbon monoliths via icetemplating and onestep pyrolysis. Carbon 95: 268–278.

78 Alhwaige, A.A., Ishida, H., and Qutubuddin, S. (2016). Carbon aerogels with excellent CO_2 adsorption capacity synthesized from clayreinforced biobased chitosan polybenzoxazine nanocomposites. ACS Sustain. Chem. Eng. 4: 1286–1295.

79 McCann, J.T., Marquez, M., and Xia, Y. (2006). Highly porous fibers by electrospinning into a cryogenic liquid. J. Am. Chem. Soc. 128: 1436–1437.

80 Zou, L., Gan, L., Lv, R. et al. (2011). A film of porous carbon nanofibers that contain Sn/SnO_x nanoparticles in the pores and its electrochemical performance as an anode material for lithium ion batteries. Carbon 49: 89–95.

81 Liang, H.W., Guan, Q.F., Chen, L.F. et al. (2012). Macroscopicscale template synthesis of robust carbonaceous nanofiber hydrogels and aerogels and their applications.

Angew. Chem. Int. Ed. 51: 5101–5105.

82 Nogi, M., Kurosaki, F., Yano, H., and Takano, M. (2010). Preparation of nanofibrillar carbon from chitin nanofibers. Carbohydr. Polym. 81: 919–924.

83 Wang, W., Sun, Y., Liu, B. et al. (2015). Porous carbon nanofiber webs derived from bacterial cellulose as an anode for high performance lithium ion batteries. Carbon 91: 56–65.

84 Qian, L., Willneff, E., and Zhang, H. (2009). A novel route to polymeric submicron fibers and their use for inorganic structures. Chem. Commun. 3946–3948.

85 Qian, L. and Zhang, H. (2010). Green synthesis of chitosanbased nanofibers and their applications. Green Chem. 12: 1207–1214.

86 Fang, W., Yang, S., Wang, X.L. et al. (2017). Manufacture and application of lignin based carbon fibers (LCFs) and ligninbased carbon nanofibers (LCNFs). Green Chem. 19: 1794–1827.

87 Liu, X., Roberts, A., Ahmed, A. et al. (2015). Carbon nanofibers by pyrolysis of self assembled perylene diimide derivative gels as supercapacitor electrode materials. J. Mater. Chem. A 3: 15513–15522.

88 Terrones, M. (2003). Science and technology of the twentyfirst century: synthesis, properties, and applications of carbon nanotubes. Annu. Rev. Mater. Res. 33: 419–501.

89 Yan, Y., Miao, J., Yang, Z. et al. (2015). Carbon nanotube catalysts: recent advances in synthesis, characterization and applications. Chem. Soc. Rev. 44: 3295–3346.

90 Ihsanullah, Abbas, A., AlAmer, A.M. et al. (2016). Heavy metal removal from aqueous solution by advanced carbon nanotubes: critical review of adsorption applications. Sep. Purif. Technol. 157: 141–161.

91 Schnorr, J.M. and Swager, T.M. (2011). Emerging applications of carbon nanotubes. Chem. Mater. 23: 646–657.

92 De Volder, M.F.L., Tawfick, S.H., Baughman, R.H., and Hart, A.J. (2013). Carbon nanotubes: present and future commercial applications. Science 339: 535–539.

93 Lee, J., Ko, S., Kwon, C.H. et al. (2016). Carbon nanotube yarnbased glucose sensing artificial muscle. Small 12: 2085–2091.

94 Bryning, M.B., Milkie, D.E., Islam, M.F. et al. (2007). Carbon nanotube aerogels. Adv. Mater. 19: 661–664.

95 Thongprachan, N., Nakagawa, K., Sano, N. et al. (2008). Preparation of macroporous solid foam from multiwalled carbon nanotubes by freezedrying technique. Mater. Chem. Phys. 112: 262–269.

96 Ozden, S., Narayanan, T., Tiwary, C.S. et al. (2015). 3D macroporous solids from chemically crosslinked carbon nanotubes. Small 11: 688–693.

97 Ozden, S., Tsafack, T., Owuor, P.S. et al. (2017). Chemically interconnected lightweight 3D–carbon nanotube solid network. Carbon 119: 142–149.

98 Koizumi, R., Hart, A.H.C., Brunetto, G. et al. (2016). Mechanochemical stabilization of threedimensional carbon nanotube aggregates. Carbon 110: 27–33.

99 Abarrategi, A., Gutiérrez, M.C., MorenoVicente, C. et al. (2008). Multiwall carbon nanotube scaffolds for tissue engineering purposes. Biomaterials 29: 94–102.

100 Nardecchia, S., Serrano, M.C., Gutiérrez, M.C. et al. (2013). Modulating the cytocompatibility of tridimensional carbon nanotubebased scaffolds. J. Mater. Chem. B 1: 3064–3072.

101 Serrano, M., Nardecchia, S., GarcíaRama, C. et al. (2014). Chondroitin sulphatebased 3D scaffolds containing MWCNTs for nervous tissue repair. Biomaterials 35: 1543–1551.

102 Nardecchia, S., Serrano, M.C., GarcíaArgüelles, S. et al. (2017). Ice as a green structuredirecting agent in the synthesis of macroporous MWCNTs and chondroitin sulphate composites. Materials 10: 355.

103 Gutiérrez, M.C., GarcíaCarvajal, Z.Y., Hortigüela, M.J. et al. (2007). Biocompatible MWCNT scaffolds for immobilization and proliferation of *E. coli*. J. Mater. Chem. 17: 2992–2995.

104 Katuri, K., Ferrer, M.L., Gutiérrez, M.C. et al. (2011). Threedimensional microchanelled electrodes in flowthrough configuration for bioanode formation and current generation. Energy. Environ. Sci. 4: 4201–4210.

105 Ouyang, A., Gong, Q., and Liang, J. (2015). Carbon nanotube–chitosan composite beads with radially aligned channels and nanotubeexposed walls for bilirubin adsorption. Adv. Eng. Mater. 17: 460–466.

106 Lau, C., Cooney, M.J., and Atanassov, P. (2008). Conductive macroporous composite chitosancarbon nanotube scaffolds. Langmuir 24: 7004–7010.

107 Gutiérrez, M.C., Hortigüela, M.J., Amarilla, J.M. et al. (2007). Macroporous 3D architectures of selfassembled MWCNT surface decorated with Pt nanoparticles as anodes for a direct methanol fuel cell. J. Phys. Chem. C 111: 5557–5560.

108 Yan, J., Wu, T., Ding, Z., and Li, X. (2016). Preparation and characterization of carbon nanotubes/chitosan composite foam with enhanced elastic property. Carbohydr. Polym. 136: 1288–1296.

109 Qi, H., Mäder, E., and Liu, J. (2013). Electrically conductive aerogels composed of cellulose and carbon nanotubes. J. Mater. Chem. A 1: 9714–9720.

110 Kwon, S.M., Kim, H.S., and Jin, H.J. (2009). Multiwalled carbon nanotube cryogels with aligned and nonaligned porous structure. Polymer 50: 2786–2792.

111 Zeng, Z., Jin, H., Chen, M. et al. (2016). Lightweight and anisotropic porous MWNCT/WPU composites for ultrahigh performance electromagnetic interference shielding. Adv. Funct. Mater. 26: 303–310.

112 Cheng, J., Gu, G., Guan, Q. et al. (2016). Synthesis of a porous sheetlike V_2O_5CNT nanocomposite using an icetemplating 'bricksandmotar' assembly approach as a high capacity, long cycle life cathode material for lithiumion batteries. J. Mater. Chem. A 4: 2729–2737.

113 Li, Y., Zhao, M., Chen, J. et al. (2016). Selfassembled $NiFe_2O_4$/carbon nanotubes sponge for enhanced glucose biosensing application. Appl. Surf. Sci. 362: 115–120.

114 Mei, H., Xia, J., Han, D. et al. (2016). Dramatic increase in electrical conductivity in epoxy composites with unidirectionally oriented laminae of carbon nanotubes. Chem. Eng. J. 304: 970–976.

115 Dong, L., Hou, F., Li, Y. et al. (2014). Preparation of continuous carbon nanotube networks in carbon fiber/epoxy composite. Compos. Part A 56: 248–255.

116 Cho, E.C., ChangJian, C.W., Hsiao, Y.S. et al. (2016). Threedimensional carbon nanotube based polymer composites for thermal management. Compos. Part A 90: 678–686.

117 He, H., Klinowski, J., Forster, M., and Lerf, A. (1998). A new structural model for graphite oxide. Chem. Phys. Lett. 287: 53–56.

118 Li, D., Müller, M.B., Gilje, S. et al. (2008). Processable aqueous dispersions of graphene nanosheets. Nat. Nanotechnol. 3: 101–105.

119 Huang, X., Yin, Z., Wu, S. et al. (2011). Graphenebased materials: synthesis, characterization, properties, and applications. Small 7: 1876–1902.

120 Sun, Y., Wu, Q., and Shi, G. (2011). Graphene based new energy materials. Energy Environ. Sci. 4: 1113–1132.

121 Zhu, C., Han, Y., Duoss, E.B. et al. (2015). Highly compressible 3D periodic graphene aerogel microlattices. Nat. Commun. 6: 6962.

122 Zhang, P., Li, J., Lv, L. et al. (2017). Vertically aligned graphene sheets membrane for highly efficient solar thermal generation of clean water. ACS Nano 11: 5087–5093.

123 Long, Y., Zhang, C., Wang, X. et al. (2011). Oxidation of SO_2 to SO_3 catalyzed by graphene oxide foams. J. Mater. Chem. 21: 13934–13941.

124 Kuang, J., Liu, L., Gao, Y. et al. (2013). A hierarchically structured graphene foam and its

potential as a largescale straingauge sensor. Nanoscale 5: 12171–12177.

125 Serrano, M.C., Patino, J., GarciaRama, C. et al. (2014). 3D freezestanding porous scaffolds made of graphene oxide as substrates for neural cell growth. J. Mater. Chem. B 2: 5698–5706.

126 Kota, M., Yu, X., Yeon, X.H. et al. (2016). Icetemplated three dimensional nitrogen doped graphene for enhanced supercapacitor performance. J. Power Sources 303: 372–378.

127 Qiu, L., Liu, J.Z., Chang, S.L.Y. et al. (2012). Biomimetic superelastic graphenebased cellular monoliths. Nat. Commun. 3: 1241.

128 Wang, S., Wang, Z., Futamura, R. et al. (2017). Highly microporousgraphene aerogel monolith of unidirectional honeycomb macrotextures. Chem. Phys. Lett. 673: 38–43.

129 Liu, T., Huang, M., Li, X. et al. (2016). Highly compressible anisotropic graphene aerogels fabricated by directional freezing for efficient absorption of organic liquids. Carbon 100: 456–464.

130 Zhang, H., Wang, D., Butler, R. et al. (2008). Formation and enhanced biocidal activity of waterdispersible organic nanoparticles. Nat. Nanotechnol. 3: 506–511.

131 Qian, L., Ahmed, A., Foster, A. et al. (2009). Systematic tuning of pore morphologies and pore volumes in macroporous materials by freezing. J. Mater. Chem. 19: 5212–5219.

132 Barg, S., Perez, F.M., Ni, N. et al. (2014). Mesoscale assembly of chemically modified graphene into complex cellular networks. Nat. Commun. 5: 4328.

133 Lv, L., Zhang, P., Cheng, H. et al. (2016). Solutionprocessed ultraelastic and strong air bubbled graphene foams. Small 12: 3229–3234.

134 Zhang, R., Cao, Y., Li, P. et al. (2014). Threedimensional porous graphene sponges assembled with the combination of surfactant and freezedrying. Nano Res. 7: 1477–1487.

135 Shao, Y., ElKady, M.F., Lin, C.W. et al. (2016). 3D freezecasting of cellular graphene films for ultrahighpowerdensity supercapacitors. Adv. Mater. 28: 6719–6716.

136 Liao, S., Zhai, T., and Xia, H. (2016). Highly adsorptive graphene aerogel microspheres with centerdiverging microchannel structures. J. Mater. Chem. A 4: 1068–1077.

137 Qiu, L., Coskun, M.B., Tang, Y. et al. (2016). Ultrafast dynamic piezoresistive response of graphenebased cellular elastomers. Adv. Mater. 28: 194–200.

138 Cheng, J.H., Chen, Y.H., Yeh, Y.S. et al. (2016). Enhancement of electrochemical properties by freezedried graphene oxide via glucoseassisted reduction. Electrochim. Acta 197: 146–151.

139 Chen, W., Huang, Y.X., Li, D.B. et al. (2014). Preparation of a macroporous flexible

three dimensional graphene sponge using an ice template as the anode material for microbial fuel cells. RSC Adv. 4: 21619–21624.

140 Bi, H., Xie, X., Yin, K. et al. (2014). Highly enhanced performance of spongy graphene as an oil sorbent. J. Mater. Chem. A 2: 1652–1656.

141 Wang, J., Gao, X., Wang, Y., and Gao, C. (2014). Novel graphene oxide sponge synthesized by freezedrying process for the removal of 2,4,6 trichlorophenol. RSC Adv. 4: 57476–57482.

142 Shin, Y.E., Sa, Y.J., Park, S. et al. (2014). An icetemplated, pHtunable self assembly route to hierarchically porous graphene nanoscroll networks. Nanoscale 6: 9734–9741.

143 Su, Y., Zhang, Y., Zhuang, X. et al. (2013). Lowtemperature synthesis of nitrogen/sulfur codoped threedimensional graphene frameworks as efficient metalfree electrocatalyst for oxygen reduction reaction. Carbon 62: 296–301.

144 Wang, J., Wang, H.S., Wang, K. et al. (2014). Ice crystals growth driving assembly of porous nitrogendoped graphene for catalyzing oxygen reduction probed by in situ fluorescence electrochemistry. Sci. Rep. 4: 6723.

145 Ye, S., Feng, J., and Wu, P. (2013). Highly elastic graphene oxide–epoxy composite aerogels via simple freezedrying and subsequent routine curing. J. Mater. Chem. A 1: 3495–3502.

146 Zhang, J., Cao, Y., Feng, J., and Wu, P. (2012). Grapheneoxidesheetinduced gelation of cellulose and promoted mechanical properties of composite aerogels. J. Phys. Chem. C 116: 8063–8068.

147 Wicklein, B., Kocjan, A., SalazarAlvarez, G. et al. (2015). Thermally insulating and fireretardant lightweight anisotropic foams based on nanocellulose and graphene oxide. Nat. Nanotechnol. 10: 277–283.

148 Ionita, M., Crica, L.E., Tiainen, H. et al. (2016). Gelatin–poly(vinyl alcohol) porous biocomposites reinforced with graphene oxide as biomaterials. J. Mater. Chem. B 4: 282–291.

149 Vickery, J.L., Patil, A.J., and Mann, S. (2009). Fabrication of graphenepolymer nanocomposites with higherorder threedimensional architecture. Adv. Mater. 21: 2180–2184.

150 Qian, L. and Lu, L. (2014). Three dimensional porous graphene–chitosan composites from iceinduced assembly for direct electron transfer and electrocatalysis of glucose oxidase. RSC Adv. 4: 38273–38280.

151 Huang, L., Li, C., Yuan, W., and Shi, G. (2013). Strong composite films with layered structures prepared by casting silk fibroin–graphene oxide hydrogels. Nanoscale 5: 3780–

3786.

152 Zhao, N., Yang, M., Zhao, Q. et al. (2017). Superstretchable nacremimetic graphene/poly(vinyl alcohol) composite film based on interfacial architectural engineering. ACS Nano 11: 4777–4784.

153 Qiu, L., Liu, D., Wang, Y. et al. (2014). Mechanically robust, electrically conductive and stimuliresponsive binary network hydrogels enabled by superelastic graphene aerogels. Adv. Mater. 26: 3333–3337.

154 D'Elia, E., Barg, S., Ni, N. et al. (2015). Selfhealing graphenebased composites with sensing capabilities. Adv. Mater. 27: 4788–4794.

155 Lian, G., Tuan, C.C., Li, L. et al. (2016). Vertically aligned and interconnected graphene networks for high thermal conductivity of epoxy composites with ultralow loading. Chem. Mater. 28: 6096–6104.

156 Sahoo, P.K., Aepuru, R., Panda, H.S., and Bahadur, D. (2015). Icetemplated synthesis of multifunctional three dimensional graphene/noble metal nanocomposites and their mechanical, electrical, catalytic, and electromagnetic shielding properties. Sci. Rep. 5: 17726.

157 Estevez, L., Kelarakis, A., Gong, Q. et al. (2011). Multifunctional graphene/platinum/nafion hybrids via ice templating. J. Am. Chem. Soc. 133: 6122–6125.

158 Sahoo, P.K., Panigrahy, B., Thakur, D., and Bahadur, D. (2017). Icetemplating synthesis of macroporous noble metal/3D–graphene nanocomposites: their fluorescence lifetimes and catalytic study. New J. Chem. 41: 7861–7869.

159 Wan, W., Yu, S., Dong, F. et al. (2016). Efficient C_3N_4/graphene oxide macroscopic aerogel visiblelight photocatalyst. J. Mater. Chem. A 6: 7823–7829.

160 Yang, J., Tang, L.S., Bao, R.Y. et al. (2016). An icetemplated assembly strategy to construct graphene oxide/boron nitride hybrid porous scaffolds in phase change materials with enhanced thermal conductivity and shape stability for lightthermalelectric energy conversion. J. Mater. Chem. A 4: 18841–18851.

161 Shen, Y., Zhu, X., Zhu, L., and Chen, B. (2017). Synergistic effects of 2D graphene oxide nanosheets and 1D carbon nanotubes in the constructed 3D carbon aerogel for high performance pollutant removal. Chem. Eng. J. 314: 336–346.

162 Lv, P., Tan, X.W., Yu, K.H. et al. (2016). Superelastic graphene/carbon nanotube aerogel: a novel thermal interface material with highly thermal transport properties. Carbon 99: 222–228.

163 Xu, X., Liu, Y., Lu, T. et al. (2015). Rational design and fabrication of graphene/carbon nanotubes hybrid sponge for high performance capacitive deionization. J. Mater. Chem. A 3: 13418–13425.

164 Ma, J., Shen, W., Li, C. et al. (2017). Graphene cryogelbased counter electrode materials freezedried using different solution media for dyesensitized solar cells. Chem. Eng. J. 319: 155–162.

165 González, M., Baselga, J., and Pozuelo, J. (2016). High porosity scaffold composites of graphene and carbon nanotubes as microwave absorbing materials. J. Mater. Chem. C 4: 8575–8582.

166 Tan, D., Zhao, J., Gao, C. et al. (2017). Carbon nanoparticle hybrid aerogels: 3D double interconnected network porous microstructure, thermoelectric, and solventremoval functions. ACS Appl. Mater. Interfaces 9: 21820–21828.

167 Wan, W., Zhang, R., Li, W. et al. (2016). Graphenecarbon nanotube aerogel as an ultralight, compressible and recyclable highly efficient absorbent for oil and dyes. Environ. Sci.: Nano 3: 107–113.

168 Kuang, J., Dai, Z., Liu, L. et al. (2015). Synergistic effects from graphene and carbon nanotubes endow ordered hierarchical structure foams with a combination of compressibility, superelasticity and stability and potential application as pressure sensors. Nanoscale 7: 9252–9260.

169 Zhang, R., Metoki, N., SharabaniYosef, O. et al. (2016). Hydroxyapatite/mesoporous graphene/singlewalled carbon nanotubes freestanding flexible hybrid membranes for regenerative medicine. Adv. Funct. Mater. 26: 7965–7974.

8
Nanomedicine via Freezedrying and Ice Templating

8.1 Introduction

There have been continued efforts to develop new pharmaceutical formulations and novel delivery methods to improve drug bioavailability, therapeutic efficacy, and patient compliance whilst attempting to reduce the dosage and side effects. Nanomedicine and associated target and responsive delivery have been intensely investigated. In simple terms, '*nanomedicine*' indicates the formulation and administering of active pharmaceutical ingredients (APIs) in the form of nanoparticles, usually in the size region of tens and hundreds of nanometres, be it drug nanocrystals, nanoencapsulation, nanoconjugation or with any form of nanocarriers [1–6]. A variety of methods have been developed and employed in nanomedicine research. In this chapter, the focus is on poorly watersoluble drug nanoformulation to address poor solubility, poor bioavailability, and delivery of drug nanoparticles, particularly via the use of the freeze drying and icetemplating methods.

8.2 Poorly Watersoluble Drugs and Drug Classifications

More than 40% of drug compounds and new chemical entities (NCEs) in the pharmaceutical industry are poorly soluble in water [2, 7]. This situation has not been made less severe with the recently adopted highthroughput synthesis and screening methodology. Poor water solubility leads to poor bioavailability, larger dosage, and hence severe side effects. As has been frequently quoted in literature, drug compounds may be termed as *soluble* or *poorly water soluble*. Poor water solubility may indicate a solubility less than ~30 mg ml^{-1}. Since water solubility is closely related to permeation and bioabsorption, these issues are often investigated or regulated together, for instance, by researchers in the pharmaceutical fields and regulation bodies such as the U.S. Food and Drug Administration (FDA). Drugs with regarding to solubility in water may be classified in more detailed categories. As shown in Table 8.1, the solubility categories include: very soluble, freely soluble, soluble, sparingly soluble, slightly soluble, very slightly soluble, and practically insoluble [8].

Table 8.1 Drug solubility classification in water.

Source: Adapted from http://pubs.acs.org/doi/abs/10.1021/mp034006h.

Solubility category	Solubility classification	Solubility range (mg ml^{-1})
Soluble in water	Very soluble	>1000
	Freely soluble	100–1000
	Soluble	33–100
Poorly water soluble	Sparingly soluble	10–33
	Slightly soluble	1–10
	Very slightly soluble	0.1–1
	Practically insoluble	<0.1

Biopharmaceutical classification systems (BCSs) have been proposed to facilitate drug development and approval by regulatory authorities. The BCS was introduced in 1996, based on solubility and permeability, to predict drug absorption [9]. The BCS classifies drug compounds into four categories: Class 1, Class 2, Class 3, and Class 4 (Figure 8.1). The criteria to determine whether a drug compound is highly soluble and/or highly permeable are also listed in Figure 8.1. The BCS system has been used by the U.S. FDA as a sciencebased approach to allow waiver of *in vivo* bioequivalence studies for BCS Class 1 drugs (highly soluble and highly permeable) [10, 11]. As per FDA regulations, the solubility should be determined in aqueous media with a pH range of 1–7.5 by a shakeflask or titration method, and analysed by a validated stabilityindicating assay. For the determination of dissolution rates, USP apparatus I (basket) at 100 rpm or USP apparatus II (paddle) at 50 rpm should be used in a defined medium (900 ml of 0.1 N HCl or simulated gastric acid, pH 4.5 buffer, and pH 6.8 buffer or simulated intestinal fluid). For the evaluation of intestinal permeability, both *in vivo* intestinal perfusion (in humans or animals) and *in vitro* permeation experiments can be performed. For *in vitro* permeability, several cell lines particularly Caco2 cell lines and Madin–Darby canine kidney (MDCK) cell lines have been widely used [6]. The *in vivo* permeability data from humans is always preferred because the *in vitro* data or *in vivo* data from animals may not produce the same results that can be applied in human medication.

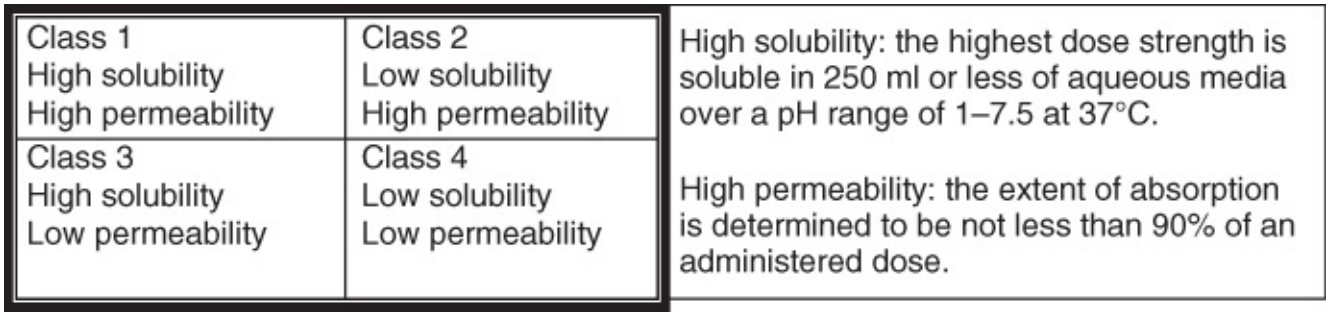

Figure 8.1 The biopharmaceutics classification system (BCS) as proposed.

Source: Amidon et al. 1995 [9]. Reprinted with permission from Springer Nature.

There are 325 medicines and 260 drugs in the WHO (World Health Organization) Essential

Drug List, of which 123 are oral drugs as immediaterelease products. These drugs have been classified based on the BCS system. Drug solubility is judged based on the dimensionless dose number, D_0. D_0 is the ratio of drug concentration in the administered volume (250 ml) to the saturation solubility of the drug in water. Drugs with $D_0 \leq 1$ are classified as highly soluble. The classification of permeability is based on log *P* or CLogP values. log *P* is the *n* octanol/water partition coefficient and can be calculated using three different fragmentation methods based on atomic contributions to lipophilicity. CLogP can be calculated using a program from BioByte Corp. log *D*, the pHdependent distribution coefficient for singly ionized species, can be calculated from log *P* and the ionization constant pK_a. The drugs with estimated log $P \geq 1.72$, CLogP ≥ 1.35, and log $D \geq -1.48$ are classified as highly permeable. Based on dose number and log *P*, among the immediaterelease drug dosages, 23.6% are in Class 1, 17.1% in Class 2, 31.7% in Class 3, and 10.6% in Class 4 [8].

A drug compound is classified as highly permeable when the fraction of dose absorbed (F_{abs}) in humans is equal to or greater than 90%. However, there are reports that high F_{abs} may not simply translate to having high permeability, as shown by the high F_{abs} of the βblocker sotalol that has low Caco2 permeability [12]. This discrepancy may be attributed to the 'local absorption' or 'average absorption', with the latter usually used for F_{abs}. However, in the different sections of the small intestine, the environmental pHs are different, which can have a significant impact on the absorption of ionizable drugs. It can be emphasized that, if a compound has a high fraction of dose absorbed, it should show high permeability in the relevant intestinal regions [12].

However, with more data available on the increasing number of drug compounds, evidence has been growing that high extent of absorption does not necessarily indicate high permeability. Wu and Benet proposed the Biopharmaceutical Drug Disposition Classification System (BDDCS) based on solubility and metabolism (Figure 8.2) [13]. The BDDCS can be primarily used to predict drug disposition and the importance of transporters in drug absorption and elimination in the intestine and liver [10]. In the BDDCS, the major route of elimination for the highly permeable Class 1 and Class 2 drugs in humans is metabolism, whilst for the poorly permeable Class 3 and Class 4 drugs the main elimination route is via renal and biliary excretion of unchanged drugs[11]. Metabolism of ≥70% is set as the cutoff value for extensive metabolism. It is noted that there are relatively few drugs where the extent of metabolism is in the range of 30–70%. Most drugs are either highly metabolized or poorly metabolized [11].

Class 1 High solubility Extensive metabolism	Class 2 Low solubility Extensive metabolism	High solubility: as used by the BCS system. Extensive metabolism: the cut-off value is not less than 70% metabolism of an administered dose.
Class 3 High solubility Poor metabolism	Class 4 Low solubility Poor metabolism	

Figure 8.2 The biopharmaceutics drug disposition classification system (BCS) as proposed.

Source: Wu and Benet 2005 [13]. Reprinted with permission from Springer Nature.

Besides the drug classification systems, 'the rule of 5' proposed by Lipinski et al. has also been widely used to predict drug absorption or permeation. The 'rule of 5' suggests that a compound is more likely to exhibit poor absorption or permeation: (i) when the compound has more than five Hbond donors (the sum of -OHs and -NHs); (ii) its molecular weight is over 500; (iii) its log *P* is over 5 (or MLogP is over 4.15); (iv) it has more than 10 Hbond acceptors (the sum of -Ns and -Os); and (v) it is not a substrate for biological transporters [14]. Antibiotics, antifungals, vitamins and cardiac glycosides are exceptions to the 'rule of 5' because their structural features allow them to act as substrates for naturally occurring transporters. Although there are exceptions, the 'rule of 5' has been very effective and useful in drug development.

8.3 Nanoformulation Approaches for Poorly Soluble Drugs

A number of approaches have been developed to address the poor water solubility problem. Although it is always nice to start from drug design and then screen lead compounds and find soluble drugs with high therapeutic potent, this has always been extremely difficult to achieve, as evidenced by the poor solubility of potent drug compounds synthesized or discovered. In addition to this, synthesis of prodrugs is a useful route to enhancing solubility. Once absorbed, the prodrugs are metabolized and then released into the systemic circulation [2]. Crystal engineering, via the preparation of cocrystals or by amorphous formulation and formation of salts, have also been exploited [1, 2].

However, nanosizing or nanoformulation techniques are probably most widely investigated and employed in research and development towards enhancing the drug solubility and bioavailability. The particle sizes can be reduced to microns and more favourably the nanosized range (e.g. 100–200 nm) [15]. The nanoparticles provide significantly increased surface area and also high surface energy. Both the dissolution rate and the saturation solubility can be improved as a result of nanosizing. The increase in dissolution rate can be described by Noyes–Whitney/Nernst–Brunner Equation [15–17]:

$$\frac{dM}{dt} = \frac{A_0 D}{h}(c_s - c),$$

where dM/dt is the dissolution rate by mass, A_0 is the total surface area of the solute, D is the diffusion coefficient, h is the thickness of the boundary layer around the solute particle, c_s is the saturation solubility and c is the solute concentration in the bulk phase at time t.

The increase in saturation solubility is given by the Ostwald–Freundlich equation [15, 17]:

$$c_{s,r} = c_{s,\infty} \exp\left(\frac{2\gamma M}{r\rho RT}\right),$$

where $c_{s,r}$ is the saturation solubility of a particle with radius r, $c_{s,\infty}$ is the saturation solubility of a particle with infinite radius, γ is the particle medium interfacial tension, M is the compound molecular weight, ρ is the particle density, R is the universal gas constant, and T is the absolute temperature.

The nanosizing techniques can be generally categorized into bottomup and topdown methods. The bottomup methods start with drug solutions (mostly organic solutions due to their poor water solubility). The commonly used approaches include encapsulation (e.g. micelles, dendrimers, emulsions, nanocapsules, microspheres, and complexation) [2, 7, 18], solid dispersions (e.g. via hot melt extrusion) [7], nanoprecipitation, antisolvent precipitation (including the use of supercritical fluids and compressed fluids) [2], spray drying [19, 20], and cryogenic techniques (which will be the focus of this chapter) [2, 21].

There are not such a variety of topdown approaches for nanosizing, with highpressure homogenization and ball milling (either dry milling or wet milling) being the mostly used techniques [15, 22–24]. Owing to simple processing, easy control of process parameters, and scaleup potential, the wet milling and homogenization methods are widely investigated and mostly used particularly in the pharmaceutical industry [1, 2, 15, 21–24].

For nanosizing formulations, it is inevitable to use nonaqueous solvents [25] and excipients [26, 27]. The solvent residual must be controlled within the limits in a drug product as required by regulatory bodies. The solvent may be categorized into three classes [28]. Class 1 solvents are human carcinogens, strongly suspected human carcinogens, or environmental hazards. These include benzene, carbon tetrachloride, 1,2dichloroethane, 1,1 dichloroethene, and 1,1,1trichloroethane. These solvents should be avoided whenever possible. Class 2 solvents are noncarcinogens and solvents suspected of other significant but reversible toxicities. Table 8.2 lists the Class 2 solvents for pharmaceuticals with permitted daily exposure (PDE) and concentration limits [28]. PDE is the maximum acceptable intake per day of residual solvent in pharmaceutical products. Class 3 solvents exhibit low toxic potential to human, with PDEs of 50 mg or more per day. The use of Class 3 solvents should be subject to good manufacturing practice (GMP) and other qualitybased requirements. Table 8.3 provides the list of Class 3 solvents [28]. There are also some solvents for which no adequate toxicological data are available: e.g. 1,1diethoxypropane, methylisopropyl ketone,

1,1dimethoxymethane, methyltetrahydrofuran, 2,2dimethoxypropane, petroleum ether, isooctane, trichloroacetic acid, isopropyl ether, and trifluoroacetic acid [28].

Table 8.2 Class 2 solvents (to be limited) for pharmaceutical products.

Source: Adapted from http://www.ich.org/products/guidelines/quality/qualitysingle/article/impuritiesguidelinefor residualsolvents.html .

Solvent	**PDE (mg d^{-1})**	**Concentration limit (ppm)**
Acetonitrile	4.1	410
Chlorobenzene	3.6	360
Chloroform	0.6	60
Cumene	0.7	70
Cyclohexane	38.8	3880
1,2Dichloroethene	18.7	1870
Dichloromethane	6.0	600
1,2Dimethoxyethane	1.0	100
N,*N*Dimethylacetamide	10.9	1090
N,*N*Dimethylformamide	8.8	880
1,4Dioxane	3.8	380
2Ethoxyethanol	1.6	160
Ethyleneglycol	6.2	620
Formamide	2.2	220
Hexane	2.9	290
Methanol	30.0	3000
2Methoxyethanol	0.5	50
Methylbutyl ketone	0.5	50
Methylcyclohexane	11.8	1180
Methylisobutylketone	45	4500
*N*Methylpyrrolidone	5.3	530
Nitromethane	0.5	50
Pyridine	2.0	200
Sulfolane	1.6	160
Tetrahydrofuran	7.2	720
Tetralin	1.0	100
Toluene	8.9	890
1,1,2Trichloroethene	0.8	80
Xylene	21.7	2170

Table 8.3 Class 3 solvents (low toxic potential to human) for pharmaceutical products.

Acetic acid	Acetone	Anisole
1Butanol	2Butanol	Butyl acetate
*tert*Butylmethyl ether	Dimethyl sulfoxide	Ethanol
Ethyl acetate	Ethyl ether	Ethyl formate
Formic acid	Heptane	Isobutyl acetate
Isopropyl acetate	Methyl acetate	3Methyl1butanol
Methylethyl ketone	2Methyl1propanol	Pentane
1Pentanol	1Propanol	2Propanol
Propyl acetate	Triethylamine	

Different excipients may be included in a pharmaceutical product to serve different purposes [26, 27]. The excipients participate in the systemic circulation like the APIs. Therefore, the safety of excipients is a very important issue but also highly complicated due to the variety of excipients used. Similarly to the APIs, the safety or toxicity of the excipients should be assessed [27]. Furthermore, the drug–excipient interaction [29] and the effect of the excipients on drug disposition [30] can have pronounced effects on excipient pharmacokinetics and profiling [31]. Sugars and polymers are the mostly used excipients for drug nanoformulations, either to protect the drug during processing or to stabilize the drug in the formulations [15, 19, 20, 26].

There are stability issues associated with nanosuspensions and solid nanoformulations. For nanosuspensions, the instabilities may include sedimentation/creaming, agglomeration, crystal growth, or crystallization of amorphous phase, and the potential chemical changes [32]. In solid formulations, the selection of excipients/bulking agents, the glass state of the matrix, and the molecular mobility (leading to nucleation/crystallization) of drugs in the matrix can have great impact on formulation stability [33].

Characterization of drug nanoparticles is an important aspect of drug nanoformulations [32]. Particle size, size distribution, and particle morphology can be obtained by scanning electron microscopy (SEM), transmission electron microscopy (TEM), and atomic force microscopy (AFM). It should be noted that these microscopic methods show the size and shape of dry nanoparticles although cryoTEM can be used to image the nanoparticles with stabilizer or hydration shell in a frozen state. Dynamic laser scattering (DLS) is an effective technique to measure the size of hydrated nanoparticles (but not particle shape) and surface charges. The data generated are very important for medical applications because the hydrated size of the nanoparticles (which can be considerably larger than the dry nanoparticles) is a good representation of the real size of nanoparticles after being administered. The crystalline state of the drug nanoparticles can be characterized by powder Xray diffraction (PXRD), wide angle Xray scattering (WAXS), small angle Xray analysis (SAXS), and differential scanning calorimetry (DSC) [22, 32].

Because one of the main purposes of employing nanosizing techniques is to enhance the drug solubility, the determination of dissolution rate and saturation stability of drug nanoparticles is crucial. It has been reported that the increase of saturation stability for drug nanoparticles is not more than 15%. Therefore, the enhancement in dissolution rate is the main contribution from nanoformulations [17]. Although the FDArecommended USP Apparatus 1 and Apparatus 2 can be employed to measure dissolution rate, questions have been asked on 'what is an appropriate dissolution method for drug nanoparticles'. Because the drug nanoparticles are small, the nanosuspension is clear and it is difficult to judge a nanosuspension from a true molecular solution. Generally, the dissolution rates for drug nanoparticles are determined by separating the drug nanoparticle from the solution (e.g. by centrifugation and membrane dialysis) and the concentration of the solution can be determined by UV–Vis analysis or high performance liquid chromatography (HPLC). This measurement may be inaccurate, particularly when the separation time is long and the dissolution rate is fast. *In situ* analytical techniques such as UV–Vis fibre optic probe, calorimetry, and turbidimetry have been used, which obviate the need to separate dissolved API. However, the shortcomings of these methods are still related to the difficulty in distinguishing small nanoparticles and the molecular solution [17]. A recent development is the use of DLS to determine the dissolution rate and the solubility. This method is based on the linear correlation between intensity and particle number in diluted nanosuspensions. The variation of particle sizes must be also considered [17, 34].

In addition to the beneficial effect it provides of enhancing dissolution rate, aqueous nanoformulations may be administered both orally and intravenously [23, 24]. Bioabsorption, stability in systemic circulation, targeted delivery, and finally elimination of drug nanoparticles from the body are the essential benefits of administering pharmaceutical nanoparticles.

8.4 Bioavailability and Delivery of Drug Nanoparticles

Bioavailability may be defined as 'the rate and extent to which the active drug ingredient or therapeutic moiety is absorbed from a drug product and becomes available at the site of drug action', as described in the Code of Federal Regulation, USA. Based on the Committee for proprietary medicinal products of the European Medicines Evaluation Agency (EMEA), bioavailability is understood to be the extent to and the rate by which a substance or its therapeutic moiety is delivered from a pharmaceutical form into the general circulation [35]. The bioavailability is achieved and governed by drug pharmacokinetics, which is the kinetics of drug absorption, distribution, metabolism, and excretion (ADME) [4, 31]. It is the same for drug nanoparticles, as shown in Figure 8.3. However, the nanoparticles can behave very differently at each stage of the ADME, compared to the dissolved drug molecules.

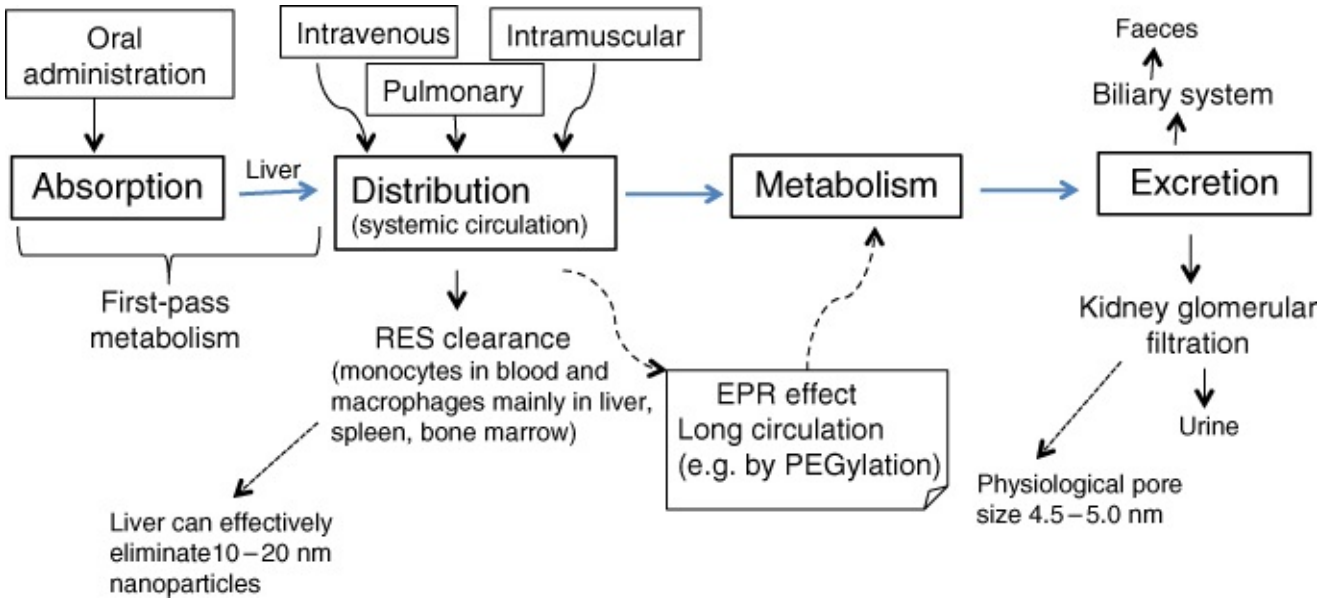

Figure 8.3 The schematic representation of the pharmacokinetic ADME for drug nanoparticles.

8.4.1 The Absorption Process

There are different administering routes, e.g. oral, intravenous, intramuscular, and pulmonary delivery. The oral administration is the most widely used, due to good patient compliance and no necessity for the presence of trained medical staff. The absorption process is involved in oral administration, pulmonary delivery, and skin delivery, etc. This section discusses oral administration and pulmonary delivery because of their wide use and because most of the processes may be adopted for other administration routes that involve absorption procedures.

8.4.1.1 The Orally Administering Route

Figure 8.4 shows how the orally administered drug nanoparticles enter the blood systemic circulation. The absorption occurs mainly in the small intestine via membrane permeation. There are three sections in the small intestine, with different pH environment, which may have significant impact on the stability and absorption of ionized or pHsensitive drug compounds [12]. The duodenum is the shortest, widest, and the least mobile section, of 20–30 cm length and 3–5 cm diameter [36, 37]. It receives digestive enzymes from the pancreas and bile via the liver and gall bladder. This is where the degradation and/or dissolution mainly take place.

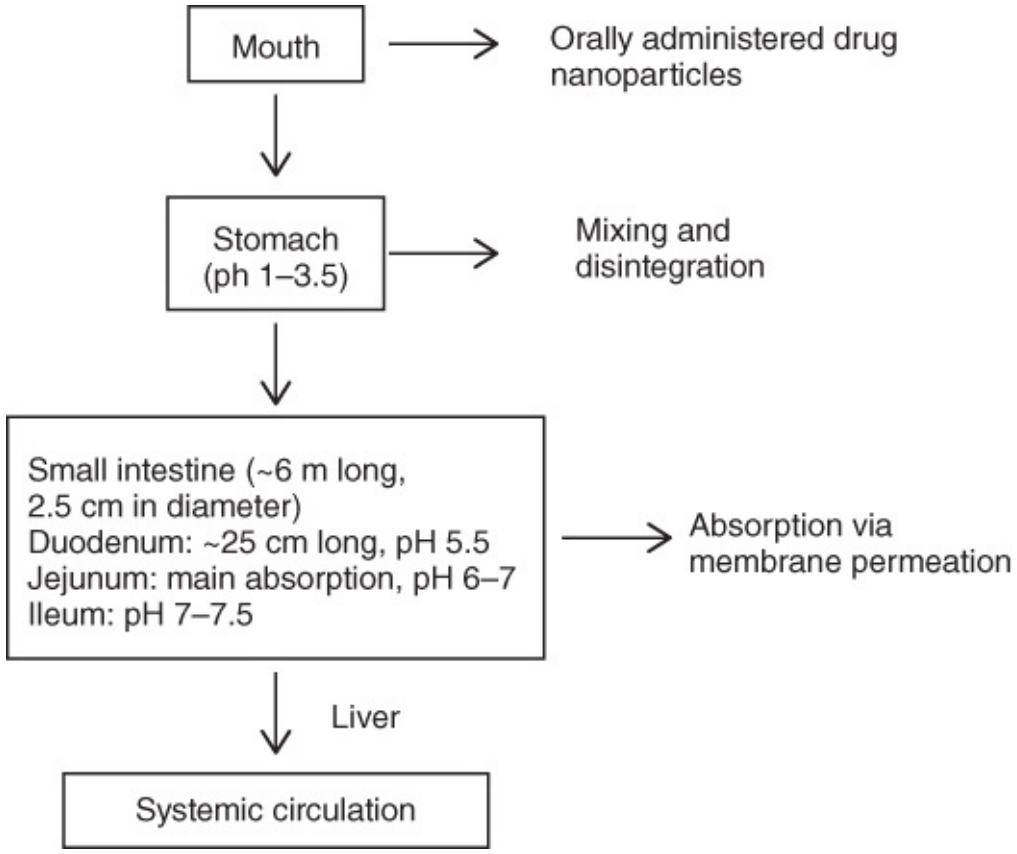

Figure 8.4 The absorption process for orally administered drug nanoparticles.

The wall of the small intestines is composed of mucosa, submucosa, muscle layers, and serosa. The serosa consists of a single layer of flattened mesothelial cells overlying some loose connective tissues. The submucosa is a network of connective tissues containing small blood vessels, lymphatic, and nerve plexus. The mucosa is at the inner surface of the intestine and is directly in contact with the intestinal fluid. The epithelium is the innermost layer facing the lumen of the bowels, consisting of a single layer of columnar epithelial cells (enterocytes), which line both the crypts and villi [37]. The presence of villi and microvilli, mostly present in the duodenum and jejunum, provides the large absorption surface area. For this reason, the small intestine is considered to be the major absorption site [38].

The small intestine lies anterior to the liver. The blood flows from the small intestine immediately into the liver by way of the portal vein. In the liver, the blood passes evenly through the hepatocytes and ultimately leaves the liver via the hepatic veins that empty into the vena cava of the general circulation. The amount of orally administered drugs can be reduced by both intestinal and hepatic metabolism. This effect is referred as *firstpass metabolism* [37] (Figure 8.3). The firstpass metabolism includes only the metabolism by the intestine during absorption and by the liver when the blood flows immediately into it from small intestine [38]. The bioavailability (F) by oral administration can then be described as [39]:

$$F = f_{abs}(1 - f_i)(1 - f_h),$$

where f_{abs} is the fraction of the dose absorbed from the intestinal lumen, f_i is the fraction of

drug metabolized by the small intestine, and f_h is the fraction of the drug metabolized by the liver.

During the absorption by the small intestine, the drug compounds or nanoparticles must first overcome the mucousal barriers. Mucousal surface protects all major portals of the body such as nose, lung, intestine, gall bladder, and reproductive tracts, by excluding pathogens and other dangerous materials. The mucousal surface is negatively charged due to the presence of sialic acids and sulfated monosaccharides in the sugar chains. The thickness of the mucous layer varies at the different parts of the body, about 300 μm in the stomach and 700 μm in the intestine [40]. As mentioned earlier, the epithelium layer lines the mucousal surface, with the two most abundant epithelial cells being absorptive cells (enterocytes) and secretory cells (goblet and Paneth). Drug nanoparticles may be predominantly taken by the M cells in the Peyer's patches of the ileum. The size of the nanoparticles can make a difference to the way the nanoparticles are absorbed. Nanoparticles with sizes less than 50 nm are transported paracellularly, whilst the nanoparticles of 50–200 nm are endocytosed by enterocytes and those of 200 nm to 5 μm are taken up by M cells of the Peyer's patches [41, 42].

The mechanism of the drug permeating across the epithelium layer can be transcellular and paracellular, as shown in Figure 8.5. Sometimes, unexpected bioavailability characteristics are observed, either higher or lower than expected. This can be attributed to the influx and efflux processes facilitated by transporter proteins, which include passive transporter (moving solutes from high concentration to low concentration or via an electrochemical gradient) and active transporter (moving solutes against the concentration or electrochemical gradient). An energyyielding chemical or photochemical reaction is required to facilitate the active transporter. Pglycoproteins can effectively utilize the ATPproduced energy to facilitate the active efflux of its substrates [39].

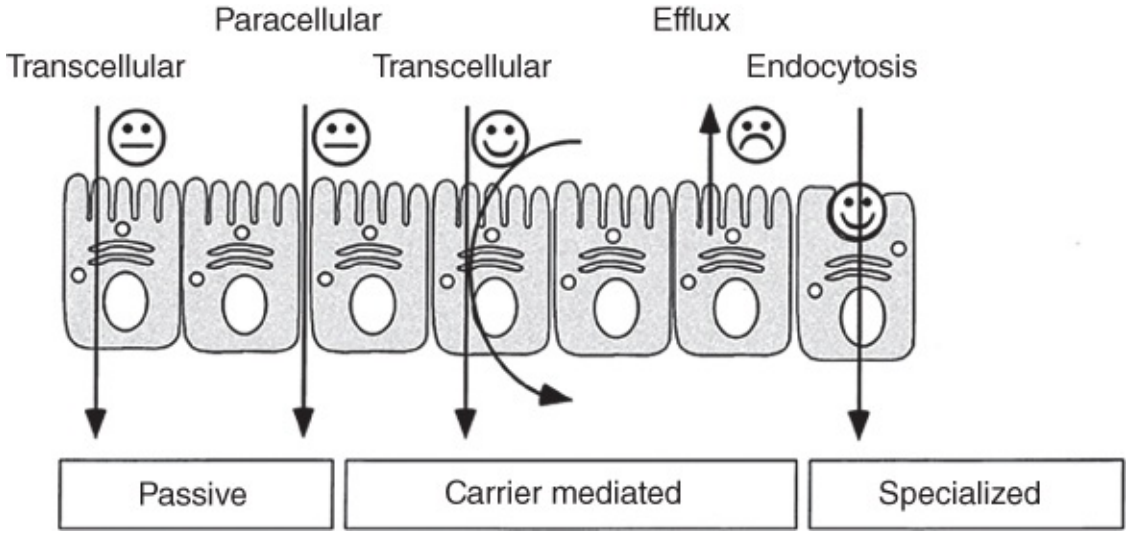

Figure 8.5 The schematic representation for the permeation pathways across the intestinal membrane.

Source: Löbenberg and Amidon 2000 [35]. Reprinted with permission from Elsevier.

For the transcellular permeation, the drug molecules or nanoparticles move across the lipid

bilayers of epithelial cells. The physicochemical properties of the compound and the structure of the lipid bilayers can exert significant impact on the permeation. In general, the bilayer can be divided into four distinct regions: (i) the first, the outermost hydrophilic region containing a high proportion of water molecules; (ii) the second, the highly packed dense region of polar heads, acting as the greatest barrier to solute diffusion; (iii) the third, the hydrophobic region containing the highest density of nonpolar tails; and (iv) the fourth, the most hydrophobic, region of the membrane, serving as a hydrophobic barrier [39]. It is clear that the lipid bilayer is a complex structure of hydrophilic and hydrophobic regions. Both highly hydrophobic and highly hydrophilic compounds lead to poor permeation. Indeed, it is suggested that the optimal partition coefficient log P_0 (based on partitioning between *n*octanol and water) for a drug is in the region of 2–7 [39] while others suggest that drugs with log P_0 in the range of 1–3 show good passive absorption across the lipid membrane [6].

During the absorption process in small intestines, blood flow in the villi as well as the adjacent regions of the submucosa is increased greatly. Drugs permeate across the villi and into the blood and then into the liver, followed by systemic circulation. The firstpass metabolism occurs in both the small intestine and the liver. Cytochromes P450 are the dominant enzymes involved in the biotransformation of drugs. The three main P450 gene families, CYP1, CYP2, and CYP3 are thought to be responsible for drug metabolism [37]. The distribution of P450 in the small intestine is not uniform, with the content higher in the proximal than in the distal part. The average total cytochrome P450 content in human intestine is about 20 pmol mg^{-1} microsomal protein, much lower than that in liver (about 300 pmol mg^{-1} microsomal protein). It is thus believed that the liver contributes significantly more to the firstpass effect. It has been found that CYP3A4 is the dominant cytochrome P450 type in the mucousal epithelium in human small intestine [37]. The drug metabolism is usually considered to be in two phases. The Phase 1 metabolism generally degrades or modifies the drug compounds via the reactions of hydrolysis, oxidation, and reduction. In the Phase 2 metabolism, the drug compound or its metabolites are conjugated to certain functional groups to make them watersoluble and be easily excreted [38].

Various methods may be employed to investigate drug absorption or firstpass metabolism in the small intestine. These include the *in vitro* method (e.g. with tissue slices, Caco2 cells/Goblet cells, rat intestine), the *in situ* method (vascular perfusion), and the *in vivo* method (e.g. perfused intestinal loops, portacaval transposition, AUC (area under curve) measurement) [38].

Despite different permeation pathways (either transcellular or paracellular), the overall absorption rates of most drugs may be commonly described by Fick's First Law, where the mass transport across the membrane is proportional to the concentration difference and the absorption area and also determined by the diffusion coefficient [35, 37]. The blood flow close to the epithelium layer can be treated as unstirred water. A high drug solubility or high concentration of nanosuspension in the intestine lumen can lead to fast absorption. A balance of hydrophobicity and hydrophilicity of the drug, allowing adequate solubility in aqueous luminal fluid and lipid membrane phase of the enterocytes, is highly important to achieve optimal

intestinal absorption.

8.4.1.2 Absorption in Lung by Pulmonary Delivery

Similar to the intestinal tract, the lung is in direct contact with the environment and can act as the first port of entry for nanoparticles into the body. The lung consists of the airways (trachea, bronchi, and bronchioles) and the alveoli (gas exchange areas). The respiratory zone includes all the structures that participate in gas exchange, beginning with the bronchioles. The gas exchange mainly occurs in the alveolar region due to the high surface area. The surface area of the human lungs is estimated to be about 75–140 m^2 in adults [43]. The mucus lines the respiratory epithelium from the nose to the terminal bronchioles. In humans, the mucous layer consists of the periciliary (sol) layer (~ 5–10 μm thick) and the luminal (gel) layer (~60 μm thick). The sol layer is close to the epithelium and more watery. The gel layer contains cilia to propel mucus up and out of the lung, acting to remove external particles [40]. The pseudostratified epithelia are different in airways and alveoli of the lungs, with a gradually thinning columnar epithelium in airways, 3–5 mm thick in the bronchial epithelium and 0.5–1 mm thick in the bronchiolar epithelium. The particles deposited in this region are either moved away from the lung by mucociliary clearance or diffuse through the thick mucus to the epithelial cells. However, in the alveolar region, there exists a thin, single cell layer. The distance between the air in the alveolar lumen and the capillary blood flow is less than 400 nm. As such, the buildup of nanoparticles in the alveolar region poses great health risks [43].

The deposition of particles in the respiratory tract can be described by three main mechanisms. The first mechanism, *inertial impaction*, occurs during the passage through the oropharynx and large conducting airways for the particles larger than 5 μm (based on the mass median aerodynamic diameter, MMMD). The second one, *gravitational sedimentation*, is responsible for the particles of 1–5 μm in smaller airways and respiratory bronchioles. The third one, *the Brownian diffusion*, is for particles less than 0.5 μm. The main factors impacting on particle deposition include: (i) particle size, density, shape, and surface properties; (ii) the structure of airways and alveoli; and (iii) ventilator parameters such as breathing pattern, flow rates, tidal volume, etc. Figure 8.6 shows the effect of particle sizes on the deposition in different parts of the human respiratory tract [44]. The optimal particle sizes to achieve delivery deep in the alveolar region are in the range of 1–3 μm. Large particles tend to deposit in the mouth and throat and airways. Smaller particles can increase both deposition (the ventilation parameters should be considered for the highly mobile and suspended nanoparticles) and diffusion in the alveolar region.

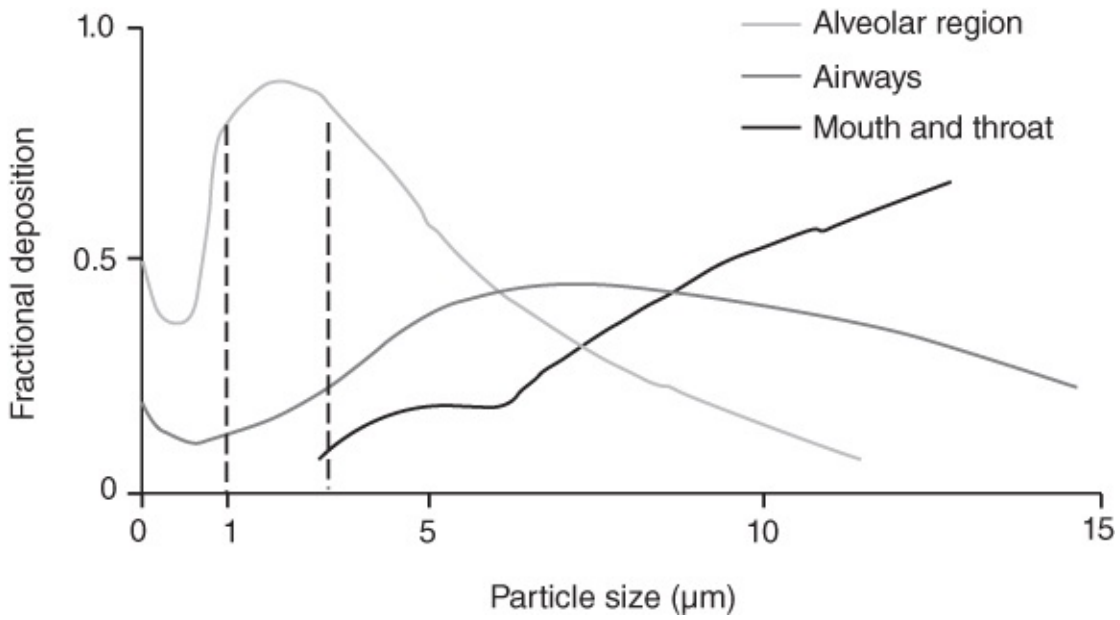

Figure 8.6 The effect of particle size on the deposition of aerosol particles in the human respiratory tract following a slow inhalation and a 5 s breath hold. Larger particles deposit in the airways or mouth and throat, whereas smaller particles deposit in the alveolar region. The optimal size range for deposition in the alveolar region is 1–3 μm.

Source: Bryon 1986 [44]. Reprinted with permission from Elsevier.

The discussion on the nanoparticle penetration across the epithelium of skin, nose, and vagina can be found elsewhere [40].

8.4.2 Nanoparticle Clearance and Distribution

Once the drug nanoparticles enter the systemic circulation, either by oral administration (with firstpass metabolism) or other routes (e.g. intravenous injection, or pulmonary delivery), the nanoparticles may be eliminated by the reticuloendothelial system (RES) (Figure 8.3). However, for the drug nanoparticles to generate therapeutic efficacy, sufficiently long circulation time and transport to the target tissue cells are required.

The RES, also known as mononuclear phagocyte system (MPS), is part of the immune system that consists of phagocytic cells, e.g. monocytes in blood and macrophages in tissues such as liver, spleen, and bone marrow. Phagocytes have receptors for molecules, termed as *opsonins*, which initiate binding and removal [45]. There are various proteins and ions in the blood, with human serum albumin being the most abundant protein. The absorption/binding of proteins and/or ions may cause nanoparticle aggregation and precipitation. More importantly, this can initiate nanoparticle opsonization. This process tags the nanoparticles, which can be subsequently recognized and taken up by phagocytic cells. This is an effective way to remove foreign particles from the body, mainly by the hepatic Kupffer cells and the marginal zone and redpulp macrophages in the spleens [4, 45]. The hepatic Kupffer cells have special features (ciliated borders and stellate branches) that facilitate the removal of foreign nanoparticles. Kupffer cells contain various receptors for selective endocytosis of opsonized foreign particles. Hepatocytes contribute considerably to endocytosis and enzymatic breakdown of

foreign particles. The nanoparticles that cannot be broken down by intracellular processes remain in the macrophages and hence in the body [46]. As a function to protect the body, the liver can efficiently capture and eliminate nanoparticles in the range of 10–20 nm (including viruses) [46].

In order to prolong the systemic circulation in blood, the nanoparticles can be surface modified with stealthshielding coating. Different polymers such as polysaccharides, polyacrylamide (PAM), and poly(vinyl alcohol) (PVA) have been used to modify the particle surface [47]. However, coating the nanoparticles with poly(ethylene glycol) (PEG) or PEG copolymer have proven to be mostly successful [47, 48]. The protective action of PEG is mainly attributed to the hydrophilic shell on the particle surface. The water molecules can form a dense shell via hydrogen bonding to the ether oxygen of PEG molecules. This hydrated surface shell can repel the protein and reduce the interaction. It is also suggested that the PEG chains can undergo spatial conformations and prevent the opsonization of particles by the macrophages of the RES [47]. Investigation on the novel coating on nanoparticles to facilitate negligible immune reactions is an exciting and emerging research area for drug delivery [48].

The transport path of the nanoparticles from blood circulation to the target cell and its nucleus is schematically shown in Figure 8.7. The nanoparticles need to permeate across the endothelium, diffuse through tissue interstitium, and arrive at the cell surface. Via endocytosis, the nanoparticles can move across the cell membrane and diffuse into different parts including the nucleus inside the cell. As described in Figure 8.7, there are different types of endothelium and different sizes of transcellular channels or fenestrations at different parts of the body [40]. In addition to particle sizes, the shape of the particles plays a significant role in the transport across the endothelium. For example, it has been reported that the cellular internalization (with the HeLa cells) of rodshaped, highaspectratio nanoparticles occurred more easily than that of the more symmetrical and lowaspectratio particles [49]. The particle size, shape, and surface chemistry can all play significant roles in cellular internalization, as evidenced in the study with gold nanorods [50]. There are two exceptional examples of endothelium. The first is the blood–brain barrier (BBB), the tightest endothelium in the body. Discovering drugs and/or functionalized nanoparticles to move across the BBB have always been a great challenge. The second one is the leaky vasculature around tumour cells, which allows the passive permeation of large nanoparticles, widely known as the enhanced permeability and retention (EPR) effect [40, 45]. The growing solid tumour requires nutrients and metabolites for growth. The resulting neovasculature is not hierarchically organized as in capillary beds. This heterogeneity can lead to variable accumulation of drug nanoparticles [45]. The pore sizes in the leaky tumour vasculatures are reported to be in the range of 380–780 nm [40] while others suggest that the highly heterogeneous cutoff pore sizes are in a wider range of 200–1200 nm [51]. Different factors can influence the transport of drug nanoparticles from blood to tumour cells. The chaotic blood flow in the tumour vasculature reduces the particle extravasation into the tumour interstitium. The higher interstitium pressure also hinders the transport into the interstitium.

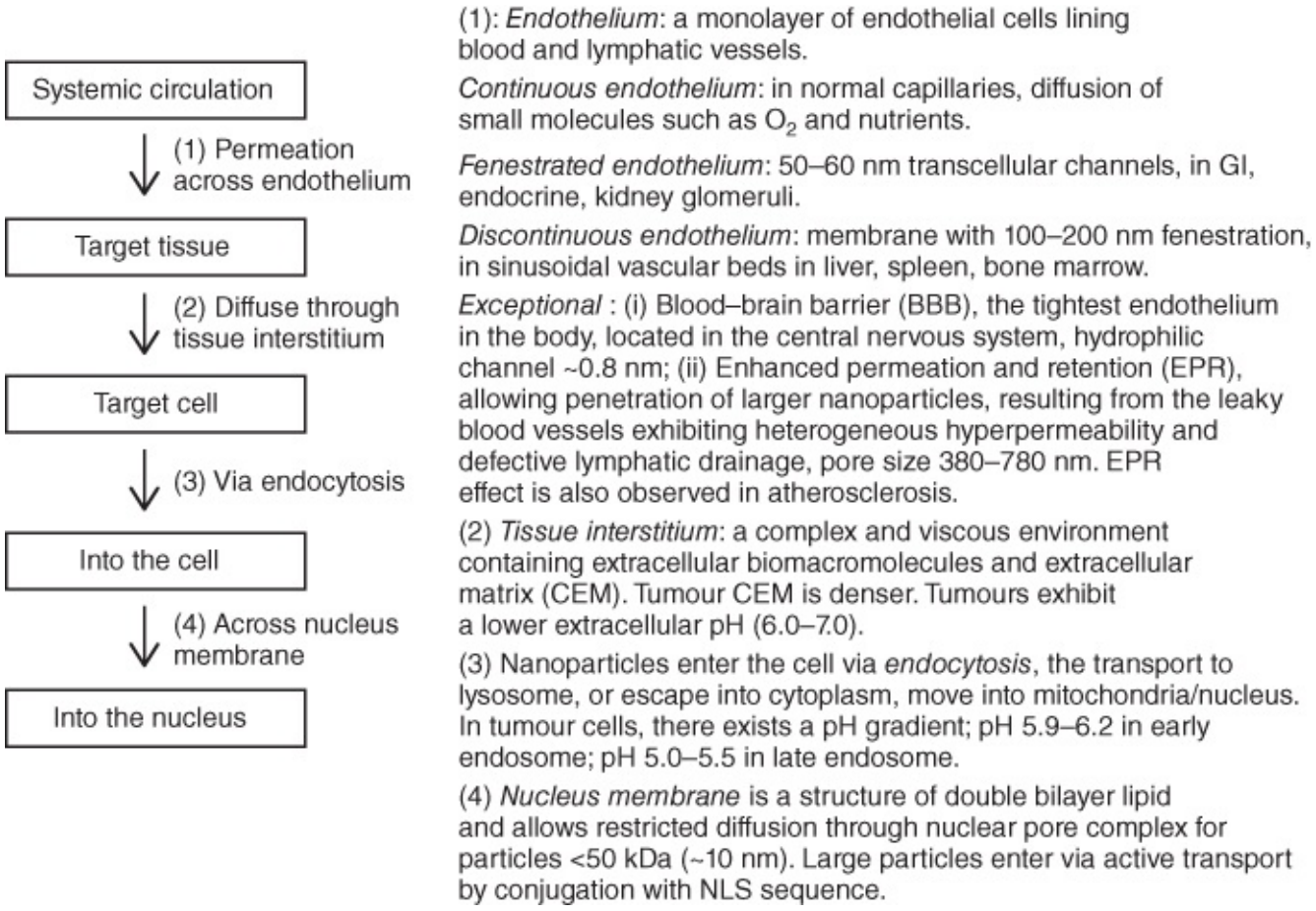

Figure 8.7 The scheme describes the delivery of drug nanoparticles from blood circulation to the target cell.

Source: Adapted from Refs. [40, 52].

As noted in Figure 8.7, there is variation of pHs in tumour tissue interstitium and tissue cells. Functional coating on the drug nanoparticles can facilitate the targeted delivery and the responsive release at the target sites. The coatings (either chemically bound or physically attached) can provide stealth shielding [47] and also prevent the rapid dissolution of drug nanoparticles before reaching the target. In addition to the long circulating polymer coating, the targetbinding ligand and/or polymers with responsive bonding or functional groups can be further attached to provide multifunctional and responsive drug nanoparticles [52]. Some examples include PEG linkage with folate/peptide/nanoplex [47], pHsensitive coating with zwitterionic chitosan derivatives [53], intracellular reductionsensitive release [54], and tumour intracellular pH responsive delivery [55].

8.4.3 Metabolism and Excretion

Once the therapeutic roles are achieved, the drug nanoparticles should be removed from the body, by metabolism and/or direct excretion via renal clearance (Figure 8.8). As many nanoparticles (e.g. quantum dots, Au nanoparticles) may not be metabolized, to avoid taking up by macrophages and accumulating in the body, excretion via urine through kidney processing is the major route. The process involves glomerular filtration, tubular secretion, and then

elimination through urinary excretion. The nanoparticles in systemic circulation enter the glomerular capillary bed via the afferent arterioles. The glomerular wall consists of fenestrated endothelium, the highly negatively charged glomerular basement membrane (GBA) and the foot processes of glomerular epithelial cells (podocytes), which are separated by filtration slits bridged by slit diaphragms. The sizes of the slit diaphragms are around 43 nm [56]. However, the physiological pore size is much smaller, only in the diameter range of 4.5–5 nm. This means that the nanoparticles less than 5 nm can be easily excreted by glomerular filtration. For the nanoparticles in the range of 6–8 nm, the glomerular filtration depends on the shape and surface charge of the nanoparticles. Owing to the negative charge of the GBA, the positively charged nanoparticles can be easily excreted [46]. However, for larger nanoparticles that do not undergo glomerular filtration, they continue to be in the circulation and may be removed by the hepatic clearance (or building up in the body) via macrophage uptake (Figure 8.8).

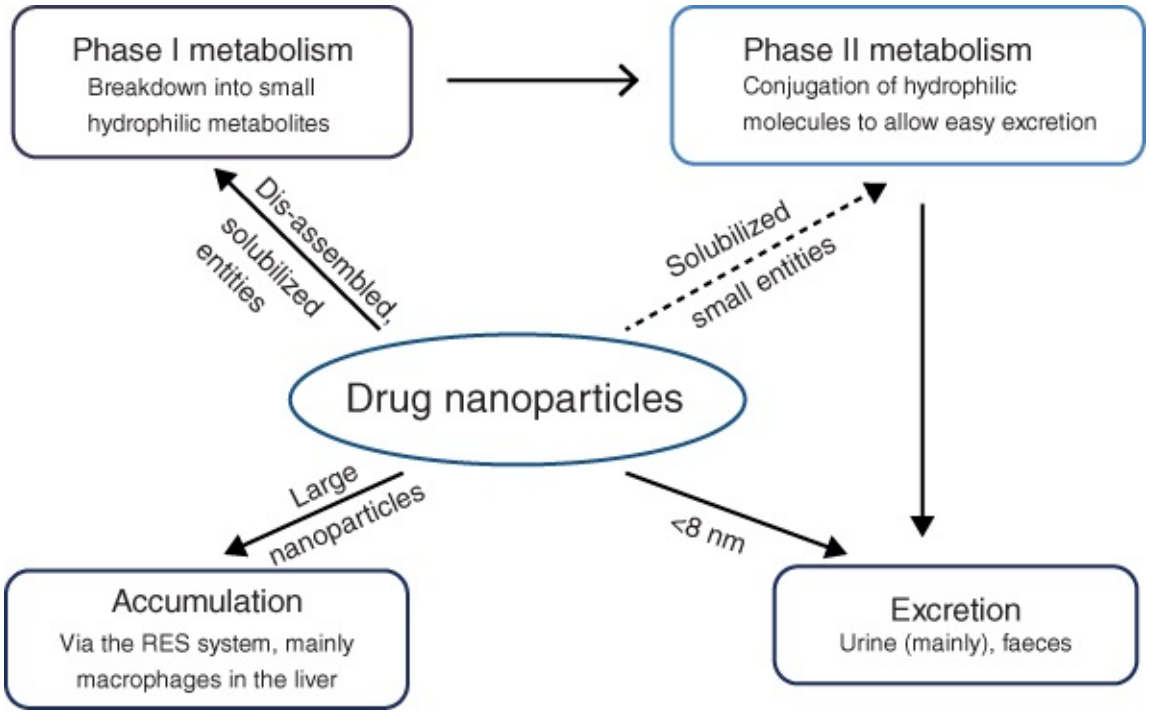

Figure 8.8 The scheme shows the fate of drug nanoparticles in the body.

Particle shapes can have significant impact on renal clearance. The nanotubes or nanorods with highaspectratios may be rapidly removed by glomerular filtration. For example, the singlewalled carbon nanotubes with average lengths of 200–300 nm could undergo rapid renal clearance. This was facilitated by the flowinduced orientation of the nanotubes [57]. However, for the sizecontrolled spherical quantum dots, efficient urinary excretion in rodents was demonstrated only for the particles with hydrodynamic diameters of ≤5.5 nm [58].

For pharmaceutical nanoformulations, the addition of excipients and/or stabilizers is unavoidable. For oral administration, the drugs need to have a balanced lipophilicity–hydrophilicity to be absorbed across the intestinal membrane. The hydrophilic excipients may be chosen so that they may have limited permeation across the biological membrane barrier, although many excipients are lipophilic [31]. Hydrophilic excipients may be easily excreted

via glomerular filtration. The hydrophilic excipients (e.g. polyvinylpyrrolidone (PVP), PVA, and PEG) with molecular weights less than 10 kDa can be readily removed from the body. The elimination $t_{1/2}$ (the time required to reduce the plasma concentration by 50%) increases with the excipient molecular weight in a sigmoidal curve shape [31].

8.4.4 Nanoparticle Toxicology

Owing to the increasing use of nanotechnology, the risks associated with the exposure to nanoparticles should be thoroughly evaluated. However, the toxicological effects of nanomaterials and the mechanisms are not well understood and indeed have not received sufficient attention. The same characteristics of nanoparticles that are attractive in nanomedicine may contribute to the toxicological consequence in biological systems.

The routes of entry into the body by nanoparticles include the respiratory system (the most important one), the skin (via exposure, cosmetics), and the gastrointestinal (GI) tract (via food, drink) [59]. The widely known example is the adverse health effect from exposure to asbestos fibres [60]. The airborne particles in air pollution are a global threat to human health, particularly in developing countries where the pollutionheavy industries are not well regulated and monitored. A typical ambient particulate matter (PM) is a highly complex mixture of particles with median diameters in the range of low nanometres to 100 μm. The fraction or concentration of the particles with median diameter of 2.5 μm or less (known as PM2.5, widely mentioned in monitoring air quality) can deposit deep into the lung and cause substantial damage [43, 44]. Inhalation of PM2.5 and ultrafine particles (0.1–2.5 μm) can cause inflammatory and granulomatous responses in lungs, lung injury via oxidative stress, and cardiovascular dysfunctions [59].

After entry into the body, the nanoparticles can diffuse/permeate across the biological membrane and into the systemic circulation. The modes of permeation and diffusion can be very similar as those of drug nanoparticles, as described in the earlier sections. The difference, however, is that these nanoparticles do not have any intended therapeutic roles but can cause toxicological consequences if they cannot be removed from the body by the RES clearance [24].

In conventional toxicology, the key parameters are concentration and time. However, for nanoparticles, the dose metric is more related to the number of the nanoparticles arriving at the site of the target organs or tissues. The increased surface area of nanoparticles contributes to the increasing surface adsorption and surface reactivity. The key parameters of the nanoparticles that influence the toxicology are the size, shape, and surface chemistry of the nanoparticles, and also the nature of the nanoparticle substance. The interaction mechanism at the nanoparticle–biological interface may be classified as chemical or physical [61]. Of the chemical mechanisms, the generation of reactive oxygen species (ROS), considered to be the main chemical process in nanotoxicology, can lead to inflammation, cell damage and even cell death [62]. The physical mechanisms mainly include the disruption of membrane, transport process, protein confirmation/folding, and protein aggregation/fibrillation [63]. Once engulfed into the cell, the nanoparticles can interfere with cell signalling process, interact with proteins

by chaperonelike activity or inducing peptide aggregation and fibrillation. However, the potential damage to DNA is not well understood but may be explained by the various chemical and physical mechanisms (particularly by the ROS route) [63]. Overall, the investigation into the toxicological impact of nanomaterials to human health (and the environment) is still at the early stage. Understanding of the entry of the nanoparticles into the body as well as of the mechanisms of interaction with the cells in various biological environments is required so that, in addition to formulation of regulation policies, proper procedures for protection may be developed.

8.5 Freezedrying of Solutions/Suspensions for Nanomedicine

Freezedrying of aqueous solutions to prepare solid biopharmaceutical formulations (mostly proteins based) is the most investigated and applied area [64]. Because freezedrying is an energyintensive and timeconsuming technique, any modifications leading to faster freeze drying are preferable. Thus, instead of generating frozen monoliths, a spray freezedrying process can be employed, where a solution or suspension is atomized into cold vapour over a cold liquid (usually liquid nitrogen) or directly atomized into liquid nitrogen (readers may refer to Figure 3.1 for the process scheme in Chapter 3) [65]. Further developments include thin film freezedrying or spin coating freezedrying [66].

When employing freezedrying for poorly watersoluble drugs, the main purpose is to reduce particle size and enhance drug dissolving rate and bioavailability. However, due to the poor water solubility, nonaqueous solvents are often added to facilitate the wettability and produce a mix solution [25]. A range of organic solvents have been used, which are usually miscible with water. These nonaqueous solvents usually have higher vapour pressure than water in the frozen state, which facilitates fast sublimation during primary drying. The mostly used cosolvent is *tert*butanol (freezing point 24 °C, vapour pressure 26.8 mmHg at 20 °C). The cosolvents with higher freezing points are usually preferred because this raises the glass transition temperature of the frozen solids. In contrast, for the cosolvents with low freezing points (e.g. ethanol, acetone, ethylacetate), a low percentage (e.g. <10%) may be only used. Otherwise, the liquid formulations may not be frozen in a commercial freezedryer or the thawing of frozen samples may occur during freezedrying. Other suitable solvents may include dimethylcarbonate (freezing point 2 °C, vapour pressure 72 mmHg at 20 °C, but limited solubility in water) or dimethylsulfoxide (freezing point 18.4 °C, vapour pressure 0.5 mmHg at 20 °C, miscible with water) [25]. In addition to the physicochemical properties, the toxicity of the solvent and the solvent residual in pharmaceutical products should be considered. As listed in Tables 8.2 and 8.3, the use of Class 2 solvents should be limited and the solvent residual must be controlled within the limit.

The BCS Class II drug celecoxib was dissolved with Phospholipid E80 and trehalose (optimal ratio 1 : 10 : 16) in *tert*butanolwater (60/40 w/w). The solution was frozen at −80 °C for 24 h and then placed in a precooled freezedryer at −60 °C. The freezedried formulation

showed enhanced dissolution rate, apparent solubility, and concentration in phosphate buffer solution (pH 6.5) [67]. Danazol was dissolved in tetrahydrofuran (THF) and then mixed with aqueous solution containing PVA (M_w = 22 K) and PVP K15. A spray freezing was applied to liquid nitrogen process to produce frozen micron powders, which were subjected to vacuum freezedrying, or atmospheric freezedrying [68].

Organic solvents are used to dissolve the poorly watersoluble drugs. For example, danazol and PVP K15 were dissolved in acetonitrile or acetonitrile/dichloromethane. The organic solutions were atomized into small droplets directly into liquid nitrogen. This processing led to the dissolution of 95% danazol in 2 min compared to 30% of the bulk danazol dissolved in 2 min, determined using USP Apparatus 2 under sink conditions [69].

However, due to the concerning issues on the toxicity, safety, and environmental impact of the organic solvents, much effort has been directed to the use of an aqueous medium. For poorly watersoluble drugs, additional procedures are required to generate the suspensions of hydrophobic drugs, which are then freezedried, mainly for storage stability, facile handling, and transport. For example, the evaporative precipitation into aqueous solution was employed to make the BCS Class II drug (danazol, itraconazole, carbamazepine) suspensions that were then processed by sprayfreezedrying. The resulting amorphous drug particles showed increased dissolution rate and increased drug bioavailability and efficacy [70]. Other approaches before freezedrying include micellar encapsulation of hydrophobic drugs [71, 72], drug encapsulation by nanoparticles [73, 74], and nanocomplex formation of cationic and anionic species [75, 76].

Freezedrying or sprayfreezedrying of nanoparticle suspensions are not limited to poorly watersoluble drug nanoparticle suspensions. These techniques are also widely used for aqueous nanoparticle suspensions containing proteins, peptides, oligonucleotides, and DNAs [77–81]. The main targets are to maintain pharmaceutical stability during storage, transport, and after reconstitution. Lyoprotectants and stabilizers are required to achieve these targets [82, 83]. More information on this topic can be found in Chapter 3.

8.6 EmulsionFreezedrying for Drug Nanoparticles

Emulsions are formed when mixing hydrophobic organic phase (water immiscible) and aqueous phase in the presence of a surfactant (or stabilizer) usually by stirring or homogenization, with the internal droplet phase dispersed in the continuous phase. Although there are emulsions formed from two immiscible nonaqueous phases, the cases are rare. The emulsions can be categorized as oilinwater (O/W) emulsions (where the oil phase is dispersed as droplets in the continuous aqueous phase) or vice versa waterinoil (W/O) emulsions [84, 85]. For hydrophobic drugs and bioactives, the O/W emulsion is an effective tool for their dispersion, absorption, and enhanced bioavailability [84–88]. Particularly for drug delivery, lipidbased emulsions have been mostly used, either for oral or parenteral administrations. Lipids are broadly defined as biological substances that are hydrophobic and usually insoluble in water [86, 87]. Lipids may be divided into ‘simple’ lipids (where the

hydrolysis reaction produces two products at most) and ‘complex’ lipids (where three or more products are formed upon hydrolysis). To facilitate the communication in the international lipids community and be compatible with informatics and lipidomics requirement, Fahy et al. divide lipids into eight categories (fatty acids, glycerolipids, glycerophospholipids, sphingolipids, sterol lipids, prenol lipids, saccharolipids, and polyketides) [89]. Fatty acids, glycerolipids, and glycerophospholipids are mostly employed in lipidbased emulsions and nanospheres. Among them, mediumchain glycerides (MCTs) with 6–10 carbons (one type of glycerolipids) are widely used as the internal oil phase for the lipidbased emulsions. Some natural sources, e.g. coconut oil and diary fat, exhibit similar properties as MCTs [90].

Based on the size of the droplets, emulsions can be categorized into emulsions (droplet sizes from submicron to 100 μm, thermodynamically unstable), nanoemulsions (droplet sizes approximately 50–500 nm, better kinetic stability), and microemulsions (clear and thermodynamically stable, droplets <100 nm in diameter) [91]. All these types of emulsions have been used for drug delivery. However, the stability of the emulsions (even for the thermodynamically stable microemulsions, but may be kinetically unstable) and chemical stability of the drugs (e.g. hydrolysis in the presence of water) are important issues that need to be addressed [91]. Thus, emulsions are freezedried to improve the stability and/or generate porous dry tablets. Most of the reported studies have focused on the stability test and/or enhanced dissolution rate [92–97]. The emulsion with MCTs (the commercial Miglyol 810/812) as internal oil phase was freezedried to produce porous tablet [96, 97]. However, considering the very low vapour pressure of the MCTs (e.g. vapour pressure < 0.0075 mmHg at 20 °C for Miglyol 812, based on the Material Safety Data Sheet from the Caesar & Loretz GmbH), it would be difficult to remove the MCT by freezedrying. However, most of the papers did not comment on what happened to MCT during freezedrying and there have been no reports (to the best of the author's knowledge) on the size of drug particles from this emulsionfreezedrying approach.

Freezedrying has been an effective route to the preparation of a variety of porous materials [98]. When emulsions are freezedried, porous materials templated by both droplets and ice crystals can be produced [84, 98]. When a polymer is dissolved in the droplet phase, porous microparticles or microcapsules can be prepared by emulsionfreezedrying [99, 100]. However, when small molecular hydrophobic compounds are dissolved in the droplets of O/W emulsions, hydrophobic organic nanoparticles (including poorly watersoluble drug nanoparticles) can be readily formed [2, 101]. The concept for the preparation of organic nanoparticles was initially demonstrated by crosslinking polymerization of an O/W emulsion followed by freezedrying (Figure 8.9) [102]. A hydrophobic dye, Oil Red O (OR), was used as the model hydrophobic compound, because it was very easy to judge from the colour/transparency of the suspension whether aqueous organic nanosuspension was formed. The emulsionfreezedrying method was then developed as a highly efficient method to produce solid drug nanoparticles and highly stable aqueous nanoparticle suspensions. The OR nanoparticles could be released linearly in hydrophilic crosslinked polymers such as PAM or in a burst fashion in response to temperature change when poly(*N*isopropyl acrylamide) (PNIPAM) was the polymer matrix (Figure 8.9e). Similarly, the reductioncontrolled release

of organic nanoparticles and the temperatureresponsive pumping release from PNIPAM have also been demonstrated [103, 104].

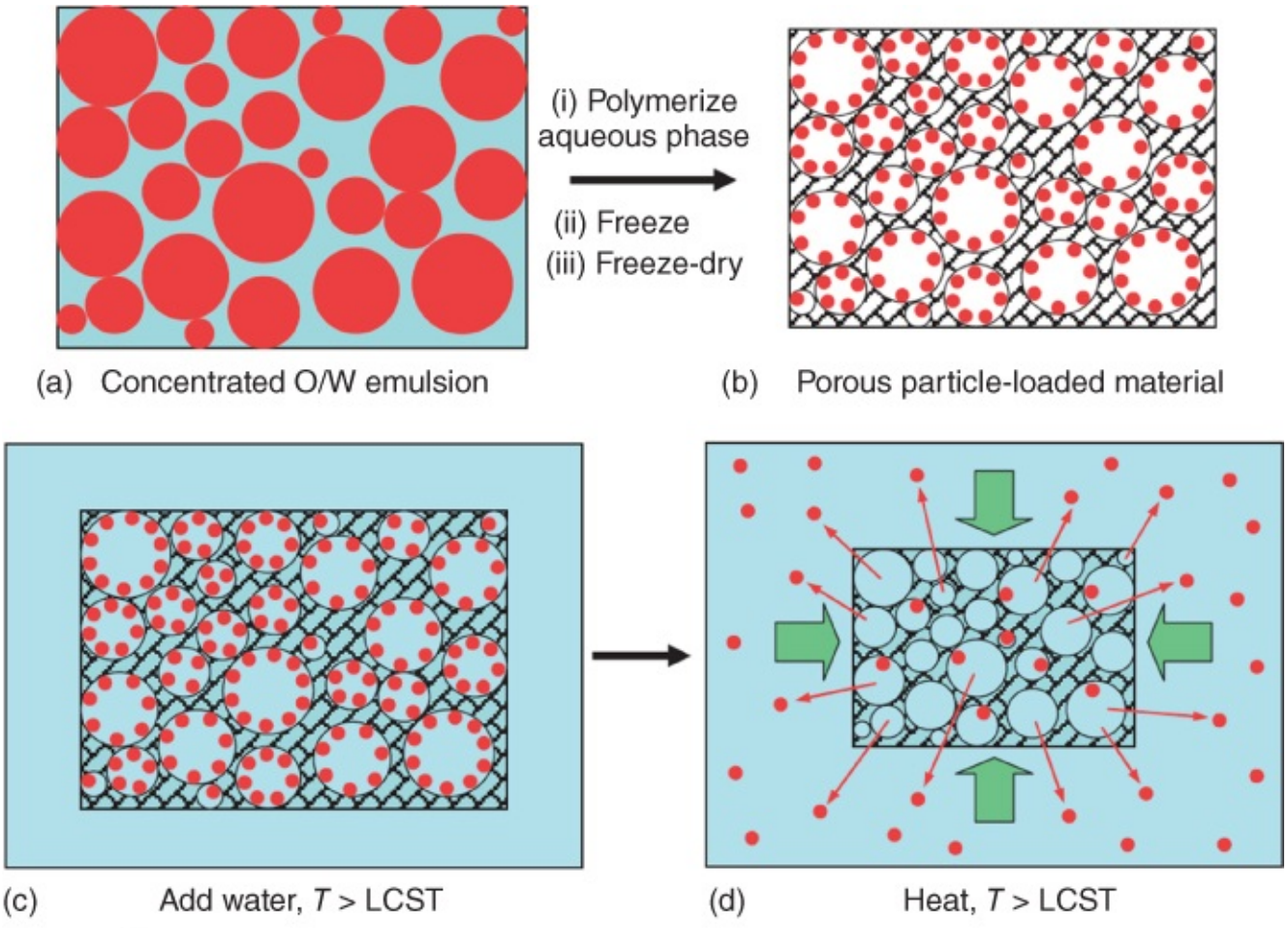

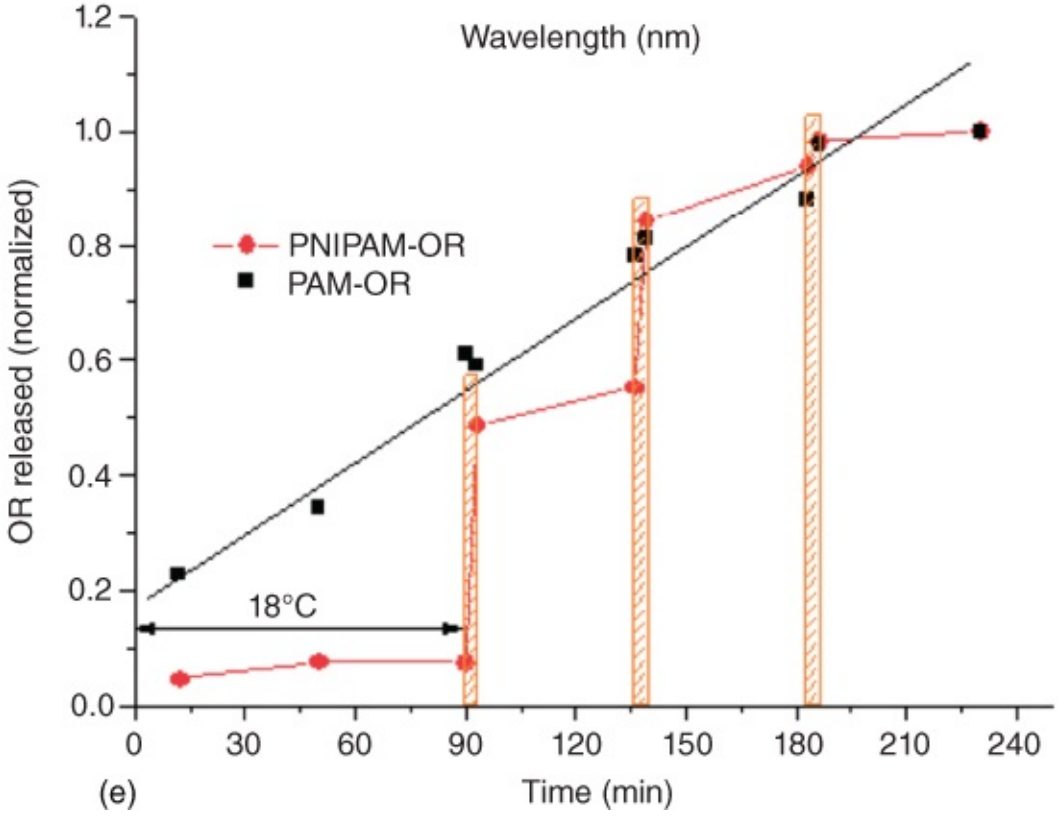

Figure 8.9 The schematic representation of formation of organic nanoparticles by emulsion templating and freezedrying and the release of organic nanoparticles. (a) An O/W emulsion is formed with a hydrophobic dye (Oil Red O) in the internal droplet phase and monomer/initiator in the continuous aqueous phase. (b) After polymerizing the emulsions followed by freezedrying, organic nanoparticles are formed in the porous polymeric matrix. (c) For temperaturesensitive polymer PNIPAM, when the temperature is less than the low critical solution temperature (LCST), the nanoparticles remain inside. (d) When the surrounding temperature is greater than the LCST, the organic nanoparticles are squeezed out into the aqueous medium. (e) The plot shows the linear release of organic nanoparticles for the hydrophilic polymer polyacrylamide (PAM) and the burse release in response to the temperature for PNIPAM.

Source: Zhang and Cooper 2007 [102]. Reprinted with permission from John Wiley and Sons.

However, the organic nanoparticles within crosslinked porous polymers [102–104] may not be a good choice for the production of poorly watersoluble drug nanoparticles because the dominant administering routes have been oral and parenteral. In both cases, a soluble matrix or an aqueous nanoparticle suspension is required. Thus, instead of polymerizing an emulsion, hydrophilic polymers (e.g. PVA) may be added to the continuous phase of an O/W emulsion. Figure 8.10 shows the result of freezedrying the O/W emulsion where OR was dissolved in the internal cyclohexane phase and PVA and anionic surfactant sodium dodecyl sulfate (SDS) in the continuous water phase [105]. This is a physical process with no chemical reactions involved. The formed emulsion was injected into liquid nitrogen and the frozen beads were then freezedried to produce the dry red beads. When water is added, the red beads can be dissolved in water rapidly, producing a clear red suspension, which looks no different from ORacetone solution. However, when the aspurchased OR is added to water, it only floats on the surface (Figure 8.10a–c). This is an indication that the OR nanoparticles are formed and well dispersed in water. Characterizing the dry beads (Figure 8.10d) shows the highly interconnected porous structure (Figure 8.10e), which contributes to the fast and instant dissolution of the red beads. Some of the nanoparticles can be seen on the pore wall by SEM imaging of the dry bead (Figure 8.10f). The OR nanosuspension was further characterized by SEM (by depositing a drop of the suspension on a copper grid and then allowing to dry) and by DLS, which shows the size of OR nanoparticles around 90 nm (Figure 8.10g,h) [105]. As a demonstration, the poorly watersoluble triclosan nanoparticles were prepared by this method. For the triclosan solution in ethanol/water, the observed MIC50 in inhibiting the bacterial (*Corynebacterium*) growth was approximately 50 ppm. In contrast, the aqueous triclosan nanodispersion was considerably more active, with the bacterial regrowth inhibited to <50% at 6.25 ppm [105].

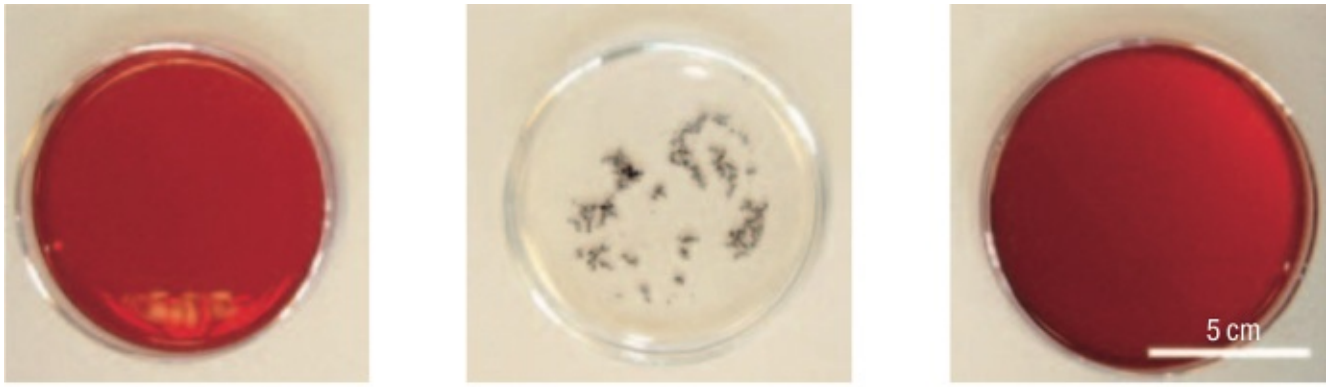
5 cm

(a) (b) (c)

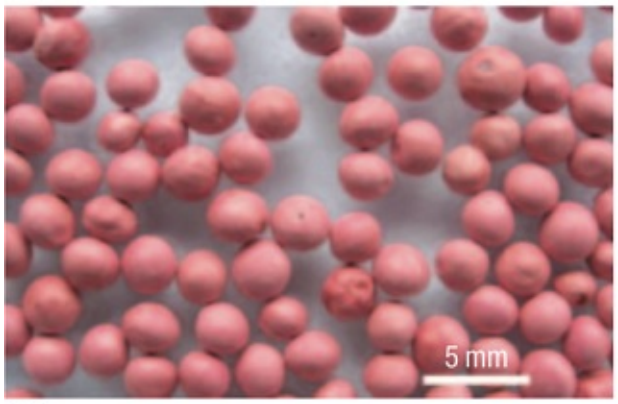
5 mm

(d)

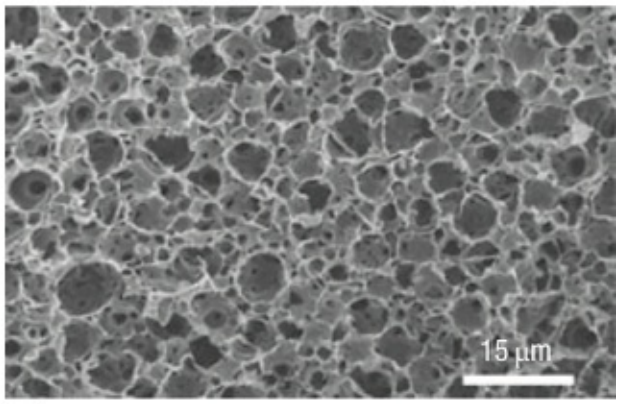
15 µm

(e)

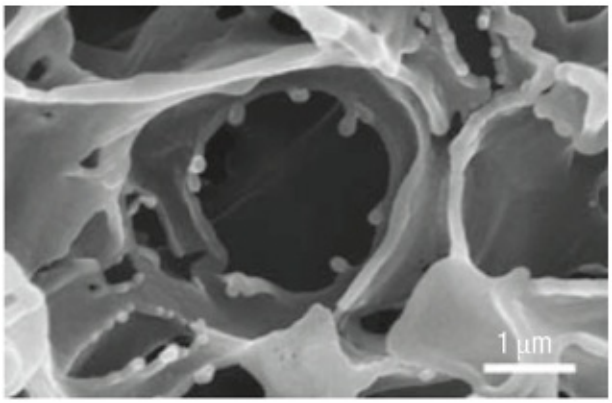
1 µm

(f)

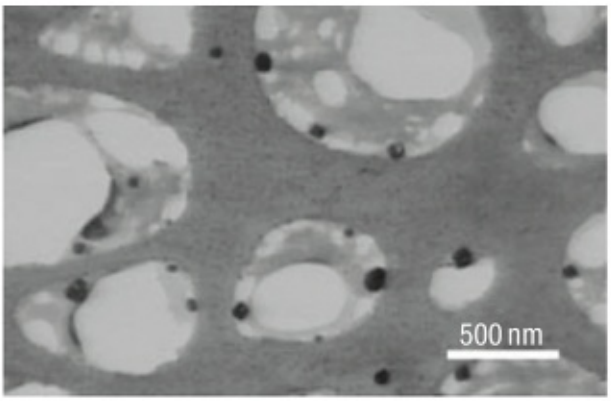
500 nm

(g)

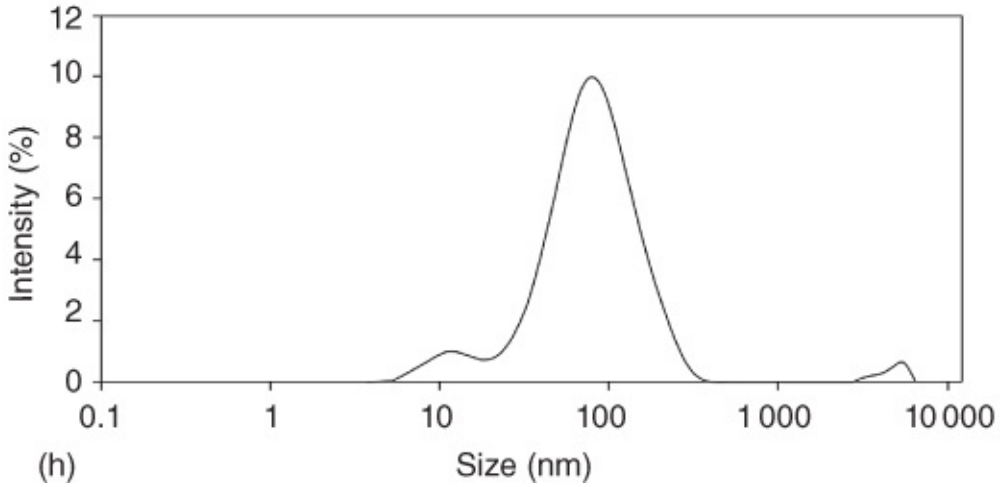
12
10
8
6
4
2
0
Intensity (%)
0.1
1
10
100
1 000
10 000
Size (nm)

(h)

Figure 8.10 Characterization of solid nanocomposites and nanodispersions. (a–c) Visual comparison of aqueous nanodispersion of Oil Red (OR) (a), OR powder added to water (b), and OR dissolved in acetone (c). (d) Highly porous nanocomposite beads containing OR. (e) SEM image of the internal porous bead structure. (f) Higher magnification showing nanoparticles on the edge of a pore. (g) STEM image of OR nanoparticles after drying the nanodispersion onto a porous carbon grid. (h) Dynamic light scattering analysis of the OR nanodispersion showing an average particle size of 90 nm.

Source: Zhang et al. 2008 [105]. Reprinted with permission from Springer Nature.

This method can be readily applied to other hydrophobic dyes and poorly watersoluble drugs [106–115]. Compared to the drug nanoparticles prepared by conventional methods such as wet milling and homogenization, the emulsionfreezedrying method can be applied to compounds of hard and soft, heatsensitive or pressuresensitive compounds, which can avoid the impurities introduced by ball milling. Importantly, the method can produce nanoparticles below 300 nm (which is considered to be the cutoff size for stable nanoparticle suspensions [1]) and prevent nanoparticle aggregation because they are stabilized in a porous solid matrix. The highly interconnected porous nature of the hydrophilic matrix allows the instant dissolution of the matrix to generate stable aqueous nanoparticle suspensions for further evaluation and application. One of the advantages with emulsions is that the volume percentage of internal phase can be varied in a wide range. When the volume percentage of the internal phase is higher than 74.05%, where the droplets are tightly packed together, the emulsion is called a high internal phase emulsion (HIPE). HIPEs can be employed as templates to produce highly interconnected porous materials [84]. When the volume percentage of the droplet phase is varied (e.g. from 20% to 80%) in an emulsion, the porosity and morphology of the resulting materials can be systematically tuned [107]. This approach may be used to effectively tune the loading of the drug nanoparticles in a formulation. The size of the nanoparticles (e.g. indomethacin) may be controlled by the concentration of the internal organic phase [108].

For the emulsionfreezedrying approach, surfactants are required to stabilize the emulsion while a hydrophilic polymer is needed to form the porous matrix to hold the nanoparticles. In the solid state, the organic nanoparticles can be very stable. Some samples have been stored over 1 year and can still produce transparent nanoparticle suspensions upon dissolution. Both the polymer and surfactant may be treated as excipients for pharmaceutical formulations. Thus the toxicity and biocompatibility of the surfactant and polymer must be considered. Some surfactants may be fine for oral administration but are not ideal for intravenous injection. With this in mind, from the point view of chemistry and materials, designing and synthesis of functional polymers to act as both stabilizers and bulking polymers should be crucial. Recently, a lightly crosslinked branched block copolymer PEG *b*PNIPAM was synthesized and used to form O/W emulsion. The polymer was present in water as core–shell nanoparticles with lightly crosslinked hydrophobic core. The emulsionfreezing approach was applied to form highly porous polymer–nanoparticles composite, which can be readily dissolved to generate stable aqueous drug nanoparticle suspensions, with the nanoparticle yields achieving as high as 100% for ketoprofen and ibuprofen [109]. With different design and synthesis, for example,

with a more hydrophobic core of poly(butyl methacrylate), there may be great potential to identify suitable functional polymers for targeted drug nanoparticles [110].

With the emulsionfreezedrying approach, it is easy to prepare multicomponent organic nanoparticles. This can be simply achieved by dissolving or dispersing different hydrophobic compounds or nanoparticles in the organic droplet phase of the O/W emulsion. For example, a donor fluorophore and an acceptor fluorophore were both dissolved in chloroform. The chloroform solution was then emulsified into an aqueous phase containing PVA (80% hydrolysed, M_w = 10 K) and Brij 58 by sonication. Freezedrying of the emulsion produced dualcomponent fluorescent nanoparticles (<200 nm) with varying compositions. These nanoparticles could be used for the investigation of cellular internalization by Caco2 cells and macrophages by fluorescence (Förster) resonance energy transfer (FRET). The breakdown of the dualcomponent nanoparticles could lead to the loss of FRET signals. The extensive wholeparticle internalization was confirmed. A mechanism for enhanced *in vivo* pharmacokinetics was proposed through further study on the cellular permeability across Coco2 monolayers [111]. In another study, threecomponent nanoparticles containing OR, a hydrophobic polymer, and oleic acidcoated Fe_3O_4 nanoparticles (15–20 nm) were prepared by a similar approach. The three hydrophobic components were dissolved/dispersed in toluene, which was then emulsified by sonication. The superparamagnetism from iron oxide nanoparticles was retained. Ibuprofen was also incorporated into the nanoparticles and evaluated for controlled release [112].

Exciting progress has been made in the use of solid drug nanoparticles in terms of biological evaluations. Efavirenz, a nonnucleoside reverse transcriptase inhibitor, is considered to be a firstline global therapy for new cases of human immunodeficiency virus (HIV) infections. But this drug has low water solubility (<10 μg ml^{-1}) and hence a large dose is required with increasing cost and side effects. The efavirenz nanoparticles were prepared by freezedrying of O/W emulsions (chloroform solution emulsified into aqueous solution containing various surfactants and polymers). The nanoparticles with sizes <400 nm were formed with nonionic surfactants αtocopherol poly(ethylene glycol) succinate (TPGS) or Tween80 with PVA (80% hydrolysed, M_w = 9500). These efavirenz nanoparticles showed reduced cytotoxicity and increased *in vitro* transport through model gut epithelium. An approximately fourfold higher pharmacokinetic exposure after oral administration was observed in the study with rodents [113]. Ritonavir (RTV) is a HIV protease inhibitor (PI) and usually used with other PIs (e.g. lopinavir (LPV)) as a booster to increase the pharmacokinetic profiles. The RTV nanoparticles prepared by the emulsionfreezedrying method showed augmented inhibition of human CYP3A4 in cellfree systems and human primary hepatocytes. In addition, higher permeability across intestinal cell membranes and lower cytotoxicity were observed [114]. Very recently, a 160component library highthroughput screening process was developed to evaluate the polymer and surfactant combinations based on the emulsionfreezedrying approach. The study employed chloroforminwater emulsions and initially focused on LPV nanoparticles (with 10% drug loading to the excipients) and then the LPVRTV (70% drug loading, LPV:RTV = 4 : 1) nanoparticles. PVA was found to be the most successful polymer in producing nanoparticles of high drug/excipient ratio, followed by hydroxypropyl

methylcellulose (HPMC). This approach could screen a large quantity of solid drug nanoparticles in a short period, thus enhancing the process of discovering and identifying optimal formulations, and speeding up the progression for clinical manufacturing [115].

8.7 Solvent Evaporation Within PorousSoluble Polymers

The main limitation of the emulsionfreezedrying approach is with the selection and suitability of the organic solvent. Firstly, to allow the emulsions to be readily freezedried in a commercial freezedryer, the freezing points should not be too low (usually greater than −50 °C depending on the grade of the freezedryer) and ideally the vapour pressure should be high. Secondly, the solvent should be immiscible with water so that O/W emulsions can be formed. This excludes the commonly used polar organic solvents such as acetone, ethanol, methanol, and THF. As for pharmaceutical products, the solvents should be in the category of Class 2 solvents (Table 8.2) and more preferably in the category of Class 3 solvents (Table 8.3). However, there are not many organic solvents available that comply with these requirements. For the drug nanoparticles prepared by emulsionfreezedrying, the solvents that have been used include cyclohexane, Oxylene, chloroform, and also toluene. However, this situation may be made worse by the fact that many poorly watersoluble drugs are only dissolved in polar organic solvent, i.e. they have very low solubility in waterimmiscible solvents.

To address this issue, a solvent evaporation method within porous soluble polymers has been developed to prepare organic and drug nanoparticles [116, 117]. Solvent evaporation from thin film on substrates can form different types of nanostructures and nanoparticles [118, 119]. It has also been successfully applied to form drug nanoparticles [120]. However, the surface area on a substrate is low. It will require a very large surface to produce a quantity of drug nanoparticles. This problem can be solved by the use of emulsionfreezedried porous polymers as the scaffold to hold up the solution and then allow the solvent to be evaporated. The O/W emulsions can be formed by an organic solvent emulsified into an aqueous solution containing a surfactant and hydrophilic polymer. Freezedrying of the O/W emulsions generates a highly interconnected porous watersoluble matrix [107]. The interconnected porosity allows the rapid uptake of organic solvent and oils. The soaked polymer matrix can be dissolved in water in seconds by shaking, which releases the oil droplets and produces an O/W emulsion on demand [121]. Different oils, including mineral oil, soy oil, and perfluorocarbon, have been used to form O/W emulsions. The size and number of the droplets in the O/W emulsions are tuneable simply by varying either the soaking time or the porosity of the porous polymers [121].

The procedures for the preparation of organic nanoparticles by solvent evaporation within porous polymers are straight forward, as shown in Figure 8.11. This method has been demonstrated with OR and poorly watersoluble drugs such as curcumin, carbamazepine, griseofulvin, and paclitaxel [116, 117]. The soluble porous polymers are prepared by freeze

drying aqueous polymer solution or O/W emulsions. The porous polymers are then soaked in organic solutions, which are formed by dissolving the organic compounds or poorly water soluble drugs in polar organic solvents (usually ethanol or acetone) or nonpolar/lesspolar solvent with low freezing points (e.g. dichloromethane). After soaking for a defined time, the soaked porous polymers are left in a vacuum oven (mostly room temperature) or simply in a fume cupboard to allow the solvent to evaporate. Drug nanoparticles are formed within the porous polymer during the solvent evaporation. Like the dry materials obtained by the emulsionfreezedrying approach, the polymers containing drug nanoparticles can be readily dissolved in water to produce stable aqueous nanoparticle suspensions. The sizes of the nanoparticles vary, depending on the polymer and/or the surfactant used. For examples, OR and curcumin nanoparticles of about 50 nm, carbamazepine nanoparticles of 130 nm, paclitaxel nanoparticles of 500 nm, and griseofulvin nanoparticles of 430 nm, have been successfully prepared by the solvent evaporation method. In general, the combination of suitable polymer, surfactant, drug, and the solvent needs to be optimized to form drug nanoparticles with smaller sizes (e.g. <300 nm) and high nanoparticle yields.

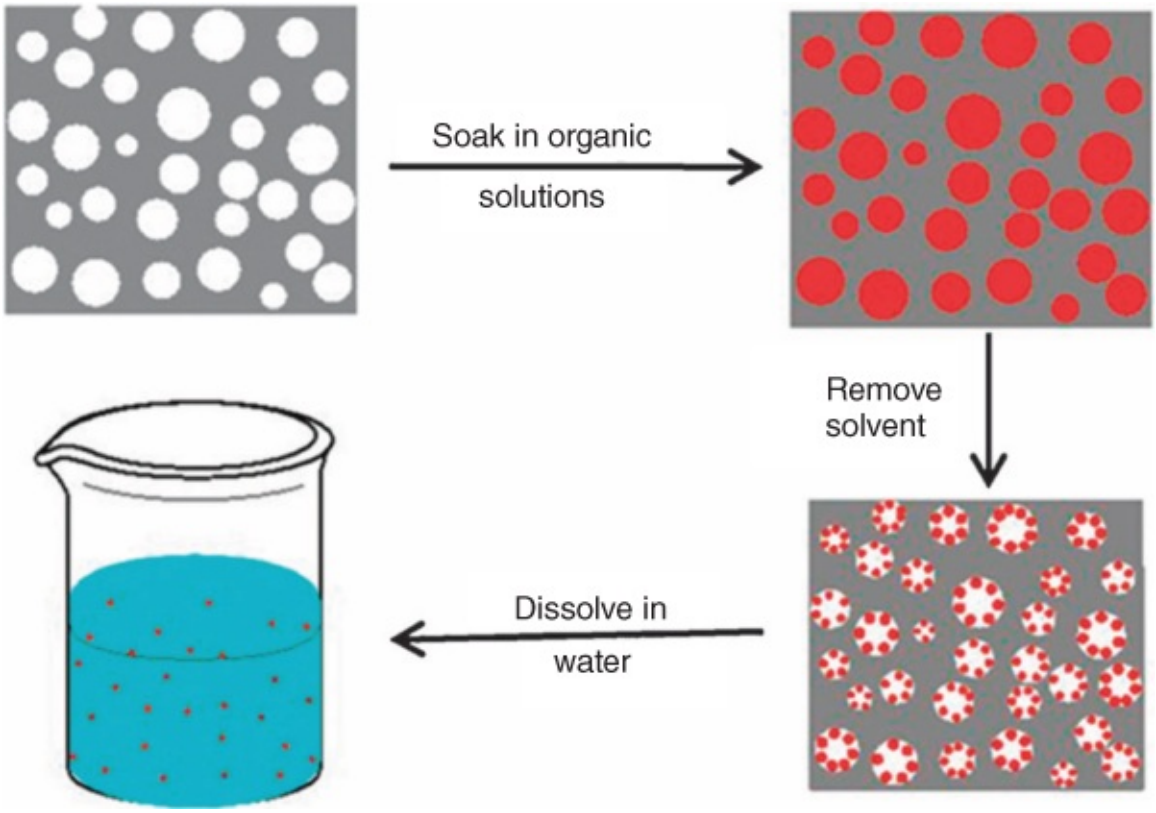

Figure 8.11 Schematic representation of the formation of drug nanoparticles by solvent evaporation within porous polymers.

Source: Qian et al. 2011 [116]. Reprinted with permission from Royal Society of Chemistry.

8.8 Summary

Nanomedicine has been extensively investigated to enhance stability, improve therapeutic efficacy, and reduce side effects. This has been highly effective for poorly watersoluble

drugs, where the poor solubility, high dosage, and low bioavailability have been the main issues. A variety of techniques are developed to produce drug nanoparticles, with wet milling and highpressure homogenization being extensively used in research and pharmaceutical production. After the introduction to bioavailability and delivery of drug nanoparticles, this chapter focuses on the freezedrying of solutions/suspensions and particularly the emulsion freezedrying approach. The freezedrying methods can be applied to heatsensitive and soft hydrophobic compounds, either in solution or emulsion approaches. The emulsion freezedrying approach can generate a stable porous soluble matrix containing hydrophobic drug nanoparticles, which can be instantly dissolved in water to produce stable aqueous nanoparticle dispersions. Similar to other pharmaceutical formulations, excipients such as hydrophilic polymers and surfactants are required to form emulsions, act as lyoprotectant, stabilize the drug nanoparticles in solid state, and facilitate fast reconstitution and stable reconstituted solution/suspensions.

Design and selection of excipients are crucial in the freezedrying approaches. This depends on the target organs/tissues where different sizes of drug nanoparticles are required. For example, extremely small nanoparticles are required to pass the BBB while submicron particles may be sufficient to be passively absorbed into the tumour tissues via the EPR effect. In other cases, it is mainly about the permeation across biological membranes and also has a sufficiently long circulation time. The targets or criteria of selecting suitable excipients are: (i) to produce the nanoparticles of required sizes; (ii) to facilitate bioabsorption; (iii) to maintain long circulation; (iv) to direct to the target tissue; and (v) to allow controlled or responsive release. Other import issues to be considered are biodegradability and elimination from the body when the therapeutic roles are completed.

Drug nanoparticles should be sufficiently characterized by physicochemical techniques and also *in vitro* characterizations. However, it is highly likely that the characteristics of the drug nanoparticles *in vitro* and *in vivo* can be considerably different. Therefore, *in vivo* characterizations and evaluations are essential for the consideration in clinical uses. Some important properties need to be considered, that may depend on the specific techniques employed. These include: (i) crystallinity (which affects stability and dissolution); (ii) dissolution rate *in vitro* and *in vivo*; (iii) the size of nanoparticles in systemic circulation (which can be very different from the sizes determined *in vitro*, due to adsorption of various proteins and other components in blood); and (iv) pharmacokinetic profiles and interaction with cells during permeation and circulation to the target cells.

References

1 Rabinow, B.E. (2004). Nanosuspensions in drug delivery. *Nat. Rev. Drug Discov.* 3: 785–796.

2 Wais, U., Jackson, A.W., He, T., and Zhang, H. (2016). Nanoformulation and encapsulation approaches for poorly watersoluble drug nanoparticles. *Nanoscale* 8: 1746–1769.

3 Riehemann, K., Schneider, S.W., Luger, T.A. et al. (2009). Nanomedicine – challenges and

perspectives. *Angew. Chem. Int. Ed.* 48: 872–897.

4 Moghimi, S.M., Hunter, A.C., and Andresen, T.L. (2012). Factors controlling nanoparticle pharmacokinetics: an integrated analysis and perspective. *Annu. Rev. Pharmacol. Toxicol.* 52: 481–503.

5 Kettiger, H., Schipanski, A., Wick, P., and Huwyler, J. (2013). Engineered nanomaterial uptake and tissue distribution: from cell to organism. *Int. J. Nanomedicine* 8: 3255–3269.

6 Pathak, K. and Raghuvanshi, S. (2015). Oral bioavailability: issues and solutions via nanoformulations. *Clin. Pharmacokinet.* 54: 325–357.

7 Savjani, K.T., Gajjar, A.K., and Savjani, J.K. (2012). Drug solubility: importance and enhanced techniques. *ISRN Pharm.* (Art. ID: 195727. doi: 10.5402/2012/195727.

8 Kasim, N.A., Whitehouse, M., Ramachandran, C. et al. (2004). Molecular properties of WHO essential drugs and provisional biopharmaceutical classification. *Mol. Pharm.* 1: 85–96.

9 Amidon, G.L., Lennernas, H., Shah, V.P., and Crison, J.R. (1995). A theoretical basis for a biopharmaceutic drug classification: the correlation of in vitro drug product dissolution and in vivo bioavailability. *Pharm. Res.* 12: 413–420.

10 Chen, M., Amidon, G.L., Benet, L.Z. et al. (2011). The BCS, BDDCS, and regulatory guidances. *Pharm. Res.* 28: 1774–1778.

11 Benet, L.Z. (2010). Predicting drug disposition via application of a biopharmaceutics drug disposition classification system. *Basic Clin. Pharmacol. Toxicol.* 106: 162–167.

12 Dahan, A., Miller, J.M., Hilfinger, J.M. et al. (2010). Highpermeability criterion for BCS Classification: segmental/pH dependent permeability considerations. *Mol. Pharm.* 7: 1827–1834.

13 Wu, C.Y. and Benet, L.Z. (2005). Predicting drug disposition via applications of BCS: transport/absorption/elimination interplay and development of a biopharmaceutics drug disposition classification system. *Pharm. Res.* 22: 11–23.

14 Lipinski, C.A., Lombardo, F., Dominy, B.W., and Feeney, P.J. (2001). Experimental and computational approaches to estimate solubility and permeability in drug discovery and development settings. *Adv. Drug Delivery Rev.* 46: 3–26.

15 Kesisoglou, F., Panmai, S., and Wu, Y. (2007). Nanosizing – oral formulation development and biopharmaceutical evaluation. *Adv. Drug Delivery Rev.* 59: 631–644.

16 Noyes, A. and Whitney, W. (1897). The rate of solution of solid substances in their own solutions. *J. Am. Chem. Soc.* 19: 930–934.

17 Anhalt, K., Geissler, S., Harms, M. et al. (2012). Development of a new method to assess

nanocrystal dissolution based on light scattering. *Pharm. Res.* 29: 2887–2901.

18 Del Valle, E.M.M. (2004). Cyclodextrins and their uses: a review. *Process Biochem.* 39: 1033–1046.

19 Sosnik, A. and Seremeta, K.P. (2015). Advantages and challenges of the spraydrying technology for the production of pure drug particles and drugloaded polymeric carriers. *Adv. Colloid Interf. Sci.* 223: 40–54.

20 Singh, A. and den Mooter, G.V. (2016). Spray drying formulation of amorphous solid dispersions. *Adv. Drug Delivery Rev.* 100: 27–50.

21 Chin, W.W.L., Parmentier, J., Widzinski, M. et al. (2014). A brief literature and patent review of nanosuspensions to a final drug product. *J. Pharm. Sci.* 103: 2980–2999.

22 Müller, R.H., Jacobs, C., and Kayser, O. (2001). Nanosuspensions as particulate drug formulations in therapy rationale for development and what we can expect for the future. *Adv. Drug Delivery Rev.* 47: 3–19.

23 MeriskoLiversidge, E. and Liversidge, G.G. (2011). Nanosizing for oral and parenteral drug delivery: a perspective on formulating poorlywater soluble compounds using wet media milling technology. *Adv. Drug Delivery Rev.* 63: 427–440.

24 Müller, R.H., Gohla, S., and Keck, C.M. (2011). State of the art of nanocrystals – special features, production, nanotoxicology aspects and intracellular delivery. *Eur. J. Pharm. Biopharm.* 78: 1–9.

25 Teagarden, D.L. and Baker, D.S. (2002). Practical aspects of lyophilisation using non aqueous cosolvent systems. *Eur. J. Pharm. Sci.* 15: 115–133.

26 Debotton, N. and Dahan, A. (2017). Applications of polymers as pharmaceutical excipients in solid oral dosage forms. *Med. Res. Rev.* 37: 52–97.

27 Pifferi, G. and Restani, P. (2003). The safety of pharmaceutical excipients. *Farmaco* 58: 541–550.

28 ICH Harmonised Guideline (2016). Impurities: guideline for residual solvents Q3C(R6), 2016 version.

29 Akers, M.J. (2002). Excipient–drug interactions in parenteral formulations. *J. Pharm. Sci.* 91: 2283–2300.

30 Buggins, T.R., Dickinson, P.A., and Taylor, G. (2007). The effects of pharmaceutical excipients on drug disposition. *Adv. Drug Delivery Rev.* 59: 1482–1503.

31 Loftsson, T. (2015). Excipient pharmacokinetics and profiling. *Int. J. Pharm.* 480: 48–54.

32 Wu, L., Zhang, J., and Watanabe, W. (2011). Physical and chemical stability of drug

nanoparticles. *Adv. Drug Delivery Rev.* 63: 456–469.

33 Janssens, S. and Van den Mooter, G. (2009). Review: physical chemistry of solid dispersions. *J. Pharm. Pharmacol*. 61: 1571–1586.

34 Lindfors, L., Forssen, S., Skantze, P. et al. (2006). Amorphous drug nanosuspensions. 2. Experimental determination of bulk monomer concentrations. *Langmuir* 22: 911–916.

35 Löbenberg, R. and Amidon, G.L. (2000). Modern bioavailability, bioequivalence and biopharmaceutics classification system. New scientific approaches to international regulatory standards. *Eur. J. Pharm. Biopharm.* 50: 3–12.

36 Moynihan, H.A. and Crean, A.M. (2009). Drug partitioning and transport across biological barriers in book, Chapter 7. In: *The Physicochemical Basis of Pharmaceuticals*, 212–254. Oxford University Press.

37 Lin, J.H., Chiba, M., and Baillie, T.A. (1999). Is the role of the small intestine in firstpass metabolism overemphasized? *Pharmacol. Rev.* 51: 135–157.

38 Doherty, M.M. and Pang, K.S. (1997). Firstpass effect: significance of the intestine for absorption and metabolism. *Drug Chem. Toxicol*. 20: 329–344.

39 Martinez, M.N. and Amidon, G.L. (2002). A mechanical approach to understanding the factors affecting drug absorption: a review of fundamentals. *J. Clin. Pharmacol*. 42: 620–643.

40 Barua, S. and Mitragotri, S. (2014). Challenges associated with penetration of nanoparticles across cell and tissue barriers: a review of current status and future prospect. *Nano Today* 9: 223–243.

41 Damgé, C., Michel, C., Aprahamian, M. et al. (1990). Nanocapsules as carriers for oral peptide delivery. *J. Controlled Release* 13: 233–239.

42 Florence, A.T. (1997). The oral absorption of micro and nanoparticulates: neither exceptional nor unusual. *Pharm. Res.* 14: 259–266.

43 Yang, W., Peters, J.I., and Williams, R.O. III (2008). Inhaled nanoparticles – a current review. *Int. J. Pharm.* 356: 239–247.

44 Bryon, P.R. (1986). Prediction of drug residence times in regions of the human respiratory tract following aerosol inhalation. *J. Pharm. Sci*. 75: 433–438.

45 Dawidczyk, C.M., Kim, C., Park, J.H. et al. (2014). Stateoftheart in design rules for drug delivery platforms: lessons learned from FDAapproved nanomedicine. *J. Controlled Release* 187: 133–144.

46 Longmire, M., Choyke, P.L., and Kobayashi, H. (2008). Clearance properties of nano sized particles and molecules as imaging agents: considerations and caveats. *Nanomedicine* 3: 703–717.

47 van Vlerken, L.E., Vyas, T.K., and Amiji, M.M. (2007). Poly(ethylene glycol)modified nanocarriers for tumortargeted and intracellular delivery. *Pharm. Res.* 24: 1405–1414.

48 BeckRoichsitter, M., Nicolas, J., and Couvreur, P. (2015). Design attributes of long circulating polymeric drug delivery vehicles. *Eur. J. Pharm. Biopharm.* 97: 304–317.

49 Gratton, S.E.A., Ropp, R.A., Pohlhaus, P.D. et al. (2008). The effect of particle design on cellular internalization pathways. *Proc. Natl. Acad. Sci. U. S. A.* 105: 11613–11618.

50 Chirthrani, B.D., Ghazani, A.A., and Chan, W.W.W. (2006). Determining the size and shape dependence of gold nanoparticle uptake into mammalian cells. *Nano Lett.* 6: 662–668.

51 Hobbs, S.K., Lonsky, W.L., Yuan, F. et al. (1998). Regulation of transport pathways in tumor vessels: role of tumor type and microenvironment. *Proc. Natl. Acad. Sci. U. S. A.* 95: 4607–4612.

52 Torchilin, V. (2009). Multifunctional and stimulisensitive pharmaceutical nanocarriers. *Eur. J. Pharm. Biopharm.* 71: 431–444.

53 Xu, P., Bajaj, G., Shugg, T. et al. (2010). Zwitterionic chitosan derivatives for pH sensitive stealth coating. *Biomacromolecules* 11: 2352–2358.

54 Cerritelli, S., Velluto, D., and Hubbell, J.A. (2007). PEGSSPPS: reductionsensitive disulfide block copolymer vesicles for intracellular drug delivery. *Biomacromolecules* 8: 1966–1972.

55 Ge, Z. and Liu, S. (2013). Functional block copolymer assemblies responsive to tumor and intacellular microenvironments for sitespecific drug delivery and enhanced imaging performance. *Chem. Soc. Rev.* 42: 7289–7325.

56 Deen, W.M., Lazzara, M.J., and Myers, B.D. (2001). Structural determinants of glomerular permeability. *Am. J. Physiol. Renal Physiol.* 281: F579–F596.

57 Lacerda, L., Herrero, M.A., Venner, K. et al. (2008). Carbonnanotube shape and individualization critical for renal excretion. *Small* 4: 130–132.

58 Choi, H.S., Liu, W., Misra, P. et al. (2007). Renal clearance of quantum dots. *Nat. Biotechnol.* 25: 1165–1170.

59 Medina, C., SantosMartinex, M.J., Radomski, A. et al. (2007). Nanoparticles: pharmacological and toxicological significance. *Br. J. Pharmacol.* 150: 552–558.

60 Kane, A.B. and Hurt, R.H. (2008). Nanotoxicology: the asbestos analogy revisited. *Nat. Nanotechnol.* 3: 378–379.

61 Nel, A.E., Madler, L., Velegol, D. et al. (2009). Understanding biophysicochemical interactions at the nanobio interface. *Nat. Mater.* 8: 543–557.

62 Nel, A., Xia, T., Mädler, L., and Li, N. (2006). Toxic potential of materials at the nanolevel. *Science* 311: 622–627.

63 Elsaesser, A. and Howard, C.V. (2012). Toxicology of nanoparticles. *Adv. Drug Delivery Rev.* 64: 129–137.

64 Manning, M.C., Chou, D.K., Murphy, B.M. et al. (2010). Stability of protein pharmaceuticals: an update. *Pharm. Res.* 27: 544–575.

65 Wanning, S., Süverkrüp, R., and Lamprecht, A. (2015). Pharmaceutical spray freeze drying. *Int. J. Pharm.* 488: 136–153.

66 Engstrom, J.D., Lai, E.S., Ludher, B.S. et al. (2008). Formation of stable submicron protein particles by thin film freezing. *Pharm. Res.* 25: 1334–1346.

67 Fong, S.Y.K., Ibisogly, A., and BauerBrandl, A. (2015). Solubility enhancement of BCS Class II drug by solid phospholipid dispersions: spray drying versus freezedrying. *Int. J. Pharm.* 496: 382–391.

68 Rogers, T.L., Nelsen, A.C., Sarkari, M. et al. (2003). Enhanced aqueous dissolution of a poorly water soluble drug by novel particle engineering technology: sprayfreezing into liquid with atmospheric freezedrying. *Pharm. Res.* 20: 485–493.

69 Hu, J., Johnston, K.P., and Williams, R.O. III (2004). Rapid dissolving high potency danazol powders produced by spray freezing into liquid process. *Int. J. Pharm.* 271: 145–154.

70 Purvis, T., Vaughn, J.M., Rogers, T.L. et al. (2006). Cryogenic liquids, nanoparticles, and microencapsulation. *Int. J. Pharm.* 324: 43–50.

71 Wang, G., Wang, J.J., Chen, X. et al. (2016). Quercetinloaded freezedried nanomicelles: improving absorption and antiglioma efficiency in vitro and in vivo. *J. Controlled Release* 235: 276–290.

72 Yang, Z.L., Li, X.R., Yang, K.W., and Liu, Y. (2007). Amphotericin Bloaded poly(ethylene glycol)–poly(lactide) micelles: preparation, freezedrying, and in vitro release. *J. Biomed. Mater. Res.* 85A: 539–546.

73 Ohshima, H., Miyagishima, A., Kurita, T. et al. (2009). Freezedried nifedipinelipid nanoparticles with longterm nanodispersion stability after reconstitution. *Int. J. Pharm.* 377: 180–184.

74 Ahmed, I.S., ElHosary, R., Shalaby, S. et al. (2016). PDPK evaluation of freezedried atorvastatin calciumloaded poly(εcaprolactone) nanoparticles. *Int. J. Pharm.* 504: 70–79.

75 Yu, H., Teo, J., Chew, J.W., and Hadinoto, K. (2016). Dry powder inhaler formulation of highpayload antibiotic nanoparticle complex intended for bronchiectasis therapy: spray drying versus spray freeze drying preparation. *Int. J. Pharm.* 499: 38–46.

76 Yu, H., Tran, T., Teo, J., and Hadinoto, K. (2016). Dry powder aerosols of curcumin chitosan nanoparticle complex prepared by spray freeze drying and their antimicrobial efficacy against common respiratory bacterial pathogens. *Colloids Surf., A* 504: 34–42.

77 Yu, Z., Garcia, A.S., Johnston, K.P., and Williams, R.O. III (2004). Spray freezing into liquid nitrogen for highly stable protein nanostructured microparticles. *Eur. J. Pharm. Biopharm.* 58: 529–537.

78 Dadparvar, M., Wagner, S., Wien, S. et al. (2014). Freezedrying of HI6loaded recombinant human serum albumin nanoparticles for improved storage stability. *Eur. J. Pharm. Biopharm.* 88: 510–517.

79 Soares, S., Fonte, P., Costa, A. et al. (2013). Effect of freezedrying, cryoprotectants and storage conditions on the stability of secondary structure of insulinloaded solid lipid. *Int. J. Pharm.* 456: 370–381.

80 Zillies, J.C., Zwiorek, K., Hoffmann, F. et al. (2008). Formulation development of freeze dried oligonucleotideloaded gelatin nanoparticles. *Eur. J. Pharm. Biopharm.* 70: 514–521.

81 Klesing, J., Chernousova, S., and Epple, M. (2012). Freezedried cationic calcium phosphate nanorods as versatile carriers of nucleic acids (DNA, siRNA). *J. Mater. Chem.* 22: 199–204.

82 Abdelwahed, W., Degobert, G., Stainmesse, S., and Fessi, H. (2006). Freezedrying of nanoparticles: formulation, process and storage considerations. *Adv. Drug Delivery Rev.* 58: 1688–1712.

83 Fonte, P., Reis, S., and Sarmento, B. (2016). Facts and evidences on the lyophilization of polymeric nanoparticles for drug delivery. *J. Controlled Release* 225: 75–86.

84 McClenments, D.J., Decker, E.A., and Weiss, J. (2007). Emulsionbased delivery systems for lipophilic bioactive components. *J. Food Sci.* 72: R109–R124.

85 Zhang, H. and Cooper, A.I. (2005). Synthesis and applications of emulsiontemplated porous materials. *Soft Matter* 1: 107–113.

86 Horpter, C.J.H., Trevaskis, N.L., and Charman, W.N. (2007). Lipids and lipidbased formulations: optimizing the oral delivery of lipophilic drugs. *Nat. Rev. Drug Discov.* 6: 231–248.

87 Hörmann, K. and Zimmer, A. (2016). Drug delivery and drug targeting with parenteral lipid nanoemulsions: a review. *J. Controlled Release* 223: 85–98.

88 Lawrence, M.J. and Rees, G.D. (2000). Microemulsionbased media as novel drug delivery systems. *Adv. Drug Delivery Rev.* 45: 89–121.

89 Fahy, E., Subramaniam, S., Brown, H.A. et al. (2005). A comprehensive classification system for lipids. *Eur. J. Lipid Sci. Technol.* 107: 337–364.

90 Marten, B., Pfeuffer, M., and Schrezenmeir, J. (2006). Mediumchain triglycerides. *Int. Dairy J.* 16: 1374–1382.

91 Morais, A.R., Alencar, E., Junior, F.H. et al. (2016). Freezedrying of emulsified systems: a review. *Int. J. Pharm.* 503: 102–114.

92 Zhao, D., Gong, T., Fu, Y. et al. (2008). Lyophilized Cheliensisin A submicron emulsion for intravenous injection: characterization, in vitro and in vivo antitumor effect. *Int. J. Pharm.* 357: 139–147.

93 Li, F., Wang, T., He, H.B., and Tang, X. (2008). The properties of bufadienolidesloaded nanoemulsion and submicronemulsion during lyophilisation. *Int. J. Pharm.* 349: 291–299.

94 Moreno, M.A., Frutos, P., and Ballesteros, M.P. (2001). Lyophilized lecithin based oil–water microemulsions as a new and low toxic delivery system for Amphotericin B. *Pharm. Res*. 18: 344–351.

95 Orr, M.T., Kramer, R.M., Barnes, V.L. et al. (2014). Elimination of the coldchain dependence of a nanoemulsion adjuvanted vaccine against tuberculosis by lyophilisation. *J. Controlled Release* 177: 20–26.

96 Corveleyn, S. and Remon, J.P. (1998). Formulation of a lyophilized dry emulsion tablet for the delivery of poorly soluble drugs. *Int. J. Pharm.* 166: 65–74.

97 Ahmed, I.S. and AboulEinien, M.H. (2007). In vitro and in vivo evaluation of a fast disintegrating lyophilized dry emulsion tablet containing griseofulvin. *Eur. J. Pharm. Sci*. 32: 58–68.

98 Qian, L. and Zhang, H. (2011). Controlled freezing and freeze drying: a versatile route for porous and micro/nanostructured materials. *J. Chem. Technol. Biotechnol*. 86: 172–184.

99 Zhang, H., Edgar, D., Murray, P. et al. (2008). Synthesis of porous microparticles with aligned porosity. *Adv. Funct. Mater.* 18: 222–228.

100 Yin, W. and Yates, M.Z. (2009). Encapsulation and sustained release from biodegradable microcapsules made by emulsification/freeze drying and spray/freeze drying. *J. Colloid Interface Sci*. 336: 155–161.

101 Wais, U., Jackson, A.W., He, T., and Zhang, H. (2017). Formation of hydrophobic drug nanoparticles via ambient solvent evaporation facilitated by branched diblock copolymers. *Int. J. Pharm.* 533: 245–253.

102 Zhang, H. and Cooper, A.I. (2007). Thermoresponsive “particle pumps”: activated release of organic nanoparticles from opencell macroporous polymers. *Adv. Mater.* 19: 2439–2444.

103 Grant, N., Wu, H., and Zhang, H. (2014). Reductioncontrolled release of organic nanoparticles from disulfide crosslinked porous polymer. *Ind. Eng. Chem. Res*. 53: 246–

252.

104 Grant, N., Cooper, A.I., and Zhang, H. (2010). Uploading and temperaturecontrolled release of polymeric colloids via hydrophilic emulsiontemplated porous polymers. *ACS Appl. Mater. Interfaces* 2: 1400–1406.

105 Zhang, H., Wang, D., Butler, R. et al. (2008). Formation and enhanced biocidal activity of waterdispersible organic nanoparticles. *Nat. Nanotechnol.* 3: 506–511.

106 Ahmed, A., Grant, N., Qian, L., and Zhang, H. (2009). Formation of organic nanoparticles by freezedrying and their controlled release. *Nanosci. Nanotechnol. Lett.* 1: 185–189.

107 Qian, L., Ahmed, A., Foster, A. et al. (2009). Systematic tuning of pore morphologies and pore volumes in macroporous materials by freezing. *J. Mater. Chem.* 19: 5212–5219.

108 Grant, N. and Zhang, H. (2011). Poorly watersoluble drug nanoparticles via an emulsionfreezedrying approach. *J. Colloid Interface Sci.* 356: 573–578.

109 Wais, U., Jackson, A.W., Zuo, Y. et al. (2016). Drug nanoparticles by emulsionfreeze drying via the employment of branched block copolymer nanoparticles. *J. Controlled Release* 222: 141–150.

110 Liu, J., Wais, U., Zuo, Y. et al. (2017). Unimolecular branched block copolymer nanoparticles in methanol for the preparation of poorly watersoluble drug nanoparticles. *J. Mater. Chem. B* 5: 423–427.

111 Giardiello, M., McDonald, T.O., Martin, P. et al. (2012). Facile synthesis of complex multicomponent organic and organic–magnetic inorganic nanocomposite particles. *J. Mater. Chem.* 22: 24744–24752.

112 McDonald, T.O., Martin, P., Patterson, J.P. et al. (2012). Multicomponent organic nanoparticles for fluorescence studies in biological systems. *Adv. Funct. Mater.* 22: 2469–2478.

113 McDonald, T.O., Giardiello, M., Martin, P. et al. (2013). Antiretroviral solid drug nanoparticles with enhanced oral bioavailability: production, characterization, and in vitro–in vivo correlation. *Adv. Healthc. Mater.* 3: 400–411.

114 Martin, P., Giardiello, M., McDonald, T.O. et al. (2015). Augmented inhibition of CYP3A4 in human primary hepatocytes by ritonavir solid drug nanoparticles. *Mol. Pharm.* 12: 3556–3568.

115 Giardiello, M., Liptrott, N.J., McDonald, T.O. et al. (2016). Accelerated oral nanomedicine discovery from miniaturized screening to clinical production exemplified by paediatric HIV nanotherapies. *Nat. Commun.* 7: 13184.

116 Qian, L., Ahmed, A., and Zhang, H. (2011). Formation of organic nanoparticles by solvent evaporation within porous polymeric materials. *Chem. Commun.* 47: 10001–10003.

117 Roberts, A.D. and Zhang, H. (2013). Poorly watersoluble drug nanoparticles via solvent evaporation in watersoluble porous polymers. *Int. J. Pharm.* 447: 241–250.

118 GomarNadal, E., PuigmartiLuis, J., and Amabilino, D.B. (2008). Assembly of functional molecular nanostructures on surfaces. *Chem. Soc. Rev.* 37: 490–504.

119 Plawsky, J.L., Fedorov, A.G., Garimella, S.V. et al. (2014). Nano and microstructures for thinfilm evaporation – a review. *Nanosc. Microsc. Thermophys. Eng.* 18: 251–269.

120 Graham, M., Yang, Y., Roberts, A.D., and Zhang, H. (2015). Poorly water soluble drug nanostructures via surface solvent evaporation. *Nano Life* 5: 1540005.

121 Qian, L. and Zhang, H. (2010). Direct formation of emulsions using watersoluble porous polymers as sacrificial scaffolds. *J. Chem. Technol. Biotechnol.* 85: 1508–1514.

9
Nanostructured Materials Fabricated via Ice Templating of Colloidal/Nanoparticle Suspensions

9.1 Introduction

Colloids and nanoparticles are used widely in the fabrication of porous materials by ice templating [1–3]. These particles may be used either as the main component [4, 5] or combined with polymers to form composites, e.g. silica/polymer [6, 7]. Indeed, many examples have been described in Chapter 5 for porous ceramics and in Chapter 6 for ceramic/polymer composites. An important feature in these studies is that the solid contents or concentrations in the suspensions are usually quite high (usually >5 wt%, more often 10–30 vol%). These particles are usually commercially available and the fine control of the size/morphology of these particles is not the focus of these studies. One exception may be the synthesis and use of carbon nanotubes and graphene/graphene oxide for porous carbonbased materials. This part has already been covered in Chapter 7. Freezedrying of polymer nanoparticles with loaded actives is also an effective route to producing solid formulations and improving storage and transport [8]. This aspect is beyond the scope of this chapter.

When dilute polymer solutions are frozen and freezedried, polymer nanofibers can be produced. This is a significant morphology change from porous polymers fabricated using relatively concentrated solutions [9, 10]. The same may be applied to nanoparticle suspensions. That is, nanostructured materials may be formed by freezedrying of dilute nanoparticle suspensions. It was shown by Kumaraswamy et al. that linear or sheetlike colloidal clusters could be formed when the particle concentrations were in the range of 10^6–10^8 particles/ml [11]. These structures from dilute suspensions appeared to be governed by particle exclusion from the growing ice crystals and accumulation between ice crystal boundaries [11]. Various design and fabrication approaches have been used to generate colloidbased structures and porous materials [12]. The selfassembly of nanoparticles (including nanowires and nanoplatelets) facilitated by ice templating has not been widely reported. However, the simple and versatile features of the icetemplating method can be highly effective, particularly for 1D nanostructures and 3D porous structures. The wide availability of some nanostructured building blocks can promote the application of the ice templating method.

A good example is cellulose nanofibers (CNFs) or cellulose nanocrystals (CNCs), which can be sourced and produced in a sustainable manner [13, 14]. CNFs may be processed to form reinforced foams/composites [14–16] and as stabilizers to produce porous materials [14, 17]. Aerogels and hybrid porous structures containing CNCs with advanced properties can be prepared [18, 19]. The icetemplating method has been used for many of these studies [13–19]. In this chapter, the focus is on the porous and nanostructured materials created by

applying the icetemplating approach to nanoparticle suspensions of different shapes, sizes, and types. Facilitated by the growing ice crystals, the arrangement and assembly of the nanoparticles is key to the formation of these porous structures and nanostructures. The nanoparticles are usually identifiable in these structures. This chapter is arranged based on the shape and composition of the nanobuilding blocks. Owing to their extensive use in various applications, CNFs and CNCs are separately described in the following section.

9.2 Cellulose Nanofibres (CNFs) and Cellulose Nanocrystals (CNCs)

Both CNFs and CNCs can be classified as cellulose nanomaterials. Some other terms are used as well, including nanoscale cellulose, cellulose nanofibrils, and cellulose nanoparticles. There is no clear definition of these names. But they are largely differentiated based on the fibre length and crystallinity. CNFs are usually long and flexible fibres but contain some highly crystalline regions that result from the alignment and intermolecular hydrogen bonding between cellulose chains. CNCs may be regarded as rodlike or needlelike nanostructures with high crystallinity and high specific surface area [13]. Ice templating has been used to make ultralight and highly porous gels from CNFs or CNCs, which are particularly useful as adsorbents for gases or as absorbents for oil/water separation. CNFs may be functionalized to enhance their dispersion in water or waterbased medium, e.g. by 2,2,6,6tetramethylpiperidine1oxyl (TEMPO)mediated oxidation [20–22]. The hydrophobicity of the CNF aerogels can be increased by surface functionalization (e.g. via trimethylsilylation) [23] or by coating with TiO_2 nanoparticles [24]. In turn, this can enhance the absorption of hydrophobic oils and aid oil/water separation. Other components may be mixed with CNF suspensions to render the formed aerogels with new functionalities. For example, *N*(2aminoethyl)3 aminopropylmethyldimethoxysilane was added to aqueous CNF dispersion. The resulting aminebased aerogel showed good performance in capturing CO_2 from air [25].

The concentration of CNF/CNC suspension is a critical factor for the icetemplating approach. It determines whether a cellular aerogel or nanofibrous aerogel is formed. In the former case, densified and aggregated CNFs form the wall of the icetemplated pores [19, 25, 26]. However, the use of dilute CNC or CNF dispersion can lead to the formation of a nanofibrous network or structure. This is analogous to the preparation of polymer nanofibres by freezedrying dilute polymer solutions [9, 10, 27] or colloidal clusters from dilute suspensions [11]. Figure 9.1 shows the morphology change of freezedried CNC and CNF structures [26]. At concentrations of ≥0.5 wt%, a porous layered structure is formed. When the concentration is reduced to 0.1 wt%, a fibrous structure starts to appear while a nanofibrous structure is produced when the concentration is further reduced to 0.05 wt%. This concentration requirement is slightly lower than that for the production of freezedried polymer nanofibres, where a concentration of 0.1 wt% is sufficient for some of the polymers investigated [9, 10]. CNCs and CNFs with different crystalline allomorphs have been investigated. At the concentration of 0.05 wt%, the fibrous structures with mean diameters of 0.57, 1.02, 1.50, and 1.00 μm are formed for CNC I, CNF I, CNC II, and CNF II, respectively

(Figure 9.1) [26]. Aerogels with fibrous structures are also formed with TEMPOoxidized CNFs (0.1 wt%) [20], CNF (0.08 wt%) and CNC (0.2 wt%) [27], and functionalized CNCs (0.5–2.9 wt%) [28]. As observed for polymer nanofibres where lower concentrations are required for polymers with larger molecular weights [9, 10], the formation of fibrous aerogels may require lower concentrations for longer CNFs/CNCs. However, this trend may change accordingly depending on the additives included in the suspension and surface functional groups of CNCs.

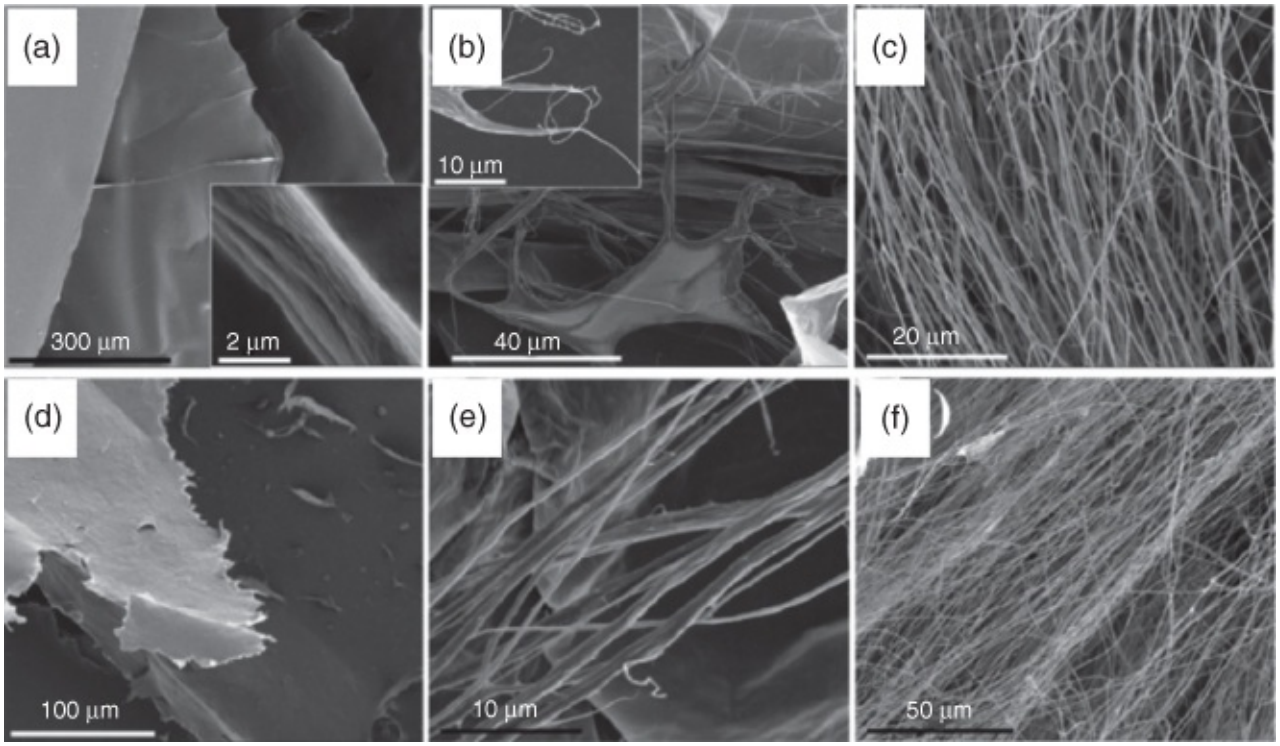

Figure 9.1 Pore structures of the freezedried CNC I at the concentration of (a) 0.5 wt%, (b) 0.1 wt%, (c) 0.05 wt % and the freezedried CNF I at the concentration of (d) 0.5 wt%, (e) 0.1 wt%, (f) 0.05 wt%. In both cases, nanofibrous structures are formed from aqueous suspensions with a concentration of 0.05 wt%.

Source: Han et al. 2013 [26]. Reprinted with permission from American Chemical Society.

Wet stretching is a common method used to produce materials with orientated nanofibres. For the icetemplating method, in addition to forming icetemplated porous structures, nanofibres can be aligned during the freezing stage, facilitated by the growing ice crystals. The degree of inplane orientation may be judged by an order parameter f, where $f = 0$ indicates random orientation while $f = 1$ means ideal alignment. A range of $f = 0.6–0.8$ is usually observed for wetstretched materials [27]. The alignment of CNCs or CNFs has been confirmed by the X ray diffraction study of freezedried foams. Figure 9.2 shows the 2D detected image and azimuthal intensity profiles of the freezedried CNC and CNF foams. The two peaks at approximately 0° and 180° indicate the alignment of the CNFs/CNCs in the direction of freezing. The sharper and more intensive peaks in Figure 9.2 suggest a higher degree of fibre alignment. The order parameter f can be calculated from the azimuthal intensity profiles along the crystalline cellulose (200) Debye–Scherrer ring. After obtaining the full width at half

maximum (fwhm) from the profile via Gaussian fitting, the order parameter can be calculated as: $f = (180 - \text{fwhm})/180$. Both the CNC and CNF foams show high and relatively constant f values (in the range of 0.7–0.8) [27].

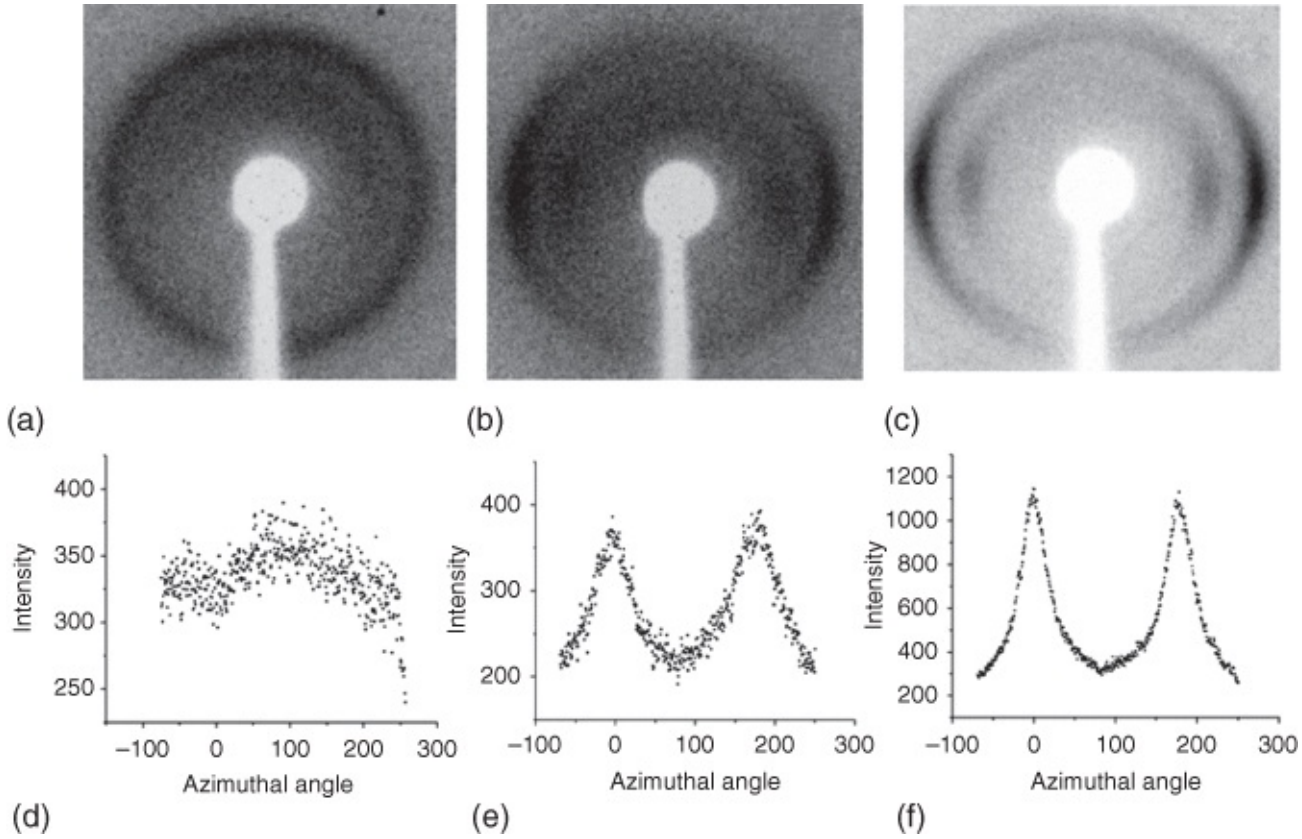

Figure 9.2 Xray diffraction investigation of freezedried CNF and CNC foams. (a–c) 2D detector images; (d–f) azimuthal intensity profiles for the samples prepared from crash frozen 0.5 wt% CNF (a and d), directional freezing of 0.5 wt% CNF (b and e), and directional freezing of 1.5 wt% CNC (c and f).

Source: Munier et al. 2016 [27]. Reprinted with permission from American Chemical Society.

The type of solvent in the CNF suspension can have a significant impact on the morphology of the freezedried aerogel. This is demonstrated by the use of water/ *tert*butyl alcohol (TBA) in the TEMPOoxidized CNF suspension. At a CNF content of 0.1 wt%, when water or water containing 10 wt% TBA was used, layered or porous CNF structures were formed. Uniform fibrous structures were produced by freezedrying the suspensions with TBA content in the range of 20–50 wt%. The optimized structure, finer fibrous network with smaller and uniform pores, was from the suspension containing 30 wt% TBA as solvent. When evaluated as air filters, this led to much lower particle penetration ratios for particles of 0.125–0.250 μm [20]. The freezing conditions, via the use of different types of cold bath with the temperatures in the range of −13 to −114 °C, were investigated for aqueous enzymatic and TEMPOoxidized CNF dispersions [21]. A colder bath gave rise to a fast freezing rate. This could result in smaller crystals and consequently smaller pores in the freezedried aerogel, a trend similar to ice templated porous materials in general [1–3].

Compared to the simple freezedried aerogel, the mechanical stability and recovering ability

can be achieved by chemically crosslinking the CNC aerogel. Aldehydefunctionalized CNC (CHO–CNC) and hydrazidemodified CNC (NHNH $_2$–CNC) in separate suspensions with the same concentration (0.5–2.0 wt%) were mixed together before freezing in a freezer (−4 °C) for 12 h. The crosslinking reaction was completed while the frozen sample was in the freezer, followed by solvent exchange with ethanol and critical drying [28]. With the increase of CNC concentration, the density of the aerogels increased while the porosity decreased (approximately from 99.7% to 98.3%). More macropores with smaller sizes occurred for the CNC aerogels with increasing concentrations. However, the mesopore size remained similar (size around 8 nm) in spite of concentration change. This is likely the result of crosslinking reactions between CNCs. The aerogel shape recovered more than 85% after 80% compression, even after 20 test cycles. The aerogels could absorb a large amount of water (160 g/g) and dodecane (72 g/g). The shaperecovering ability in water was superior [28].

An acid hydrolysis process is usually employed to produce CNCs or CNFs. They can be produced from different sources, mainly lignocellulosic fibres (both woody and nonwoody plants) and also animal, algae, and bacteria [13]. Bacterial CNCs have been frequently used to produce cellulose materials, due to their high mechanical stability, high chemical purity, and high crystallinity. For example, bacterial cellulose hydrogel was washed with water and solvent exchanged with TBA, and then freezedried to produce nanofibrous aerogel with the diameters of the nanofibres in the range of 20–80 nm [23]. This aerogel was modified to increase hydrophobicity by surface reaction with trimethylchlorosilane. The hydrophobic aerogel showed excellent compressibility and oil adsorption capacity. The maximum oil absorption capacity by mass gain was 185 g/g for chloroform. For the absorption of diesel, the capacity (120 g/g) remained unchanged after 10 cycles by compression, washing, and re absorption [23].

In addition to freezing and freezedrying, a freeze–thaw process may be applied to generate nanocellulose aerogels. After a defined number of freeze–thaw (at −20 °C for 15 h and room temperature for 9 h, respectively) cycles (1–3), the TEMPOoxidized CNF hydrogels were formed, which were solvent exchanged with TBA, frozen, and freezedried to get the dry aerogels [29]. The freezeinduced selfassembly of CNFs was observed at a concentration of 0.05% while macroporous structures were formed with concentrations ≥0.2%. The aerogels prepared by three cycles of freeze–thaw and TBA exchange showed a surface area of 118 m^2 g^{-1}, a pore volume of 1.16 cm^3 g^{-1}, and a water absorption capacity of 116 g/g. Full and repetitive shape recovery of the aerogel was achieved in 4 s when the waterabsorbed aerogel was squeezed and reabsorbed for at least 20 cycles [29].

9.3 Nanoparticles and Colloids

Owing to the high surface area, nanoparticles tend to aggregate. The presence of stabilizers promotes the formation of stable nanoparticle suspensions. Freezedrying of nanoparticle suspensions has been an effective route to fabricating aerogels. This has been demonstrated by Bigall and coauthors with Au, Ag, Pd, Pt, Fe $_2O_3$, and CdSe/CdS nanoparticles [30]. The

formed aerogels were selfsupporting with densities in the range of 20–60 mg cm $^{-3}$. Figure 9.3a shows the fluffy Pd aerogel containing a wellinterconnected porous network of 10–100 nm thin sheets. At a higher magnification, it can be seen that the sheetlike structure consists of Pd nanoparticles contacting with each other (Figure 9.3b) [30]. By directional freezing of relatively dilute nanoparticle suspensions, porous networks with aligned microwires may be formed, as demonstrated with Au nanoparticle suspensions [6]. When injecting Au nanoparticle suspension directly into liquid nitrogen followed by freezedrying, porous beads with a randomly porous outer shell (due to the fast freezing process when in contact with liquid nitrogen) and a radially porous internal structure (resulting from the directional freezing from outside of the drop to the core of the drop) are formed (Figure 9.3c) [31]. Both the randomly porous region and the aligned porous region contain Au nanowires (Figure 9.3d and e). The size of the Au nanoparticle is around 15 nm. From Figure 9.3f, it is difficult to see the individual Au nanoparticles (AuNPs). Instead, the Au nanoparticles are aggregated to form bigger clusters that are assembled to produce the Au nanowires. The aggregation of AuNPs is also confirmed by the colour change from dark red to black [31]. Owing to the high surface energy of AuNPs and nanowires, these freezedried structures could be heated in air under relatively mild conditions to fuse the nanoparticles together and form quite smooth Au nanowires without the loss of highly porous icetemplated aerogel structures [31].

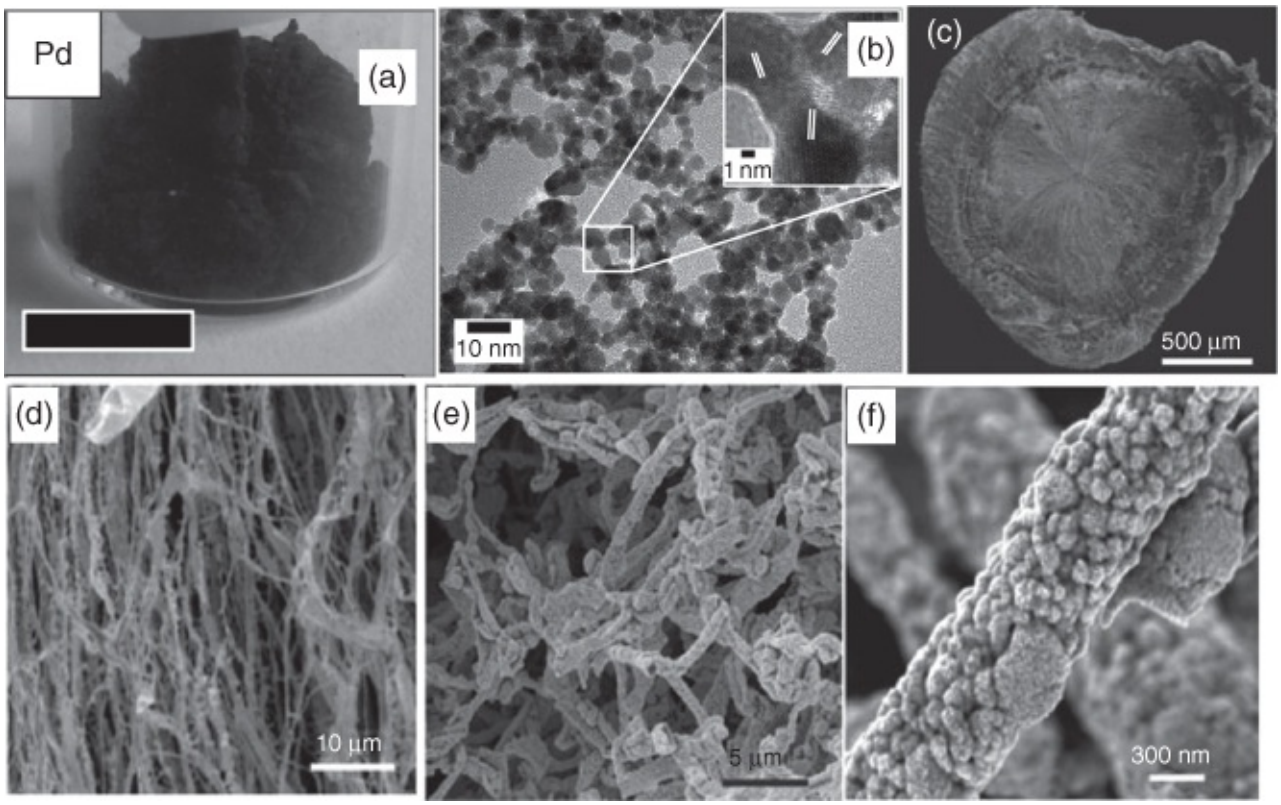

Figure 9.3 Porous structures made from Pd nanoparticles and Au nanoparticles. (a) Photo of the Pd aerogel. (b) The Pd nanoparticles assemble together (in direct contact) to form the structure. ; (c) The structure of the porous bead prepared by injecting Au nanoparticle suspension into liquid nitrogen and subsequent freezedrying. (d) The aligned structure from the radially aligned part of the bead in (c). (e) The randomly porous structure consisting of nanowires in the outer shell of the beads in (c). (f) The freezeinduced nanowire consisting of aggregated Au nanoparticles.

Source: Zhang et al. 2008 [31]. Reprinted with permission from John Wiley and Sons.

Source: Reprinted with permission from Ref. [30]

The assembly of AuNPs into chains and superstructures by a simple freezing process has been demonstrated by Chen and coauthors [32]. Figure 9.4a shows the AuNP chain by freezing aqueous AuNP suspension on a Si substrate at the concentration of 3.8×10^{12} particles/ml. The triangular prism shape is clearly shown in Figure 9.4b, with the width around 450 nm. When the concentration was reduced to 3.8×10^{9} particles/ml, only short chains with narrow width were obtained. At the concentration of 6×10^{10} particles/ml, chains with lengths up to 100 µm and with single, double, triple, and quadruplelines of AuNPs could be produced.
Similar chain structures could be produced with Au nanorods (AuNRs), with most of the AuNRs accommodating endtoend conformation with the neighbouring particles (Figure 9.4c and d). The AuNP chains can also be produced by freezing a small volume of AuNP suspension instead of spreading on the Si substrate. The chain structures were observed when freezing 0.5 ml of AuNP solution with the concentration of 6×10^{10} particles/ml in a −80 °C freezer or ethanol. An example of the single chain consisting of the assembled AuNPs is shown in Figure 9.4e, which was prepared by freezing in −80 °C ethanol and then allowed to melt at

room temperature. The suspension containing the AuNP chains was mixed with the reactive solution containing aniline and other suitable reagents. The polymerization of aniline in the presence of AuNP chains was completed at room temperature without stirring for 24 h. The structures of AuNP chains encapsulated by polyaniline could be produced (Figure 9.4f–h) [32]. These unbranched and long chains can be important for plasmonic coupling and for the development of plasmonic waveguides.

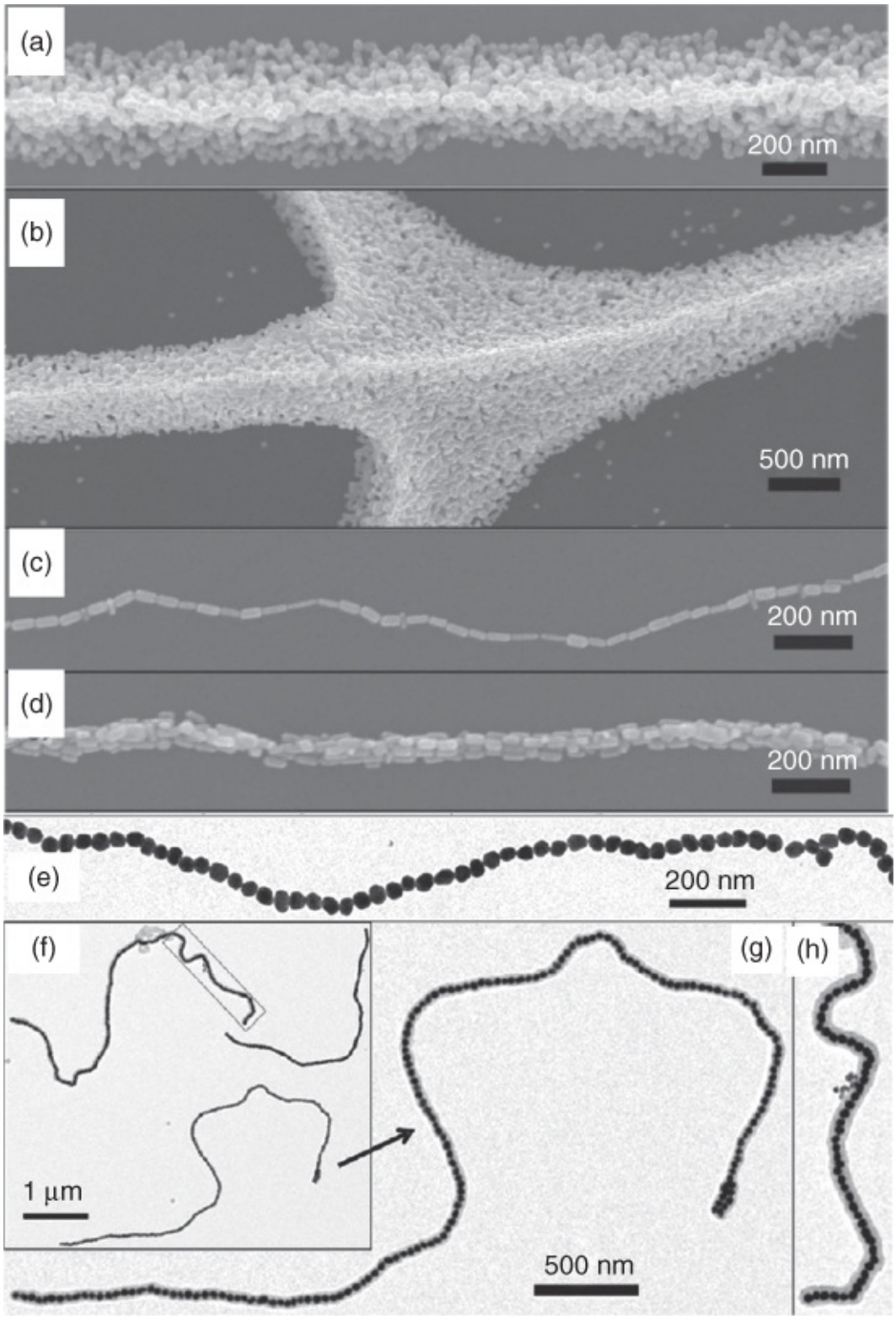

Figure 9.4 Selfassembly of Au nanoparticles and Au nanorods on Si substrate by ice templating and the encapsulation within polyaniline. (a and b) A typical chain and a node shaped structure obtained from 40 nm Au nanoparticles; (c and d) Single chain and multiple layered chains formed from Au nanorods; (e) A single line chain of Au nanoparticles formed by freezing the nanoparticle suspension in −80 °C ethanol; (f–h) The chain of Au nanoparticles encapsulated by polyaniline.

Source: Shen et al. 2011 [32]. Reprinted with permission from American Chemical Society.

In addition to 3D aerogels and 1D chains, 2D surface patterned structures can be fabricated by controlled freezing of thin films of nanoparticle suspension on a substrate. This was demonstrated by the aligned patterns of the assembled AuNPs [6]. The distance or the spacing between the aligned ridges can be readily tuned by varying the freezing rates [6, 33]. Figure 9.5a shows how the spacings change with the freeze rates [33]. In order to produce the aligned patterns, the addition of a stabilizing polymer is often necessary. Figure 9.5b and c illustrates the morphology of the aligned patterns of silica particles with a small percentage of stabilizer polymers such as sodium carboxymethylcellulose (SCMC) or polyvinyl alcohol (PVA). The silica nanoparticles (in the region of 10–15 nm) in Figure 9.5b are too small to be seen at this magnification. However, the freezeinduced selfassembled surface patterns can be clearly demonstrated with the silica microparticles (diameters ~1 μm) (Figure 9.5c). This method could be used to create aligned surface patterns with biodegradable polymer nanoparticles or biocompatible polymers such as chitosan to guide the growth of stem cells [33].

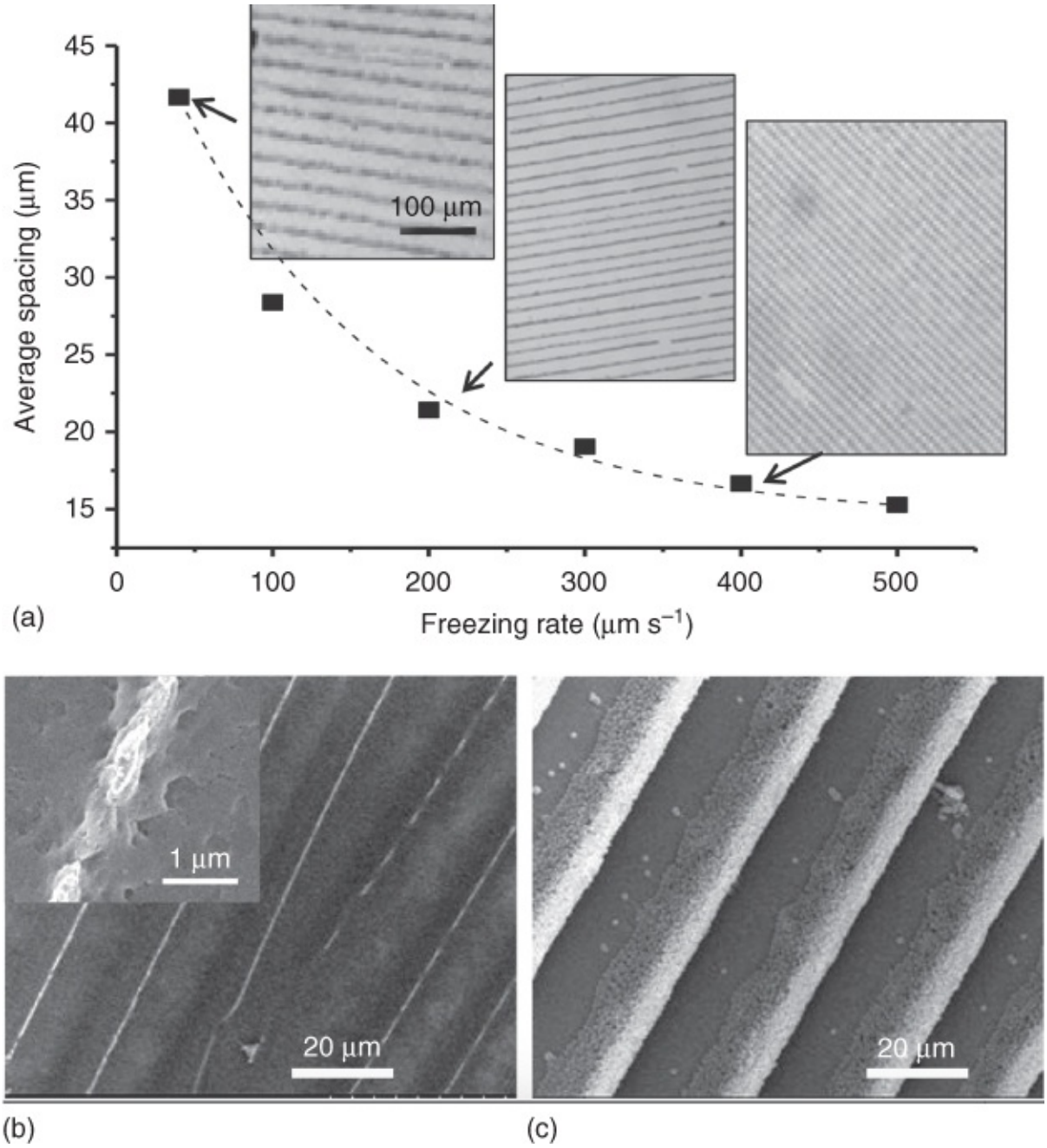

Figure 9.5 Aligned surface patterns fabricated by directional freezing of liquid suspension thin film on substrates. (a) The spacing between the ridges decrease with the increase of freezing rate, demonstrated with the aqueous suspension containing 5 wt% HS30 silica colloids and 5 wt% poly(vinyl alcohol). (b) The structure prepared from aqueous suspension of 15 wt% HS30 colloids and 1.5 wt% SCMC. (c) The aligned patterns with the selfassembled silica microspheres fabricated from the suspension containing 15 wt% silica microspheres and 5 wt% PVA.

Source: Qian et al. 2015 [33]. Reprinted with permission from Elsevier.

Polymer nanoparticles are also processed by the icetemplating method to create 1D nanowires or microwires. Aqueous polystyrene (PS) nanoparticle dispersion (1 wt%, nanoparticle size 80 nm) was subjected to a directional freezing process. After freezedrying, a fibrous structure containing bundles of microwires was formed (Figure 9.6a) [34]. Under

higher magnifications, it could be seen that PS nanoparticles were assembled tightly together to form the microwires with diameters around 1.5 μm (Figure 9.6b and c). When this structure was subjected to a chemical vapour deposition (CVD) process with silane molecules, the fibrous structure was retained but the mechanical stability was reinforced [34]. Lee et al. showed that by directional freezing of aqueous polypyrrole (PPy) nanoparticle suspension (prepared by miniemulsion polymerization, size 20–50 nm), PPy nanofibres (with diameters in the range of 200–500 nm) consisting of the assembled nanoparticles could be produced (Figure 9.6d). The PPy nanofibres were further used as vapour sensors to detect nitrogencontaining explosive chemicals based on the conductivity/current change [35]. Larger PS colloids with diameters around 450 nm could also be assembled by the directional freezing process (Figure 9.6e) [31]. Porous structures containing the colloidsassembled microwires were formed after freezedrying the PS colloidal suspensions (Figure 9.6f). Interestingly, by heating this structure in air to 150 °C, the PS colloids softened and fused together to form smooth microwires without damaging the 3D fibrous structure (Figure 9.6g) [31].

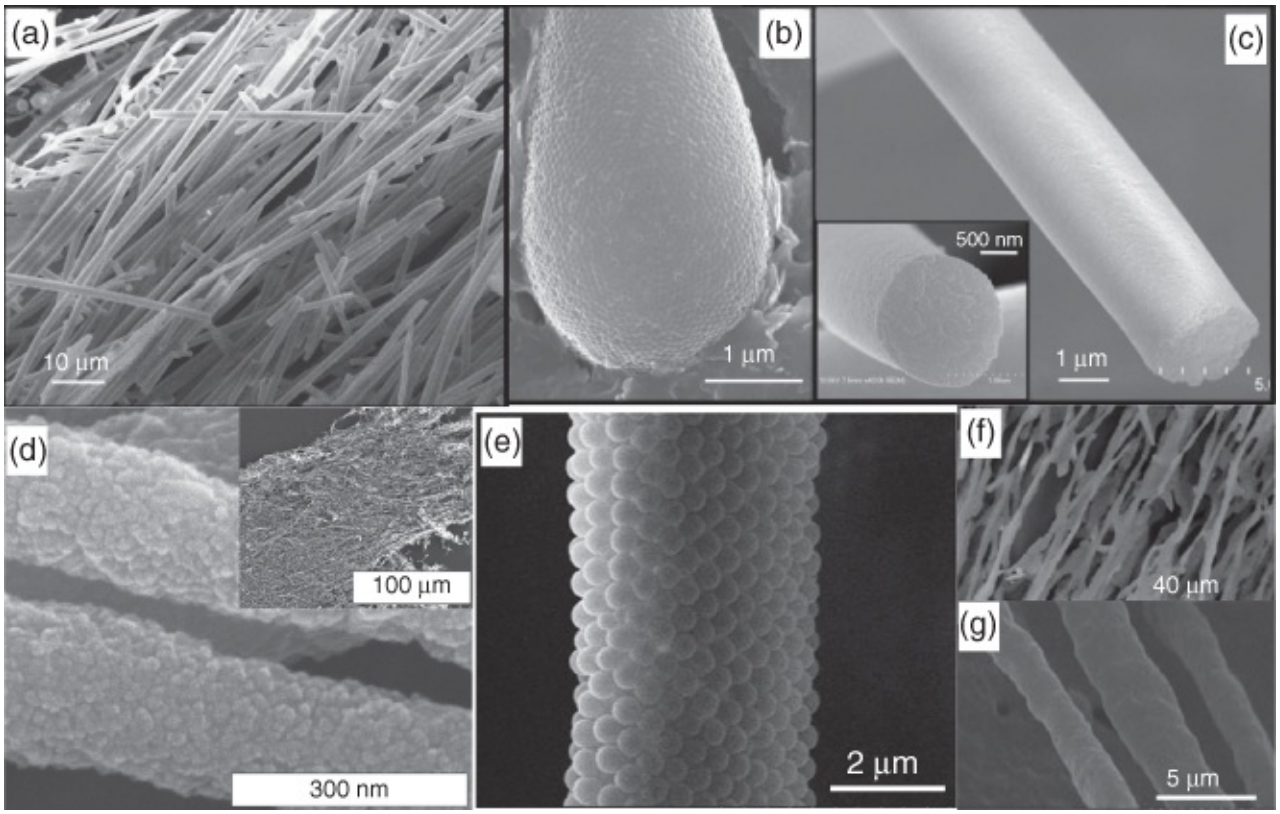

Figure 9.6 1D structures fabricated by directional freezing of polymer nanoparticle/colloid suspensions. (a–c) The structures prepared from polystyrene nanoparticles (80 nm). (d) The nanofibers obtained from polypyrrole nanoparticles (20–50 nm). (e–g) The structures fabricated from polystyrene colloids (450 nm).

Source: Zhang et al. 2008 [31]. Reprinted with permission from John Wiley and Sons.

Source: Reprinted with permission from Ref. [35].

Source: Reprinted with permission from Ref. [34].

Polymeric microgels have also been freezedried, mostly to form 3D macroporous structures. Poly(*N*isopropylacrylamide) (PNIPAM) microgels were prepared with *N*,*N*methylenebis

acrylamide and allylamine by precipitation polymerization [36]. The porous gels were fabricated by directly freezedrying the microgel suspension or with bacteria and microbes. 3D macroporous structures were formed via the assembly of microgel particles, with the microbes identifiable [36]. The oppositely charged microgels, poly(*N*vinylcaprolactamco diethylaminoethyl methacrylate) (PVCLDEAEMA) and poly(*N*vinylcaprolactamco acrylic acid) (PVCLAA) particles, were assembled to form aligned hydrogels by directional freezing and thermally triggered electrostatic selfassembly [37]. A fast temperature responsive PNIPAM macroporous gels with the walls consisting of the assembled microgel particles could be similarly prepared via the icetemplating approach [38].

In addition to the examples discussed, the icetemplating approach can be used to assemble a wide range of metal nanoparticles, silica particle, and different types of metal oxide nanoparticles to produce porous aerogels or structures consisting of assembled microwires [30, 31]. Different types of nanoparticles may be mixed together to fabricate complex porous structures, which is detailed in the last section of this chapter.

9.4 Nanowires and Nanofibres

3D porous structures can be equally fabricated from nanowires or nanofibres via the ice templating approach. Aqueous suspensions of Ag nanowires with lengths of 4–15 μm were frozen and freezedried to generate freestanding macroporous networks when the concentration was not less than 10 mg ml^{-1} (Figure 9.7a) [39]. Different concentrations and different freezing temperatures could be used to tune the porosity and the macropore morphology. Figure 9.7b shows that the pore wall consists of bundled Ag nanowires with some alignment. These networks exhibit a very high electrical conductivity of 21.5 S cm^{-1} at an ultralow density of 25 mg cm^{-3}. Similar structures were also prepared from Cu nanowires. Polydimethylsiloxane (PDMS) could be infiltrated into the 3D Ag fibrous structure and the resulting composites showed excellent electromechanical stability with a great potential for highperformance stretchable and flexible conductors [39].

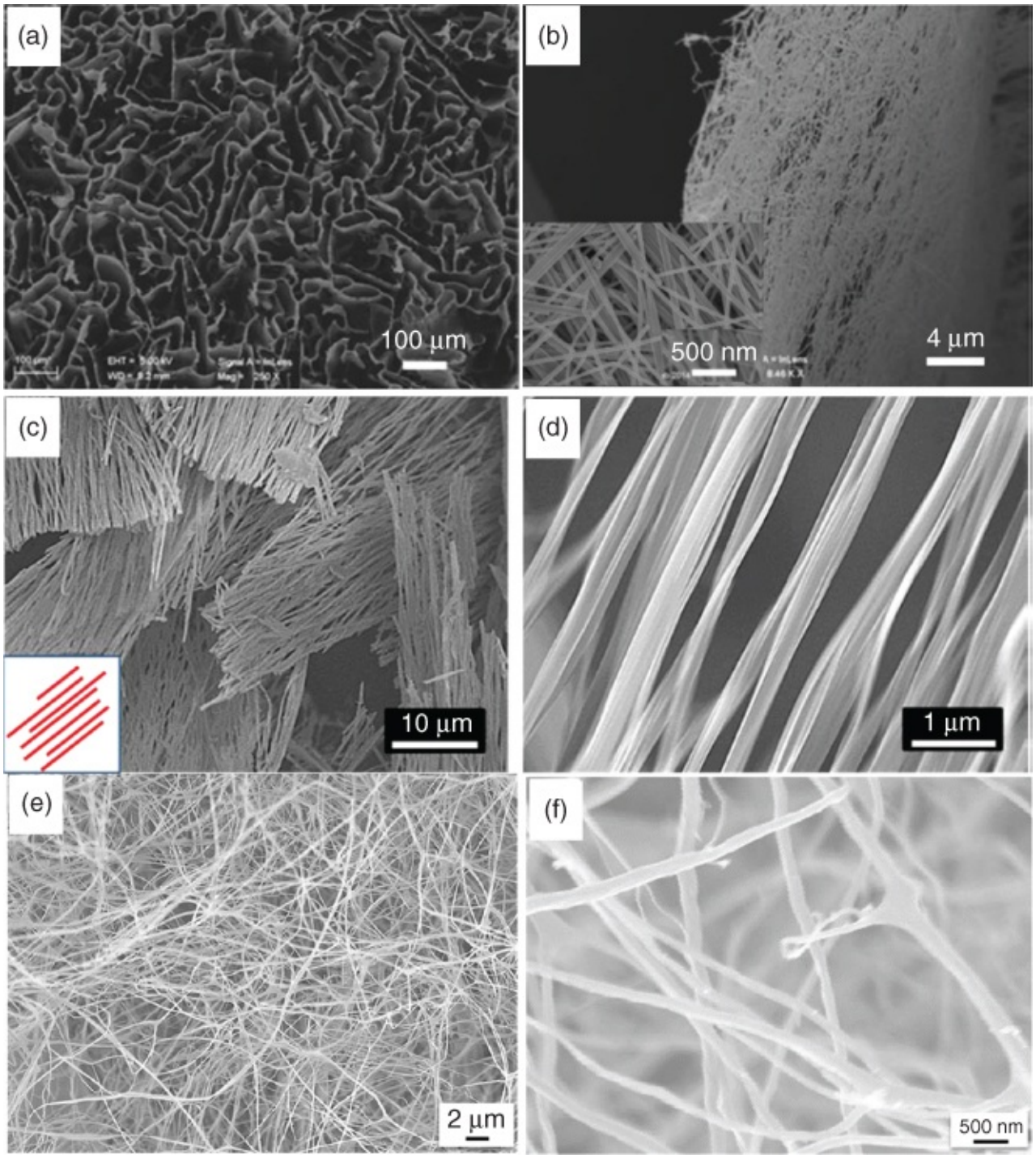

Figure 9.7 3D structures fabricated from nanowires via ice templating. (a and b) The porous structures from Ag nanowires. The inset shows the original Ag nanowires. ; (c and d) Aligned nanofibrous networks from phenylalanine nanofibers. ; (e and f) The nanofibrous networks generated from chitin nanofibers.

Source: Wu and Meredith 2014 [41]. Reprinted with permission from American Chemical Society.

Source: Reprinted with permission from Ref. [40]

Source: Reprinted with permission from Ref. [39]

Phenylalanine nanofibres with diameter of ~160 nm and lengths of tens of micrometres were employed to produce 3D nanofibrous networks [40]. Depending on the freezing temperature,

the alignment of the fibres could be quite random (freezing at −20 °C) or highly ordered (freezing at −196 °C in liquid nitrogen, Figure 9.7c and d). The nanofibrous networks were formed with the suspension concentrations in the range of 10–150 mM. Higher concentrations gave a denser network. The fibrous materials were also formed with phenylalanine nanofibres/polyethylenimine and phenylalanine nanofibres/PVA, which may be highly useful as scaffold materials for tissue engineering [40].

Chitin nanofibres with average diameter of 50 nm were prepared via fibrillation of purified chitin by high shear homogenization. When aqueous suspension of chitin nanofibres was frozen at −20 °C and freezedried, a white and opaque material was formed [41]. The SEM images in Figure 9.7e and f show the formation of nanofibrous networks. The nanofibres have an average diameter of 220 nm, in the range of 150–350 nm, and are randomly positioned. However, when the suspensions were frozen at −80 or −196 °C, orientated sheetlike porous structures were obtained, instead of the nanofibrous network [41]. The authors argued that the chitin nanofibres could have more time to assemble to larger nanofibres when the freezing rate was low at −20 °C [41].

9.5 Platelets and Nanosheets

Microplatelets can be assembled by the growing ice crystals. Figure 9.8 shows the assembled boron nitride (BN) triggered by the moving ice front [42]. The faster freezing rate promotes the assembly of the microplates, with a thinner wall and condensed packing [42]. This method was employed to assemble alumina platelets into strong nacrelike porous scaffolds, with an improvement factor of 1.5–4 [43]. This concept has also been employed to produce nacre mimetic tough composites from alumina platelets (7 μm in diameter and 500 nm in thickness), alumina nanoparticles (100 nm), and smaller nanoparticles of silica–calcia phase (20 nm) [44].

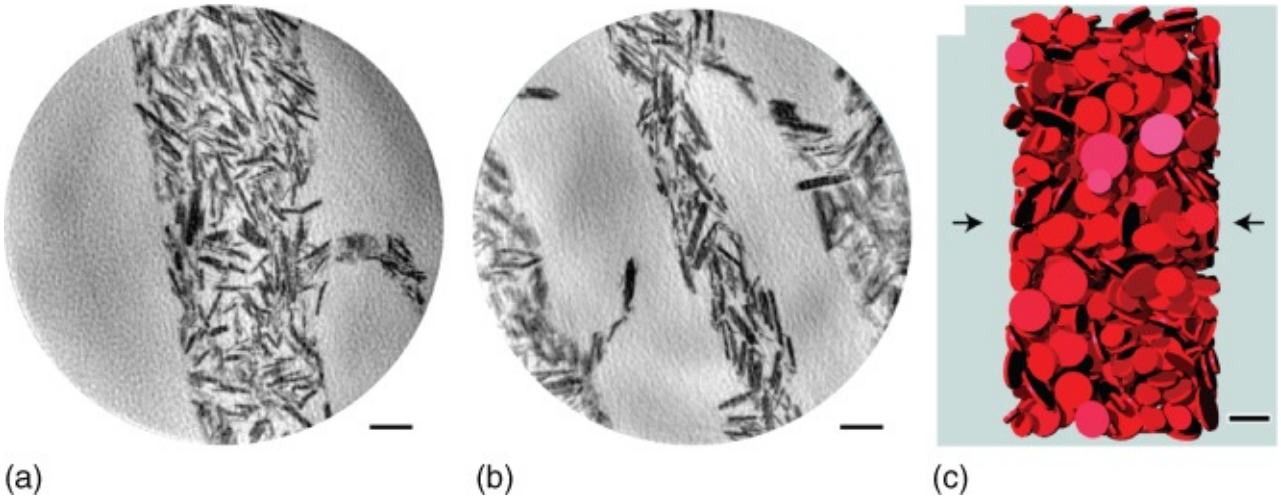

Figure 9.8 Freezeinduced selfassembly of boron nitride microplates. (a) The structure obtained at the flow rate of 15 μm s^{-1}. (b) The structure from a fast freezing rate of 25 μm s^{-1}. (c) The scheme showing the assembly of the microplates. Scale bar 10 μm.

Source: Bouville et al. 2014 [42]. Reprinted with permission from American Chemical Society.

Nanosheets can be employed to fabricate functional aerogels and superelastic porous networks. For example, Liu et al. reported the preparation of ultralight aerogels from the self assembly of MnO_2 nanosheets by ice templating [45]. The aerogels had low density of ~0.53 mg cm^{-3} and were effective in the adsorption of toxicreducing gas such as N $_2H_4$ [45]. Graphene and graphene oxides are probably the mostly used nanosheets for fabrication of functional porous materials by ice templating. This has been covered in Chapter 7.

9.6 Mixing Colloids and Core–Shell Nanoparticles

Colloids may be simply mixed before the freezing process, to offer additional functions or porosity in the prepared materials. Kim et al. showed the fabrication of silica monoliths with icetemplated microhoneycomb structures and highly ordered and interconnected macroporous walls (Figure 9.9) [46]. This was achieved by directional freezing of a mixture of particle suspensions containing silica nanoparticles (8–11 nm) and poly(styrene(co2 hydroxyethyl methacrylate)) latex particles (385 nm). The freezing process induced the self assembly of both particles, with polymer colloids closely packed and the smaller silica nanoparticles assembled within the interstices of the packed polymer particles. After calcination to remove the polymer particles, the ordered and interconnected macroporous wall was formed. The size of the macropores was about 300 nm, smaller than the size of the polymer colloids, due to the shrinkage caused by calcination. The surface area of the resulting silica monolith was 281 m^2 g^{-1}, with mesopore size distribution around 3.6 nm [46]. Bon and coauthors used a mixture of large ‘soft’ polymer latexes (size in the range of 200–500 nm, e.g. poly(vinyl laurate) latexes) and small ‘hard’ nanoparticles (e.g. Ludox colloidal silica, alumina nanoparticles) to fabricate reinforced foams via the icetemplating approach [47]. Carbon black particles (120 nm) could be added at a percentage of 14 wt% to produce conductive foams that were used as sensors to detect the vapour of organic solvent such as toluene and ethanol, based on the resistance change [47].

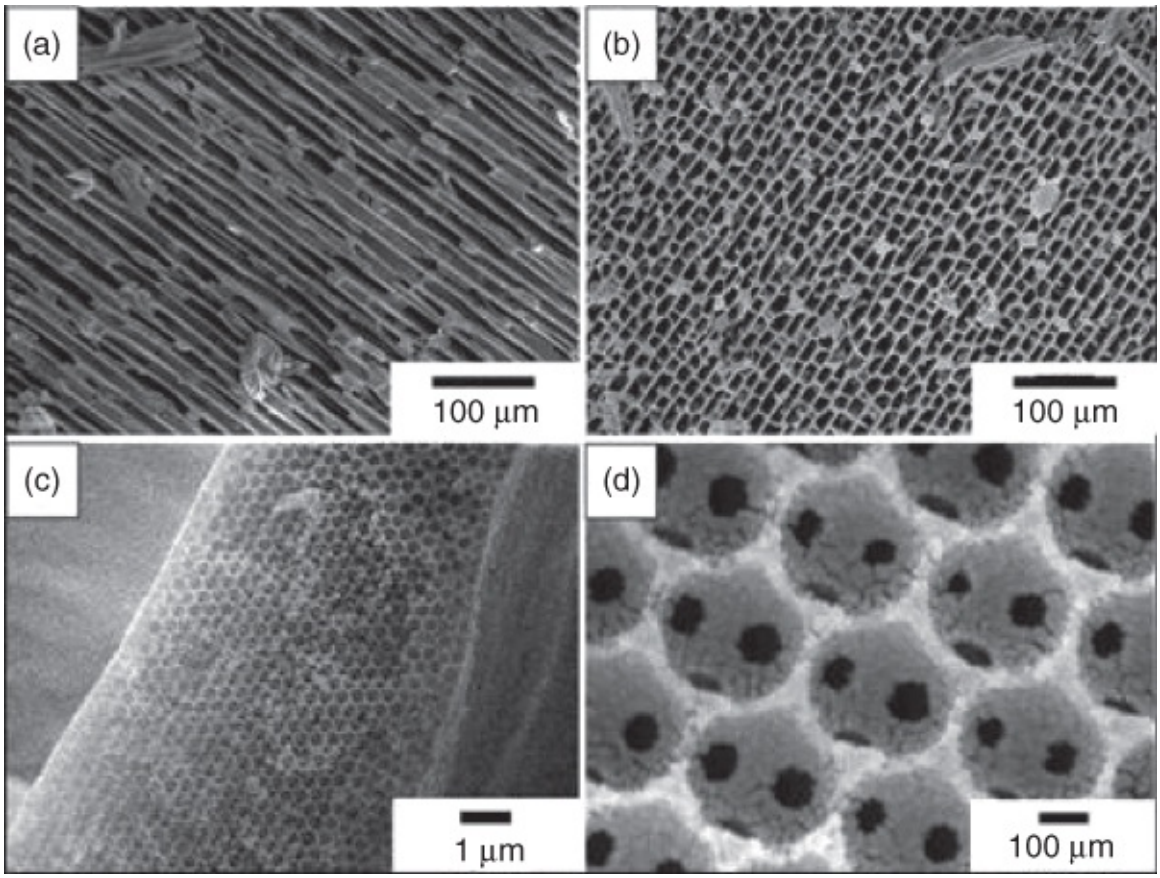

Figure 9.9 The silica monoliths with microhoneycomb structure and ordered, interconnected macroporous walls fabricated by ice templating with silica nanoparticles and polymer colloids and subsequent removal of polymer colloids by calcination. (a) The crosssectioned area parallel to the freezing direction; (b) the crosssectioned surface perpendicular to the freezing direction; (c) the magnified area parallel to the freezing direction; (d) the polymer colloid templated macropores.

Source: Kim et al. 2009 [46]. Reprinted with permission from American Chemical Society.

The freezedrying of nanoparticle suspensions usually result in fragile porous structures, particularly for those 'hard' inorganic particles. One way to address this issue is to modify the surface of the nanoparticles and crosslink the icetemplated structures. This was demonstrated by a study from Rajamanickam et al. [48]. Polyethyleneimine was adsorbed on silica particles (Ludox, 26 nm) with a coverage of ~1 mg m^{-2}. Poly(ethylene glycol) diglycidyl as crosslinker was added to the polyethyleneiminemodified silica suspension. The crosslinking was completed during the frozen state at −10 °C for 24 h [48]. The resulting structure showed good elastic mechanical response. This concept was also employed to fabricate soft scaffolds from hydroxyapatite particles and gelatin, and crosslinked via the EDC chemistry in the frozen state [48].

The inorganic nanoparticles may be made 'soft' by forming a polymeric shell onto the surface. Uniform silica nanoparticles prepared by the Stöber method were coated with PNIPAM of varied shell thickness. Aqueous dispersions of the core–shell microgels (1 wt%) was frozen in a −80 °C bath. The porous structures consisting of interwoven fibres were produced after

freezedrying [49]. Figure 9.10a gives an overview of the fibres made from silica nanoparticles (250 nm) with 50 nm of PNIPAM shell. The assembled particles can be clearly seen in Figure 9.10b. The microgel surface of the core–shell particles facilitated the holding together of the particles to form the fibres. The procedure was also successfully applied to prepare ZrO_2@SiO_2@PNIPAM and also γFe $_2O_3$@SiO_2 core–shell nanoparticles [49].

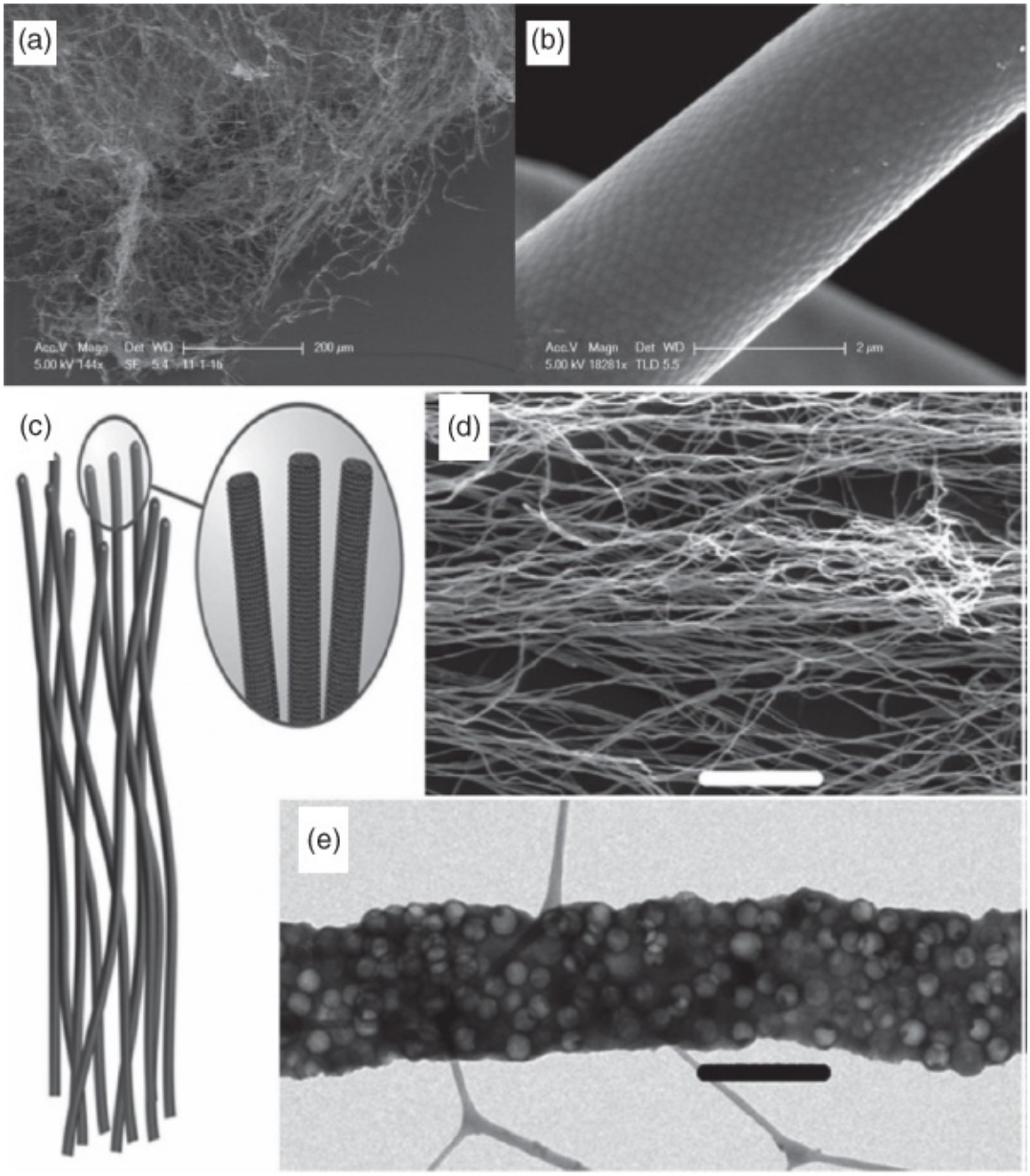

Figure 9.10 Nanofibrous structures prepared by ice templating from core–shell particles. (a and b) The structures made from silica nanoparticles (250 nm) with poly(*N* isopropylacrylamide) shell. (c) The scheme showing the selfassembly of core–shell nanoparticles. (d) The nanofibers prepared from SiO_2@polyacrylonitrile particles. Scale bar 50 μm. (e) The nanofiber consisting of hollow carbon capsules after carbonization and etching silica with NaOH solution. Scale bar 200 nm. (c–e)

Source: Shi et al. 2008 [50]. Reprinted with permission from American Chemical Society.

Source: Shi et al. 2007 [49]. Reprinted with permission from John Wiley and Sons.

When the shell polymer has a high carbon content, this method can be applied to fabricate carbon fibres. For example, polyacrylonitrile (PAN) was used for such a purpose. Figure 9.10c shows schematically how the fibres are formed from the nanoparticles by the ice

templating method. Silica nanoparticles with a PAN shell (SiO_2@PAN) were dispersed in a 0.1 wt% PVA aqueous solution and then frozen in a −80 °C bath [50]. Figure 9.10d demonstrates the fibres formed after the freezedrying process. When these fibres were annealed at 200 °C in air for 1 h, carbonized at 800 °C under Ar and treated with 10 M NaOH solution to remove the silica core, fibres consisting of hollow carbon capsules were formed (Figure 9.10e). When the core–shell SiO_2@ZrO_2@PAN particles were employed, the fibres of carbon–metal oxide hollow capsules were obtained [50].

9.7 Summary

Nanoparticles (including nanofibers, nanosheets, and platelets) are excellent building blocks for porous materials and composites via the icetemplating approach. Nanoparticles are usually processed with surfactants and polymers in order to produce relatively stable freeze dried materials. The use of nanoparticles by ice templating is mostly for the fabrication of aerogels, which may be thermally treated subsequently. The freezing of dilute nanoparticle suspensions is usually essential in order to fabricate fibrous and nanostructures from nanoparticles as building blocks. The freezeinduced selfassembly leads to the formation of 1D nano/microfibers, 2D aligned surface patterns, and 3D fibrous networks. Different types of nanoparticles, polymer colloids, and core–shell particles can be used in the fabrication process. It provides a simple but highly effective route to the fabrication of nanochains, nanofibers, patterns, and ultralight aerogels, which may have various potential applications in different areas. Owing to their weak mechanical stability, the direct use of the freezedried structure is not well reported. But they may be posttreated, e.g. by thermal sintering process and chemical crosslinking, or by incorporating a second phase material to form composites, to improve mechanical stability while maintaining the original functionality so that the materials may be suitable for enhanced target applications.

References

1 Gutiérrez, M.C., Ferrer, M.L., and del Monte, F. (2008). Icetemplated materials: sophisticated structures exhibiting enhanced functionalities obtained after unidirectional freezing and icesegregationinduced selfassembly. *Chem. Mater.* 20: 634–648.

2 Qian, L. and Zhang, H. (2011). Controlled freezing and freeze drying: a versatile route for porous and micro/nanostructured materials. *J. Chem. Technol. Biotechnol.* 86: 172–184.

3 Deville, S. (2013). Icetemplating, freeze casting: beyond materials processing. *J. Mater. Res.* 28: 2202–2219.

4 Ahmed, A., Clowes, R., Myers, P., and Zhang, H. (2011). Hierarchically porous silica monoliths with tuneable morphology, porosity, and mechanical stability. *J. Mater. Chem.* 21: 5753–5763.

5 Kar, M., Pauline, M., Sharma, K. et al. (2011). Synthesis of polylglutamic acid grafted

silica nanoparticles and their assembly into macroporous structures. *Langmuir* 27: 12124–12133.

6 Zhang, H., Hussain, I., Brust, M. et al. (2005). Aligned two and threedimensional structures by directional freezing of polymers and nanoparticles. *Nat. Mater.* 4: 787–793.

7 Gutiérrez, M.C., Jobbágy, M., Rapún, N. et al. (2006). A biocompatible bottomup route for the preparation of hierarchical biohybrid materials. *Adv. Mater.* 18: 1137–1140.

8 Abdelwahed, W., Degobert, G., Stainmesse, S., and Fessi, H. (2006). Freezedrying of nanoparticles: formulation, process and storage considerations. *Adv. Drug Deliv. Rev.* 58: 1688–1713.

9 Qian, L., Willneff, E., and Zhang, H. (2009). A novel route to polymeric submicron fibers and their use for inorganic structures. *Chem. Commun.* 3946–3948.

10 Qian, L. and Zhang, H. (2010). Green synthesis of chitosanbased nanofibers and their applications. *Green Chem.* 12: 1207–1214.

11 Kumaraswamy, G., Biswas, B., Choudhury, C., and K. (2016). Colloidal assembly by ice templating. *Faraday Discuss.* 186: 61–76.

12 Phillips, K.R., England, G.T., Sunny, S. et al. (2016). A colloidoscope of colloidbased porous materials and their use. *Chem. Soc. Rev.* 45: 281–322.

13 Trache, D., Hussin, M.H., Haafiz, M.K.M., and Thakur, V.K. (2017). Recent progress in cellulose nanocrystals: sources and production. *Nanoscale* 9: 1763–1786.

14 Salas, C., Nypelö, T., RodriguezAbreu, C. et al. (2014). Nanocellulose properties and applications in colloids and interfaces. *Curr. Opin. Colloid Interface Sci.* 19: 383–396.

15 Liu, D., Ma, Z., Wang, Z. et al. (2014). Biodegradable poly(vinyl alcohol) foams supported by cellulose nanofibrils: processing, structure, and properties. *Langmuir* 30: 9544–9550.

16 Zhai, T., Zheng, Q., Cai, Z. et al. (2015). Poly(vinyl alcohol)/cellulose nanofibril hybrid aerogels with an aligned microtubular porous structure and their composites with polydimethylsiloxane. *ACS Appl. Mater. Interfaces* 7: 7436–7444.

17 Cervin, N.T., Andersson, L., Ng, J.B.S. et al. (2013). Lightweight and strong cellulose materials made from aqueous foams stabilized by nanofibrillated cellulose. *Biomacromolecules* 14: 503–511.

18 Yang, X., Shi, K., Zhitomirsky, I., and Cranston, E.D. (2015). Cellulose nanocrystals aerogels as universal 3D lightweight substrates for supercapacitor materials. *Adv. Mater.* 27: 6104–6109.

19 Chu, G., Qu, D., Zussman, E., and Xu, Y. (2017). Iceassisted assembly of liquid crystalline cellulose nanocrystals for preparing anisotropic aerogels with ordered structures.

Chem. Mater. 29: 3980–3988.

20 Nemoto, J., Saito, T., and Isogai, A. (2015). Simple freezedrying procedure for producing nanocellulose aerogelcontaining, highperformance air filters. *ACS Appl. Mater. Interfaces* 7: 19809–19815.

21 Martoïa, F., Cochereau, T., Dumont, P.J.J. et al. (2016). Cellulose nanofibril foams: links between icetemplating conditions, microstructures and mechanical properties. *Mater. Des.* 104: 376–391.

22 Pan, Z.Z., Nishihara, H., Iwamura, S. et al. (2016). Cellulose nanofiber as a distinct structuredirecting agent for xylemlike microhoneycomb monoliths by unidirectional freezedrying. *ACS Nano* 10: 10689–10697.

23 Sai, H., Fu, R., Xing, L. et al. (2015). Surface modification of bacterial cellulose aerogels' weblike skeleton for oil/water separation. *ACS Appl. Mater. Interfaces* 7: 7373–7381.

24 Korhonen, J.T., Kettunen, M., Ras, R.H.A., and Ikkala, O. (2011). Hydrophobic nanocellulose aerogels as floating, sustainable, reusable, and recyclable oil absorbents. *ACS Appl. Mater. Interfaces* 3: 1813–1816.

25 Gebald, C., Wurzbacher, J.A., Tingaut, P. et al. (2011). Aminebased nanofibrillated cellulose as adsorbent for CO_2 capture from air. *Environ. Sci. Technol.* 45: 9101–9108.

26 Han, J., Zhou, C., Wu, Y. et al. (2013). Selfassembling behaviour of cellulose nanoparticles during freezedrying: effect of suspension concentration, particle size, crystal structure, and surface charge. *Biomacromolecules* 14: 1529–1540.

27 Munier, P., Gordeyeva, K., Bergström, L., and Fall, A.B. (2016). Directional freezing of nanocellulose dispersions aligns the rodlike particles and produces lowdensity and robust particle network. *Biomacromolecules* 17: 1875–1881.

28 Yang, X. and Cranston, E.D. (2014). Chemically crosslinked cellulose nanocrystal aerogels with shape recovery and superabsorbent properties. *Chem. Mater.* 26: 6016–6025.

29 Jiang, F. and Hsieh, Y.L. (2014). Super water absorbing and shape memory nanocellulose aerogels from TEMPOoxidized cellulose nanofibrils via cyclic freezingthawing. *J. Mater. Chem. A* 2: 350–359.

30 Freytag, A., SanchezParadinas, S., Naskar, S. et al. (2016). Versatile aerogel fabrication by freezing and subsequent freezedrying of colloidal nanoparticle solutions. *Angew. Chem. Int. Ed.* 55: 1200–1203.

31 Zhang, H., Lee, J.Y., Ahmed, A. et al. (2008). Freezealign and heatfuse: microwires and networks from nanoparticle suspensions. *Angew. Chem. Int. Ed.* 47: 4573–4576.

32 Shen, X., Chen, L., Li, D. et al. (2011). Assembly of colloidal nanoparticles directed by the

microstructures of polycrystalline ice. *ACS Nano* 5: 8426–8433.

33 Qian, L., Ahmed, A., GlennonAlty, L. et al. (2015). Patterned substrates fabricated by a controlled freezing approach and biocompatibility evaluation by stem cells. *Mater. Sci. Eng. C* 49: 390–399.

34 Yan, J., Chen, Z., Jiang, J. et al. (2009). Freestanding allnanoparticle thin fibers: a novel nanostructure bridging zero and onedimensional nanoscale features. *Adv. Mater.* 21: 314–319.

35 Lee, D., Zhang, C., and Gao, H. (2014). Facile production of polypyrrole nanofibers using a freezedrying method. *Macromol. Chem. Phys.* 215: 669–674.

36 Kirsebom, H., Mattiasson, B., and Galaev, I.Y. (2009). Building macroporous materials from microgels and microbes via onestep cryogelation. *Langmuir* 25: 8462–8465.

37 Yao, X., Yao, H., and Li, Y. (2009). Hierarchically aligned porous scaffold by ice segregationinduced selfassembly and thermally triggered electrostatic selfassembly of oppositely charged thermosensitive microgels. *J. Mater. Chem.* 19: 6516–6520.

38 Kirsebom, H., Mattiasson, B., and Galaev, I.Y. (2010). Ultrafast responsive poly(*N* isopropylacrylamide) gel produced by cryostructuring of selfcrosslinkable polymer microgels. *Macromol. Rapid Commun.* 31: 1095–1100.

39 Gao, H.L., Xu, L., Long, F. et al. (2014). Macroscopic freestanding hierarchical 3D architectures assembled from silver nanowires by ice templating. *Angew. Chem. Int. Ed.* 53: 4561–4566.

40 Wang, X., Chen, Y.C., and Li, B. (2015). Aligning 3D nanofibrous networks from self assembled phenylalanine nanofibers. *RSC Adv.* 5: 8022–8027.

41 Wu, J. and Meredith, J.C. (2014). Assembly of chitin nanofibers into porous biomimetic structures via freeze drying. *ACS Macro Lett.* 3: 185–190.

42 Bouville, F., Maire, E., and Deville, S. (2014). Selfassembly of faceted particles triggered by a moving ice front. *Langmuir* 30: 8656–8663.

43 Hunger, P.M., Donius, A.E., and Wegst, U.G.K. (2013). Platelets selfassembly into porous nacre during freeze casting. *J. Mech. Behav. Biomed. Mater.* 19: 87–93.

44 Bouville, F., Maire, E., Meille, S. et al. (2014). Strong, tough and stiff bioinspired ceramics from brittle constitutes. *Nat. Mater.* 13: 508–514.

45 Liu, Z., Xu, K., She, P. et al. (2016). Selfassembly of 2D MnO_2 nanosheets into high purity aerogels with ultralow density. *Chem. Sci.* 7: 1926–1932.

46 Kim, J.W., Tazumi, K., Okaji, R., and Ohshima, M. (2009). Honeycomb monolith structured silica with highly ordered, threedimensionally interconnected macroporous walls.

Chem. Mater. 21: 3476–3478.

47 Colard, C.A.L., Cave, R.A., Grossiord, N. et al. (2009). Conducting nanocomposite polymer foams from icecrystaltemplated assembly of mixtures of colloids. *Adv. Mater.* 21: 2895–2898.

48 Rajamanickam, R., Kumari, S., Kumar, D. et al. (2014). Soft colloidal scaffolds capable of elastic recover after large compressive strains. *Chem. Mater.* 26: 5161–5168.

49 Shi, Q., An, Z., Tsung, C.K. et al. (2007). Icetemplating of core/shell microgel fibers through 'brickandmortar' assembly. *Adv. Mater.* 19: 4539–4543.

50 Shi, Q., Liang, H., Feng, D. et al. (2008). Porous carbon and carbon/metal oxide microfibers with wellcontrolled pore structure and interface. *J. Am. Chem. Soc.* 130: 5034–5035.

10
Other Developments and Perspectives in the Fabrication of New Materials Facilitated by Freezing and Freezedrying

The icetemplating approach for the preparation of porous and functional materials is a two stage process. The templates are first created by a freezing step and then removed in the second stage, usually by a freezedrying process. Ice templating is often applied to solutions or suspensions (mostly waterbased), with the solutes or dispersants to determine what materials may be fabricated. The icetemplating method may be also used in systems based on organic solvents or in combination with other techniques, in order to produce materials with better control in porosity/morphology or more functions. Some of these have been mentioned in previous chapters but will be highlighted in this chapter. There are also developments in preparation of new materials, which are promoted by the freezing stage or the freezedrying step. These will be also discussed. A general summary and perspective is given at the end of the chapter.

10.1 Combining Icetemplating and Other Techniques

10.1.1 Ice Templating and Emulsion Templating

Emulsion templating is an effective route to the preparation of porous materials. When increasing the volume of the internal droplets to above 74.05 v/v%, the emulsions are called high internal phase emulsions (HIPEs). HIPEs can be used to fabricate highly interconnected macroporous materials [1]. While the continuous phase containing monomers may be polymerized to lock in the emulsion structure [2], the emulsions can be frozen and freeze dried to remove the solvents from both the continuous phase and droplet phase. The resulting porous materials exhibit both emulsiontemplated cellular pores and icetemplated pores [3]. By choosing suitable precursor materials, the scaffolds prepared via the combined approaches can be better for targeted applications, e.g. for bone tissue engineering [4]. In principle, any emulsion can be frozen and freezedried. However, most reports are based on oilinwater (O/W) emulsions [1]. Considering the limitations of the freezedryer used, the selected organic solvents should have relatively high boiling points so that the freezedrying process can be completed without damage or partial collapse of the emulsiontemplated structure.

In addition to the emulsions formed with surfactants or polymers, Pickering emulsions (where particles are used as the stabilizers) may be freezedried to produce porous structures. For example, a Pickering emulsion was formed by emulsifying hexane into aqueous medium containing silica nanoparticles (24 wt%) and poly(*N*isopropylacrylamide)based microgels

(0.8 wt%). The emulsion was freezedried and then calcined at 950 °C for 2 h [5]. As shown in Figure 10.1, the resulting material exhibits emulsiontemplated macropores (10–30 μm), interconnected windows (3–5 μm), and nanoporous walls (80 nm, from the microgel templating). Starch granules were also employed to form emulsion. When nonvolatile oils such as Miglyol 812 and peanut oil were used as the internal phase, the freezedrying process produced oilcontaining (as high as 80%) powders that could be readily reconstituted [6]. The porous polymer structures fabricated by emulsionfreezedrying have been used as scaffolds to absorb organic solution or oils. In the former case, after evaporation of organic solvent, organic nanoparticles were formed within the porous materials. Aqueous nanoparticle (organic or drug) dispersions are produced upon dissolution of the composites [7, 8]. When oils (both volatile and nonvolatile) are absorbed into the porous polymer, the composites can be readily dissolved, resulting in instant formation of emulsions [9].

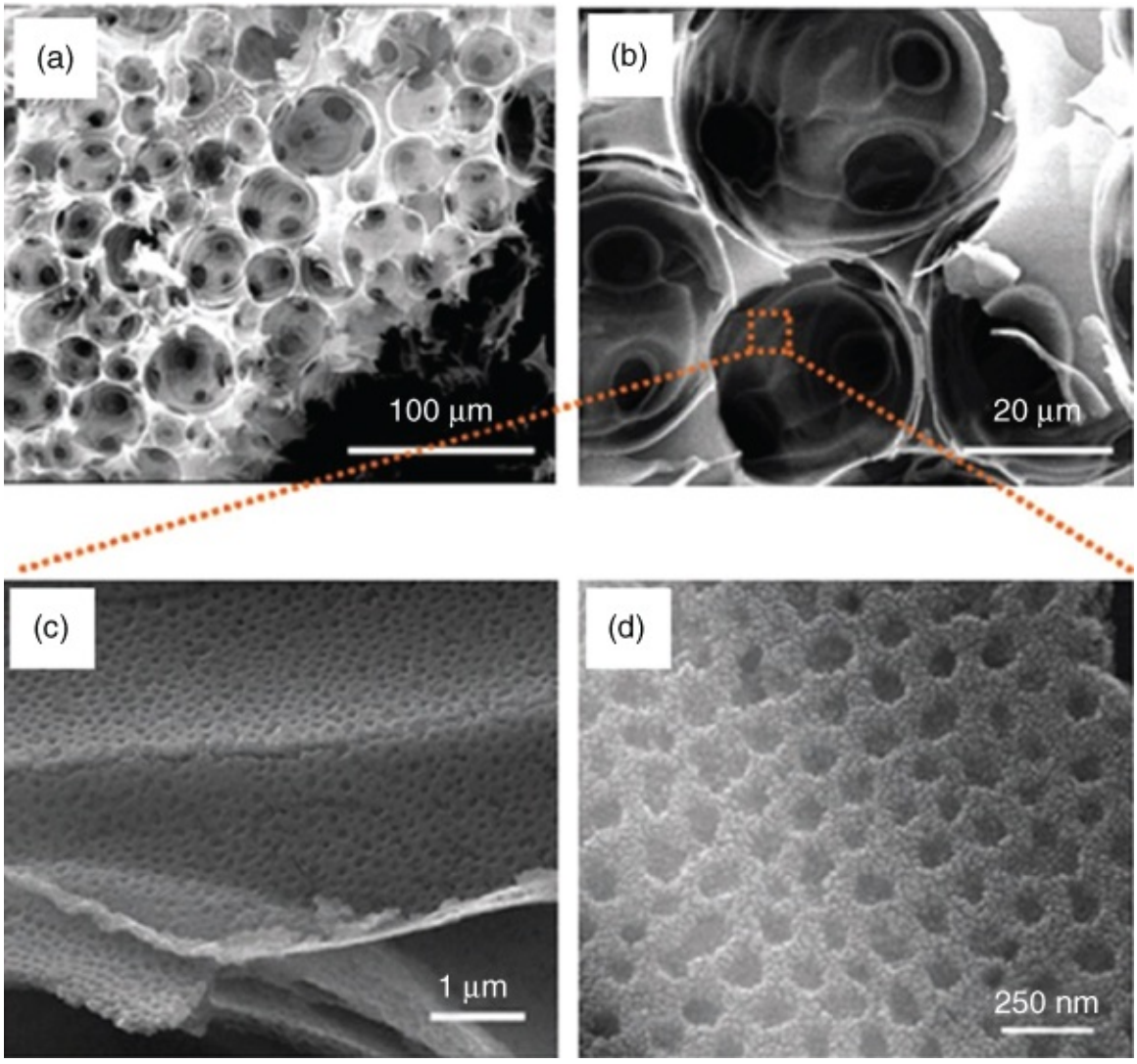

Figure 10.1 SEM images show the porous structures prepared by freezedrying a Pickering emulsion using silica nanoparticles (40 nm) and polymer microgel (250 nm) as stabilizers. (a) and (b) The interconnected emulsiontemplated cellular pores; (c) and (d) The pore structure of the cellular walls after removing microgel particles by calcination at 950 °C for 2 h.

Source: Li et al. 2010 [5]. Reprinted with permission from Royal Society of Chemistry.

Porous materials are produced when freezedrying the emulsions where the internal droplets consist of solvent only. When a solution is emulsified into another solution containing surfactant and/or polymer, the freezedrying process can lead to in situ formation of nanoparticles or microparticles within the porous structures. This has been demonstrated by the formation of organic nanoparticles or drug nanoparticle within porous polymers [10, 11]. An organic solution (hydrophobic dye Oil Red O dissolved in cyclohexane) was dispersed in aqueous solution containing surfactant and hydrophilic polymer poly(vinyl alcohol) (PVA) [10]. Similarly, organic solutions containing hydrophobic drug compounds could be used [11]. The freezedrying of the emulsions led to the formation of hydrophobic nanoparticles within porous PVA, all in one step. The porous PVA could be dissolved to release the nanoparticles and stable aqueous nanoparticle dispersions were formed instantly. If monomers instead of polymers are present in the continuous phase, the monomers can be polymerized and crosslinked first, followed by emulsion freezedrying. The organic nanoparticles formed may be either released by simple diffusion or facilitated by triggers such as temperature change [12]. However, porous microparticles embedded in the porous matrix can be formed when a hydrophobic polymer is dissolved in the internal organic phase, after freezedrying the emulsions. A directional freezing process results in the production of uniquely aligned porous microparticles [13]. In a recent progress, emulsions have been formed from lightly crosslinked branched block copolymers only. The emulsionfreezedrying approach was then employed to generate drug nanoparticles with high yield [14].

10.1.2 Gelation/Crosslinking and Ice Templating

Conventionally, solutions or suspensions are directly freezedried. This usually produces powders or fragile porous materials. In order to enhance the mechanical stability, the solutions or suspensions may be crosslinked physically or chemically and subsequently subjected to a freezedrying process. Gelatin is one of the most commonly used gelation systems, particularly when preparing porous ceramics. Gelatin can be dissolved in warm solution and the gelation conveniently occurs when the warm solution/suspension cools down [15]. Additional templates such as salt particles may be incorporated to tune the porosity of the freezedried scaffolds [16]. Another widely used gelation system is the freezing and thawing of PVA solution. The gelation is induced by hydrogen bonding and crystallization of contacted chains. The number of freeze–thaw cycles can influence the crystallites' crosslinking density and the strength of the gels. The freeze–thaw process is usually carried out in a freezer (−20 °C) and then allowed to thaw at room temperature. Recently, when a directional freezing process was employed during the freezing step, PVA hydrogel with gradient stiffness was produced and was further used to investigate stem cell differentiation and cell migration in terms of scaffold stiffness [17]. Monomer solutions (e.g. resorcinol–formaldehyde resins) or emulsions containing monomers in the continuous phase [12] can be polymerized and crosslinked. The subsequent freezedrying process produces highly porous materials with minimal shrinkage. Similarly, a sol–gel process (e.g. from silica sol) can be combined with a freezedrying process to fabricate stable monoliths with welldefined icetemplated macropores [18].

10.1.3 Ice Templating with Green Solvents

There are many occasions where water cannot be used as solvent. For example, hydrophobic polymers or organic compounds are insoluble in water. The compounds or the biomolecules may be hydrolysed or destabilized by the presence of water. This is the reason for organic solutions or suspensions being employed in icetemplating processes [19]. In an effort to replace organic solvents with a green solvent, sugar acetate solutions in compressed CO_2 were prepared (a high pressure vessel with valves required) and then frozen in liquid nitrogen [20]. Unlike the use of organic solvents where the freezedrying step is usually required to remove the frozen solvent, the frozen CO_2 solution could be easily allowed to warm up (e.g. in a fume hood at room temperature) and released as gaseous CO_2 with the valves open [20]. There is no residual solvent in the resulting material and, therefore, this method can be potentially very useful for biomaterials. However, the limitations for this method are that high pressure vessels or reactors have to be used and that not many compounds or polymers are soluble in compressed CO_2 or swollen by CO_2.

Another type of green solvents is ionic liquids (ILs). ILs are usually regarded as molten salts with melting points below 373 K [21]. The selection of anions and cations is crucial as the interactions between them destabilize the tendency to form solidphase crystals. The common properties of ILs include high electrical conductivity, liquid phase in a wide temperature range, and negligible vapour pressure [21, 22]. ILs are often regarded as green solvents because of the negligible vapour pressure. For the same reason, it is not possible to remove ILs by freezedrying. Gutièrrez et al. developed a method to incorporate bacteria in deep eutectic solvents (DES) via freezedrying for enhanced biocatalytic reactions [23]. DES are a class of ILs obtained by complexion of quaternary ammonium salts with hydrogen bond donors. The presence of water hydrates the ions and destroys the properties of the ILs. By dispersing bacteria in minimal media in an aqueous solution of DES, the freezedrying process then removes the water and incorporates the bacteria in pure DES [23].

The freeze–thaw process has been applied to lignocellulose–IL solutions. Lignocellulose aerogels were produced after rinsing ILs with acetone [24] or water [25], followed by supercritical CO_2 drying. The processing parameters included freeze–thaw temperatures (e.g. −20 to 20 °C [24, 25], −196 to 20 °C), cycles and frequency of freeze–thaw, and solvents used to wash ILs. These parameters could make a difference in producing 2D sheetlike structures or 3D fibrous networks [24, 25]. Song et al. employed a directional freezing process to make aligned porous scaffolds of PVA containing halloysite nanotubes [26]. The scaffolds could absorb the IL 1butyl3methylimidazolium tetrafluoroborate, generating a composite with anisotropic ionic conductivity. The ionic conductivity reached 5.2×10^{-3} S cm^{-1} at 30 °C in the direction parallel to the freezing direction, which was more than 500 times higher than the value obtained in the direction perpendicular to the freezing direction [26].

10.2 Freezinginduced Selfassembly

The selfassembly of particles, including nanospheres, nanowires, and platelets, can be facilitated by the freezing process. The selfassembly is the result of particle concentration and exclusion from the moving ice front. Recently, Albouy et al. reported the selfassembly of amphiphilic molecules, the commercial block copolymer P123, induced by the freezing process [27]. The freezing process was monitored using in situ small angle Xray scattering (SAXS). At the start, there were only unimers. The freezing ice front excluded P123 molecules and concentrated P123 and led to the selfassembly of P123 micelles to form ordered mesophases (Figure 10.2). Ordered structures such as hexagonally closed packed (hcp) sphere aggregates and 2D hexagonal phase were detected by SAXS. This phenomenon is similar to the evaporationinduced surfactant selfassembly where the evaporation of the solvent concentrates the solution and induces the selfassembly of the surfactant molecules into different mesophases [28]. The evolution of P123 selfassembly induced by the freezing process was summarized using a concentration–temperature diagram [27]. This finding may be very useful for the construction of soft matters and mesoporous materials.

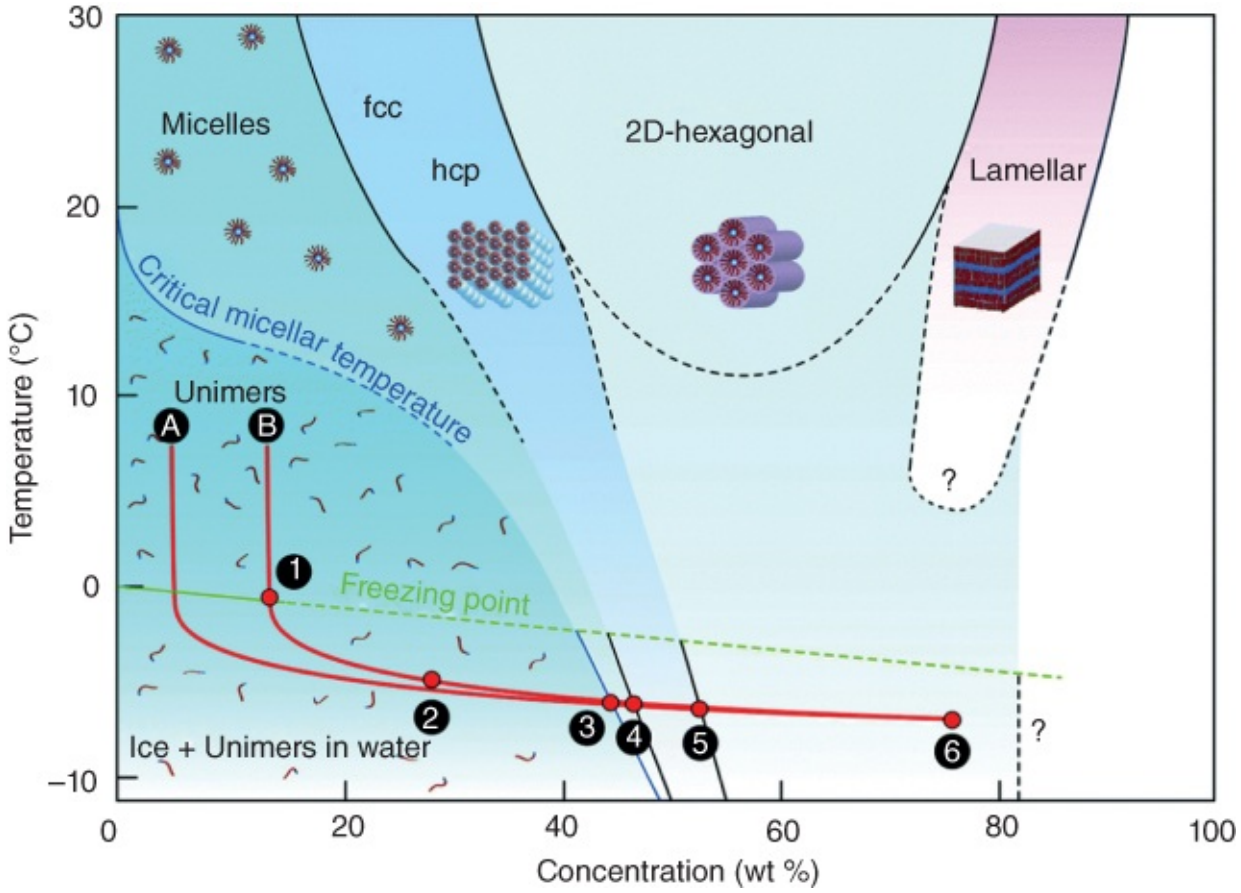

Figure 10.2 Scheme showing the freezinginduced selfassembly of P123 in water in a concentration–temperature diagram.

Source: Albouy et al. 2017 [27]. Reprinted with permission from Royal Society of Chemistry.

10.3 Reaction and Polymerization in Frozen Solutions

Chemical reactions usually occur smoothly and fast under the freely diffusing condition in

homogeneous solutions. However, some reactions have been reported to be accelerated in the frozen state [29]. It should be pointed out that a frozen solution is not a frozen solid. For solutions containing two or more components, the frozen solution usually refers to the temperature below the freezing point of the solvent while the frozen solid state indicates the solution frozen below the eutectic point (Figure 10.3) [29]. In the frozen state, due to the effect of freezing point depression resulting from solution concentration, there are concentrated liquid solutions still present, which may accelerate the reactions in spite of low temperatures [29, 30]. For a solution containing both water and an organic solvent such as methanol, below the icefreezing temperature, there are puddles of methanol that can induce reactions in frozen solutions [31]. The other acceleration mechanisms include: (i) the position effect induced by solvent crystallization and orientation of reactants; (ii) the catalytic activity offered by the surface of the frozen solvent; and (iii) enhanced proton or electron transfer in the frozen solution [32, 33]. For accelerated reactions in frozen state, it is usually difficult to point out the exact mechanism. It is possible that multiple mechanisms may contribute to the acceleration. Naidu et al. reported the highly chemoselective Michael addition of amines and thiols to the dehydroalanine side chain of nocathiacins in water with good yields. The reactions were carried out at −20 °C. The selectivity and yields were much better than the reactions performed at room temperature [34]. Accelerated glycosylation using thiomethyl glycosides in *p*xylene was observed when the reactions were performed below the freezing point of *p*xylene. High yields were recorded in frozen *p*xylene while only marginal yields were obtained for the reactions at room temperature [35].

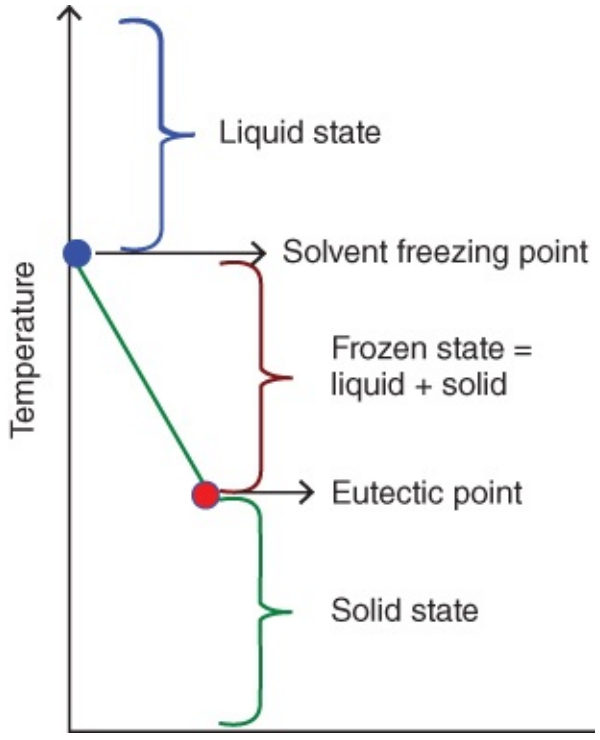

Figure 10.3 Diagram of a solution containing two or more components under different states.

Source: Adapted from Pincock 1969 [29]. http://pubs.acs.org/doi/abs/10.1021/ar50016a001?journalCode=achre4.

Accelerated polymerization has also been reported in frozen solvents. For example, the polymerization rates of *N*carboxyamino acid anhydrides were found to be at least 10 times

higher in frozen dioxane between +5 °C and −26 °C than in liquid systems [32]. The ice crystals may be also employed as templates in fabricating nanofibers and 3D porous structures. Ma et al. fabricated polyaniline microflakes by freezing aqueous solution containing $H_4SiW_{12}O_{40}$, $FeCl_3$ and aniline in freezer at −10 °C for 20 days [36]. The solutes were excluded from the ice crystals and polymerized between the layered ice crystals, producing microflakes. At a higher magnification by electron microscopic imaging, it was revealed that the microflakes consisted of polyaniline nanofibers in the range of 22–32 nm [36].

Interfacial polymerization involving the frozen solvent crystals has been used to produce porous or nanostructured materials. Qi et al. prepared highly conductive polypyrrole films by freezing a twophase system (pyrrole in cyclohexane + water containing ammonium persulfate (APS) as oxidant and HCl as dopant) in a freezer at −20 °C for 4 days [37]. Figure 10.4 shows schematically how the interfacial polymerization method works. After freezing, liquid aniline is excluded from frozen cyclohexane and fills the interstices between ice crystals due to gravity and capillary effects. The oxidant and dopant are also excluded from the ice crystals that initiate the redox polymerization of pyrrole. The polypyrrole film prepared this way showed a high conductivity up to 2000 S cm^{-1} [37]. When a solvent with lower melting point is mixed with aqueous solution and a frozen polymerization is followed, polymer capsules may be fabricated. For example, when diethyl ether was added and mixed with aqueous solution containing $H_4SiW_{12}O_{40}$, $FeCl_3$ and aniline and the resulting suspensions were frozen at −18 °C for 20 days, hollow hemispheres of polyaniline were produced (Figure 10.5) [38]. This resulted from the droplets of diethyl ether in ice crystals and the excluded solutes reacting at the interface between ice and diethyl ether droplets. The formed polyaniline nanoparticles at the curved interface precipitated to eventually generate hollow hemispheres [38].

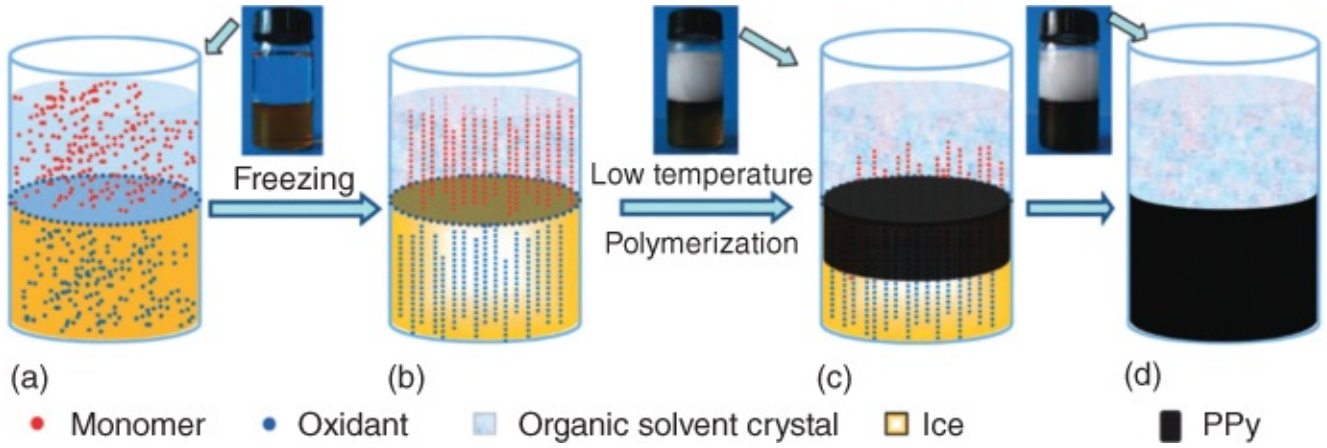

Figure 10.4 Schematic shows the preparation of polypyrrole films via freezing interfacial polymerization.

Source: Qi et al. 2012 [37]. Reprinted with permission from Royal Society of Chemistry.

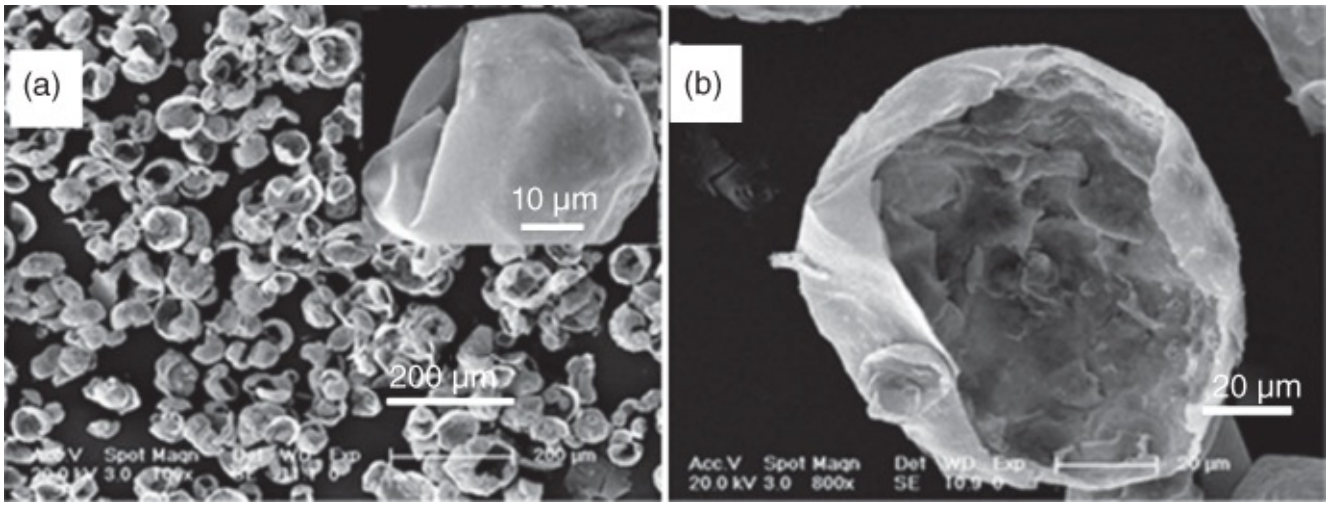

Figure 10.5 Polyaniline hemispheres synthesized via an icetemplating method with the addition of diethyl ether into the aqueous solution containing reactants. (a) An overview of the hemispheres, with the inset showing the surface of one hemisphere. (b) The magnified internal structure of one hemisphere.

Source: Ma et al. 2010 [38]. Reprinted with permission from John Wiley and Sons.

Wang et al. reported the formation of uniform polyaniline nanotubes by combining freezing and nanorod templating to control the diffusion of aniline and APS at the polyaniline interface [39]. Aniline and amino acids were complexed to form nanorods in the solution. After freezing, APS was excluded from the ice crystals and diffused to the nanorods for the reaction with aniline. As the reaction occurred in the frozen solution, the diffusion of both aniline and APS across the polyaniline interface was similar to the preparation of hollow inorganic nanotubes via the Kirkendall effect. As shown in Figure 10.6, these polyaniline nanotubes are quite uniform, with an average outer diameter of 45 nm and inner diameters in the range of 5–10 nm. Ndoped carbon nanotubes could be readily formed by carbonization of polyaniline nanotubes in argon at 800 °C [39].

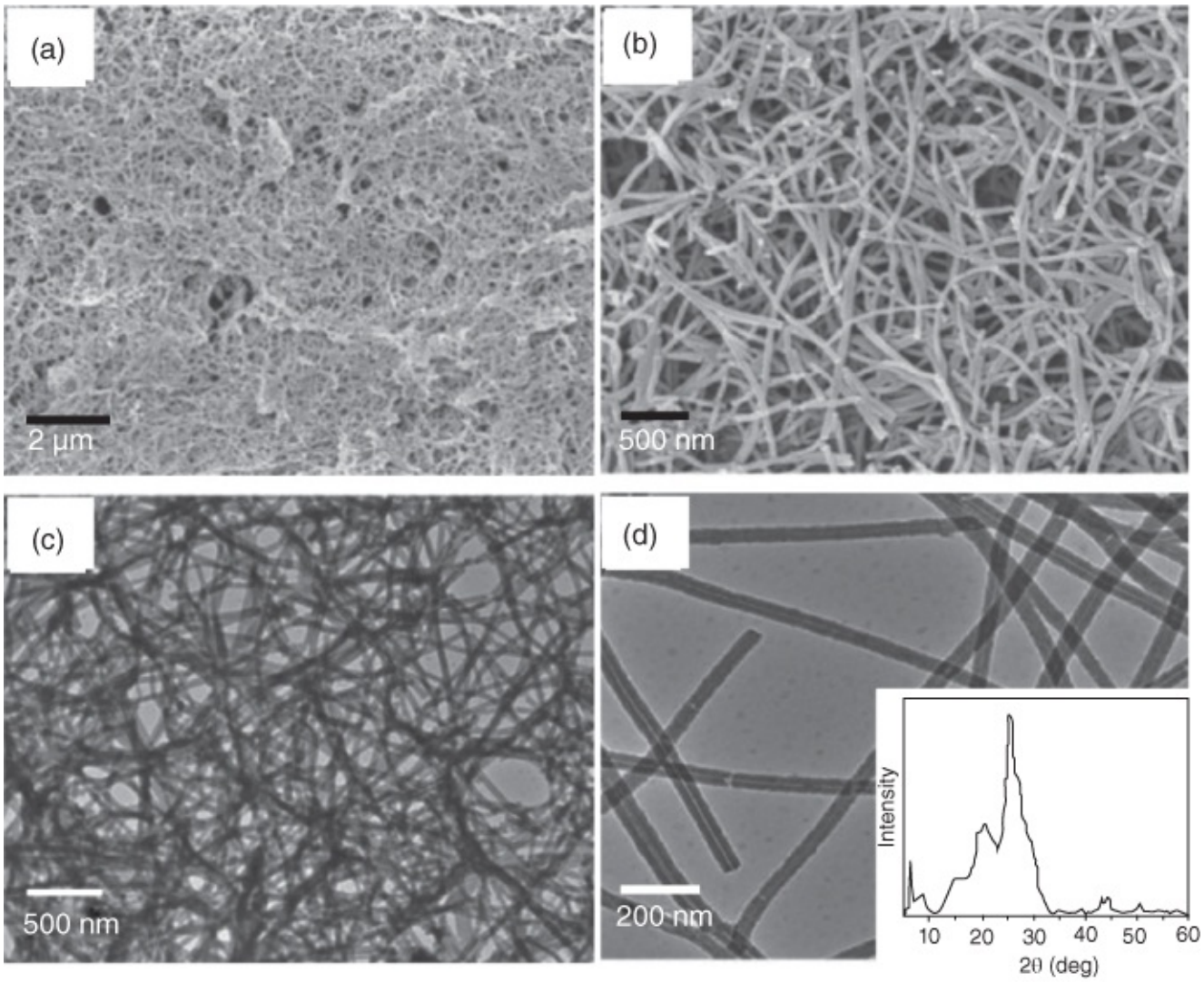

Figure 10.6 The morphology of polyaniline nanotubes synthesized via a frozen polymerization approach. (a) and (b) SEM images at different magnifications. (c) and (d) TEM images at different magnifications. The inset shows the XRD pattern of the nanotubes.

Source: Wang et al. 2015 [39]. Reprinted with permission from John Wiley and Sons.

Cryogels have been widely investigated by frozen polymerization, which is covered in Chapter 4. Instead of simply placing the solutions in a freezer for extended times, UVfacilitated frozen polymerization has been used [40, 41]. These systems usually contain acrylate monomers and photoinitiators. This method can produce highly crosslinked and strong porous polymers or anisotropic hydrogels, templated from the orientated ice crystals [40, 41].

10.4 Icetemplated Hierarchically Porous Materials Containing Micropores

Owing to the size of the ice crystals, icetemplated materials always exhibit macropores in the range of microns. By choosing different additives, e.g. dextran, it is possible to reduce the icetemplated pores to the nanometer range [42]. By using mixing solvents at eutectic points, mesopores in icetemplated materials can be generated [43]. Mesopores may be also formed

from the interstitial spaces between packed particles after freezedrying particle suspensions [44]. However, by all means, it is highly challenging to generate micropores in the ice templated materials (i.e. with the presence of icetemplated pores) although the freeze drying process is effective in producing aerogels or microporous metal–organic frameworks (MOFs) [45, 46].

This issue may be addressed by applying the icetemplating method to soluble microporous materials, the precursors of microporous materials, or the suspensions of particles containing micropores. There are many types of microporous materials, for example, zeolites, carbon, polymers of intrinsic microporosity (PIM) [47], MOFs [48], organic cages, and covalent organic frameworks (COFs) [49]. The icetemplating process always begins with a solution or suspension. It is therefore straightforward to directly freezedry the suspensions of the abovementioned particles with microporosity. This can fabricate the icetemplated materials with microporosity. However, there is a disadvantage associated with this process. Because surfactants and polymeric stabilizers are usually required to form stable suspensions before the freezedrying process, the presence of these additives may block the micropores or at least reduce the microporosity proportionally.

The icetemplating approach by processing solutions can address this problem. However, many of the microporous materials are crosslinked or frameworks and they are insoluble in common solvents. These include zeolites, carbon, COFs, and MOFs. Some of the microporous materials, organic cages and PIMs can be dissolved in organic solvents. As such, these microporous materials are dissolved in organic solvents and processed via the icetemplating procedures to produce hierarchical monoliths with microporosity. Owing to its high solubility in chloroform, the organic cage CC13 solution in chloroform was directionally frozen and freezedried to generate a monolith [50]. Figure 10.7a and b shows the aligned macropores by scanning electron microscopic (SEM) imaging. This macroporosity, with the pore sizes in a wide range but mainly around 100 μm, is also confirmed by Hg intrusion porosimetry (Figure 10.7c). The gas sorption data based on H_2 and N_2 uptake show the presence of micropores (Figure 10.7d). H_2 uptake at 77 K and 1 bar was around 4.5 mmol g^{-1} while N_2 uptake was only about 1.9 mmol g^{-1} with a BET surface of 80 m^2 g^{-1}. The surface area is much lower than that of the crystalline CC13. This is attributed to the constraining of the pathway through the structure by the loss of order, limiting the access of relatively large molecules. Similarly, PIM1 was dissolved in chloroform. After directional freezing and freezedrying of the solution, a monolith with wellaligned macropores and porous walls was formed. This monolith exhibited an intrusion volume of 4.21 cm^3 g^{-1} and a BET surface area of 766 m^2 g^{-1}. Mesopores up to 30 nm and a sharp peak around 1 nm were obtained from N_2 sorption for this material [50].

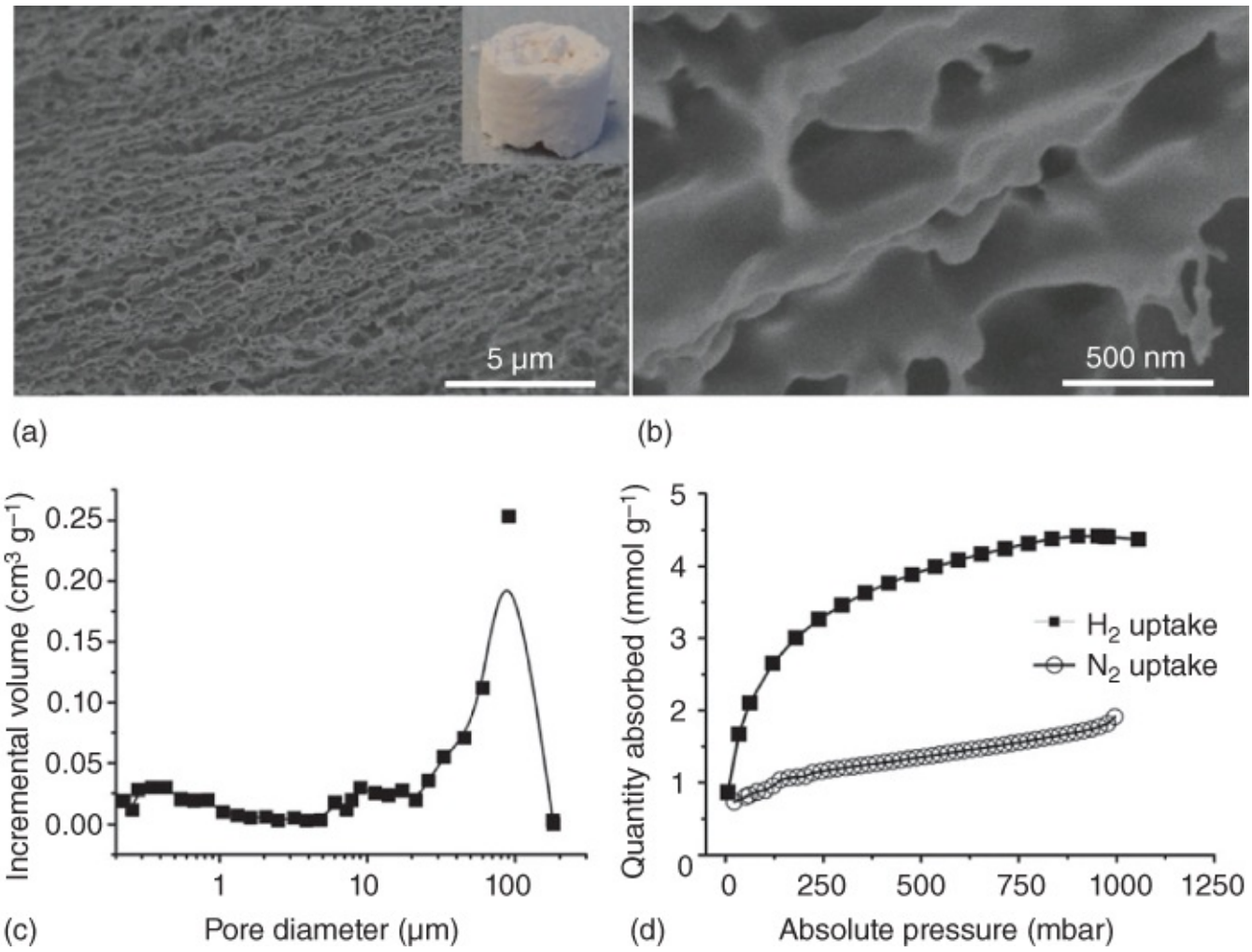

Figure 10.7 The aligned porous organic cage (CC13) prepared by directional freezing and freezedrying of CC13 solution in chloroform. (a) and (b) The pore structure. (c) The macropore size distribution measured by Hg intrusion porosimetry. (d) The H_2 and N_2 uptake of the CC13 monolith.

Source: Ahmed et al. 2015 [50]. Reprinted with permission from Royal Society of Chemistry.

HKUST1 is one of the earliest and most widely investigated MOFs and can be synthesized under mild conditions. Ahmed et al. prepared HKUST1 monolith in a steel column by simply mixing the precursor powders of copper acetate and benzene tricarboxylate (BTC), soaked with a mixture solvent of ethanol:H_2O, and then heated at mild temperatures of 25–120 °C [51]. The synthesized monolith showed a surface area of 1240 $m^2\ g^{-1}$ and enhanced mechanical stability. In addition to the intrinsic micropores of HKUST1, this monolith exhibited mesopores that were generated from the aggregated nanoparticles during the synthesis. An icetemplating method was further developed to fabricate HKUST1 monoliths with macropores [50]. In this method, the solution of copper acetate + BTC in dimethyl sulfoxide (DMSO) was directionally frozen and freezedried to produce a monolith with the ice templated aligned pores. The monolith showed the typical powder Xray diffraction (PXRD) pattern of HKUST1 but the crystallinity could be further improved by posttreatment in ethanol at 120 °C. As shown in Figure 10.8a and b, the aligned macropores can be clearly seen

while the pore wall surface is quite smooth. The N_2 sorption analysis gave a surface area of 870 $m^2\ g^{-1}$, a micropore volume of 0.406 $cm^3\ g^{-1}$ (with a sharp peak around 1 nm, Figure 10.8c), and a mesopore volume of 0.271 $cm^3\ g^{-1}$. The bimodal macropore size distribution (aligned macropores around 10 μm and the macropores of 0.4 μm in the wall) was characterized by Hg intrusion porosimetry and is shown in Figure 10.8d [50]. A high intrusion volume of 8.30 $cm^3\ g^{-1}$ was obtained. It was believed that the monolith was formed during the freezedrying stage because the freezing process was fast and the temperature (in liquid nitrogen) was very low. Indeed, freezedrying is an effective technique for the synthesis of cocrystals and the manufacture of pharmaceutical dosage forms. The cocrystals can be formed via the amorphous phase during the solvent sublimation stage for the amorphous materials with glass transition temperatures at or below ambient temperature [52].

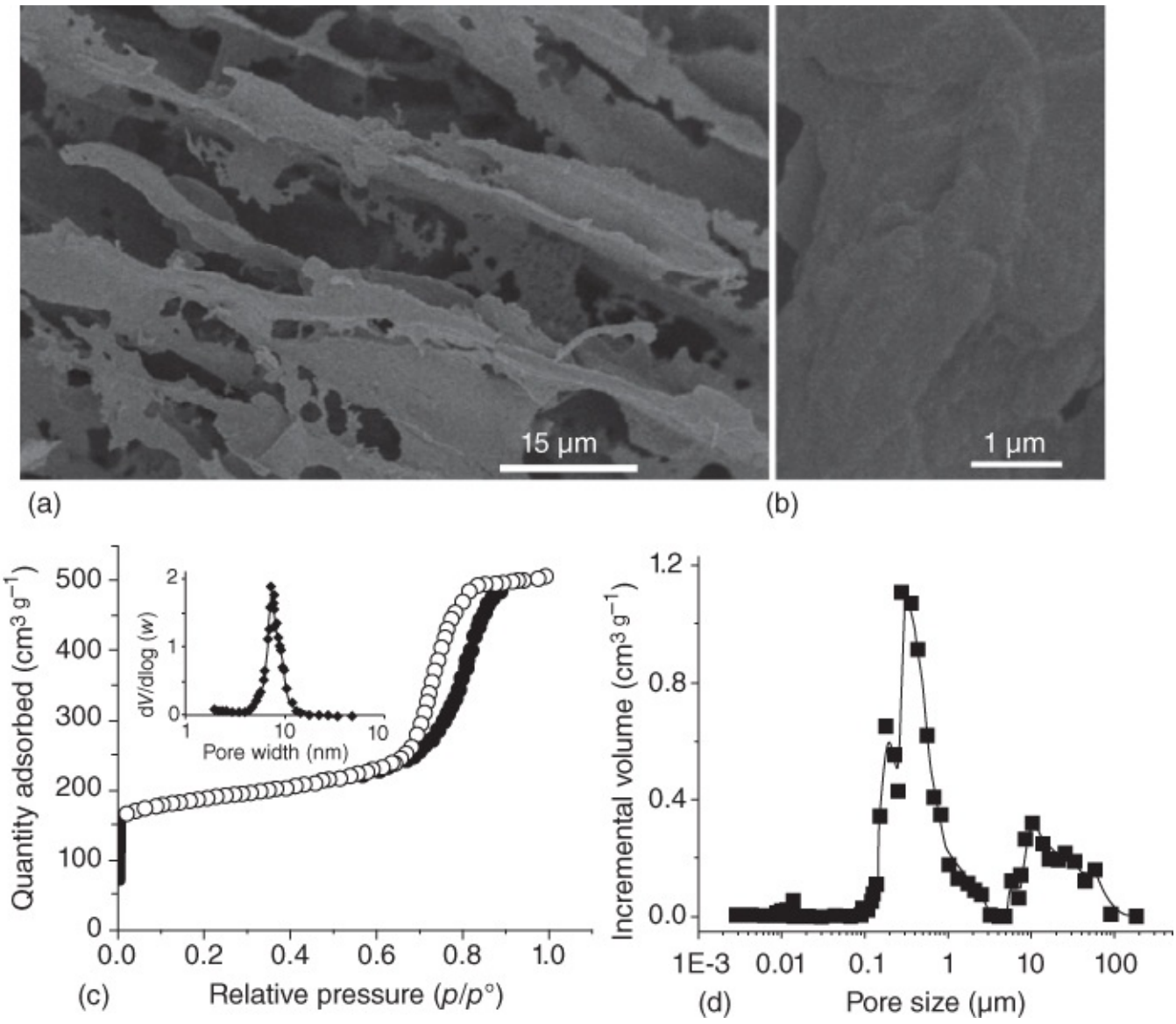

Figure 10.8 Characterization of aligned porous MOF (HKUST1) monolith fabricated by an icetemplating approach. (a) The pore structure. (b) The surface morphology. (c) The N_2 sorption isotherm with the inset showing the micropore size distribution. (d) The macropore size distribution by Hg intrusion porosimetry.

Source: Ahmed et al. 2015 [50]. Reprinted with permission from Royal Society of Chemistry.

10.5 General Summary and Perspectives

Freezing and freezedrying are the key steps of the icetemplating method although the frozen solvent may be removed by other methods instead of freezedrying. Freezing of solutions and colloids has been known in nature (e.g. sea ice, frost heaving) and widely used in cryopreservation and food engineering (e.g. ice cream, frozen dessert) [53]. With regards to freezing, freezedrying has been a highly effective drying technique for pharmaceutical formulations and materials science. In this book, we have focused on the use of ice templating and freezedrying for different types of porous materials and the use of freezedrying for pharmaceutical and food studies is also described. The emphasis has been on the fabrication

methods, processing parameters, and description of the typical applications of each type of icetemplated materials. We believe that most types of the icetemplated materials are covered in this book. The aim is to give the readers a clear picture of how the icetemplating method may be used for preparation of various materials. In spite of our best efforts, there is a possibility that some unique materials fabricated by ice templating may not be included. Hopefully, this will be improved in a future edition.

With the progress so far, ice templating has been demonstrated to be highly efficient for materials fabrication. The uniqueness of this method lies in its simplicity and versatility. The prepared materials exhibit highly interconnected pore structures, anisotropic pores (aligned channels or layered structure), and fibrous networks, which may be further used to produce strong and functional composites or other nanostructured materials. Other procedures or techniques may be employed in combination with ice templating to enhance mechanical properties or offer additional functionalities. However, the challenges remain on the production of largescale materials with reproducible pore morphology and porosity. Formulations, processing parameters, and novel freezing procedures/devices will be continuously developed and optimized for this purpose. To better control the structure of materials, the development of freezing theory and experimental observation to provide evidence for freezing mechanisms are still the essential part in the use of the icetemplating method. For materials engineers and scientists, we believe the focus will be on selecting functional building blocks and developing methods and procedures to produce materials with required pore structure, strength, functionality and other properties for the target applications. Therefore, it is important to understand what materials and their characteristics are required and how the icetemplating (freezing, freezedrying) method, or in combination with other techniques, may be developed accordingly to obtain the desired materials.

References

1 Zhang, H. and Cooper, A.I. (2005). Synthesis and applications of emulsiontemplated porous materials. *Soft Matter* 1: 107–113.

2 Zhang, H. and Cooper, A.I. (2002). Synthesis of monodisperse emulsiontemplated polymer beads by oilinwaterinoil (O/W/O) sedimentation polymerization. *Chem. Mater.* 14: 4017–4020.

3 Qian, L., Ahmed, A., Foster, A. et al. (2009). Systematic tuning of pore morphologies and pore volumes in macroporous materials by freezing. *J. Mater. Chem.* 19: 5212–5219.

4 Sultana, N. and Wang, M. (2012). PHBV/PLLAbased composite scaffolds fabricated using an emulsion freezing/freezedrying technique for bone tissue engineering: surface modification and in vitro biological evaluation. *Biofabrication* 4: 015003.

5 Li, Z., Wei, X., Ming, T. et al. (2010). Dual templating synthesis of hierarchical porous silica materials with three orders of length scale. *Chem. Commun.* 46: 8767–8769.

6 Marefati, A., Rayner, M., Timgren, A. et al. (2013). Freezing and freezedrying of Pickering emulsions stabilized by starch granules. *Colloid Surf. A* 436: 512–520.

7 Qian, L., Ahmed, A., and Zhang, H. (2011). Formation of organic nanoparticles by solvent evaporation within porous polymeric materials. *Chem. Commun.* 47: 10001–10003.

8 Roberts, A.D. and Zhang, H. (2013). Poorly watersoluble drug nanoparticles via solvent evaporation in watersoluble porous polymers. *Int. J. Pharm.* 447: 241–250.

9 Qian, L. and Zhang, H. (2010). Direct formation of emulsions using watersoluble porous polymers as sacrificial scaffolds. *J. Chem. Technol. Biotechnol.* 85: 1508–1514.

10 Zhang, H., Wang, D., Butler, R. et al. (2008). Formation and enhanced biocidal activity of waterdispersible organic nanoparticles. *Nat. Nanotechnol.* 3: 506–511.

11 Grant, N. and Zhang, H. (2011). Poorly watersoluble drug nanoparticles via an emulsionfreezedrying approach. *J. Colloid Interface Sci.* 356: 573–578.

12 Zhang, H. and Cooper, A.I. (2007). Thermoresponsive "particle pumps": activated release of organic nanoparticles from opencell macroporous polymers. *Adv. Mater.* 19: 2439–2444.

13 Zhang, H., Edgar, D., Murray, P. et al. (2008). Synthesis of porous microparticles with aligned porosity. *Adv. Funct. Mater.* 18: 222–228.

14 Wais, U., Jackson, A.W., Zuo, Y. et al. (2016). Drug nanoparticles by emulsionfreeze drying via the employment of branched block copolymer nanoparticles. *J. Control. Release* 222: 141–150.

15 Fukushima, M. and Yoshizawa, Y. (2014). Fabrication of highly porous silica thermal insulators prepared by gelationfreezing route. *J. Am. Ceram. Soc.* 97: 713–717.

16 Alizadeh, M., Abbasi, F., Khoshfetrat, A.B., and Ghaleh, H. (2013). Microstructure and characteristic properties of gelatin/chitosan scaffold prepared by a combined freeze drying/leaching method. *Mater. Sci. Eng. C* 33: 3958–3967.

17 Kim, T.H., An, D.B., Oh, S.H. et al. (2015). Creating stiffness gradient polyvinyl alcohol hydrogel using a simple gradual freezingthawing method to investigate stem cell differentiation behaviors. *Biomaterials* 40: 51–60.

18 Minaberry, Y. and Jobbágy, M. (2011). Macroporous bioglass scaffolds prepared by coupling solgel with freeze drying. *Chem. Mater.* 23: 2327–2332.

19 Qian, L. and Zhang, H. (2011). Controlled freezing and freeze drying: a versatile route for porous and micro/nanostructured materials. *J. Chem. Technol. Biotechnol.* 86: 172–184.

20 Zhang, H., Long, J., and Cooper, A.I. (2005). Aligned porous materials by directional freezing of solution in liquid CO_2. *J. Am. Chem. Soc.* 127: 13482–13483.

21 Hayes, R., Warr, G.G., and Atkin, R. (2015). Structure and nanostructure in ionic liquids. *Chem. Rev.* 115: 6357–6426.

22 Ahmed, E., Breternitz, J., Groh, M.F., and Ruck, M. (2012). Ionic liquids as crystallisation media for inorganic materials. *CrystEngComm* 14: 4874–4885.

23 Gutièrrez, M.C., Ferrer, M.L., Yuste, L. et al. (2010). Bacteria incorporation in deep eutectic solvents through freezedrying. *Angew. Chem. Int. Ed.* 49: 2158–2162.

24 Li, J., Lu, Y., Yang, D. et al. (2011). Lignocellulose aerogel from woodionic liquid solution (1allyl3methylimidazolium chloride) under freezing and thawing conditions. *Biomacromolecules* 12: 1860–1867.

25 Lu, Y., Sun, Q., Yang, D. et al. (2012). Fabrication of mesoporous lignocellulose aerogels from wood via cyclic liquid nitrogen freezingthawing in ionic liquid solution. *J. Mater. Chem.* 22: 13548–13557.

26 Song, H., Zhao, N., Qin, W. et al. (2015). Highperformance ionic liquidbased nanocomposite polymer electrolytes with anisotropic ionic conductivity prepared by coupling liquid crystal selftemplating with unidirectional freezing. *J. Mater. Chem. A* 3: 2128–2134.

27 Albouy, P.A., Deville, S., Fulkar, A. et al. (2017). Freezinginduced selfassembly of amphiphilic molecules. *Soft Matter* 13: 1759–1763.

28 Brinker, C.J., Lu, Y., Sellinger, A., and Fan, H. (1999). Evaporationinduced self assembly: nanostructures made easy. *Adv. Mater.* 11: 579–585.

29 Pincock, R.E. (1969). Reactions in frozen systems. *Acc. Chem. Res.* 2: 97–103.

30 Pincock, R.E. and Kiovsky, T.E. (1966). Kinetics of reactions in frozen solutions. *J. Chem. Ed.* 43: 358–360.

31 Wang, S.Y. (1961). Photochemical reactions in frozen solutions. *Nature* 190: 690–694.

32 Grant, N.H., Clark, D.E., and Alburn, H.E. (1966). Accelerated polymerization of *N* carboxyamino acid anhydrides in frozen dioxane. *J. Am. Chem. Soc.* 88: 4071–4074.

33 Chen, P. and Meyer, T.J. (1996). Electron transfer in frozen media. *Inorg. Chem.* 35: 5520–5524.

34 Naidu, N., Li, W., Sorenson, M.E. et al. (2004). Organic reactions in frozen water: Michael addition of amines and thiols to the dehydroalanine side chain of nocathiacins. *Tetrahedron Lett.* 45: 1059–1063.

35 Takatani, M., Nakano, J., Arai, M.A. et al. (2004). Accelerated glycosylation under frozen conditions. *Tetrahedron Lett.* 45: 3929–3932.

36 Ma, H., Gao, Y., Li, Y. et al. (2009). Icetemplating synthesis of polyaniline microflakes

stacked by onedimensional nanofibers. *J. Phys. Chem. C* 113: 9047–9052.

37 Qi, G., Huang, L., and Wang, H. (2012). Highly conductive free standing polypyrrole films prepared by freezing interfacial polymerization. *Chem. Commun.* 48: 8246–8248.

38 Ma, H., Li, Y., Gao, F. et al. (2010). Facile synthesis of polyaniline hemispheres in diethyl ether/ice mixture solvent and growth mechanism study. *J. Polym. Sci. A* 48: 3596–3603.

39 Wang, F., Wang, Z., Tana, M.B., and He, C. (2015). Uniform polyaniline nanotubes formation via frozen polymerization and application for oxygen reduction reactions. *Macromol. Chem. Phys.* 216: 977–984.

40 Barrow, M., Eltmimi, A., Ahmed, A. et al. (2012). Frozen polymerization for aligned porous structures with enhanced mechanical stability, conductivity, and as stationary phase for HPLC. *J. Mater. Chem.* 22: 11615–11620.

41 Barrow, M. and Zhang, H. (2013). Aligned porous stimuliresponsive hydrogels via directional freezing and frozen UV initiated polymerization. *Soft Matter* 9: 2723–2729.

42 Nishihara, H., Iwamura, S., and Kyotani, T. (2008). Synthesis of silicabased porous monoliths with straight nanochannels using an icerod nanoarray as a template. *J. Mater. Chem.* 18: 3662–3670.

43 Borisova, A., De Bruyn, M., Budarin, V.L. et al. (2015). A sustainable freezedrying route to porous polysaccharides with tailored hierarchical meso and macroporosity. *Macromol. Rapid Commun.* 36: 774–779.

44 Ahmed, A., Clowes, R., Myers, P., and Zhang, H. (2011). Hierarchically porous silica monoliths with tuneable morphology, porosity, and mechanical stability. *J. Mater. Chem.* 21: 5753–5763.

45 Eychmüller, A., Ziegler, C., Wolf, A. et al. (2017). Modern inorganic aerogels. *Angew. Chem. Int. Ed.* 56: 13200–13221.

46 Ma, L., Jin, A., Xie, Z., and Lin, W. (2009). Freeze drying significantly increases permanent porosity and hydrogen uptake in 4,4connected metal–organic frameworks. *Angew. Chem. Int. Ed.* 48: 9905–9908.

47 McKeown, N.B. and Budd, P.M. (2006). Polymers of intrinsic microporosity (PIMs): organic materials for membrane separations, heterogeneous catalysis and hydrogen storage. *Chem. Soc. Rev.* 35: 675–683.

48 Howarth, A.J., Peters, A.W., Vermeulen, N.A. et al. (2017). Best practices for the synthesis, activation, and characterization of metal−organic frameworks. *Chem. Mater.* 29: 26–39.

49 Slate, A.G. and Cooper, A.I. (2015). Functionalled design of new porous materials. *Science* 348: 989–999.

50 Ahmed, A., Hasell, T., Clowes, R. et al. (2015). Aligned macroporous monoliths with intrinsic microporosity via a frozensolventtemplating approach. *Chem. Commun.* 51: 1717–1720.

51 Ahmed, A., Forster, M., Clowes, R. et al. (2014). Hierarchically porous metal–organic framework monoliths. *Chem. Commun.* 50: 14314–14316.

52 Eddleston, M.D., Patel, B., Day, G.M., and Jones, W. (2013). Cocrystallization by freeze drying: preparation of novel multicomponent crystal forms. *Cryst. Growth Des.* 13: 4599–4606.

53 Deville, S. (2017). Freezing Colloids: Observations, Principles, Control, and Use. Springer International Publishing AG.

Index

b

c

d

f

g

h

i

j

k

l

m

o

p

q

t

WILEY END USER LICENSE AGREEMENT

Go to www.wiley.com/go/eula to access Wiley's ebook EULA.

WILEY-VCH

Haifei Zhang

Ice Templating and Freeze-Drying for Porous Materials and Their Applications